



## **Novus Scientia 2023**

# **20. Medzinárodná vedecká konferencia doktorandov strojnícckých fakúlt technických univerzít a vysokých škôl**

**Novus Scientia 2023**

**Zborník príspevkov z XX. Medzinárodnej vedeckej konferencie doktorandov  
strojnícckých fakúlt technických univerzít a vysokých škôl**

**26.01.2023**

**Strojnícka fakulta**

**Technická univerzita v Košiciach**

## Zameranie konferencie:

- Automatizácia, mechatronika a robotika
- Technologické a materiálové inžinierstvo
- Manažment, priemyselné a digitálne inžinierstvo
- Konštrukčné a procesné inžinierstvo
- Špeciálne inžinierske procesológie

## Vedecký a organizačný výbor konferencie

### Patronát konferencie

**Dr.h.c. mult. prof. Ing. Jozef Živčák, PhD., MPH**

Technická univerzita v Košiciach, Slovensko

### Garant konferencie

**prof. Ing. Ján Slota, PhD.**

Technická univerzita v Košiciach, Slovensko

### Vedecký výbor konferencie

prof. Ing. Jozef Bocko, CSc., Technická univerzita v Košiciach, Slovensko

prof. Ing. Radovan Hudák, PhD., Technická univerzita v Košiciach, Slovensko

prof. Ing. Michal Kelemen, PhD., Technická univerzita v Košiciach, Slovensko

prof. Ing. Ervin Lumnitzer, PhD., Technická univerzita v Košiciach, Slovensko

prof. Ing. Emil Spišák, CSc., Technická univerzita v Košiciach, Slovensko

prof. Ing. Tomáš Brestovič, PhD., Technická univerzita v Košiciach, Slovensko

doc. Ing. Ján Kráľ, PhD., Technická univerzita v Košiciach, Slovensko

doc. Ing. Peter Frankovský, PhD., Technická univerzita v Košiciach, Slovensko

prof. Ing. Michal Hatala, PhD., Technická univerzita v Košiciach, Slovensko

prof. Ing. Eva Tillová, PhD., Žilinská univerzita v Žiline, Slovensko

prof. Ing. Stanislav Ďuriš, PhD., Slovenská technická univerzita v Bratislave, Slovensko

prof. Ing. Peter Šugár, CSc., Slovenská technická univerzita v Bratislave, Slovensko

prof. Ing. Ivan Křupka, Ph.D., Vysoké učení technické Brno, Česká republika

doc. Ing. Miroslav Mahdal, Ph.D., VŠB Technická univerzita Ostrava, Česká republika

prof. Ing. Tomáš Jirout, Ph.D., ČVUT Praha, Česká republika

doc. Ing. Petr Lepšík, Ph.D., Technická univerzita v Liberci, Česká republika

doc. Ing. Václav Vaněk, Ph.D., Západočeská univerzita v Plzni, Česká republika

dr hab. inż. Andrzej Burghardt, prof. PRz, Politechnika Rzeszowska, Poľsko

Dr inż. Tomasz Jachowicz, Politechnika Lubelska, Poľsko

### Organizačný výbor

prof. Ing. Ján Slota, PhD.

Ing. Viktória Krajňáková, PhD.

Ing. Jaroslav Melko  
Ing. Matúš Matiscsák  
Ing. Ján Kopec  
Ing. Laura Lachvajderová  
Ing. Dominika Sukopová  
Ing. Marek Mizerák

**Príspevky publikované v zborníku z konferencie boli recenzované recenzentmi uvedenými v nasledovnom zozname.**

### **Recenzenti**

prof. Ing. Ján Slota, PhD., Technická univerzita v Košiciach, Slovensko  
prof. Ing. Tomáš Brestovič, PhD., Technická univerzita v Košiciach, Slovensko  
prof. Ing. Janette Brezinová, PhD., Technická univerzita v Košiciach, Slovensko  
prof. Ing. Robert Grega, PhD., Technická univerzita v Košiciach, Slovensko  
prof. Ing. Michal Kelemen, PhD., Technická univerzita v Košiciach, Slovensko  
prof. Ing. Jozef Kuľka, PhD., Technická univerzita v Košiciach, Slovensko  
prof. Ing. Milan Oravec, PhD., Technická univerzita v Košiciach, Slovensko  
prof. Ing. Ildikó Maňková, CSc., Technická univerzita v Košiciach, Slovensko  
prof. Ing. Marek Sukop, PhD., Technická univerzita v Košiciach, Slovensko  
prof. Ing. Jozef Svetlík, PhD., Technická univerzita v Košiciach, Slovensko  
doc. Ing. Michaela Balážiková, PhD., Technická univerzita v Košiciach, Slovensko  
doc. Ing. Ján Semjon, PhD., Technická univerzita v Košiciach, Slovensko  
doc. Ing. Dagmar Draganovská, PhD., Technická univerzita v Košiciach, Slovensko  
doc. Ing. Ivan Gajdoš, PhD., Technická univerzita v Košiciach, Slovensko  
doc. Ing. Anna Guzanová, PhD., Technická univerzita v Košiciach, Slovensko  
doc. Ing. Róbert Huňady, PhD., Technická univerzita v Košiciach, Slovensko  
doc. Ing. Euboš Kaščák, PhD., Technická univerzita v Košiciach, Slovensko  
doc. Ing. Ružena Králiková, PhD., Technická univerzita v Košiciach, Slovensko  
doc. Ing. Marián Lázár, PhD., Technická univerzita v Košiciach, Slovensko  
doc. Ing. Silvia Maláková, PhD., Technická univerzita v Košiciach, Slovensko

doc. Ing. Martin Mantič, PhD., Technická univerzita v Košiciach, Slovensko

doc. Ing. Miroslav Pástor, PhD., Technická univerzita v Košiciach, Slovensko

doc. Ing. Miriam Pekarčíková, PhD., Technická univerzita v Košiciach, Slovensko

doc. Ing. Juraj Šebo, PhD., Technická univerzita v Košiciach, Slovensko

doc. Ing. Teodor Tóth, PhD., Technická univerzita v Košiciach, , Slovensko

doc. Ing. Pavol Liptai, PhD., Technická univerzita v Košiciach, , Slovensko

Ing. Marek Moravec, PhD., Technická univerzita v Košiciach, Slovensko

Ing. Marek Schnitzer, PhD., Technická univerzita v Košiciach, Slovensko

## Novus Scientia 2023

Zborník príspevkov z XX. Medzinárodnej vedeckej konferencie doktorandov  
strojnícych fakúlt technických univerzít a vysokých škôl

<b>Názov:</b>	Novus Scientia 2023
<b>Editor:</b>	© prof. Ing. Ján Slotá, PhD. © Ing. Matúš Matiscsák © Ing. Ján Kopec © Ing. Laura Lachvajderová © Ing. Dominika Sukopová © Ing. Marek Mizerák
<b>Vydavateľ:</b>	Technická univerzita v Košiciach, Strojnícka fakulta, Letná 1/9, 042 00 Košice-Sever
<b>Rok:</b>	2023
<b>Náklad:</b>	70 výtlačkov
<b>Rozsah:</b>	337 strán
<b>Miesto konania:</b>	Strojnícka fakulta, Technická univerzita v Košiciach
<b>Dátum konania:</b>	26.01.2023
<b>ISBN</b>	<b>978-80-553-4369-3</b>

# OBSAH

<b>Autorský kolektív a názov príspevku</b>	<b>Strany</b>
<b>Miroslava Badidová, Lýdia Sobotová</b> Analysis of Emissions Emitted by Laser Technology	9 - 17
<b>Tomáš Balint, Jozef Živčák, Samuel Lancoš, Miroslav Kohan, Tomáš Jaroš</b> Overview of materials for the production of biomedical filaments	18 - 23
<b>Tomas Breskovic, Norbert Ferencik, Gabriela Dancakova, Radovan Hudak</b> Overview of trends in tissue engineering	24 - 29
<b>Jozef Brindza, Michal Demko, Filip Dominik, Marek Vrabel, Peter Ižol</b> Cylinder head modifications of internal combustion engine	30 - 35
<b>Denis Cmorej, Luboš Kaščák</b> Numerical simulation of clinch-riveting of HX420LAD steel sheets	36 - 41
<b>Gabriela Dancáková, Teodor Tóth, Viktória Rajtúková, Dominika Belvončíková, Tomáš Breškovič, Jozef Živčák, Radovan Hudák</b> Development and production of in-ear hearing aids (ITE) using additive manufacturing	42 - 48
<b>Filip Duda, Natália Jasmínská</b> Structural design and strength analysis of non-standardized metal hydride vessel for mobile applications	49 - 53
<b>Maksym Grytsiv, Marek Sukop, Dušan Mlinarček, Dávid Kovaluk</b> Mapping of the surrounding environment of the mobile robot based on the LiDAR localization system	54 - 59
<b>Július Hajduk, Janka Majerníková</b> Evaluation of Mechanical Properties of Selected Types of Thin Steel Sheet	60 - 65
<b>Ján Hašul, Janette Brezinová</b> Increasing the technological life of molds for high-pressure aluminum casting by applying PVD coatings	66 - 71
<b>Sára Janigová, Peter Palička</b> Influence of the thickness of carbon nanostructures on their mechanical properties	72 - 77
<b>Erik Janoško, Anna Guzanová, Nikita Veligotski</b> Corrosion resistance of steel HX340LAD+Z after deformation	78 - 83
<b>Elena Jurgovská, Ervin Lumnitzer, Anna Yehorova</b> Changes in the intensity of electromagnetic fields at base stations of mobile operators	84 - 89
<b>Matúš Kačír, Robert Grega</b> Dual-mass flywheel for hybrid propulsion	90 - 93
<b>Ivana Koláriková, Tatiana Kelemenová, Barbora Hudáková</b> Verification of the properties of linear position sensors	94 - 100
<b>Petra Kolembusová, Radovan Hudák, Norbert Ferencík</b> Review of bioreactor systems in tissue engineering	101 - 106
<b>Ján Kopec, Miriam Pekarčíková, Marek Mizerák</b> Presentation of the 3D laboratory in a virtual environment	107 - 111
<b>Juliy Martyn Kulya, Miroslav Tomáš</b> The strain distribution at the Limit Dome Height test of dual phase steel and correlation of experiment-simulation results	112 - 117
<b>František Kupec, Michal Fabian</b> Use of CFD method for research of aerodynamic elements of passenger car	118 - 125

<b>Laura Lachvajderová, Jaroslava Kádárová, Ernesto Juliá Sanchis, Denisa Rybárová</b> Industry 5.0 - A Sustainable Human-Centric Solution	126 - 130
<b>Samuel Lancoš, Miroslav Kohan, Gabriela Dancáková, Tomáš Balint, Teodor Tóth, Radovan Hudák</b> Technological process of filament production from PPSU material and the effect on its biocompatibility	131 - 135
<b>Matúš Lavčák, Pavol Tarbajovský, Michal Puškár</b> ANALYSIS OF MOTORCYCLE EMISSION PARAMETERS IN THE USE OF SUSTAINABLE FUELS	136 - 139
<b>Wanda Mamrilla, Zuzana Molčanová, Beáta Ballóková, Dóra Zalka, Karel Saks, Radovan Hudák</b> Effect of Mn addition on the mechanical properties of Zinc alloys	140 - 145
<b>Matúš Matiscsák, Peter Trebuňa</b> Comparison of RFID robots	146 - 150
<b>Tomas Merva, Ivan Virgala</b> A survey of integrated task and motion planning	151 - 154
<b>Ivan Mihálik, Tomáš Brestovič</b> Design of a hydrogen distribution system implemented in a hydrogen bus	155 - 158
<b>Marek Mizerák, Peter Trebuňa, Ján Kopec</b> Digitization of production data through RTLS technology	159 - 164
<b>Róbert Moro, Dagmar Draganovská</b> Application of a conversion layer by phosphating in the pre-treatment of steels for bonding	165 - 170
<b>Alžbeta Nováková, Kristián Pástor, Miroslav Badida</b> Analysis of the influence of the porosity of recycled rubber crumb on its acoustic properties	171 - 174
<b>Jan Kral, Dominik Novotny</b> Antimicrobial photocatalytic devices	175 - 180
<b>Štefan Ondočko, Jozef Svetlík, Tomáš Stejskal, Michal Šašala</b> Use of Matlab - Simulink for calculating the kinematic variables of the mechanism	181 - 188
<b>Bibiána Ondrejová, Branko Štefanovič, Monika Michalíková, Lucia Bednarčíková, Jozef Živčák</b> 3D PRINTED CUSTOMIZED CAST FOR A CHILD WITH UPPER EXTREMITY FRACTURES: A CASE STUDY	189 - 193
<b>Peter Palička, Róbert Huňady, Sára Janigová</b> Homogenization of composite material reinforced with discontinuous fibers	194 - 198
<b>Kristián Pástor, Miroslav Badida, Alžbeta Nováková, Anna Badidová</b> Analysis of the sound of selected automobile powertrains using psychoacoustic methods	199 - 204
<b>Denisa Porubčanová, Kristína Lengyelová, Miroslav Čička, Ferdinand Kóča, Michaela Balážiková</b> Ergonomic Assessment of Physical Load in the Mechanical Engineering Industry	205 - 210
<b>Vladimír Rohal, Emil Spišák</b> THE QUALITY EVALUATION OF THE CUTTING SURFACE BY MICROSCOPIC ANALYSIS	211 - 219
<b>Jaroslav Romančík, Marek Vagaš</b> Development and testing of collaborative workplace with 2D camera system	220 - 225
<b>Svetlana Rusnáková, Jozef Živčák</b> Detection of nickel and chromium release in the oral cavity in patients with metal-ceramic dental prostheses	226 - 232

<b>Henrich Sailer, Janette Brezinova</b> Evaluation of the quality of renovation layers in tribological conditions	233 - 238
<b>Peter Ján Sinčák , Ivan Virgala, Martin Varga</b> Continuum robot control based on reinforcement learning	239 - 244
<b>Samuel Sivák , Silvia Maláková, Matúš Virostko</b> Introduction of Generative Design for Spur Gear Wheel Bodies	245 - 251
<b>Domínika Sukopová, Jaroslava Kádárová, Juraj Kováč</b> Digitization and virtual reality in industrial enterprises	252 - 257
<b>Michal Sasala, Jozef Svetlík, Tomas Stejskal, Stefan Ondocko</b> Analysis of available torque on the output shaft for Universal Rotary Module prototype	258 - 263
<b>Branko Štefanovič, Lucia Bednarčíková, Richard Staško, Jozef Živčák</b> Individual arm and forearm orthosis CAD design	264 - 269
<b>Pavol Štefčák, Ivan Gajdoš, Ján Slota</b> Design and setup of a robotic workstation for additive manu-facturing	270 - 275
<b>Pavol Tarbajovský, Michal Puškár, Matúš Lavčák</b> Advanced exhaust system for vehicles' emission footprint reduction	276 - 282
<b>Martin Varga, Ivan Virgala, Michal Kelemen</b> New trends in industrial robot research and application: re-dundant robots	283 - 288
<b>Patrik Varga, Radovan Hudák, Teodor Tóth, Marek Schnitzer</b> Evaluation of accuracy and porosity of FDM 3D printed PEEK implants	289 - 292
<b>Nikita Veligotskyi, Erik Janoško, Anna Guzanová</b> Influence of selected process parameters on joint formation by thermal drilling technology	293 - 301
<b>Samuel Vilkovský, Janka Majerníková</b> Analysis of deep drawing simulation using Simufact software	302 - 307
<b>Matúš Virostko, Martin Mantič, Samuel Sivák</b> Introduction to Generative Design	308 - 312
<b>Anna Yehorova, Ervin Lumnitzer, Elena Jurgovská</b> Assessment of the acoustic performance of different categories of drones	313 - 319
<b>Lucia Žuľová, Robert Grega, Marián Siman</b> Verification of the causal dependence of noise and vibration on a mechanical drive with a piston compressor.	320 - 324
<b>Jana Demeterová, Marianna Trebuňová, Darina Bačenková, Jozef Živčák</b> 3D bioprinting using stem cells in regenerative medicine	325 - 330
<b>Ľuboš Chromý, Viktória Rajťúková, Radovan Hudák</b> Proposal of a methodology for evaluating the placement of dental implants using dental surgical guides	331 - 336



# Analysis of Emissions Emitted by Laser Technology

Miroslava Badidová <sup>1,\*</sup>, Lýdia Sobotová <sup>2</sup>

<sup>1</sup>. Technical University of Košice, Faculty of Mechanical Engineering, Department of Environmental Engineering 1; miroslava.badidová@gmail.com

<sup>2</sup>. Technical University of Košice, Faculty of Mechanical Engineering, Department of Environmental Engineering 2; lydia.sobotova@tuke.sk

\* Correspondence: [miroslava.badidová@gmail.com](mailto:miroslava.badidová@gmail.com), tel. : +421 55 602 2793

**Abstract:** *Laser cutting machines are sophisticated machines with a certain amount of simplicity built into their design. The nature of plug-and-play lasers and corresponding vapour extraction systems makes pairing the two functions seemingly easy. It is important that dust and fumes are collected from the source and that particles are properly stored and disposed of. Therefore, in this presented publication, the composition of the materials of the test samples and aerosols are analysed, the classification is performed and the current state of laser cutting technology is examined. On this basis, the emission of pollutants during laser cutting and the corresponding control of pollution are the main conditions and solution of the proposed method and equipment.*

**Keywords:** laser 1; marking 2; dust 3; aerosols 4; Filtration 5

## 1. Introduction

In conjunction with new advanced technologies such as laser and plasma technologies used for cutting material, welding, spot-welding or additive technologies, for example in the automotive industry, the environmental safety of workplaces must be respected in addition to high accuracy, repeatability, cost-effectiveness. Compared to other cutting technologies, laser cutting offers the advantages of better material utilization in cutting, scoring and engraving materials while observing strict environmental and safety regulations. This publication examines the composition, classification and current state of laser cutting technology. Emissions of pollutants in laser cutting and corresponding measurement methods and pollution control devices were investigated.

## 2. Laser cutting equipment

Laser cutting equipment consists of an automated system integrating the laser beam, servo-motor control, electrical control, detection technology and an industrial computer. The laser cutting machine is characterized by a light source, power and cutting dimensions. Well-known options for laser cutting technology include evaporation, fusion, reactive fusion, and controlled fracture cutting. During the process of dividing or cutting, dust, smoke and aerosols are released, which is an environmental problem and poses a threat to public health. The choice of the method of ventilation, dedusting and the design of the equipment should take into account the rate of dust removal from the workstation, the initial investment costs, maintenance costs, and so on. [1 - 5, 13 - 15]

The process of laser cleaning technology, for example, degreasing, removing corrosive parts of the surface of the material, takes place in a closed cabin due to the imminent risk of laser beam-induced radiation arising or dust being produced, which is harmful to

human health. In the cabin of the device, Fig. 1, there is a work table, which contains grooves for the overflow of the generated waste. The workplace where the laser cutting process takes place is equipped with a ventilation device that absorbs the unwanted dust generated. The entire workstation is bounded by columns that delimit the safe zone during the operation of the equipment. Overall, this machinery has a considerable impact on the space used in the workplace hall. [1 - 6]

The device includes a fully enclosed safety design. During operation, the device's state of processing can be monitored from the front window of the security door, ensuring safety for the operator. In laser machines, multi-stage filtration is used. [1,2, 10]

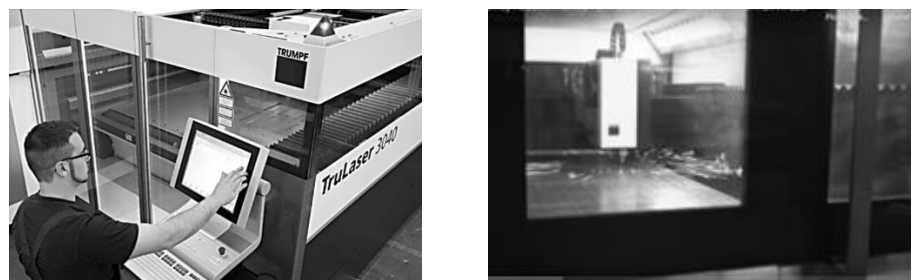


**Figure 1.** Laser cutting device during parameter input and material division [1,2].

### 3. Pollution generation and air filtering

The most important physical factors in the environment in workplaces using laser technologies include [7-12]:

- noise
- lighting
- microclimate - temperature, humidity,
- electromagnetic fields,
- dustiness,
- solid aerosols.

During the cutting process, large amounts of dust, smoke and aerosols are produced, which causes environmental concerns and poses a threat to the health of workers [5, 9]. The amount of smoke and dust emitted by laser cutting is related to the cutting speed and the setting of the cutting air pressure parameters. If the specialist correctly sets the technological parameters of cutting, the smoke emission from laser cutting is significantly reduced. In addition, the material of the workpiece has a significant impact on emissions. When cutting 6 mm thick low-carbon steel material, the amount of smoke and dust emitted per 1 m of cut is 440 mg. When cutting 6 mm thick chromium-nickel material or galvanized steel sheet, smoke and dust emissions per 1 m of cut are 2000 mg. For cutting 6 mm thick low-carbon steel, 39.6 g/hour of smoke and dust can be released at a cutting

speed of 1500 mm/min. Smoke and dust contain particles of metal oxides such as iron oxide and alumina [5- 8].

Smoke, dust and aerosols are released in the process of laser cutting of metal materials. The particle size of the dust generally exceeds 10  $\mu\text{m}$ , and the particle size of the aerosols is less than 10  $\mu\text{m}$ .

The primary threats to a worker or employee who works with laser technology can be considered to be mainly solid aerosols and dustiness.

The determination of dustiness is one of the most difficult to identify in the field of chemicals. The risk of solid aerosols is determined not only by their concentration, but also by a number of other factors such as size composition (dispersion) or chemical composition. [10,11,12]

When treating metallic materials with a laser, the following substances are released into the air:

- dust (particle size greater than 1 mm),
- aerosols (particle size less than 1 mm),
- gases. [16]

In terms of the action of dust on humans, there are differences between:

- dust having a predominantly specified effect,
- dust with fibrogenic action,
- dust with an irritating effect,
- mineral fibrous dust. [8, 9]

The measurement of aerosol size distribution is important for the design of appropriate filtration systems, Fig. 2. There is no filtration system or medium that can absorb all the smoke, dust, vapours, gas, or debris resulting from the use of lasers. With strict emission pollution limits, multiple treatment systems or hybrid systems with different filtration methods are necessary to control pollution in some cases. Modern dedusting technologies include mesh filtration, pocket filtration, electrostatic filtration and activated carbon filtration [91–94]. Among them, electrostatic systems have several obvious advantages. First of all, it is possible to clean the filter and there is no need to replace it, eliminating the cost of repeatedly replacing the filter repeatedly. Secondly, a well-designed system can provide high rates of removal of soot and smoke particles removal at a submicron scale. Another advantage is the very small loss of air flow when dirt accumulates on the filter. During the operation of the laser, air loaded with pollutants is first sucked out through the prefilter. Then it enters the high-density ionization zone filled with smoke and soot particles. Charged particles pass through the collecting chamber, which is composed of alternating voltage and a grounded plate. A cylindrical filter is used for capture. [3, 10,11,12]

#### **4. Exposure to dust and consequent health effects**

Exposure to dust and consequent health effects can take various forms. Skin contact with some dusts, such as most organic dusts, can cause irritation or allergic responses,

especially in sensitive people. The respiratory tract is the most common and main route of entry of dust particles into the human body, Fig. 3 [12].

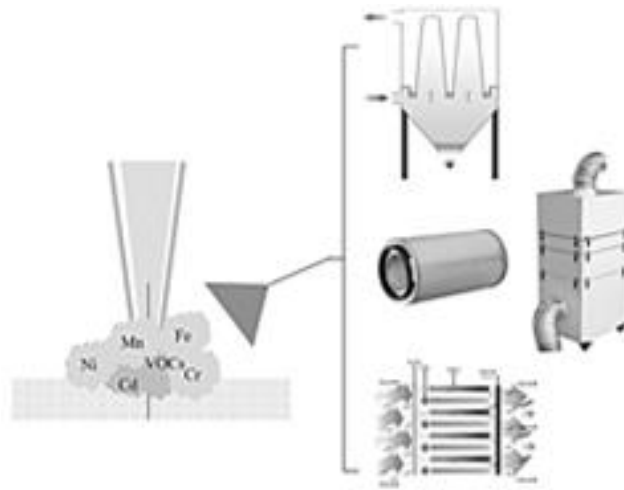


**Figure 2.** Pollution control strategy for laser cutting(5).

The effect of irritating dusts is primarily manifested in terms of mechanical irritation of the mucous membranes of the respiratory tract, skin and conjunctiva of the eyes. With more sensitive individuals, allergic reactions may also appear. In particular, dust of organic origin can provoke hypersensitivity, manifested in the form of bronchial asthma. Infectious dust, which often contains germs trapped on dust particles, can cause serious diseases in certain cases. This also includes bacterial and fungal infections. Toxic dust, in addition to the local effect on the respiratory system of a person, can cause systematic intoxication. Dust that contains toxic substances is absorbed by the blood and leads to an adverse effect on the tissue and organs of the human body. Carcinogenic dust in people who are exposed to these effects, if inhaled, can cause an oncological disease. [4, 10-14]

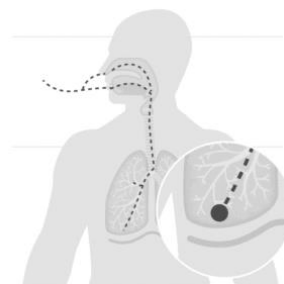


**Figure 3.** Inhalation of dust and aerosols by man [4].

## 5. Experimental section and evaluation

Experimental tests were carried out at the Department of Environmental Engineering, SĽ TUKE, at Trumpf Slovakia, s.r.o. and at U.S.S. Košice, a.s.

For experimental tests, galvanized sheet metal with dimensions: 25 mm width, 105 mm height, 1.6 mm thickness, Fig. 4 was used.



**Figure 4.** Galvanized sheet metal used for the experiment.

The experimental samples were surface treated with a laser on a Laser Trumpf TruMark Station 5000, Fig. 5.

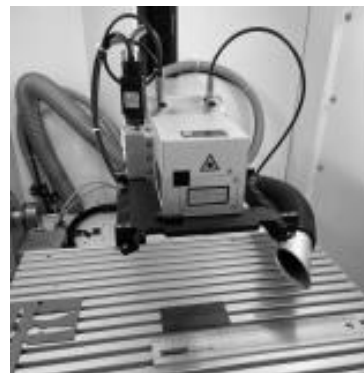


**Figure 5.** Laser Trumpf TruMark Station 5000.

During the preparation of the test samples, the surface of the galvanized sheet was treated, where at position 3 means that the laser beam passed three times over the selected surface, and a position 1 - the laser beam passed only once on the test surface, Fig. 6



**Figure 6.** Galvanized sample tested.

During surface treatment, the places where the test samples were glued – targets – were defined to determine the fumes and type of aerosols after laser work had been carried out, Fig. 7.

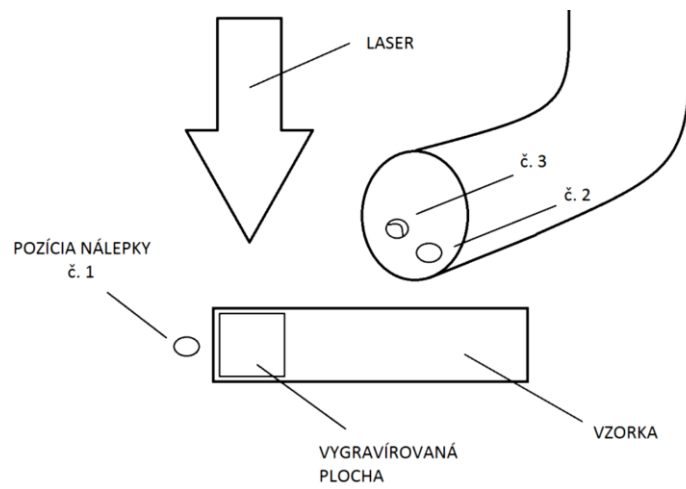


**Figure 7.** Location of targets in the suction process.

In Fig. 8, particles are captured at 200 times magnification from the target when a laser beam passes through the surface of the sheet once.

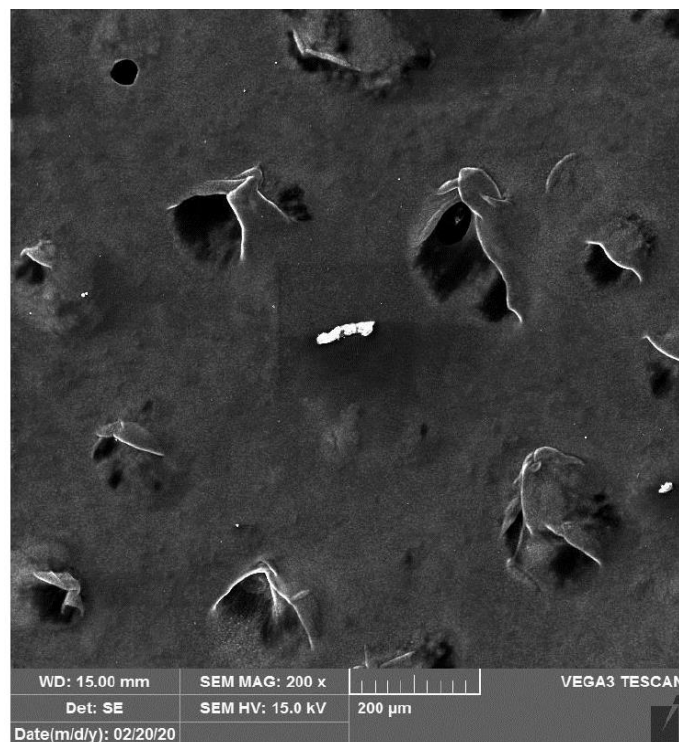


**Figure 8.** Area passed over once at 200x zoom.

After conducting the experiments, the targets were divided into groups, Fig. 9 and evaluated using a TESCAN VEGA3 raster electron microscope, Fig.10.

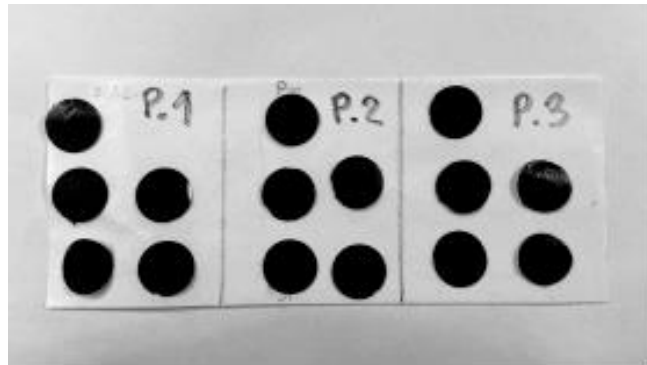


Figure 9. Targets with trapped dirt during suction.



Figure 10. Raster electron microscope TESCAN VEGA3.

Particle analysis was carried out and analysis was performed on the residues of various materials that were trapped on the surface of the applied stickers on the ventilation pipe in close proximity to the laser head, Fig. 11.

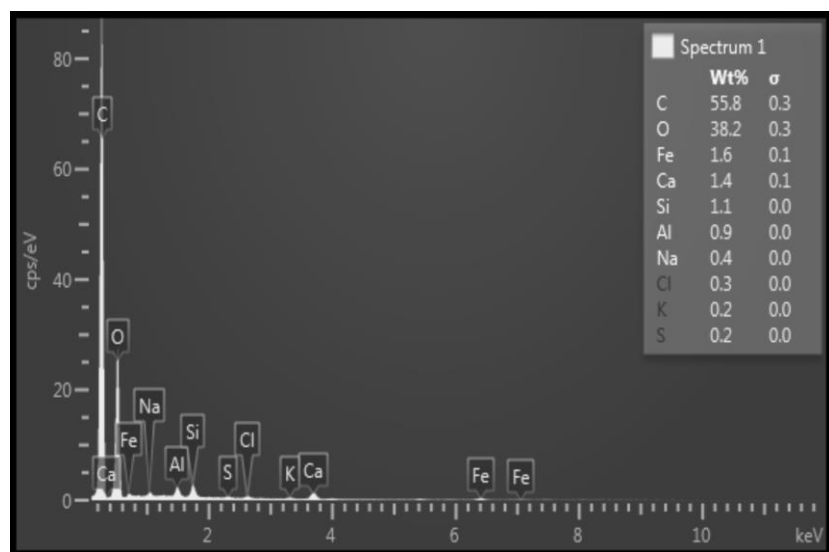


Figure 11. Analysis of particles of chemical elements after conducting the experiment.

When analyzing the targets under a microscope, it was concluded that when the laser operates for a short period of time, a large amount of dirt is not released into the working environment. On other hand, over a longer interval, various elements are released from the machined material.

Traces of carbon, oxygen, iron and calcium were detected when the laser beam first passed across the sample surface. It was possible to clearly identify the remnants of zinc only with three passes of the laser. Failure to maintain sufficient ventilation may result in inhalation of these harmful impurities and damage to the health of the person operating the laser.

## CONCLUSION

In conjunction with the rapidly growing demands for metal cutting, it is necessary to develop technologies for rapid material cutting with increased accuracy, environmental safety and cost-effectiveness. Well-known options for laser cutting technology include evaporation, fusion and reactive melt cutting. During the cutting process, dust, smoke and aerosols are formed, i.e., dustiness is created from physical factors, which is an ecological concern and poses a threat to the health of operators. Modern dedusting technologies include mesh filtration, pocket filtration, electrostatic filtration and activated carbon filtration.

In some cases, with strict pollution emission limits, multiple treatment systems or to control pollution, hybrid systems with different filtration methods are required. Laser cutting technology is suitable, although there are still some process challenges in dedusting. The design of the dedusting method should take into account the removal of dust, aerosols, soot, but also the initial cost of capital and maintenance costs.

Multi-stage filtration in combination with activated carbon filtration or electrostatic filtration is accepted and in demand for the given beam technologies.

**Acknowledgments:** This paper was created as part of the KEGA 009 TUKE-04/ 2021 project.

**Conflicts of Interest:** "The authors declare no conflict of interest."

## References

1. Kellerusa: Extraction dust to protect personel and machinery, Laser cutting, Dostupné na internete: <https://www.kellerusa.com/laser-processing/laser-cutting>.
2. Robovent: Total air filtration, Dostupné na internete: [www.robovent.com](http://www.robovent.com).
3. How to control Laser cutting Dust, 2022, Dostupné na internete: <https://www.fabricatingandmetalworking.com/2017/08/how-to-control-laser-cutting-dust/>.
4. DownDraft: Laser fume extraction systems, No.9, 2017, Dostupné na internete: <https://downdraft.com/laser-fume-extraction/#>.
5. Yingyong He. - Honghu Xie - Yongjun Ge - Yishan Lin - Zhitong Yao - Binhui Wang - Meiqing Jin - Jie Liu - Xinyang Chen - Yuhang Sun: Laser Cutting Technologies and Corresponding Pollution Control Strategy, Processes, 2022, No.10, p.732, Dostupné na internete: <https://doi.org/10.3390/pr10040732>.
6. All about laser cutter. Laser maintenance, 2022, Dostupné na internete: <https://learn.adafruit.com/all-about-laser-cutters/maintenance>.
7. Cleaning the laser cutter extractor filter, 2022, Dostupné na internete: <https://discourse.southlondonmakerspace.org/t/cleaning-the-laser-cutter-extractor-filter/11545>.
8. TRUMPF Slovakia, a.s., Katalógová literatúra, 2022, Dostupné na internete: [www.trumpf.com](http://www.trumpf.com).
9. BADIDA, M.- SOBOTOVÁ, L. - DZURO, T. et al: Strojárska výroba a životné prostredie, 2. vyd. Košice : TU, 2017. - 355 s. - ISBN 978-80-553-2674-0

10. LUMNITZER, E. - BADIDA, M. -ROMÁNOVÁ,M.: Hodnotenie kvality prostredia / - 1. vyd - Košice : Sjf TU - 2007. - 275 s. - ISBN 978-80-8073-836-5.
11. BADIDA, M. - LUKÁČOVÁ, K. - SZABÓ, R.: Pevné aerosóly v pracovnom prostredí - 1. vyd. - Košice : Sjf TU - 2015. - 209 s.. - ISBN 978-80-553-2458-6.
12. SOBOTOVA, L.: Environment and laser technology /- 2017. In: Scientific Letters of Academic Society of Michal Baludansky. Roč. 5, č. 5 (2017), s. 173-175. - ISSN 1338-9432.
13. SOBOTOVÁ, L. - BADIDA, M.: Laser marking and environmental hazards / 2018. In: Scientific Letters of Academic Society of Michal Baludansky. - Košice (Slovensko) : Akademická spoločnosť Michala Baluďanského Roč. 6, č. 6A (2018), s. 102-107 [print]. - ISSN 1338-9432
14. SOBOTOVÁ, L. - BADIDA, M.: Laser marking as environment technology, Spôsob prístupu: <https://www.degruyter.com/view/j/eng.2017.7.issue-1/eng-2017-0030/eng-2017-0030.xml?format=INT...> - 2017. In: Open Engineering. Vol. 7, no. 1 (2017), p. 303-316. - ISSN 2391-5439.



# Overview of materials for the production of biomedical filaments

Tomáš Balint<sup>1</sup>, Jozef Živčák<sup>1</sup>, Samuel Lancos<sup>1</sup>, Miroslav Kohan<sup>1</sup>, Tomáš Jaroš<sup>1</sup>

<sup>1</sup> jozef.zivcak@tuke.sk, samuel.lancos@tuke.sk, miroslav.kohan@tuke.sk, tomas.jaros@tuke.sk

Corresponding author: tomas.balint@tuke.sk

**Abstract:** This scientific research deals with an overview of polymers suitable for implementation in the field of tissue engineering, regenerative medicine and implantology and brings significant findings to the field. An overview of biocompatible materials such as PLA, PHB and PDO brings new application possibilities. From selected medically certified materials, the scientific team proceeded to the production of the filament. All production processes were optimized, resulting in a final product with a constant diameter. Subsequently, modeling and 3D printing of the aorta was started using additive FFF technology. The aorta model was printed at a printing temperature of 175 degrees with a heated pad. This model was intended for pressure simulation. The simulation produced interesting results, which are described in the conclusion of this study.

**Keywords:** 3D printing, extrusion, filament, polymers, biodegradation

## 1. Introduction

Natural and synthetic polymers are considered biodegradable materials. Polymers can be broadly defined as macromolecules composed of covalently bonded monomers. Natural-based polymers include starch, chitosan, hyaluronic acid derivatives, collagen, fibrin gels, and silk. Undesirable properties of these polymers include low mechanical strength, unknown degradation rate, repellency and high physiological activity. Various scientific studies show that synthetic polymers have a wide range of uses and satisfactory properties compared to natural polymers [1]. Among the important properties of polymers is the rate of degradation, which can vary depending on the type of arrangement of the polymer chain and its crystallinity. The glass transition temperature affects the flexible properties of polymers, so it is essential that the polymers are biodegradable above normal body temperature. Commonly used biodegradable polymers include polyglycolic acid (PGA), polylactic acid (PLA), poly- $\beta$ -hydroxybutyrate (PHB), poly(lactic-co-glycolic acid) (PLGA), and poly- $\epsilon$ -caprolactone (PCL). Among these polymers, PLA, PGA and PLGA are used for the production of degradable rivet connections (sutures). PLA has been synthesized from natural sources such as starch and corn. Crystalline PLA (L-PLA) is less resistant to hydrolysis than amorphous PLA (DL-PLA). PGA, a synthetic polymer, has high crystallinity, low solubility and high degradation rate. The high degradation rate of PGA reduces its mechanical strength after implantation. PCL is an aliphatic polyester used in medical implantology. PCL is typically used for long-term implants and as a drug delivery system due to its crystallinity and permeability. PCL also has high flexibility and molding capabilities to create different shapes. PHB belongs to another type of biodegradable polymer with high crystallinity, however, due to its brittleness, it is not used for practical applications, but is mixed with other polymers. Poly-para-dioxanone (PPD) is another biodegradable polymer commonly used for its biodegradability, resorbability, compatibility and flexibility as a medical implant for internal fixation of fractures and in

the form of films, foams, pressed products and coatings. Studies have shown the possibility of complete disintegration of PPD implants within 6-7 months after implantation by changing their molecular weight, crystallinity and melting temperature. When choosing biodegradable polymers for applications in biomedical engineering, their desired properties, such as their chemical, physical and mechanical properties, have a great influence. Degradation of polymers takes place by hydrolysis of ester bonds, which leads to a change in their chemical structure. The physical biodegradation process occurs when microorganisms interact with the surface of polymers, leading to hydrolysis. However, chemical biodegradation occurs due to the enzymatic interaction of the microorganism with the polymers, which leads to the conversion to CO<sub>2</sub> and H<sub>2</sub>O. Implants in places with high loads require high mechanical strength, so materials such as ceramics and metals are preferred. However, these materials have undesirable properties such as inflammation at the implantation site, corrosion and loss of bone mass. To solve these negative properties, it is necessary to change the material in the form of polymers. Polymers are widely considered for their tensile strength, modulus of elasticity and non-corrosive properties. Non-viable properties include loss of mechanical strength with increasing implantation time due to degradation/resorbability. Currently, polymers such as PGA, PLA and PLGA are widely used for bone implants [1, 2, 3].

## **2. Overview of resorbable materials for clinical use**

### *2.1. Polylactic acid (PLA)*

Social and economic development has stimulated considerable scientific and engineering efforts in the discovery, development and use of polymers. Polylactic acid (PLA) is among the most researched biopolymers because it can be produced from non-toxic renewable raw materials. PLA has a high application for biomedical applications due to its properties, such as biocompatibility, biodegradability, mechanical strength and processability. PLA is derived from lactic acid (LA). LA is the building block for the synthesis of PLA. LA is a chiral molecule existing in l and d isomers. Lactic acid (LA) can be obtained by fermenting sugars obtained from renewable sources such as corn and sugar cane. Thus, PLA is an ecological non-toxic polymer with properties that allow use in the human body. Despite the wide spectrum in biomedical applications, there are also certain limitations, such as slow degradation rate, hydrophobicity. Blending PLA with other polymers such as PHB offers convenient options to improve properties or to create new blends for targeted bio-medical applications. Various PLA blends have been explored for various biomedical applications during ongoing scientific research. PLA and their copolymers are becoming widely used in tissue engineering to restore the function of damaged tissues due to their excellent biocompatibility and mechanical properties. The use of PLA has great justification in biomedical applications (Figure 1). It is used for the production of scaffolds for tissue engineering, various bioresorbable medical implants and sutures in dermatology and cosmetics. To improve the properties, it is mixed in different proportions with other polymeric or non-polymeric components. The finished implant thus meets the required properties for application in the patient's body. Various surface modification strategies, such as physical, chemical, plasma, and radiation-induced methods, have been used to create the desired surface properties of PLA biomaterials [4, 5].

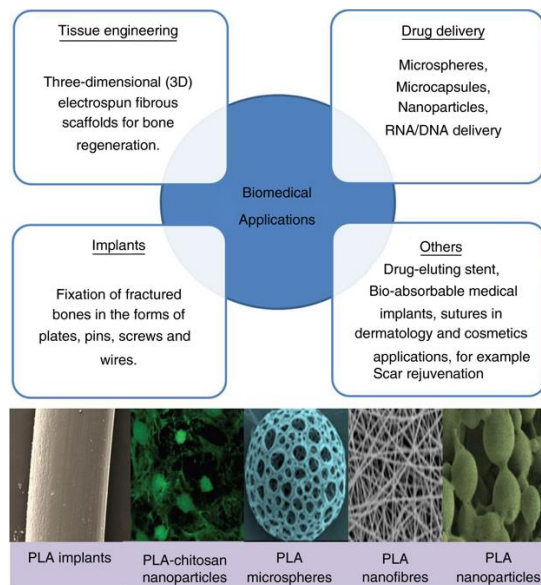


**Figure.1.** Biomedical applications of PLA [4].

### 2.2. Polyhydroxybutyrate (PHB)

Poly(hydroxybutyrate) (PHB) has become an increasingly attractive biomaterial in research and development in recent years. PHB is a natural bio-based aliphatic polyester produced by many species of bacteria. Thanks to its biodegradable, biocompatible and ecological nature, it can be used in a wide range of applications. However, high production costs, thermal instability and poor mechanical properties limit its desired applications. Therefore, it is necessary to incorporate PHB with other materials or biopolymers to develop some new bio-based composites. The development of biodegradable PHB-based biocomposites with improved mechanical properties could be used to overcome the limitations of PHB alone. As previously mentioned, PLA is a biodegradable polyester that could be used to develop composites with PHB. PLA has a brittle nature and stands out as an excellent material for the development of biocomposites with improved mechanical properties. Various scientific studies have prepared PLA/PHB based composites with improved properties such as increased elongation at break and reduced tensile strength. In many cases, mixing PLA/PHB improved the thermal stability of the composite [5-7].

### 2.3. Polydioxanone (PDO)

Polydioxanone (PDO) is another polyester that is commonly used to make biodegradable medical devices. It is also known as PDS, poly-p-dioxanone, PDX or PDDX. Polydioxanone is a synthetic and absorbable colorless polyester that was first produced in the early 1980s. It is synthesized by polymerization of p-dioxanone in the presence of an organometallic catalyst and heat. This polymer is considered non-antigenic and non-pyrogenic and has been found to induce minimal tissue reaction during absorption after implantation. Due to the duration of absorption (182–238 days) and synthetic nature, it is widely used in medical devices. The glass transition temperature is in the range of  $-10^{\circ}\text{C}$  to  $0^{\circ}\text{C}$  and the melting temperature is between  $110-115^{\circ}\text{C}$ . These properties allow the production of stitches by the extrusion process at the lowest temperature. In the medical field, it is implanted in various shapes and sizes. It is most often used in surgical procedures as a suture material (Figure 2), due to its high flexibility due to the presence of an ether oxygen group in the polymer chain [7-9].



Figure.2. Suture material PDO.

### 3. Production of biomedical filament

From biomedically certified pellets, we produced filament on the filament maker Composer series under the investigated temperature melting conditions of PLA/PHB material and plasticizer (Figure 3). The temperature range of extrusion varied between 150 and 170 degrees.



Figure.3. Filament extrusion process under optimized conditions.

All extrusion parameters were optimized. Production took place in a sterile environment under optimal environmental temperature conditions. The most important parameter, which is the diameter of the filament, was recorded and controlled by software from 3devo (Figure 4). The filament diameter plot shows a uniform flow in the desired range for the subsequent 3D printing of the aorta model.



Figure.4. Filament progress graph recorded using 3devo software.

#### 4. 3D printing and simulation of the aorta model

Using FFF additive manufacturing technology, we printed an aorta model from the manufactured medical filament. The printing settings were as follows: printing temperature 175 degrees, plate temperature 90 degrees, used nozzle with a diameter of 0.4 mm. After printing the object, we proceeded to the pressure simulation on the walls of the aorta (Figure 5). We set the tubular to a diameter of 32 mm and a wall thickness of 2.8 mm. The simulation was performed with pressure on the inner walls, non-linearly distributed pressure, so that the pressure is highest in the center and decreases towards the ends. The pressure was set at 48 kPa.

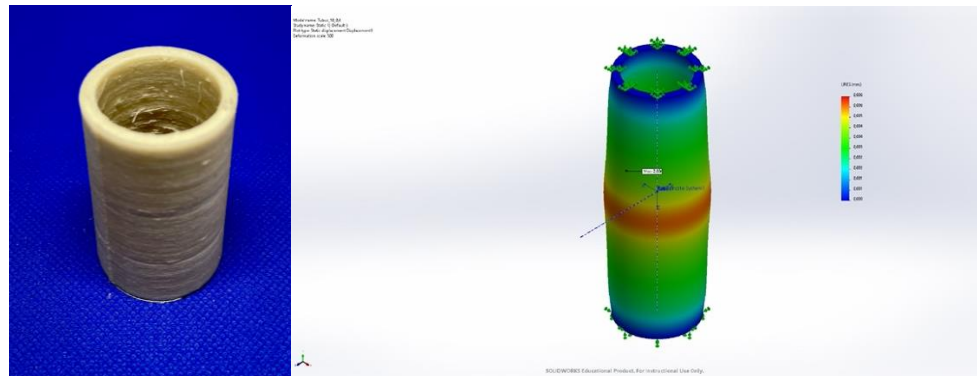


Figure.5. Aortic model and simulation.

#### 5. Conclusion

This scientific article presents theoretical as well as practical outputs from the field of material engineering, filament production, additive manufacturing and the actual simulation of the final implant. The mentioned scientific study brings new knowledge to material engineering and is the theoretical output of the production of filaments that will be used in the field of medical applications. Nowadays, the emphasis is placed on the research of new biodegradable materials and their possible use. The production of filaments based on biodegradable polymers brings new knowledge and connects medicine with engineering. When using filament in additive technologies, it is essential that it meets the requirements necessary for high-quality 3D printing of implants suitable for tissue replacement. Desirable filament properties include strength, good surface finish and constant diameter. All these features contribute to the quality of the final print. Biocompatibility and biodegradability are important in medical applications.

**Acknowledgment:** This scientific study was created thanks to support under the Operational Program Integrated In-frastructure for the project "Center for Medical Bioadditive Research and Production (CEMBAM), code ITMS2014 +: 313011V358, Operational Program Integrated Infrastructure for the project: Open Scientific Community for Modern Interdisciplinary Research in Medicine (OPENMED), code ITMS2014 +: 313011V455, co-financed by the European Regional Development Fund and thanks to support under the Operational Program Integrated infrastructure for the project: Center for Advanced Therapies of Chronic Inflammatory Diseases of the Musculoskeletal System (CPT ZOPA), code ITMS2014 +: 313011W410, co-financed by the European Regional Development Fund, co-financed by the European Regional Development Fund", with the support of the projects KEGA 044TUKE- 4/2022 and KEGA 023TUKE-4/2020 with the support of the project Design solution and biomechanical analysis of personalized instruments for arthroscopic applications (VEGA 1/0599/22) and also Development and testing of systems for controlled simulation of cell growth in a bioreactor environment using computer vision (VEGA 1/0387/22).

## References

1. MYTHILI, P. et al., 2017. Biodegradable Materials and Metallic Implants—A Review. In: *J Funct Biomater*. Vol. 8(4), pp. 44.
2. M.S. SINGHVI, S.S. ZINJARDE, GOKHALE, G. V., 2019. Polylactic acid: synthesis and biomedical applications. In: *Journal of Applied Microbiology*. Vol. 127, no. 6.
3. MIRÓN, V., FERRÁNDIZ, F., JUÁREZ, D., MENGUEL, A.: Manufacturing and characterization of 3D printer filament using tailoring materials. *Procedia manufacturing*. 2017. Available on the internet: <https://www.sciencedirect.com/science/article/pii/S2351978917307886>.
4. CHANFREAU, S., MENA, M., PORRAS-DOMINGUEZ, J.R., RAMÍREZ-GILLY, M., GIMENO, M., ROQUERO, P., TECANTE, A. AND BARZANA, E., 2010. Enzymatic synthesis of poly-L-lactide and poly-L-lactide-co-glycolide in an ionic liquid. In: *Bio-process Biosyst Eng*. Vol. 33, 629–638.
5. KARTHIK, T., UDAYABHANU, J., WEISMAN. A. J., 2019. 3D Printing Custom Bioactive and Absorbable Surgical Screws, Pins, and Bone Plates for Localized Drug Delivery. In: *J. Funct. Biomater*. Vol.10(2), no. 17.
6. ZULFIQAR, A. R., SAFA, N., SHANZA, K., 2019. Recent developments in the synthesis of poly(hydroxybutyrate) based bio-composites. In: *Biotechnology Progress*. Vol. 35, no. 5.
7. ÇANTI, E., AYDIN, M., YILDIRIM, F.: Production and Characterization of Composite Filaments for 3D Printing. *Journal of Polytechnic*. 2018. Available on the internet: [https://www.researchgate.net/publication/322903568\\_Production\\_and\\_Characterization\\_of\\_Composite\\_Filaments\\_for\\_3D\\_Printing](https://www.researchgate.net/publication/322903568_Production_and_Characterization_of_Composite_Filaments_for_3D_Printing).
8. MENČÍK, P., PŘIKRYL, R. et al., 2018. Effect of Selected Commercial Plasticizers on Mechanical, Thermal, and Morphological Properties of Poly(3-hydroxybutyrate)/Poly(lactic acid)/Plasticizer Biodegradable Blends for Three-Dimensional (3D) Print. In: *Materials*. Vol. 11, no. 10.
9. ZEERATKAR, M., D. DE TULLIO, M., PERCOCO, G., 2021. Fused Filament Fabrication (FFF) for Manufacturing of Microfluidic Micromixers, an Experimental Study on the Effect of Process Variables in Printed Microfluidic Micromixers. In: *Micromachines*. Vol. 12(8), pp. 858.



# Overview of trends in tissue engineering

Tomas Breskovic <sup>1,\*</sup>, Norbert Ferencik <sup>2</sup>, Gabriela Dancakova <sup>3</sup> and Radovan Hudak <sup>4</sup>

<sup>1</sup> Technical University of Kosice; tomas.breskovic@tuke.sk

<sup>2</sup> Technical University of Kosice; norbert.ferencik@tuke.sk

<sup>3</sup> Technical University of Kosice; gabriela.dancakova.2@tuke.sk

<sup>4</sup> Technical University of Kosice; radovan.hudak@tuke.sk

\* Correspondence: Ing. Tomas Breskovic, Technical University of Kosice, Faculty of Mechanical Engineering, Department of Biomedical Engineering, Letna 9, 042 00 Kosice tomas.breskovic@gmail.com; Tel.: +421 55 602 2042

**Abstract:** Tissue engineering has emerged as an interesting field nowadays; it focuses on accelerating the tissue's self-healing mechanism rather than organ transplantation. It involves the implantation of in vitro cultured initiating tissue, or a scaffold filled with tissue-regenerating components into the damaged area. Bioreactors are commonly used to apply biophysically relevant stimuli to tissue engineering to investigate how these stimuli affect tissue development, healing and homeostasis and offer great flexibility as key properties of the stimuli (e.g., duty cycle, frequency, amplitude, and duration) can be controlled to elicit the desired cellular response.

**Keywords:** tissue engineering 1; bioreactor 2; cultivation 3

## 1. Introduction

Tissue engineering is based on the collaboration of several disciplines, where biological sciences and technical principles are applied to the development of substitutes to restore and improve the function of a tissue or organ. [1][2] Currently, tissues obtained from the patient himself (autologous transplants) or tissues from a human or animal donor (allogeneic and xenogeneic transplants) are commonly used. However, in both cases, a number of problems arise. In the case of autologous tissues, a limiting factor may be the lack of suitable tissue for transplantation, while tissues from donors may cause unwanted immune reactions that may even lead to de-healing (if they are perceived as foreign) of the tissue or the entire organ.[2] The goal of regenerative medicine is to repair structurally and functionally damaged, dead tissues and organs. Methods in regenerative medicine use tissue-specific cells, biomaterials, and biologically active molecules to enhance regeneration and support the formation of new and functional tissues. A tissue engineering bioreactor can be defined as a device that uses mechanical means to influence biological processes. Mechanical stimulation in a bioreactor is used to transform stem cells into a desired cell phenotype. Bioreactors can provide biochemical and physical regulatory signals that direct differentiation. They also create an optimal environment by stabilizing the temperature, humidity, pH level and oxygen level, which provides the most suitable conditions necessary for cell growth and differentiation. In tissue engineering, bioreactors can be used in several areas. In the beginning, we need bioreactors for cell expansion. The cells are intended for direct transplantation. Second, we use bioreactors to grow 3D tissues before implantation, such as skin, cartilage, bone, blood vessels, and others.[3][4]

## 2. Trends in tissue engineering

In the last two decades of research in the field of 3D tissue engineering, significant progress has been achieved, mainly by using progressive research in the field of biomaterial engineering and 3D additive technology. Some of these tissue-engineered, medical products have been transplanted IN VIVO as tissue substitutes or to support tissue regeneration.

- **Polymer-salt microfibers**

At the Technical University of Messachussk, scientists are working on the development of microfibers based on polymer and salt. Printing scaffolds from these experimental polymer-salt microfibers has potential in nerve tissue regeneration or transplantation. Using a basic diagram representing spinal cord nerve injuries, American scientists predictively designed a microchannel scaffold with a corresponding cross-section to support the regeneration of the damaged area. A porogen (sodium chloride, NaCl) was used in the creation of the necessary broad-spectrum fibers to precisely control their pore sizes, which was previously inserted into the polymers for the production of pre-forms. The NaCl crystals are first sieved to separate the required grain size and then mixed with the polymer. The polymer/salt solution is spread on the surface to form thin films, which are then rolled and consolidated around a polystyrene rod used as the core of the composite. The composite preforms created in this way is wrapped again in polystyrene to create the perimeter structure. The fiber structure created in this way is fed to the nozzles, is melted, thermally drawn, and applied in such a way as to create an optimal scaffold structure. [5]

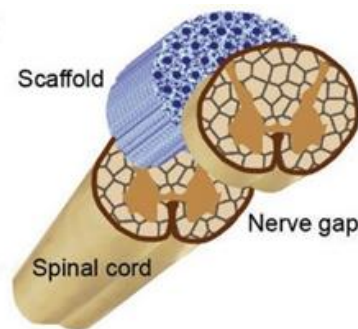


Figure 1 Demonstration of inserting the treated scaffold into the spinal cord.

- **Phonometric bioreactor**

At the Medical University of Graz, Australia, a phonemimetic bioreactor has been developed as a potential method for culturing vocal cord tissue. This bioreactor construction has a case custom designed using 3D CAD software to which the BioFlex board can be connected. For the production of the bioreactor, 6-well plates with a flexible, thin-walled, silicone base 0.51 mm thick and with a surface area of 9.62 cm<sup>2</sup> per well were used (BioFlex, Flexcell International Corporation, Burlington, NC, USA). These plates were developed for a commercially available computer-controlled bioreactor that operates in a vacuum, where positive air pressure drives the movement of a cylindrical loading column that cyclically applies stress to the cells. However, this system offered a maximum frequency of only 5 Hz and therefore did not meet the requirements for more complex stimulation (50 Hz - 250 Hz). To overcome this limitation, custom boards were created that allowed us to stimulate the silicone membranes directly through sound waves, thus creating any stimulation pattern with high amplitudes and frequencies up to 10 kHz. The speaker consists of an anodized aluminum cone; solid aluminum basket made of die-cast material; elastic, rubber frame and Kapton coil, which is able to sufficiently withstand the

conditions in the cell culture incubator (37 ° C, 100% humidity.) The sounds during the research were edited and generated with the open-source sound application Audacity. (audacityteam.org, registered trademark of Dominic Mazzoni) [6]

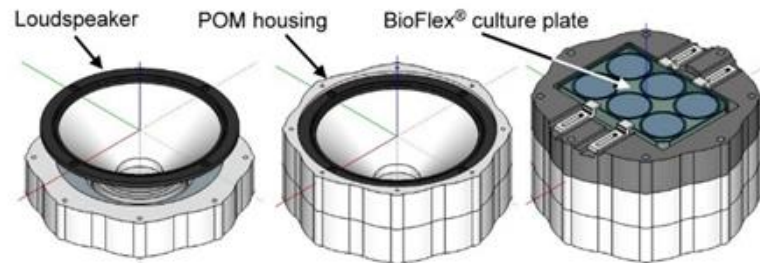


Figure 2 Phonometric bioreactor and its basic parts.

- **Cellular scaffold based on hydrogel.**

Omentum tissue (the omentum as a membranous double layer of fatty tissue that covers and maintains the intestines and organs in the lower abdomen) is extracted from the patient and, after decellularization of the tissue, the extracellular matrix is processed into a personalized, thermoresponsive hydrogel. The cells are reprogrammed to become pluripotent and then differentiate into cardiomyocytes and endothelial cells. Differentiated cells are encapsulated in a hydrogel and thus a so-called bioink (bioink) is created, which can be used to print personalized tissue. Subsequently, vascularized surfaces or complex cellular structures can be created by 3D printing. The resulting autologous engineered tissue can be transplanted back into the patient as a cellular replacement for a damaged or destroyed organ with a low risk of rejection. [7] In the picture we see an example of printing personalized vascular tissue inside the extracellular matrix of hydrogel.

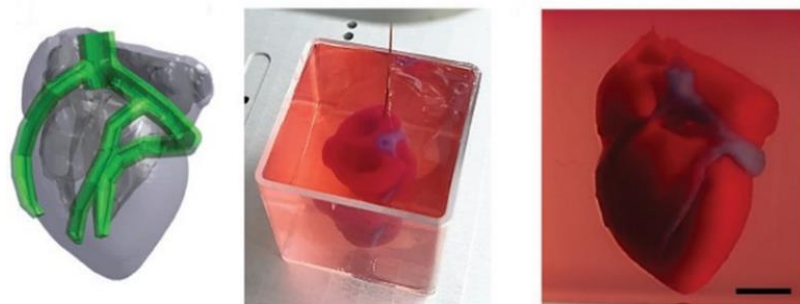


Figure 3 Personalized vascular tissue inside a hydrogel extracellular matrix.

- **Bioreactor system intended for the cultivation of heart valves.**

A developmental bioreactor system intended for the cultivation of heart valves was developed at Harvard University in the USA. With this system, it is possible to create live valve implants by simulating suitable flow and hydrodynamic conditions. The main flow path uses a dominant pulsatile pump to generate flow through the valve lumen and other components to achieve the desired simulations of pressures above and below the valve during the cardiac cycle. Nutrient flow circulates between the heating, oxygenated reservoir and valve chamber. Another flow circuit brings nutrients from the valve chamber to monitor pO<sub>2</sub>, pCO<sub>2</sub> and pH. The circulation circuit for stabilizing the gas atmosphere ensures the uniform supply of a mixture of 95% air and 5% CO<sub>2</sub> to the central reservoir during cultivation. The body of the valve chamber is filled with cellular culture medium. The tissue valve is placed between the connectors on the valve chamber lid to

ensure a quick installation. A borescope camera is positioned above the outflow side of the tissue flap to monitor the development of the tissue construct in detail during culture. The afterload generator (afterload as the amount of vascular resistance that the left ventricle must overcome in order for blood to flow out of the heart) is located on the outflow side of the tissue valve and consists of a stabilization chamber and a safety valve. The elasticity of the aorta and large elastic arteries is simulated through the stabilization chamber, while the safety valve helps to control the maximum systolic pressure. [8]

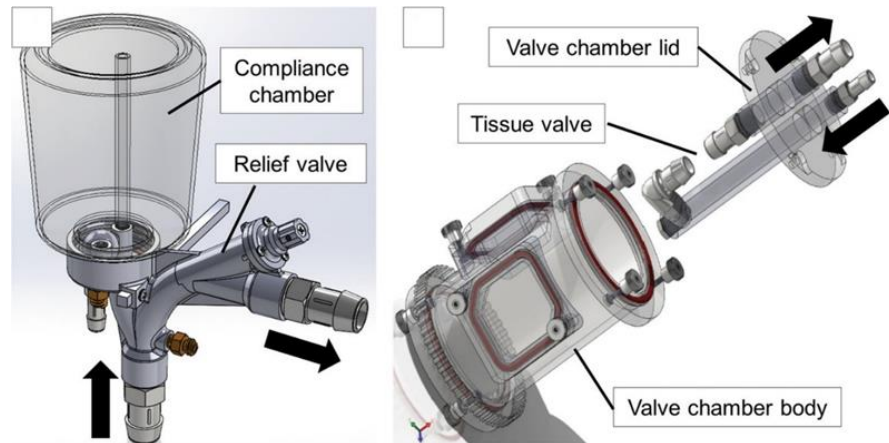


Figure 4 Basic parts of a flap culture bioreactor.

- **Bioreactor for the cultivation of intervertebral discs**

Design of a mechanical device for cultivation, bovine, movement segments of the spine. This two-degree-of-freedom bioreactor was developed to culture intervertebral discs under standard atmospheric conditions (i.e., 37 °C, 5% CO<sub>2</sub>, and 100% humidity). The drive unit makes it possible to perfectly adapt the culture chamber to the length of the sample and the biasing mechanism. Perfect adaptation is ensured by means of a screw piston, which can be used to adjust the cultivation chamber downwards. When the sample and the pressure, titanium plate are in contact, the split shaft begins to move and applies a preload depending on the stiffness of the spring. Also, the torque transmission mechanism on the top cover transmits the torque through the shaft to the bottom of the cultivation chamber. In this design of a two-degree-of-freedom bioreactor to optimally determine degeneration and regeneration of disc tissue in vitro, it was shown that some type of "physiological" loading is necessary for proper development of intervertebral disc tissue. It has also been shown that it is necessary to keep the disc matrix in continuous circulation of the culture solution. [9]

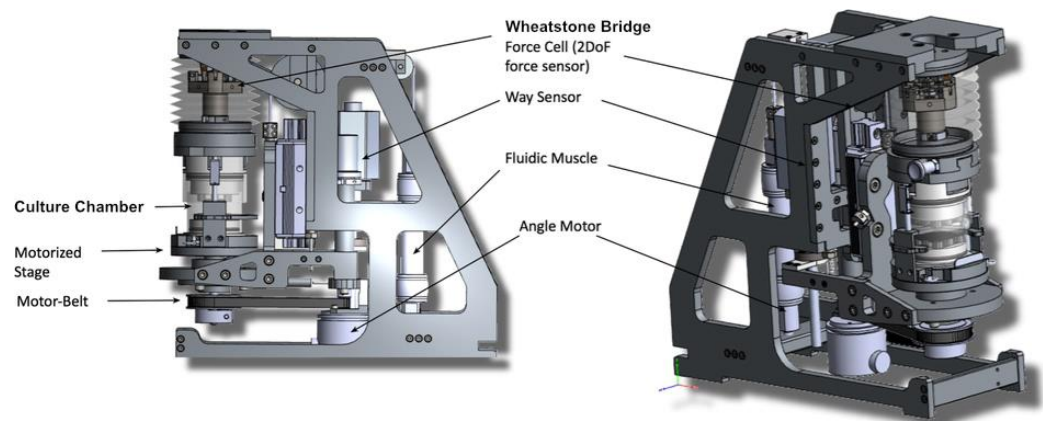


Figure 5 Basic parts of the bioreactor for the cultivation of intervertebral discs.

- **Bioreactor for the cultivation of tendons**

Bioreactor using traction force in combination with circular circulation. This system should be able to create implants that could be used to repair damaged tendons. (Oscillating Stretch-Perfusion Bioreactor (OSPB)) The OSPB chamber was designed using 3D CAD computer software (Solid Edge ST6, Siemens). Subsequently, the flow rates of the cultivation chamber were designed by computer simulation in such a way as to achieve a uniform flow of liquid/cultivation medium. The cultivation assembly is composed of a sterile part (that is, a cultivation chamber), a mechanism for inducing tensile forces and a support disc. The chamber is composed of two holders for anchoring the tissue, flexible silicone rubber, silicone tube hardened with platinum and three connectors for filling and changing the culture medium. All these components are connected in a closed loop. The cultivation chamber is placed on a 3D printed support disc of cyclic shape. The carrier disc also contains all the mechanical parts to activate the stretching phase during the dynamic cultivation process through a mechanism for inducing tensile forces. The tissue anchor holder consists of two main parts, a stainless steel clamp and a clamp cover made of delrin, a biocompatible material. All components were custom made with high precision machining. With such a production process, a firm anchoring of the tendon was achieved by means of holders during the stimulation and cultivation phase. The clamp system has been designed to be accessible via external control, allowing sterility to be maintained. To ensure a firm grip, the clamp system has been designed with two alternating rows of serrated patterns that interlock when the clamps are closed. The drive device consists of a step linear drive; two miniaturized, linear guide rods with high precision; load cell and two supports for fastening the cultivation chamber. The traction force was generated by a linear magnetic drive and transferred to the cultured tendon through a movable shaft. The load acting on the cells was in the capacity of 600 N. The culture chamber allows performing an unlimited perfusion flow simultaneously in combination with stretching, in an automatic manner, without the need for user manipulation. [10]

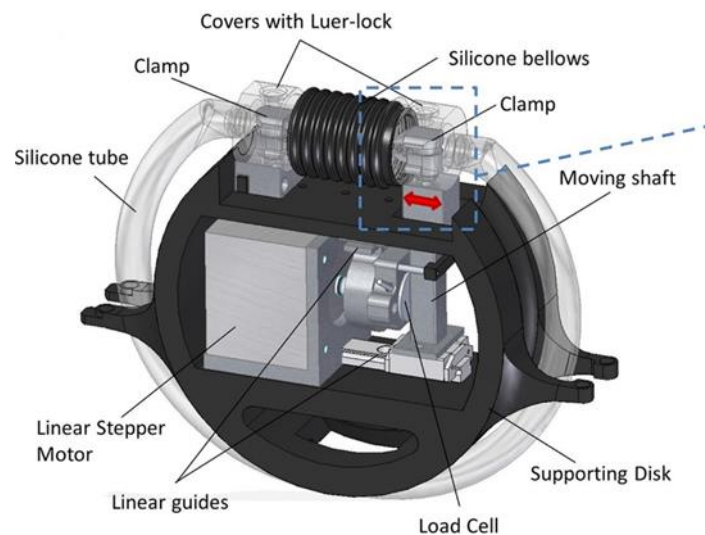


Figure 6 Bioreactor for the cultivation of tendons and its basic parts.

### 3. Conclusions

Cultivation of living tissue is one of the main clinical challenges, but unfortunately this challenge is limited due to the insufficient amount of building living tissue after cultivation. Because the growth of a cellular product in a stable culture facility has a limited supply of the necessary resources. The multiplication of cells in a passive culture device is dependent exclusively on the passive dispersion of nutrients, which means insufficient distribution of the necessary nutrients for cultivation, resulting in insufficient viability of

the cultured tissue. A static culture device does not have the necessary microenvironment for proper cell growth of living tissue. During static cultivation, cells are often placed unevenly on the surface, but also inside the scaffold, and there is no overgrowth and cell viability across the entire diameter of the cultured cross-section.

**Acknowledgments:** This article was developed with support Slovak Research and Development Project KEGA 044TUKE-4/2022 Implementation of progressive technologies in prosthetics and orthotics education and support integration with practice, project KEGA 023TUKE-4/2020 Increasing the synergy of methods of teaching biophysics using laboratory equipment and diagnostic devices aimed at measuring physical and is the result of the project implementation, VEGA 1/0387/22 Development and testing of systems for controlled stimulation of cell growth in a bioreactor environment using computer vision, VEGA 1/0599/22 Design solution and biomechanical analysis of personalized instruments for arthroscopic applications, CEMBAM - Center for Medical Bioadditive Research and Production, ITMS2014+: 313011V358 supported by the Operational Programme Integrated Infrastructure funded by the European Regional Development Fund.

**Conflicts of Interest:** The author(s) declared no potential conflicts of interest with respect to the research, authorship, and/or publication of this article.

## References

1. L. Roseti, V. Parisi, M. Petretta et al., (2017), "Scaffolds for bone tissue engineering: state of the art and new perspectives," *Materials Science and Engineering: C*, vol. 78.
2. Yoshito Ikada, (2006), *Tissue Engineering: Fundamentals and Applications*, CHAPTER 4: CHALLENGES IN TISSUE ENGINEERING
3. LISA E. FREED et al., (2007), *Advanced Tools for Tissue Engineering: Scaffolds, Bioreactors, and Signaling*, DOI: 10.1089/ten.2006.12.3285
4. Junjie Zhao et al., *Bioreactors for Tissue Engineering: An Update*, *Biochemical Engineering Journal*, dostupné na: <http://dx.doi.org/10.1016/j.bej.2016.01.018>
5. Noor, N., Shapira, A., Edri, R., Gal, I., Wertheim, L., Dvir, T., 3D Printing of Personalized Thick and Perfusable Cardiac Patches and Hearts. *Adv. Sci.* 2019, 6, 1900344. <https://doi.org/10.1002/advs.201900344>
6. Tefft BJ, Choe JA, Young MD, Hennessy RS, Morse DW, Bouchard JA, Hedberg HJ, Consiglio JF, Dragomir-Daescu D, Simari RD, Lerman A. Cardiac Valve Bioreactor for Physiological Conditioning and Hydrodynamic Performance Assessment. *Cardiovasc Eng Technol.* 2019 Mar;10(1):80-94. doi: 10.1007/s13239-018-00382-2. Epub 2018 Oct 11. PMID: 30311149; PMCID: PMC6541400.
7. *Developing Bioreactors to Host Joint-Derived Tissues That Require Mechanical Stimulation*, *Journal: Reference Module in Biomedical Sciences*, : 2019, ISBN: 9780128012383
8. Talò G, D'Arrigo D, Lorenzi S, Moretti M, Lovati AB. Independent, Controllable Stretch-Perfusion Bioreactor Chambers to Functionalize Cell-Seeded Decellularized Tendons. *Ann Biomed Eng.* 2020 Mar;48(3):1112-1126. doi: 10.1007/s10439-019-02257-6. Epub 2019 Apr 8. PMID: 30963381; PMCID: PMC7015956.
9. Sidi A. Bencherif, R. Warren Sands, Deen Bhatta, Praveen Arany, Catia S. Verbeke, David A. Edwards, David J. Mooney, Injectable preformed scaffolds, *Proceedings of the National Academy of Sciences* Nov 2012, 109 (48) 19590-19595; DOI: 10.1073/pnas.1211516109
10. Rosso, F., Marino, G., Giordano, A., Barbarisi, M., Parmeggiani, D. and Barbarisi, A. (2005), Smart materials as scaffolds for tissue engineering. *J. Cell. Physiol.*, 203: 465-470. <https://doi.org/10.1002/jcp.20270>



# Cylinder head modifications of internal combustion engine

Jozef Brindza <sup>1\*</sup>, Michal Demko <sup>2</sup>, Filip Dominik <sup>3</sup>, Marek Vrabel <sup>4</sup> and Peter Ižol <sup>5</sup>

<sup>1</sup> Prototyping and Innovation centre, Faculty of Mechanical Engineering, Technical University of Kosice, Slovak republic; jozef.brindza@tuke.sk

<sup>2</sup> Prototyping and Innovation centre, Faculty of Mechanical Engineering, Technical University of Kosice, Slovak republic; michal.demko@tuke.sk

<sup>3</sup> Prototyping and Innovation centre, Faculty of Mechanical Engineering, Technical University of Kosice, Slovak republic; filip.dominik@tuke.sk

<sup>4</sup> Prototyping and Innovation centre, Faculty of Mechanical Engineering, Technical University of Kosice, Slovak republic; marek.vrabel@tuke.sk

<sup>5</sup> Department of Technology, Materials and Computer Supported Production, Faculty of Mechanical Engineering, Technical University of Kosice, Slovak republic; peter.izol@tuke.sk

\* Correspondence: jozef.brindza@tuke.sk; Tel.: +421 940 772 427

**Abstract:** The purpose of the paper is to design a machine technology for modifying cylinder head channels and to describe the fundamental understanding of the topic in specific modification areas that may be further improved. The paper includes an analysis of the issue, broken down into parts based on the technological requirements to carry out a successful head modification, the design of the technological procedure of the modification, the implementation of the proposed procedure in light of the theoretical knowledge obtained from the analysis of the issue, and the evaluation of the results obtained in which at the same time, better alternative solutions are proposed.

**Keywords:** cylinder head, modifications, CAM system, milling, 5-axis CNC

## 1. Introduction

In motor sports, it is common to modify car parts in order to increase the performance of the vehicle. Car conversions are aimed at improving driving characteristics, safety and especially at increasing engine performance. When modifying the engine, as well as other parts, it is necessary to keep certain technological procedures in order to achieve the desired result. The activities described were aimed at adjusting the cylinder head of the combustion engine, more precisely at adjusting the intake and exhaust channels. Modifications of these channels is normally done by hand machining. The disadvantage of this approach is that the same shapes are not achieved in each channel, which is desirable for maximum effect. In motorsport, even a small difference in performance can mean a lot, so it is worth investigating how the modification can be done mechanically [1].

The surface of the serial intake and exhaust channels is rough and imprecisely shaped, which is due to the technology used in the serial production of these parts. In some castings, displacement of the mold cores is also visible. These facts cause flow losses during intake and exhaust of cylinder capacity. To reduce these losses and to increase the filling efficiency of the engine, the walls of the channels are smoothed, their shape changes and the cross-section increases. Due to the thickness of the wall, the cross-section of the channels can be increased by only a few millimeters [2]. Other modifications of the cylinder heads are:

- lowering of the cylinder head,
- enlargement of the valve seats,
- modification of valves and their springs.

All components that are related to these modifications must be properly coordinated, thus ensuring their functionality and, consequently, an overall increase in performance. In order to start modifications, it is necessary to know how the finished channel should look [3].

Due to the construction of the head, the channels have a radius, affecting the filling efficiency of the engine. The bend of the channel enlarging cause increase the losses in the flow, which reduces the use of the cross-section of the intake channel, but at the same time, a larger bend enables a simpler head design. Therefore, channel shapes are a compromise among head design, cylinder fill rate, and cylinder vortex formation. In sports engines, there is an effort to fill the cylinder as much as possible [4].

An important rule for modifications is: the bend of the channel must be as large as possible so that its entire cross-section is used and at the same time that the flow of the mixture flows evenly around the valve during filling. However, it is not easy due to the design of the cylinder head. With a small curvature, when filling the cylinder, the flow moves to the wrong places, where flow restriction occurs. By increasing the radius of curvature, the flow is moved closer to the saddle, resulting in a similar flow on the opposite side as well [5, 6].

## 2. Design and implementation of modifications

Modification of engine head channels is normally done using hand powered or hydraulic tools with grinding wheels and cutters. During manual processing, various deviations will arise between the individual channels, which can cause an uneven supply of the mixture to the individual cylinders. Manual modification is time-consuming, therefore it is more efficient to implement machine modification for repeated modifications of selected heads. However, the preparation for machining is lengthy and therefore not suitable for one-piece modifications. The selected cylinder head from the Škoda 1.3 MPi 50 kW engine is commonly used in rally cars. The problem with machining is mainly the lack of knowledge of the original shape of the head geometry. Therefore, the first step in the modification is the creation of a cylinder head model with the help of reverse engineering. After the original geometry has been distorted, the geometry is adjusted to the desired one. For this case, the dimensions of the channels were specified according to the proven long-term experience of experts [6].

The required channel modification is as follows:

- On the intake side, the intake channel should start at a diameter of  $\varnothing 30$  mm and continue like a funnel to the beginning of the valve guide, where it narrows uniformly to a diameter of  $\varnothing 29$  mm. After the narrowing, there is an expansion to a diameter of  $\varnothing 32$  mm and a subsequent narrowing to a diameter of the valve seat of  $\varnothing 30$  mm opening into the combustion chamber.
- The exhaust channel also needs to be enlarged, but its geometry is no longer so important, it is important to enlarge it so that the volume of exhaust gases can leave the combustion chamber without increasing the load on the engine. It increases from the combustion chamber to the exhaust system uniformly from a diameter of  $\varnothing 28$  mm to an oval of  $28 \times 42$  mm.
- Realization of modifications.

### 2.1. Finding the original geometry

The original geometry of the channels needs to be determined in order to correctly position the new, modified channel. It is necessary to take into account that a part that contains many other functional elements is being modified. These elements must remain untouched, such as valve seats, holes for valve guides, mounting threads and especially the cooling circuit of the cylinder head. The original channel has its own specific shape, and the wall between the cooling circuit of the head and the channels has a certain thickness. If the trajectory of the original channel remained unknown, there would be a risk of breaking through the wall to the cooling circuit during the implementation of the

modification. The thickness of this wall is between 4 and 6 mm and cannot be clearly determined without special equipment.

Engine heads are produced by casting from aluminum alloy. The original geometry is unknown, either due to secrecy by the manufacturer or the age when the documentation no longer exists. In order to determine the original geometry, the simplest available and feasible method was chosen, namely measurement using common gauges and a coordinate measuring machine (CMM), which was used to determine the trajectory, axes and diameters of the channels.

The basic geometry, the rough dimensions of the casting and the proportional distribution of the shape elements were transferred to paper and then scanned using a regular scanner. A simpler way would be to use a photograph, but due to the curvature of the camera lens, a distorted geometry would be obtained, introducing further inaccuracies into the process.

Subsequently, the scans were transferred to free planes in the CAD system and basic shapes were sketched from them, such as the outer shape, the positions of the holes, etc. – figure 1. The holes ensuring the position when fitting the head to the other engine components were chosen as a reference for creating the geometry. At the same time, they were chosen as bases for measurements on the CMM machine and also for determining the reference point for the exact setting of the head on the CNC milling machine. The remaining dimensions of the holes, necessary for the creation of the model, were compensated against the scanned dimensions according to the measurements and partially adjusted according to the found center planes. These planes were found to be intermediate dimensions between the valve guides. The position of the guides is accurate because it is a machined part of the head and not a cast one.

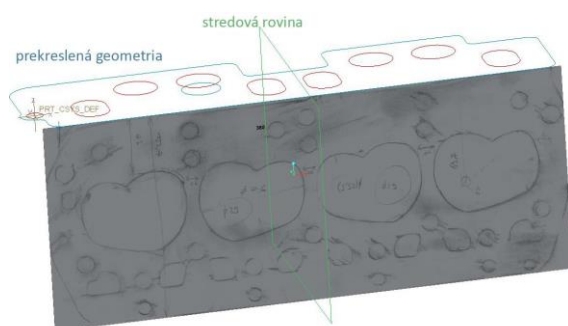


**Figure 1.** Scans transferred to the CAD system.

Using the CMM, the coordinates of the points in the plane that represent the lower curve of the intake channel were determined, as well as the positions of the selected reference points, essential for the creation of the geometry. The scanned points were transferred to the CAD system, where they helped to model the original channel geometry. The scanned points are shown in figure 2.

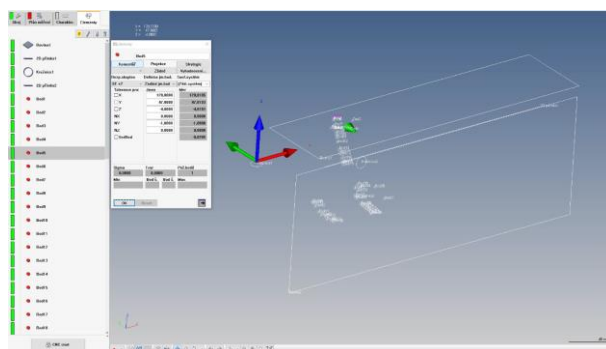


**Figure 2.** Output from the CMM, scanned points for creating a guide curve.

Based on these points, a guide curve was created. The curve is the basic element for channel modeling with the "Sweep" tool. This tool is used to create objects with the same or variable cross-section linked to the guide curve. Both types of channels - intake and exhaust - were created with this tool. The created guide curve is shown in figure 3.

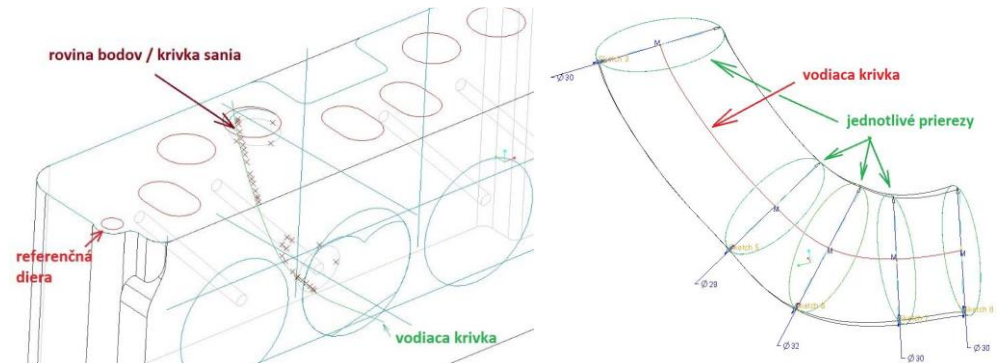


**Figure 3.** A guide curve created based on the scanned points.

## 2.2 Creation of NC program

A 5-axis continuous milling machine DMU 60 eVo was chosen for the production of internal shaped surfaces. The first step was choosing a suitable tool. Since it is an enlargement of the cast hole, no pre-drilling or rough milling operations were necessary. Due to the complexity of the surfaces and the difficult access to them, a tool was needed that could also handle the so-called undercutting operations. Undercutting is the machining of surfaces to which standard cutting tools cannot be positioned. Therefore, it was necessary to use a special cutter. The geometry of the selected tool enables a cut up to 280°.

Creating an NC program begins with choosing the right strategy and determining the geometric and technological parameters. The geometric parameters include the machined and control surfaces, the curves bounding the machined surfaces and the guide curves of the tool. Technological parameters are important for the correct guidance of the tool, for perfect machining of selected surfaces, for movement during approaches and retracts, for the way the tool is guided in possible collision, etc. The last step is optimization the process. The chosen strategy is 5-axis continuous Morph milling, which has circular toolpaths. This strategy requires the determination of the machined surfaces and the boundaries of these surfaces, as well as the determination of the tool guide curve. The following cutting conditions were chosen: spindle speed  $S = 10\,000$  ot./min.; feed  $F = 1\,500$  mm/min. The accuracy achieved after modification of the channels was approximately 0.1-0.2 mm, because of the inaccuracy of the tool used, which was not intended for CNC machining, and the tool could also be pushed off during machining. The final shape of the tool paths can be seen in figure 4.

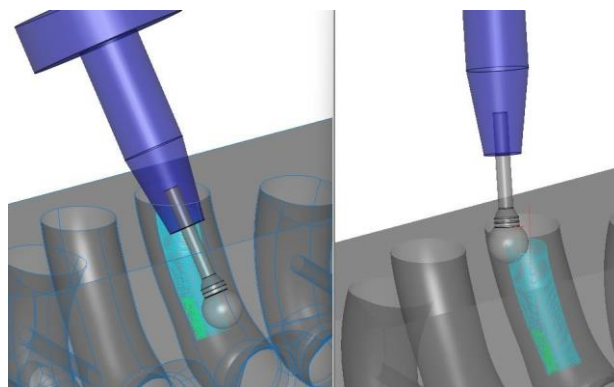


**Figure 4.** Final tool paths.

### 2.3. Realization of production

The head could be clamped in a vise, because of available parallel surfaces. The head is a rough cast from the underside and does not have a flat surface. To set it in the horizontal plane, setting screws with nuts, placed in the grooves of the machine table, were used. By adjusting the height of the nuts, the head was set in a horizontal position and the flatness was checked using a dial indicator.

After positioning and detenting the head in the working space of the machine, the position of the head, its rotation and the defined position of the zero point were determined using a touch probe. These operations were followed by production itself. Production records are shown in figure 5.



Figure 5. Production records.

### 3. Results

In the paper, a procedure and a method of modification the cylinder head of a standard internal combustion engine were proposed so that the engine could be used for sports purposes. The presented procedure was based on the available options regarding the need to modify one piece of the head. In addition to the described modifications to the intake and exhaust channels in the engine head, the following adjustments were made:

- Lowering the cylinder head.
- Enlargement of valve seats.
- Modifications of valves.
- Replacement of valve guides [5].

The finished modified head is shown in figure 6 and is ready for assembly and testing. The expected final effect of the modifications is an increase in engine power by 30 to 40 horsepower.

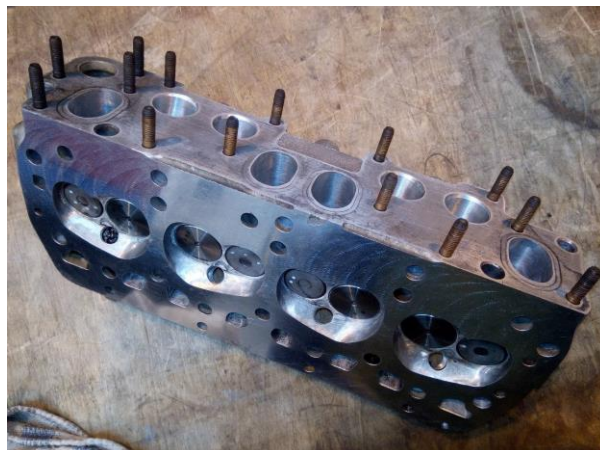


Figure 6. Finished modified engine head.

#### 4. Conclusions

Several improvements have been proposed for future modifications of combustion engine heads, should they be implemented on a larger scale.

The chosen method of creating the geometry was the simplest, but lengthy, considering the current possibilities. For repeated modification, this procedure is inefficient. A more advantageous way is to use 3D scanning. By scanning the head, especially its cavities, a polygonal model is obtained, which is then imported into CAD software. Based on a 3D scan, it is possible to proceed to the actual creation of the adjusted channel geometry in a fraction of the time.

A professional solution for the modification of heads from touch scanning to production itself is the use of specialized Centroid machines, in which, among other things, cycles for 5-axis probing of internal surfaces are available. The advantage is that all activities can be performed in one clamping (probing, geometry modification, program creation, machining) [8].

Although the proposed clamping method was the simplest, it did not provide sufficient access to the cavities from both sides. The consequence was setting the head twice. For repeated production, it is advantageous to use a fixture. The fixture is designed as a clamping block cut by 45°. The reason for this cut is the accessibility of the cavity from both sides and the sufficient height of the head above the worktable of the machine, so that there is no interference between the table and the headstock. The clamping plate contains holes for fixing it to the worktable with screws, screws for setting flatness of the head in relation to the axes of the machine and clamping screws. The design of the fixture with the visualization of the clamping on the milling machine is shown in figure 7.

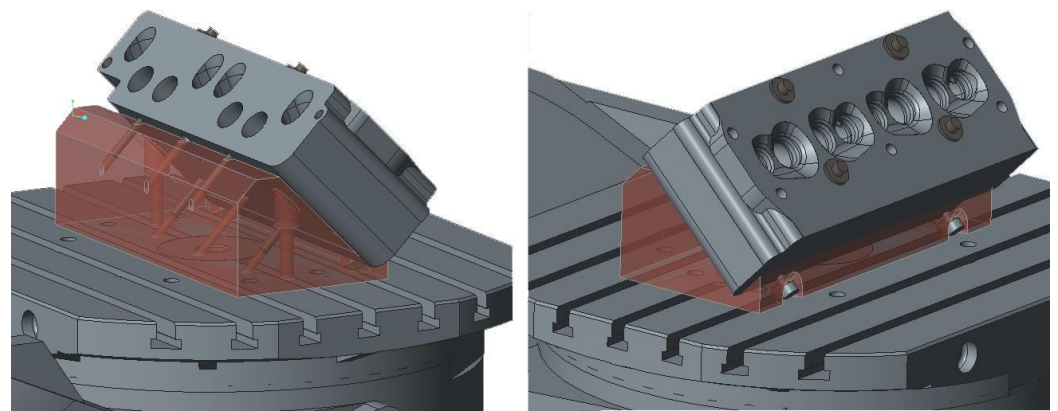


Figure 7. The designed fixture and its visualization of clamping on the milling machine.

**Conflicts of Interest:** The authors declare no conflict of interest.

#### References

1. Dominik, F. Design and realization of technology for modification to the intake and exhaust ports of the combustion engine. *Thesis, Master study, Technical University of Košice, Košice*, 13.05.2022.
2. Úprava hlavy valcov: Spôsob ako zvýšiť výkon motora. Available online: <https://autoride.sk/uprava-hlavy-valcov-sposob-ako-zvysit-vykon-motora> (accessed on 16-04-2022).
3. Basshuysen R., Schafer F. *Internal Combustion Engine Handbook*, 2nd ed. SAE International, 2016; 1150 p.
4. Mackerle, J. *Motory závodních automobilů*. 1. ed. Státní nakladatelství technické literatury, Praha, 1980; 196 p.
5. Vizard, D. *David Vizard's How to Port & Flow Test Cylinder Heads*, 1. ed. CarTech, 2012; 160 p.
6. Nishad, K.; Ries, F.; Li, Y.; Sadiki, A.; Numerical Investigation of Flow through a Valve during Charge Intake in a DISI -Engine Using Large Eddy Simulation. *Energies* **2019**, *12*, 20 p.
7. Tips for Machined Parts With Undercuts. Available online: <https://www.americanmicroinc.com/resources/tips-machined-parts-undercuts/> (accessed on 30-04-2022).
8. Centroid. Available online: [https://www.centroidcnc.com/cnc\\_porting\\_machine.html](https://www.centroidcnc.com/cnc_porting_machine.html) (accessed 01-05-2022).



# Numerical simulation of clinch-riveting of HX420LAD steel sheets

Denis Cmorej <sup>1</sup>, Ľuboš Kaščák <sup>2</sup>

<sup>1</sup> Affiliation 1; denis.cmorej@tuke.sk

<sup>2</sup> Affiliation 2; lubos.kascak@tuke.sk

\* Correspondence: denis.cmorej@tuke.sk; Tel.: +421 55 602 3519

**Abstract:** Currently, there are several important reasons for using high-strength steel in the automotive industry. Car manufacturers choose steel with good fatigue, good formability resistance, and the ability to absorb impact energy. HSLA steels can fulfill these mentioned criteria. The application of HSLA steel sheets has led to the development of new progressive joining techniques. Mechanical joining - clinch-riveting, is an innovative technique to join these progressive materials. In practice, simulation programs are used to predict and optimize the joining processes before the joining process is realized. One of the most used software for simulating the clinch-riveting process is Simufact Forming. Simufact Forming software was used to simulate the joining of HX420LAD steel sheets. Due to the axisymmetric nature of the clinch-riveting process, the simulation was simplified to a 2D representation. The result of the simulation was compared with metallographic images after the clinch-riveting process.

**Keywords:** clinch-riveting, Simufact Forming, numerical simulation

## 1. Introduction

One of the most significant problems in the automotive industry is the lightweight, safe design, and the enhanced crash response of specific car-body parts. These objectives lead to the increasing adoption of HS (high-strength) steel sheets for specific parts of car-body structures [1].

One of the best known high-strength steels is HSLA (high-strength low-alloy) steel. HSLA steels are fine-grained steels with a ferritic or ferritic-pearlitic structure, while they are micro-alloyed with a minor addition of one or more elements such as aluminium, titanium, niobium, vanadium. In general, HSLA alloys are much stronger and tougher than ordinary plain carbon steels. The low-alloy steel sheets have good machinability and hardenability properties [2-3].

Clinch-riveting technology is an innovative technique to join these progressive materials. In this technology, a rivet of defined dimensions is pressed into the joined sheets by a punch. The main advantage of this technology is that it is not necessary to pre-drill a hole in the joined sheets before joining the sheets. Joints created by using clinch-riveting technology achieve higher values of load-bearing capacity compared to joints created by clinching technology [4-6].

In practice, simulation programs are used to predict and optimize the joining processes such as mechanical joining – clinch-riveting before the joining process is realized. One of the most used software for simulating the process of clinch-riveting is Simufact Forming [7-8]. The paper deals with the comparison of the simulation and metallographic images after the process of clinch-riveting.

## 2. Materials and Methods

In the experiment, one type of material was used. This steel is marked as HX420LAD. The thickness of the tested steel sheet was 1.5 mm. HX420LAD steel sheet was a zinc coating - hot-dip galvanized on both sides. Table 1 shows the basic mechanical properties of the HX420LAD. The chemical composition of the steel sheets is shown in Table 2. It was not necessary to clean the samples before the process of clinch-riveting. Figure 1 shows a test sample according to STN 05 1122.

**Table 1.** Basic mechanical properties of the observed materials

Material	Thickness [mm]	Rp <sub>0,2</sub> [MPa]	Rm [MPa]	A <sub>80</sub> [%]
HX420LAD	1.5	490	565	19.5

**Table 2.** Chemical composition of the observed materials (% wt)

Material	Chemical composition			
	C	Mn	Si	Al
HX420LAD [1.5 mm]	0.09	1.2	0.02	0.035
	Nb	Ti	P	
	0.0055	0.015	0.016	

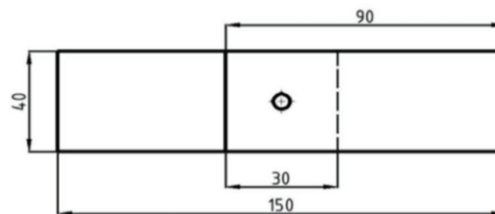


**Figure 1.** Sample dimensions according to STN 05 1122

### Clinch-riveting

Clinch-riveting is a new, innovative technique to join progressive materials. The clinch-riveting technique consists in pressing a solid rivet into the upper and lower plate; the upper plate is mechanically wedged into the lower plate, similarly to the clinching technology (shown in Fig.2). The active parts of the clinch-riveting tools are punch, die, and a sheet holder. The rivet placed directly in the joint ensures an increase in the load-bearing capacity of the joint in the critical area of the joint.

**Table 3.** The parameters of clinching

Material	Pressing force F [kN]	Rivet dimensions [mm]	Die diameter
HX420LAD (1.5 mm)	90	Ø5 x 5	Ø8 mm

The pressing force was the same for all joints made. The die with a diameter of Ø8 mm had moving segments. Steel rivets with a diameter of Ø 5 mm and a height of 5 mm were applied to create the joint. The parameters of clinching as technology are described in Tab.3. Sample created by clinch-riveting is shown in Fig. 3.

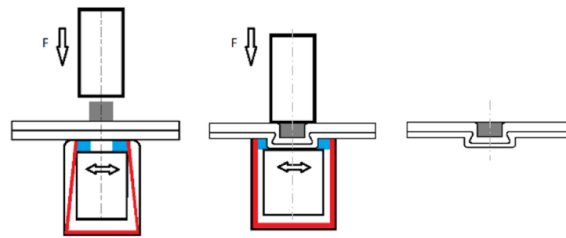


Figure 2. The process of clinch-riveting

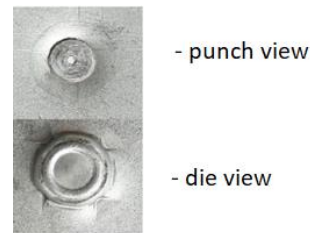


Figure 3. Joint sample created by clinch-riveting technology

### Simulating the process of clinch-riveting in the Simufact Forming software

Simufact Forming is a simulation software for users working with the technology of forming. Simufact Forming software allows for both two-dimensional (axisymmetric and planar) and three-dimensional simulations on the same graphical user interface. To simulate the technology of forming, we can use different types of common materials using mentioned software. In practice, simulation software is used to optimize the processes of joining before the joining process is implemented [7-8]. The working environment of the used simulation program is shown in figure 4.

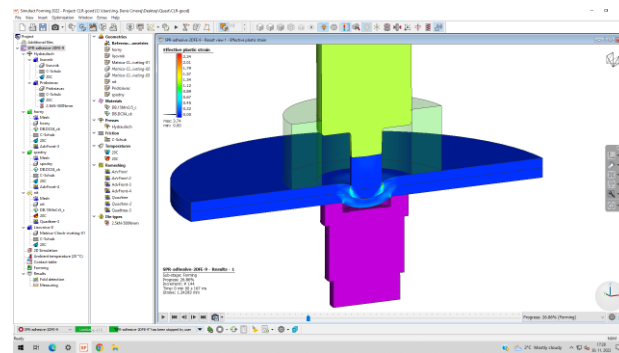


Figure 4. The working environment of the Simufact Forming

The parameters of the clinch-riveting process, necessary when defining the simulation itself include the special friction coefficient, the holding force, and the specific distance of the punch stroke. In the simulation process of the clinch-riveting, the specially shaped punch can only be moved in the specific - vertical position, with the punch making a specific vertical downward movement at a punch stroke.

The contacts between the tools and joined sheets as well as the contacts between the joined sheets were defined as frictional contacts. Between punch/die and sheets was defined as a friction coefficient of 0.12 and between sheets was defined special friction coefficient of 0.2. The important boundary condition is a holder force of sheets - 100 N that acts on the upper sheet to fix the joined sheets. At the exact moment, the distance of the stroke height has been reached, the punch performs a backward movement to the starting position. At the same time, the special force of the sheet holder stops to working. The specially shaped punch, specially shaped die, and sheet holder was specified as perfectly

stiff and non-deformable bodies. The joined sheets and rivet were defined as deformable bodies.

**Metallographic observation**

In this analysis, the changes in the microstructure of HX420LAD material were observed– see Figure 5. A microscopic analysis of metallographic sections was performed by light optical microscopes KEYENCE VHX- 5000.

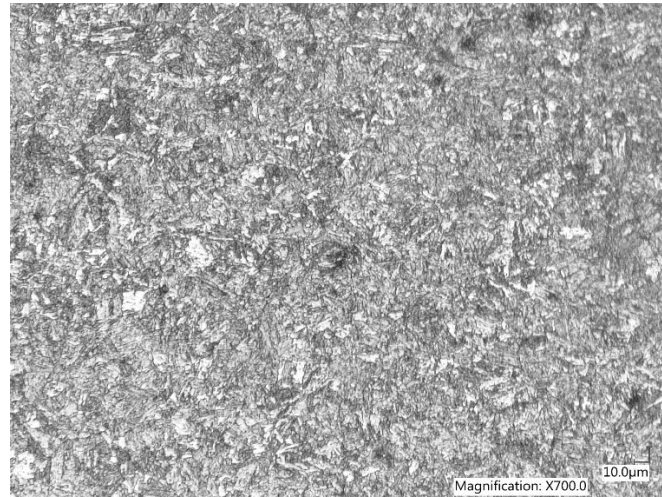


**Figure 5.** the microstructure of HX420LAD material – magnification x 700.00

**3. Results**

Figure 6 shows the development of plastic deformation during the joining process of HX420LAD steel sheets in the 4 characteristic steps.

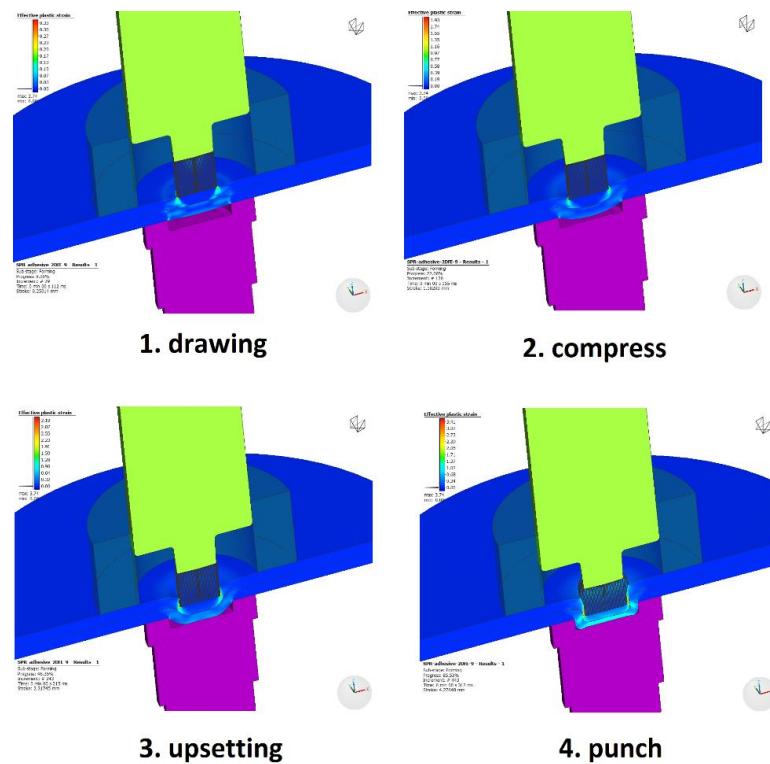


**Figure 6.** development of plastic deformation during the clinch-riveting process

For better visibility of the presented results, the view of finite element mesh was used. The most critical area of the joint during the clinch-riveting process is the sheet metal on the punch side. The value of the maximum plastic deformation during the process of clinch-riveting is located just in the upper sheet at the point where it is excessively thinned (area of the neck of the joint). It is possible to verify the simulation and compare it to the results of a real joining process - clinch-riveting. Figure 7 shows a comparison of the cross-sections between the real joint created by clinch-riveting and the joint resulting from the simulation.

Based on the results, real values of the process of clinch-riveting can be compared with values after simulation, such as the position and shape of the rivet, the thickness of individual sheets, or the interlocking between the rivet and joined sheets. Comparison of the cross-sections between the real joint created by clinch-riveting technology and the joint resulting from the simulation (see Fig.7). Fig. 7 also contains the dimensions - the thickness of the sheets in the bottom, on the side and the dimensions of the rivet. After comparison we can deduce, that the deviations are significantly different.

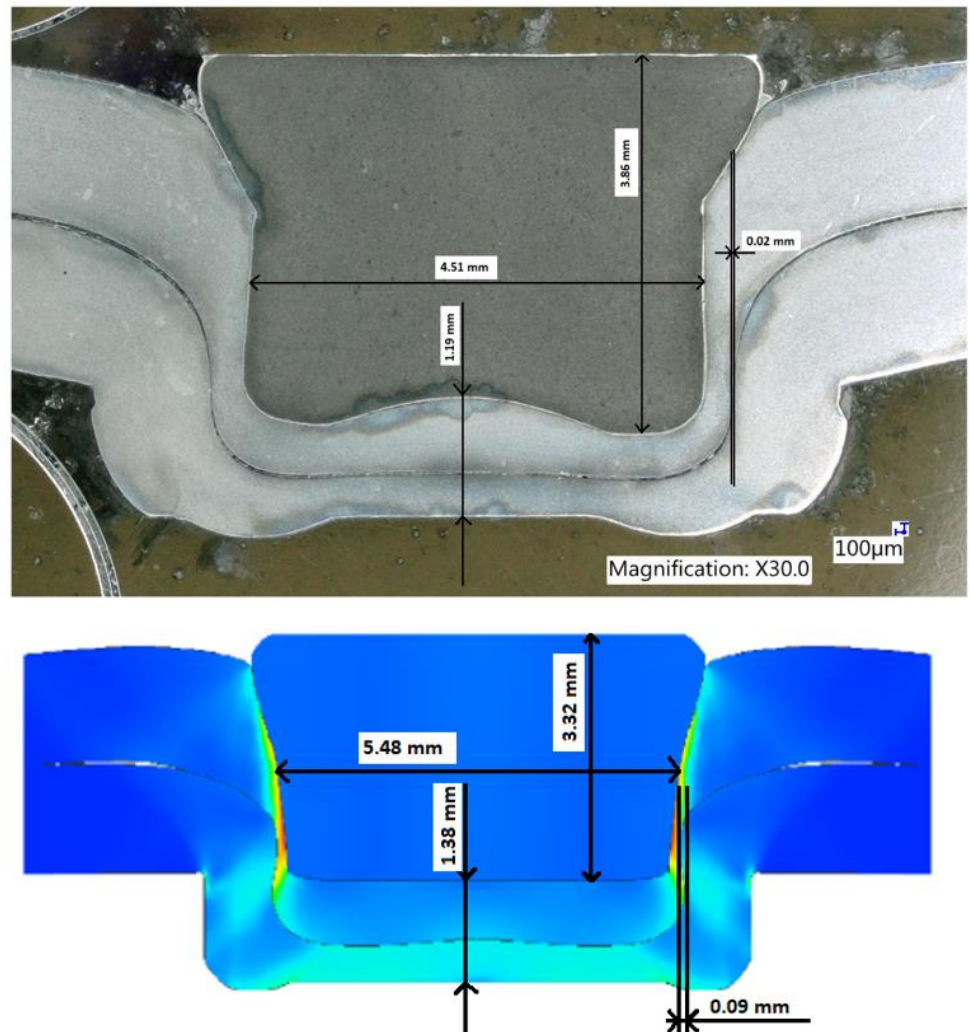


**Figure 7.** Comparison of the cross-sections between the real joint created by clinch-riveting technology and the joint resulting from the simulation.

## 5. Conclusions

The paper presented the simulation of the clinch-riveting process. The simulation has been simplified into 2D conditions based on the axial symmetry of the process of clinch-riveting. The results of the simulation of the process of clinch-riveting in the form of the representation of the plastic deformation in the steel sheets during the individual mechanical joining stages were observed.

Based on the results of the performed experiments and based on the simulation, it can be stated:

- The joints created by using technology such as clinch-riveting are classified as joints created by environmentally friendly joining techniques, they are less harmful to the environment, especially when joining hot-dip galvanized steel sheets.
- Based on the results, real values of mechanical joining as clinch-riveting can be compared with values after simulation, such as the position and shape of the rivet, the thickness of individual sheets, or the interlocking between the joined sheets (called the "S" shape of the sheets).
- Based on the visual cross-section comparison of the results, it is possible to state that the result of the simulation does not correspond to the real experiment, there is a significant difference. The rivet is not equally deformed, neither the upper sheet nor the bottom sheet when comparing the results of simulation and real clinched joint.

**Acknowledgments:** The author is grateful for the support of experimental works by project **VEGA 1/0259/19** - Research of innovative forming and joining methods to improve the performance of thin-walled components.

## References

1. E. Kaščák, et al.; Application of modern joining methods in car production. Processes Examples Strength. Rzeszów, pp.143.
2. R. Kuziak, et al.; Advanced high strength steels for automotive industry, Archives of Civil and Mechanical Engineering, 2008, vol.8, issue 2, pp.103-117.
3. E. Kaščák, et al.; Clinchrivet as an alternative method to resistance spot welding, Acta Mechanica et Automatica, 2013, vol. 7, pp.79-82.
4. E. Spišák, et al.; Joining materials used in car body production by clinching, Chemické listy, 2012, vol. 106, No. S, pp. 541-544.
5. C. Shi, et al.; Experimental investigation of the flat clinch-rivet process. Thin-Walled Structures, 2022, vol. 171, 108612.
6. K. Mori et al.; Mechanism of superiority of fatigue strength for aluminium alloy sheets joined by mechanical clinching and self-pierce riveting, 2012, vol. 212, issue 9, pp. 1900-1905.
7. E. Kaščák, et al.; Finite element calculation of clinching with rigid die of three steel sheets. Strength of Materials. 2017; vol. 49, pp. 488-499.
8. L. Potgorschek, et. al.; Numerical simulation of hybrid joining processes: self-piercing riveting combined with adhesive bonding. Procedia Manufacturing. 2020, vol. 47, pp. 413-418.



# Development and production of in-ear hearing aids (ITE) using additive manufacturing

Gabriela Dancáková<sup>1,\*</sup>, Teodor Tóth<sup>1</sup>, Viktória Rajtúková<sup>1</sup>, Dominika Belvončíková<sup>1</sup>, Tomáš Breškovič<sup>1</sup>, Jozef Živčák and Radovan Hudák<sup>1</sup>

<sup>1</sup> Department of Biomedical Engineering and Measurement, Faculty of Mechanical Engineering, Technical University of Kosice, Kosice; gabriela.dancakova.2@tuke.sk

<sup>2</sup> Trauma Surgery Clinic, L. Pasteur University Hospital Kosice

\* Correspondence: gabriela.dancakova.2@tuke.sk; Tel.: +421 55 602 26 55

**Abstract:** The publication is focused on the development and production of in-ear hearing aids (ITE - in the ear). The study describes the manufacturing process of an in-ear hearing aid using 3D modeling and additive technology. It also provides a closer look at the variants and circumstances involved in the production of a hearing aid cup. The publication describes in more detail the individual stages of production - from taking and scanning the impression of the patient's ear, to the physical production of the cup (shell), in which the electronic components of the hearing aid are placed. At the end of the publication, the benefits that the production process using additive technology provides for practice, science, research and, last but not least, education are summarized.

**Keywords:** ITE 1; hearing aid 2; shell 3; 3D printing 4; CDLP 5

## 1. Introduction

Hearing is one of the five basic senses. It is the most sensitive human sense that perceives sound, which in this context can mean speech, music, noise, etc. Hearing enables a person to identify and recognize objects in the world based on the sound they produce hearing enables communication using sound [1].

A healthy, young auditory system can silently detect tones with frequencies from about 20 to 2,000 Hz. The auditory field (or hearing area) is the range of all sounds that the human ear can perceive. At each frequency there is a different difference in intensities that we hear. The human auditory organ is most sensitive in the frequency range of 1–5 kHz [2,3,4].

People can perceive sound in several ways. Through the air, when the waves spread from the external environment through the entire auditory system, i.e., through the outer, middle, and inner ear to the brain. Another method of sound transmission is the bone path, where the sound vibration is transmitted through the bones of the skull directly to the cochlea of the bony labyrinth [1].

Hearing disorders are caused by damage to the auditory system, that is, when any of its parts is disabled [5]. If we talk about reduced function of the auditory system, it is possible to talk about hearing impairment, reduced hearing acuity, unilateral hearing impairment, hearing loss or deafness [6].

A hearing aid is an electronic aid that enables a person with a hearing impairment to better hear sounds from the environment and to understand speech more clearly. This results in an overall improvement of the client's communication skills. Hearing aids are able to automatically emphasize sound coming from a certain direction, focus on speech, suppress ambient noise, or compress sound frequencies so that they are audible to the ear [6,8].

An in-the-ear hearing aid (ITE) is an electroacoustic amplifier that amplifies weak sound to the intensity needed to accommodate the ear. It can be adapted to different hearing losses. If the hair cells in the cochlea are damaged, the remaining cells can pick up the amplified sound and send it as an electrical signal to the brain [7].

All hearing aids use the same basic parts to transmit sounds from the environment to the ear and amplify them. Most hearing aids are digital, and all are powered by either a traditional hearing aid battery or a rechargeable battery. Small microphones collect sounds from the environment. A computer chip with an amplifier converts the incoming sound into a digital code. The device analyzes and adjusts the sound based on the patient's hearing loss, listening needs and the level of sounds around the user. The amplified signals are then converted into sound waves and reach the ears through speakers [7,9,10].

Currently, there are several types of ITE devices on the market [10,11]. The focus of this publication is the production of an ITE shell using the method of additive technology. The topic of the publication is highly topical considering the increasing number of people with hearing impairments. The reality is that, according to information, no company is currently involved in the physical production of hearing aid structures in Slovakia. Listening devices are loaded into shells that were manufactured abroad and imported to Slovakia. Alternatively, electronic components will only be set up in Slovakia.

## 2. Materials and Methods

To determine a suitable digitization process to produce an ITE shell, it is necessary to determine the materials, equipment, and method of the procedure. These important parameters are described in the next chapter.

Materials: Silicone impression material of medical quality, scanner E3 (3Shape, Copenhagen, Denmark) - stationary scanner, object scanning accuracy up to 7 micrometers [11]. Modeling using the 3Shape Shell Designer software (3Shape, Copenhagen, Denmark) [11], this is a medical software directly intended for modeling and designing the design of a hearing aid shell. A VIDA device (EnvisionTEC, Detroit, Michigan) was used for 3D printing, which uses Continuous digital light processing (CDLP) technology. The Shell model was then transferred to the software Perfactory RP 3.2.3594 (EnvisionTEC, Detroit, Michigan), which is used to prepare the data for the 3D printer. The material e-shell 300 methacrylate (EnvisionTEC, Detroit, Michigan), transparent color, was used for 3D printing of the ITE device of the ITC type. An Otoflash UV oven (EnvisionTEC, Detroit, Michigan) was used for final curing of the model. The finalization of hearing aids, such as the application of electronic components, is carried out in designated companies.

Procedure method: After the ear impression is made, the model is scanned using the E3 scanner. The scanner scans the imprint geometry as a cloud of points, then an STL file is created (Fig. 1A). The model was designed taking into account the anatomical features of the ear impression, such as canal, opening, concha, tragus/antitragus, notch, crus, cymba/anticymba.

Designing the final shape of the hearing aid shell is a process where a virtual STL model of the ear canal that has been created by scanning is modified. After entering the digitized impression model into the 3Shape Shell Designer software, the ITE appliance category, as well as its size and coil integration, are selected. It is also necessary to enter the optional components that will be displayed during the "Simulation of electronic components" step, and also indicate whether it is the right or left ear. The "Plane cut" function, which cuts the bottom of the scan, creates a cavity inside the scan, into which the components are inserted. The plane is drawn in the software with a classic line across the lower part of the imprint. For ITE devices, this also defines the length of the device. This plane should pass through the tragus, antitragus and anticymbuses. With ITE, it is necessary to remove part of the cymbal, with ITC/CIC, the cut is applied only at the place of the crus, and with invisible types of ITE, the cut is applied only at the opening, so that the device is completely in the canal. As part of this step, it is also possible to

set "Surface offset", which creates an offset (enlarged) model from the original scan. This step is similar to covering the stamp with wax in the conventional production method. The step is necessary because the ear is a dynamic element, or the stiffness of the canal varies among patients - some have stiff ear canals, others have rather soft ones. During mandibular movements, this leads to enlargement of the auditory canal. Based on the study by R. Oliveira, R. Babcock et al. and the studies of A. Delnavaz and J. Voix, it is possible to say that the volume of the channel can increase by up to  $20 \text{ mm}^3 / \text{mm}$  or an increase in the diameter of the channel by 2 mm [13,14]. Therefore, ITE devices can fall out, and the offset from the scan of the impression is an important step. When modeling, it is also necessary to know whether it is a pediatric patient in whom the auditory canal is softer. The thickness is offset evenly. The size determines the offset between the inner and outer walls. There is usually an "offset" of 0.4 mm (Fig. 1B). Using the "Sculpt" function, it is possible to modify any artifacts, add or remove material. To smooth the final model, the software offers several options such as "Spline", "Tube", "Brush", "Spray" or "Edge Smoothness". The "Fillet" function cuts off the top of the stamp and rounds it off. The step determines how deep into the ear canal the ITE device will be placed. The 'Tip Fitting' feature allows you to select a tip fitting type and then by positioning the cutting plane it changes the depth of cut along the center line of the tip. The size refers to rounding. Using the available control points of the plane, it is possible to tilt and taper it (Fig. 1C). The addition of a vent or Vent, a tubular structure that runs along the entire length of the shell allows air to pass through the listening device (by inserting the ITE device into the ear, the air pressure inside the user's ear canal will be the same as the ambient air outside the ear). The vent also provides low-frequency reduction in the sub-1000 Hz region. "Step vent" allows you to create and determine the optimal place at the top of the channel for the placement of the vent. This step is performed to prevent occlusion (Fig. 1D).

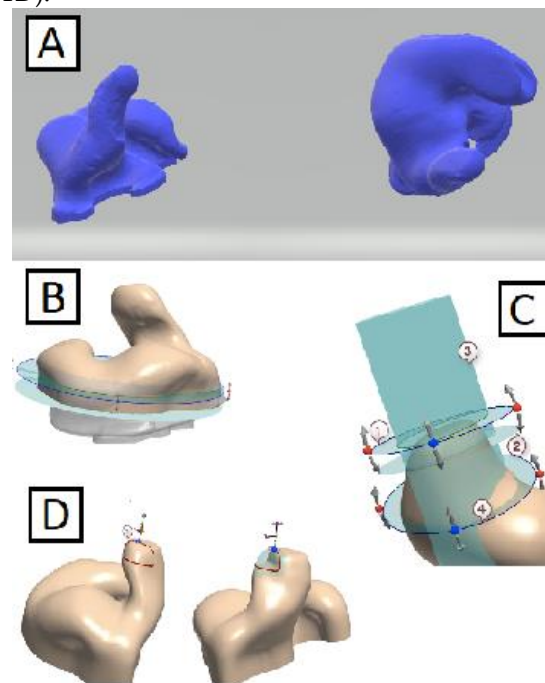


**Figure 1.** Scanned impression of the left ear (A). Using the function "Plane cut" and "Offset" (B). Using the "Fillet" function (C). "Step vent" function (D).

The "Component placement" function allows the simulation of the placement of electronic components in real time (Fig. 2A; 2B). The finalization of the ITE 3D design focuses on the shape of the device. Using the "Spline" curve, a cut is defined on the plate with a "faceplate" that is glued to the shell after production (Fig. 2C). When the shape of the device is fixed, the vent path is adjusted using the "Vent" function (Fig. 2D). It fol-

allows the simulation of the storage of the components and the addition of the "faceplate". As the last step of the 3D design, the identification of the device is placed on the surface of the cover, usually from the inside. The identification is specific to each manufacturing company, as well as the device according to the client to which it is intended (Fig. 2E).

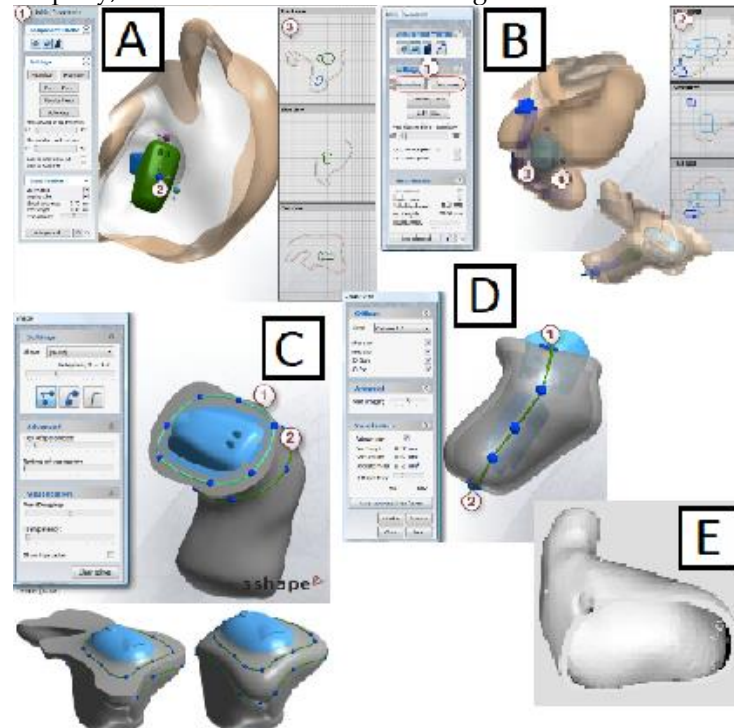


**Figure 2.** "Component placement" function (A). Editing the model and component placement (B). "Shape" function (C). Creating a vent path (D). Final 3D model of the ITE apparatus created for test printing

A VIDA 3D printer was used to produce the shell of the ITE hearing aid. It is a 3D printer using Continuous digital light processing (CDLP) technology, which creates a printout from an acrylic stock using LED light source curing. The accuracy of the 3D printing of the apparatus was set to 100 microns. The transparent color e-shell 300 methacrylate material was used to produce the ITE shell device of the ITC category. The shell model is ported to Perfactory RP 3.2.3594 software, for platform placement and support structure settings. The total 3D printing time was 64 minutes (Fig. 3A).

After printing, the print was removed from the platform (Fig. 3B). Subsequently, the supporting structures were also separated. During 3D printing, they ensured that the printout was not placed directly on the platform and thus damaged or otherwise deformed when separating from the platform. Subsequently, the shell is cleaned with isopropyl alcohol and placed in the Otofash UV curing oven. Two light bulbs in the lower part of the oven operate at a frequency of 10 flashes/second. Flashes produce very intense light radiation in the 300-700 nm spectrum. Thanks to this, additional hardening of the material is possible, which improves the final physical properties, as well as a lower content of residual monomer in the material. Also, by using a UV oven for this purpose, it is possible to harden the shell without emitting heat, which would cause deformation of the shape of the shell, which must not occur. The total time for curing the print did not exceed 700ms (Fig. 3C).

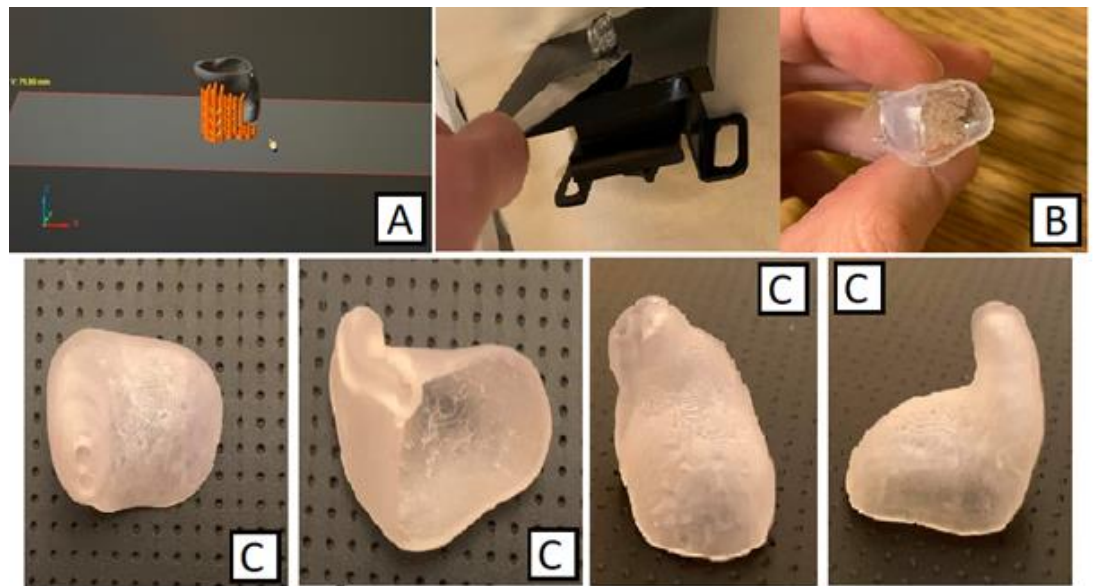


**Figure 3.** Placing the 3D model on the platform with the addition of the support structure (A). Removing the printout from the platform; the print together with the supporting structure (B). The final component of an ITE hearing aid manufactured using additive technology from different angles (C).

### 3. Results and discussion

#### 3.1. Benefits of additive technology in the production of hearing aids

The advantages of applying additive technology in the field of hearing aid production brings benefits for the technical worker as well as benefits for production.

The use of hypoallergenic material to produce the shell is attractive from the point of view that all photopolymers undergo extensive testing to ensure this property, while the curing method, which changes the chemical structure of the material (decomposes the monomer), also helps. Another advantage of these materials is increased resistance to pressure and external influences.

Among the main advantages of 3D design, reproducibility can be included, i.e., the possibility of re-3D printing of the shell model of the device previously stored in the database. This reduces the waiting time for the patient, as well as the fact that it is not necessary for the ear impression to be taken again in case of loss or malfunction of the device. 3D scanning ensures an improved retention position of the appliance, which is important due to the dynamic nature of the ear canal. It consists of cartilaginous and bony parts. The cartilaginous part of the canal moves together with the entire temporomandibular apparatus. In some cases, this leads to retention problems, but when modeling using a CAD system and 3D printing, this problem is eliminable. This advantage is especially important for invisible types of ITE.

From a technological point of view, the same thickness of the wall of the entire shell as well as of the vent is especially noteworthy, where this feature could not be guaranteed during conventional production, as it depended to a large extent on the knowledge of the technician. With the knowledge and experience of the technical worker, in the case of the conventional production method, more detailed modifications are also related. Using modeling software, it is possible to correct imperfections on the scan of the original imprint.

Due to the high accuracy of printing 3D devices, it is possible to produce the smallest possible devices. This feature is given by the possibility of additive manufacturing and especially by accurate modeling, while the designer relies to a large extent on "elec-

tronic components simulation" and "collision control" for the selected software. This allows the electronics to not be in contact with each other or with the shell wall. The selected electronic components can thus be tightly stored inside the 3D printed cup.

In addition to the mentioned advantages for the technician, or additive manufacturing is advantageous for the patient as well. It mainly concerns a better and more accurate geometry of the product, as well as its complexity. When manufacturing the shells of ITE devices, it is a highly complex geometry on a small scale and therefore requires high precision manufacturing. More accurate production is also directly related to material consumption. When using additive technology, there is a reduction in excess material stocks and thus also waste. The elimination of multiple grinding and trimming in production is in the context of high precision manufacturing in additive manufacturing. It is not necessary to gradually sand and trim the cured photopolymer in the process. Instead, it is enough to sand down the support structures that were used in 3D printing.

Due to the fact with which 3D devices work with precision, the risk of errors is also reduced.

The software and equipment used in this production are designed intuitively, and thus it is possible to quickly train personnel without previous experience in working with such equipment and software.

With the possibility of placing shells within the 3D device platform, it is also possible to talk about serial production. Despite the fact that each print is unique, which was a problem with the conventional production method, when adapting additive manufacturing, this is not the case. Today it is possible to produce/print several shell models at the same time. The only limitation is the size of the 3D printer platform. The entire production process is thus cheaper and faster.

From the above-mentioned advantages of additive technology compared to conventional methods of manufacturing ITE cochlear hearing aids, it can be concluded that additive technology could be beneficial in this area, mainly due to its accuracy and speed of production of individual cochlear hearing aids.

**Acknowledgments:** This research was supported by project KEGA 023TUKE-4/2020 Increasing the synergy of methods of teaching biophysics using laboratory equipment and diagnostic devices aimed at measuring physical and technical quantities. This research was supported by project KEGA 021TUKE-4/2022 Implementation of computed tomography in an interdisciplinary technical and scientific space. This research was supported by project VEGA 1/0387/22 Development and testing of systems for controlled stimulation of cell growth in a bioreactor environment using computer vision.

**Conflicts of Interest:** The authors declare no conflict of interest.

## References

1. Oghalai, J.S., Browell W.E., Lalwani, A.K.: CURRENT Diagnosis & Treatment in Otolaryngology - Head & Neck Surgery. 3rd ed. LALWANI, A.K. (ed.), The McGraw-Hill Companies, Untined States, 2012
2. Dobie, R.A., Van Hemel S.B.: Basics of Sound, the Ear, and Hearing. Hearing Loss: Determining Eligibility for Social Security Benefits. National Academies Press, Washington, 2004. 1st ed., s. 10
3. Møller, A.R.: Hearing – Anatomy, physiology, and disorders of the auditory system. 2nd ed. Elsevier, London, 2006, s. 128-140
4. Grandjean, P., Nexer, G.: Infrasound and Ultrasound: Risks and the means of protection. [https://www.hearingprotech.com/pdf/en/Pub\\_Infrasound-and-ultrasound-risks-and-means-of-protection.pdf](https://www.hearingprotech.com/pdf/en/Pub_Infrasound-and-ultrasound-risks-and-means-of-protection.pdf), 2015
5. Balkany, T.J., Brown K.D.: The ear book – A complete guide to ear disorders and health. Johns Hopkins University Press, Baltimore, 2017
6. Olusanya. B.O., Davis A.C., Hoffman H.J.: Hearing loss grades and the International classification of functioning, disability and health. Bull World Health Organ. 97 (10), 2019, s. 725–728
7. Hearing Aid. MadeHow. Vol. 2. <http://www.madehow.com/Volume-2/Hearing-Aid.html>
8. Breaker, D.: Hearing Aid Buyer's Guide: Types of Hearing Aids. MD Hearing aid. <https://www.mdhearingaid.com/en/blog/types-of-hearing-aids-buyersguide>, 2018
9. Instructions for use. FCC ID. <https://fccid.io/U28FUIITE01/User-Manual/User-Manual-770755>, 2007

10. Čo je načúvaci prístroj. Akustik. <https://www.akustik.sk/a/12/co-je-nacuvaci-pristroj>
11. Medical software ShellDesigner™. MedicalExpo by virtualexpo group. <https://www.medicalexpo.com/prod/3shape/product-71366-674175.html>
12. Unitron, Inc. Unitron custom products reference guide. [https://www.unitron.com/content/dam/unitron-2014/documents/gc-specific/US/Custom%20ITE%20Page/2349%20MANL%20028-5347-03%2001-16%20Custom%20Product%20Reference%20Guide\\_mediumres.pdf](https://www.unitron.com/content/dam/unitron-2014/documents/gc-specific/US/Custom%20ITE%20Page/2349%20MANL%20028-5347-03%2001-16%20Custom%20Product%20Reference%20Guide_mediumres.pdf), 2015
13. Oliveira, R., Babcock, M., Venem, M., Hoeker, G.: The Dynamic Ear Canal and Its Implications. Hearing review. <https://www.hearingreview.com/practice-building/practice-management/the-dynamic-ear-canal-and-its-implications>, 2005
14. Delnavaz, A. Voix, J.: Ear canal dynamic motion as a source of power for in-ear devices. Journal of Applied Physics. 113, 2013, s. 1-9



# Structural design and strength analysis of non-standardized metal hydride vessel for mobile applications

Filip Duda <sup>1\*</sup>, Natália Jasminská <sup>2</sup>

<sup>1</sup> Technical University of Košice, Faculty of Mechanical Engineering, Department of Power engineering  
filip.duda@tuke.sk

<sup>2</sup> Technical University of Košice, Faculty of Mechanical Engineering, Department of Power engineering  
natalia.jasminska@tuke.sk

\* Correspondence: filip.duda@tuke.sk.

**Abstract:** The article describes the design and strength calculation of a low-pressure steel vessel, which has a non-standardized shape and is used to store hydrogen in the structure of TiFe-based metal alloys. The design of the structure is made of three parts, namely the elliptical part, the connecting part and the cylindrical parts in which the passive heat exchangers are placed. The strength calculation was carried out as a result of the determination of the ideal thickness of the vessel wall for the implementation of the required vessel in operating conditions.

**Keywords:** Hydrogen, metal alloy, metal hydride reservoir, hydrogen storage, strength calculation, non-standardized shape

## 1. Introduction

Hydrogen is receiving more and more attention in Europe and around the world. The most important aspect is the fact that the energy recovery of green hydrogen in fuel cells produces no air emissions. Thus, it represents a possible solution to partially decarbonize industrial processes and economic sectors.

Today, several EU member countries as well as other developed economies - the United States of America and Japan - are testing the possibilities of using hydrogen technologies in the field of individual and mass transport through the implementation and introduction of hydrogen solutions for means of transport. One of the basic challenges is increasing the safety of hydrogen fuel storage. Currently, hydrogen fuel is stored at extremely high pressures of 35-95 MPa. Today, there are options for storing hydrogen in various compounds that provide better storage options.

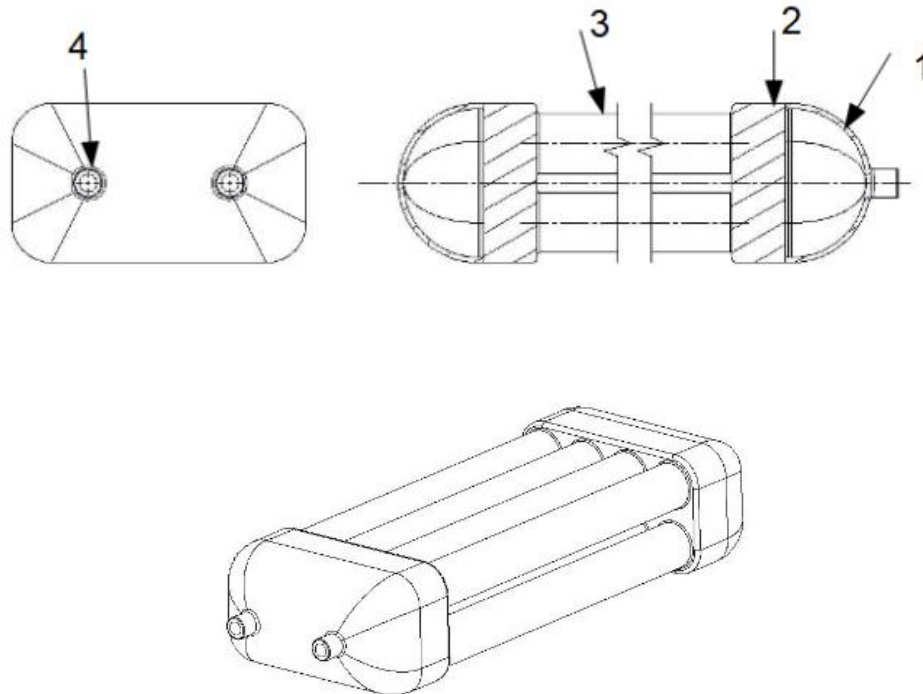
The implementation of hydrogen technologies with metal hydride vessels provides scope for increasing the safety and storage of H<sub>2</sub> at lower pressures. Metal hydride storage vessels have some advantages over other storage options. They are characterized by a relatively high volumetric energy density.

This paper focuses on the design of an efficient hydrogen storage system using a metal hydride alloys. It solves the problem of the design of a non-standardized metal-hydride vessel with internal heat exchangers, which serve to remove the generated heat during the absorption of hydrogen into the structure of the metal-hydride alloy.

## 2. Structural design of non-standardized metal hydride vessel

The structure consists of three parts, namely the bottom of a rectangular shape, the connecting part and the cylindrical tubes in which there are passive heat exchangers. The structural design of the non-standardized vessel was solved so that all circumferential welds on the structure were controllable. The connecting part connects the rectangular bottom with the cylindrical pipes shown in Figure 1. The cylindrical pipes are wrapped in a casing that serves for the flow of cooling liquid. The material of which the vessel is

made out of is stainless steel 316L-1.4404. The mechanical properties of this steel are shown in Table 1.



1- rectangular bottom of atypical shape, 2- connecting part,  
 3- cylinder tubes with passive internal heat exchangers,  
 4-Flange NPT ¼"

**Figure 1.** Structural design of the metal hydride vessel

**Table 1. Mechanical properties of stainless steel 316L-1.4404**

0.2% Re (MPa)	Rm (MPa)	$\rho$ (kg·m <sup>-3</sup> )	$\mu$	E (MPa)
205	515	7950	0.3	2.1·10 <sup>5</sup>

Where: Re-yield strength, Rm-strength strength,  $\rho$ -density,  $\mu$ -poisson's number and E-Young's modulus of elasticity.

Table 2 shows the individual parameters of the designed vessel.

**Table. 2 Parameters of the designed vessel**

The weight of the empty vessel	19 kg
Weight of metal hydride	22.557 kg
Total weight of the vessel with MH	41.557 kg
Metal hydride volume	6.44·10 <sup>-3</sup> m <sup>3</sup>
Mass of stored hydrogen	0.31 kg
Volume of hydrogen	4.28 m <sup>3</sup>

Generated heat

37060.5 kJ

### 3. Strength calculation of the non-standardized metal hydride vessel

The strength calculation of the reservoir was carried out in the ANSYS Static Structural program. At the beginning of the simulation, it is necessary to define the boundary conditions and determine the material values for stainless steel 316L-1.4404. Boundary conditions used in simulations:

- Adjustment of fixed support, which is located at the bottom of the vessel
- A pressure setting of 3 MPa, which represents the maximum working pressure, and later the internal pressure was changed to 4.7 MPa, which represents the maximum test hydraulic pressure above atmospheric.
- Command hydrostatic pressure with density of  $7000 \text{ kg}\cdot\text{m}^{-3}$  in the inside area of the vessel, which represents the metal hydride load.
- Temperature condition of  $60 \text{ }^\circ\text{C}$ , which represents the maximum working temperature with the use of a metal alloy and is also considered the limiting temperature for the absorption of the alloy by hydrogen.
- Standard Earth gravity upon vessel has been set.

In Figure 2, it is possible to see the maximum stresses that arise on the vessel and are considered safe, because the values of the maximum stresses did not approach the value of the yield strength point of the selected material.

Table 3 shows the simulation results at a working pressure of 3 MPa, and Table 4 shows the simulation results at a maximum test pressure of 4.7 MPa above atmospheric.

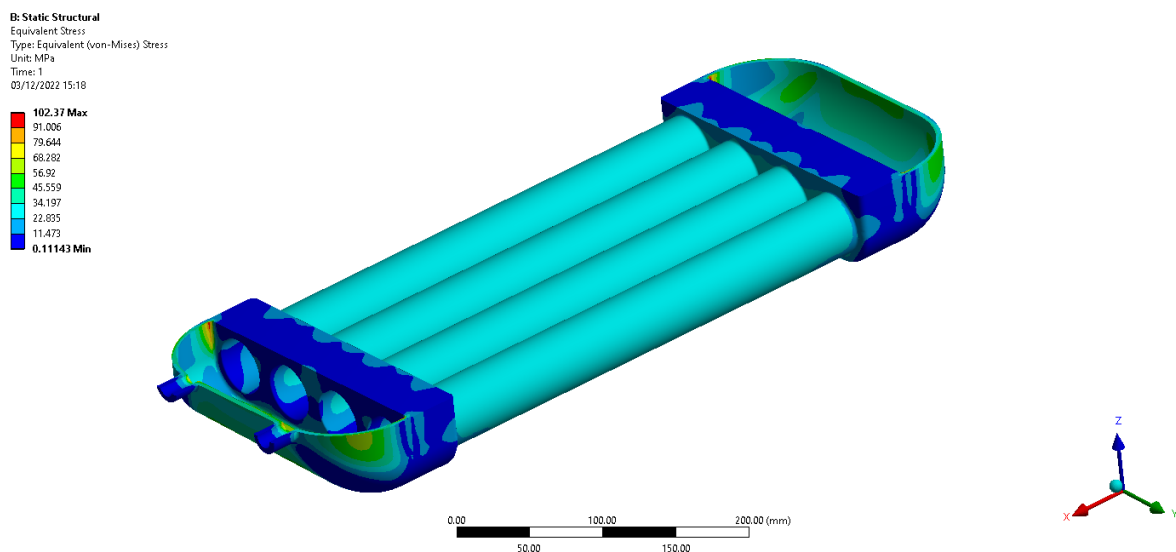


Figure 2. Emerging stresses on the vessel at a working pressure of 3 MPa

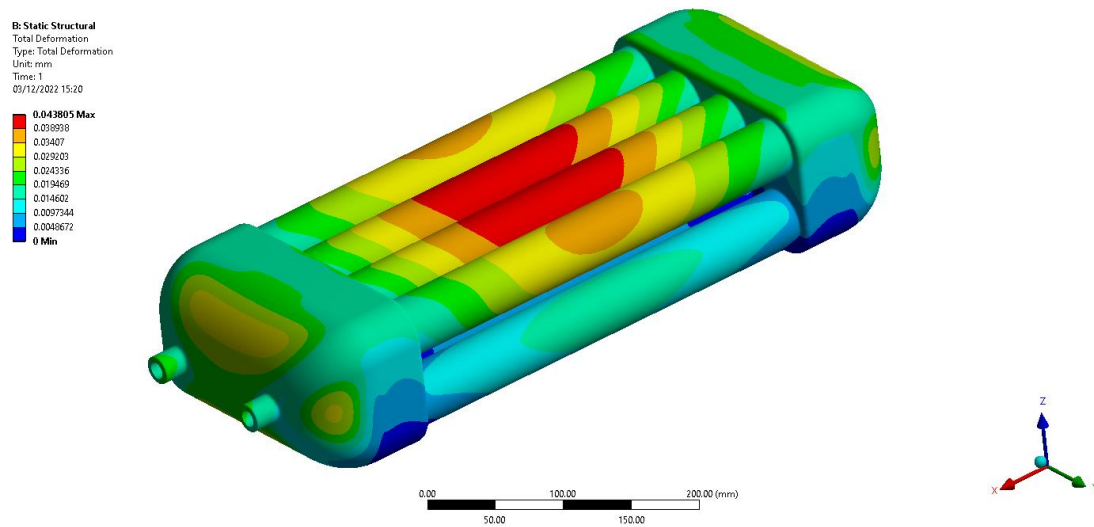


Figure 3. Emerging total deformations on the vessel at a working pressure of 3 MPa

Table 3. Simulation results at an internal pressure of 3MPa

<b>Total deformation</b>	0.04 mm
<b>Directional deformation in x-axis</b>	0.031 mm
<b>Directional deformation in z-axis</b>	0.04 mm
<b>Field of reduced stresses according to Von Misses</b>	102 MPa

Table 4. Simulation results at an internal pressure of 4.7MPa

<b>Total deformation</b>	0,0687 mm
<b>Directional deformation in x-axis</b>	0,049 mm
<b>Directional deformation in z-axis</b>	0,068 mm
<b>Field of reduced stresses according to Von Misses</b>	160.37 MPa

#### 4. Discussion

From the simulation in the Ansys Static structural program, it was found that the non-standardized vessel fully meets the requirements for the operational parameters of hydrogen storage from a strength point of view. With the help of simulation, suitable thicknesses of individual parts of the vessel structure were chosen with respect to the required structural strength, but also with respect to the distribution of the temperature field during the absorption and desorption of hydrogen.

#### 5. Conclusion

From the results of the simulation, it was found that the tension that arose on the vessel at the maximum test hydraulic pressure above the atmospheric 4.7 MPa did not exceed the yield point of the selected material 316L-1.4404. The next step in solving the designed atypical metal hydride reservoir would be to verify the spread of heat transfer

through simulation and to propose a suitable method of cooling the reservoir during the hydrogen absorption process.

**Acknowledgments:** This paper was written with the financial support from the VEGA granting agency within the project solutions No. 1/0626/20, No. 1/0532/22, and No. 1/0224/23 from the KEGA granting agency within the project solutions No. 012TUKÉ-4/2022 and with financial support from the granting agency APVV within the Project Solution No. APVV-15-0202, APVV-21-0274 and APVV-20-0205.

## References

1. Murín, Justín; Hrabovský, Juraj; Kutiš, Vladimír. *Metóda Konečných Prvkov Vybrané kapitoly pre mechatronikov*, Slovenská technická univerzita v Bratislave 2014
2. BOCKO, Jozef; Lengvarský, Pavol; Huňady, Róbert; Delyová, Ingrid. *Simulácia v programe ANSYS*. Stojnícka fakulta, Technická Univerzita v Košiciach, 2020.
3. Lototsky, Mykhaylo; Tolj, Ivan; Klochko, Yevgeniy; Wafeeg Davids, Moegamat; Swanepoel, Dana; Linkov, Vladimir. *Metal hydride hydrogen storage for fuel cell utility vehicles*, HySA Systems Competence Centre, South African Institute for Advanced Materials Chemistry, 2019.
4. Babu, Rajesh; Gugulothu, Santosh Kumar; *CFD analysis of heat transfer enhancement by using passive technique in heat exchanger*, Department of Mechanical Engineering, GITAM University, India, 2015.
5. Kumar, Mukesh; Chandrasekar. *CFD analysis on heat and flow characteristics of double helically coiled tube heat exchanger handling water nanofluids*, Department of mechanical engineering, University College of Engineering, India, 2019.
6. Masaryk, Michal; Ferstl, Karol; *Prenos Tepla*, Strojnícka fakulta, Slovenská Technická Univerzita v Bratislave, Bratislava, 2011

# Mapping of the surrounding environment of the mobile robot based on the LiDAR localization system

Maksym Grytsiv <sup>1\*</sup>, Marek Sukop <sup>1</sup> Dušan Mlinarček, Dávid Kovaľuk

<sup>1</sup> Technical University of Kosice, Department of Production Technology and Robotics.

\* Contact: maksym.grytsiv@tuke.sk; Tel.: +421 55 602 3156

**Abstract:** This article describes the possibilities of using LiDAR laser scanning systems and their use in localization and spatial mapping for mobile robotics. Using distance data to surrounding objects from 2D scanning is an opportunity to localize the position of the robot. The work is divided into two parts. The first part is about the possibilities of 2D scanning and the second part compares the obtained results with different LiDAR settings. Of course, to obtain an autonomous robot, these data must be processed by the processor installed on the robot, for which the program will be written.

**Keywords:** Mobile robot, Measurements, LiDAR, Localization, 2D scanning.

## 1. Introduction

Testing was performed based on LiDAR (Figure 1) from Slamtec – RPLiDAR A2M8 360° and Frame grabber application for monitoring, setting LiDAR and obtaining measurement results [1]. There are many implementations of 2D SLAM and 3D mapping with different sensor configurations. Most hardware configurations use a dedicated sensor for 2D SLAM along with additional sensors used for 3D data collection. This article discusses the basics of 2D mapping with the help of a single LiDAR sensor and for the future use of the most suitable methods of scanning the environment of indoor spaces with effective settings in robot localization.

To obtain the results, a base was used - the construction of a mobile robot (Figure 2), on which the LiDAR system was installed. The sensor is directly connected to the computer to receive and process the received data.



Figure 1 RPLiDAR A2M8 360°

By recording not only the time it takes for the laser beam to return, but also the angle at which it bounces, LiDAR data can be combined with other information to create highly accurate 3D maps. Professional LiDAR systems are often paired with GPS devices, another technology now widely used [6].

Basic sensor data:

Model		A2M8
Measurement range		0.2 m - 12 m
Sampling frequency		8000 fps
Rotation speed		10Hz (5Hz-15Hz)
Angular resolution		0.45°

Tab.1 Features LiDAR

RPLiDAR A2M8 is an improved version of the 2D laser scanner (LiDAR). The system can perform 2D 360-degree scanning with a range of up to 12 meters (Tab. 1). The generated 2D data creates point clouds that can be used for mapping, localization, and modeling of objects/environment.

### 2. Testing LiDAR

The test space, assembled from a base plate measuring 1.2x1.2m, was continuously delimited around by randomly arranged walls (Figure 2). The LiDAR was connected via an adapter and cable directly to the computer.



Figure 2 Test space

On the left side of the picture, the real location of the robot with the sensor in the test area is shown, while on the right you can see the results from the LiDAR sensor in the form of point clouds that create a map.

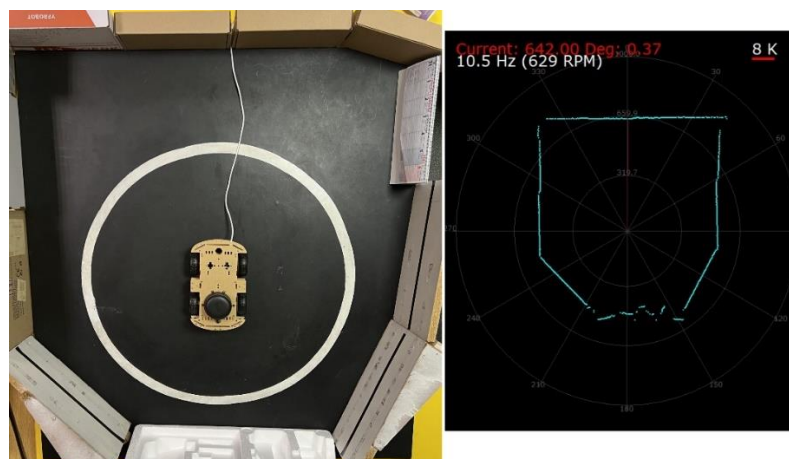


Figure 3 LiDAR mapping result

To achieve the necessary results, we will use the settings of the laser sensor according to the possibilities of the application, and we will test the different frequency of revolutions of the measuring head of the sensor.



Figure 4 Mode and speed settings

Each mode has its own humidity, sampling quality and number of created points. When applying an autonomous robot, it will also be necessary to consider the energy consumption of these variants. At high revolutions, we have a better sensor response, but more energy consumption, a smaller number of points.

### 3. Measurement results

All measurements were performed at one point in approximately the middle position on the test surface and were repeated 10 times for each LiDAR scanning mode. The results of those measurements are shown in the graph on Figure 5. For a better representation of the results of the number of measurements, additional graphs were created for different modes: "standard", "express" and "boost" Figure 7.

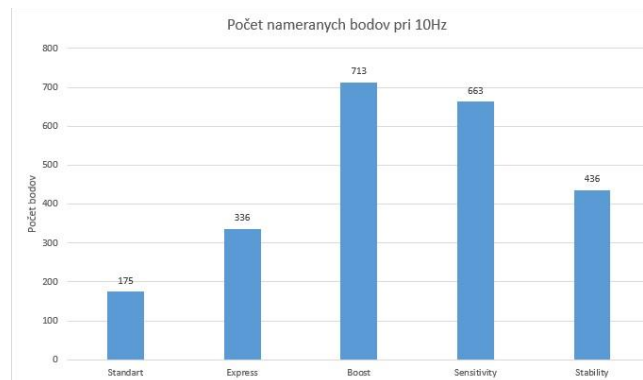


Figure 5 The number of scanned points in different modes

Standard	175
Express	336
Boost	713
Sensitivity	663
Stability	436

Tab. 2 Number of scanned points

According to Tab. 2, it can be seen that the largest number of points and, consequently, the best mapping quality is with the "Boost" mode. The worst results were obtained using the "Standard" mode. In the graphs in Figure 7, we compare three modes, where we find that the first mode has one point per 2, compared to "Boost", this value is equal to 0.5, thus the cloud point density is much greater.

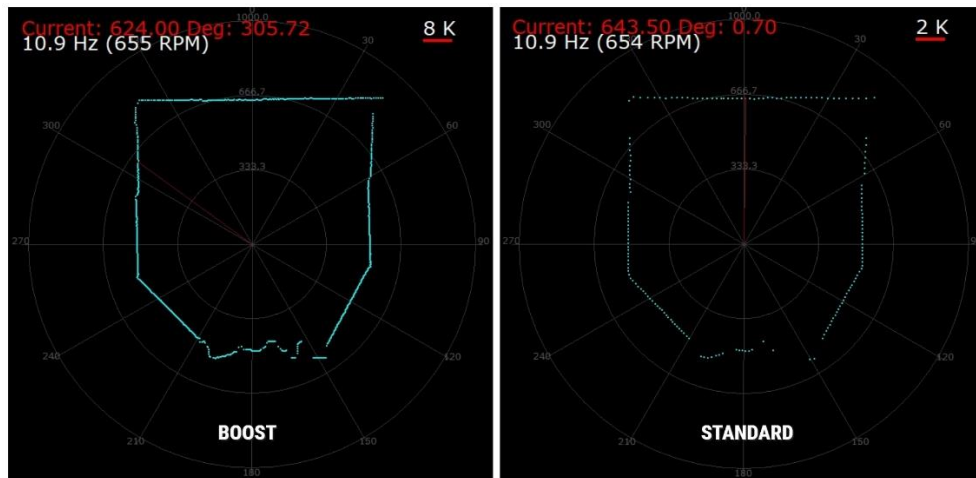


Figure 6 Comparison Boost a Standard

According to Figure 6, we define that "Standard" mode is not suitable for mapping, especially for large spaces. The problem arises at the corners of the space, where the measurement range of 2° is too low to reach the necessary points. For better quality and number of points, it is correct to select "Boost" mode.

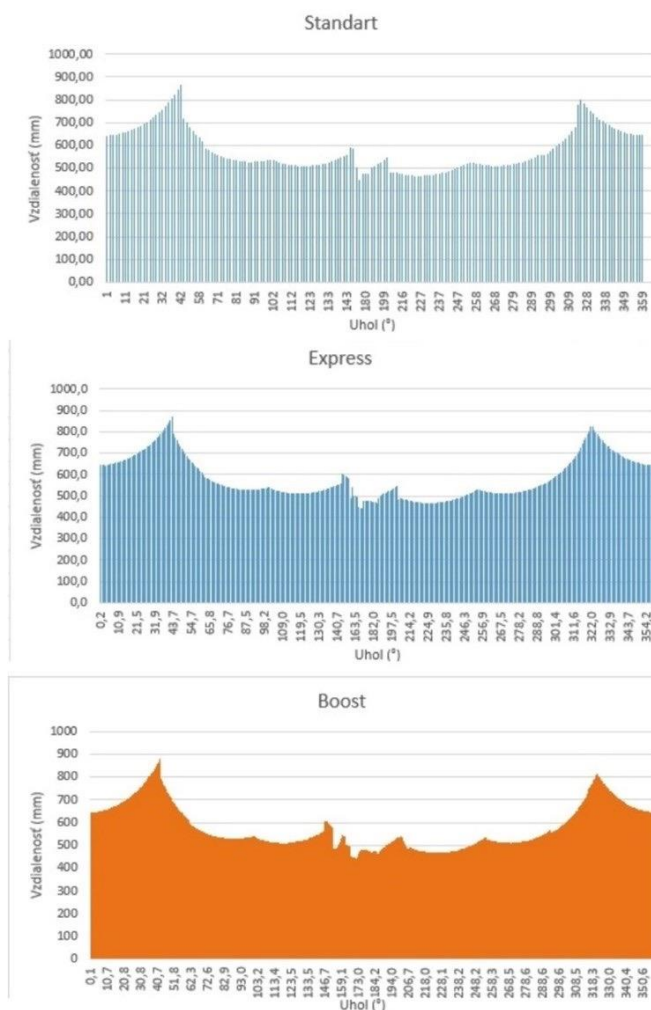


Figure 7 Accuracy of measurements in different modes

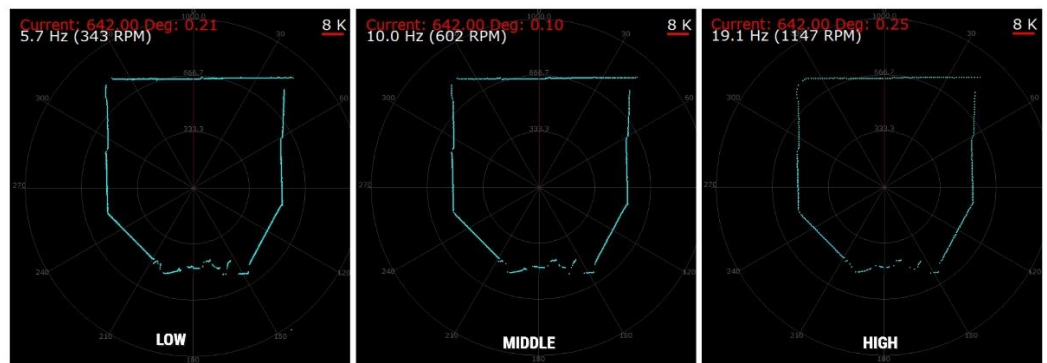


Figure 8 the difference in the number of revolutions per scan result

The dependence of the rotation frequency of the sensor head on the number of points reached is very high (Figure 8). According to the graph in Figure 9, it can be seen how the quality of mapping rapidly decreases due to the decrease in the number of created points in 2D space. But at the same time, each created point at a high frequency (19.1Hz) is renewed more often, which allows the robot to have a faster response, which is necessary at high movement speeds. The recommended frequency is 10 Hz. With such a frequency, we will get a sufficiently high-quality map, with many points, but also a sufficiently fast response.

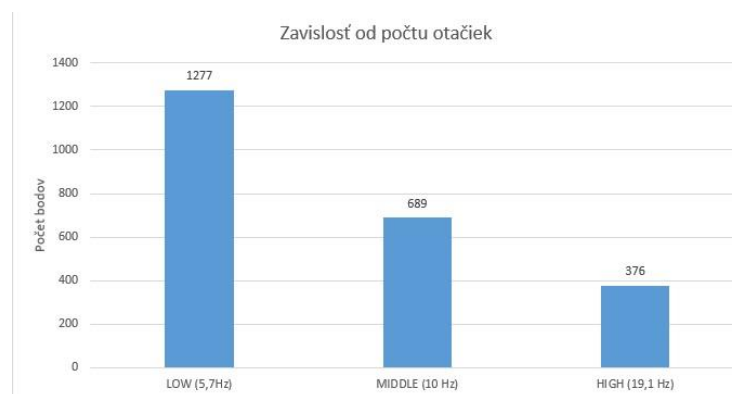


Figure 9 The dependence of the number of points on the speed of the sensor head

#### 4. Conclusion

According to the achieved results, it is possible to claim that for the further use of the laser sensor for the purposes of localization, mapping (SLAM) and for enough of the resulting points reached during the robot's movement, we need to choose a suitable LiDAR mode and suitable revolutions. It is also necessary to test this function for longer distances, for example a room with dimensions of 10m x 10m, and to find out the necessary parameters for the functioning of the autonomous robot (especially the speed of movement in space and energy consumption for the selected mode).

#### 5. Acknowledgment

This article was created thanks to the support of the KEGA project: 020TUKE-4/2022 Development and implementation of new approaches in the teaching of industrial and collaborative robotics.

## References

1. D208\_SLAMTEC\_rplidar\_datasheet\_A2M8. Slamtec [online]. 2017. Dostupné z: [https://bucket-download.slamtec.com/20b2e974dd7c381e46c78db374772e31ea74370d/LD208\\_SLAMTEC\\_rplidar\\_datasheet\\_A2M8\\_v2.6\\_en.pdf](https://bucket-download.slamtec.com/20b2e974dd7c381e46c78db374772e31ea74370d/LD208_SLAMTEC_rplidar_datasheet_A2M8_v2.6_en.pdf)
2. H. Durrant-Whyte and T. Bailey, Simultaneous localization and mapping (SLAM): part I The Essential Algorithms, *Robotics & Automation Magazine*, vol. 2, pp. 99-110, 2006.
3. J. Engel, T. Schöps, D. Cremers. "LSD-SLAM: Large-Scale Direct Monocular SLAM", in Proc. of European Conf. on Computer Vision (ECCV), Zurich, Switzerland, 2014, pp. 834-849.
4. F. Pomerleau, F. Colas, R. Siegwart et al., "A review of point cloud registration algorithms for mobile robotics", *Foundations and Trends® in Robotics*, vol. 4, no. 1, pp. 1-104, 2015.
5. C. Stachniss, J.J. Leonard and S. Thrun, "Simultaneous localization and mapping" in *Springer Handbook of Robotics*, Springer, pp. 1153-1176, 2016.
6. R. Kümmerle, B. Steder, C. Dornhege, M. Ruhnke, G. Grisetti, C. Stachniss, et al., "On measuring the accuracy of slam algorithms", *Autonomous Robots*, vol. 27, no. 4, pp. 387, 2009.
7. T. Bailey and H. Durrant-Whyte, "Simultaneous localization and mapping (SLAM): part II," *IEEE Robotics and Automation Magazine*, vol. 13, no. 3, pp. 108–117, Sept 2006.
8. J. Leonard and H. Durrant-Whyte, "Simultaneous map building and localization for an autonomous mobile robot," *Proceedings IROS '91:IEEE/RSJ International Workshop on Intelligent Robots and Systems '91*, no. 91, pp. 1442–1447, 1991
9. M. Montemerlo, S. Thrun, D. Koller, B. Wegbreit, et al., "Fastslam: A factored solution to the simultaneous localization and mapping problem," *Aaai/iaai*, vol. 593598, 2002.
10. T. Bailey, J. Nieto, J. Guivant, M. Stevens, and E. Nebot, "Consistency of the ekf-slam algorithm," in *Int. Conference on Intelligent Robots and Systems (IROS)*, pp. 3562–3568, IEEE, 2006.



# Evaluation of Mechanical Properties of Selected Types of Thin Steel Sheet

Július Hajduk<sup>1</sup>, Janka Majerníková<sup>2</sup>

<sup>1</sup> Technical University of Košice, Faculty of Mechanical Engineering, Department of Technologies, Materials and Computer Aided Production, Mäsiarska 74, 040 01 Košice, Slovakia, julio.haduk@centrum.sk,

<sup>2</sup> Technical University of Košice, Faculty of Mechanical Engineering, Department of Technologies, Materials and Computer Aided Production, Mäsiarska 74, 040 01 Košice, Slovakia, janka.majernikova@tuke.sk

**Abstract:** The future and survival of industries in Slovakia in a highly competitive environment depends on the use of high value-added materials and reducing production costs with respect to the environment. One of the materials that meet these conditions is high-strength steel plates, which are needed for the production of high-quality and high-performance parts in the automotive, food, electrical and other industries. We need to know their mechanical, technological, physical and chemical properties, with regard to the specified requirements of processors, for their correct and appropriate processing and use. In this paper, we are dealing with the evaluation of two types of steels, microalloyed steel and TRIP steel. The results from two process tests, uniaxial tensile test and biaxial tensile test are compared. Finally, the results of the tests are evaluated.

**Keywords:** Uniaxial tensile test, biaxial tensile test, mechanical properties, TRIP steel, microalloyed steel

## 1 Introduction

Nowadays we are facing new challenges and one of them is the most efficient use and processing of semi-finished products into final products. One of the materials processed in the automotive industry, and not only in the automotive industry, is thin steel sheets. Steel is a material with significant innovation potential. The innovative and performance capability of steel is particularly evident in the development of high-strength and ultra-high-strength steels. In order to reduce the amount of steel sheet used in the manufacture of final products, manufacturers are inclining towards reducing the thickness of steel sheet. However, this reduction must not be at the expense of mechanical properties. [1]

These requirements are met by a group of steels where we include high strength steels (HSS), advanced high strength steels (AHSS) and ultra high strength steels (UHSS). All these material groups have suitable mechanical properties to meet all stringent environmental standards, customer requirements along with economic availability for the manufacturer. For their appropriate and efficient use, we need to know their chemical composition, formability and mechanical-technological properties. Therefore, in this paper we are concerned with the evaluation of the properties of thin steel plates by uniaxial tensile test and biaxial tensile test. [2-4]

## 2 Materials and Methods

### 2.1 Materials

For the evaluation of the mechanical properties we used two types of steels, microalloyed steel with the designation H220PD Z100MBO, thickness  $a_0 = 0.80$  mm (hereinafter referred to as "M") and transformation-induced plasticity steel designated TRIP RAK40/70 Z100MBO, thickness  $a_0 = 0.75$  mm (hereinafter referred to as "T").

Both evaluated M and T steel plates were electrogalvanized on both sides and the amount of zinc is 100 g/m<sup>2</sup> (designation Z100MBO). The chemical composition of the materials is given in Table 1.

**Table 1.** Chemical Composition for Materials M, T.

Material	Chemical composition %						
	C	Si	Mn	P	S	Nb	Ti
M	0.04	0.1	0.415	0.042	0.004	0.026	0.037
T	2.4	0.2	1.683	0.018	0.003	0.004	0.009
	Cr	Cu	Ni	Zr	Mo	Al	
M	0.031	0.011	0.017	0.001	0.005	0.035	
T	0.055	0.028	0.018	0.007	0.008	1.73	

## 2.2 Methods

### 2.2.1 The uniaxial tensile test

The uniaxial tensile test is the most widespread test in which the basic mechanical characteristics of the sheet are obtained. The aim of the test, the conditions and shape of the test sample, indicating the standards STN EN ISO 6892-1, is to obtain the values of the basic mechanical characteristics. The results of this test are to assess the formability, especially deep drawing sheets, considerable importance [2].

To obtain anisotropic properties of the material, samples are taken in the 0°, 45° and 90° direction with respect to the rolling direction for the tensile test. The tensile strength  $R_e$ , tensile strength  $R_m$ , total elongation  $A_{80}$ , and uniform elongation  $A_H$  are preferably evaluated from the tensile test. The materials were tested on a TIRA- test 2300 tearing machine, which is shown in Fig. 1. A MYTUTUYO caliper with an accuracy of 0.01 mm and a Carl Zeiss Jena optical length gauge with an accuracy of 0.001 mm were also used. A flat test sample was used for the test, the dimensions of which are shown in Fig. 2. [8].



**Figure 1.** Tearing machine - TIRA-test 2300

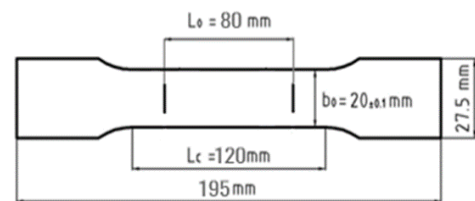


**Figure 2.** Test sample shape

For the experimental research, 3 pcs of test samples from each direction were fabricated for both materials. The measured mechanical values are shown in Table 2 and 3.

**Table 2.** Mechanical properties of Material M

Mechanical properties of sample M			
Direction [°]	Rp <sub>0.2</sub> [MPa]	Rm [MPa]	A80 [%]
0°	221	387	35
45°	228	370	37.9
90°	240	384	36.3

**Table 3.** Mechanical properties of Material T

Mechanical properties of sample T			
Direction [°]	Rp <sub>0.2</sub> [MPa]	Rm [MPa]	A80 [%]
0°	444	773	28.3
45°	443	764	25.9
90°	452	768	26.4

#### 2.2.1.1 Evaluations of the experiment

### Yield strength

Taking into account the rolling direction, the maximum value of the yield strength  $R_{p0,2}$  of the tested sheet M reaches a maximum value in the 90° direction and a minimum value in the 0° direction. Taking into account the rolling direction, the maximum yield strength  $R_{p0,2}$  of the tested sheet T reaches a maximum value in the 90° direction and a minimum value in the 45° direction.

### Tensile strength

Taking into account the rolling direction, the maximum tensile strength  $R_m$  of the tested sheet M reaches a maximum value in the 0° direction and a minimum value in the 45° direction. Taking into account the rolling direction, the maximum tensile strength  $R_m$  of the tested sheet T reaches a maximum value in the 0° direction and a minimum value in the 45° direction.

### Ductility

Taking into account the rolling direction, the maximum value of the ductility  $A_{80}$  of the tested sheet M reaches a maximum value in the 45° direction and a minimum value in the 0° direction. Taking into account the rolling direction, the maximum value of the ductility  $A_{80}$  of the tested sheet T reaches a maximum value in the 0° direction and a minimum value in the 45° direction.

#### 2.2.2 Biaxial tensile test

The principle of the test consists in bulging tested sheet metal with hydraulic fluid supplied under pressure. The sheet metal to be tested is clamped firmly between the bottom plate and the draw bar. The supplied pressurised fluid (hydraulic oil) bulges the test plate until it breaks. The ductile properties of the tested plate are measured by the height of the spherical cap at breaking, the pressure of the injected fluid which is sensed by a sensor, the shape of the crack after breaking and the surface of the ball cap. [9,10]

From the height of the spherical cap it is possible to determine the logarithmic deformation  $\varphi$  (or the intensity of deformation  $\varphi_i$ ) or the relative deformation  $\varepsilon$ . As an approximation, the crack shape is also used to assess the ductile properties of the sheet under investigation. [5-7]

A schematic of the device is shown in Fig. 3. The same materials were used for the test as for the uniaxial test. A 130 x 130 mm sheet was cut from each material. We evaluated 5 samples from material M and 3 samples from material T.

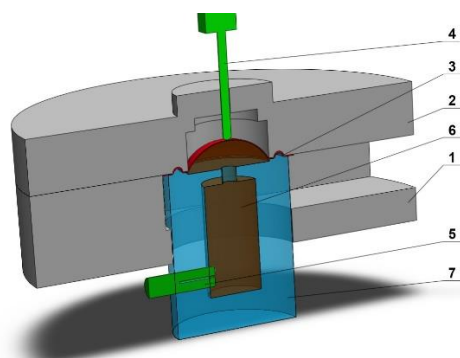


Fig. 3 Schematic diagram of the biaxial tensile testing machine

1 - bottom plate, 2 - draw bar, 3 - tested plate, 4 - bulge height sensor, 5 - fluid pressure sensor, 6 - hydraulic oil, 7 - draw bar

The stress in the material during cap extrusion is calculated for thin-walled vessels according to Laplace's equation: [1]

$$\sigma = \frac{p \cdot R}{2 \cdot s_0} \quad (1),$$

where:  $p$  - fluid pressure [MPa],  $s_0$  - actual material thickness [mm],  $R$  - radius of curvature of the spherical cap [mm].

The plastic properties of the investigated material can also be expressed by the relative plastic deformation (or ductility  $A$  given in %) expressed by the formula:

$$\varepsilon = \frac{l - l_0}{l_0} \quad [\%] \quad (2),$$

where:  $l$  - is the length of the spherical cap after breaking [mm],  $l_0$  - length before plastic deformation (diameter of the tensile rod) [mm].

The device for the biaxial tensile test was constructed at the Department of Technology, Materials and Computer Support of Production, Faculty of Mechanical Engineering, Technical University in Košice and is shown in Fig. 4. Fig. 5 shows the samples after the biaxial test.



Figure 4. Biaxial test device

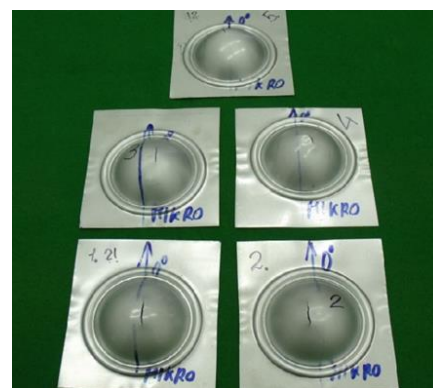


Figure 5. Material M after Bulge test

Table 4 shows the average material M values obtained by the Bulge test.

Table 4. Measured values of material M

Sample	h [mm]	$R_e$ [MPa]	$\sigma_{conv.}$ [MPa]	$\sigma_{actu.}$ [MPa]	$\varepsilon$ [%]	$\varphi_i$ [%]
M	27.9	333	449	566	29.5	52.1

Tab. 5 shows the average material T-values obtained by the Bulge test

Table 5. Measured values of material T

Sample	h [mm]	$R_e$ [MPa]	$\sigma_{conv.}$ [MPa]	$\sigma_{actu.}$ [MPa]	$\varepsilon$ [%]	$\varphi_i$ [%]
T	18.1	496	603	716	13.8	25.9

### 3. Results and Discussion

This section compares the measured and calculated material M and T values for the uniaxial and biaxial tests.

Fig. 6 shows the yield strength values measured in the uniaxial and biaxial tests. The highest yield strength value for the uniaxial test was obtained for material M at 90° rolling direction, namely 240 MPa. For the biaxial test, a value of 333 MPa was measured. The highest yield strength in the uniaxial test was achieved by material T at 90° rolling direction, 452 MPa. For the biaxial test, a value of 496 MPa was measured.

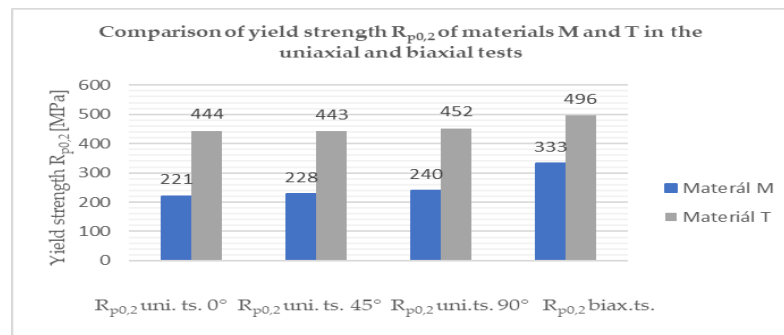


Fig. 6 Comparison of yield strength of materials M and T

Fig. 7 shows the tensile strength values measured in the uniaxial and biaxial tests. The highest value of tensile strength in the uniaxial test was obtained by material M at 0° rolling direction, i.e. 387 MPa. In the biaxial test, a value of 449 MPa was measured. The highest yield strength value in the uniaxial test was obtained by the material T at 0° rolling direction, i.e. 773 MPa. In the biaxial test, the test was aborted after reaching 603 MPa.

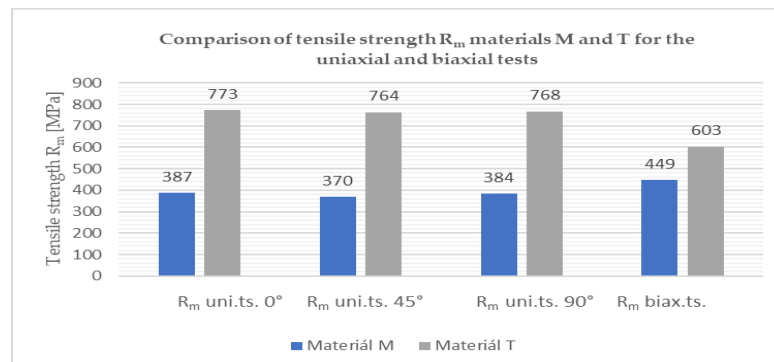


Fig. 7 Comparison of tensile strength of M and T materials

Fig. 8 shows the ductility values measured for the uniaxial and biaxial tests. The highest ductility value in the uniaxial test was achieved by material M at 45° rolling direction, 37.9%. For the biaxial test, we obtained  $\epsilon$  and  $\phi_i$  values of 29.5% and 52.1%, respectively. The highest ductility value in uniaxial test was obtained by material T at rolling direction 0°, namely 28.3%. For the biaxial test, we obtained  $\epsilon$  values of 13.8% and  $\phi_i$  of 25.9% due to the premature termination of the test.

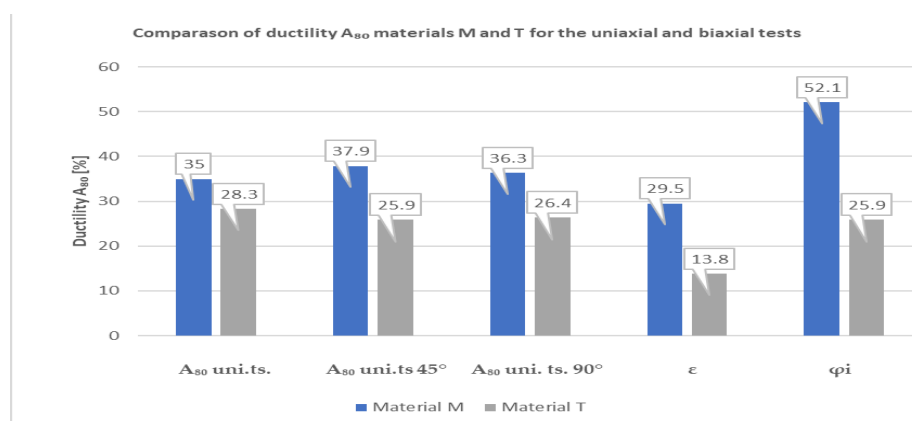


Fig. 8 Comparison of ductility of M and T materials

## 5. Conclusions

The appropriate use and processing technology for steel plate can be recommended based, among other things, on the values of mechanical properties. This paper describes the basic characteristics of the evaluation of the mechanical properties of thin high-strength plates obtained by uniaxial tensile testing and biaxial tensile testing. Although considerable efforts have been made so far to find only one universal test to characterize the suitability of the material for tensile testing, this goal has not been achieved. A single evaluation test cannot unambiguously determine all the properties that affect the processing of thin steel plates.

Based on the resulting values mechanical properties, surface anisotropy, of the normal anisotropy coefficient and the exponent deformation strengthening can be stated: TRIP steel RAK40/70 has almost double higher strength compared to microalloyed steel H220PD, while the areal anisotropy parameters mechanical properties are more pronounced for H220PD microalloyed steel. Microalloyed steel H220PD has TRIP steel RAK40/70 higher ductility.

From the results of the tests we have conducted on the tested materials, it can be concluded that the differences are not only depending on the test carried out, but also depending on the rolling direction.

**Acknowledgments:** The authors are grateful to VEGA 1/0384/20 and KEGA 036TUKE-4/2021.

## References

- SUTAR, V., DHARANKAR, C.S., THIRUPATHI RAJU, B.: High Strength Steel for Automotive Applications. International Research Journal of Engineering and Technology. Vol. 3, Issue 5, (2016), p. 966-968. ISSN 2395 -0056
- SPIŠÁK, E., MAJERNÍKOVÁ, J.: Thin steel plates-methods of evaluation of their properties, Košice, 2016, ISBN: 978-80-553-2647-4
- SPIŠÁK, E.: Limit states in tension of thin steel plates and their modelling. Inaugural lecture, Košice, 2000
- SPIŠÁK, E. et al.: Materials for conventional and advanced technologies, Košice, 2012
- SPIŠÁK, E., MAJERNÍKOVÁ, J.: Analysis of variance of mechanical properties of sheets as the input parameters for simulation of processes. Acta Metallurgica Slovaca. Vol. 18, no. 2-3., 2013, p. 109-116
- SLOTA, J., SPIŠÁK, E.: Determination of flow stress by the hydraulic bulge test, Metalurgija, 47(1), 2008, 13-17
- SPIŠÁK, E., SLOTA, J., TOMÁŠ, M., EVIN, E., MAJERNÍKOVÁ, J.: Optical Measuring of 3D Deformation in Sheet Metal Forming. Acta Mechanica Slovaca 15 (4): 74 - 81, 2011
- FARIDMEHR, Iman et al. Correlation between Engineering Stress-Strain and True Stress-Strain Curve. American Journal of Civil Engineering and Architecture [online].2014, 2(1), 53-59 [cit. 2017-05-02]. DOI: 10.12691/ajcea-2-1-6.
- CAMPOS, H.; SANTOS, A.D.; MARTINS, B.; ITO, K.; MORI, N.; BARLAT, F. Hydraulic bulge test for stress-strain curve determination and damage calibration for ITO-GOYA model. In Proceedings of the World Congress on Computational Congress XI, Barcelona, Spain, 20–25 July 2014.
- ABENDROTH, M. FEM analysis of small punch tests. In Proceedings of the 3rd Annual International Conference SSTT, Graz, Austria, 23–25 September 2014

# Increasing the technological life of molds for high-pressure aluminum casting by applying PVD coatings

Ján Hašul<sup>1,\*</sup>, Janette Brezinová<sup>1</sup>

<sup>1</sup> Technical University of Košice, Faculty of Mechanical Engineering, [jan.hasul@tuke.sk](mailto:jan.hasul@tuke.sk),  
[janette.brezinova@tuke.sk](mailto:janette.brezinova@tuke.sk)

**Abstract:** The paper is focused on the assessment of surface wettability using contact angle measurement. To increase the lubrication effects in the production of Al-based castings, the surface of the PVD coatings was textured using laser beam technology (LBT). Two types of textures were created. Distilled water and 2 types of separation agents Safety Lube 7815 and Safety Lube 8801 were used to determine surface wettability.

**Keywords:** casting, PVD, texture, contact angle, wettability

## 1. Introduction

Recently, the high-pressure casting process is often used to produce castings from aluminum and its alloys intended mainly for the automotive industry. In this process, molten aluminum is injected into the mold cavity at a temperature in the range of 670-710 °C at a speed of 30-100 m.s<sup>-1</sup> and under a pressure of up to 120 MPa. However, these conditions lead to wear of the forms and thus reduce their technological life [1]. Basic wear mechanisms include fatigue wear, high-temperature corrosive wear, erosive wear, metal sticking to the surface of the mold (die soldering) and thermal fatigue wear [2]. High temperature corrosion is characterized by the loss of matrix material from the mold surface. The metal bonding process can be divided into 2 groups [3]: (a) *metallurgical*, which is characterized by a high number of cycles and a high temperature of the mold surface; (b) *mechanical*, which is characterized by a low number of cycles and high melt. The layers formed during this process are usually the product of the simultaneous action of metallurgical and mechanical bonds [4]. Mechanical and thermal fatigue wear is caused by repeated cycles of the process, or voltage changes caused by alternating heating and cooling of the mold surface during the high-pressure casting process. The formation of cracks from thermal fatigue wear leads to losses of mold material as small fragments are peeled off from the mold surface [4,5]. Figure 1 cracks in the zones of sharp transitions of the surfaces of the shaped parts of the mold [6]:

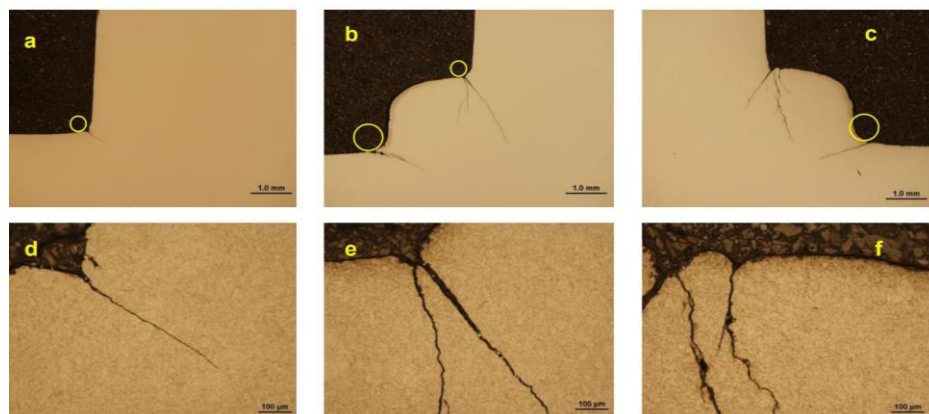


**Figure 1.** Cracks in the zones of sharp transitions of the surfaces of the shaped parts of the mold

The alloys used in the high-pressure casting process are based on Al-Si and are referred to as Silumins. The castability of high pressure die casting (HPDC) alloys was reported to be principally related to the die temperature, the in-gate velocity of melt, and casting pressure. It was found that the combination of die temperature, the mould filling capacity of molten metal, the geometrical complexity of parts and cooling rate during die casting significantly affect the integrity of cast components. In addition, the slow forwarding speed of melt in the shot sleeve was found to be able to minimize the gas entrainment in the HPDC process and increase the mechanical properties of castings [7].

## 2. Materials and Methods

Uddeholm Dievar tool steel was used for the experiment as a base material (BM), which is used to produce molds used for high-pressure casting of aluminum and its alloys. This tool steel is alloyed with elements Cr, Mo, and V. It has very good resistance to high temperatures, coarse cracking, hot wear, and plastic deformation. Also, the material excels with good toughness and ductility, good strength at high temperatures and, at the same time, dimensional stability at high temperatures during the high-pressure casting process. Among the basic areas of use of the material are mainly high-pressure casting, forging, hot pressing of sheet metal and others. Table 1 shows the chemical composition of the Uddeholm Dievar material.

**Table 1.** Chemical composition of Uddeholm Dievar

Element	C	Si	Mn	Cr	Mo	V
Weight %	0.38	0.2	0.5	5	2.3	0.6

Wettability of the mold surface and the effect of texturing on surface wettability were evaluated by measuring the contact angle on the Advex device using the trapped bubble method according to the ISO 19403 standard. Distilled water, two separation agents Safety Lube 7815 and Safety Lube 8801, which are used in the high-pressure casting process of Al and its alloys, were used as test fluids.

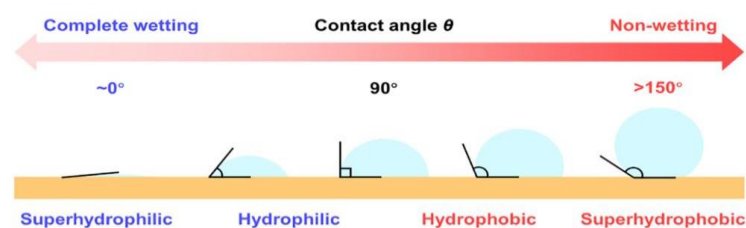


**Figure 2.** Contact angle determination scheme

Two types of samples with a non-textured and a textured surface were made for the measurements. In the case of non-textured samples, their surface was modified by wet sandblasting technology. Texturing of the surface of the samples was performed using the LBT (laser beam texturing) method. A Piranha II Multi FL205 type Yb laser device (Figure 3) with a power of 20 W was used to create dimple textures that serve as a separation agent reservoir in the process of high-pressure casting of aluminum and its alloys.



**Figure 3.** Laser texturing device

Three PVD coatings (AlTiN G, AlXN<sub>3</sub>, nACRo<sup>4</sup>) were applied to the thus prepared surfaces. AlTiN is a high-performance gradient coating that is used for machining materials that have higher strength and hardness. It solves many tribological problems in practice. The main area of application of this coating is coating of drilling tools, coating of molds for high-pressure aluminum casting. The coating can be applied at temperatures of 450 °C to 475 °C. AlXN<sub>3</sub> is a duplex coating consisting of: X=Cr; CrN layer + Al/CrN nanomultilayer + AlN layer. It is a tough coating that has high resistance to abrasion at high temperatures and is also used in solving various tribological problems. Molds for high-pressure casting are coated with it to reduce abrasive wear, but also tools for cutting solid materials to reduce tool wear during the cutting process. The nACRo<sup>4</sup> nanocomposite coating belongs to the group of 4th generation nanocomposite coatings. It has high toughness and is resistant to abrasion and suitable for high temperatures. Tools for machining non-ferrous metals, as well as molds designed for high-pressure casting of aluminum and its alloys, are coated with it. The nACRo<sup>4</sup> coating consists of the following layers: The first layer is made of CrN – this layer is referred to as the adhesive layer. An AlCrN gradient layer is applied to the adhesive layer. Subsequently, thin AlCrN nanolayers are applied to the gradient layer. The final top layer is made of nc-AlCrN/a-Si<sub>3</sub>N<sub>4</sub>.

**Table 2.** Basic properties of used coatings

Coating	AlTiN G	AlXN <sub>3</sub>	nACRo <sup>4</sup>
Max. temperature used [°C]	900	900	1100
Hardness [GPa]	38	32	40

### 3. Results

#### 3.1 Texturing of the surface

Laser random and organized laser large, dimpled textures were created on the surface of the samples. Dimple textures were purposely created to serve as a separating agent reservoir in the repetitive process of high-pressure casting. It was found that it is possible to apply stochastic (laser random) textures to the surface of the mold, because the shape parts of the molds are complex in shape, they have different roundings and bevels, therefore large textures cannot be applied to the shape parts of the molds. Figure 4 shows examples of stochastic (laser random) texturing (Fig.4a) and organized (laser large) texturing (Fig.4b)

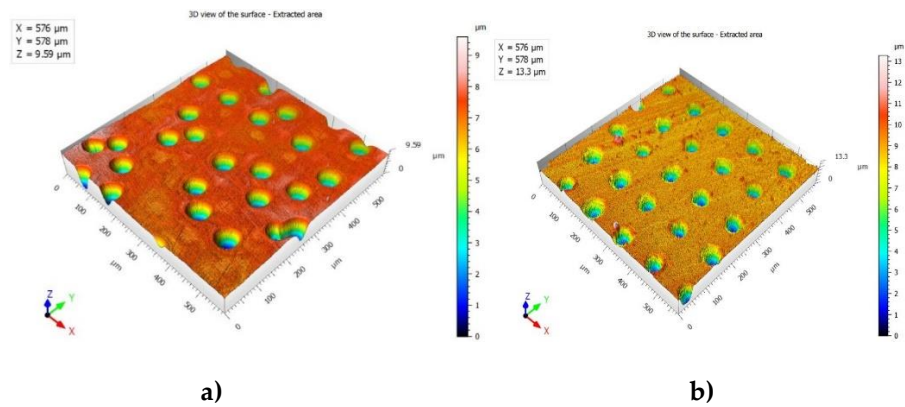


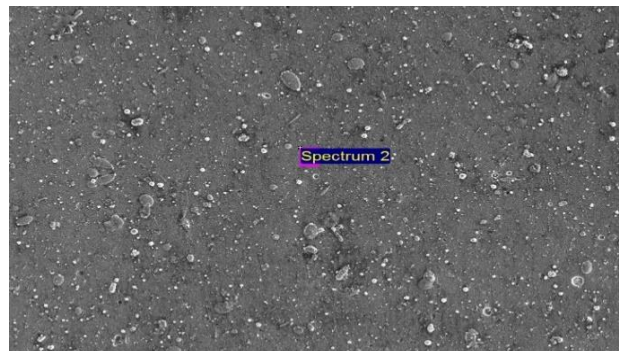
**Figure 4.** Texturing of surface: a) stochastic (laser random), b) organized (laser large)

### 3.2 EDX analysis of PVD coatings

The chemical composition of the AlTiN G coating was determined by EDX analysis (Table 3). The highest proportion of titanium was found in the coating. Other elements also appeared, namely carbon, nitrogen, and aluminum.

**Table 3.** EDX analysis of AlTiN G coating

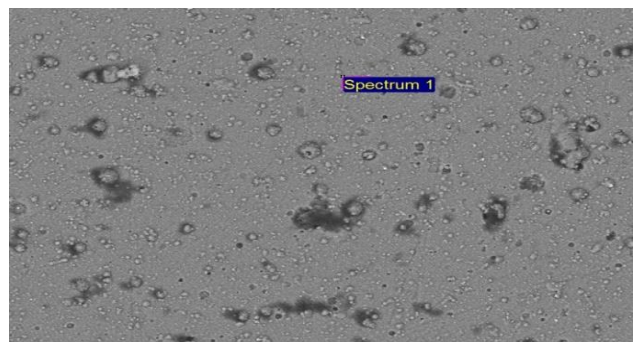
AlTiN G coating	
Element	Weight%
C K	4.18
N K	32.24
Al K	30.89
Ti K	32.69
Totals	100.00



The highest proportion of chromium and nitrogen elements was found in the AlXN<sub>3</sub> coating (Table 4). A higher proportion of aluminum was found and a small percentage of carbon in the coating.

**Table 4.** EDX analysis of AlXN<sub>3</sub> coating

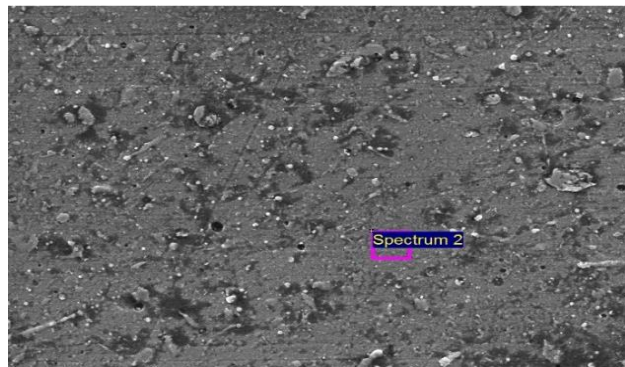
AlXN <sub>3</sub> coating	
Element	Weight%
C K	3.63
N K	31.28
Al K	28.12
Cr K	36.97
Totals	100.00



A certain proportion of silicon was detected in the nanostructured coating nACrO<sup>4</sup> (Table 5). Silicon improves the mechanical properties of the surface. Silicon is an element dependent on the formation of a nanocomposite structure. During coating deposition, silicon tends to segregate along grain boundaries as SixNy and forms an amorphous compound during deposition.

**Table 5.** EDX analysis of nanocomposite nACro<sup>4</sup> coating

nACro <sup>4</sup> coating	
Element	Weight%
C K	2.50
N K	31.39
Al K	17.92
Si K	3.84
Cr K	44.34
Totals	100.00



### 3.3. Measurement of contact angles

The average values of the contact angles of the untextured surface of the pure base material as well as the material with PVD coatings were measured (Table 6).

**Table 6.** Average values of the contact angles of the non-textured surface with PVD coatings

Used fluid	Average value of contact angles without texture				
	BM (ground)	BM (polished)	AlTiN G	nACro <sup>4</sup>	AlXN <sub>3</sub>
Distilled water	67.6	65.8	78.2	77	78.6
Safety Lube 7815	45.5	46.8	42.5	38.5	37.2
Safety Lube 8801	29	32	30.4	28.4	28.9

The best wettability of the surface was achieved by the separating agent Safety Lube 8801, where the smallest values of contact angles were achieved. When distilled water encountered the surface, worse wettability was found compared to the used separation agents, and the highest values of contact angles were measured (Table 6).



**Figure 5.** Outputs from contact angle measurements – a) Distilled water; b) Safety Lube 8801

During measurements of the surface with created dimple textures, the average values of the contact angles of the base material without and with PVD coatings were measured, which are shown in Table 7.

**Table 7.** Average values of the contact angles of the textured surface with PVD coatings

Used fluid	Average value of contact angles with texture			
	BM	AlTiN G	nACro <sup>4</sup>	AlXN <sub>3</sub>
Distilled water	73.7	72.3	62.6	64.8
Safety Lube 7815	46.2	46.1	44.8	44.4
Safety Lube 8801	31.9	28.2	27	28.5

The best surface wettability was achieved by the separating agent Safety Lube 8801. When distilled water was used as the test liquid, higher values of contact angles were found compared to the Safety Lube separating agents, which means worse surface wettability (Table 7).



**Figure 6.** Outputs from contact angle measurements – a) Safety Lube 7815; b) Safety Lube 8801

#### 4. Conclusions

The experimental work was aimed at evaluating the wettability of non-textured and textured surfaces. The best wettability of both non-textured and textured surfaces was measured with Safety Lube 8801 separating agent with small contact angles compared to Safety Lube 7815 separating agent and distilled water. The largest values of contact angles were measured during measurements with distilled water. In the next stage of the experiment, the influence of texturing in the measurement of tribological properties will be investigated, where texturing should reduce the resulting values of the friction coefficient compared to a non-textured surface. In the next parts of the experiment, attention will be paid to the evaluation of the effect of surface texturing on the quality of coatings during cyclic immersion tests in molten AlSi9Cu3 alloy 10 and 20 times for 15 min.

#### Acknowledgments

The contribution is the result of the implementation of the project: APVV-20-0303, VEGA no. 1/0597/23 and KEGA 046TUKE-4/2022.

#### References

1. D. Mellouli, N. Haddar, A. Koster, H.F. Avedi: Thermal fatigue failure of brass die – casting dies, In: Engineering Failure Analysis, 2012, Volume 20, pp. 137-146
2. J. Wang et.al.: On the failure mechanism for high pressure die casting A390 hypereutectic alloy in low cycle and high cycle fatigue, In: Materials Science & Engineering A, 2018, Volume 723, pp. 48-55
3. K. Domkin, J.H. Hattel, J. Thorborg: Modelling of high temperature and diffusion-controlled die soldering in aluminum high pressure die casting, In: J. Mater. Process. Technol., 2019, Volume 8, pp. 4051-4061
4. R. Ding et.al: Failure analysis of H13 steel die for high pressure die casting Al alloy, In: Engineering Failure Analysis, 2021, Volume 124, 105330
5. D. Abid, A. Ktari, D. Mellouli, N. Gafsi, N. Haddar: Failure analysis of shot sleeves used in brass high pressure die casting process, In: Engineering Failure Analysis, 2019, Volume 104, pp. 177-188
6. Special Steels for High pressure Die Casting. [online] [ cit. 2022-11-28]. Available on the Internet: <https://matmatch.com/suppliers/dest-deutsche-edelstahlwerke-dew-/examples/special-steels-for-high-pressure-die-casting>
7. N. Zhicao et.al.: Effect of high pressure die casting on the castability, defects and mechanical properties of aluminum alloys in extra-large thin-wall casting, In.: Journal of Materials Processing Tech., 2022, Volume 303, 117525



# Influence of the thickness of carbon nanostructures on their mechanical properties

Sára Janigová <sup>1</sup>, Peter Palička <sup>2</sup>

<sup>1</sup> sara.janigova@tuke.sk, Technical University in Košice, Faculty of Mechanical Engineering, Department of Applied Mechanics and Mechanical Engineering, Slovakia

<sup>2</sup> peter.palicka@tuke.sk, Technical University in Košice, Faculty of Mechanical Engineering, Department of Applied Mechanics and Mechanical Engineering, Slovakia

**Abstract:** Nanotechnology allows, thanks to the ability to manipulate the modeling of substances at the atomic level, to create materials with a unique structure and new improved properties. Finite element method (FEM) is a standard method of analysis and simulation of structural and mechanical elements, but its role in the field of nanostructures' numerical simulation is still growing. The European Commission defines nanomaterials as substances whose parts have at least one size dimension between 1 and 100 nanometers. However, there appears to be a larger variance between the theoretically and numerically determined values of the thickness of the carbon nanostructures. This challenge of standardizing the physical thickness of a graphene sheet along with its mechanical properties is referred to within the scientific community as the Yakobson's paradox. If the expected thickness of graphene is the same as the interlayer distance of graphite, the value of Young's modulus is around 1 TPa. In the works that use the shell model in the analysis, the estimate of the elastic modulus is around 5 TPa. Finally, the article shows the dependences between the thickness and the modulus of elasticity, in-plane and bending stiffness.

**Keywords:** nanomaterials; graphene sheets; Yakobson; thickness; mechanical properties; finite element method

## 1. Introduction

Nanotechnology has been developed as a field of science with wide applications in various fields. Reducing the particle size and tuning the particle morphology of materials from micro- to nanoscale results in unique properties and the creation of new generations of materials and structures. The reason why nanomaterials show enhanced properties is the large surface-to-volume ratio and the quantum confinement effect. It is therefore essential to understand their nature and possible ways of their analysis [1].

Graphene and its associated nanostructures have been investigated in detail over the past decade using experimental and numerical methods. Graphene is a planar array of carbon atoms that are linked by  $sp^2$  C-C covalent bonds to form the hexagonal cells that are the basic structure of graphite. Graphene can be understood as a two-dimensional crystal. The distance between neighboring atoms is  $d_{CC} = 1.42 \text{ \AA}$ . A remarkable detail of graphene crystals is that they preferentially break at crystal edges of two types: zig-zag edge runs parallel to the graphene lattice vector, armchair edge runs parallel to carbon bonds (Figure 1) [2].

The graphene geometry is defined by the chiral vector  $C_h$  and the chiral angle  $\theta$ . A chiral vector is represented by two unit vectors  $a_1$  and  $a_2$  and two integers  $m$  and  $n$ , as shown in the equation below [3]:

$$C_h = na_1 + ma_2, \quad (1)$$

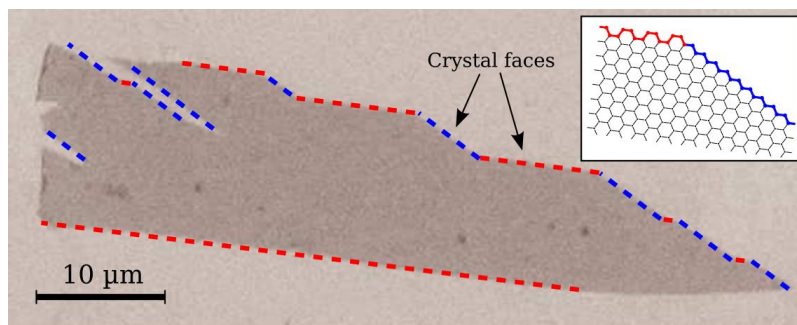


**Figure 1.** STM image of a large graphene monolayer obtained through exfoliation. The edges of the crystal are preferably oriented in a zig-zag (red) or armchair (blue) shape [4].

The basic configuration of graphene sheet can be defined based on the chiral vector or the chiral angle  $\theta$ , as shown in Figure 2. This results in three different configurations, which include chiral (if  $0^\circ < \theta < 30^\circ$  or  $m \neq n \neq 0$ ), zig-zag (if  $\theta = 0^\circ$  or  $m = 0$ ), and armchair (if  $\theta = 30^\circ$  or  $m = n$ ) graphene structure [3].

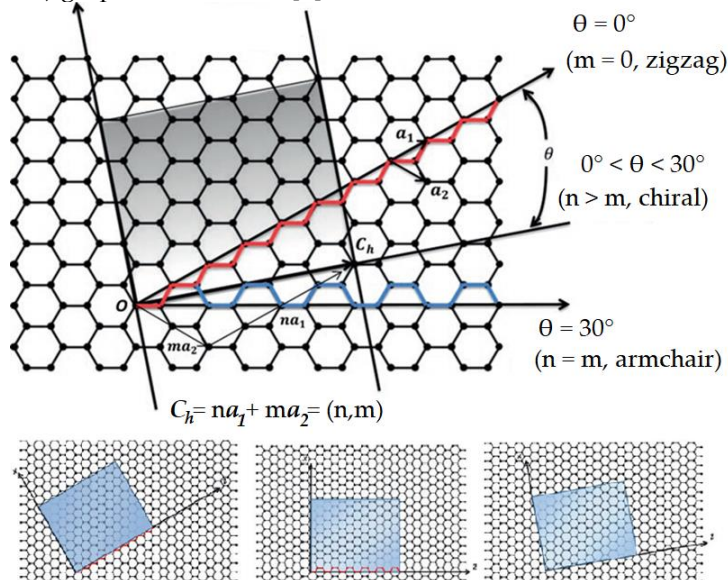


**Figure 2.** Graphene sheet scheme and definition of its geometric parameters to describe zig-zag (left), armchair (middle) and chiral (right) structure [3].

**2. Materials and Methods**

The most commonly used way to represent the graphene sheet in FEM analysis is to consider each carbon atom to be a node, while the covalent bond between them is represented by a finite element. The mechanical properties of this bond, such as  $E$  (Young’s modulus) and  $G$  (shear modulus), can be determined by the equations representing the equivalence between the deformation energy and the harmonic potential of a hypothetical beam of length  $L$  [2]:

$$\frac{k_r}{2} (\delta r)^2 = \frac{EA}{2L} (\delta r)^2, \tag{2}$$

$$\frac{k_\tau}{2} (\delta \varphi)^2 = \frac{GJ}{2L} (\delta \varphi)^2, \tag{3}$$

$$\frac{k_\theta}{2} (\delta \theta)^2 = \frac{EI}{2L} \frac{4 + \Phi}{1 + \Phi} (\delta \theta)^2, \tag{4}$$

where  $\delta r$  is bond stretching,  $\delta\theta$  is bond angle change and  $\delta\varphi$  is twist angle change,  $k_r$  is a force constants of bond stretching resistance,  $k_\theta$  is a bond bending resistance and  $k_\tau$  is twisting resistance (the values of constants are  $k_r = 6.52 \times 10^{-7} \text{ Nmm}^{-1}$ ,  $k_\theta = 9,00 \times 10^{-10} \text{ N nm rad}^{-2}$  a  $k_\tau = 2,78 \times 10^{-10} \text{ N nm}^{-1} \text{ rad}^{-2}$ ),  $A$  is the cross section area,  $J$  is the polar moment of inertia,  $I$  is the second moment of area,  $\Phi$  is the shear deformation constant.

Graphene sheets in the molecular mechanics are considered as large molecules consisting of carbon atoms with atomic nuclei considered as mass points whose motions are governed by force field. Based on the equivalence of molecular mechanics and structural mechanics for interaction between carbon atoms, it is possible to derive relations between force field constants (molecular mechanics) and stiffness quantities of the beam (structural mechanics). If we take into account that the deformation energies from the molecular and structural mechanics correspond to each other, we obtain relations that express the dependence between the constants of the force field (parameters of molecular mechanics) and the stiffness quantities of the beam (parameters of structural mechanics) [5]:

$$k_r = \frac{EA}{L}, \quad (5)$$

$$k_\theta = \frac{EI}{L}, \quad (6)$$

$$k_\tau = \frac{GJ}{L}. \quad (7)$$

The last three equations are the basic relationships used in the finite element analysis of nanomaterials. Supplementary equations, which serve as input for modeling graphene spatial structures in numerical analysis programs, are expressed as follows [5]:

$$d = 4 \sqrt{\frac{k_\theta}{k_r}}, \quad (8)$$

$$E = \frac{k_r^2 L}{4\pi k_\theta}, \quad (9)$$

$$G = \frac{k_r^2 k_\tau L}{8\pi k_\theta^2}. \quad (10)$$

The above equations will provide a procedure for determining a unique value of the bond diameter,  $d$ , which is equal to the wall thickness of the nanostructure. However, different thicknesses of carbon based nanostructures are often used in scientific works, which presents a problem when comparing the obtained results. For this reason, it is advisable to perform calculations for different wall thickness values [6].

Based on atomistic computations, it is possible to obtain only an estimate of the in-plane stiffness, i.e. " $D = Eh$ " where  $E$  is the Young's modulus and " $h$ " is the thickness of the graphene sheet. In most properly performed numerical analyses from different sources there is an agreement on the numerical value of  $Eh$ . In many cases it is not necessary to know the value of  $E$ . However, there are also studies where a specific value of the modulus of elasticity is required, and therefore in that case it is necessary to make an estimate of the thickness  $h$  for the calculation. According to Huang et. al., hence the wide spread in the published values of  $E$  [7].

The thickness of the element in the form of its diameter  $d = 0.1486 \text{ nm}$  can be calculated based on the equation (8), while  $k_r$ ,  $k_\theta$  and  $k_\tau$  are known as their values are available in AMBER or MORSE format in the literature [8]. The condition is that the cross-section of the element representing the carbon bond is considered circular. Calculation models of nanostructures with such a thickness have been experimentally and analytically verified, therefore it is possible to draw the conclusion that it is appropriate to calculate

the thickness  $d$  from force constants and implement them in atomistic models. However, if the carbon nanostructure is represented by continuum elements, e.g. shell or plate, the tensile stiffness

$$T = \frac{Eh}{1 - \mu^2}, \quad (11)$$

as well as the bending stiffness

$$B = \frac{Eh^3}{12(1 - \mu^2)} \quad (12)$$

are calculated. Their ratio leads to the expression for thickness

$$h = \frac{\sqrt{12B}}{T}. \quad (13)$$

In that case it is usual to assume a thickness of 0.34 nm. This thickness of 0.34 nm is derived based on the interatomic/interplanar distances between carbon atoms in multi-layer graphene systems [9].

### 3. Results

The graphene sheets are generated in the Nanotube modeler program, from which their xyz coordinates and connectivities are obtained. These data are exported in PBD format and transferred using a script created in the Matlab program to a program designed for numerical analysis (Ansys). The nanostructures are then simplified - carbon atoms represent nodes of finite elements and interatomic interactions are represented using finite elements (beam type BEAM4). Thus, graphene sheets are modeled as spatial frame structures using beam elements that will be immaterial, with all mass concentrated at the nodes.

The stiffness of an object expresses its resistance in response to an applied load. If the original length is  $L$ , and after loading by uniaxial tension, it increases to  $L + \Delta L$  under the influence of external force  $F$ , then using Hooke's law, the Young's modulus of the graphene sheet can be calculated according to the following equations [10]:

$$\sigma = \text{normal stress} = F/A, \quad (14)$$

$$\varepsilon = \text{deformation} = \Delta L/L, \quad (15)$$

$$E = \text{Young's modulus} = \sigma/\varepsilon, \quad (16)$$

$$\mu = \text{Poisson's ratio} = -\varepsilon_w/\varepsilon_L. \quad (17)$$

where  $A$  is a cross-sectional area of the graphene sheet,  $\varepsilon_w$  is absolute elongation along the width of the graphene sheet and  $\varepsilon_L$  is absolute elongation along the length of the graphene sheet.

Along with the above mentioned relations for the in-plane stiffness  $D$  and the bending stiffness  $B$  (equation (12)), the values of Young's modulus, in-plane and bending stiffness can be calculated for different thickness of the graphene sheet. Since the Poisson's ratio does not depend on the thickness of the graphene sheet, it will not change with the changing thickness.

Two types of graphene sheets are modeled – first with a thickness equal to the thickness of the element in the form of its diameter  $d = 0.1486$  nm and second with a thickness of 0.34 nm, which is derived from the interatomic/interplanar distances between carbon atoms in multilayer graphene systems. The analyzed graphene sheet has chirality (14,0), width  $w = 3,4457$  nm and length varying from 3,4 to 17 nm. In the analysis, one side of the sheet is fixed and the opposite one is loaded by the force  $F$  according to Figure 3.

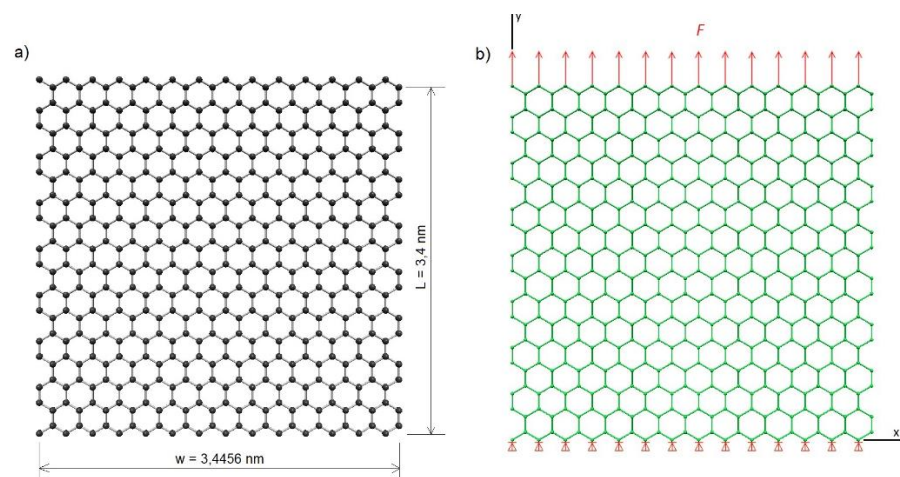


Figure 3. a) geometry of analyzed graphene sheet, b) applied boundary conditions and loading.

The obtained values of Young's modulus, in-plane and bending stiffness are shown in Figure 4 to Figure 6.

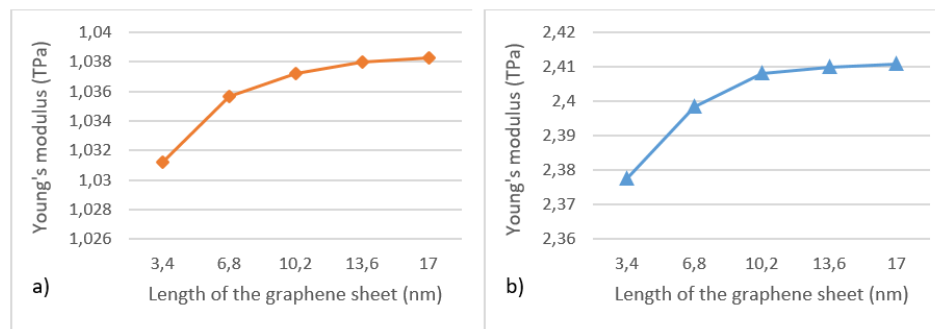


Figure 4. Values of Young's modulus for thickness a)  $d = 0.34$  nm, b)  $d = 0.1486$  nm.

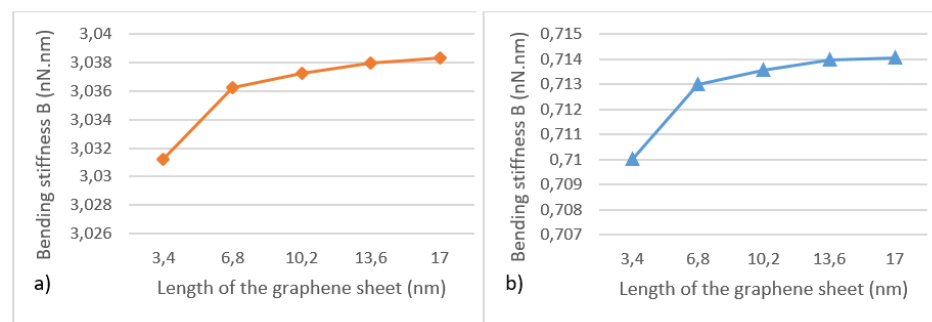


Figure 5. Values of bending stiffness  $B$  for thickness a)  $d = 0.34$  nm, b)  $d = 0.1486$  nm.

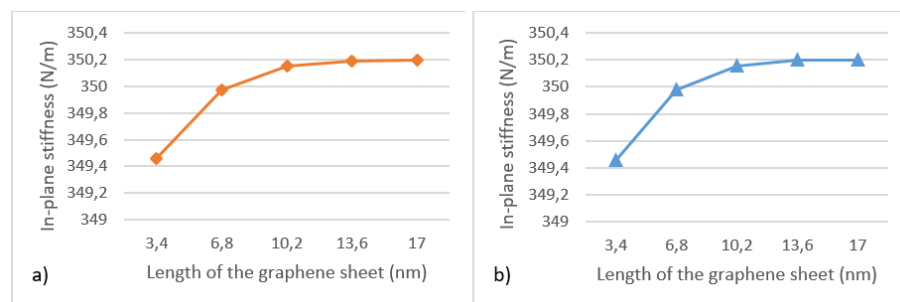


Figure 6. Values of in-plane stiffness for thickness a)  $d = 0.34$  nm, b)  $d = 0.1486$  nm.

#### 4. Discussion

It can be determined from the computations that the Young's modulus is around 1 TPa for thickness 0.34 nm but increases into approximately 2.4 TPa when thickness equal to the diameter 0.1486 nm is applied. There is also a slight increase with the increasing length of the graphene sheet caused by the boundary conditions. Bending stiffness expressed for two thicknesses of carbon sheets also changes with the changing thickness. It can be seen that its values depend on the chosen thickness and the calculated Young's modulus according to equation (12). Figure 6 shows the in-plane stiffness which is not affected by the change in the thickness. On the other hand, it is clear that it depends on the dimensions of the graphene sheets.

**Acknowledgments:** This paper was supported by the Ministry of Education of Slovak Republic under grant project VEGA No. 1/0500/20.

**Conflicts of Interest:** The authors declare no conflict of interest.

#### References

1. Cho W. S. To; Bending and shear moduli of single-walled carbon nanotubes. *Finite Elements in Analysis and Design*, Volume 42, Issue 5, February 2006; pp 404-413.
2. Mehdipour I.; Barari A.; Kimiaefar A.; Domairry G.; Vibrational analysis of curved single-walled carbon nanotube on a Pasternak elastic foundation. *Advances in Engineering Software*. Volume 48(1):1–5, June 2012, DOI:10.1016/j.advengsoft.2012.01.004
3. Yengejeh S. I.; Öchsner A.; Kazemi S. A.; A Primer on the Geometry of Carbon Nanotubes and Their Modifications, Publisher: Springer International Publishing, January 12, 2015; ISBN: 9783319149868
4. Geim A. K.; Novoselov K. S.; The rise of graphene. *Nature Materials*, Volume 6, 2007, pp 18-24, doi:10.1038/nmat1849
5. Cao Q. X.; Huaipeng G.; Pengjie W.; Aaron W.; Yucheng Lan L.; Peng Q.; A Review of Current Development of Graphene Mechanics. *Crystals* [online]. 2018, Volume 8(9), pp 1-30, doi.org/10.3390/cryst8090357
6. Jomehzadeh E.; Pugno N.M.; Bending stiffening of graphene and other 2D materials via controlled rippling, *Composites Part B: Engineering*, Volume 83, 15 December 2015, pp 194-202, doi.org/10.1016/j.compositesb.2015.08.002
7. Sharma P.; Why is the reported elastic modulus of carbon nanotube so scattered? "Yakobsons Paradox" and Perspective from Huang et. al.; iMechanica web of mechanics and mechanicians (online blog), 2007, Available online: <https://imechanica.org/node/791> (accessed on November 10, 2022).
8. Giannopoulos G.I.; Georgantzinou S.K.; Katsareas D.E.; Anifantis N.K.; Numerical Prediction of Young's and Shear Moduli of Carbon Nanotube Composites Incorporating Nanoscale and Interfacial Effects *Computer Modeling in Engineering and Sciences*. February 2010; Volume 56(3): pp 231-248, DOI:10.3970/cmesci.2010.056.231
9. Sun Y. W.; Papageorgiou D. G.; Humphreys C. J.; Dunstan D. J.; Mechanical properties of graphene. *Applied Physics Review*. 2021, Volume 8, DOI: 10.1063/5.0040578ff.
10. Berinskii I. E.; Krivtsov A. M.; Kudarova A. M.; Bending Stiffness of a Graphene Sheet. *Physical Mesomechanics*. November 2014, 17(4): pp 356-364; DOI:10.1134/S1029959914040134.



# Corrosion resistance of steel HX340LAD+Z after deformation

Erik JANOŠKO<sup>1</sup>, Anna GUZANOVÁ<sup>1</sup>, Nikita VELIGOTSKI<sup>1</sup>

<sup>1</sup> Technical University of Košice, Faculty of Mechanical Engineering, Department of Technologies, Materials and Computer Aided Production, Slovakia; [erik.janosko@tuke.sk](mailto:erik.janosko@tuke.sk); [anna.guzanova@tuke.sk](mailto:anna.guzanova@tuke.sk); [nikita.veligotskyi@tuke.sk](mailto:nikita.veligotskyi@tuke.sk)

\* Correspondence: [erik.janosko@tuke.sk](mailto:erik.janosko@tuke.sk)

**Abstract:** The paper deals with the measurement of corrosion resistance of galvanized, high strength low alloyed steel HX340LAD+Z after different degrees of deformation. Electrochemical impedance spectroscopy and linear polarization were evaluated. Polarization resistance  $R_p$  and corrosion rate were evaluated. The dependence between the degree of deformation and the corrosion rate was found.

**Keywords:** electrochemical impedance spectroscopy, linear polarization, deformation, HX340LAD+Z

## 1. Introduction

Galvanized steel sheets are used in many industries due to their resistance to corrosion. This is mainly the automotive industry, where the basic steel sheet is protected by a Zn layer. Since many parts are processed and deformation occurs in various processes of forming, it is important for the automotive industry that the coating shows good formability. Since the Zn coating during the forming process can be disturbed, the base material can be exposed to an aggressive environment [1]. The Zn layer in the forming process adapts to compressive stresses without peeling from the base material, which is an advantage of such a coating [2].

The corrosion resistance of deformed galvanized steel was investigated by Sacco et al. [2], who investigated the linear polarization of deformed galvanized steel. They found an increased rate of corrosion with the degree of deformation [3]. Other studies were carried out [4-6] to determine the behavior of Zn coating on steel sheets in the forming process, but these investigations were focused on limit deformations during forming, changes in the coefficient of friction, lubrication characteristics, etc. and not for corrosion resistance after the forming process.

This article deals with a galvanized steel sheet that was deformed by uniaxial tension at four different degrees of deformation. The goal was to determine the corrosion resistance of the coating and determine the dependence of the corrosion rate on the degree of deformation. Accelerated corrosion laboratory measurements such as electrochemical impedance spectroscopy (EIS) and linear polarization (LP) were used to forge these measurements.

## 2. Materials and Methods

### 2.1 Material

HX340LAD+Z microalloyed steel with a thickness of 0.8 mm and a Zn layer of 100 g/m<sup>2</sup> was used to perform this experiment. The chemical composition and mechani-

cal properties can be found in Table 1 and 2. Mechanical properties were determined by static tensile test.

Table 1 Chemical composition of the material, wt. %.

C	Mn	Si	P	S	Al min	Nb	Ti
0.07	0.6	0.007	0.016	0.007	0.034	0.025	0.001

Table 2 Mechanical properties of the material.

Rp 0,2 [Mpa]	Rm [Mpa]	A80 [%]
351±1.3	427±1.7	26±0.1

## 2.2 Deformation of samples

The samples were deformed by uniaxial tension on the Tiratest 2300, universal tensile test machine. Traverse speed was 10 mm/min. Before the test, uniaxial tensile measurements were made, and then the deformation points on the measured curve were selected. The chosen degrees of deformation (Figure 1) were 5%, 10%, 15% and 20%.

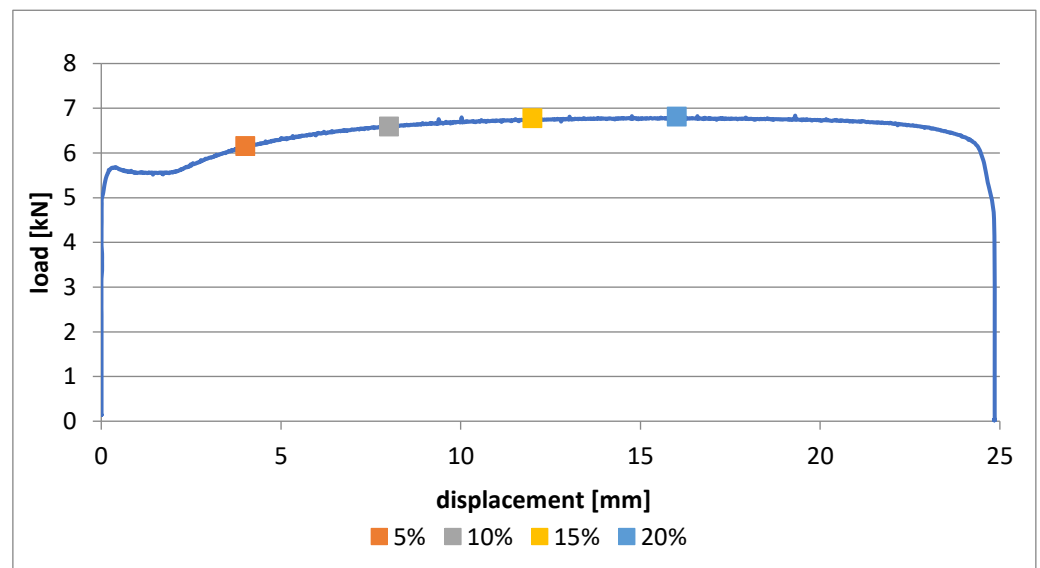


Figure 1. Diagram of the tensile test of the material with marked degrees of deformation

## 2.3 Corrosion studies

A BioLogic SP-150 potentiostat was used for experimental determination of corrosion resistance. The tested area of the samples was 0.636 mm<sup>2</sup>. The temperature of the laboratory during the tests was 23±1 °C. Sample preparation consisted of degreasing with nitrocellulose thinner C 6000 and subsequent rinsing with demineralized water. Measurement of corrosion resistance was performed in electrolyte - 3.5% NaCl solution, which simulates an aggressive environment. The samples were placed in this solution for 24h (i.e. settling time). A three-electrode connection was used for the measurement. Platinum was used as the counter electrode, supersaturated calomel electrode (SCE) was the reference electrode, and the sample was the working electrode. The beginning of each test was the stabilization of the working electrode, i.e. the stabilization of the open circuit potential (OCP).

The following parameters were used for electrochemical impedance spectroscopy (EIS) settings. The frequency range was from 10mHz to 100kHz, a sinusoidal amplitude

of  $\pm 10\text{mV}$  was used. The number of frequencies per decade was 10 (a total of 51 different frequencies).

Linear polarization (LP) settings were  $\pm 0.2\text{ V}$  from  $E_{\text{corr}}$  and scan rate was  $0.5\text{ mV/s}$ .

Each measurement was made at least 3 times. The measurements were processed using the EC-Lab v11.27 software.

### 3. Results

#### 3.1 Potentiostatic Electrochemical Impedance Spectroscopy

The equivalent circuit in Figure 2 was used to process the measured results. In this circuit, R1 represents the resistance of the electrolyte, R2 represents the resistance of the zinc layer, and R3 represents the resistance of the base material. The variable capacitance Q1 is located at the interface between the electrolyte and the zinc layer, the variable capacitance Q2 is located at the interface between the zinc layer and the base material.

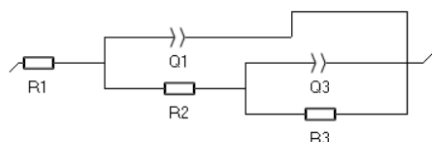


Figure 2. Equivalent circuit used to analyze the PEIS results.

The results were processed in the Nyquist coordinate system. In Figure 3, the analysis of the measured data with an iteration curve (Z-fit) is shown.

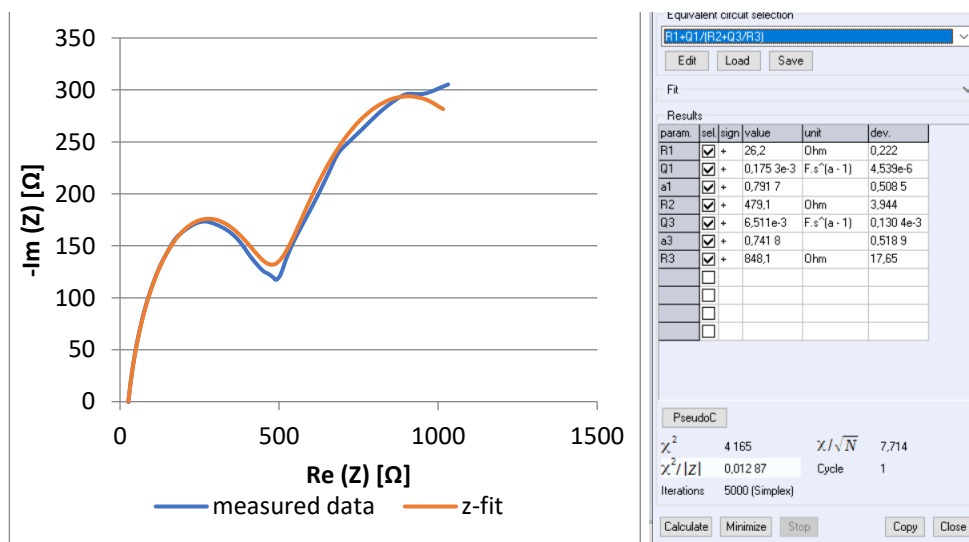


Figure 3. Measured PEIS data with analysis.

The course of the PEIS measurement is shown in Figure 4. The main parameter that indicates the resistance of deformed samples in our case is the R2 value (see Table 3), which represents the polarization resistance of the zinc layer. The measurement showed that the value of R2 for all degrees of deformation is very low and decreasing with degree of deformation. In Figure 4 this value is represented by the first impedance loop, and we can therefore say that the zinc layer protects the base material during deformations up to 20%.

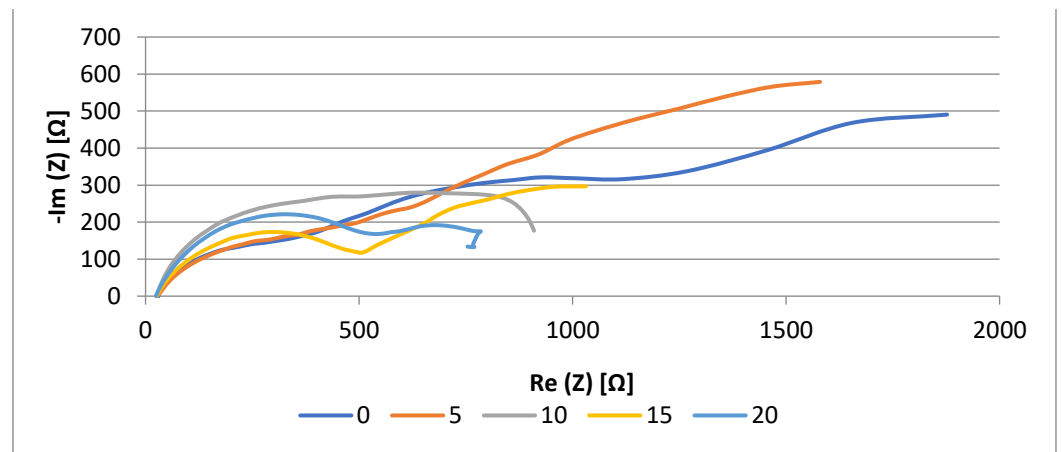


Figure 4. PEIS measurements after different degrees of deformation.

Table 3. Measured values after PEIS analysis.

Deformation [%]	R1 [Ω]	R2 [Ω]	R3 [Ω]	Q1 [F.s]	Q3 [F.s]
0	28±1	492±198	1827±207	0.221±0.018	2.284±0.253
5	28±1	460±14	1675±95	0.135±0.120	1.494±0.968
10	27±2	437±63	886±142	0.151±0.010	1.270±0.300
15	26±1	415±95	639±182	0.186±0.014	5.059±2.231
20	25±1	423±21	230±85	0.191±0.044	5.416±3.071

### 3.2 Linear Polarization

The analysis of the measured LP data can be found in Figure 5 using Tafel fit. During the processing of the measured data, emphasis was placed on the fact that the tangents  $\beta_a$  and  $\beta_c$  were drawn through the measured data in strongly linear regions.

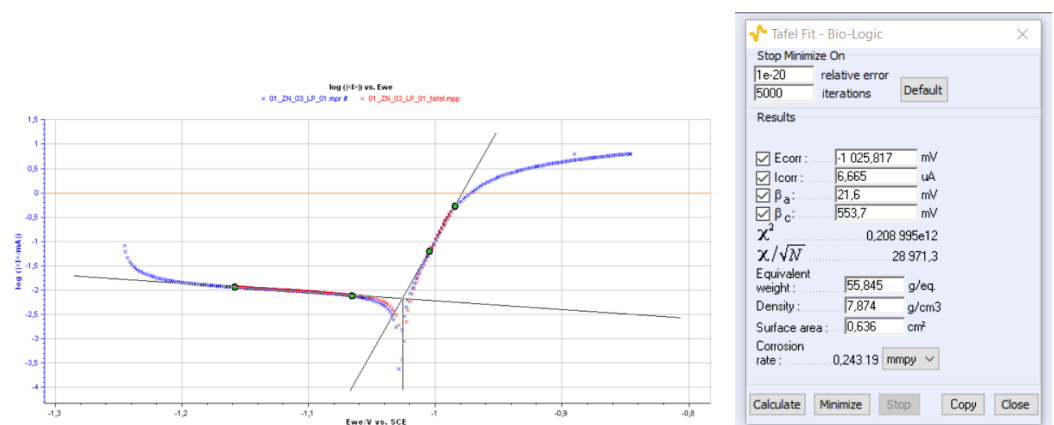


Figure 5. LP analysis method using Tafel curves.

The measured curves are shown in Figure 6. The important parameters in our case are: corrosion potential  $E_{corr}$ , corrosion current  $I_{corr}$  and corrosion rate. As the degree of deformation increases, the potential  $E_{corr}$  becomes increasingly negative. Also, with increasing degree of deformation,  $I_{corr}$  increases. So we can say that, with the increasing degree of deformation, the corrosion process accelerates, while a thin layer of Zn corrosion products is formed on the surface.

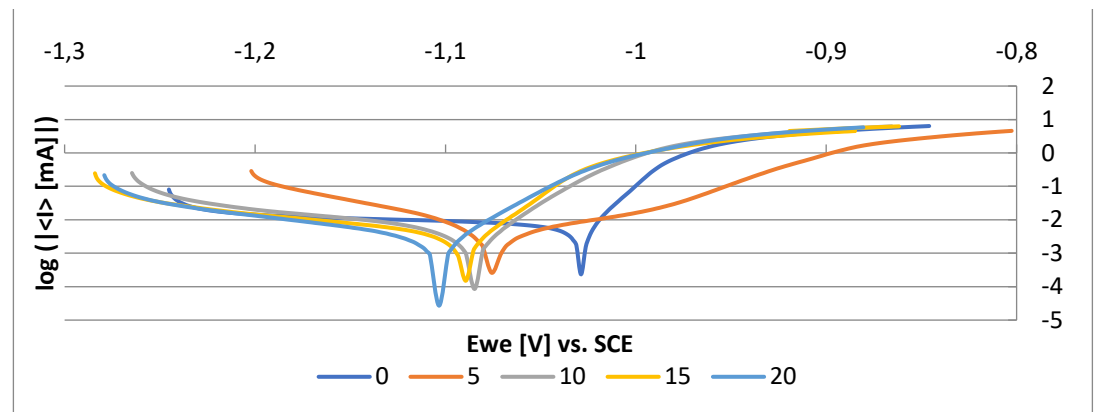


Figure 6. LP measurements after different degrees of deformation.

In Table 4, the measured data are analyzed using Tafel analysis. With an increase in the degree of deformation,  $I_{corr}$  increases, which is an accelerated evolution of hydrogen  $H_2$  ( $H^+ + e \rightarrow (1/2) H_2$ ).

Table 4. Analysis of measured LP data

Deformation [%]	$E_{corr}$ [mV]	$I_{corr}$ [ $\mu$ A]	$\beta_c$ [mV]	$\beta_a$ [mV]	corr. rate [mmpy]
0	-1042.5±23.3	4.6±0.6	307.5±65.7	22.1±3.1	0.168±0.024
5	-1073.9±9.3	9.1±0.2	125.3±21.0	316.7±20.9	0.257±0.027
10	-1078.1±9.6	7.2±0.4	176.9±70.6	70.1±1.1	0.262±0.150
15	-1088.8±6.2	11.3±0.1	252.8±15.5	30.5±0.6	0.413±0.003
20	-1126.5±22.4	10.6±0.5	109.2±20.6	100.5±2.6	0.484±0.017

Figure 7 shows the dependence of the corrosion rate on the degree of deformation of the steel sheet. If measurement deviations are taken into account, measured dependence can be considered linear. So we can say that an increase in the degree of deformation leads to very gentle decrease in protective function of Zn layer, the exposure of the basic steel material to aggressive environment and reaction with the electrolyte.

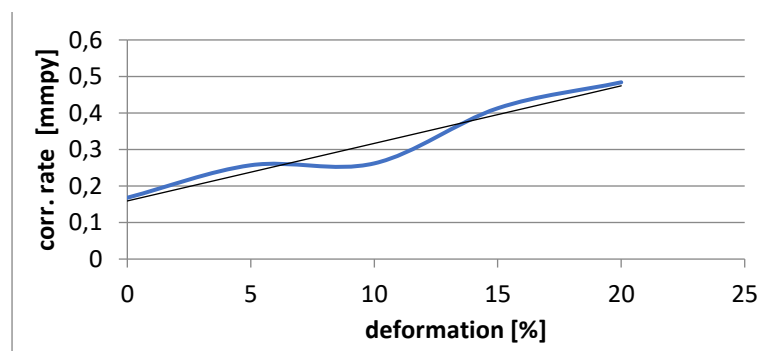


Figure 7. Dependence of the corrosion rate on the degree of deformation.

### 5. Conclusions

By analyzing the results of the measurements, the following conclusions can be established:

- PEIS measurements proved the high resistance of the Zn layer after all degrees of deformation. This cannot be said about the base material, where the polarization resistance of the base material decreased significantly with the increasing degree of deformation.
- Through LP analysis, it was found a linear relationship between the corrosion rate and the degree of deformation. It was also found by measurement that  $i_{corr}$  and corrosion rate increase with the increasing the degree of deformation.

**Funding:** This research was funded by the Scientific Grant Agency of the Ministry of Education, Science, Research and Sports of the Slovak Republic under project VEGA 1/0154/19: Research into the combined technologies of joining dissimilar materials for automotive industry.

## References

1. J.Z. Gronostajski, W.J. Ali, M.S. Ghattas . *Adv. Technol. Plast.*, volume 1 (1987), p. 423
2. E.A. Sacco, N.B. Alvarez. *Coat. Technol.*, volume 168 (2003), p. 115
3. C. Perez, A. Collazo. *Corros. Sci.*, 44 (2002), p. 481
4. T.H. Muster, I.S. Cole. *Corros. Sci.*, 46 (2004), p. 2319
5. K.L. Lin, C.H. Chue, B.C. Kou. *Mater. Chem. Phys.*, 50 (1997), p. 82
6. V. Barranco, S. Feliu Jr., S. Feliu. *Corros. Sci.*, 46 (2004), p. 2203



# Changes in the intensity of electromagnetic fields at base stations of mobile operators

Elena Jurgovská <sup>1\*</sup>, Ervin Lumnitzer <sup>1</sup>, Anna Yehorova<sup>1</sup>

<sup>1</sup> Technical University of Košice, Faculty of Mechanical Engineering, Department of Environmental Engineering

\* Correspondence: elena.jurgovska@tuke.sk

**Abstract:** Mobile operators are reacting to an increasing number of mobile phone users by building new base stations. The reaction is an increase in residents' concern about possible health damage due to increased electromagnetic field intensity values. The contribution is aimed at comparing the EMF intensity before and after the addition of a new operator at a particular base station. The expert measurement was carried out by a frequency-selective method, whereby we were able to perform a more detailed analysis of data intentions in the mobile operators used in the frequency range. A specific base station was chosen because both mobile operators were transmitting in the same frequency range - 800 and 900 MHz. In the experiment, attention was also paid to the assessment of the human impact of electromagnetic fields in a particular municipality and its comparison with action values within the meaning of the legislation in force.

**Keywords:** mobile operators, base stations, intensity, electromagnetic fields, legislative

## 1. Introduction

Exposure to the electromagnetic field generated by mobile operators' base stations is subject to currently valid legislation. In an article by Boo, SF et al. [1], the authors conducted an experiment comparing the radiated power levels of base stations with the International Commission on Non-Ionizing Radiation Protection (ICNIRP) safety guidelines. The measured EMF levels were lower than the ICNIRP exposure limits. Similarly, in [2], household exposure to electric, magnetic, or electromagnetic fields (EMF) was measured. The article reported that all measurement results were well below the ICNIRP guidelines. In [3], the authors carried out measurements, the results of which showed that the maximum measured exposure value to the electromagnetic field exceeded the reference levels of exposure of the public to ICNIRP by 2,5% of the places, and the Serbian national reference levels by 15,6% of the places. It should be stressed that values exceeding the reference levels were only observed in the external environment. In the indoor environment, the total strength of the electromagnetic field did not exceed the defined reference levels.

The contribution describes an experiment in which we carry out measurements of the intensity of electromagnetic fields at selected locations. Measurements were made twice at 4 measuring points. The first measurement was carried out during the operation of one mobile operator. After adding the second mobile operator to the base station, we repeated the measurements at the same measurement points. The measurements were carried out using a frequency-selective method, with the help of which we more closely analyzed the used frequency range at the given base station. The measured EMF intensity values were compared with the permissible action values laid down in the legislation currently in force in Slovakia. The purpose of the contribution is to assess the impact of the EMF by measuring, evaluating, and aligning it with the allowed values.

## 2. Materials and Methods

In the context of this topic, we have carried out a measurement of the exposure of the population to an electromagnetic field. We carried out the experimental measurement at the base station, which is located above the village in Slovakia. This base station was chosen due to the increase in the number of mobile operators. The aim of this increase is to cover the village with the signal from a further operator. The residents of the municipality were interested in seeing how the intensity of the electromagnetic field would increase.

The measurements were performed at 4 measurement points before and after the addition of a new mobile operator. The first measurement was carried out during the operation of one mobile operator using 4 transmitter antennas in the directions of the main radiating lobe of  $110^\circ$  and  $255^\circ$  to cover the village by signal. The second measurement was made after adding the second mobile operator. The number of radiating antennas was increased by two, where the main direction of radiation remained the same.

The measuring points (Figure 1) are positioned as follows:

- M1, and M2 - are positioned in the direct direction of the transmitting antennas
- M3 – First house near the base station
- M4 – In the middle of the village

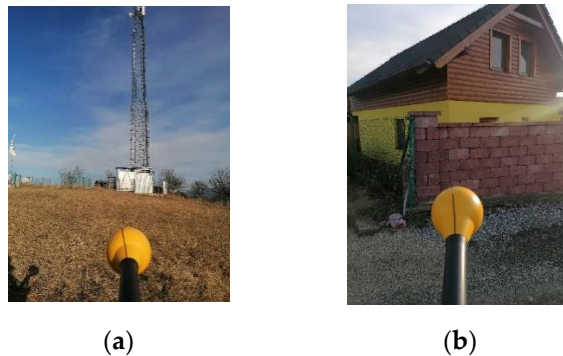


**Figure 1.** (a) measurement point M1; (b) measurement point M3

Measurements were performed at each measurement site using a Narda SRM-3006 measuring instrument consisting of a spectrum analyzer and a probe for measuring the electric field component. The measuring instrument was placed on a carbon tripod at a height of 1.5 m. The output of the measurements is the frequency spectrum and cumulative values of the electromagnetic spectrum intensity at each measurement site during individual measurements. The measurement time was set to six minutes. The measurement was performed in the frequency band of the measurement chain from 420 MHz to 6 GHz. During the measurement, the dynamic measurement range was set on the instrument to 5V/m, RBW – 5MHz, the minimum display frequency  $F_{\min}$  – 700 MHz, and the maximum display frequency  $F_{\max}$  – 3500 MHz.

Given the measurement method used, the measurement instruments, and the measurement conditions, the uncertainty in Table 1 was considered in the results. The uncertainty is determined by an internal operating procedure of an accredited test laboratory.

**Table 1.** Measurement uncertainty.

Quantity	Measurement range	Measurement uncertainty %
Electric field strength - E	420 MHz – 1600 MHz	26,4
Electric field strength - E	1600 MHz – 6000 MHz	29,7

According to announcements of the Ministry of Health SR 534/2007 Coll [4], these values have been compared with the action values for continuous exposure of the popu-

lation. In table 2 the exposure action values for the electrical, magnetic, and electromagnetic fields (effective values for continuous exposure) related to the frequency interfaces of mobile base stations are shown.

**Table 2.** Reference levels for exposure, averaged over 30 min and the whole body, to electromagnetic fields from 400MHz to 300 GHz [4].

Frequency range	Electric field strength	Magnetic field	Magnetic induction	Plane-wave equivalent incident
	E (V/m)	strength H (A/m)	B (μT)	power density Seq (W/m)
400MHz to < 2000MHz	$1,375 \times f^{1/2}$	$0,0037 \times f^{1/2}$	$0,0046 \times f^{1/2}$	$f/200$
2 GHz to 300 GHz	61	0,16	0,2	10

Note:

1. f is the frequency in units specified in the frequency range column.
2. For frequencies in the range of 100 kHz to 10 GHz, seq, E2 shall be averaged over a 6-minute interval.
3. For frequencies above 10 GHz, seq, E2 must be averaged over 68 / f1,05-minute intervals (f in GHz).

### 3. Results

#### 3.1. Full spectrum of measurement

The frequency range  $F_{min}$  700 MHz and  $F_{max}$  3500MHz have been set for the measurement. In general, this spectrum is used by operators to operate their services. Figure 2 shows the frequency spectrum graphs from the M1 measuring point for a given range in the operation of one operator and both at the same time.

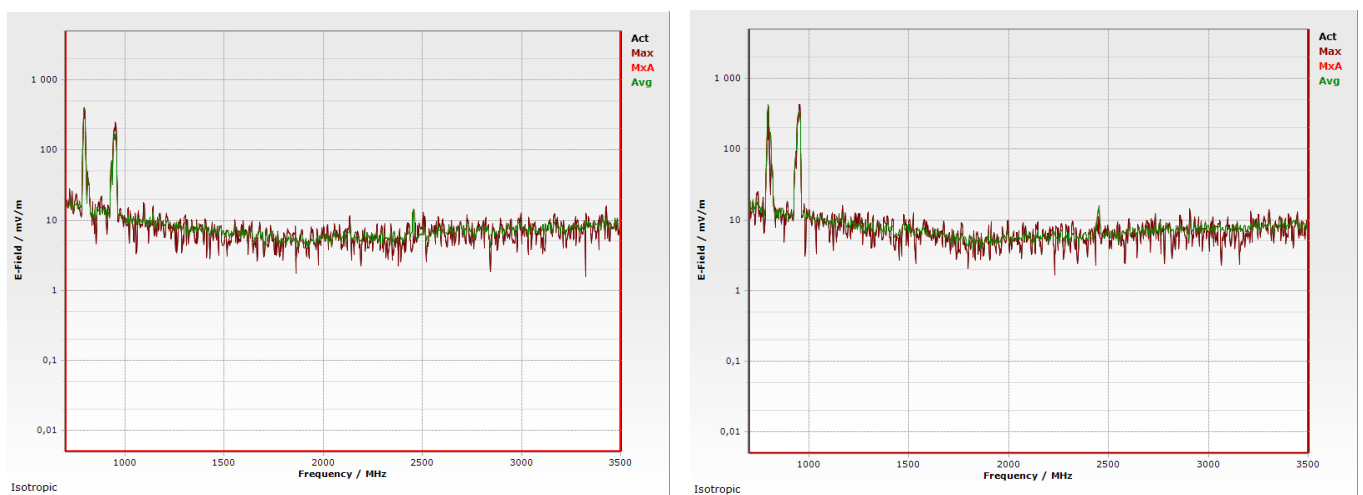


**Figure 2.** (a) Frequency spectrum M1.1 – one operator; (b) Frequency spectrum M1.2 – two operators

The output of the measurements are cumulative values (table 3) from the frequency range  $F_{min}$  700 MHz –  $F_{max}$  3500MHz, which show us the differences in the intensity of electromagnetic fields during the measurements of one operator and both mobile operators together.

**Table 3.** Cumulative values from frequency range 700 ÷ 3500 MHz

Cumulative values (V/m)	M1	M2	M3	M4
1 operator	0,693	0,285	0,473	0,250
2 operators	0,766	0,302	0,263	0,238

#### 3.2. Analysis of transmission frequencies

In order to better assess the added operator, we have carried out a frequency range analysis of the operators' frequencies of 800 MHz and 900 MHz. We've been scanning the frequency range from  $F_{\min}$  700MHz to  $F_{\max}$  1000MHz. Figures 3 and 4 show the frequency spectrum from the M1, and M3 measurement points for one operator and both mobile operators simultaneously (marked M1.1, M1.2, etc.).

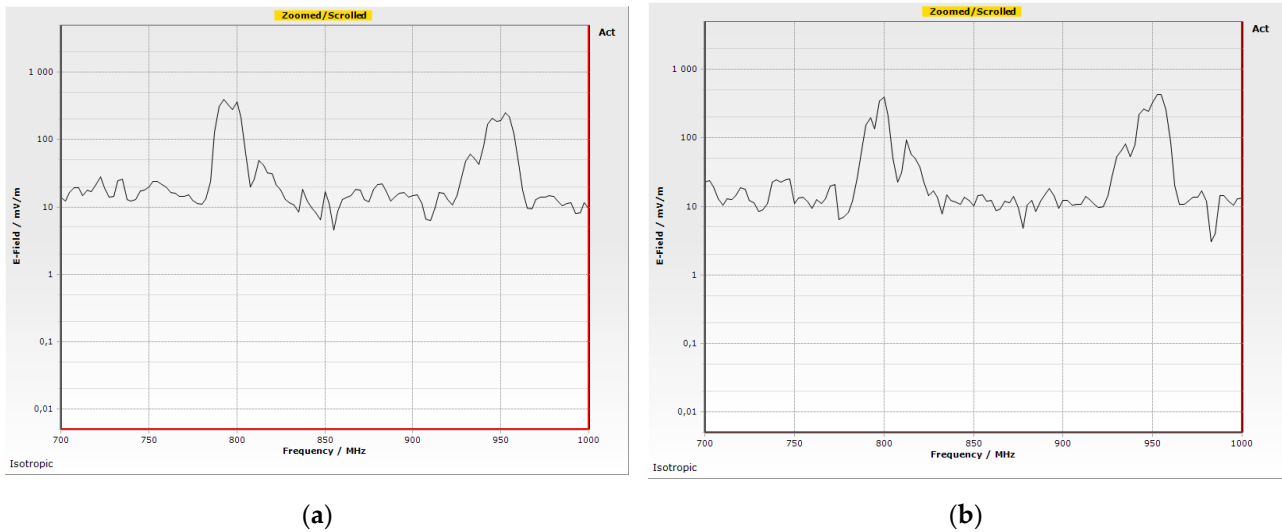


Figure 3. (a) Frequency spectrum M1.1 – one operator; (b) Frequency spectrum M1.2 – two operators

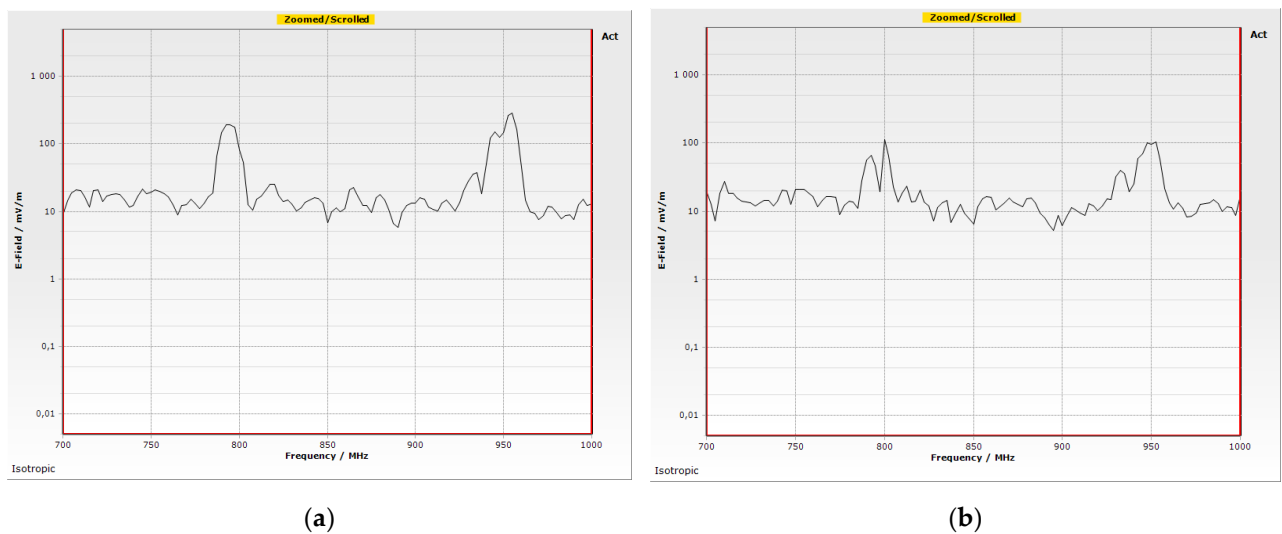


Figure 4. (a) Frequency spectrum M3.1 – one operator; (b) Frequency spectrum M3.2 – two operators

Table 4 shows the cumulative values from the frequency range of 700 ÷ 1000 MHz and Figure 5 gives a graphical representation of these values in V / m.

Table 4. Cumulative values from frequency range 700 ÷ 1000 MHz.

Cumulative values (V/m)	M1	M2	M3	M4
1 operator	0,676	0,239	0,447	0,194
2 operators	0,750	0,261	0,212	0,181

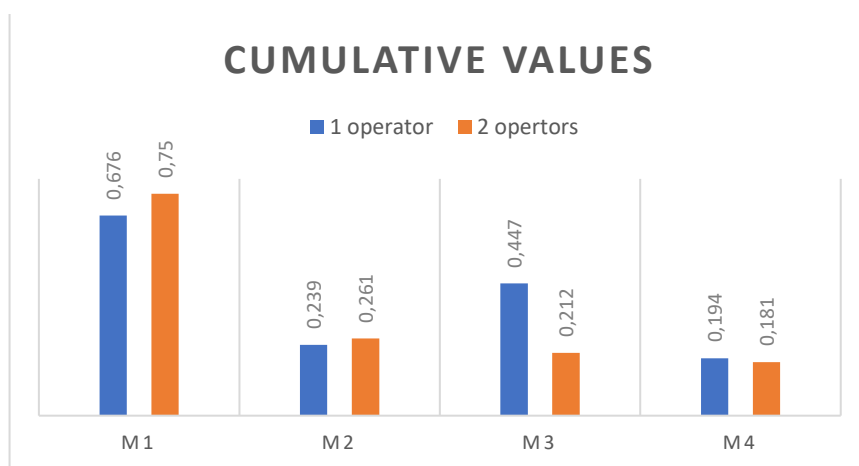


Figure 5. graphical representation of cumulative values in V/m

Assessment of the analysis of transmission frequencies

- M1, M2 - by adding a mobile operator, the EMF intensity increased by only 0.074 V/m or by 0.022 V/m.
- M3, M4 – Conversely, at the measuring points M3 and M4, which were located at the dwelling house, the EMF intensity was measured at 0,235 and 0,013 V / m respectively lower for both operators. This difference may be due to several factors, such as the timing of the measurement, the maintenance of the services of the first mobile operator in a particular dwelling, or the first measurement also capturing another domestic source, such as Wi-Fi.

3.3 Assessment of population exposure

The environmental impact assessment of the population has been carried out in the range of 700 MHz to 1000 MHz. The measure to be assessed under the legislation in force is the cumulative value of the EMF intensity in the frequency range of the resource to be assessed. Table 5 shows the values measured, the values assessed the legislative action values, and their comparison.

Table 5. Results of the electric field intensity measurement – impact on the population.

Measurement site	Frequency range	Measured Effective Value Electrical Field Intensity Eef (V/m)	Effective electric field force value to be assessed EefP (V/m)	Action Values (Decree No. 534/2007) Ea (V/m)	(EefP/Ea) <sup>2</sup>
M1.1	700 ÷ 1000 MHz	0,676	0,85	36,4	5,52E-04
M2.1	700 ÷ 1000 MHz	0,239	0,30	36,4	6,90E-05
M3.1	700 ÷ 1000 MHz	0,447	0,57	36,4	2,41E-04
M4.1	700 ÷ 1000 MHz	0,194	0,25	36,4	4,54E-05
M1.2	700 ÷ 1000 MHz	0,750	0,95	36,4	6,79E-04
M2.2	700 ÷ 1000 MHz	0,261	0,33	36,4	8,22E-05
M3.2	700 ÷ 1000 MHz	0,212	0,27	36,4	5,43E-05
M4.2	700 ÷ 1000 MHz	0,181	0,23	36,4	3,96E-05

- 1) The value to be considered is the measured value plus the measurement uncertainty from the tab. 1
- 2) The action value was taken as the lowest allowed value in the range of the frequency range being evaluated (e.g., for the range of 700 to 1000 MHz, the action value for the frequency of 700 MHz is calculated).

In the case of frequency measurement, the  $\sum (EefP / Ea)^2$  – the sum of all signals with a level greater than 30 dB below the maximum measured level must be less than 1.

From the measured and calculated values, it was found that the assessed values of the EefP electric field from the M1-M4 measuring points do not exceed the action values of the Ea electric field. The population exposure is in accordance with the provisions of the Act NR SR 355 / 2007 Z Coll. and announcements of the Ministry of Health Communication SR 534 / 2007 Coll.

#### 4. Conclusions

The interest in mobile phone services continues to grow. It is essential that potential operators ensure data services for everyone equally. That is why the construction, the expansion of base stations for mobile operators, is essential. However, there is also a greater interest on the part of residents or users in the negative effects resulting from the operation of these base stations.

In the contribution, we described the experimental measurement of EMF intensity at the mobile base station where the new mobile operator was added. Measurements before and after the addition of a new operator have been evaluated for the frequency range of 700 ÷ 1000 MHz because both mobile operators use frequencies in this frequency range. The increase in values after the addition of the mobile operator was only recorded in the vicinity of the base station. Measurements in the municipality of the houses recorded lower EMF intensities than in the operation of a single operator. This may be due to the time difference when the measurement was performed or to the data services, they use in the vicinity of the measuring point. It follows from the above that the extension of the station by one operator with specified performance and technical regulation has a negligible impact on the population.

Based on the measured values of the EMF intensity of the individual measuring points, we have carried out a comparison with the permissible action values laid down in the legislation in force in the Slovak Republic. All values are well below the EMF action values set out in the legislation in force. Nevertheless, it is essential to monitor these changes closely.

**Acknowledgments:** This article was prepared with support from the project titled APVV-21-0120 „Research of an innovative method of monitoring the noise load generated by overhead power lines“ and KEGA 011TUKE-4/2021 „Implementation of current scientific, technical and methodological solutions in the field of environmental engineering by the educational process in universities“.

**Conflicts of Interest:** The authors declare no conflict of interest.

#### References

1. Boo, SF.; Pang, WL.; Wong, SK.; Chan, KY.; Alkhateb, L. Investigation of Electromagnetic Fields from LTE Base Station. *Advanced Science Letters* 23, 2018, pp.11494-11497.
2. Tomitsch, J.; Dechant, E.; Frank, W. Survey of Electromagnetic Field Exposure in Bedrooms of Residences in Lower Austria. *Bioelectromagnetics* 31, 2010, pp. 200-208.
3. Koprivica, M., Slavkovic, V., Neskovic, N., & Neskovic, A. Statistical analysis of electromagnetic radiation measurements in the vicinity of GSM/UMTS base station installed on buildings in Serbia. *Radiation Protection Dosimetry*, 168(4), 2015, pp. 489–502
4. Decree of the Ministry of Health of the Slovak Republic no. 534/2007 Coll. on details and requirements for sources of electromagnetic radiation and on the limits of exposure of residents to electromagnetic radiation in the environment. (Slovak language)

# Dual-mass flywheel for hybrid propulsion

Matúš Kačír<sup>1\*</sup>, Robert Grega<sup>2</sup>

<sup>1</sup> Technical University of Košice, Faculty of Mechanical Engineering, Department of Construction and Transport Engineering, [matus.kacir@tuke.sk](mailto:matus.kacir@tuke.sk)

<sup>2</sup> Technical University of Košice, Faculty of Mechanical Engineering, Department of Construction and Transport Engineering, [robert.grega@tuke.sk](mailto:robert.grega@tuke.sk)

\* Correspondence: [matus.kacir@tuke.sk](mailto:matus.kacir@tuke.sk); Tel.: +421 55 602 2355

**Abstract:** Electrification of passenger cars is a common part of the design and production of cars thanks to decreasing emission standards. We most often encounter hybrid cars on the road, while these cars are powered by an internal combustion engine and electric motor. If the electric motor is directly connected to the vehicle's drivetrain, it is affected by the effects of torsional oscillations, which causes a reduction in the efficiency of the electric motor. For this reason, it is necessary to eliminate torsional oscillation as much as possible. To eliminate torsional oscillation, a dual-mass flywheel with a certain load characteristic is currently used. Our effort is to design a dual-mass flywheel where we could change the load characteristic to a certain extent as needed. Such a dual-mass flywheel could be used in combustion engines, in hybrid drives, but also in engines with cylinder deactivation.

**Keywords:** dual-mass flywheel, hybrid propulsion, torsional vibration

## 1. Introduction

Due to current and future environmental and ecological requirements, car manufacturers have been forced to apply various technologies to combustion engines, resulting in lower fuel consumption and lower emissions. Such technologies and design changes can be considered, for example, downsizing, down speeding or cylinder deactivation [1]. However, these technologies adversely affected the formation of crankshaft torsional oscillation. Historically, several measures have been taken to control the torsional vibrations of the powertrain. For engines with high torque, a dual-mass flywheel (DMF) was designed to eliminate torsional oscillation [2, 3]. Figure 1 shows the elimination of crankshaft vibration.

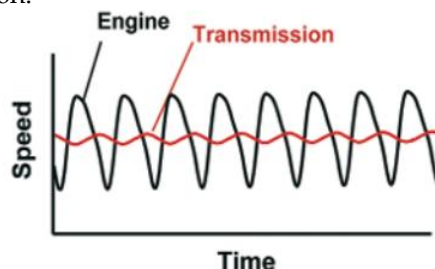


**Figure 1.** The elimination of crankshaft vibration with application of DMF [4].

The current trend to reduce emissions is the electrification of vehicles and the transition to so-called hybrid electric vehicles (HEV) [2,3]. By combining an internal combustion engine and an electric motor, car manufacturers achieved the required emission production value. The hybrid powertrain is an electromechanical system that is sensitive to vibrations. This fact is different from the problems of a vehicle with combustion engine.

propulsion. Therefore, it is inevitable to suppress the unwanted torsional vibrations of the hybrid vehicle as much as possible.

## 2. Defining the problem

In recent years, much effort has been devoted to DMF research with the aim of improving driving comfort by eliminating vibrations and reducing stress on individual vehicle components. Wang et al proposed a multi-level torsional stiffness DMF [5]. Pflieger and his team designed an electromagnetic damping system for a dual-mass flywheel [6]. Hu et al. analysed the working principle of a torsional vibration damper with a radial spring of a dual-mass flywheel [7]. Chen et al. created a nonlinear torsional vibration system with two degrees of freedom of a long arc DMF spring [8].

The disadvantage of these designs and improvements is the unchanging load characteristic of damping torsional oscillations. Eliminating torsional oscillations is suitable, for example, in cars with cylinder deactivation [9].

The suppression of torsional vibrations is essential for the driving performance of a hybrid vehicle. The main aim of this proposal is to build a model with flexible members that will provide optimal damping of torsional oscillations and eliminate vibrations.

In the issue of piston combustion engines, there is an effort to reduce the torsional oscillation entering the electric motor located on the input shaft of the transmission [9]. Schematic drive of a hybrid car is shown in following figure. The drive consists of combustion engine (1), DMF (2), electric motor (3), gearbox (4) and gearbox output shaft (5).

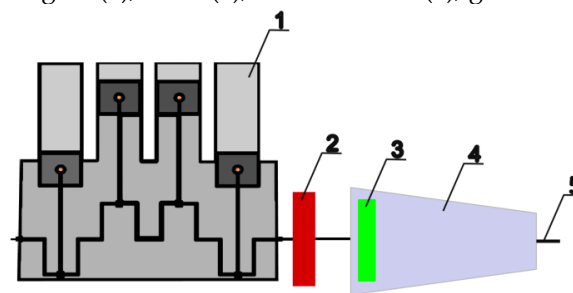


**Figure 2.**Schematic drive of a hybrid car.

Torsional oscillation adversely affects the operation of the electric motor and thereby reduces its efficiency and lifespan. In different driving modes and under different conditions, such as the excitation force of the engine, excitation from the road, wheel imbalance, or when the car starts, gears or brakes [9]. All this can disrupt the proper operation of the electric motor and other parts of the car. One of the possibilities to eliminate the torsional vibration of the crankshaft more effectively is to develop an element based on the principle of a dual-mass flywheel. The dual-mass flywheel, which can be used, is shown in figure 3.

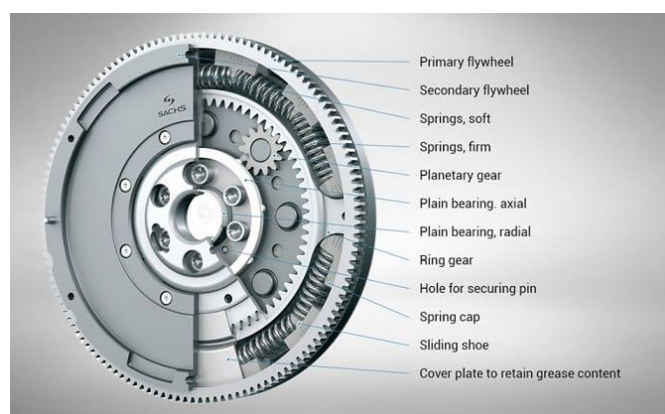


**Figure3.** Dual mass flywheel [10]

### 3. Design of a pneumatic dual-mass flywheel

Our proposal is a dual mass flywheel in which we can smoothly change the torsional stiffness and thereby achieve optimal regulation of torsional oscillations. Torsional stiffness regulation consists of changing the pressure of the gas medium in the vibration dampers. Such type of a pneumatic dual-mass flywheel can be seen in Fig. 4.

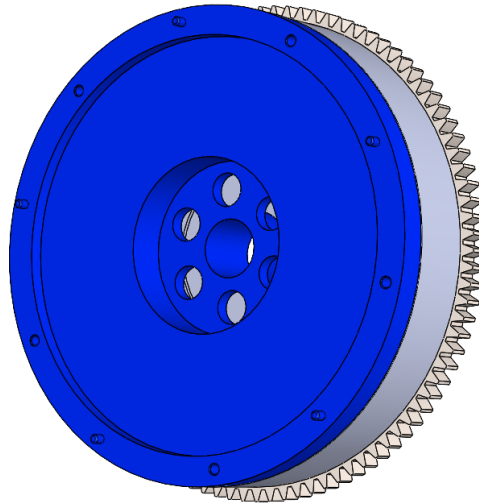


**Figure 4.** Pneumatic dual mass flywheel.

The procedure consisted in the design of a dual-mass flywheel using linear pneumatic cylinders, which will allow us to smoothly change the torsional stiffness. Pneumatic cylinders transfer the torque from the primary to the secondary mass.

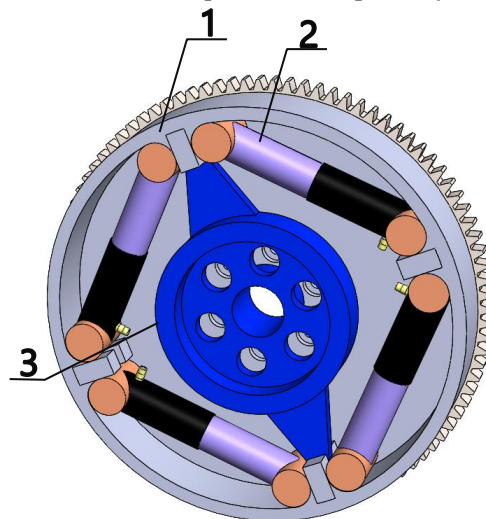


**Figure 5.** Section of pneumatic dual-mass flywheel.

Fig. 5 shows a section of a pneumatic dual-mass flywheel. The principle of use consists in the fact that the primary mass (1) is screwed onto the crankshaft. The engine torque is transmitted to the secondary mass via pneumatic cylinders (2). Inside the pneumatic cylinders, it is possible to change the pressure of the gas medium and thereby eliminate torsional oscillation more efficiently. The torque is transmitted to the secondary part of the flywheel and from there by means of a coupling to the transmission input shaft.

#### 4. Conclusion

The use of dual-mass flywheels in the automotive industry is commonplace today. Historical development, increasing driving comfort and lowering emission limits forced car manufacturers to develop new components and technologies. Our aim is to design a dual-mass flywheel with the possibility of regulating the damping of crankshaft torsional oscillations. In the next research we would like to focus on the numerical analysis of the designed two-mass flywheel, the results of which will be verified by experimental measurements in the laboratory at our workplace.

**Acknowledgments:** This paper was written in the framework of Grant Project **VEGA:** „1/0528/20 and **KEGA** 029TUKE-4/2021.

**Conflicts of Interest:** The authors declare no conflict of interest.

#### References

- FRIDRICHOVÁ, K., DRÁPAL, L., VOPAŘIL, J. and DLUGOŠ, J. Overview of the potential and limitations of cylinder deactivation. *Renewable and Sustainable Energy Reviews*. 2021. Vol. 146, p. 111196. DOI 10.1016/j.rser.2021.111196.
- MARTINEZ, C. M., HU, X., CAO, D., VELENIS, E., GAO, B. and WELLERS, M. Energy Management in plug-in Hybrid Electric Vehicles: Recent progress and a connected vehicles perspective. *IEEE Transactions on Vehicular Technology*. 2017. Vol. 66, no. 6p. 4534–4549. DOI 10.1109/tvt.2016.2582721.
- FRIDRICHOVÁ, K., DRÁPAL, L., VOPAŘIL, J. and DLUGOŠ, J. Overview of the potential and limitations of cylinder deactivation. *Renewable and Sustainable Energy Reviews*. 2021. Vol. 146, p. 111196. DOI 10.1016/j.rser.2021.111196.
- BALASHOV, D., BURKOVSKI, L., FERDERER, F., FIDLIN, A., KREMER, M., PENNEC, B. and SEEBACHER, R. Simulation Bei Drehschwingungsdämpfern. *ATZ - Automobiltechnische Zeitschrift*. 2006. Vol. 108, no. 12p. 1038–1045. DOI 10.1007/bf03221845.
- WANG, Y., QIN, X., HUANG, S. and DENG, S. Design and analysis of a multi-stage torsional stiffness dual mass flywheel based on vibration control. *Applied Acoustics*. 2016. Vol. 104, p. 172–181. DOI 10.1016/j.apacoust.2015.11.004.
- PFLEGHAAR, J. and LOHMANN, B. The electrical dual mass flywheel -an efficient active damping system. *IFAC Proceedings Volumes*. 2013. Vol. 46, no. 21p. 483–488. DOI 10.3182/20130904-4-jp-2042.00046.
- HU, J., QIN, D., ZHAO, Y. and LIU, Y. Study on natural torsional vibration characteristics of dual mass - flywheel radial spring type torsional vibration damper. *SAE Technical Paper Series*. 2009. DOI 10.4271/2009-01-2062.
- CHEN, L., ZENG, R. and JIANG, Z. Nonlinear dynamical model of an automotive dual mass flywheel. *Advances in Mechanical Engineering*. 2015. Vol. 7, no. 6p. 168781401558953. DOI 10.1177/1687814015589533.
- Yücesan, A., & Mugan, A. (2021). Development and control of an active torsional vibration damper for vehicle powertrains. *Proceedings of the Institution of Mechanical Engineers, Part K: Journal of Multi-Body Dynamics*, 235(3), 452–464. <https://doi.org/10.1177/14644193211019943>
- Thorat, S. (2020, February 19). What is dual mass flywheel: Types , working. *Learn Mechanical Engineering*. Retrieved November 13, 2022, from <https://learnmech.com/what-is-dual-mass-flywheel-types-working>



# Verification of the properties of linear position sensors

Ivana Koláriková <sup>1\*</sup>, Tatiana Kelemenová <sup>1</sup> and Barbora Hudáková <sup>1</sup>

<sup>1</sup> Technical University of Košice, Faculty of Mechanical Engineering, Department of Biomedical Engineering and Measurement, Letná 1/9, 042 00 Košice, Slovak Republic

\* ivana.kolarikova@tuke.sk, tatiana.kelemenova@tuke.sk

**Abstract:** Linear position sensors are designed to measure the distance between a physical object and a point of reference, as well as changes in position. Linear position sensors are designed to measure the distance between a physical object and a point of reference, as well as changes in position. Linear position sensors play an important role in automated machinery. Therefore, it is essential that these sensors are highly accurate and have low measurement errors. In this article there were verified properties of two small linear position sensors. They were mounted on a measuring stand and detected a change in the position of a reflecting surface. There were created transformation and calibration characteristics and there were calculated regression equations, standard deviations and combined standard uncertainties from obtained data. From the point where both sensors showed a voltage change, the working range was evaluated. Both sensors have different working range and one of them will be chosen to be used on inclination tribometer for sensing the position of the body.

**Keywords:** linear position sensor; measurement; uncertainty; proximity

## 1. Introduction

Linear position sensors measure by converting displacement into an electrical output. A wide variety of measurement principles can be used to make precise and reliable measurements for a broad range of applications. Linear position sensors and measurement systems are used in industrial applications as well as in scientific laboratories. There are many different types of linear position sensing technology available: capacitive, inductive, magnetic, photoelectric and ultrasonic [1 – 5].

Capacitive sensors are non-contact type of linear sensors and work by measuring the difference in voltage applied between the sensor and its target. Capacitive sensors can either be used in conductive and non-conductive material but is sensitive to environmental parameters such as air. The principle of inductive sensors consists in the transformation of the measured position to the change of coil's own inductance, or the coil's mutual inductance. The main part of the sensor is one or more coils. The displacement of the measured object changes the electrical and magnetic properties of the sensor. Magnetic proximity sensors detect permanent magnets. At first glance they look the same as inductive sensors, but they allow the object to be detected even through non-magnetic metallic materials (aluminum, gold, etc.). They have a relatively long range and small dimensions. Photoelectric sensors include fiber optic, optical triangulation, and optical time of flight. They function by using the projection and detection of light. Ultrasonic sensors work similarly to photoelectric sensors by using the projection and detection of sound [1 – 5].

For purpose of this work two different position sensors were chosen: photoelectric and ultrasonic sensor. There are many differences between them, they are used in different industrial applications and the aim of this work is to verify their properties in order to choose one of them for the next research.

## 2. Sensors and Measurement Methodology

Ultrasonic sensor UB 800-18 GM 40-1-V1 Pepperl + Fuchs has analog output in the form of electric current, but for the purposes of this article, a resistor with a value of  $500\ \Omega$  was used. The resistor was connected to the current output of the sensor, and then the drop in electric voltage on this resistor was measured. This modification was implemented in order to make the results comparable with another sensor tested in this article. The principle of the sensor consists in non-contact detection of the measured object. A measuring stand (Figure 1 left) was created with a linear guide with a range of 1000 mm and an adjustable sensor holder specially designed for this purpose and printed on a 3D printer from PLA material. On this stand, there was another holder holding reflective surface, which served as the detected object, and it was placed on the linear guide. The mutual distance between the sensor and the reflecting surface was gradually adjusted during the measurement using gauge blocks with a step of 2.5 mm from 40 to 80 mm and a step of 10 mm from 80 to 850 mm, 10 measurements for each step under the same measurement conditions. Sensor was connected to the power supply and multimeter Mastech MY74 (Figure 1 right).

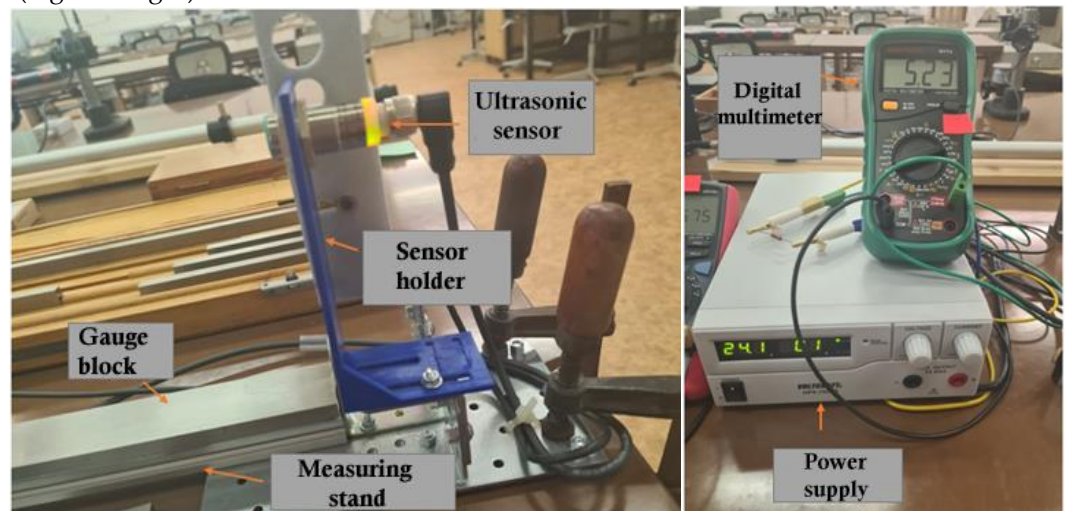


**Figure 1.** Measuring chain with ultrasonic sensor.

The Panasonic HG – C1400-P photoelectric non-contact sensor used the same measuring stand (Figure 2 left) as the ultrasonic sensor for the measurements, therefore the same reflective surface was used as the detected object. There was also 3D printed sensor holder. In this case, the mutual distance between the sensor and the reflecting surface was also set using gauge blocks (Figure 3) with a step of 10 mm from 200 mm to 600 mm, and the measurements were carried out 10 times under the same conditions. In this article, white matte paper was used as a reflective surface (Figure 3). Sensor was connected to the power supply and multimeter UNI-T UT 71E (Figure 2 right).

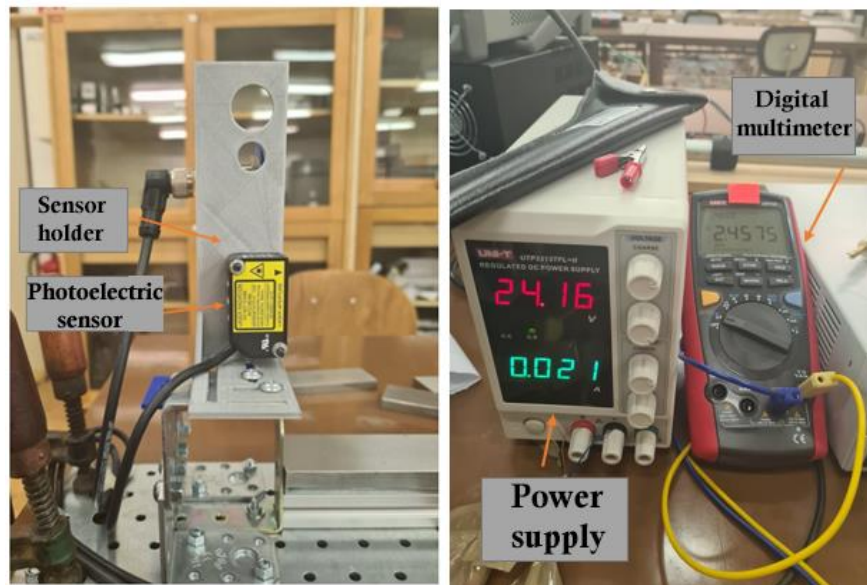


Figure 2. Measuring chain with photoelectric sensor.

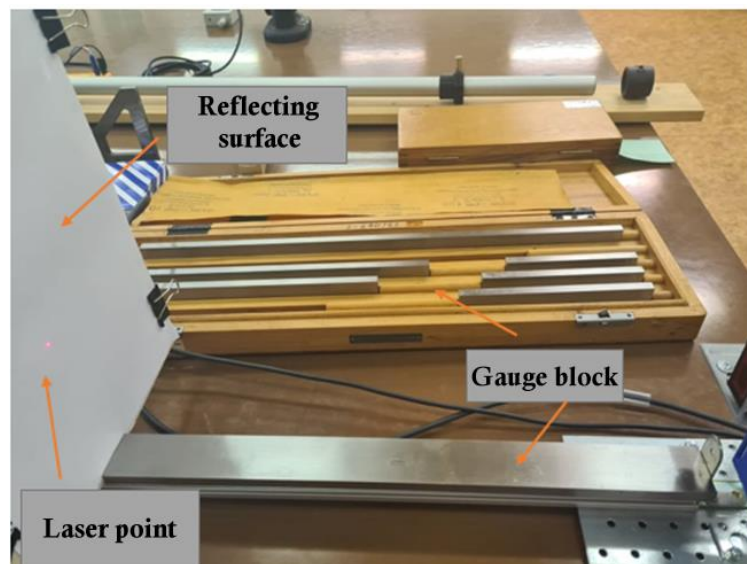


Figure 3. Measuring chain and reflecting surface.

### 3. Results

A total of 1350 measurements were performed. The results of the verification measurements of sensors were processed into a graphic form as a transformation and calibration characteristic. From the point of view of practical application, the usable measurement ranges of these sensors were determined. A regression curve was analyzed on the graph of the calibration characteristic, from which the regression equation and model were calculated. This will allow to recalculate the output electrical voltage to the measured position and equation can be further applied to the electronic unit (PLC or microcontroller) to which the sensor will be connected. Both characteristics for sensors can be seen in Figure 4, Figure 5, Figure 6 and Figure 7.

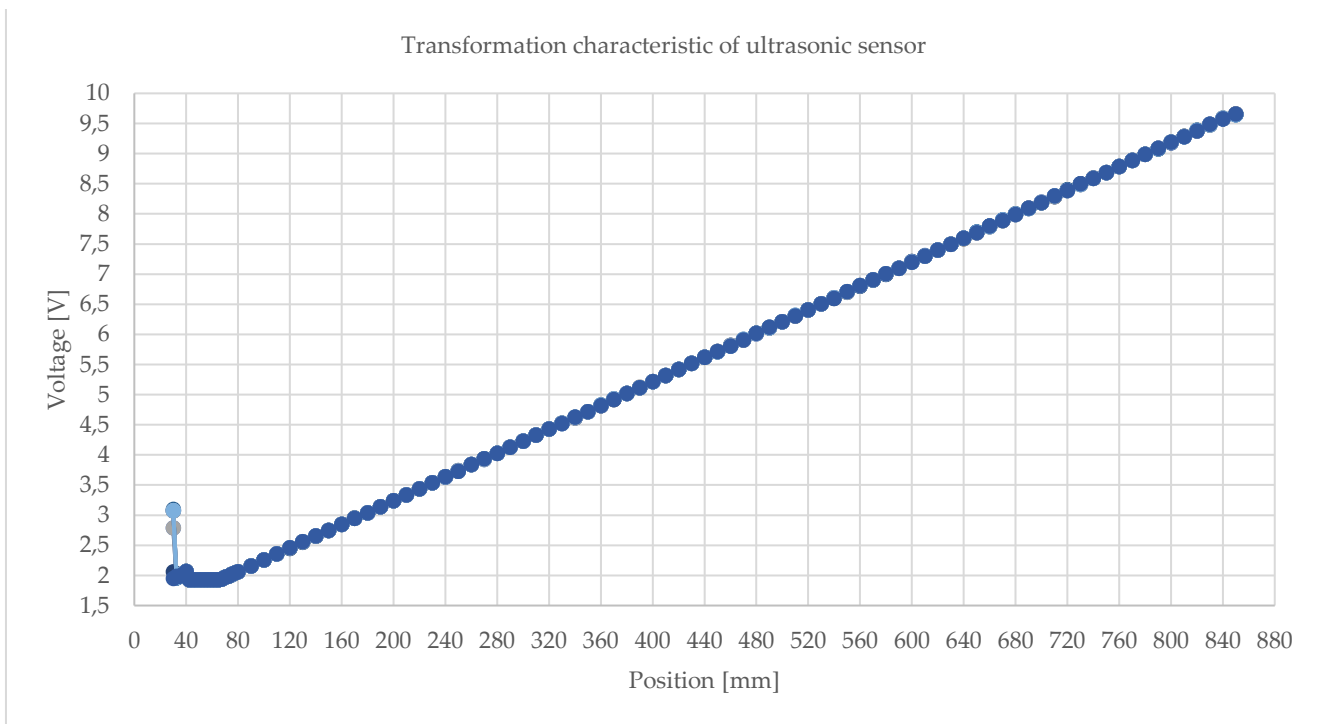


Figure 4. Dependence of the average output voltage of ultrasonic sensor on the position.

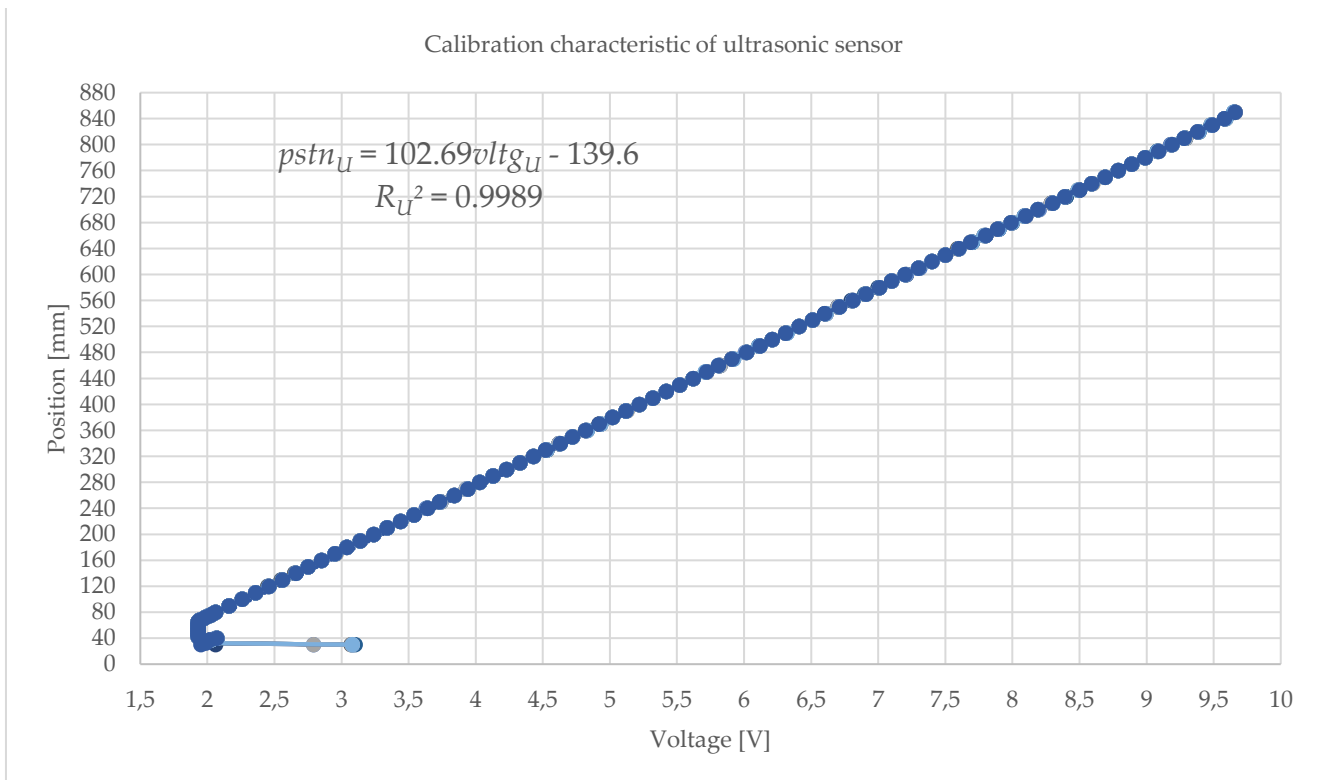


Figure 5. Dependence of the position on the average output voltage of ultrasonic sensor.

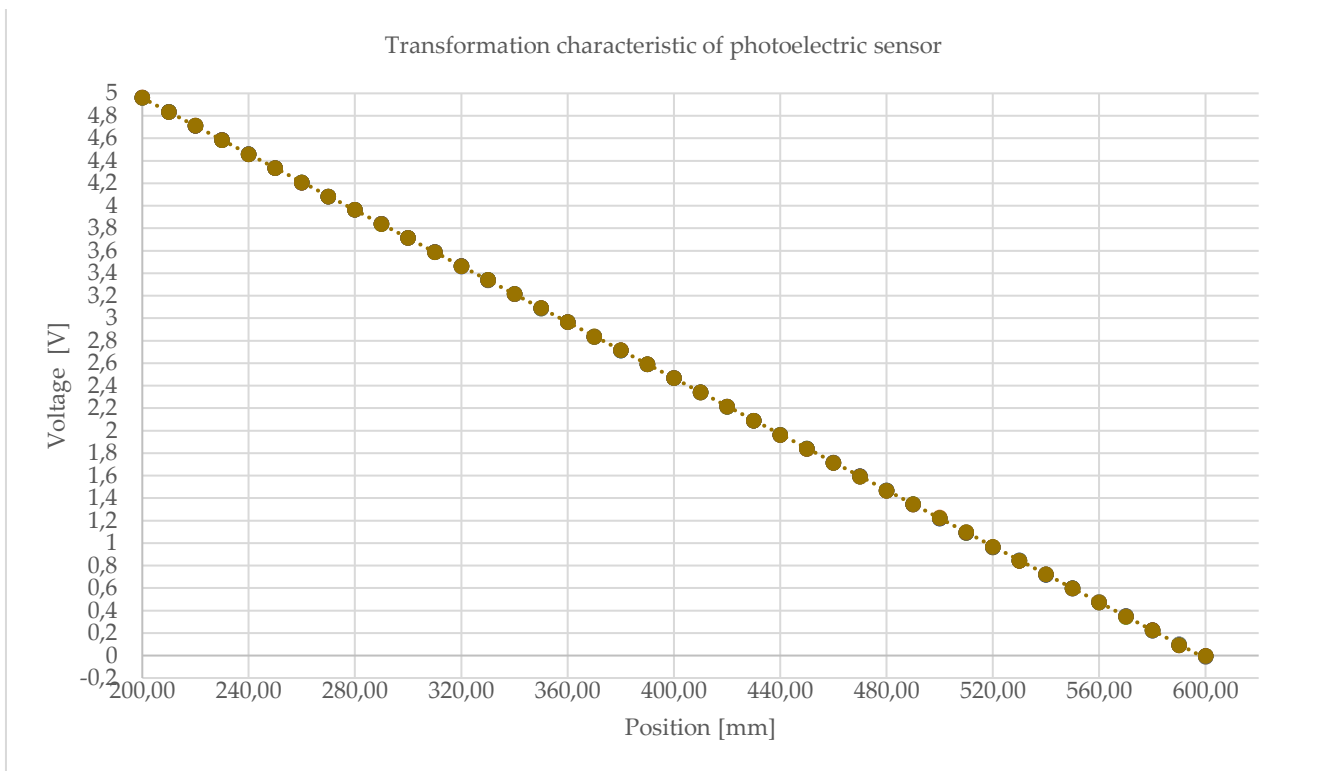


Figure 6. Dependence of the average output voltage of photoelectric sensor on the position.

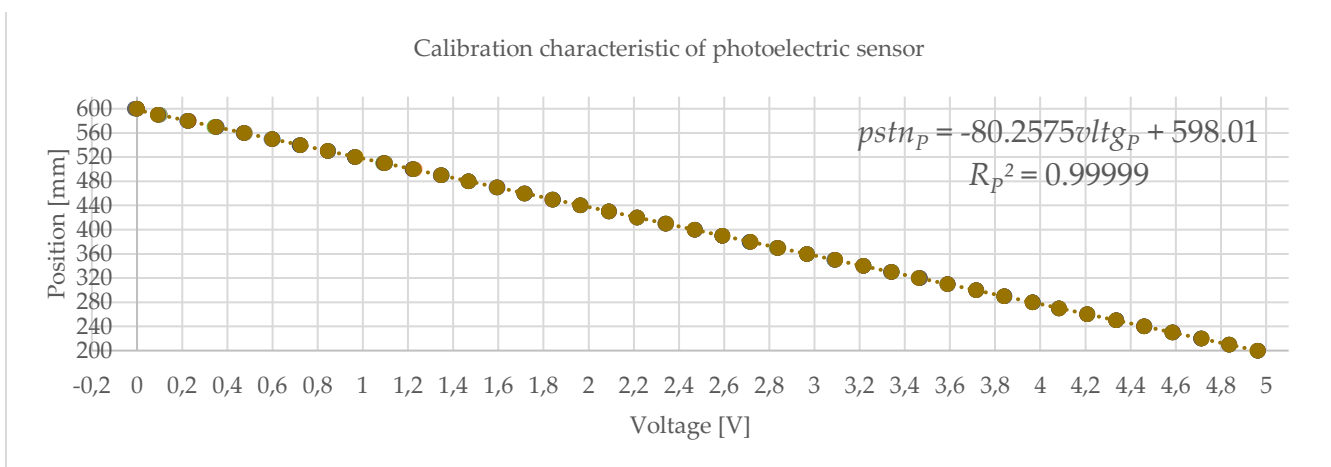


Figure 7. Dependence of the position on the average output voltage of photoelectric sensor.

There were calculated type B evaluations of standard uncertainties from datasheets. According to manufacturer of UB 800-18 GM 40-1-V1 Pepperl + Fuchs [6] repeat accuracy is  $\pm 0.5\%$  of full-scale value, therefore  $u_B$  was:

$$u_{BU} = \frac{0.5\% * 750}{\sqrt{3}} = \pm 2.2 \text{ mm} \tag{1}$$

Output voltage from ultrasonic sensor was displayed on multimeter Mastech MY74. According to manufacturer of the multimeter Mastech MY74 [7], maximum permissible error (MPE) of DC voltage for range from 200 mV to 200 V is:

$$MPE_{MY74} = 0.5\% * \bar{U} + 0.01 * 2 \tag{2}$$

According to manufacturer of Panasonic HG – C1400-P [8] repeatability is 300 μm of measuring distance 200 to 400 mm and 800 μm of measuring distance 400 to 600 mm, therefore  $u_B$  was:

$$u_{B P1} = \frac{0.3}{\sqrt{3}} = 0.17 \text{ mm} \quad u_{B P2} = \frac{0.8}{\sqrt{3}} = 0.46 \text{ mm} \quad (3)$$

According to manufacturer of the multimeter UNI-T UT 71E [9],  $MPE$  of DC voltage for range from 200 mV to 1000 V is:

$$MPE_{71E} = 0.025\% * \bar{U} + 0.001 * 5 \quad (4)$$

There were calculated type B evaluations of standard uncertainties of multimeters and type A evaluations of standard uncertainties of measurements and therefore, combined standard uncertainty could be calculated too. These uncertainties can be seen in Figure 8 and Figure 9.

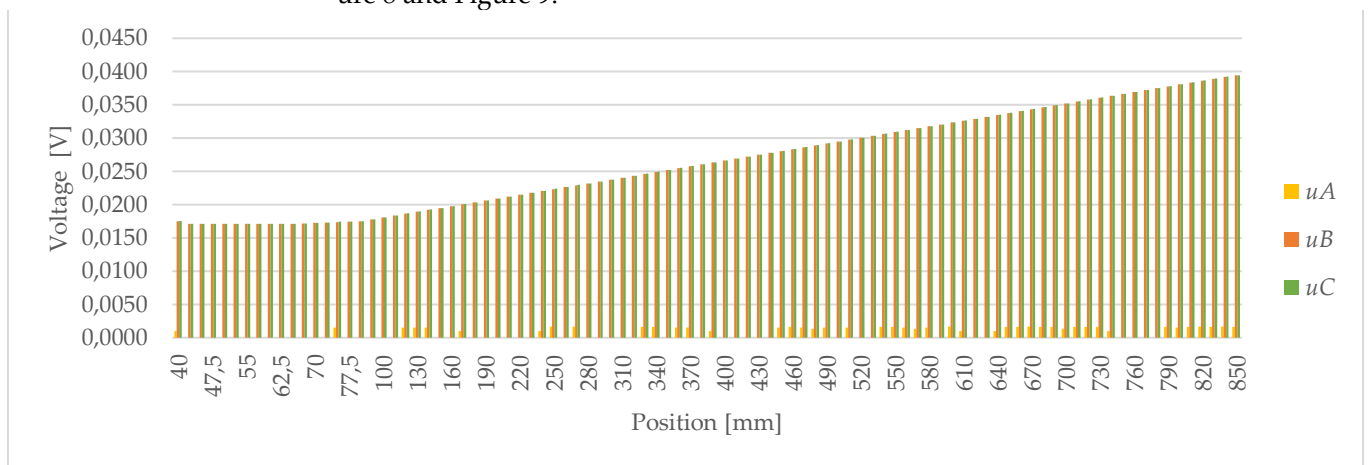


Figure 8. Standard uncertainty  $u_A$ ,  $u_B$ ,  $u_C$  of ultrasonic sensor.

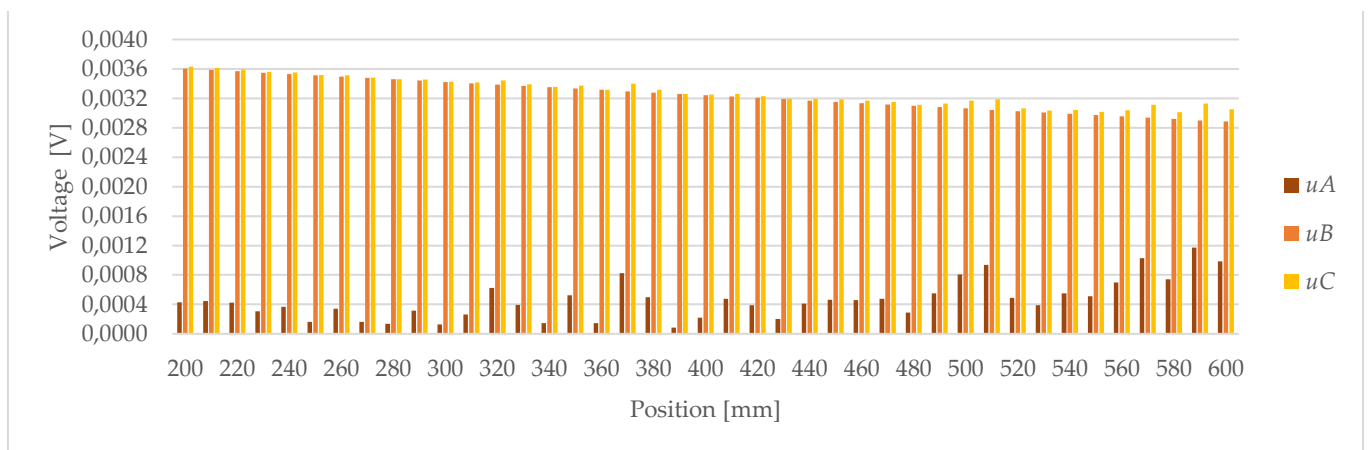


Figure 9. Standard uncertainty  $u_A$ ,  $u_B$ ,  $u_C$  of photoelectric sensor.

#### 4. Discussion

From the results processed into graphs can be evaluated that in the Figure 4 of the ultrasonic sensor average output voltage started at 2.069 V at 40 mm and had similar values of voltage until 70 mm. Therefore, these values cannot be used for measuring distance because they are in a dead band. At 70 mm the voltage started to increase in a linear manner up until 9.656 V at 850 mm. Then the working range would be from 70 to 850 mm. In the Figure 6 of the photoelectric sensor average output voltage started at 4.9625 V

at 200 mm and was decreasing in linear manner until  $-0.0021$  V at 600 mm. Therefore, the working range would be from 200 to 600 mm.

Calibration characteristic could be described as dependence of the position on the average output voltage and in the graphs, there were analyzed regression curves from which there were calculated regression equations and model. In the Figure 5 (ultrasonic sensor) regression equation was linear  $pstn_U = 102.69vltg_U - 139.6$  and regression model was close to  $R^2 = 1$ :  $R_U^2 = 0.9989$ . In the Figure 7 (photoelectric sensor) regression equation was linear  $pstn_p = -80.2575vltg_p + 598.01$  and regression model was very close to one  $R_p^2 = 0.99999$ .

In the Figure 8 for ultrasonic sensor can be seen dependence of the type A, type B and combined standard uncertainty results on the position. The type A standard uncertainty was as low as 0 V and maximum was 0.0017 V. Therefore, it can be hardly seen in the graph. The type B standard uncertainty depended on the chosen multimeter and until 80 mm values ranged between 0.0171 V to 0.0175 V. From 90 mm it increased in linear manner up to 0.0394 V. Type B standard uncertainty and combined standard uncertainty values were very similar, because type A standard uncertainty was very low.

In the Figure 9 for photoelectric sensor can be seen dependence of the type A, type B and combined standard uncertainty results on the position. The type A standard uncertainty values ranged from 0.0001 to 0.0012 V. Because for photoelectric sensor was used multimeter with higher accuracy the results for the type B standard uncertainty were from 0.0029 V to 0.0036 V. The values decreased with increasing distance in linear manner. Combined standard uncertainty was also very similar to the type B uncertainty for the same reasons as for the previous sensor.

## 5. Conclusion

According to the obtained data both sensors had great results and low standard uncertainties in their measured range. A great option for use on an inclination tribometer, where it is necessary to sense the position of the body set in motion, would be ultrasonic sensor due to the lower value of the distance that can be registered by the sensor. Therefore, the tribometer would not have to be long.

**Acknowledgments:** This study was supported by projects VEGA 1/0168/21 1/0168/21 Research and development of testing and measuring methods in coordinate metrology and KEGA 016TUKE-4/2021 New educational technologies of metrologists for monitoring of production processes and post-processing of products.

**Conflicts of Interest:** The authors declare no conflict of interest. The funders had no role in the design of the study; in the collection, analyses, or interpretation of data; in the writing of the manuscript, or in the decision to publish the results.

## References

1. Althen sensors. Available online: <https://www.althensensors.com/sensors/linear-position-sensors/> (accessed on 20. 11. 2022).
2. Variohm. Available online: <https://www.variohm.com/products/linear-position-sensors-> (accessed on 20. 11. 2022).
3. Positek. Available online: <https://www.positek.com/products/linear-position-sensors> (accessed on 21. 11. 2022).
4. Automatizace. Available online: <https://automatizace.hw.cz/magneticke-senzory-priblizeni.html> (accessed on 23. 11. 2022).
5. Virgala, I.; Miková, L.; Lipták, T.; Šarga, P.; Vagáš, M.; Kelemen, M. Snímače a převodníky, ISBN 978-80-553-2912-3, Košice 2018.
6. Pepperl+Fuchs. Available online: [https://www.pepperl-fuchs.com/global/en/classid\\_186.htm?view=productdetails&prodid=39580](https://www.pepperl-fuchs.com/global/en/classid_186.htm?view=productdetails&prodid=39580) (accessed on 23. 11. 2022).
7. Mastech Group. Available online: [https://mastech-group.com/resources/QSG+%E8%AA%AA%E6%98%8E%E6%9B%B8/GLO+%E8%AA%AA%E6%98%8E%E6%9B%B8/GLO%E8%AA%AA%E6%98%8E%E6%9B%B8\\_MY70\\_MY74.pdf](https://mastech-group.com/resources/QSG+%E8%AA%AA%E6%98%8E%E6%9B%B8/GLO+%E8%AA%AA%E6%98%8E%E6%9B%B8/GLO%E8%AA%AA%E6%98%8E%E6%9B%B8_MY70_MY74.pdf) (accessed on 23. 11. 2022).
8. Conrad. Available online: <https://asset.conrad.com/media10/add/160267/c1/-/en/001416060DS01/datasheet-1416060-panasonic-hg-c1400-p-laser-range-finder-1-pcs-24-v-dc-max-range-open-field-400-mm-l-x-w-x-h-44-x-20-x-25-mm.pdf> (accessed on 23. 11. 2022).
9. Micronix. Available online: <https://eshop.micronix.sk/data/sk/att/004/6928-7792.pdf> (accessed on 23. 11. 2022).



# Review of bioreactor systems in tissue engineering

Petra Kolembusová <sup>1,\*</sup>, Radovan Hudák <sup>1</sup> and Norbert Ferenčík <sup>1</sup>

<sup>1</sup> Department of Biomedical Engineering and Measurement

\* Correspondence: petra.kolembusova@tuke.sk

## Abstract:

The aim of this review is to make an overview of existing bioreactors in tissue engineering and their parameters for cell and tissue cultivation. Types of tissue engineering bioreactors can be divided into many groups depending on which parameter we consider. We decided to make a list of bioreactors depending on how they stimulate cells during cultivation process. Based on that list we named parameters which are dependent on those bioreactors. The outcome from this review is a table of designs of bioreactors and important parameters for mimicking physiological phenomena.

**Keywords:** bioreactor, tissue engineering, regenerative medicine, cultivation

## 1. Introduction

Tissue engineering uses a combination of the structural, biological, and physico-chemical characteristics of cells, engineering, and materials science to create solutions for the replacement, repair, and regeneration of tissues and organs [1].

There are several other applications for bioreactors, both on a micro- and larger scale; small- and micro-bioreactors are frequently used in manufacturing to design new production processes prior to full-scale fabrication, as well as lab-on-a-chip applications. This review, however, is not about these. Rather, this review will focus on the design of bioreactors that will address functional mimics of an in vivo environment [1].

Bioreactors are devices used for tissue culture and simulation of the in vivo environment. Most bioreactors are designed with a specific tissue type in mind so that the precise physiological environment for the tissue type can be produced [2].

## 2. Materials and Methods

During the design process, the specific use of the bioreactor must be kept in mind to ensure that all design conditions are met. If various parameters such as pH, nutrient concentration or oxygen levels are to be monitored, these sensors should be built into the design. If a pump or motor is to be used, it must be small enough to fit in the incubator and also usable in a humid environment. The forces required for cell stimulation are very small, so it is important to ensure that the pump/motor has the sensitivity to accurately exert small forces. In any structure involving fluids, fluid sealing problems may occur, and the need for seals should be minimized as far as possible. If a bioreactor prototype is being designed, it is worth thinking about innovative improvements from the very beginning. This may mean designing a device that can be scaled up relatively easily without changing its properties—a bioreactor that can use more than one cell carrier at a time [3].

The choice of materials is very important, as it must be ensured that the materials do not have negative effects and reactions with the cells during cultivation in the bioreactor. Any material that will be in direct contact with cells must be biocompatible and bioinert.

Several criteria determine the design of the bioreactor. The criteria may vary for different tissue types being developed, but in general the bioreactor must be designed to meet the following requirements (see **Figure 1**) [3]:

- Permanent control of the physical and chemical environment;
- Constant monitoring of cell and tissue quality;
- Ensuring that the process takes place under sterile conditions;
- Determining the exact number of distributed cells per cell carrier;
- Ensuring that cells have sufficient exchange of nutrients and waste with the environment;
- Exposure of the developing tissue to the necessary mechanical forces according to the type of tissue;
- Maintain a high level of cell proliferation;
- Ensure bioreactor materials are cell/tissue compatible.

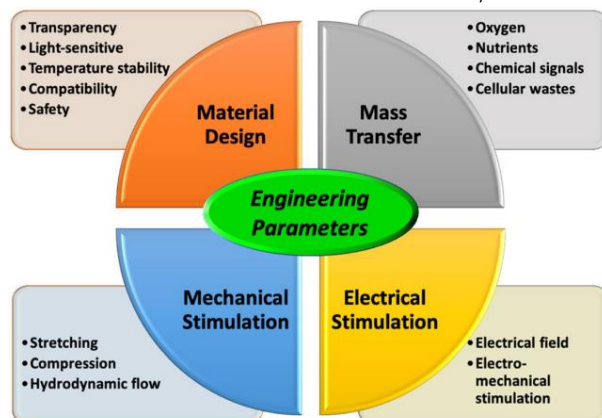


Figure 1. Schematic diagram of engineering parameters for bioreactor design [3]

Bioreactor systems offer the opportunity to study cellular function, cell-to-cell interactions, and tissue development within controlled 3D models that are designed to provide cells with the conditions of their natural environment. In this regard, various culture systems have been developed to support tissue engineering constructs. These cultivation systems can basically be divided into two main categories [3, 5]:

1. Static cultivation systems (traditional method);
2. Dynamic cultivation systems.

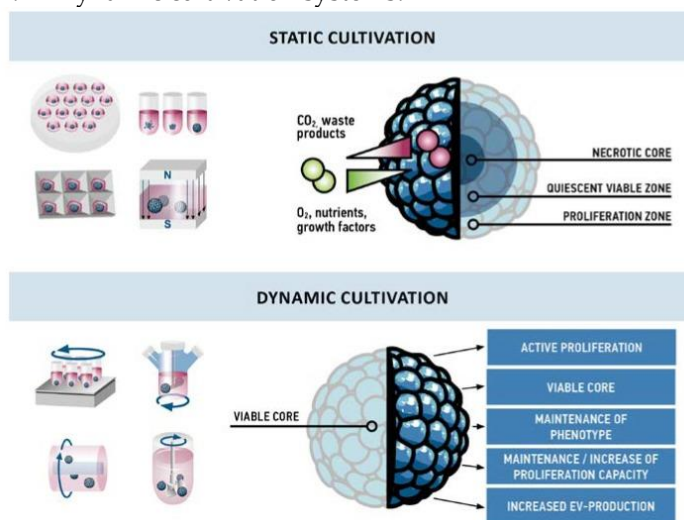


Figure 2. Comparison of effects observed in static and dynamic cultivation [6]

This traditional method of tissue cultivation does not meet all the conditions for the regeneration of a functional organ. When 3D tissues are cultured in a static culture system, the cells on the outer surface of the scaffold are viable, while the cells inside are less active or necrotic. By regularly supplying oxygen and maintaining its level in a static 3D culture, it was shown that an oxygen gradient was formed from the surface of the carrier towards

the center. As a result, thin tissues (e.g. skin) and tissues that are naturally vascular (e.g. cartilage) grow more easily in static culture systems than thicker vascular tissues [3].

In contrast to static culture conditions, the use of bioreactors has the potential to achieve a more dynamic, organ- or tissue-specific culture by providing better conditions and improving nutrient supply. Development of artificial tissues in bioreactors generally involves less handling than static culture methods to significantly reduce the risk of contamination [3, 5]. You can see the difference between static and dynamic cultivation on **Figure 2**.

### 2.1. Dynamic bioreactor systems in tissue engineering

There are different types of dynamic bioreactor systems (see **Figure 3**):

- Bioreactors with a rotating bank;
- Bioreactors with rotating walls;
- Bioreactors with hollow fibers;
- Direct perfusion bioreactors;
- Bioreactors that apply controlled mechanical forces.

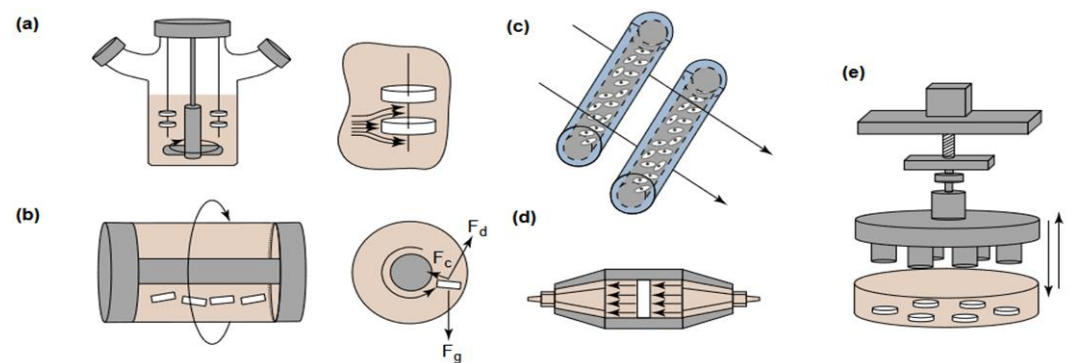


**Figure 3.** Types of dynamic bioreactor systems in tissue engineering [7]

**Rotating bank bioreactors** are used to seed cells into 3D scaffolds and to subsequently cultivate the constructs [7].

**Rotating wall bioreactors** provide constructs with a dynamic culture environment with low shear stress and high mass transfer rates. The walls rotate at a rate that allows the drag force ( $F_d$ ), the centrifugal force ( $F_c$ ) and the net gravitational force ( $F_g$ ) on the structure to be balanced [7].

**Hollow fiber bioreactors** can be used to enhance mass transfer during the cultivation of highly metabolic and sensitive cell types. In one configuration, the cells are embedded in a gel inside the lumen of the permeable hollow fibers and the medium is perfused through the outer surface of the fibers [7].

**Direct perfusion bioreactors** are systems in which the medium flows directly through the pores of the scaffold [7].

**Bioreactors** that apply controlled **mechanical forces**, such as dynamic compression, to cultured tissue can be used as model systems for tissue development under physiological stress conditions [7].

### 2.2. Bioreactor parameters

There are parameters that must be controlled and adjusted appropriately to maintain controlled, reproducible experiments. The parameters are:

- pH;
- Oxygen diffusion;
- Transport of nutrients an;
- Waste removal.

These parameters are crucial to maintain in a properly constructed bioreactor. In particular, mass transport and diffusion limitation problems related to oxygen transport have

severely limited efforts to create tissues that normally have high vascularity and/or cellularity [9]. For more parameters go to **Table 1**. Bioreactor properties [9].

**Table 1.** Bioreactor properties [9]

Biochemical properties	Biomechanical properties
Nutrients	
pO <sub>2</sub> and pCO <sub>2</sub>	Flow intensity
Vaste	Cultivation chamber volume
pH	Pressure
Temperature	Tension and other mechanical stimulations
Humidity	

The growth and differentiation of many cell types and consequently the structure and architecture of tissue is regulated by four main sources of extrinsic signaling. These include:

1. Soluble growth and differentiation factors;
2. The nature and organization of the insoluble and soluble components of the extracellular matrix (ECM) ;
3. Intercellular interactions;
4. Environmental stress induced by fluid flow and/or mechanical stimuli such as dynamic, static or shear forces, as well as other physical stimuli such as oxygen tension and pH effects.

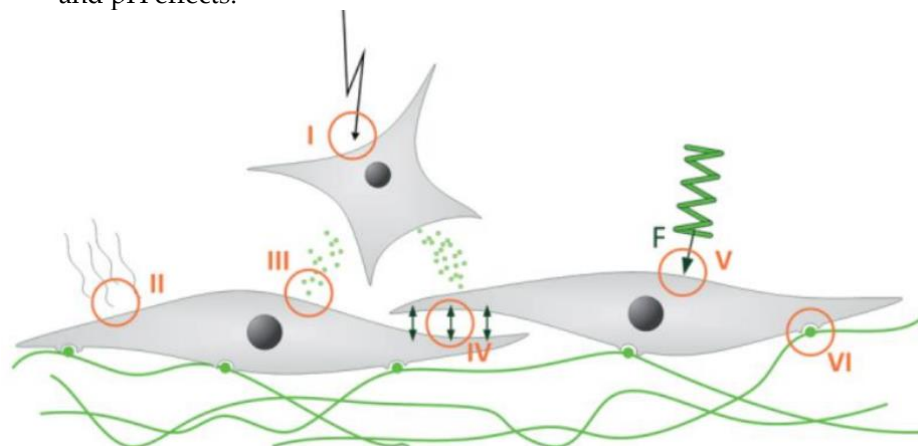


**Figure 4.** Stimuli controlling cell behavior [8]

In a complex environment (**Figure 4**), the cell is exposed to electrical (I), electromagnetic (II) and biochemical (III) stimuli. In addition, cell-cell interactions (IV), mechanical forces (V) or cell-matrix interactions (VI) can influence cell development.

For outcome of this review follow to **Table 2**. Designs of bioreactors and important parameters for mimicking physiological phenomena [10- 30]

**Table 2.** Designs of bioreactors and important parameters for mimicking physiological phenomena [10- 30]

Physiological phenomena	Physical / biological stimuli	Design	Parameters
Blood supply through the capillary network	Sufficient supply of O <sub>2</sub> , growth factors and nutrients	Rotating walls Perfusion	Flow rate and velocity
Weight-bearing joints during locomotion	Mechanical compression leading to tissue pressurization	Bioreactors with pressure and tension application	Static/dynamic compression Stroke length and frequency

Stretching of muscles and tendons	A tensile force that pulls tissue and cells	Uni-/bi-pull movement Radial thrust movement	Traction force Tensile tension Frequency
Fluid flow through cells	Hydrostatic/dynamic shear force	Perfusion in a thin wall 3D perfusion	Shear stress Fluid flow rate Simulation based flow
Joint movement	Shear force	Sliding surfaces	Rýchlost pohybu a trenie
Development, wound healing, nerve impulse	Electric current and potential difference	Electric stimulator Electromagnetic current	Voltage and current Frequency (pulsating alternating current and direct current)
Muscle contraction	The electrical signal that depolarizes the cells	Electric stimulator	Voltage and current Frequency
Cell adhesion to the tissue matrix	Cell-substrate attachment through antigens and protein bonds	Substrate for micro sampling	Substrate composition, spatial distribution and stiffness
Communication cell - cell	Local cellular contact	Microcontact printing Contact surface	Cell type Cell density Cell surface area
In vivo response of multiple cell types, factors and properties	Tissue response in vivo cell type and stimulatory factors	Implantation in vivo	Complex tissue development, formation and function

### 3. Results

The review paper is devoted to the analysis of the current state of bioreactor systems and their parameters. In this work, it was possible to summarize all the necessary information for the design and function of simple bioreactor system. We were successful in naming all requirements for bioreactor design:

- Material properties;
- Biomechanical parameters;
- Biochemical parameters.

### 4. Discussion

Knowing the characteristics of cells and tissues as well as how they behave in their natural environments is a fundamental requirement for advancement in tissue engineering and regenerative medicine so that theory may be put into reality. This review sought to provide a summary of existing tissue engineering bioreactors before designing a bioreactor system.

Over the last decade, there have been significant improvements in the design and construction of bioreactor systems. Systems have been developed that allow robust and reproducible culture conditions to be maintained. Specific bioreactor design is critical to the production of useful systems that can predict performance when based on the natural niche of cells from in vivo physiology.

#### Conflict of interest

The authors declare that there is no conflict of interest.

#### Ethical approval

This work does not contain any studies with human or animal subjects performed by any of the author.

## References

1. Ingber, Donald E. et al., "Tissue engineering and developmental biology: going biomimetic." *Tissue engineering* 12, no. 12 (2006): 3265-3283.
2. L. Roseti, V. Parisi, M. Petretta et al., (2017), "Scaffolds for bone tissue engineering: state of the art and new perspectives," *Materials Science and Engineering: C*, vol. 78.
3. Lim, D., Renteria, E.S., Sime, D.S., Ju, Y.M., Kim, J.H., Criswell, T., Shupe, T.D., Atala, A., Marini, F.C., Gurcan, M.N., Soker, S., Hunsberger, J., in Yoo, J.J. (2021) *Bioreactor design and validation for manufacturing strategies in tissue engineering*
4. LISA E. FREED et al., (2007), *Advanced Tools for Tissue Engineering: Scaffolds, Bioreactors, and Signaling*, DOI: 10.1089/ten.2006.12.3285
5. Junjie Zhao et al., *Bioreactors for Tissue Engineering: An Update*, *Biochemical Engineering Journal*, DOI: <http://dx.doi.org/10.1016/j.bej.2016.01.018>
6. Egger D, Tripisciano C, Weber V, Dominici M, Kasper C. Dynamic Cultivation of Mesenchymal Stem Cell Aggregates. *Bioengineering (Basel)*. 2018 Jun 19;5(2):48. doi: 10.3390/bioengineering5020048.
7. S. Partap, N. A. Plunkett, F. J. O'Brien, (2010), *Bioreactors in Tissue Engineering*, *Tissue Engineering*, Daniel Eberli (Ed.), ISBN: 978-953-307-079-7
8. Kasper C., van Griensven M., Pörtner R. (eds) *Bioreactor Systems for Tissue Engineering*. *Advances in Biochemical Engineering/Biotechnology*, vol 112
9. Bhumiratana, S., Bernhard, J., Cimetta, E., & Vunjak-Novakovic, G. (2014). Principles of Bioreactor Design for Tissue Engineering. *Principles of Tissue Engineering*, 261–278. doi:10.1016/b978-0-12-398358-9.00
10. Zhong JJ. Recent advances in bioreactor engineering, (2010), *Korean Journal of Chemical Engineering*
11. Chen HC, Hu YC, (2006), *Bioreactors for tissue engineering*. *Biotechnology Letters*
12. Mauck et al., (2000), Functional tissue engineering of articular cartilage through dynamic loading of chondrocyte-seeded agarose gels. *J Biomech Eng*
13. Huang CY, Hagar KL, Frost LE, Sun Y, Cheung HS., (2004), Effects of cyclic compressive loading on chondrogenesis of rabbit bone-marrow derived mesenchymal stem cells
14. Elder BD, Athanasiou KA., (2009), Hydrostatic pressure in articular cartilage tissue engineering: from chondrocytes to tissue regeneration. *Tissue Eng Part B Rev*
15. Elder BD, Athanasiou KA., (2009), Effects of temporal hydrostatic pressure on tissue-engineered bovine articular cartilage constructs. *Tissue Eng Part A*
16. Nugent et al., (2006), Dynamic shear stimulation of bovine cartilage biosynthesis of proteoglycan 4. *Arthritis Rheum*
17. Hronik-Tupaj M, Kaplan DL., (2012), A Review of the Responses of Two- and Three-Dimensional Engineered Tissues to Electric Fields. *Tissue Engineering Part B-Reviews*
18. Schwartz et al., (2008), Pulsed electromagnetic fields enhance BMP-2 dependent osteoblastic differentiation of human mesenchymal stem cells. *Journal of Orthopaedic Research*
19. Borschel GH, Dennis RG, Kuzon WM., (2004), Contractile skeletal muscle tissue-engineered on an acellular scaffold
20. Discher DE, Janmey P, Wang Y-L., (2005), Tissue Cells Feel and Respond to the Stiffness of Their Substrate
21. Engler AJ, Sen S, Sweeney HL, Discher DE., (2006), Matrix Elasticity Directs Stem Cell Lineage Specification
22. Hui EE, Bhatia SN., (2007), Micromechanical control of cell-cell interactions. *Proc Natl Acad Sci USA*
23. Folch A, Toner M., (2000), Microengineering of cellular interactions. *Annu Rev Biomed Eng*
24. Fukuda et al., (2006), Micropatterned cell co-cultures using layer-by-layer deposition of extracellular matrix components. *Biomaterials*
25. Yamato M, Konno C, Utsumi M, Kikuchi A, Okano T., (2002) Thermally responsive polymer-grafted surfaces facilitate patterned cell seeding and co-culture. *Biomaterials*
26. Irimia D, Liu SY, Tharp WG, Samadani A, Toner M, Poznansky MC., (2006), Microfluidic system for measuring neutrophil migratory responses to fast switches of chemical gradients. *Lab On A Chip*
27. Park JY et al., (2009), Differentiation of Neural Progenitor Cells in a Microfluidic Chip- Generated Cytokine Gradient
28. Baumert H et al., (2007) Development of a seeded scaffold in the great omentum: feasibility of an in vivo bioreactor for bladder tissue engineering
29. Emans PJ et al., (2010), Autologous engineering of cartilage. *Proceedings of the National Academy of Sciences of the United States of America*
30. Warnke PH et al., (2006), Man as living bioreactor: Fate of an exogenously prepared customized tissue-engineered mandible



# Presentation of the 3D laboratory in a virtual environment

Ján Kopec <sup>1</sup>, Miriam Pekarčíková<sup>2</sup>, Marek Mizerák <sup>3</sup>

<sup>1</sup> Department of industrial and digital engineering, jan.kopec@tuke.sk, Technical University of Košice, Park Komenského 9, 04001 Košice

<sup>2</sup> Department of industrial and digital engineering, miriam.pekarcikova@tuke.sk, Technical University of Košice, Park Komenského 9, 04001 Košice

<sup>3</sup> Department of industrial and digital engineering, marek.mizerak@tuke.sk, Technical University of Košice, Park Komenského 9, 04001 Košice

\* Correspondence: jan.kopec@tuke.sk

**Abstract:** The aim of this article is to point out the possibility of creating a virtual model of the laboratory using Pixyz and SolidWorks. The level of enterprise development advances with science and technology. Virtual reality is among the latest technical elements that find their application in the teaching process as well as in the field of industry. Virtual reality offers an environment in which various equipment and user integrations with the virtual world can be created. Precisely because of its feature of integration, virtual reality is very useful in the process of presentation or teaching. The PiXYZ program is a means of combining models from the SolidWorks program into a virtual environment where objects can be manipulated.

**Keywords:** PiXYZ, virtual reality, education, VR labs

## 1. Introduction

The laboratory is most often used for the presentation of logistics processes and assembly process training. Students and teachers within the faculty use this laboratory for the teaching program. The construction of this laboratory required careful planning and financial resources. To support laboratory training, a virtual model is created in which the assembly process takes place using virtual reality. The entire process must be established even before students perform actual exercises in a real lab. Especially connecting the virtual model to the Oculus Rift S.

Smartphones and computers are now one of the main parts of everyday life. This is the first alternative for using the virtual model.

The second option is the use of virtual technology on gaming devices that support the use of virtual reality. Virtual reality can display objects exactly as they do in real life. The use of virtual reality in the laboratory can increase the safety and simplicity of laboratory activities, in this case, the process of assembly and logistics processes.

One of the competencies needed in this era of digitization is the subject of digital engineering. Digital engineering is a good competitive skill that can face the industrial era 4.0. Digital data and communication are the most used currently. Knowledge of digital engineering is the basis of programming and development from machines in this era [1].

## 2. Virtual reality

Virtual reality is a computer-simulated environment that provides the user with integration and changes perception because of sensory information sent to the human brain. Virtual reality, in its current form, is the result of years of technology development and the implementation of microprocessors capable of performing a huge number of calculations [1-2].

Like any technological innovation, virtual reality is also going through the process of implementation in various industries at a rapid pace. Figure 1 graphically shows the percentage use of virtual reality in different areas.

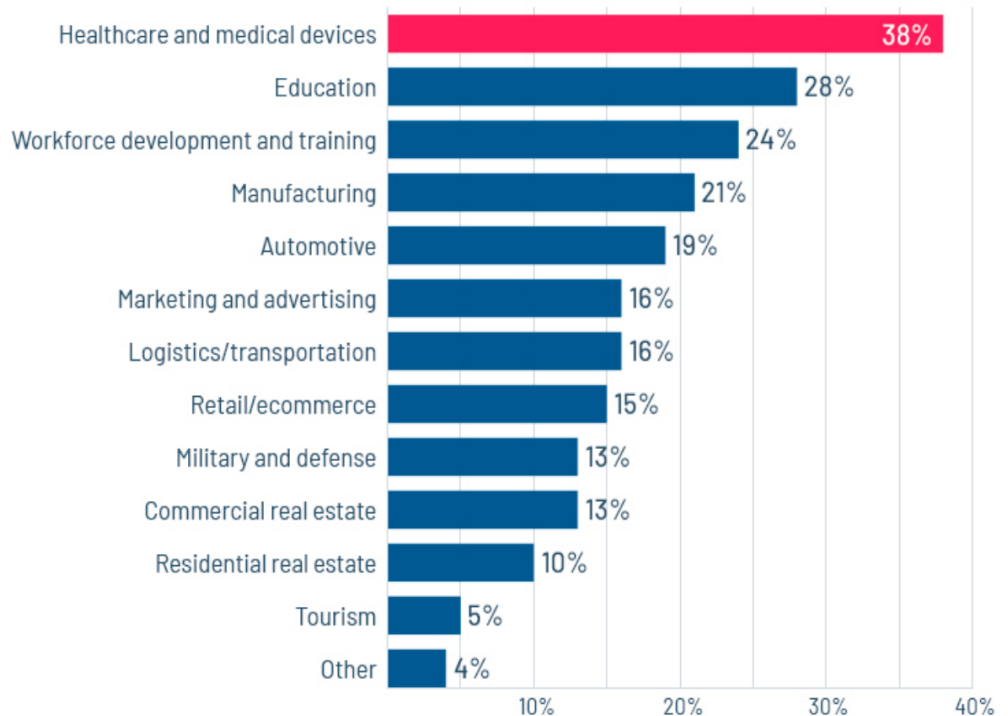


**Figure 1.** Percentage use of virtual reality in different areas [source: Perkins Coie[4]]

The virtual laboratory shows a room and a set of objects, such as computer equipment and office objects, such as tables, chairs, cabinets, and stands, which serve to simulate logistics processes from a real manufacturing plant.

2.1. *Virtual laboratory design*

Virtual labs are created using virtual reality, which is projected for students using the Oculus Rift S. The virtual environment is created to resemble a real conventional training place. Movement control is provided by PiXYZ software. where embedded components are added as individual parts, and for each, it is necessary to set free movement axes in the PiXYZ software environment. There are several processes that users can perform in the virtual environment. Figure 2 shows the flowchart of the virtual laboratory [3].

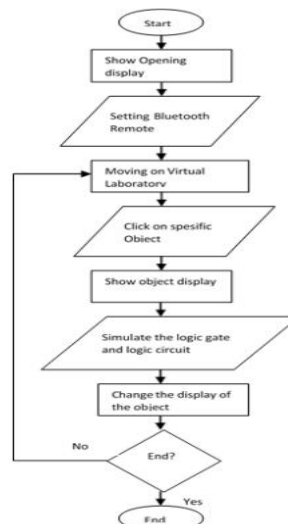


**Figure 2.** Flowchart of the virtual process [source: ResearchGate]

The following figure shows the appearance of a virtual laboratory that was created in the Solidworks program. If this process of creating virtual models and rooms begins, the student will also be able to work with this program, because the program for 2D and 3D modeling is taught. The first step to creation is to create your own 3D models or download them from internet sources. If the equipment of the laboratory is secured, we proceed to the second step, which is the creation of the walls of the room. We will then combine everything into one unit within the Solidworks program in the Assembly section.



**Figure 3.** Creating a virtual form of the laboratory in the SolidWorks program

Only a 2D/3D model of the laboratory can be created within the program. Now what is needed is PiXYZ review software that can provide a virtual environment. It provides flexibility and control over a virtual object for which degrees of freedom are defined in the PiXYZ program.

Another software element used in the process of creating and using a virtual model is the Oculus and Steam VR applications. As part of the PiXYZ program, it is then possible to start a virtual environment and manipulate entities with the help of controllers.

Figure 4 shows the environment of the PiXYZ program, which was used to integrate several programs and components in the creation of a virtual laboratory.

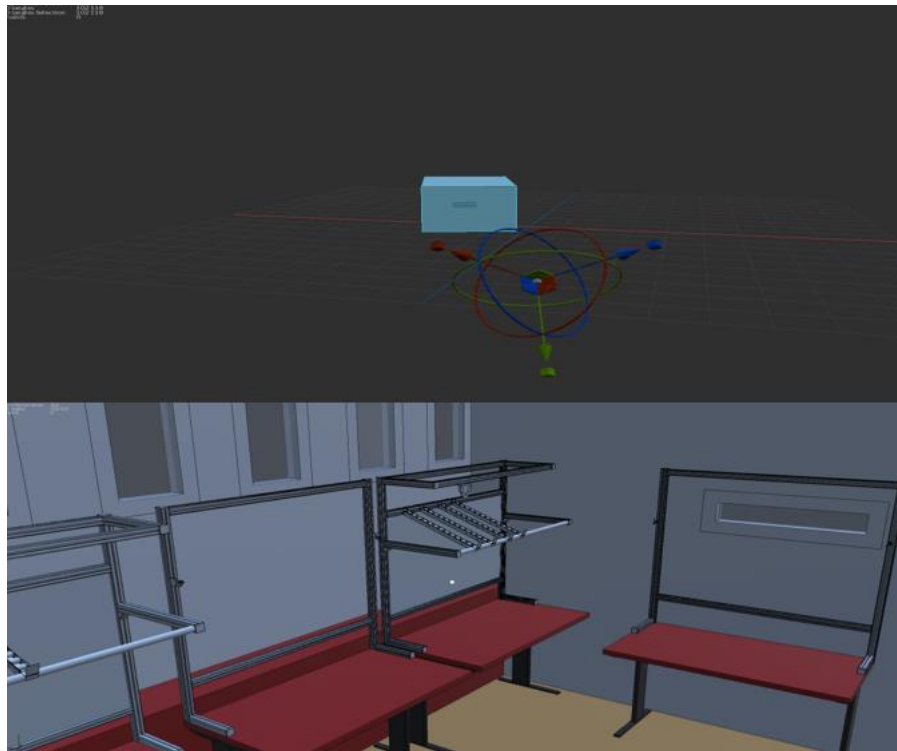


**Figure 4.** The environment of the PiXYZ program

## 5. Conclusions

This article is a description and at the same time instruction on how to create a virtual laboratory. The article describes the individual steps and the software that needs to be connected.

The article also develops a virtual laboratory as part of digital engineering. Many advantages result from this virtual laboratory, such as broadening horizons for students when they collaborate on production or directly train environment control and manipulation in a virtual environment. Another advantage is the readiness of the virtual environment in case of a pandemic or the impossibility of working in a real environment. In a virtual environment, a real logistics process is tested, which is a big plus, when the company does not need to test innovations on a real process, but primarily in a virtual environment, where it is much easier to make changes if necessary than in a real environment.

However, during the creation of the virtual laboratory, the collective of authors also revealed shortcomings in the chosen procedure or cooperation between software. For example, the SolidWorks program, with complex components that are represented in large quantities, creates a great burden for computer software equipment. It also has consequences (overheating, program crashes, and long loading times). When uploading the virtual laboratory to its environment, the PiXYZ program repeatedly forced itself to shut down for no reason, then a restart was necessary.

This article is the first step towards the creation of a functional environment where the time security of processes will be investigated, for example, the assembly of a component in a real environment and the time required for assembly in a created virtual environment.

## Acknowledgements

This article was created by the implementation of the grant projects: APVV-17-0258 Digital engineering elements application in innovation and optimization of production flows. APVV-19-0418 Intelligent solutions to enhance business innovation capability in the process of transforming them into smart businesses. VEGA 1/0438/20 Interaction of digital technologies to support software and hardware communication of the advanced production system platform. KEGA

001TUKÉ-4/2020 Modernizing Industrial Engineering education to Develop Existing Training Program Skills in a Specialized Laboratory. VEGA 1/0508/22 „Innovative and digital technologies in manufacturing and logistics processes and system“.

### References

1. Hamdi Serin, Virtual Reality in Education from the Perspective of Teachers, Articulo de investigacion, 2020, Vol.9, online
2. Khairudin, M. et.al. : Mobile Virtual Reality to Develop a Virtual Labororium for the Subject of Digital Engineering, International Journal of Interactive Mobile Technologies, 2019, Vol.14, online
3. Soliman, M.; Pesyridis, A.; Dalaymani-Zad, D.; Gronfula, M.; Kourmpetis, M. The Application of Virtual Reality in Engineering Education. Appl. Sci. 2021, 11, 2879. <https://doi.org/10.3390/app11062879>
4. Blagojevic, I.; Virtual reality Statistics, [online], <https://99firms.com/blog/virtual-reality-statistics/#gref>



# The strain distribution at the Limit Dome Height test of dual phase steel and correlation of experiment-simulation results

Juliy Martyn Kulya <sup>1\*</sup> and Miroslav Tomáš <sup>1</sup>

<sup>1</sup> Department of Automotive Production, Faculty of Mechanical Engineering, Technical University of Kosice; miroslav.tomas@tuke.sk

\* Correspondence: juliy.martyn.kulya@tuke.sk; Tel.: +421 55 602 3528

**Abstract:** The article deals with formability testing of dual phase steel DP 800 that is used for production of part used in the rear deformation zone of the car-body. The thickness of steel was 1.5 mm and Limit Dome Height test was performed on an Erichsen 145-60 testing machine. Specimens of different width were stretched up to the fracture and the punch path and force were measured. Specimens were etched to create deformation grid of dots in order to measure strain distribution by photogrammetric system Argus. Then, the simulation model of LDH test was created and the average punch path was set to calculate the strain distribution as well, when constitutive equations Hill 48 and Hollomon model described the material. Results of strain distribution measured experimentally were compared to those one numerically simulated.

**Keywords:** LDH test, stretching force, punch path, experiment, simulation

## 1. Introduction

Demands of making cars lighter weight to achieve lower emissions during their operation, but still keeping passengers safety, steel grades like AHSS steels are implemented in the body structure. These steels offer using lower steel sheets thickness for stamped part due to their higher strength. Dual phase steels are commonly used in certain car-body parts because of their good combination of strength and ductility and low production costs [1].

Formability, defined as the ability of sheet metal to be stamped without any fracture, depends on several interacting factors [2]. The total formability can be classified as a material one and process one [3]. Material formability can be easily tested by the tests which lies on simple tensile or compression test. Otherwise, process formability includes several process-depending factors when combined with material properties. Due to different stress-strain distribution in each stamped part region, there is no single testing procedure for satisfying to test formability in a simple way. Thus, different simulative tests are used, such as Erichsen, Engelhardt, Cup test, Limit Dome height etc. [2-4]

Limit dome height test (LDH), introduced by Ghosh and modified by Hecker, was developed to simulate the fracture conditions under plane-strain deformation, which was identified by the Hecker as more than 80 % of the stamping failures [5,6]. Furthermore, the test was modified to use metal sheet strips with different width, material thickness and laser welded dissimilar materials. Sahu [7] applied LDH test to study deformation properties of very thin brass sheet. They modelled biaxial, plane-strain and uniaxial strain paths by scaling down the tool and specimen dimensions and evaluated limit strains as well. Xie and Nakamachi [8] predicted the formability of high-strength steels and by using elastic/crystalline viscoplastic FE analyses of standard LDH tests. From LDH formability test they confirmed that the combination of high-strength steel with a little proportion of gamma texture components could lead to significant improvement of formability. Kuramae et al [9] performed modified LDH test on four automotive sheetmetals (3x aluminium and

steel H220PD). They performed formability analysis from the view of microcrystalline texture evolution during plastic deformation by the multi-scale LDH test analysis, which was done by using multiscale parallel finite element procedure. As a result, they compared the results of FE prediction of fracture to the LDH test performed with flat head punch for various strain path conditions. Katragadda et al [10] conducted LDH test for different steel grades used in automotive industry. Results of experiments compared to the simulations when applied Hill 48 and Hollomon's equation as constitutive equations to describe material behavior. Bandyopadhyay et al [11] conducted formability tests for laser welded tailor welded blanks of dissimilar materials (DP980/DP600 and DP980/IFHS). They found out the decrease of formability for LDH and Erichsen cupping test were approximately following similar trend, and hence, the punch size played a minor influence.

The aim of the article is to compare results of LDH tests reached experimentally when testing dual phase steel DP800 to those one reached by numerical simulation of the test. Otherwise, major and minor strains will be measured by photogrammetric system Argus and compared to the strains calculated in simulation software PamStamp.

## 2. Materials and Methods

### 2.1 Material – DP800

Formability of dual phase high strength steel DP800 with thickness 1.5 mm was assessed by the limit dome height test (LDH). Mechanical properties of experimental material were tested according to standard: ISO 6892-1, plastic strain ratio according to ISO 10113 and strain hardening exponent according to ISO 10275. Samples for mechanical tests were taken in rolling direction 0°, 45° and 90° to describe material anisotropy. Three specimens were measured in each direction and average values are shown in Table 1. Tests were done on TIRA test 2300 testing machine equipped with longitudinal and transversal extensometers with precision 0.001 mm. Plastic strain ratio was evaluated at uniform elongation level and strain hardening exponent within the range 5% to uniform elongation.

**Table 1.** Mechanical properties of dual-phase steel DP 800, thickness 1.5 mm

	$R_{p0.2}$ [MPa]	$R_m$ [MPa]	$A_{80}$ [%]	$r$ [-]	$r_m$ [-]	$n$ [-]	$n_m$ [-]
0°	527	828	19.9	0.873		0.126	
45°	508	830	18.2	0.907	0.917	0.125	0.125
90°	496	838	18.4	0.979		0.123	

### 2.2 Limit Dome Height (LDH) Test

The limiting dome height test, also known as LDH test is a method used to determine sheet metal forming properties. The limiting dome height test is used to determine the ductility of sheet metals and is comparable to a Nakajima test. A hemispherical die strains the clamped specimen until break. Testing is performed on specimens with various width. For each specimen the maximum attainable dome height and strain at break are determined. Experiments were conducted on Erichsen 145-60 testing machine with Nakajima tooling setup. The Erichsen 145-60 is a universal deep-drawn sheet metal testing machine from the German manufacturer Erichsen. The maximum force of this equipment is 600 kN. This test equipment is electro-hydraulically controlled. Test sequences can be controlled automatically or manually as required. The machine control unit takes care of the error-free operation and control of the test equipment. The pulling force is displayed digitally along with the holding force.

For our experiment we used blanks with widths of 196, 133, 108, 70, 39 and 26 millimeters. There are illustrated in Fig.1.



**Figure 1.** Types of blanks.

The deformation mesh was applied to the samples by electrochemical etching on an ÖSTLING EU Classic 300. The principle is to cover the sample with a matrix through which the electrolyte is fed via a graphite electrode. The electrode moves evenly over the entire surface of the sample. Both the sample and the electrode are connected to a DC voltage. Rectangular deformation grid consisted of dots with diameter of 1mm and spacing 2mm in rows and columns. The Argus 3D optical system from the German company GOM was used to measure the applied deformation mesh. It is a well-established and frequently used device for the evaluation of various types of forming processes due to its complexity.

### 2.3 Simulation model of LDH test

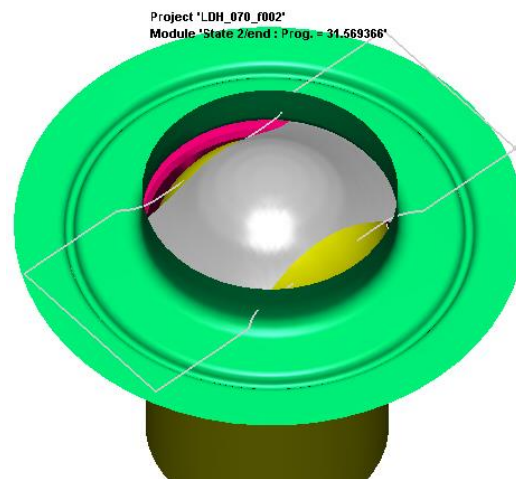


**Figure 2.** Simulation model.

The simulation model is shown in Fig.2. It consists of three parts – die (green), punch (yellow), pink (blank holder), and blank (grey). These parts were meshed during importing CAD model of the tool and set as rigid surface tools. The picture shows one type of blanks with a width of 70mm. Blanks were meshed by square elements 2x2mm. Yield law and hardening curve describing material behavior were defined as follows:

Hill 48 anisotropic plasticity model:

$$\sigma_1^2 = \frac{r_0(1 + r_{90})}{r_{90}(1 + r_0)} \sigma_2^2 - \frac{2r_0}{1 + r_0} \sigma_1 \sigma_2 = (\sigma_1^y)^2 \quad (1)$$

Hollomon hardening model (Eq. 2).

$$\sigma = K \cdot \varphi^n, \quad (2)$$

where  $K$  is material constant,  $n$  is strain hardening exponent and  $r_0, r_{45}, r_{90}$  are plastic strain ratios (Lankford's coefficients) in specified direction.

### 3. Results and discussion

The results of the measurement of the maximum tensile forces and the punch path up to the specimen fracture for the individual widths of the samples are given in Table 2. For the individual widths, 3 measurements were carried out and the average value of the maximum force and the average value of the path at fracture were calculated. In the simulation model, this average value of the path was used to define the path of the punch. Table 2 shows the results of the maximum force from the numerical simulation and Fig. 2 illustrates the progression and comparison of the forces obtained experimentally and from the numerical simulation.

**Table 2.** Measured values of the maximum force and the punch path at fracture

	Experiment			Simulation	
	Max. Force [kN]	Average value	Stroke [mm]	Max. Force [kN]	Stroke [mm]
196	211.31	211.4	34.44	234.7	36.6
	205.68		33.16		
	217.22		36.62		
133	133.88	131.3	25.4	152.85	24.91
	127.39		24.54		
	132.75		25.16		
108	97.53	97.9	23.4	112.92	23.5
	92.67		22.52		
	103.76		24.58		
070	110.11	112.3	30.86	123.6	31.57
	114.52		32.28		
039	60.45	60.2	29.42	62.74	29.52
	61.29		30.16		
	58.86		28.98		
026	37.91	37.5	26.16	35.77	25.45
	37.37		24.46		
	37.36		25.74		

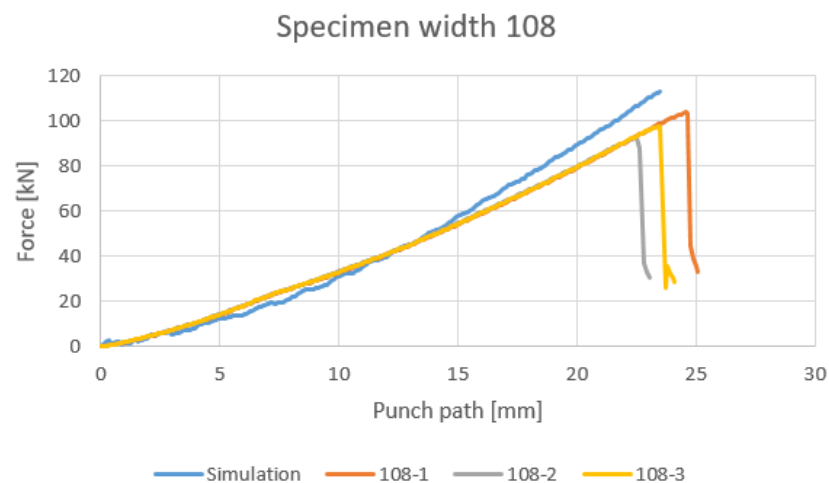


**Figure 2.** Comparison of force-punch path for a 108 mm blank width.

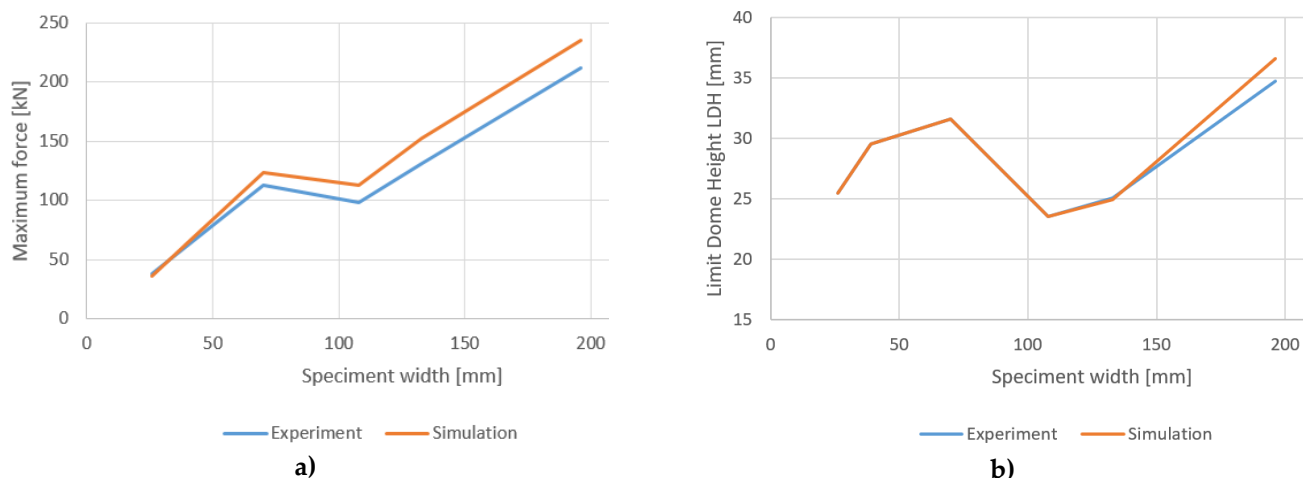


**Figure 3.** LDH test results: a) dependence of the maximum force on the blank width; b) dependence of the dome height at fracture on the blank width

Fig. 2a shows a graphical representation of the measured data from the previous table. From this image it can be stated that the force measured in the simulation is slightly higher than the force measured in the real experiment. You can also see in the image that the forces measured on the larger blank widths differ more than those of the smaller blank widths. The larger the diameter of the blank, the greater the difference in force between the simulation and the experiment. This graph also shows a small jump in force values for blanks with a width of 108 mm. As the blank width is reduced from 196mm to 108mm, the maximum stretching force decreases. It is possible to observe a discontinuity of decrease in the range of specimen width 108mm to 70mm, then the pulling force decreases as well.

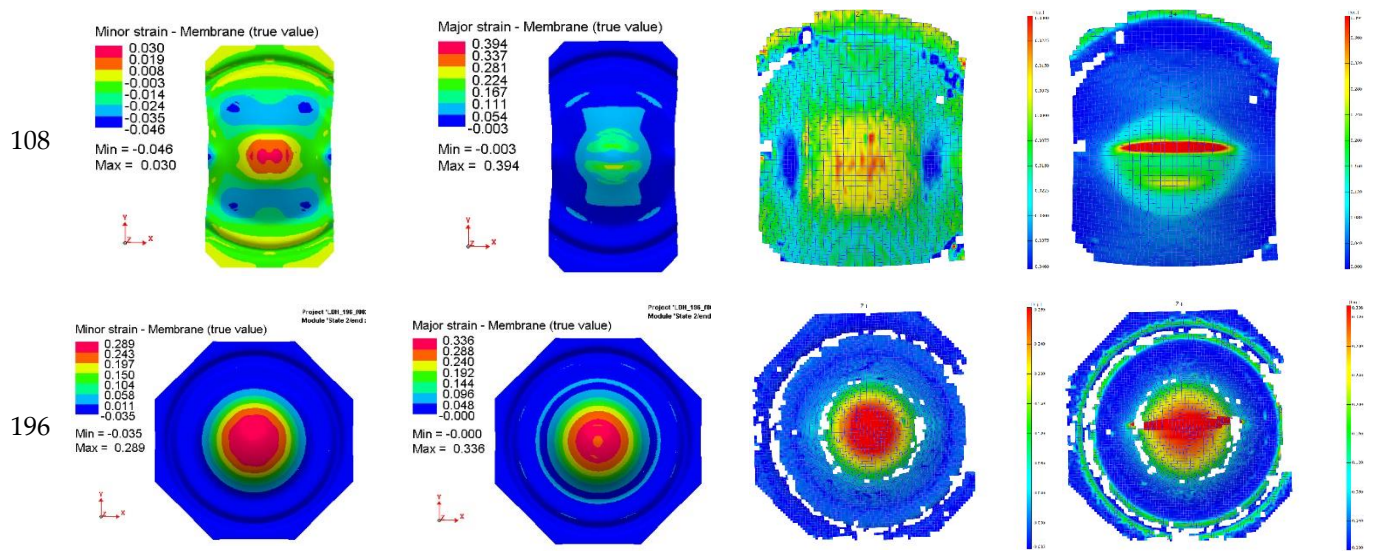
Fig. 2b shows a comparison of the achieved punch path for each specimen width. The minimum value of punch path - LDH parameter - was recorded for a specimen width of 108mm (LDH = 23.5 ± 1.5 mm) which is considered as plain-strain state. The results comply to the results of Takahashi, which performed LDH test on AHSS steel [12,13].

The results of the strain distribution measured by the Argus system and determined by numerical simulation are given in Tab. 3. Major strains of the fracture zone when measured by Argus were significantly larger than those of the safety zone [14]. Even though the results of numerical simulations depend on yield law-hardening law combination, it is possible to state a good agreement between the results of experimental measurements and numerical simulation.

**Table 3.** Comparison of major and minor strain measured experimentally and calculated by numerical simulation

Simulation		Experiment	
Minor strain	Major strain	Minor strain	Major strain
<p>Minor strain - Membrane (true value)</p> <p>0.004 -0.013 -0.030 -0.048 -0.065 -0.082 -0.099 -0.116</p> <p>Min = -0.116 Max = 0.004</p>	<p>Major strain - Membrane (true value)</p> <p>0.293 0.251 0.209 0.167 0.125 0.083 0.041 -0.001</p> <p>Min = -0.001 Max = 0.293</p>		

039



## 5. Conclusions

The article presents the result of LDH test conducted on dual phase steel DP800. This steel is being used to make stamped part for rear deformation zone of cars. The minimal punch path, i.e. LDH parameter was reached for plane-strain condition modelled by specimen width 108mm. It was confirmed by measuring the strain distribution using ARGUS photogrammetric system. The results of strain distribution for selected samples were also correlated to the numerical simulation of LDH test. Further research will be focused to the evaluation of limit strains and its correlation to the numerical simulation.

**Acknowledgments:** The work was done under the grant project VEGA 2-0080-19 “Prediction of weldability and formability for laser welded tailored blanks made of combined high strength steels with CAE support”

## References

1. Oliver S., Jones T.B., Fourlaris G., Dual phase versus TRIP strip steels: Microstructural changes as a consequence of quasi-static and dynamic tensile testing. *Materials Characterization*, **2007**, Volume 58, p. 390-400.
2. Hrivňák A., Evin E. Formability of metal sheets, 1st ed.; Kosice : Technical University, Slovakia, 2004; pp. 223.
3. Mielnik E.M., *Metalworking Science and Engineering*, McGraw-Hill, 1991, p. 976.
4. Hosford W.F., Caddell R.M., *Metal Forming , Mechanics and Metallurgy*, 3rd edition, Cambridge University Press, 2012.
5. Narasimhan K., Miles M.P., Wagoner R.H., A better sheet-formability test, *Journal of Materials Processing Technology* **1995**, Volume 50, p. 385-394.
6. ASM Handbook, *Forming and Forging*, ASM International, 9th Edition Metals Handbook, 1988.
7. Sahu J., Mishra S., Limit dome height test of very thin brass sheet considering the scaling effect. *Journal of Physics Conference Series* **2016**.
8. Xie C.L., Nakamachi E., The effect of crystallographic textures on the formability of high-strength steel sheets. *Journal of Materials Processing Technology* **2002**, p. 104-111.
9. Kuramae H., Ikeya Y., Sakamoto H., Morimoto H., Nakamachi E., Multi-scale parallel finite element analyses of LDH sheet formability tests based on crystallographic homogenization method. *International Journal of Mechanical Sciences* **2010**, p. 183-197.
10. Katragadda S.C., Ramulu P., Investigation of forming behavior prediction of different steel grade materials using numerical simulation, 5 th International & 26th All India Manufacturing Technology, Design and Research Conference, India, 2014.
11. Bandyopadhyay K., Panda S.K., Saha P., Padmanabham G., Limiting drawing ratio and deep drawing behavior of dual phase steel tailor welded blanks: FE simulation and experimental validation. *Journal of Materials Processing Technology* **2015**, p. 48-64.
12. AHSS Guidelines, Available online: <https://www.worldautosteel.org/projects/advanced-high-strength-steel-application-guidelines/>.
13. Takahashi M., “Development of High Strength Steels for Automobiles,” Nippon Steel Technical Report No. 88 (July **2003**).
14. Sun, L.; Cai, Z.; He, D.; Li, L. Aluminum Alloy Sheet-Forming Limit Curve Prediction Based on Original Measured Stress–Strain Data and Its Application in Stretch-Forming Process. *Metals* **2019**, *9*, 1129. <https://doi.org/10.3390/met9101129>



# Use of CFD method for research of aerodynamic elements of passenger car

František Kupec <sup>1\*</sup>, Michal Fabian <sup>2</sup>

<sup>1,2</sup> Technical university of Kosice, Faculty of Mechanical Engineering, Department of Automotive Manufacturing, Slovakia; frantisek.kupec@tuke.sk, michal.fabian@tuke.sk

\* Correspondence: frantisek.kupec@tuke.sk; Tel.: +421 55 602 3530

**Abstract:** The paper provides insight into the process of using numerical airflow simulation in the development of vehicle aerodynamics. For the increasingly common use in the automotive industry, it highlights the process of solving such a problem, using the design of a new aerodynamic vehicle body element to do so. The aim is to investigate the effect on the well-known phenomenon of the A-pillar vortex in the flow around a selected vehicle body. It highlights the importance of adapting the geometry of the car for the desired airflow and achieving good aerodynamic results.

**Keywords:** car aerodynamics; CFD method; A-pillar vortex.

## 1. Introduction

The automotive industry is one of the most progressive areas of engineering. It is involved in the continuous application development of technologies and materials, but at the same time supports the development of related scientific fields. As the car consumes energy not only for propulsion but also for overcoming driving resistance, the dominant one being aerodynamic resistance, the development of aerodynamics plays an important role in efficiency. Further aerodynamic advances are continuously being explored to improve driving comfort, reduce energy consumption and improve the driving and safety characteristics of cars. The research and application of new aerodynamic features in mass-produced passenger cars is coming to the fore. As well as the development teams of automotive companies, scientific teams are also working on research into new geometrical features that optimise airflow around vehicle bodies. One area that is the subject of much study is the phenomenon of the so-called A-pillar vortex of the automobile. The effect of this phenomenon on the overall airflow around an experimental car body via the CFD (Computational Fluid Dynamic) method was published in [1] by Murad et al. The study of the formation and understanding of the A-pillar vortex phenomenon of a car via the CFD method was addressed by Bonitz et al. in [2]. The generation of experimental data for validation of numerical methods in the design and study of A-pillar car vortex was published in [3] by Wood, et al.

## 2. Research of car aerodynamics by CFD method

CFD (Computational Fluid Dynamics), belongs to the field of CAE (Computer Aided Engineering). It is the computational analysis of fluid or air flow as well as heat transfer in various industrial fields. It has been part of the development of automotive aerodynamics for several decades. At the vehicle development stage, it provides a high-resolution representation of the complete flow field around the vehicle, from which changes can be made for better aerodynamic results.

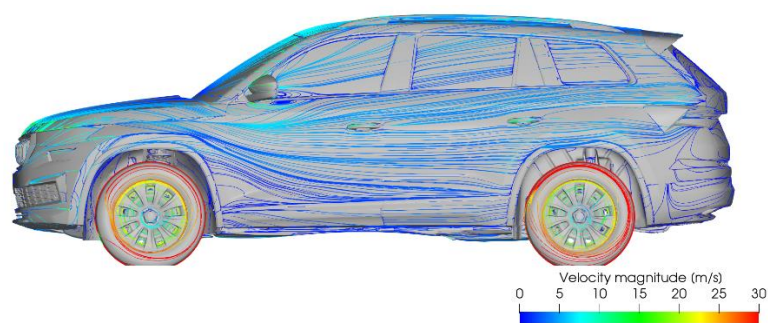


**Figure 1** Example of a display of streamlines around the body of a vehicle with a colour scale distinguishing their speed in different areas [8]

The main reason for using CFD is that it allows for faster development cycles and cost savings compared to traditional wind tunnel testing, which has been used in the past as the main tool for aerodynamic testing. The ability to predict aerodynamic properties in a fast, iterative and highly accurate manner allows engineers to optimise the aerodynamic elements of a car right from their workstation, before any parts are manufactured and deployed in mass production. By simultaneously using a combination of CFD methods and verification of results on a physical prototype in a wind tunnel, accurate and directional results can be achieved for automotive development [4-6].

The CFD method finds high application in the research of new, previously unused aerodynamic elements of automobile bodies. By creating a virtual geometry of the car, it is possible to apply any geometric change and observe the behavior and changes in the airflow around the modified part. By applying the knowledge of airflow, the geometry of the element can be modified and optimized in incremental steps to its most optimal shape. The physical prototype, tested in a wind tunnel to confirm the results obtained virtually, is then geometrically the closest to the final solution intended for approval for series production, thanks to the optimisation by CFD.

### 2.1 Principle of the CFD method

The computational methods contained in the CFD solvers are based on the laws of conservation of mass, conservation of momentum and conservation of energy. The Navier-Stokes equations describing the flow of an incompressible Newtonian fluid are based on these laws. The description of the flow is a system of nonlinear partial differential equations of 2nd order. CFD methods only solve these equations to an approximation - the equations are simplified in various ways in terms of physical phenomena. Exact solutions of the Navier-Stokes equations (NSE) exist only for special cases, and only a few are relevant for automotive engineering. Thus, only simplified versions of the NSE for which a numerical solution is possible and feasible are used in automotive aerodynamics development. [4]

Examples of simplifications include: neglected viscous effects, non-rotating flow or time averaging of flow quantities in the flow field. All of these NSE simplifications idealize the physics and move away from the actual natural conditions.

The second category of simplification is mathematical in origin, introduced by the way selected equations are solved. In principle, the differential equations describing the continuum are discretized together with specific boundary conditions (i.e., they are applied to small but finite volumes in the computational domain). These simplifications are made in the interest of speeding up the computation but to the extent that the relevance of the result is maintained. The accuracy of the CFD method can be adjusted individually depending on the desired result. CFD simulation options provide the specification of accurate boundary conditions for a particular wind tunnel, including models of the support systems for accurate ride simulation [5].

## 2.2 Steps of the CFD method

The main steps of CAE computational methods are pre-processing, processing and post-processing. In the context of passenger vehicle aerodynamics research, the CFD method according to [5] can be more specifically described as follows.

Pre-processing involves processing the imported data, discretizing the computational domain, and setting boundary conditions. The flow medium is partitioned by the finite element method into a finite number of elements in a three-dimensional space, each with its associated local and global coordinates. It is essential to adjust the size of the grid elements, especially if the research case is at a certain scale compared to the real size of the car. In automotive development, methods of densifying the mesh in areas of high significance - e.g. front A-pillar, brake disc area for more accurate analysis of flow in these areas - are well established. The refinement strategies are varied, one of which is shown in Figure 2.

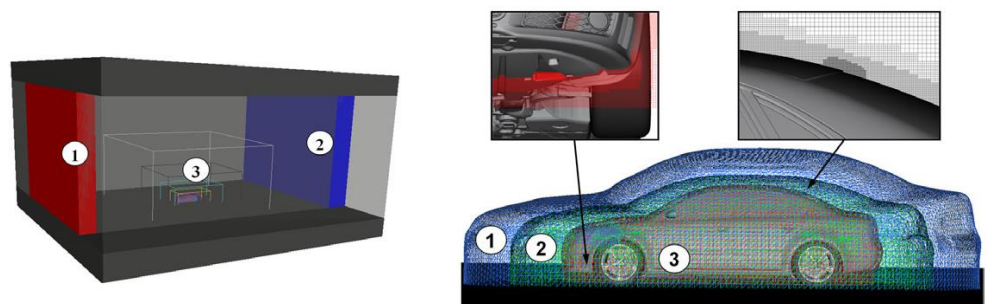


**Figure 2** Pre-processing – varied discretization of the flow regions, distributed from the coarsest (1) to the finest (3) in the boundary layer closest to the vehicle body [4]

Processing involves solving the numerical equations for each of the discretized elements using the finite element method. Pressure fields, velocity vectors, transport equations and momentum equations are calculated by converting partial differential equations into systems of linear equations. Several iterations are performed and the goal is to reach a certain region of convergence of the result of each quantity, from which the final results are determined by the chosen method.

Post-processing involves detailed analysis and visualization of the results of individual variables. The analysis is performed by means of visualisation tools that graphically plot the individual aerodynamic forces and moments as dimensionless coefficients distributed over the vehicle surface geometry under investigation. They are depicted by a colour scale and by plotting three-dimensional shapes to visualise the vortices. [4, 5]

## 3. An example of using the CFD method in the design of a new aerodynamic element

The demonstration of the use of the CFD method in this paper is the design of a node optimization in the A-pillar region of a passenger car. At this point, the airflow splitting and subsequent coupling occurs, resulting in the formation of the A pillar vortex, in which the energy losses of the flow medium and the contribution of the increase of the air drag coefficient  $c_D$ , which is one of the main data characterizing the aerodynamic quality of the vehicle. It is a dimensionless coefficient which is calculated according to the relation:

$$c_D = \frac{2 \cdot F_D}{\rho \cdot v^2 \cdot A'} \quad (1)$$

where:

- $F_D$  is the force acting against the movement of the vehicle,
- $\rho$  is the density of the following medium (air)
- $v$  is speed of the vehicle,
- $A$  is the projection of the frontal surface area content of the vehicles.

As shown in Figure 3, the airflow on the A-pillar splits into two directions - along the side of the vehicle body, over the vehicle body (blue-green). Their separation and subsequent merging in the area above the first side glass causes turbulent flow (red). The A-pillar vortex discussed above is formed here.

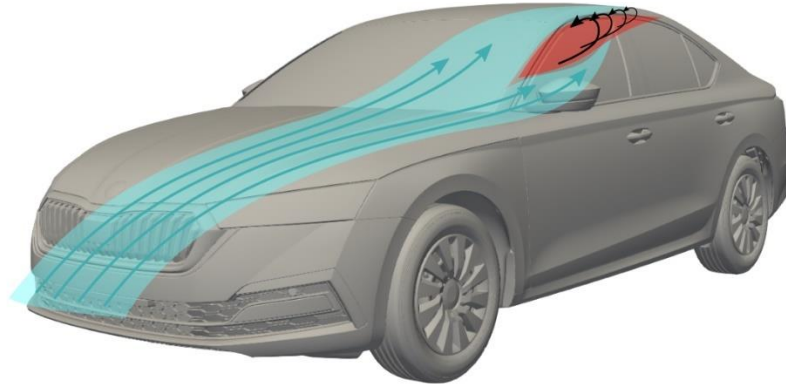


**Figure 3** Airflow distribution (blue-green) over and along the side of the body, formation of A-pillar vortex (red)

### 3.1. The solution proposal

In this step, the design objective is to achieve the elimination of the A-pillar vortex, or the separation of the air streams over and along the side of the body. This achieves airflow close to the body with the potential to reduce flow energy losses. The proposed solution with the expected result is shown in Figure 4.

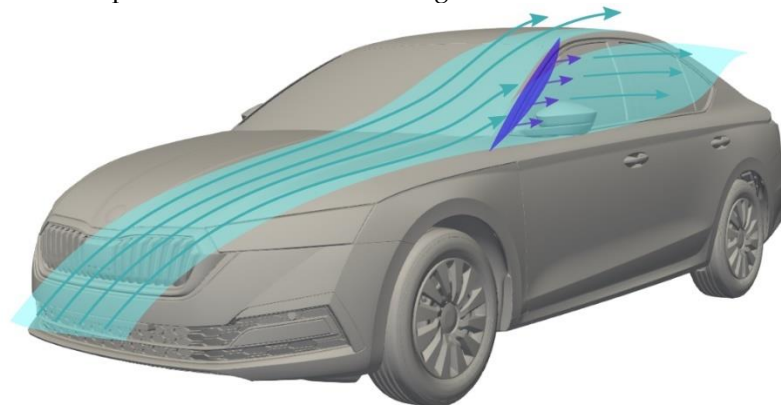


**Figure 4** Expected change in airflow (green-blue) due to the application of an aerodynamic element (purple)

### 3.2. Car selection and element geometry creation

For the purpose of the research of the experimental aerodynamic element, a car from the D-SUV category - Skoda Kodiaq (2021) was selected. The rationale for the selection is the increasing popularity of the SUV segment, which does not achieve the aerodynamic qualities of passenger cars precisely because of their size. The choice of the Škoda vehicle is justified by the cooperation with the development centre of ŠKODA AUTO, a.s. on this experiment.

An aerodynamic element was proposed that would not structurally interfere with the original car, being glued to the body of the car. This is a spoiler that contains a space - a channel between the original A-pillar and the proposed geometry, where the airflow will be directed along the side of the body along the side windows.

The geometry was created in the professional non-parametric 3D modelling CAD (Computer Aided Design) software ICEM Surf for the creation of A-class quality surface

data. These are surfaces defined by design and technology requirements with controlled light incidence. The proposed geometry is shown in Figure 5.

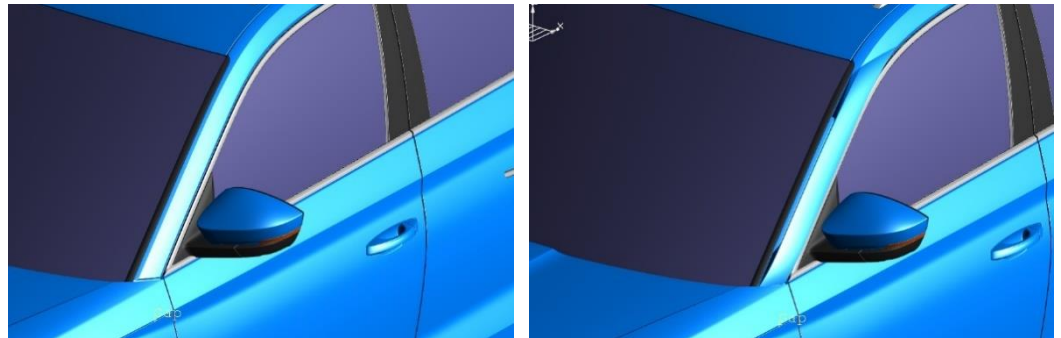


**Figure 5** Proposed spoiler glued to the A-pillar of the vehicle - left without spoiler, right with spoiler

### 3.3. CFD analysis

The proposed geometry was modified for the purpose of CFD simulation using ANSA software. The full geometry preparation is understood as the creation of a complete surface model of the car including the internal functional openings, with the output being the geometry for meshing by the CFD tool. [4,9]

The STAR CCM+ software tool was selected for the CFD analysis. It automatically defines the surface and volume mesh based on the input geometry. The aim is to set the ideal number of grid cells for a sufficiently accurate description of the investigated areas. If necessary, an automatic surface correction is also performed by the software, which corrects the generated surface mesh by either ignoring or modifying the edges of the individual elements. [9, 10]

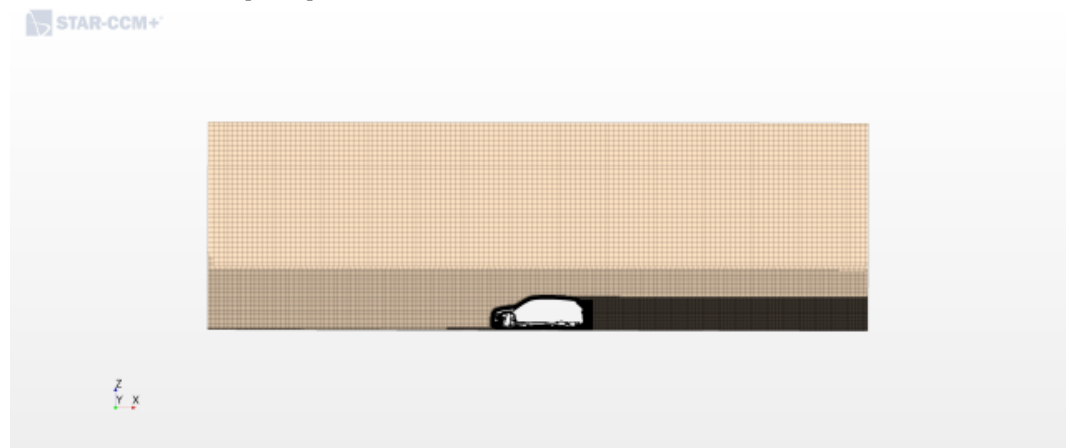


**Figure 6** Volumetric network of the flowing medium in the cross-section of the X0 plane created by the software CFD tool STAR CCM+

The numerical method used was the Reynolds Averaged Navier-Stokes (RANS) method of modelling stationary turbulent flow, which is a reduced form of the general Navier-Stokes equations. The Star-CCM+ program [2] offers several turbulent models based on the Boussinesq hypothesis. The Spalart-Allmaras model in two variants is used as a representative of the single-equation models. In the field of two-equation models, variants of the k-Epsilon ( $k - \epsilon$ ), k-Omega ( $k - \omega$ ), Elliptic Blending and V2F ( $k - \epsilon$ ) models figure. [11]

The CFD simulation of the vehicle aerodynamics is performed with constant airflow and no crosswind. The driving simulation was set to a speed of 140 km/h, wheel rotation modulus and tire deformation with bulging at the bottom of the tire due to contact with

the road were used. The calculation process is completed by settling the convergence of the force effects in the specified range. Postprocessing involves the generation of a set of images with colour maps representing the pressure fields according to the calculated simulation equations under the specified boundary conditions.

#### 4. Discussion

The effect of the spoiler on the flow and the formation of the A-pillar vortex can be observed in the post-processing images generated by the STAR CCM+ software. Selected analysis figures 7-9 have been used for the discussion, which show the effect on the change in the A-pillar flow. On the left are images of the studied body without the experimental spoiler, on the right using the spoiler

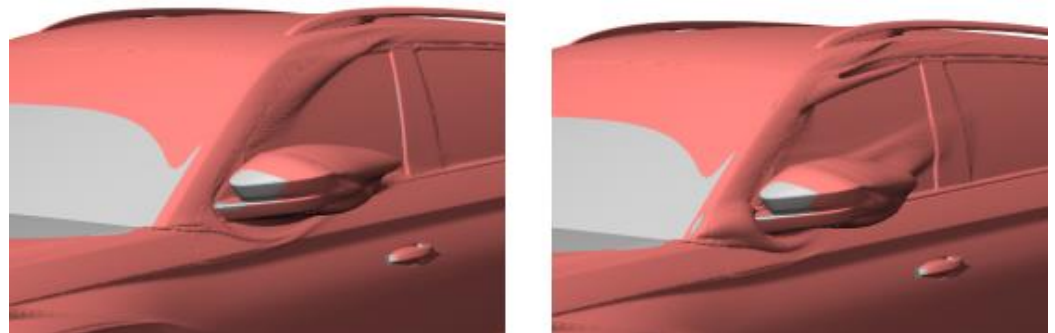


**Figure 7** Vortex visualisation using ISO surfaces plotted against the total pressure coefficient

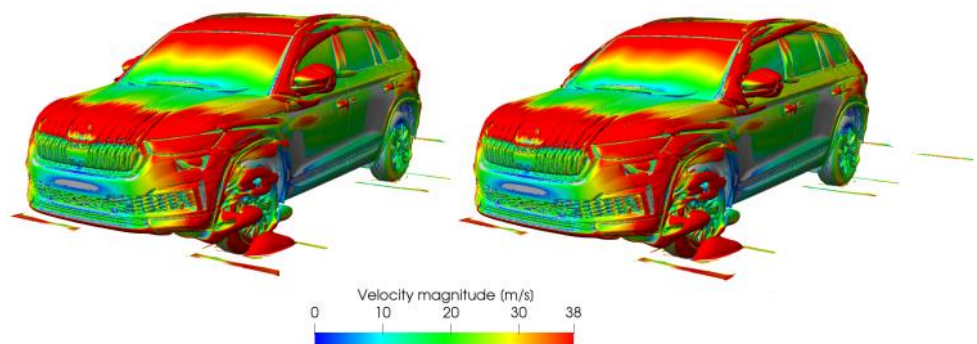


**Figure 8** Vortex visualisation using ISO surfaces plotted by the Q criteria method with a colour map of the velocities of the individual parts of the vortices - isometric view

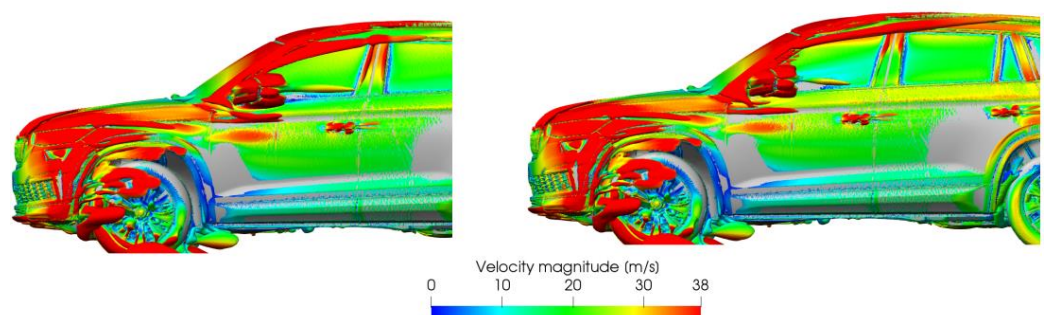


**Figure 9** Vortex visualisation using ISO surfaces plotted by the Q criteria method with a colour map of the velocities of the individual parts of the vortices - view from the left side of the vehicle

By comparison in Figure 7, the elimination of the main A-column vortex and its splitting can be observed, which can be considered as a benefit. The negative effect is the formation of smaller vortices in different regions that slow down the airflow. This can be better observed in the comparative figures 8 and 9 plotted using the Q-criterion [12], where the orange coloration of the end of the vortex over the rear window of the modified vehicle demonstrates the loss of flow velocity. The separation of the A-pillar vortex from the body is beneficial, but the goal is to eliminate it completely, which the preparation of this spoiler variant did not achieve.

**Table 1.** Influence of the spoiler on the aerodynamic coefficient of drag.

	Without spoiler	With spoiler
$c_D$	0,3171	0,3218
$\Delta c_D$	-	<b>+0,0047<sup>1</sup></b>

<sup>1</sup> Data obtained from internal CCX post-processing tools.

As shown in Table 1, there was an increase of 4.7 aerodynamic points for the comparison based on the air drag coefficient  $c_D$ . This change can also be observed in the differential plot in Figure 10.

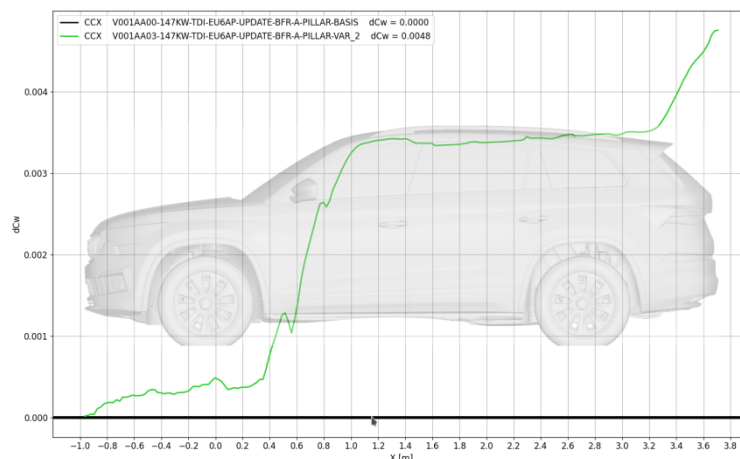


**Figure 10** Difference plot of air resistance coefficient  $c_D$  - comparison of the basic version (black on the graph) with the modified version (green)

## 5. Conclusions

The proposed new aerodynamic element of the vehicle A-pillar spoiler verified by CFD method met the expectations in terms of A-pillar vortex mitigation. The concomitant effect of the expected aerodynamic improvement is the reduction of the air drag coefficient  $c_D$ . In this case, the flow at the rear of the vehicle is disturbed, the excitation area of the mirror and the drift behind the vehicle is increased, which increases the air drag coefficient  $c_D$ . It is therefore necessary to modify the geometry by further analysis to eliminate the A-pillar vortex, reduce the drift behind the vehicle and reduce the air drag coefficient  $c_D$ .

**Acknowledgments:** The author is grateful for the support of works by project VEGA 1/0318/21 "Research and development of innovations for more efficient use of renewable energy sources and reducing the carbon footprint of vehicles". This article was prepared thanks to the cooperation of the Faculty of Mechanical Engineering of TUKE with ŠKODA AUTO, a.s.

**Conflicts of Interest:** The authors declare no conflict of interest.

## References

1. Murad, N. et al.: Computational fluid dynamics study of vehicle A-pillar aero-acoustics. *Applied Acoustics*, 74(6), 882–896. 2013. doi:10.1016/j.apacoust.2012.12.01.
2. Bonitz, S. et al.: "Numerical Investigation of Crossflow Separation on the A-Pillar of a Passenger Car." *ASME. J. Fluids Engineering*. November 2018; 140(11): 111105. <https://doi.org/10.1115/1.4040107>.
3. Wood, D. et al.: Experimental Data for the Validation of Numerical Methods - SAE Reference Notchback Model. *SAE International Journal of Passenger Cars - Mechanical Systems*, 7(1), 2014, 145–154. doi: 10.4271/2014-01-0590.
4. Schuetz, T.: *Aerodynamics of Road Vehicles*, Fifth Edition, Warrendale, Pennsylvania, USA, 2016 SAE International, eISBN 978-0-7680-8253-1.
5. Sharma, A., *Introduction to Computational Fluid Dynamics*, Mumbai, Maharashtra, India, 2022, ISBN 978-3-030-72883-0.
6. Hoffmann, K. A., & Chiang, S. T., *Computational fluid dynamics*, Vol. 1-3, Kansas: Engineering Education System, 2000, 67208-1078.
7. Galyard, A. P., *The Appropriate Use of CFD in the Automotive Design Process*, Jaguar Land Rover, 2009 SAE International, 2009-01-1162.
8. Interné materiály ŠKODA AUTO, a.s.
9. Frank M., *Fluid Mechanics*, Seventh edition, University of Rhode Island, 2011, ISBN 978-0-07-352934-9.
10. Fischer, S.: Vehicle aerodynamics CFD simulation in Simcenter STAR-CCM+. June 23, 2021. Online: <<https://blogs.sw.siemens.com/simcenter/vehicle-aerodynamics-cfd-simulation-in-simcenter-star-ccm/>>
11. CD-ADAPCO. STAR-CCM+® Documentation: Version 12.02. CD-adapco®, 2017.
12. Baker, M.: Q-criterion for Vortex Visualization. March 16, 2021. Online: <<https://www.m4-engineering.com/q-criterion-for-vortex-visualization/>>



# Industry 5.0 - A Sustainable Human-Centric Solution

Laura Lachvajderová <sup>1\*</sup>, Jaroslava Kádárová <sup>1</sup>, Ernesto Juliá Sanchis <sup>2</sup> and Denisa Rybárová <sup>1</sup>

- 1 Technical University of Kosice, Faculty of Mechanical Engineering, Institute of Industrial Engineering, Management and Environmental Engineering, Department of Industrial and Digital Engineering, jaroslava.kadarova@tuke.sk, denisa.rybarova@tuke.sk
  - 2 Universitat Politècnica de València - Campus d'Alcoi, Dep. de Mecànica dels Medis Continus i Teoria d'Estructures, erjusan@mes.upv.es
- \* Correspondence: laura.lachvajderova@tuke.sk

**Abstract:** Industry 5.0 is an effort to address the human impacts of the fourth Industrial Revolution. It starts from the belief that businesses want to do more than just maximize profit and provides pathways for integrating social and environmental concerns into technological innovation. This article is dedicated to the theoretical definition of the topic of the fifth industrial revolution. It describes the differences between the last two industrial revolutions and defines three basic elements that are crucial for Industry 5.0. In the end, the scientific output is devoted to the description of specific ways in which simulation can help in the transition to Industry 5.0 and at the very end a summary, the challenges and requirements that Industry 5.0 brings.

**Keywords:** Industry 5.0, Human-Centricity, Sustainability, Resilience

## 1. Introduction

The manufacturing industry has been going through its fourth major transition since artisans gave way to workshops and factories. The first of these revolutions was mechanization and the use of steam power, which later succeeded by the adoption of electricity. Then came computerization, and today that's being followed by the arrival of cyber-physical systems and advanced analytics, otherwise known as Industry 4.0.

Industry 5.0 however is not a typical succession to 4.0. Neither is it a marketing term conceived by an overworked advertising agency. Industry 5.0 refers to the human side of 4.0 and seeks to address the issues raised by 4.0 adoption. Industry 5.0 is a framework for re-imagining the future of energy, manufacturing, mobility, and supply chains that build upon and complement the meaningful groundwork paved by the vision of Industry 4.0.

Industry 5.0 uses collaborative robots and artificial intelligence to bring a human touch to the concept of digital transformation. Promoted by the European commission and other governmental bodies, Industry 5.0 emphasizes a triple-bottom-line of economic, environmental, and societal impact, bringing ESG (Environment, Social and Governance) perspective and balance to what have often been technology-led and economic-driven choices [1].

## 2. Understanding Industry 5.0

Industry 4.0 -- a phenomenon since the industrial revolution -- deals with the integration of innovation and new technologies into the manufacturing production process. Though Industry 4.0 has delivered industrial automation and other significant positive impacts, it sometimes has replaced humans in the workflow process. Industry 5.0 seeks to correct that imbalance, using the concepts of cognitive computing, cyber-physical systems, and artificial intelligence to ensure humans have a role in the digital transformation that is continuing to evolve.

Industry 4.0 is a technological revolution that will have far-reaching human impacts. In manufacturing, increasing automation means that many many workers may get displaced, not only on the factory floor but in administrative and even professional functions. Meanwhile, very little has been done to address some of the biggest challenges facing manufacturers, like where to find the next generation of workers, how to move towards a circular economy, and how to become more resilient in the face of unexpected change and supply chain disruption. Championed by the European Union, Industry 5.0 is an effort to address the human impacts of the fourth Industrial Revolution. It starts from the belief that businesses want to do more than just maximize profit and provides pathways for integrating social and environmental concerns into technological innovation [2].

Altruism plays a part in this, but there's also a strong element of self-interest. Young people want to work for socially aware organizations and people want to buy from companies that behave responsibly. So, by adopting Industry 5.0 principles, organizations wish to safeguard their futures. One of Industry 5.0 challenges is to make processes more human-centric. Part of the motivation is to mitigate the concerns and resistance to automation from labor unions and politicians concerned that Industry 4.0, in theory, could create crises of technological unemployment. From the start of the cycle of innovation during the industrial revolution, the goal of manufacturers has been to enable technologies that would make the production process more efficient. From a practical perspective, this benchmark has been achieved – highly automated processes can deliver highly consistent and repeatable outputs. But this does not address the need to provide increasingly customized or personalized products (as customer expectations become increasingly sophisticated). Human-machine collaboration is the key to unlocking these benefits [3].

### **3. Elements of Industry 5.0**

Perhaps the most important distinction of Industry 5.0 is the reintroduction of the human element into the manufacturing process. In one sense, the human element brings the soul back to manufacturing by enabling collaborative production – the imagination and flexibility of the human worker become empowered and advanced with the ability to harness cyber-physical systems like collaborative robots (or cobots). The combination of smart machines, cognitive computing, cloud computing, and savvy humans will allow for true “mass personalization” and more nimble production.

#### *3.1. Human-Centricity*

Industry 5.0 seeks to restore a human-centric approach to business that some would say was lacking with an Industry 4.0 approach. The symbiosis of humans and machines is essential to creating more jobs, leveraging productivity and efficiency, and attracting and retaining talent. Particularly to technology-centred organizations, human capital is the most strategic asset and businesses will need to accommodate the growing cohort of Gen-Z and Millennials' changing needs. For younger generations of workers, the commitment to environmental and social factors becomes increasingly important in their choice of employer, and this may include a commitment to community initiatives, flex working arrangements, and the cultivation of historically underrepresented minorities in leadership roles. The human-centric vision also critically involves re-thinking how workers and machines collaborate. Traditionally static manufacturing processes can be updated with digital twins, and new collaborative robotics (cobots) with line workers empowered to exercise greater flexibility in production. A healthy and happy workforce with opportunities for creative personal and professional advancement is likely to create lasting value for the business [4].

This proposes that workers be viewed as investments and not costs. Thus, rather than seeking to drive down labor costs, manufacturers should look at how to maximize the return from their employees. This leads to the view that processes should be adapted to

suit workers, and workers should be given the tools to help them do their jobs better. Some of the key components that support the human-centric approach are:

- Exoskeletons
- Augmented reality
- Virtual reality
- Wearables
- Cobots
- Analytics

Furthermore, to maximize the benefits of these new technologies, which include higher productivity, less waste, and lower accidents, workers should be included in their design and deployment. As part of this, it's believed that there is a clear need for upskilling and reskilling [5].

### 3.2 Sustainability

Industry 5.0 seeks to create a manufacturing environment that is both sustainable and resilient, while also being human-centric. With the growing regulatory and investor emphasis on reducing carbon emissions and environmental impact, businesses need to evaluate their resource footprint that supports their manufacturing process. This may involve analyzing the source of raw materials, the proportion of waste generated, along with an evaluation of the environmental impact, the energy efficiency of processes, as well as the sources of energy.

Businesses want to reduce their environmental impact by using alternative energy sources to minimize their footprint. At the same time, it is important to lower the operational costs but also attract young talents. Businesses are realizing that it is the right thing to do and they are adding sustainability plans to their strategy. One reason is to lower operating costs by cutting resource consumption and waste. Another is because it's what employees and younger recruits want to see. And a third reason is that it's the right thing to do. Many firms have committed to specific reductions of fossil fuels and clean energy generation sources. Additionally, the adoption of new materials and composites (away from petroleum-based for instance) can reduce environmental impact while increasing smart manufacturing practices, such as recycling and repurposing materials, to achieve objectives for socio-ecological sustainability [6].

Industry 5.0 addresses how manufacturers and others can move towards a circular economy where recycling is integral to production and consumption. With an emphasis on this, plus re-use and repurposing, Industry 5.0 encourages adopting artificial intelligence (AI) and additive manufacturing to avoid resource depletion and environmental degradation [7].

### 3.3 Resilience

In the Industry 4.0 paradigm, businesses have been forced to cope with increased uncertainties and adapt to cope with change. That's why Industry 5.0 bolsters resilience for companies looking to balance man and machine. It's important for organizations to engage in planning exercises that account for potential disruptions across the value chain, from the factory floor to the supplier network, to transportation channels, to regulatory and geopolitical changes that can promote the achievement of societal goals.

Digital technologies and methodologies (simulations and AI-enhanced modeling) can help identify optimal alternative paths in the event of a disruption, weighing different factors such as cost, substitution, quality, and logistical concerns into the mix. Start with identifying the greatest points of vulnerability (whether in process or supply chain), isolate the key inputs, and then formulate contingency planning for any disruptions [8].

Some tools and capabilities that will play a part in this are:

- Deployment of modular factories
- New materials (and the ability to transition seamlessly between sources)

- Remotely operated factories
- Real-time risk monitoring
- Enhanced cybersecurity

Any perception that Industry 5.0, (and also Industry 4.0,) is only for deep-pocketed global manufacturers is incorrect. Small and medium enterprises (SMEs) are just as capable of adopting these new technologies and perspectives as their larger brethren, and perhaps more so [9]. For many of the trends and technologies discussed above, implementation is as dependent on open minds and a willingness to change as on financial resources, and these are areas where SMEs often excel [3].

#### 4. Industry 5.0 Transition Support

Factories and manufacturing processes are becoming smarter, and competitors never stop looking for an “edge.” Against this background, it’s more important than ever to keep changing and improving, but also to do it faster and to avoid mistakes.

Manufacturing simulation plays a key role in all three elements of Industry 5.0. By modeling existing or proposed manufacturing systems, it provides a so-called “virtual sandbox” that enables risk-free exploration of ideas and alternatives. It’s used to gain a deeper understanding of complex operations and relationships, to identify potential problems or conflicts, and to identify opportunities and solve current problems [10]. Specific ways in which simulation supports an Industry 5.0 transition include:

- Creation of digital twins
- Virtual commissioning
- Modeling supply chain disruptions
- Travel avoidance
- Risk-free experimentation
- Upskilling

A digital twin is a complete and accurate representation of part or all of the production process. Most importantly, by connecting it to sensors installed on the physical system, it maintains fidelity to real-world conditions. With this, it’s possible to evaluate changes and the impact of disruptions and come up with alternative production schedules. It also helps with debugging problems and can avoid the need for technicians to travel to work sites or factories. Virtual commissioning uses a digital twin to accelerate the implementation of new equipment and processes [11].

#### 5. Conclusions

The essential Industry 5.0 strategy is designed to ensure a framework for industry that combines competitiveness and sustainability, allowing industry to realize its potential as one of the pillars of transformation. It is a strategy focused on emphasizing the impact of alternative modes of (technology) governance for sustainability and resilience. An effective Industry 5.0 strategy empowers workers using digital devices, endorsing a human-centric approach to technology; builds transition pathways towards environmentally sustainable uses of technology; expands the remit of corporation's responsibility to their whole value chains; and, finally, introduces indicators that show, for each industrial ecosystem, the progress achieved on the path to well-being, resilience, and overall sustainability.

Preparing for Industry 5.0 is not inconsequential, but there are multiple forces arraying to compel businesses to adopt the core principles of human-centricity, resilience, and sustainability. It’s far better to take the opportunity to prepare ahead of time, rather than react to an unanticipated shock to the system. Beyond better, cheaper, and faster, the technology-enhanced mantra Industry 5.0 promises to lead the next generation into a balance of decisions that support smarter, cleaner, and more resilient industries. Realizing the updated vision for Industry 5.0 will require new economic priorities to measure industry performance, new structure and design of business models, value chains and supply

chains, updated objectives for digital transformation, innovative approaches to policy-making that better align the interests with business and industry, new ways to drive innovation and research capabilities, while better aligning the interests of businesses with broader society, government, and environment. The lessons learned from the pandemic underscore the compelling need to build resilience across value chains while securing jobs and economic security.

**Acknowledgments:** This article was created with the support of projects: KEGA 009TUKE-4/2020 “Transfer of Digitization into Education in the Study Program Business Management and Economics”, VEGA 1/0340/21 “The impact of a pandemic and the subsequent economic crisis on the development of digitization of enterprises and society in Slovakia”, VEGA 1/0438/20 “Interaction of digital technologies to support software and hardware communication of the advanced production system platform”, KEGA 001TUKE-4/2020 “Modernizing Industrial Engineering education to Develop Existing Training Program Skills in a Specialized Laboratory” and KEGA 020TUKE-4/2023 “Systematic development of the competence profile of students of industrial and digital engineering in the process of higher education”.

## References

1. Lachvajderová, L.; Kádárová, J.: Industry 4.0 Implementation and Industry 5.0 Readiness in Industrial Enterprises. *Management and Production Engineering Review* **2022**, Volume 13(3), pp. 102-109. DOI: 10.24425/mper.2022.142387
2. Lachvajderová, L.; Kádárová, J.; Rybárová, D.; Trebuňa, M.: Vplyv digitalizácie a udržateľnosti na malé a stredné podniky na Slovensku. *Maneko: MANažment a EKOnomika podniku* **2022**, Volume 14(1), pp. 38-48. ISSN 1337-9488
3. Ghobakhloo, M.; Iranmanesh, M.; Mubarak, F. M.; Mubarik, M.; Rejeb, A.; Nilashi, M.: Identifying industry 5.0 contributions to sustainable development: A strategy roadmap for delivering sustainability values. *Sustainable Production and Consumption* **2022**, Volume 33, pp. 716-737, ISSN 2352-5509, DOI: <https://doi.org/10.1016/j.spc.2022.08.003>
4. Coronado, E.; Kiyokawa, T.; Garcia Ricardez, A. G.; Ramirez-Alpizar, G. I.; Venture, G.; Yamanobe, N.: Evaluating quality in human-robot interaction: A systematic search and classification of performance and human-centered factors, measures and metrics towards an industry 5.0, *Journal of Manufacturing Systems* **2022**, Volume 63, pp. 392-410, ISSN 0278-6125, DOI: <https://doi.org/10.1016/j.jmsy.2022.04.007>
5. Kolade, O.; Owoseni, A.: Employment 5.0: The work of the future and the future of work, *Technology in Society* **2022**, Volume 71, 102086, ISSN 0160-791X, DOI: <https://doi.org/10.1016/j.techsoc.2022.102086>
6. Yin, S.; Yu, Y.: An adoption-implementation framework of digital green knowledge to improve the performance of digital green innovation practices for industry 5.0, *Journal of Cleaner Production* **2022**, Volume 363, 132608, ISSN 0959-6526, DOI: <https://doi.org/10.1016/j.jclepro.2022.132608>
7. Javaid, M.; Haleem, A.; Singh, R. P.; Suman, R.; Santibañez Gonzalez, E.: Understanding the adoption of Industry 4.0 technologies in improving environmental sustainability, *Sustainable Operations and Computers* **2022**, Volume 3, pp. 203-217, ISSN 2666-4127, DOI: <https://doi.org/10.1016/j.susoc.2022.01.008>
8. Doyle-Kent, M.; Kopacek, P.: Adoption of Collaborative Robotics in Industry 5.0. An Irish industry case study, *IFAC-PapersOnLine* **2021**, Volume 54(13), pp. 413-418, ISSN 2405-8963. DOI: <https://doi.org/10.1016/j.ifacol.2021.10.483>
9. Lachvajderová, L.; Kádárová, J.: Attitude of European SMEs to digitalization and digital transformation during the COVID-19 pandemic, *Novus Scientia* **2022**, Volume 19, pp. 101-106, ISBN 978-80-553-4085-2.
10. Kopec, J.; Pekarčíková, M.; Lachvajderová, L.; Mizerák, M.: Simulation methods for logistics processes in solidworks, *Research, Production and Use of Steel Ropes, Transport and Handling Equipment - International Conference* **2022**, Volume 21, pp. 43-50, ISBN 978-80-553-4084-5.
11. Pekarčíková, M.; Kopec, J.; Dic, M.; Petriková, A.: Intensification of modelling tools through simulation, *Research, Production and Use of Steel Ropes, Transport and Handling Equipment - International Conference* **2022**, Volume 21, pp.113-121, ISBN 978-80-553-4084-5



# Technological process of filament production from PPSU material and the effect on its biocompatibility

Samuel Lancoš <sup>1\*</sup>, Miroslav Kohan <sup>1</sup>, Gabriela Dancáková <sup>1</sup>, Tomáš Balint <sup>1</sup>, Teodor Tóth <sup>1</sup> and Radovan Hudák <sup>1</sup>

<sup>1</sup> Technical University of Košice, Faculty of Mechanical Engineering, Department of Biomedical engineering and measurement; samuel.lancos@tuke.sk

\* Correspondence: samuel.lancos@tuke.sk

**Abstract:** The article describes the complete methodology and process of printing filament production as well as the description of the basic parameters of the machine. The medically certified PPSU material in the form of granules was used to produce filaments that are used for additive manufacturing. Filament maker equipment (Precision series) and dryer from 3Devo (Netherlands) were used for the production of filaments. Cytotoxicity tests in vitro were subsequently performed on the produced filament - a test on extracts. 6 samples for 100 and 75 percent media were used for evaluation. The benefit of the work was the creation of a usable filament with a deviation of  $1.75 \pm 0.1$ mm, which is sufficient for use in 3D printing. The cytotoxicity test proved that the specific material is not cytotoxic, as there was no decrease in metabolic activity below 70 percent.

**Keywords:** polyphenylsulfone; cytotoxicity; extrusion; filament

## 1. Introduction

When it comes to new biomaterials and biomedical devices, thermoplastic and thermoset polymers represent a suitable choice mainly due to their mechanical behavior, chemical stability and physicochemical versatility. Whether considering the fields of research or industry, the successful use of plastics has been reported in a variety of biomedical applications, including the coating of medical devices, the fabrication of novel biomedical devices, selective and accurate detection and diagnostics, specific drugs, and personalized engineering. The attractive and adaptable properties associated with thermoplastic polymers have gained impressive attention and enable the assembly of specialty compounds for modern biomedical applications. In certain cases, some materials can also be used in the field of regenerative engineering [1,2]. In the case of biomedical polymers, the current challenge is to adjust the mixing and processing procedures to make adequate use of their characteristic properties and to manage the presence of any residual material that contains toxic potential. During the last decades, several experimental techniques have been tested and selected for the development of biomedical materials and devices based on plastics (injection molding, electrospinning, extrusion, and others).

Among the most widely used additive manufacturing technologies is an extrusion-based process in which a filament of thermoplastic material is liquefied and extruded through a nozzle to create a three-dimensional object in a layer-by-layer fashion. One of the challenges of this technology is the limited availability of materials [1,3].

When choosing a polymer material for biomedical applications, it must meet specific mechanical conditions such as strength, impact resistance or stiffness. There are some thermoplastics that have suitable mechanical properties over a wide range of temperatures, such as PC, PEEK, PPSU and nylon. Among biomaterials, PPSU is considered dimensionally stable because it has uniform shrinkage and deformation over wide temperature ranges, allowing it to maintain tight tolerances in close abutment with bone structure [4].

The main challenge in using synthetic polymers for biomedical applications is almost always the lack of biocompatibility, which is often associated with inflammatory reactions. In direct connection with the aspects of surface contact, biocompatibility is an essential element in the field of biomaterials. Biocompatibility has been officially defined as “the ability of a material to work with an appropriate host response in a specific application. This broad definition includes the term "bioactivity", where the material produces a desired effect in living tissue, and thus the opposite of inertness [5]. We can also include a cytotoxicity test among the basic biocompatibility tests.

The cytotoxicity test is an economical method with the advantages of a relatively simple test method, high repeatability, accurate result, and extensive evaluation as a result of standardization. Different cell lines are used for cytotoxicity assessment in accordance with the target application [6,7].

## 2. Materials and Methods

The granulate material used in the production of filaments: PPSU (Grade: Radel R-5000NT), from the manufacturer Solvay. Based on information from the manufacturer, this material offers hydrolytic stability, toughness and excellent thermal coverage. The material transformation process was carried out on equipment from the manufacturer 3Devo (Netherlands).

### 2.1. Granulate preparation

The material was delivered in the form of granules, protected from moisture and light by opaque vacuum packaging. Nevertheless, the materials were subjected to a drying process in a Dryer from 3Devo (Figure 1b). The drying of the granulate was carried out at a temperature of 100°C and lasted for 3 hours. The rotating blades of the device mix the material during the drying process, while evenly distributing the heat emitted by the dryer. The drying process was chosen for the purpose of eliminating moisture in the materials.

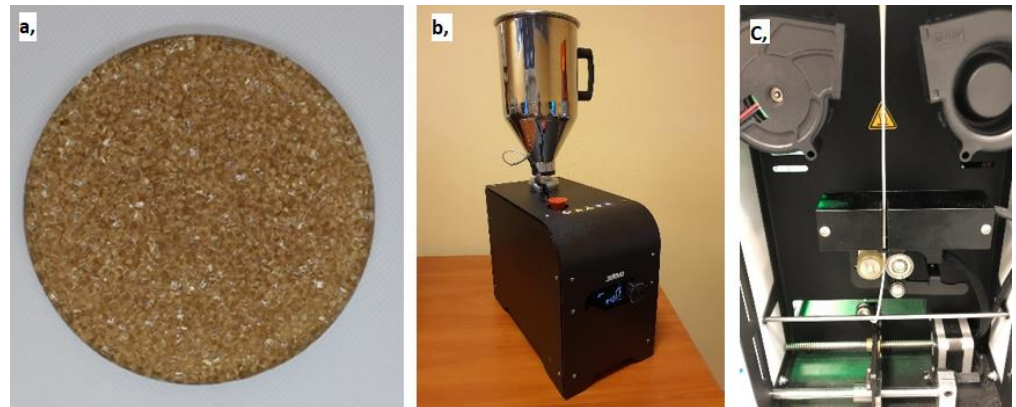


**Figure 1.** (a) PPSU material in form of granulate; (b) Dryer – 3Devo; (c) extrusion process

### 2.2. Extrusion process

Extrusion was performed on a filament maker (Precision series) (Figure 1c). The device was placed in a room with air conditioning to maintain a constant temperature. The temperatures on all four heating bodies of the filament maker were set to 350°C. This temperature was chosen based on knowledge of the melting point of the PPSU material. To achieve such a high temperature, we needed transit materials, because few materials can withstand such a wide temperature range (15-400°C). 3 transit materials were used:

- HDPE - temperature range 180-280°C;
- Devoclean MidTemp - temperature range 180-320°C;
- Devoclean HighTemp - temperature range 320-420°C.

During the subsequent lowering of the temperatures of the individual heat bodies, we tried to achieve that the range of the drawn current was from 2050-2150mA. During extrusion, other important parameters were also monitored, such as: the speed of rotation of the sliding screw and cooling by the respective fans. With a suitable combination of these parameters, we tried to achieve a filament with a diameter of 1.75 mm. The final parameter combinations are summarized in Table 1. The filament was then wound into a spool (Figure 2a). You can see the graph showing the thickness of the filament in Figure 2b.

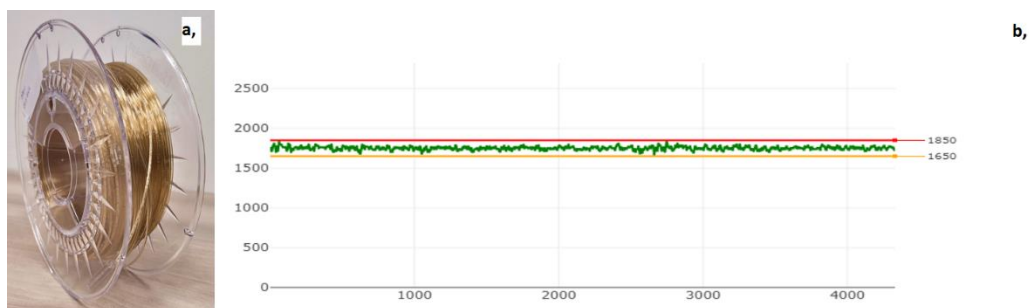


**Figure 2.** (a) PPSU spool produced; (b) Diameter [µm] / time [s]

**Table 1.** Extrusion parameters for pure PPSU material

Pure PPSU				
Heating element	#4	#3	#2	#1
Set temperature [°C]	~345	~347	~347	~347
Round per minute	5			
Fan percentage output [%]	70			

### 2.3. Cytotoxicity test

In order to determine the behavior of the material towards the organism, it was necessary to perform an in vitro test on the cytotoxicity of the PPSU material. The purchased Radel R-5000NT material from Solvay has a medical certification of biocompatibility. After the filament production process, it was necessary to find out whether the material production method does not affect the biocompatibility of the PPSU material. The test was performed in accordance with ISO 10993-5:2009 and ISO 10993-12:2021. The cell line L929 (ATCC® CCL-1™) was used to evaluate cell proliferation. The extraction medium was MEM (MEM (Sigma M0446) + 5% FBS (Sigma F7524) + ATB (Sigma A5955)). The extraction conditions were: 24 h, 37°C, 120 RPM. 2 types of extracts were used: 100%- fresh (undiluted extract) and 75% extract (1 part extract + 3 parts medium).

Chronological course of the exam:

1. Day:
  - insertion of sterile samples into MEM+5% FBS+ATB medium
  - 37°C shaking (120RPM)
  - 24-hour extraction
  - seeding 10<sup>5</sup> cells in a 96-well array
  - 24-hour incubation
2. Day:
  - media control
  - 24-hour incubation
3. Day:
  - measurement of metabolic activity

- preparation of resazurin in MEM
- 1-hour incubation
- fluorescence measurement (ex/em = 560/590nm)

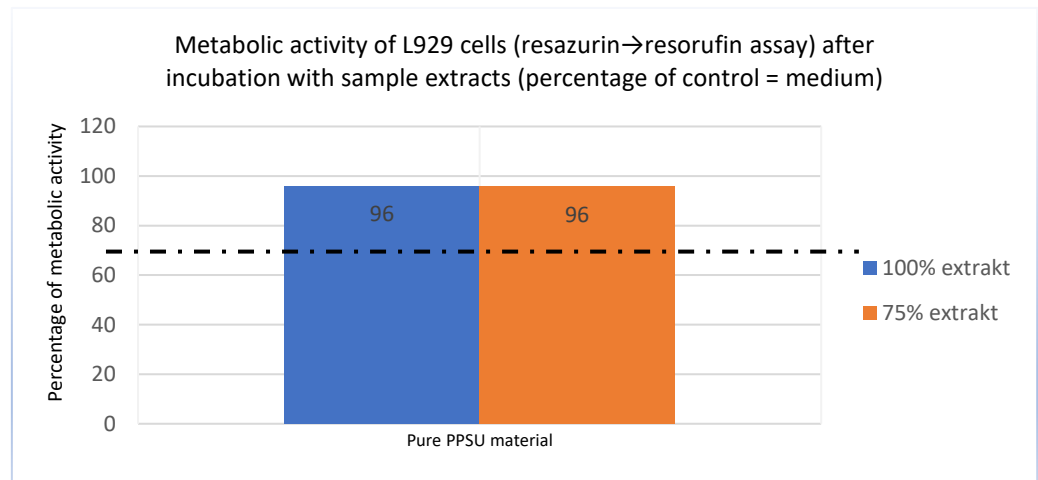


**Figure 2.** Measured metabolic activity; resazurin – resorufin assay

#### Test results (quantitative):

None of the extracts of the tested material caused a decrease in the metabolic activity of the cells below 70%. In the tested samples of both percentage variants the metabolic activity was slightly reduced compared to the negative control and to reference material. Four percentage reduction of cells in means that tested material is not cytotoxic. Based on visual inspection, an increase in the number of cells was evident after 24 hours of cultivation. Cells after culture with extracts are morphologically comparable to unaffected cells.

### 3. Conclusions

The theoretical output of the article is the presentation of the reasons why the PPSU material is suitable for use in the field of biomedical engineering. Based on a suitable optimization of the equipment, the material was transformed from the form of pellets to the form of filament. Based on the sensor, it was evaluated as suitable for future use in FDM printing. Subsequently, the material was tested for cytotoxicity with a positive result. The measured values of cell proliferation were unchanged based on control on 6 samples.

#### Acknowledgments:

This publication is the result of the project implementation CEMBAM - Center for Medical Bioadditive Research and Production, ITMS2014+: 313011V358 supported by the Operational Programme Integrated Infrastructure funded by the European Regional Development Fund. This research was supported by project VEGA 1/0599/22 Design solution and biomechanical analysis of personalized instruments for arthroscopic applications. This research was supported by project KEGA 021TUKÉ-4/2022 Implementation of computed tomography in an interdisciplinary technical and scientific area. This research was supported by project VEGA 1/0308/22 The use of biocomposite materials in the therapy of fractures of long tubular bones in birds.

### References

1. WATANABE, Narumi. Computational and experimental investigation of reinforced polymers for material extrusion additive manufacturing. 2016. PhD Thesis. Georgia Institute of Technology.
2. TEOH, Swee Hin. Engineering materials for biomedical applications. World scientific, 2004.
3. STELL, Adam L., et al. Systematic evaluation of clinically used biomaterials to determine their suitability for fabrication of beta cell delivery devices. Journal of Immunology and Regenerative Medicine, 2022, 16: 100055.

4. BÎRCĂ, Alexandra, et al. Introduction in thermoplastic and thermosetting polymers. In: *Materials for Biomedical Engineering*. Elsevier, 2019. p. 1-28.
5. BERNARD, Mélisande, et al. Biocompatibility of polymer-based biomaterials and medical devices—regulations, in vitro screening and risk-management. *Biomaterials science*, 2018, 6.8: 2025-2053.
6. ZHOU, W. R.; ZHENG, Y. F. Characterization of modified magnesium and magnesium alloys for biomedical applications. In: *Surface modification of magnesium and its alloys for biomedical applications*. Woodhead Publishing, 2015. p. 263-282.
7. LEE, Gang Ho; KIM, Jeong-Tae. *Ultrasmlal lanthanide oxide nanoparticles for biomedical imaging and therapy*. Woodhead Publishing, 2014.



# ANALYSIS OF MOTORCYCLE EMISSION PARAMETERS IN THE USE OF SUSTAINABLE FUELS

Matúš Lavčák<sup>1</sup>, Pavol Tarbajovský<sup>2</sup> Michal Puškár<sup>3</sup>

<sup>1</sup> Faculty of Mechanical Engineering, TU Košice, Letná 9, 040 01 Košice, Slovak Republic; matus.lavcak@tuke.sk

<sup>2</sup> Faculty of Mechanical Engineering, TU Košice, Letná 9, 040 01 Košice, Slovak Republic; pavol.tarbajovsky@tuke.sk

<sup>3</sup> Faculty of Mechanical Engineering, TU Košice, Letná 9, 040 01 Košice, Slovak Republic; michal.puskar@tuke.sk

\* Correspondence matus.lavcak@tuke.sk; Tel.: 0944 344 186;

**Abstract:** Fossil fuels, which are the primary contributors to climate change and global warming, are currently having a significant negative impact on the environment. Therefore, it would be advantageous to create sustainable alternative fuels. A potential fuel, bioethanol is environmentally friendly and renewable. In this study, a single-occupancy car was propelled by a mixture of bioethanol and gasoline. Power, torque, and emissions served as the metrics used to measure bioethanol performance. The blend's bioethanol percentage was 5%, 10%, 30%, and 50%. Performance was worse than expected compared to 5% bioethanol, especially at higher engine speeds. Power and torque numbers were highest with the E5 blend. However, burning a mixture of bioethanol and gasoline produced

**Keywords:** analysis; sustainable fuels; performance

## 1. Introduction

Fossil fuels, which are a major contributor to climate change and global warming, are currently having a significant negative impact on the environment. It would therefore be appropriate to develop sustainable alternative fuels. A potential fuel, bioethanol, is environmentally friendly and renewable. In this study, a single-passenger vehicle was powered by a mixture of bioethanol and gasoline. Power, torque, and emissions served as the indices used to measure the performance of the bioethanol. The proportion of bioethanol in the blend was 5%, 10%, 30% and 50%. The performance was worse than expected compared to 5% bioethanol, especially at higher engine speeds. The power and torque values were highest for the E5 blend.

## 2. Materials and Methods

Bioethanol testing (torque and power) on a motorcycle was performed in this study on an engine running at 4000 to 8000 rpm. A dynamometer test was used to measure the torque and power testing. A gas analyzer was used to test emissions when the engine was running at 500 to 4000 rpm. Different bioethanol and gasoline fuel blends (5%, 10%, 30%, and 50%) were tested. After combining the fuel, a 125cc Yamaha motorcycle's performance was tested. DYNOJET i250 dynamometer used for evaluating torque and power.

### 3. Experimental results and discussion

Figure 1 depicts the power output generated at various speeds and fuel combinations. Over 6 Kw of power was produced at 7500 revolutions per minute using E5 gasoline. As a result of using E10, the parameters subsequently declined. Higher bioethanol concentration was used, and while the performance parameters stabilized, they were somewhat less than with E5. The investigation demonstrates that the biofuel enhances performance by enhancing detonation resistance, but for the improvements to truly take effect, the compression ratio must be increased. [4,5]

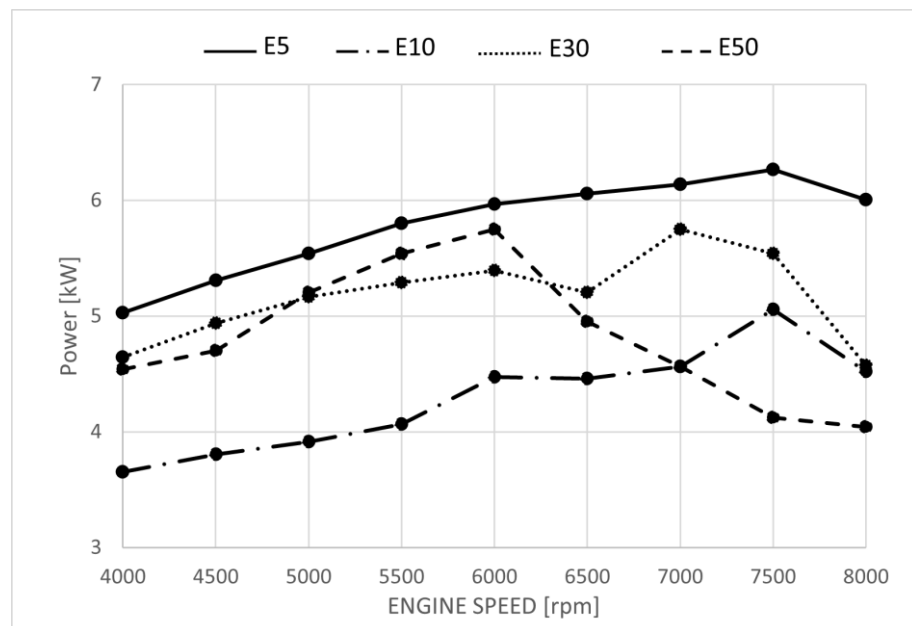


Figure 1 Performance at different fuel mixtures

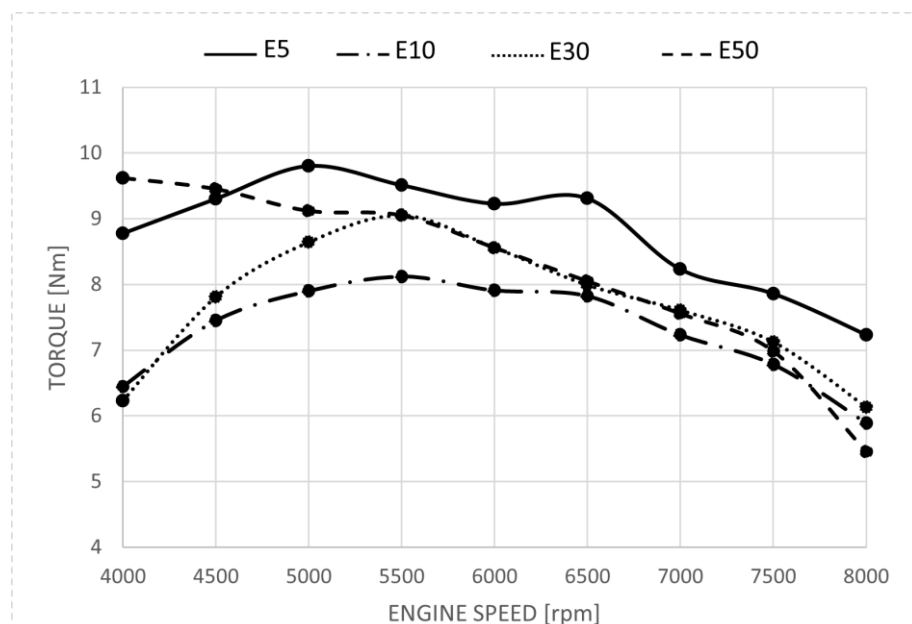


Figure 2 Torque waveform for different fuel mixture

Figure 2 depicts the torque fluctuation with engine speed for a bioethanol/gasoline combination. The bioethanol-gasoline blends should, on the whole, deliver better torque performance than regular gasoline. [7,9]

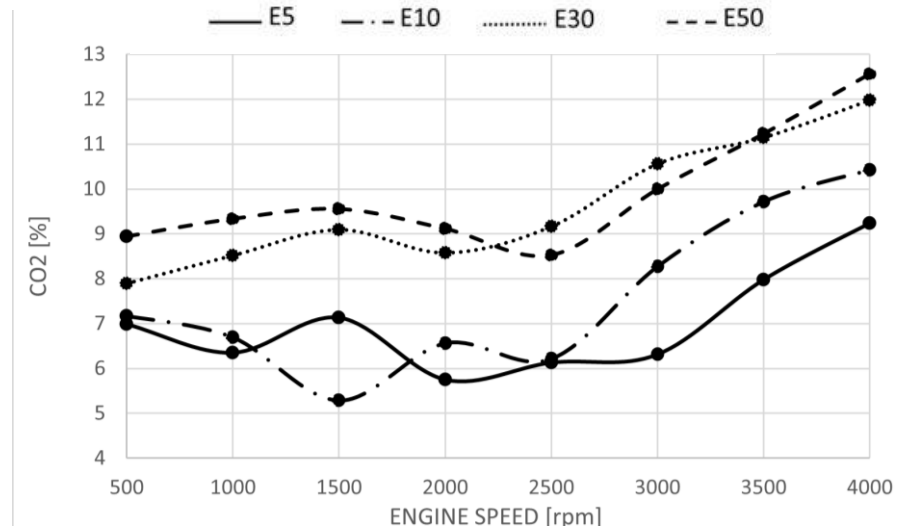


Figure 3 Analysis of CO2 emission

One of the many reasons for doing this is that oxidized gasoline enables improved fuel combustion outcomes, which increases torque. Additionally, because bioethanol and gasoline blends include more oxygen than pure gasoline, they may burn more effectively. Because good acceleration requires a lot of torque, the crankshaft rotates with a bigger moment of inertia, which results in more economical fuel use. [5,6]

Figure 3 displays the results of the measurement of the CO2 content of the exhaust gases at engine speeds ranging from 500 to 4000 rpm. Compared to pure gasoline, a bioethanol-gasoline blend emits more carbon dioxide (CO2). Engine speed has an impact on the amount of CO2 emitted. The graph shows that the amount of CO2 emissions in bioethanol-gasoline blends is higher than that in pure gasoline and rises when more bioethanol is utilized. The E50 blend has the greatest CO2 emission content [1,7]. E5 blends had the lowest CO2 content, though. The higher oxygen percentage in the fuel blend is what's causing the increase in CO2 emissions [4].

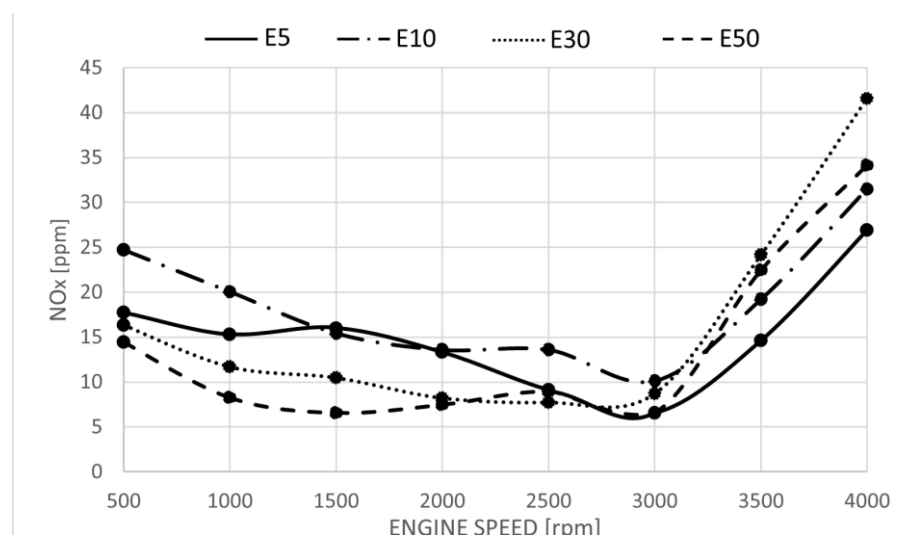


Figure 4 NOx emission analysis

Figure 4 shows how engine speed affects NOx emissions. Nitric oxide (NO) and nitrogen dioxide (NO<sub>2</sub>) combine to form the NO<sub>x</sub> molecule when oxygen and nitrogen gases in the air are burned. The three critical factors that affect NO<sub>x</sub> formation are flame burning temperature, oxygen concentration, and combustion time [4]. Figure 4 shows the trend of lower NO<sub>x</sub> emissions occurring in the interval 500 - 3000 rpm, followed by an increase in NO<sub>x</sub> content from 3000 rpm onwards. All blends of bioethanol and gasoline typically emit less NO<sub>x</sub> than conventional gasoline. The E30 and E50 blends produced the lowest NO<sub>x</sub> values. [3,9].

#### 4. Conclusions

This study was successful in examining how bioethanol and gasoline mixtures performed. The analyses proved that bioethanol should offer better fuel efficiency. [4,5,8] The issue was that the fuel mixture had a different specific gravity than air, which made mixing with it difficult. The anti-detonation qualities have been improved, which has resulted in a temporary decline in performance metrics at a particular compression ratio and standard fuel map. In other words, the engine design did not take advantage of the fuel performance. Compression must be raised and the fuel map must be changed in order to fully use the fuel mixture's potential. [1,2,3]

**Acknowledgments:** This work was supported by the Slovak Research and Development Agency under the Contract no. APVV-19-0328. The article was written in the framework of Grant Projects: VEGA 1/0318/21 "Research and development of innovations for more efficient utilization of renewable energy sources and for reduction of the carbon footprint of vehicles" and KEGA 007TUKE-4/2023 "Transfer of innovations and advanced technologies, determined for more ecological and more efficient vehicle drive systems, into the educational process."

**Conflicts of Interest:** The authors declare no conflict of interests.

#### References

1. Puškár, M.; Bigoš, P. Method for accurate measurements of detonations in motorbike high speed racing engine. *Measurement* 2012, 45, 529–534. ISSN 0263-2241.
2. Lamas, M.I.; Rodriguez, C.G.; Rodriguez, J.D.; Telmo, J. Internal modifications to reduce pollutant emissions from marine engines. A numerical approach. *Int. J. Naval Archit. Mar. Eng.* 2013, 5, 493–501, doi:10.2478/IJNAOE-2013-0148.
3. Chen H, Su X, He JJ, Xie B. Investigation on combustion and emission characteristics of a common rail diesel engine fueled with diesel/n-pentanol/ methanol blends. *Energy* 2019;167:297–311.
4. Manigandan S, Gunasekar P, Devipriya J. Emission and injection characteristics of corn biodiesel blends in diesel engine. *Fuel* 2019;235:723–35.
5. van Niekerk AS, Drew B, Larsen N, et al. Influence of blends of diesel and renewable fuels on compression ignition engine emissions over transient engine conditions. *Appl Energy* 2019;255:113890.
6. Etim, Anietie O.; Musonge, Paul; Eloka-Eboka, Andrew C. Effectiveness of biogenic waste-derived heterogeneous catalysts and feedstock hybridization techniques in biodiesel production. *BIOFUEL BIOPROD BIOR*, 14 (3): 620-649 MAY 2020
7. Puškár, M.; Bigoš, P. Output Performance Increase of Two-stroke Combustion Engine with Detonation Combustion Optimization. *Strojarstvo: Časopis za teoriju i praksu u strojarstvu* 2010, 52, 577–587. ISSN 0562-1887.
8. Geng LM, Xiao YG, Li SJ, Chen H, Chen XB. Effects of injection timing and rail pressure on particulate size-number distribution of a common rail DI engine fueled with fischer-tropsch diesel synthesized from coal. *J. Energy Inst* 2020. <https://doi.org/10.1016/j.joei.2020.08.008>.
9. Zhang MM, Hong W, Xie FX, et al. Effects of diluents on cycle-by-cycle variations in a spark ignition engine fueled with methanol. *Energy* 2019;182:1132–40.



# Effect of Mn addition on the mechanical properties of Zinc alloys

Wanda Mamrilla<sup>1,2\*</sup>, Zuzana Molčanová<sup>2</sup>, Beáta Ballóková<sup>2</sup>, Dóra Zalka<sup>2,3</sup>, Karel Saks<sup>2</sup>, Radovan Hudák<sup>1</sup>

<sup>1</sup> Technical University of Košice, Faculty of Mechanical Engineering ; [wanda.mamrilla@tuke.sk](mailto:wanda.mamrilla@tuke.sk), [radovan.hudak@tuke.sk](mailto:radovan.hudak@tuke.sk)

<sup>2</sup> Slovak Academic of Science, Institute of materials research; [wmamrilla@saske.sk](mailto:wmamrilla@saske.sk), [molcanova@saske.sk](mailto:molcanova@saske.sk), [bbalokova@saske.sk](mailto:bbalokova@saske.sk), [ksaksl@saske.sk](mailto:ksaksl@saske.sk)

<sup>3</sup> University of Pavol Jozef Safarik, Faculty of Science : [dzalka@saske.sk](mailto:dzalka@saske.sk)

\* Correspondence: [wanda.mamrilla@tuke.sk](mailto:wanda.mamrilla@tuke.sk)

**Abstract:** Zn-based metallic alloys are the next generations of the biodegradable materials in biomedical implant applications. These materials shows perfect biocompatibility and their corrosion rates are lower compared to Mg-based alloys. The advantage of degradation process of Zn is absence of evolution excessive H<sub>2</sub> gas. In the present study, Zn-Mg-Ca alloy microalloyed with Mn was studied. Alloys was fabricated by gravity casting and processed by hot extrusion. Mechanical properties and corrosion resistance were evaluated in comparison with pure zinc. After hot extrusion process the microhardness was improved by an average by 25%. With the addition of Mn, the microhardness of the extruded alloys increased by 40%. The highest microhardness value of 133.8±12.0 was measured for the Zn-0.4Mg-0.4Ca-1.1Mn alloy after hot extrusion. The lowest corrosion rate of 0.117 mm/year was measured for the sample Zn-0.4Mg-0.4Ca-0.6Mn. It should be noted that corrosion rate of studied Zn-based materials was close to the 0.2mm/year, which is ideal corrosion rate for biodegradable alloys.

**Keywords:** biodegradable metallic materials, zinc-based alloys, mechanical properties, corrosion resistance

## 1. Introduction

The fundamental role of zinc in the human body was discovered in 1961, when Iranian farmers discovered that people who ate zinc-poor foods (bread, potatoes, and milk) suffered from syndromes such as anemia, hypogonadism, and dwarfism. Since this discovery, interest in the biochemical and clinical aspects of zinc has greatly increased [1]. It is now well known that zinc is one of the most abundant nutritional elements in the human body. Zinc is present in all organs, tissues, fluids and body secretions, with 86% found in skeletal muscle and bone, 6% in skin, 5% in liver, 1.5% in brain, and the rest distributed among other tissues [2][3]. At the cellular level, 30–40% is found in the nucleus, 50% in the cytoplasm, organelles and vesicles, and the remaining part is found in the cell membrane. The human body is able to absorb zinc from the environment, regulate its concentration in body fluids, ensure its transport to places where its presence is needed, and safely excrete the excess through the kidneys [2].

Zinc plays an important role in the formation and mineralization of bone and bone mass and can also be found in the bone extracellular matrix, where it is deposited together with calcium hydroxyapatite. Lack of zinc in the bone matrix correlates with aging of the skeleton and causes various diseases [4].

Zinc and zinc-based alloys have only recently entered the list of bioresorbable metallic materials as promising alternatives to magnesium and iron.

Zinc exhibits high chemical activity, with an electrode potential ( $-0.762$  V) falling between that of magnesium ( $-2.372$  V) and iron ( $-0.444$  V) [5]. Therefore, pure zinc metal shows intermediate degradation rate (it degrades faster than Fe and its alloys, but slower than the fast-degrading Mg and its alloys) due to passive layers formed by corrosion products [6].

Zinc and its alloys are easier to cast and process due to their low melting points, low chemical reactivity and good machinability. Unlike Mg-based alloys, the melting of zinc alloys can be carried out in air [7].

Pure Zn shows the lowest ultimate tensile strength  $\sigma_{UTS}$ , tensile yield strength  $\sigma_{TYS}$  and elongation  $\epsilon$  among all metallic biomaterials (Tab.1). Therefore, the development of zinc alloys with higher  $\sigma_{UTS}$ ,  $\sigma_{TYS}$ , and  $\epsilon$  is one of the main challenges to its suitability as a candidate material for biomedical applications. The mechanical properties of Zn alloys can be enhanced by alloying strengthening and thermodeformation treatment [8].

**Table 1.** Comparison of physical and mechanical properties of bone tissues along with existing non-biodegradable and biodegradable metallic materials [8].

Tissue/Material	$\rho$ (g/cm <sup>3</sup> )	$\sigma_{UTS}$ (MPa)	$\sigma_{TYS}$ (MPa)	E (GPa)	$\epsilon$ (%)
<b>Cortical bone</b>	1.8-2.0	35-283	105-114	5-23	1.07-2.1
<b>Trabecular bone</b>	1.0-1.4	1.5-38	1-12	0.01-1.6	2.20-8.5
<b>316L stainless steel</b>	8.0	450-650	200-300	190	30-40
<b>Co-Cr alloys (ASTM F90)</b>	9.2	860	310	210	20
<b>Ti-6Al-4V (annealed)</b>	4.4	895-1025	825-869	110-114	6-10
<b>Pure Mg</b>	1.7-2.0	90-190	65-100	41-45	2-10
<b>Pure Fe</b>	7.8	180-210	120-150	211.4	40
<b>Pure Zn (As cast a hot rolled)</b>	7.14	18-140	10-110	1.2-2.1	0.3-36

Alloying is usually the first choice in the design, with the purpose of improving the mechanical properties of the base metal, which can be achieved by creating solid solutions or precipitation strengthening. As shows Tab. 2, the alloying elements Mg, Ca, Mn in resorbable Zn alloys has a different contribution in strengthening mechanisms.

**Table 2.** Selected alloying elements and their effect on zinc alloys [9].

Element	Daily Allowance	Effect on zinc alloys
Mg	700 mg	↑mechanical properties ↑corrosion rates
Ca	800 mg	↑mechanical properties ↑corrosion rates
Mn	4 mg	Mn improves the casting process. ↑susceptibility of galvanic micro-cell corrosion

In the present work, the novel zinc alloys have been designed considering the benefits of Zn, Mg, Ca and a minor amount of Mn to develop the Zn-Mg-Ca-Mn alloys and evaluated their chemical composition, mechanical properties and in vitro corrosion behavior.

## 2. Materials and Methods

### 2.1. Materials' preparation

A series of Zn alloys were prepared, specifically: Zn-0.4Mg-0.4Ca-xMn (x=0, 0.2, 0.4, 0.6, 0.8 wt.%) with pure Zn (99.995%, Heneke, Mazak, bulk), pure Mg (99.98%, Alfa Aesar, lumps), pure Ca (99.5% Alfa Aesar, granules) and pure Mn (99.3% Alfa Aesar, powder). Mg, Ca, Mn were chosen because they are non-toxic and biocompatible to living organisms, they also improve mechanical properties and help maintain mechanical integrity for the required application time. The mentioned series of alloys was prepared by conventional gravity casting in a graphite mold under protective Ar atmosphere to prevent the possible formation of oxides in the alloy.

Alloy ingots were machined into diameter 15 mm and height 20 mm and then hot extruded by hydraulic press at 250°C with extrusion ratio 14:1 to diameter 4 mm.

### 2.2. Methods of materials' characterization

Actual chemical composition of the extruded ingots were analyzed by scanning electron microscope Tescan Vega 3 LMU supplemented by elemental EDX analysis (Energy-Dispersive X-ray analyzer- Bruker Nano Xflash 410M) from the area 0,5 x 0,5 mm using magnification 230x and acceleration voltage 20kV.

The specimens for microstructure characterization were embedding in electrically conductive material (PolyFast, Struers), in the Buehler SimpleMet 1000 device. The embedding process conditions were: temperature 180°C, pressure 30 MPa, time 15 minutes. Subsequently, these samples were ground and polished to ensure a smooth surface without grooves and scratches. Microstructure analysis was performed by optical microscope Olympus GX 71. Before this observation, the surfaces of the metallographic grindings were etched using Nital (Ethanol 96% and HNO<sub>3</sub> 4%) to highlight the microstructures. Images were taken under non-polarized light, using a microscope lens providing 1000x magnification.

Microhardness measurements on the samples were performed on a Wilson-Wolper Tukon 1102 microhardness tester with a Vickers indenter. The applied load was 0.1 kg with duration of 10 s, and thus a microhardness of HV<sub>0.1</sub> was determined. 10 indentations were performed on each sample and the arithmetic mean of the recorded data was determined along with the determination of the measurement error.

The measurement of the instantaneous corrosion rate was carried out after hot extrusion using a potentiostat from the company Metrohm Autolab. The measurement was carried out in a volume of Hank's solution of 50 ml. Ag/AgCl reference electrode and platinum working electrode were used for measurement. Data were recorded in Intello software from Metrohm. The potential range was chosen from -0.9 V to -2 V and the scan rate was 5 mV/s. We obtained corrosion potential values from the measured data E and logarithmic values of current density log j. The corrosion rate (mm/year) was determined from equation:

$$v_{corr} = 3,27 \times 10^3 \frac{i_{corr} \times M_w}{\rho \cdot z} \quad (1)$$

where  $i_{corr}$  is the electrochemical current density,  $M_w$  is the molar mass,  $\rho$  is the density, and  $z$  is the number of exchanged electrons.

## 3. Results

### Chemical composition

Table 3 shows actual chemical composition of the prepared alloys. The actual chemical composition varies from the required to 0.07wt%.

**Table 3. Chemical composition of prepared alloys in [wt%]**

EDX	Mg	Ca	Mn
Zn-0.4Mg-0.4Ca	0.44	0.39	-
Zn-0.4Mg-0.4Ca-0.2Mn	0.41	0.39	0.15
Zn-0.4Mg-0.4Ca-0.4Mn	0.47	0.38	0.35
Zn-0.4Mg-0.4Ca-0.6Mn	0.44	0.43	0.55
Zn-0.4Mg-0.4Ca-0.8Mn	0.38	0.42	0.75
Zn-0.4Mg-0.4Ca-1.1Mn	0.48	0.38	1.1

### Microstructure and microhardness

Hot extrusion process resulted in grain refinement (Fig 1.), which is accompanied by hardening of the alloys. As the addition of Mn increases, further additional solid solution hardening of the alloys occurs. The highest microhardness value of  $134 \pm 12.0$  was measured for the Zn-0.4Mg-0.4Ca-1.1Mn alloy after hot extrusion. Thus with the increasing of Mn content from 0 to 1.1 wt% the microhardness of prealloys increases from  $83 \pm 5$  to  $109 \pm 9$  and microhardness of extruded samples increases from  $83 \pm 3$  to  $134 \pm 12$  ( Fig. 2.).

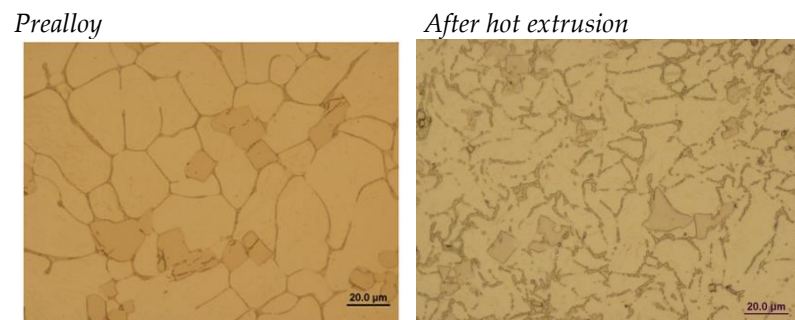
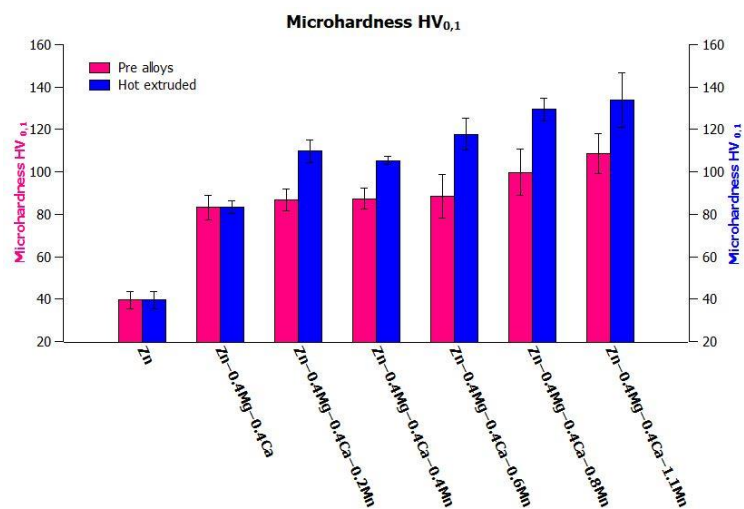


Figure 1. Comparison of microstructures of prealloys and extruded sample

Figure 2. Microhardness HV<sub>0.1</sub> of prealloys and after hot extrusion

### Corrosion properties

Table 4 shows that there is a positive shift in the corrosion potential  $E$  with a simultaneous decrease in the corrosion rate. The lowest corrosion rate of 0.117 mm/year was measured for the sample Zn-0.4Mg-0.4Ca-0.6Mn. However, all alloys have a 3 to 5 times lower instantaneous corrosion rate compared to pure zinc, which, together with improved mechanical properties, favors them as materials for future implants.

**Table 4. Corrosion rate of prepared alloys**

Sample	Corrosion potential $E_{cor}$ [V]	Corrosion current $I_{cor}$ [ $\mu\text{A}/\text{cm}^2$ ]	Corrosion rate $v$ [mm/year]
Zn	-0.998 $\pm$ 0.05	42.364	0.634
Zn-0.4Mg-0.4Ca	-0.967 $\pm$ 0.05	10.519	0.224
Zn-0.4Mg-0.4Ca-0.2Mn	-0.968 $\pm$ 0.05	8.974	0.213
Zn-0.4Mg-0.4Ca-0.4Mn	-0.983 $\pm$ 0.05	10.839	0.287
Zn-0.4Mg-0.4Ca-0.6Mn	-0.940 $\pm$ 0.05	4.055	0.117
Zn-0.4Mg-0.4Ca-0.8Mn	-0.947 $\pm$ 0.05	6.622	0.207
Zn-0.4Mg-0.4Ca-1.1Mn	-0.971 $\pm$ 0.05	4.677	0.164

### 4. Discussion

Zinc based alloys were recently suggested as a promising biodegradable materials, due to their excellent biocompatibility and electrode potential fallen in between that of magnesium and iron. In the present work, we examine the mechanical properties, corrosion properties and microstructure of Zn-Mg-Ca-Mn alloys.

From the point of view of mechanical properties the microhardness was improved by 25% after extrusion process as shown Fig 2. Microhardness was higher than similar alloy Zn-1Mg-0.1Mn after hot rolling, which showed microhardness 107.82 Hv [10]. The largest impact on mechanical properties had micro-alloying with Mn. The highest microhardness value of 134 $\pm$ 12.0 was measured for the Zn-0.4Mg-0.4Ca-1.1Mn alloy after hot extrusion.

From electrochemical measurements, the corrosion rate was estimated. The lowest corrosion rate of 0.117 mm/year was measured for the sample Zn-0.4Mg-0.4Ca-0.6Mn. It should be noted that corrosion rate of novel Zn-based materials was close to the 0.2mm/year, which is ideal corrosion rate of biodegradable alloys for instance in cardiovascular stent application. Corrosion rates of these alloys are comparable with alloy Zn-1Mg-0.1Mn which showed 0.25 mm/year [10].

This novel Zn-based alloys had potential to meet the requirements in mechanical properties for biodegradable materials especially Zn-0.4Mg-0.4Ca-0.6Mn, Zn-0.4Mg-0.4Ca-0.8Mn, Zn-0.4Mg-0.4Ca-1.1Mn which have acquired the highest values of microhardness and required corrosion rates for vascular stents.

## 5. Conclusions

The Zn-0.4Mg-0.4Ca-xMn (x=0, 0.2, 0.4, 0.6, 0.8, 1.1 wt.%) alloys were fabricated and after hot extrusion process the improvement of mechanical properties was occurred. The highest value 134 Hv was demonstrated for the alloy Zn-0.4Mg-0.4Ca-1.1Mn. All prepared alloys shows corrosion rate close to the 0.2 mm/year. In the present study, hot extruded Zn-0.4Mg-0.4Ca-xMn alloys had been shown as a candidate for biodegradable implant materials due to its appropriate corrosion rates and potential good mechanical properties.

**Acknowledgments:** The article was created with the support of projects: Development of new bioresorbable alloys for intracellular implants APVV-20-0068. Development of biodegradable zinc-based alloys for biomedical applications: "06/TUKE/2022". VEGA 1/0387/22 Development and testing of systems for controlled stimulation of cell growth in a bioreactor environment using computer vision.

## References

1. R. H. Nazanin Roohani, K. Roya, and S. Rainer, "Zinc and its importance for human health: An integrative review," *Journal of Research in Medical Sciences*, 2013. [https://www.researchgate.net/publication/271201421\\_Zinc\\_and\\_its\\_importance\\_for\\_human\\_health\\_An\\_integrative\\_review](https://www.researchgate.net/publication/271201421_Zinc_and_its_importance_for_human_health_An_integrative_review) (accessed Feb. 23, 2022).
2. L. M. Plum, L. Rink, and H. Haase, "The Essential Toxin: Impact of Zinc on Human Health," *OPEN ACCESS Int. J. Environ. Res. Public Heal.*, vol. 7, p. 7, 2010, doi: 10.3390/ijerph7041342.
3. M. J. Jackson, "Physiology of Zinc: General Aspects," pp. 1–14, 1989, doi: 10.1007/978-1-4471-3879-2\_1.
4. H. F. Li *et al.*, "Development of biodegradable Zn-1X binary alloys with nutrient alloying elements Mg, Ca and Sr OPEN," 2015, doi: 10.1038/srep10719
5. X. Liu *et al.*, "Effects of alloying elements (Ca and Sr) on microstructure, mechanical property and in vitro corrosion behavior of biodegradable Zn-1.5Mg alloy," *J. Alloys Compd.*, vol. 664, pp. 444–452, Apr. 2016, doi: 10.1016/J.JALLCOM.2015.10.116.
6. T. Huang, Y. Zheng, and Y. Han, "Accelerating degradation rate of pure iron by zinc ion implantation," *Regen. Biomater.*, vol. 3, no. 4, pp. 205–215, Dec. 2016, doi: 10.1093/RB/RBW020.
7. J. Niu *et al.*, "Research on a Zn-Cu alloy as a biodegradable material for potential vascular stents application," *Mater. Sci. Eng. C. Mater. Biol. Appl.*, vol. 69, pp. 407–413, Dec. 2016, doi: 10.1016/J.MSEC.2016.06.082.
8. H. Kabir, et al. Recent research and progress of biodegradable zinc alloys and composites for biomedical application: Biomechanical and biocorrosion perspectives. *Bioactive Materials* 6 (2021) 836–879
9. G. K. Levy, J. Goldman, and E. Aghion, "The Prospects of Zinc as a Structural Material for Biodegradable Implants—A Review Paper," *Met.* 2017, Vol. 7, Page 402, vol. 7, no. 10, p. 402, Oct. 2017, doi: 10.3390/MET7100402
10. X. Liu *et al.*, "Micro-alloying with Mn in Zn-Mg alloy for future biodegradable metals application," *JMADE*, vol. 94, pp. 95–104, 2015, doi: 10.1016/j.matdes.2015.12.128.



# Comparison of RFID robots

Matúš Matiscsák<sup>1,\*</sup> and Peter Trebuňa<sup>2</sup>

<sup>1</sup> Department of Industrial and Digital Engineering, Institute of Industrial Engineering, Management and Environmental Engineering, Technical University of Košice, Park Komenského 9, 040 01 Košice, Slovakia; matus.matiscsak@tuke.sk

<sup>2</sup> Department of Industrial and Digital Engineering, Institute of Industrial Engineering, Management and Environmental Engineering, Technical University of Košice, Park Komenského 9, 040 01 Košice, Slovakia; peter.trebuna@tuke.sk

\* Correspondence: matus.matiscsak@tuke.sk; Tel.: +421 55 602 3223

**Abstract:** The main objective of this paper is to compare two RFID robots in a particular company based on basic parameters and tests. The company has opted for two tests which are described in detail in the article and the exact results are also given. At the beginning of the article, the RFID technology and the RFID robot are described to understand the background and results of the research. The conclusion of the article is devoted to the evaluation of the tests performed by the company.

## 1. Introduction

Process streamlining is the alpha omega of the emerging Industry 4.0 era. SMART FACTORY's task is to achieve the fusion of machines with IT technology and the Internet. The Internet of Things (IoT) shifts previously autonomously acting isolated links (people, techniques, processes) into one coherent, independently functioning whole. And it is RFID technology that brings a globally understandable and accurate way to identify objects. RFID (Radio Frequency Identification) technology is the technology most used to wirelessly identify objects with special tags. The main initiator of this technology was Wal-Mart, which in the past upgraded its identification system from barcodes to RFID technology. Nowadays it is becoming more and more popular, and we meet it every day. The reason for its popularity is its increasing availability and the great advantages resulting from its use. The main advantage of using this technology in the identification of objects is the possibility of identifying them over long distances and the elimination of the need for direct visibility of the identified object. In recent years, there have also been efforts to use this technology for motion sensing, which has significant advantages and disadvantages over commonly used systems. However, RFID is not only used to identify goods, but also, for example, in the healthcare sector it is associated with the identification of patients and medicines, or is used for contactless payment using payment cards, etc.

## 2. RFID technology

Radio Frequency Identification (RFID) system is based on an electromagnetic field to automatically identify and thus track tags attached to objects. The information is stored electromagnetically on the tags. Based on whether the tags have their own source or not, they can be classified as passive, semi-passive or active. Passive tags collect radio wave energy from a transmitter near the RFID reader. Active tags are characterized by a local power source (e.g., a battery) and can operate at several meters from the RFID reader. Compared to a barcode, tickets do not need to be positioned so that readers have direct visibility of the ticket. RFID is also used as a method for automatic identification and data collection [1]. The characteristics of the RFID system are shown in Table 1.

**Table 1.** Characteristics of the RFID system [2]

Type	Low Frequency	High Frequency	Ultra-high frequency	
			Active	Passive
<b>Frequency</b>	125 -135 KHz	13,56 Mhz	860 – 960 Mhz	860 – 960 Mhz
<b>Range</b>	< 10 cm	< 1 m	< 100 m	< 10 m
<b>Interference</b>	Weak sensitivity	Medium sensitivity	High sensitivity	High sensitivity
<b>Data transfer</b>	Weak	Weak	High	High
<b>Price tag</b>	Medium	Low	High	Low
<b>Positives</b>	Meets global standards	Meets global standards	Very large range, lots of transmitted data	Good range, easy production of transferred data
<b>Negatives</b>	Small scale, data capacity, amount of data	Small range	High cost, interference with metals and liquids	High interference with metals and liquids

Active RFID systems are made up of active RFID elements. The active RFID element has a built-in power source and allows to change the information in memory. It is used to collect information, evaluate, and then transmit the data. The disadvantage is the limited lifetime, which depends on the power source used [3,4].

Passive RFID systems are made up of passive RFID elements that do not have a built-in power source and derive their energy from the magnetic pole of the reading device to operate. The memory size of these RFID elements ranges from 32 to 128 bits and the data stored in them cannot be modified. They are used for identification and are being considered as a future replacement for barcodes. Compared to active RFID elements, they require higher power reading devices and can communicate over a shorter distance [3,4].

Based on the characteristics of the RFID system, we can say that currently the prevalence of passive tags is much larger than the prevalence of active tags. This fact seems to be the case in the global environment, not only in Slovakia. The main reason for this is their cost, despite the wider possible application of active tags. In the future, however, this situation may change (with the advent of new technological approaches and decreasing prices of tags).

### 3. RFID robots

The fields of robotics, automation and artificial intelligence have seen tremendous growth and innovation in recent decades. RFID inventory accuracy using handheld RFID readers could reach 98% or more, but faulty procedures and human error reduce this accuracy to 85-95%. An RFID robot is a mobile and autonomous RFID system that automatically performs an inventory of a given area, for example in logistics or retail, giving us higher RFID inventory accuracy compared to manual readers. The RFID robot operates completely autonomously: the user specifies when the inventory is to be taken and the robot starts when it is scheduled. The RFID robot also locates each tagged item in two dimensions (x and y). This information can be processed to create a planogram of the items in the space. The information generated by the RFID robot is used to help employees detect misplaced items, speed up pick and return management, and other operational processes. Today, most RFID robots can already move in all directions because they can rotate on the spot without displacement. Therefore, it can easily move around any space. Each RFID robot has a fixed speed that is synchronized with the tag reading to maximize the reading speed. The RFID robot includes: an RFID system with a certain number of antennas, which depends on the size of the RFID robot in question [5,6].

#### 3.1. Differences of RFID robots

The company in which the comparison and selection of a suitable RFID robot was carried out chose two specific RFID robots from two different companies. The first RFID

robot is the StockBot from PAL Robotics. The second RFID robot that the company chose is TORY RFID from MetraLabs.



Figure 1. RFID robots

In Table 2 we can see the basic parameters of RFID robots, which also played an important role in the selection of a particular RFID robot.

Table 2. Basic parameters of RFID robots [7,8]

	StockBot	TORY RFID
<b>Dimensions (HxLxW)</b>	190 x 50 x 50 cm	210 x 50 x 50 cm
<b>Speed</b>	1,0 m/s	1,0 m/s
<b>Battery autonomy</b>	12 h	8 h
<b>Charging time</b>	4 h	2 -3 h
<b>Antennas</b>	8	16
<b>Efficiency</b>	>99% (up to 500 tags/s)	>99% (up to 1000 tags/s)

Table 2 shows that the dimensions of the two RFID robots are almost identical, with only a difference in height of 20 cm. The movement speed of the robots is identical at 1.0 m/s. The first major difference that we can see is in the battery life per charge. The StockBot from PAL Robotics can last approximately 12 hours on a single charge, which is 4 hours more than the TORY RFID. This implies that the StockBot will take longer to charge, approximately one hour longer than the TORY RFID. One of the most important parameters in an RFID robot is the number of antennas that read RFID tags. The StockBot has 8 antennas, while the TORY RFID has up to 16 antennas, which increases the sensing efficiency. Therefore, TORY RFID can capture up to approximately 1000 tags per second.

#### 4. Result of comparison

The RFID robots were tested in the company's pilot store. The area of the store where the testing took place is 4,300 m<sup>2</sup> and there were approximately 93,000 pieces in the store. The comparison of the performance, efficiency, speed, and quality of the specific RFID robots described in subsection 3.1 consisted of the following two tests:

1. Inventory of the entire store (4300 m<sup>2</sup>)
2. Manual inventory of 50 specific products (8700 pieces)

The first robot tested was the RFID robot StockBot from PAL Robotics. The StockBot took exactly 5 hours to inventory the entire store. Then, a manual inventory of 50 specific products was performed to determine the accuracy of the RFID robot's inventory performance. In Figure 2, we can see the percentage success rate of the inventory on the specifically selected products.

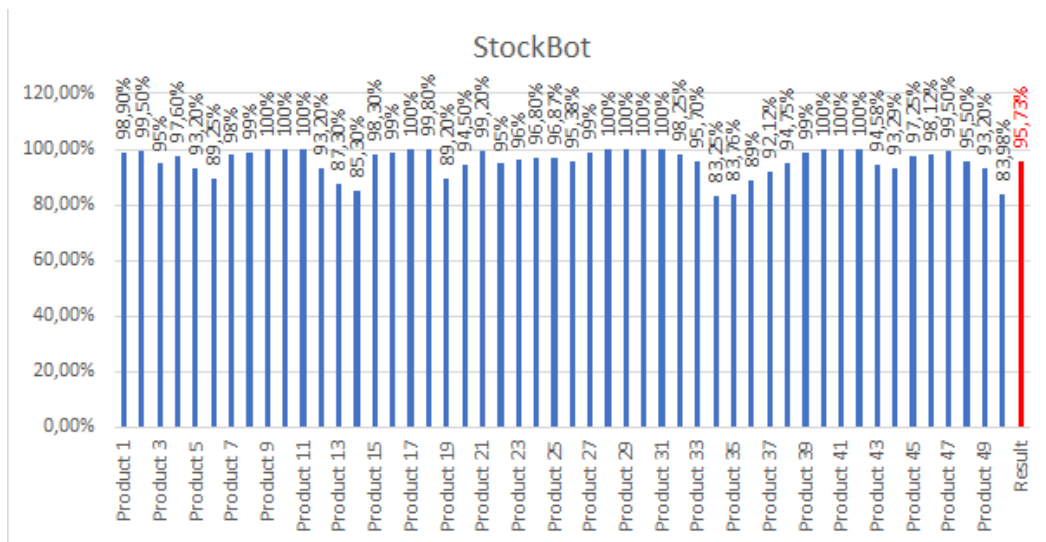


Figure 2. StockBot inventory success rate

The overall success rate of the RFID robot StockBot on a specific 50 products, representing 8700 units, was 95,73%.

The TORY RFID robot from MetraLabs was tested as the second one. TORY RFID took 3 hours and 30 minutes to inventory the entire store. Subsequently, a manual inventory was also carried out on 50 specific products. The success rate on specific products can be seen in Figure 3.

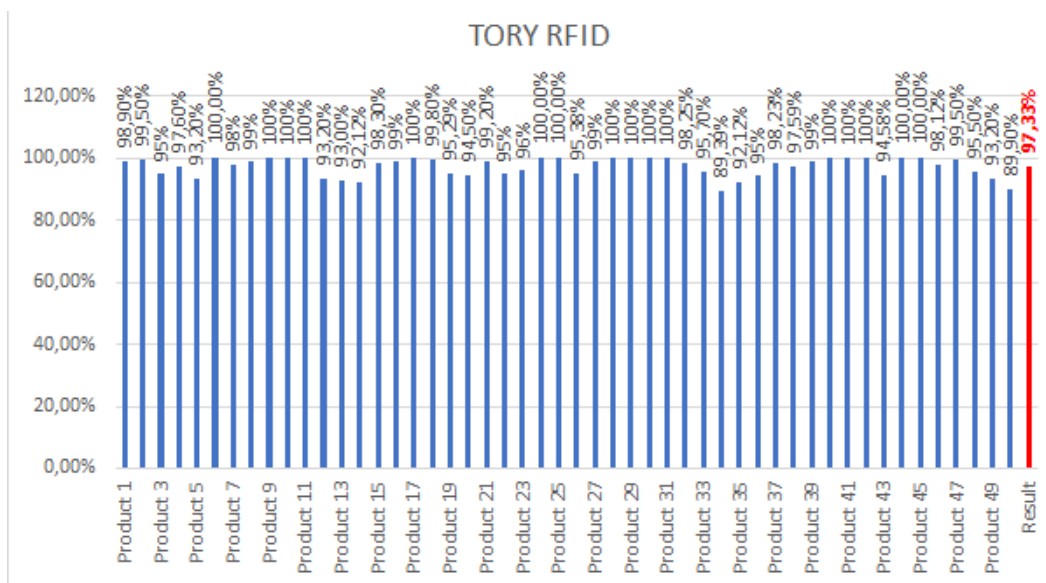


Figure 3. TORY RFID inventory success rate

The overall success rate of the RFID robot TORY RFID on a specific 50 products, representing 8700 units, was 97,33%.

## 5. Conclusions

For RFID robots, a very important parameter is how many RFID antennas it contains. The more of them it has, the better the quality and accuracy of RFID tag reading. In our case, we compared two RFID robots, one had 8 antennas and the other had 16 antennas. The inventory success rate of the TORY RFID robot with 16 antennas on a particular 50 products was 97.33% which is 1.6% more than the robot StockBot which has 8 antennas. Another important parameter for RFID robots is how many tags it can capture in one second.

From the results, we can see that speed is not an important parameter as both robots have the same speed and one has done the inventory of the whole store in 3 hours and 30 minutes and the other in 5 hours. The time depended on the speed at which the RFID tags were captured.

Based on a comparison of basic parameters and tests performed, the company chose the TORY RFID robot from MetraLabs.

**Acknowledgments:** This article was created by the implementation of the grant projects: APVV-17-0258 Digital engineering elements application in innovation and optimization of production flows. APVV-19-0418 Intelligent solutions to enhance business innovation capability in the process of transforming them into smart businesses. VEGA 1/0438/20 Interaction of digital technologies to support software and hardware communication of the advanced production system platform. KEGA 001TUKE-4/2020 Modernizing Industrial Engineering education to Develop Existing Training Program Skills in a Specialized Laboratory. VEGA 1/0508/22 „Innovative and digital technologies in manufacturing and logistics processes and system “. KEGA 020TUKE-4/2023 “Systematic development of the competence profile of students of industrial and digital engineering in the process of higher education”.

## References

1. Filippo Costa, Simone Genovesi, Michele Borgese, Andrea Michel, Francesco Alessio Dicandia, Giuliano Manara, "A Review of RFID Sensors, the New Frontier of Internet of Things", *Sensors*, vol.21, no.9, pp.3138, 2021.
2. EPCglobal: EPC Radio-Frequency Identity Protocols Generation-2 UHF RFID, Specification for RFID Air Interface, Protocol for Communications at 860 MHz 960 MHz, Version 2.0.1 Ratified. 2015. Available on: [http://www.gs1.org/sites/default/files/docs/epc/Gen2\\_Protocol\\_Standard.pdf](http://www.gs1.org/sites/default/files/docs/epc/Gen2_Protocol_Standard.pdf).
3. Amal Gunatilake, Sarath Kodagoda, Karthick Thiyagarajan, "A Novel UHF-RFID Dual Antenna Signals Combined With Gaussian Process and Particle Filter for In-Pipe Robot Localization", *IEEE Robotics and Automation Letters*, vol.7, no.3, pp.6005-6011, 2022. Available on: <https://ieeexplore.ieee.org/document/9745833>
4. PEKARČÍKOVÁ, M., TREBUŇA, P., KLIMENT, M., EDL, M., ROSOCHA, L.: Transformation the logistics to digital logistics: theoretical approach. In: *Acta logistica. - Košice (Slovensko) : 4S go Roč. 7, č. 4 (2020)*, s. 217-223 [online]. ISSN 1339-5629.
5. M. Morenza-Cinos, V. Casamayor-Pujol, J. Soler-Busquets, J. L. Sanz, R. Guzmán and R. Pous, "Development of an RFID inventory robot (AdvanRobot)" in *Robot Operating System (ROS)*, Cham, Switzerland:Springer, pp. 387-417, 2017. Available on: [https://link.springer.com/chapter/10.1007/978-3-319-54927-9\\_12#Tab2](https://link.springer.com/chapter/10.1007/978-3-319-54927-9_12#Tab2)
6. MARSCHALL, M.; GREGOR, M.; DURICA, L.; VAVRIK, V.; BIELIK, T.; GRZNAR, P.; MOZOL, S.: Defining the Number of Mobile Robotic Systems Needed for Reconfiguration of Modular Manufacturing Systems via Simulation. *Machines* 2022, 10 (5), 316. Available on: <https://doi.org/10.3390/machines10050316>. <https://www.webofscience.com/wos/woscc/full-record/WOS:000804335800001>
7. PAL Robotics, "STOCKBOT TECHNICAL SPECIFICATIONS" Available on: [http://pal-robotics.com/wp-content/uploads/2016/04/StockBot\\_Datasheet.pdf](http://pal-robotics.com/wp-content/uploads/2016/04/StockBot_Datasheet.pdf)
8. MetraLabs, "TORY RFID TECHNICAL SPECIFICATIONS" Available on: [https://www.metralabs.com/wp-content/uploads/2022/02/tory\\_datenblatt\\_en.pdf](https://www.metralabs.com/wp-content/uploads/2022/02/tory_datenblatt_en.pdf)



# A survey of integrated task and motion planning

Tomas Merva<sup>1,\*</sup> and Ivan Virgala<sup>1</sup>

<sup>1</sup> Department of Industrial Automation and Mechatronics, Technical University of Kosice

\* Correspondence: tomas.merva@tuke.com

**Abstract:** There is an increased demand for robots that are capable of autonomously working in complex human-inhabited environments. However, to accomplish tasks in such complex environments, a robot needs to autonomously find a sequence of actions that it must execute before achieving the requested goal. Using task and motion planning algorithms separately does not scale well and therefore there is a motivation to integrate both in such a way, which they can guide one another. This integration can handle tasks that classical approaches fail, but it also creates significant challenges. This survey provides a brief introduction to the families of such methods, especially towards the optimization-based algorithm.

**Keywords:** motion planning, task planning, robotics, constraints

## 1. Introduction

Each robotic application, regardless if it is located in an industrial or human-inhabited environment, requires a sequence of actions that a robot must execute in order to achieve a user-defined goal. Even in a simple pick&place application, the robot's actions are guided by a certain form of logic. The most used forms are finite state machines and behaviour trees that are very suitable for simple repetitive tasks. However, in the case of tasks, which require more sophisticated strategies as a result of the increased complexity of environments, these two widely used forms of logic do not scale well. Using them in a straightforward combination with a motion planner produces many challenges. Firstly, a user needs to define conditions and corresponding actions for all possible combinations of states that increase exponentially with the number of objects within an environment. Secondly, if the motion planner fails to find a feasible robot trajectory based on the task plan, the task planner freezes. Thirdly, most environments are dynamic, stochastic and not fully observable, so the policy can change over time or consists of additional actions to gain more knowledge about the environment, which is hard to implement using a finite state machine. Finally, the unguided task and motion replanning takes a lot of time, which is a crucial factor in the applicability of these approaches. [1][9]

The motivation behind integrated task and motion planning (TAMP) is to solve the aforementioned reasons. The main idea is to combine a "high-level" task planner and a "low-level" motion planner in such a way, that they can guide themselves with the intention of solving the complex task in the shortest time possible. Task planning has been a research area of the AI community for decades and they have successfully developed very effective domain-independent methods, unfortunately, these methods work only in discrete state space. On the other hand, the motion planning algorithms works very well for finding a solution within continuous state space. However, in a complex task, there can be additional state variables that are not geometric or kinematic and therefore cannot be handled by motion planners. In the case of TAMP, algorithms have to be capable of utilizing AI and robotics approaches to find a solution for this hybrid state space. Nonetheless, this class of problems creates significant challenges in terms of computation and new powerful algorithms. [1][3][4][8]

This survey is organized as follows. In the first part, the general principles and classification of TAMP algorithms are introduced. The second part is focused on the optimization-based approach Logic-Geometric Programming (LGP) [2] and its implementation within ROS is discussed in the last part. The contribution of this paper is twofold:

1. General introduction to TAMP
2. Description of the LGP algorithm

## 2. TAMP categories

The found solution of TAMP consists of two parts: an action sequence and continuous variables of those actions. We consider actions as discrete decisions that a robot needs to execute, for example: move without holding any object, pick an object A, move to the oven while holding an object A, place an object A into the oven, and cook an object A. An action sequence is also called an action skeleton. The second part of the solution is continuous variables of the action skeleton, e.g. exact trajectory to an object A or a grasp pose for an object A. For a simple example of picking a pizza (object A) and cooking it in the oven, the solution could look as follows: [1]

$$\pi = \left[ \begin{array}{l} \text{moveF}(q_0, \tau_1, q_1), \text{pick}[A](q_1, p_A, g_2), \text{moveH}[A](q_1, \tau_3, q_3), \\ \text{place}[A](q_3, p_A, g_2), \text{cook}[A](p_A) \end{array} \right] \quad (1)$$

Finding a solution consists of two steps. The first step is to find an action sequence. There are many domain-independent state-of-the-art algorithms from the AI community such as FastDownward [3], but the issue is how to efficiently use it in collaboration with motion planning. The step is to solve the hybrid constraint satisfaction problem (H-CSP). There are two popular approaches for solving H-CSP, which are sampling-based methods and optimization-based methods, the same as it is in motion planning. [1]

The order of these two steps matters and the TAMP methods can be classified accordingly. There are three major types of the overall control flow of TAMP methods:

1. Sequence before satisfaction – The algorithm first tries to find an action sequence and thereafter finds continuous variables for a given action sequence that satisfy all constraints. The necessary property of these methods is to have some way of backtracking in case the hybrid constraint satisfaction problem fails. [2] The schematic of the approach is shown in Fig. 1.
2. Satisfy before sequencing – The algorithm generates valid samples of continuous state space, mostly by sampling, that are used for discrete search using a task planner. These approaches leverage the task planning speed in finite discrete spaces. The success of these methods depends on the number of valid samples. The most famous example of this approach is PDDLStream [5]. The schematic of the approach is shown in Fig. 2.
3. Interleaved – It is possible to combine both approaches into one and try to utilize the advantages of both of them. Since the most expensive part in terms of computational speed is motion planning, it is possible to just sample robot configuration space and use it for more efficient sequencing thereafter. After finding an action sequence, we can find the rest of the variables that satisfy constraints. [4]

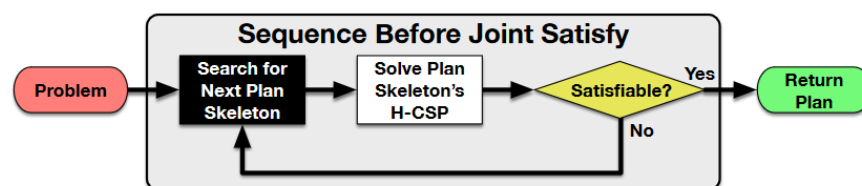


Figure 1. Sequence before satisfaction control flow [1]



Figure 2. Satisfy before sequencing control flow [1]

### 3. Logic-Geometric Programming

Marc Toussaint formulated the TAMP problem as a mathematical program. This novel framework satisfies all constraints within a given action sequence jointly. This proves to be very effective since by optimizing jointly, we can take into account the long-term effects of early actions. The other advantage is that we can solve the task according to arbitrary objective function  $\psi(x(T))$  of the final configuration. This cannot be achieved by the “satisfy before sequencing” methods. The TAMP problem is formulated as follows: [2]

$$\begin{aligned}
 & \min_{x, a_{1:K}, s_{1:K}, t_{1:K}} \int_0^T c(x(t), \dot{x}(t), \ddot{x}(t)) dt + \psi(x(T)) \\
 & \text{s.t.} \quad \forall_{k=1:K} s_k = \text{succ}(a_k, s_{k-1}) \\
 & \quad \quad s_K \models \mathfrak{g} \\
 & \quad \quad \forall_{k=1}^K h_{\text{switch}}(x(t_k) | a_k, s_{k-1}) = 0 \\
 & \quad \quad \forall_{k=1}^K g_{\text{switch}}(x(t_k) | a_k, s_{k-1}) \leq 0 \\
 & \quad \quad \forall_{t \in [0, T]} h_{\text{path}}(x(t), \dot{x}(t) | s_{k(t)}) = 0 \\
 & \quad \quad \forall_{t \in [0, T]} g_{\text{path}}(x(t), \dot{x}(t) | s_{k(t)}) \leq 0 .
 \end{aligned}$$

The optimization of this mathematical program is divided into three approximation levels. For this explanation, we will assume that Monte Carlo Tree Search (MCTS) is used as a task planner. MCTS generates potential action sequences. The first level of approximation optimizes over the final configuration  $x(T)$  for each action sequence. After that, evaluates each final configuration and then chooses the best action sequence accordingly. The best action sequence is sent to the second level, which optimizes over each action of a given action sequence. If it is possible to find actions' continuous variables, then we continue into the third level, which performs the trajectory optimization between each action (waypoints/phases). If the optimization fails in any of the previous levels, then the information about it is used as a heuristics for MCTS and the whole process is repeated. (Fig. 3) [2][6]

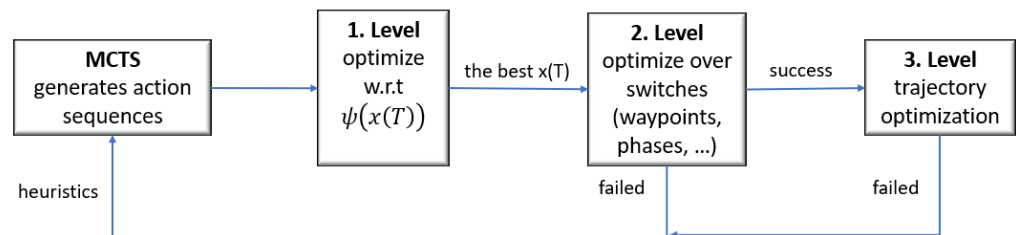


Figure 3. Satisfy before sequencing control flow

#### 4. Conclusions

The objective of this paper was to present a brief introduction to the research area of integrated task and motion planning. TAMP is motivated by solving complex tasks that cannot be effectively solved by standard, well-known methods. The aim of the first part is to inform a reader about the reasons for the failures of standard methods for many sequential tasks, as well as provide the core ideas behind different categories of TAMP methods. The second part is dedicated to the Logic-Geometric Programming algorithm, which is the state-of-the-art formulation of a TAMP problem that is capable of solving TAMP problems based on an arbitrary objective function and satisfying all constraints jointly. The future work will consist of using LGP offline plan as a platform to build on for the reactive task and motion planning that could handle perturbations within dynamic environments.

**Acknowledgements:** The authors would like to thank the Slovak Grant Agency VEGA 1/0201/21, VEGA 1/0436/22 and KEGA 030TUKE-4/2020.

**Conflicts of Interest:** The authors declare no conflict of interest. The funders had no role in the design of the study; in the collection, analysis, or interpretation of data; in the writing of the manuscript; or in the decision to publish the results

#### References

- [1] C. R. Garrett, R. Chitnis, R. Holladay, B. Kim, T. Silver, L. P. Kaelbling and T. Lozano-Pérez, "Integrated Task and Motion Planning," *Annual Review of Control, Robotics, and Autonomous Systems*, vol. 4, p. 265–293, 2021.
- [2] M. Toussaint, "Logic-geometric programming: an optimization-based approach to combined task and motion planning," in *Proceedings of the 24th International Conference on Artificial Intelligence*, Buenos, 2015.
- [3] M. Helmert, "The Fast Downward Planning System," *Journal of Artificial Intelligence Research*, vol. 26, p. 191–246, July 2006.
- [4] L. P. Kaelbling and T. Lozano-Pérez, "Hierarchical task and motion planning in the now," in *2011 IEEE International Conference on Robotics and Automation*, 2011.
- [5] C. R. Garrett, T. Lozano-Pérez and L. P. Kaelbling, "PDDLStream: Integrating Symbolic Planners and Blackbox Samplers via Optimistic Adaptive Planning," 2020.
- [6] M. Toussaint and M. Lopes, "Multi-bound tree search for logic-geometric programming in cooperative manipulation domains," in *2017 IEEE International Conference on Robotics and Automation (ICRA)*, 2017.
- [7] E. Aertbeliën and J. De Schutter, "eTaSL/eTC: A constraint-based task specification language and robot controller using expression graphs," in *2014 IEEE/RSJ International Conference on Intelligent Robots and Systems*, 2014.
- [8] R. E. Fikes and N. J. Nilsson, "Strips: A new approach to the application of theorem proving to problem solving," *Artificial Intelligence*, vol. 2, p. 189–208, December 1971.
- [9] K. Hauser and J.-C. Latombe, "Multi-modal Motion Planning in Non-expansive Spaces," *The International Journal of Robotics Research*, vol. 29, p. 897–915, June 2010.



# Design of a hydrogen distribution system implemented in a hydrogen bus

Ivan Mihálik<sup>1\*</sup>, Tomáš Brestovič<sup>2</sup>

<sup>1</sup> Technical University of Košice, Faculty of Mechanical Engineering, Department of Power Engineering, Vysokoškolská 4, 042 00 Košice; ivan.mihalik@tuke.sk

<sup>2</sup> Technical University of Košice, Faculty of Mechanical Engineering, Department of Power Engineering, Vysokoškolská 4, 042 00 Košice; tomas.brestovic@tuke.sk

\* Correspondence: ivan.mihalik@tuke.sk

**Abstract:** The article discusses the design and construction of hydrogen distribution system for the modified Iveco Daily 70C chassis platform supplied by ROŠERO - P. The basic issues of the design of hydrogen distribution system and storage vessels are discussed. The system was designed to meet the EC79 regulation, valid at the time the solution was designed, as well as other safety requirements. Individual components were chosen according to the EC79 regulation, while due to the design of an experimental vehicle intended for research and development in the field of low-pressure metal hydride tanks, some of the components received a legislative exception for use.

**Keywords:** hydrogen; metal hydride; public transport

## 1. Introduction

Due to the tightening requirements for reducing CO<sub>2</sub> emissions in transport in the territory of the European Union, vehicle manufacturers are increasingly focusing on the development of alternative drives of vehicles. In addition to battery-electric vehicles (BEV), alternatives with a high potential for use in the future undoubtedly include hydrogen drive, especially in the field of heavy-duty transport. Thanks to hydrogen technologies, it could also be possible to meet the requirements set by European Green Deal to reduce 90 % of greenhouse gases produced by transport by 2050 compared to the situation in 1990.

## 2. Design of hydrogen circuit

The vast majority of current Fuel Cell Electric Vehicles (FCEV) use high-pressure compressed hydrogen tanks for hydrogen storage. In conventional FCEV buses, the pressure in the vessels reaches a value of 350 bar [1,2]. The main difference in the proposed solution lies in the use of low-pressure vessels MNTZV-159, which store hydrogen using metal hydrides at a maximum operating pressure of 25 bar.

High pressure up to 350 bar occurs only in a relatively small part of the hydrogen circuit, specifically in the area between the fuel filler neck and the first reduction valve. In addition to the mentioned components, pipes and fittings, there is also an electronic pressure sensor. Due to the high working pressure in this area of the hydrogen circuit, particularly high safety requirements are placed on these components. For this reason, components that meet the EC79 regulation were chosen in the high-pressure part of the circuit.

In the area of the hydrogen circuit behind the first reduction valve, the pressure is reduced to a maximum level of 25 bar. In this part of the circuit between the first and second reduction valves, there is, for example, a system of vessels equipped with filters, an electronic pressure sensor, various valves, and safety elements of the circuit, such as

thermally activated pressure relief device (TPRD) and a safety valve. Of the components used in this area of the distribution system, the electronic pressure sensor and TPRD comply with EC79 regulation. Other components could be applied to the hydrogen circuit considering the low operating pressure with a declaration from the manufacturer, as they are not “class 0 components”, i.e. high-pressure hydrogen components containing hydrogen at a nominal working pressure above 3 MPa.

The temperature sensor applied on the surface of the vessel does not need to meet the EC79 regulation or does not need a declaration from the manufacturer, as it is only used for surface temperature measurement and the sensor is not used as a hydrogen circuit safety device.

The second reduction valve reduces the pressure in the system to a value of 0.8 MPa. This pressure reduction is necessary due to the operating parameters of the fuel cell applied in the hydrogen bus. These three parts of hydrogen circuit with different maximum operating pressure are shown in Figure 1.

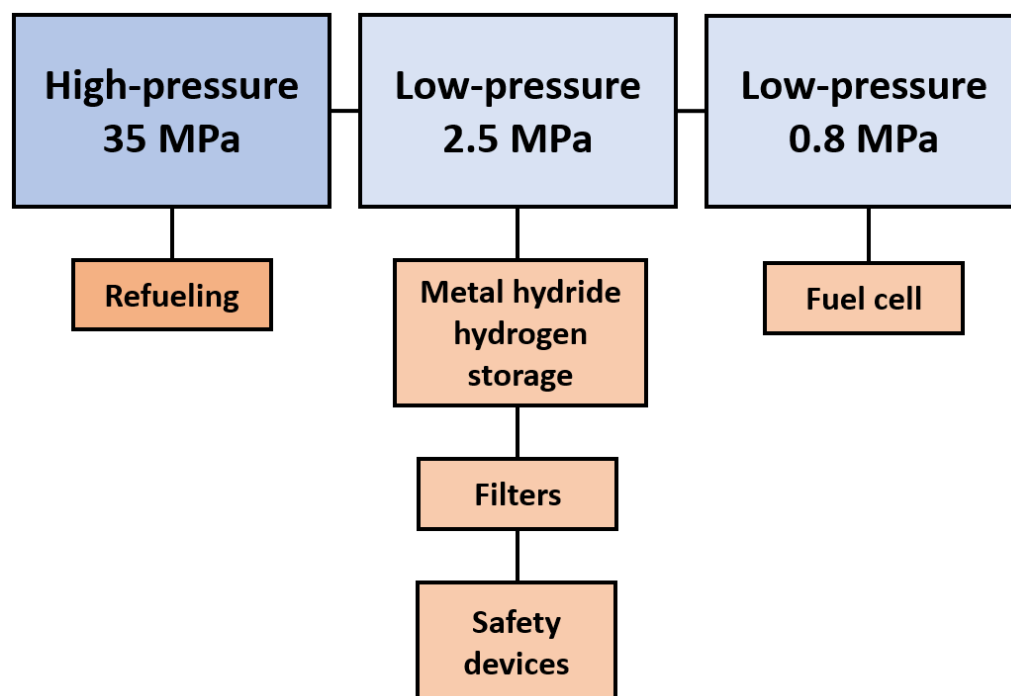


**Figure 1.** Simplified scheme of designed hydrogen circuit.

### 3. Low-pressure vessels for hydrogen storage

The vessel array is defined as two or more vessels interconnected by pipes, securely enclosed in a casing or protective frame [3]. Each vessel array implemented in the hydrogen bus consists of three pieces of certified MNTZV-159, which were designed at the Faculty of Mechanical Engineering at Technical University of Košice according to the STN EN 13322-2 standard (Figure 2). There are two vessel arrays installed in the front part of the chassis (Figure 3). Each vessel consists of a primary and secondary section and is made of 316L stainless steel. The primary part of the vessel is the main body, and the secondary part is the outer shell of the vessel.

In the resulting space between the primary and secondary parts of the vessels flows a cooling liquid, which ensures the temperature management of metal hydride hydrogen storage system. Temperature management is essential for enabling low-pressure storage of hydrogen in metal hydrides. When hydrogen is absorbed into the alloy during refueling, it is necessary to cool the vessels. On the other hand, when hydrogen is desorbed

during bus operation, it is necessary to heat the vessels. To ensure optimal heat transfer, the vessels are equipped with an internal heat transfer intensifier [4].

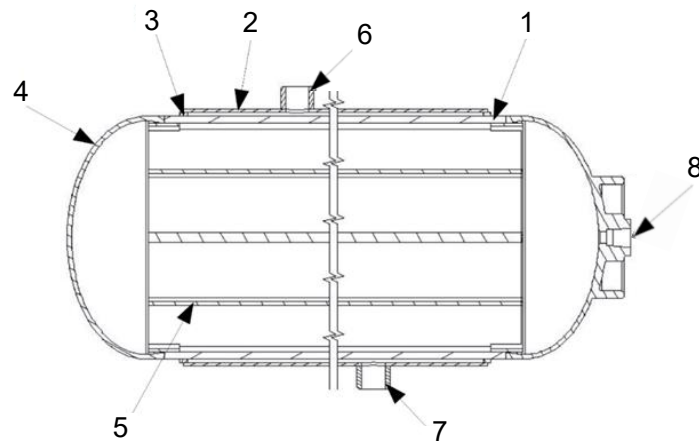


**Figure 2.** Construction of the low-pressure hydrogen vessel MNTZV-159 with an internal heat transfer intensifier. 1 – main cylindrical body of the vessel; 2 – cylindrical outer shell of the vessel; 3 – flange for the cylindrical outer shell; 4 – elliptical bottom; 5 – internal heat transfer intensifier; 6 – flange for coolant inlet; 7 – flange for coolant outlet; 8 – flange for hydrogen inlet/outlet

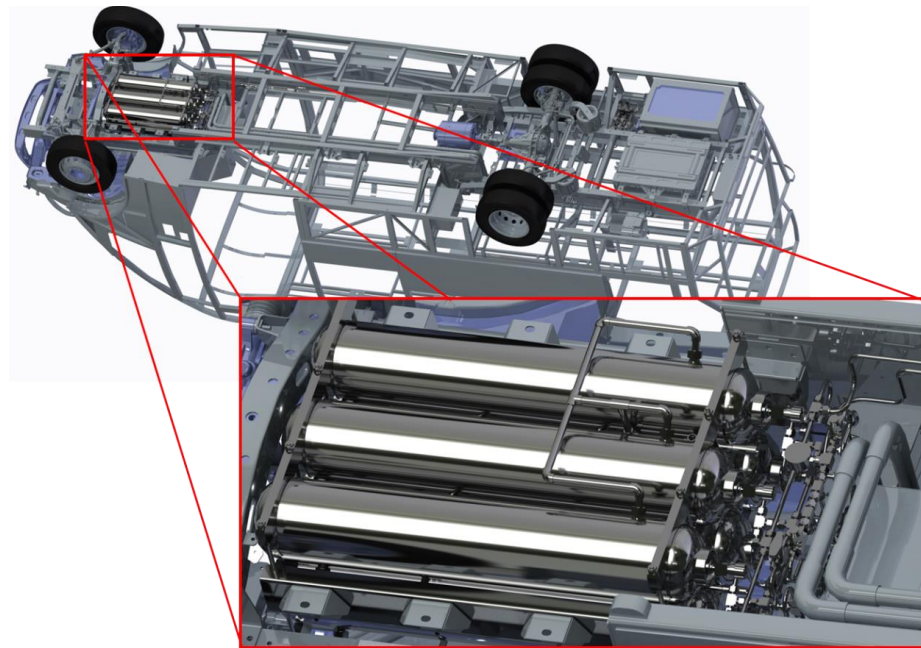


**Figure 3.** Placement of hydrogen storage vessels in the front part of the bus chassis.

Powdered metal hydride alloy Hydralloy C5 is applied in the storage vessels. The size of its grains is in the range of 0 – 2 mm. During the activation of the alloy and during the filling cycles, small cracks appear in the grains, which result in the splitting of the grains into microparticles [5]. To prevent contamination of the hydrogen circuit and its individual components with these microparticles of the metal hydride alloy, it is necessary to equip the vessels with a 5-micron filter.

#### 4. Safety devices installed in the hydrogen circuit

Safety devices are located in the second part of the hydrogen circuit, where the maximum operating pressure is 25 bar. These are devices such as TPRD and pressure relief valve.

The TPRD is a device designed to empty the hydrogen tanks if the system overheats, preventing them from rupturing due to fire. This device does not reclose after thermal activation. There are two basic types of TPRD. Devices of the first type are activated by melting the metal fuse at temperatures of 104 – 110 °C. The second type of TPRD uses a glass bulb containing a fluid. The fluid expands due to the high temperature, causing the glass bulb to break [6]. TPRD with metal fuse is implemented in the designed hydrogen bus.

The TPRD must be installed in such a way that, in the event of activation, the hydrogen is diverted to the atmospheric discharge pipe, from where it is further discharged outside the vehicle. Hydrogen must not be discharged from the vehicle to non-insulated electrical switches, under the wheel fender, horizontally in front of and behind the vehicle, or from the sides of the vehicle. For this reason, the hydrogen is released to the roof of the vehicle.

The vehicle is also equipped with a pressure relief valve which, if activated when the maximum allowed working pressure of 30 bar is exceeded, releases hydrogen into the same atmospheric pipe as the TPRD.

## 5. Conclusions

The proposed hydrogen distribution system must meet strict requirements in mobile applications not only in terms of functionality, but also in terms of safety. Since this is an innovative and not widespread technology of low-pressure hydrogen storage in mobile applications, the design of the system faces many challenges. The EC79 regulation valid during the design of the hydrogen circuit was repealed in July 2022. It is important to mention that type approvals which were granted before this date will not be invalidated.

In the future, however, only Regulation (EU) 2021/535 and UN Regulation No 134 remains valid, which may cause uncertainty due to their narrow scope of focus. Some of the hydrogen components will be left with no applicable type approval framework. Therefore, in future designs, it is necessary to pay close attention not only to solving technological challenges, but also to potential changes in regulations.

**Acknowledgments:** This paper was written with the financial support from the VEGA granting agency within the project solutions No. 1/0626/20 and No. 1/0532/22 from the KEGA granting agency within the project solutions No. 012TUKE-4/2022 and with financial support from the granting agency APVV within the Project Solution No. APVV-15-0202, APVV-21-0274 and APVV-20-0205.

## References

1. Caponi, R. et al, 2022. Single-tank storage versus multi-tank cascade system in hydrogen refueling stations for fuel cell buses. In: *International Journal of Hydrogen Energy*. 2022, Volume 47, Issue 64, p. 27633 – 27645.
2. Caponi, R. et al, 2022. Hydrogen refueling stations and fuel cell buses four year operational analysis under real-world conditions. In: *International Journal of Hydrogen Energy* [online]. 2022; Available at: <https://doi.org/10.1016/j.ijhydene.2022.10.093>
3. Regulation (EC) No 79/2009. *Regulation of the European Parliament and of the Council on type-approval of hydrogen-powered motor vehicles*.
4. Duda, F.; Jasminská, N.; Brestovič, T., 2022. Construction design of a heat transfer intensifier for low-pressure vessel for storing hydrogen. In: *Novus Scientia 2022*. Košice: Technical University of Košice, Faculty of Mechanical Engineering, p. 254 – 259. ISBN 978-80-553-4085-2.
5. Weckerle, C.; Bürger, I.; Linder, M., 2017. Novel reactor design for metal hydride cooling systems. In: *International Journal of Hydrogen Energy*. 2017; Volume 42, Issue 12, p. 8063 – 8074.
6. Tamura, Y.; Sato, K., 2017. The possibility of an accidental scenario for marine transportation of fuel cell vehicle – Hydrogen releases from TPRD by radiant heat from lower deck. In: *International Journal of Hydrogen Energy*. 2017; Volume 42, Issue 12, p. 7560 – 7564.



# Digitization of production data through RTLS technology

Marek Mizerák<sup>1\*</sup>, Peter Trebuňa<sup>2</sup> and Ján Kopec<sup>3</sup>,

<sup>1</sup> Marek Mizerák1; marek.mizerak@tuke.sk

<sup>2</sup> Peter Trebuňa2; peter.trebuna@tuke.sk

<sup>3</sup> Ján Kopec3; jan.kopec@tuke.sk

<sup>1,2,3</sup> Department of Industrial and Digital Engineering, TUKE, Slovakia

\* Correspondence: marek.mizerak@tuke.sk, Tel.: + 421 55 602 3232

**Abstract:** This article is dedicated to the digitization elements that are oriented towards the progressive RTLS localization system. This system is designed to create analyzes through Sewio software, as in this case it will create localization safety zones to protect workers in production. This is software that can be used to increase the efficiency of production, the safety of not only workers but also production technology and equipment. Among other applications, the software can analyze the movements of workers and handling equipment, locate employees in crisis situations such as fires and other accidents and thus prevent injuries. The article will further focus on a selected part of production in a company dedicated to heavy engineering.

**Keywords:** RTLS, technology, production

## 1. Introduction

Real Time localization system (hereafter referred to as RTLS) is a term for technology that monitors the location of people, equipment, and machines in real time. This technology is based on the UWB principle, which will be described below. It is important to understand the principle that if we want to point to something, we must know its exact location. Therefore, even manufacturing companies are trying to increase their profits by implementing processes that ensure, for example, shorter times for finding material or tools using localization RTLS technology. Another important application is the safety of workers in production. By this we can understand the finding of an injured person, for example, in warehouses or a digital presentation in dangerous situations such as fires. Regarding safety in production, the RTLS system, in cooperation with software support, can create a system of digital virtual zones that ensure the safety of workers in dangerous areas, such as the movement of machines, robots, logistics vehicles, and the like.

## 2. RTLS UWB location technology and its parts

UWB stands for ultra-wideband signal technology. It is a communication technology used in wireless networks that uses low power consumption to achieve high-speed connectivity. In other words, it is designed to transmit large volumes of data over short distances without high power consumption.

This technology is designed for monitoring that takes place inside buildings, halls, or other facilities. In fact, it can be said to complement the Global Positioning System (GPS) in its philosophy. Due to the investment in the installation of an appropriate number of anchors, UWB RTLS technology is a suitable solution in applications where objects such as people, material as well as logistics assets move frequently.

RTLS is thus a platform mostly used in manufacturing, in-house logistics, warehouses, shops or sports activities.



Figure 1 Sewio UWB RTLS technology

For the purpose of this article, the technology from Sewio was chosen. We use this technology at the Department of Industrial and Digital Engineering in two specialized laboratories, in the micro logistics laboratory and in Testbed 4.0. This software-hardware platform provides the entire technology platform in a package of hardware (tags, anchors) and software (RTLS Studio).



Figure 2 Hardware and software platform from Sewio

The Sewio UWB RTLS platform consists of two types of hardware: signal transmitters, called tags, used to track entities, and signal receivers, called anchors, used to receive signals from tags.

Tags are small electronic devices that are attached to any object or individual that needs to be tracked. The tags act as a transmitter and emit flashes that are received by the anchors and sent to the location server to calculate the tag positions.

Anchors are electronic devices that detect UWB pulses emitted by UWB tags and then forward them to a location server to calculate the tag positions. To cover an area with an indoor tracking system, a set of anchors must be installed above the area to create the location infrastructure.

For accurate estimation of tag positions, it is generally recommended to deploy anchors at a distance of approximately 15-20 meters apart. These conditions are based on the synchronization technology used, where the automatically selected anchors communicate with the RTLS server over a dedicated Ethernet cable network that must be installed before the anchors are deployed. The anchors can be powered via POE (Power over Ethernet) through a passive POE splitter. UWB packets coming from the anchors pass through the POE splitters and IP switches directly to the RTLS server.

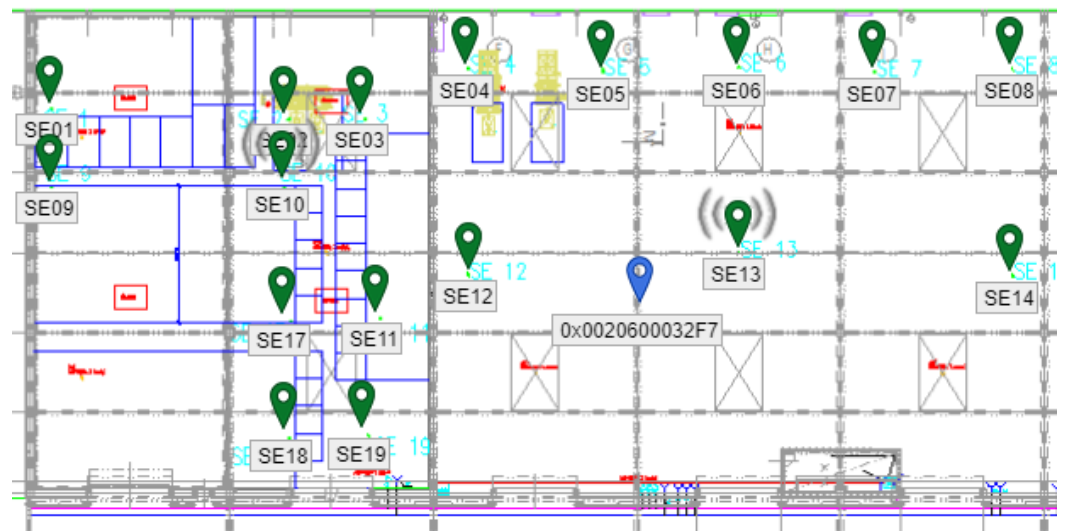


Figure 3 Example of location network layout in production

## 2.1 System setup and accuracy

Setting up the system is greatly simplified thanks to the RTLS Manager web-based tool, which is one of the modules of Sewio's RTLS Studio software platform. This module optimally sets up the system according to the quality parameters obtained from the system installation environment. This essentially means uploading the layout of the production area to the software environment.

The RTLS platform requires fixed anchor coordinates stored on the RTLS server. This can be done via the drag & drop function integrated into the Sensmap framework, or directly in the RTLS Manager, by inserting the exact coordinates of each anchor. The anchors have their own IP addresses and therefore their configuration and management are clear and efficient. RTLS Manager allows you to check radio and IP configuration and remotely upload new settings in a user-friendly environment.

Based on active communication with customers integrating and installing the RTLS platform in various environments, it has been proven that the Sewio RTLS platform achieves an accuracy of up to half a meter. An accuracy of 20-30 centimeters can be achieved if the solution meets the condition of direct visibility between UWB devices. In some solutions, it may be necessary to increase the density of anchors, especially in narrow aisles or production halls. The RTLS platform provides a very stable position estimate also thanks to the complex rules and filters applied to the algorithmic process.

## 3. Converting static RTLS technology to mobile technology

Since RTLS technology is primarily static, which is normally mounted on poles or walls of production halls. The main idea of this article is to create a digitization network

for the purpose of collecting production data, but with the possibility of tracking one specific part of the production. Therefore, its hardware part was mounted on classic photographic tripods. Subsequently, a network was created using UTP cables, which were connected to a switch that then sends information directly to the localization server.



*Figure 4 Vista DirectFive anchor on a photo tripod*

In the case of the measurement attempt, a company focused on the heavy industry was selected, which is dedicated to the custom production of spare parts for cargo machines (buckets, arms). As part of the production, the machining center was monitored, namely the horizontal milling cutter WTF13 and WTF13R. The main task was to supplement the digital protection zone.



*Figure 5 Horizontal milling machine WTF13*

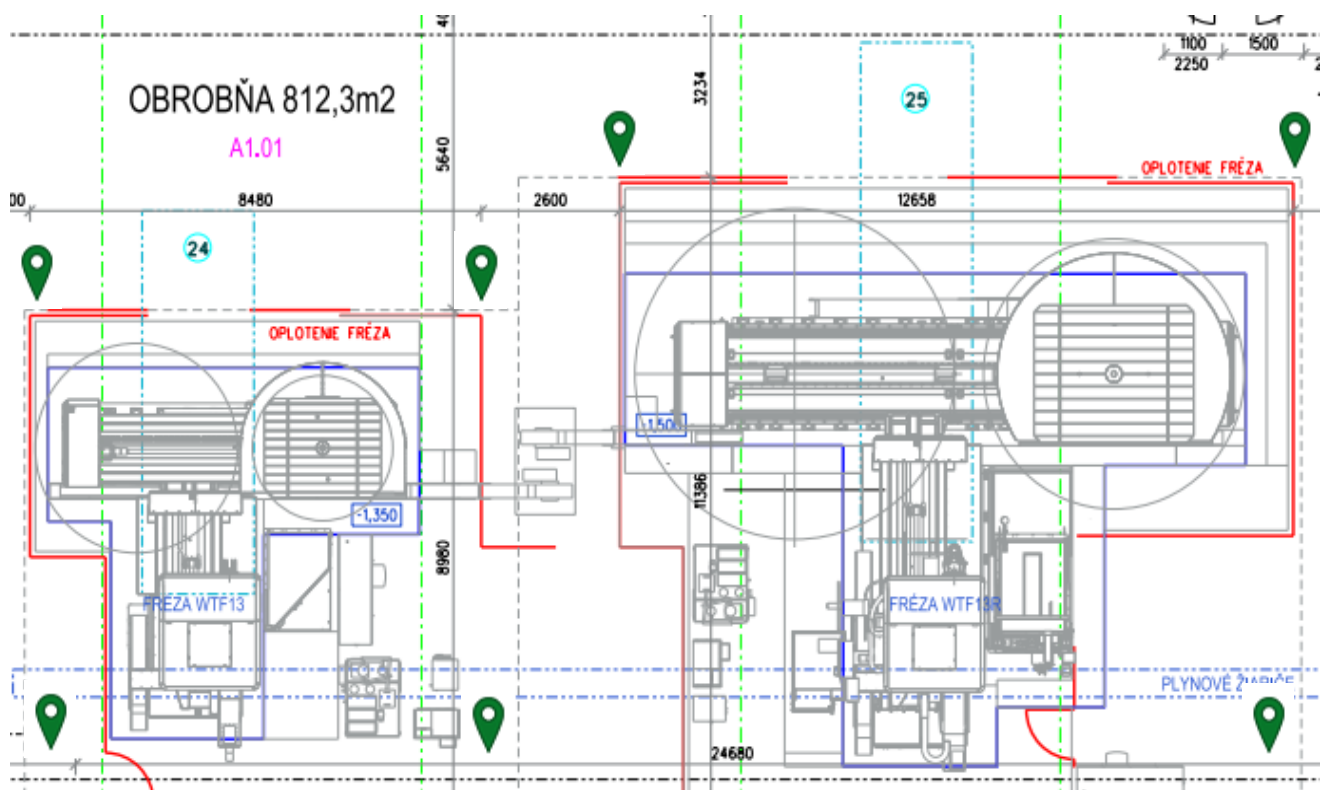


**Figure 2.** Machining center with two horizontal cutters WTF13 and WTF13R; (Note - green marks indicate the most suitable position for signal receivers, which will ensure the creation of a localization network)

## 5. Conclusions

If a company wants to be competitive today and wants to be included among the companies that use the pillars of Industry 4.0, it must also implement these exponential technologies, such as RTLS localization systems. Nowadays, these technologies are coming to the fore, and their importance is also realized by top managers, for whom it brings remarkable results and analyzes on which it is possible to create individual optimizations of production processes, material flows, as well as logistics and worker protection in production. The localization network should always be designed to cover the measurement area as best as possible but with the least amount of hardware.

In the case of this article, the creation of an application for the initialization of movement in the protective zone of the machine tool is considered as a possible continuation of the research. The WebSocket web interface has direct configurability to the localization software RTLS Studio and thus offers the user the possibility of creating his own application according to the requirements.

**Acknowledgments:** This article was written with the support of the projects VEGA 1/0438/20 Interaction of digital technologies to support software and hardware communication platform of advanced manufacturing system, KEGA 001TUKE-4/2020 Modernization of industrial engineering teaching to develop the skills of the existing educational program in r. specialized laboratory, APVV-17- 0258 Application of elements of digital engineering in innovation and optimization of production flows, APVV-19-0418 Smart solutions to increase the innovative capacity of companies in the process of their transformation into smart companies. VEGA 1/0508/22 Innovative and digital technologies in production and logistics processes and systems.

## References

1. Digitálny podnik. [cit. 25/02/2016]. Available on the Internet: <[http://www.priemyselneinzierstvo.sk/?page\\_id=1534](http://www.priemyselneinzierstvo.sk/?page_id=1534)>. Country, 2007; Volume 3, pp. 154–196.
2. Sewio Networks. Technology comparison. General information Dostupné na internete - <https://www.sewio.net/uwb-technology/rtls-technology-comparison/>
3. Sewio Networks. Uwb. General information Dostupné na internete - <https://www.sewio.net/real-time-location-system-rtls-on-uwb/>
4. EDL, M. - KUDRNA, J.: Metody průmyslového inženýrství. 1. vyd. Plzeň : Smart Motion, s.r.o., 2013, ISBN: 978-80-87539-40-8
5. MALIK, M.: RTLS for Dummies, Eiley Publishing, Hoboken, JJ,, 2009.
6. RIZOS, C., Demplster, B. Indoor positioning techniques based on wireless lan. 2007.
7. SILANICAY M., Lokalizačný systém na sledovanie mobilných objektov – nová stratégia rozvoja podnikov. [online] Dostupné na internete: <https://opac.crzp.sk/?fn=docviewChild0003B032>
8. TREBUŇA, P.: Plánovanie merania v priemyselnom inžinierstve, In: Strojárstvo : strojárstvo extra. Č. 1-2 (2010), s. 74/8-75/9. - ISSN 1335-2938.
9. Mozolova, L.; Grznár, P.; Mozol, Š.; Furmanová, B.: Development of digital support tools; 2021.[https://www.researchgate.net/publication/355218064\\_Development\\_of\\_digital\\_support\\_tools](https://www.researchgate.net/publication/355218064_Development_of_digital_support_tools)
10. Burganova, N.; Grznár, P.; Mozol, Š.: Challenges of factory of future in the context of adaptive manufacturing; 2021. [https://www.researchgate.net/publication/355218272\\_Challenges\\_of\\_factory\\_of\\_future\\_in\\_the\\_context\\_of\\_adaptive\\_manufacturing](https://www.researchgate.net/publication/355218272_Challenges_of_factory_of_future_in_the_context_of_adaptive_manufacturing)
11. Stefanik, A.; Grznar, P.; Micieta, B.: Tools for Continual Process Improvement - Simulation and Benchmarking. In Annals of DAAAM for 2003 & Proceedings of the 14th International DAAAM Symposium: intelligent manufacturing & automation: focus on reconstruction and development; Katalinic, B., Ed.; Daaam Int Vienna: Wien, 2003; pp 443–444. <https://www.webof-science.com/wos/woscc/full-record/WOS:000245326200218>

# Application of a conversion layer by phosphating in the pre-treatment of steels for bonding

Róbert Moro <sup>1</sup>, Dagmar Draganovská <sup>2</sup>

<sup>1</sup> robert.moro@tuke.sk

<sup>2</sup> dagmar.draganovska@tuke.sk

**Abstract:** The contribution is focused on the analysis of surface roughness after applying the conversion layer using phosphating. Two types of basic materials were used in the experiment – uncoated deep-drawn steel DC 04 and hot-dip galvanized microalloyed steel HX340LAD+Z. During the application of the conversion layer, surface roughness changes were studied with respect to the phosphating time, which was 3, 5 and 10 minutes. The achieved results provide information for other technological operations such as the creation of lapped joints using gluing, where the correct anchoring of the adhesive is important for sufficient surface division.

**Keywords:** conversion layer, roughness, phosphating

## 1. Introduction

In practice, steel materials are modified by applying a conversion layer through the phosphating process. The term conversion coatings collectively refers to chemical pre-treatments of metal materials, which are created by a chemical reaction between the metal and the applied coating. The result of this chemical reaction is the formation of a surface layer - coating. are created by immersing a metal object in a chemical solution with or without applying an electric current to the object.

We classify phosphating as a simple technology, which in the final result is intended to create an intermediate layer, for better adhesion of glue or other surface treatments or to increase the resistance of the base material to corrosion. [1,2,3,4]

An important point is to observe the correlation between the duration of the phosphating process and the resulting changes in the surface of the material, which would lead to an optimal anchoring of the adhesive on a sufficiently fragmented surface for the subsequent joining of the materials. The paper analyzes the changes in surface roughness during the application of the conversion layer due to different phosphating times.

## 2. Materials and Methods

### Used materials:

DC04 (1.0338) and HX340LAD+Z (1.0933) steels with dimensions of 100 x 25 x 8 mm were used as basic materials for the experiment.

DC04 steel is an uncoated deep-drawn steel, particularly suitable for demanding external and internal parts in car bodies, or for other extrusions.

HX340LAD+Z steel is a hot-dip galvanized microalloy steel. The chemical composition of the materials is in Table 1, and their mechanical properties and surface condition upon delivery is in Table 2.

### 2.1 Pretreatment of the surface

The surface of the test samples of DC steels was without any surface treatments, and the surface of HX type steels was coated with hot-dip galvanizing.

**Table 1.** Chemical composition of used steels.

Material	C	Mn	P	Si	S	Nb	Ti
DC	0,04%	0,25%	0,01%	-	0,01%	-	-
HX	0,07%	0,60%	0,02%	0,01%	0,01%	0,03%	0,00%

**Table 2.** Mechanical properties of materials and surface condition upon delivery from the supplier.

Properties	DC	HX
Re (MPa)	197	414
Rm (Mpa)	327	473
A80 (%)	39	28,4
Zn (g.m <sup>-2</sup> )	-	111
Surface condition	Matte	Improved surface
Oiling (g.m <sup>-2</sup> )	0,5 - 2,5	0,6 - 2,5

The tested samples of both materials were classified into two categories:

1. Surfaces without further treatment – a steel sample is used for testing in the state in which it was delivered from the manufacturer. The sheet surface was preserved by electrostatic oiling with an intensity of 0.5-2.5 g.m<sup>-2</sup>, which protects it from corrosion.

2. Surfaces with the addition of a conversion layer of zinc phosphate - during the phosphating process, small crystals form on the surface of the material, creating a phosphate layer that serves as protection against corrosion or as a base layer to improve adhesion when applying additional layers and when gluing.

A total of 8 types of samples were used for the experiment. Samples DC 0 and HX 0 were samples of DC and HX type steels, the surface of which was not treated with a zinc phosphate conversion layer. The other samples used in the experiment were treated with a layer of zinc phosphate with different immersion times of the sample in the phosphating bath, namely 3, 5 and 10 minutes. In Table 3 shows the labels of the samples according to their phosphating times.

**Table 3.** Designation of samples.

Sample	Steel type	Time of phosphating
DC 0	DC04	Sample
DC 3	DC04	3 min
DC 5	DC04	5 min
DC 10	DC04	10 min
HX 0	HX340LAD+Z	-
HX 3	HX340LAD+Z	3 min
HX 5	HX340LAD+Z	5 min
HX 10	HX340LAD+Z	10 min

## 2.2 Phosphating process

For the phosphating of the samples, the technology of phosphating with Pragofos 1500, manufactured by Pragochema s.r.o., applied by immersion, was used. The phosphate layer has the task of protecting the material from corrosion or serves as a base layer

before applying other layers. Before the phosphating process itself, the treated steel surface was degreased with an alkaline, medium-emulsifying preparation Pragolod 57 N from Pragochema s.r.o. The preparation was applied to remove preservative oils and other impurities from the surface of the steel samples. Its effectiveness is also high on modern types of biodegradable oils such as rapeseed oil or oils based on acid esters of vegetable oils. The dispersant contained in the preparation is effective on graphite and metal particles, which are more complicated to remove from the surface. Pragolod 57 N was applied by immersing the sample in a bath.

Before applying the phosphate layer after the application of the degreaser Pragolod 57 N, the rinse in the bath was diluted with the activating rinse Pragofos 1007 at a concentration of 0.3% at room temperature with a mixing time of 3 minutes. DC04 type steel samples were subsequently phosphated, as recommended manufacturer Pragochema s.r.o., in a Pragofos 1501 bath at a temperature of 60°C for 3, 5 and 10 minutes. Pragofos 1501 is a concentrate for the preparation of a phosphating bath, the main components of which are zinc phosphate and chlorate. HX340LAD+Z steel samples were phosphated in a bath mixed with Pragofos 1501 and Pragofos 1502 products from Pragochema s.r.o., used to treat hot-dip galvanized steel. The preparation Pragofos 1502 is a preparation containing fluorides. The conversion phosphate layer was applied at a temperature of 60 °C for 3, 5 and 10 min. After the phosphating process, the samples were rinsed with demineralized water and dried with hot air. [5,7]

### 2.3 Surface roughness measurement methodology

The surface roughness of the individual samples was measured by the touch measurement method with a profilometer of the type SurfTest SJ-201 from the Japanese manufacturer of metrological equipment Mitutoyo. The measurement took place in accordance with the standard STN 4287. [5] For the purpose of the experiment, parameters were chosen that could accurately describe the differences in the roughness of the evaluated surfaces.[6]

The following parameters were selected:

Ra [ $\mu\text{m}$ ] – mean arithmetic deviation of the surface

Rz [ $\mu\text{m}$ ] – average value of the largest profile heights

RSm [ $\mu\text{m}$ ] - average width of profile elements

RPc [-/cm] - number of profile elements per cm of length

### 3. Measurement results and evaluation

The resulting average values of the measurement of individual roughness parameters are shown in Table 4. It follows from the measurements that the value of the parameter Ra does not change significantly for individual materials and surface treatments, it varies in the range:

- for DC material from 0.96 to 1.05  $\mu\text{m}$ ,

- for HX material from 0.80 to 1.05  $\mu\text{m}$ .

The parameter Rz is also relatively stable:

- for DC material it ranges from 5.21 to 5.43  $\mu\text{m}$

- for HX material from 5.13 to 5.97  $\mu\text{m}$ .

However, the differences between individual surface treatments were more clearly manifested in other parameters, namely RSm and RPc. The density of protrusions per centimeter of surface length, expressed by the RPc parameter, increased in DC material compared to the original surface, more clearly in the zinc phosphate surface with a phosphating time of 10 min. However, it should be noted that the difference in the RPc value for the phosphating duration of 5 min versus 10 minutes was relatively small (9 protrusions per  $\text{cm}^{-1}$ ) and therefore it is possible to apply phosphating for DC material even for 5 minutes in order to achieve lower production costs.

The zinc phosphate on the surface consists of a number of insoluble phosphate crystals that grew on the surface in the phosphating process and the density of the protrusions

increased. The surfaces of the modified HX material rather just copy the original surface, so the density of the protrusions did not change significantly. This means that even in this case the phosphating process can be carried out for 5 minutes.

An increased density of protrusions per centimeter of length means an increase in modified surfaces. In the case of using such surfaces for the formation of adhesive joints, it is possible to expect an increase in the contact area between the adhesive and the surface-treated material. An increase in the contact area could be manifested by an increase in the bearing capacity of the joint. However, it is necessary to consider the assumption that the adhesion of the created phosphate layer to the base material will be higher than the adhesion of the glue to this created layer. In the case of the DC material, this happened after surface treatment phosphating to increase the number of protrusions compared to the untreated state.

The surfaces of the HX treated material show approximately the same density of RPc protrusions. However, it is necessary to take into account the fact that the number of protrusions of the HX material was already double that of the DC material in its original state, and after surface treatment by phosphating, the number of protrusions of the HX material is significantly higher than that of the DC material with the same treatments. It is therefore possible to conclude that the original surface profile was only copied during the phosphating of the HX material.

**Table 4.** Measured values of roughness parameters

Sample	Measured values of roughness parameters			
	Ra [ $\mu\text{m}$ ]	Rz [ $\mu\text{m}$ ]	RPc [-/mm]	RSm [ $\mu\text{m}$ ]
DC 0	1,04 $\pm$ 0,10	5,43 $\pm$ 0,49	44,78 $\pm$ 7,80	230 $\pm$ 39
DC 3	1,05 $\pm$ 0,11	5,28 $\pm$ 0,37	47,17 $\pm$ 6,72	216 $\pm$ 34
DC 5	1,00 $\pm$ 0,12	5,35 $\pm$ 0,47	47,54 $\pm$ 9,87	218 $\pm$ 41
DC 10	0,96 $\pm$ 0,10	5,21 $\pm$ 0,57	56,57 $\pm$ 12,85	186 $\pm$ 46
HX 0	1,05 $\pm$ 0,01	5,88 $\pm$ 0,44	91,90 $\pm$ 12,40	104 $\pm$ 10
HX 3	0,80 $\pm$ 0,08	5,13 $\pm$ 0,53	96,08 $\pm$ 17,84	101 $\pm$ 24
HX 5	0,97 $\pm$ 0,12	5,97 $\pm$ 0,97	99,86 $\pm$ 21,41	98 $\pm$ 24
HX 10	0,87 $\pm$ 0,12	5,83 $\pm$ 1,18	98,14 $\pm$ 13,21	97 $\pm$ 27

In the case of DC material, the number of protrusions increased after surface treatment by phosphating compared to the untreated state. The surfaces of the HX treated material show approximately the same density of RPc protrusions. The Abbot-Firestone curve is different for both materials in their original state as you can see on Figure 1. The surface of the DC material shows a convex character as on, while the HX material has a more concave surface character.

From the above results, it follows that, from the point of view of microgeometry, the HX material and its modified variants in the case of adhesive joining of materials have a greater possibility to create a joint with a high load-bearing capacity compared to the DC material, as it shows a higher number of protrusions (RPc parameter) and a more favorable slope of the Abbot-Firestone curve.

### 3.1 SEM appearance of the base material and pretreatment samples

All types of surfaces were also documented by microscopic analysis with a JEOL JSM-6390LV scanning electron microscope. The appearance of the surfaces of all samples is shown in Fig. 2. Microscopic analysis documents that with a phosphating time of 3 minutes, for both materials, zinc phosphate crystals are excluded in the form of needles in a lower density than with phosphating times of 5 and 10 minutes.

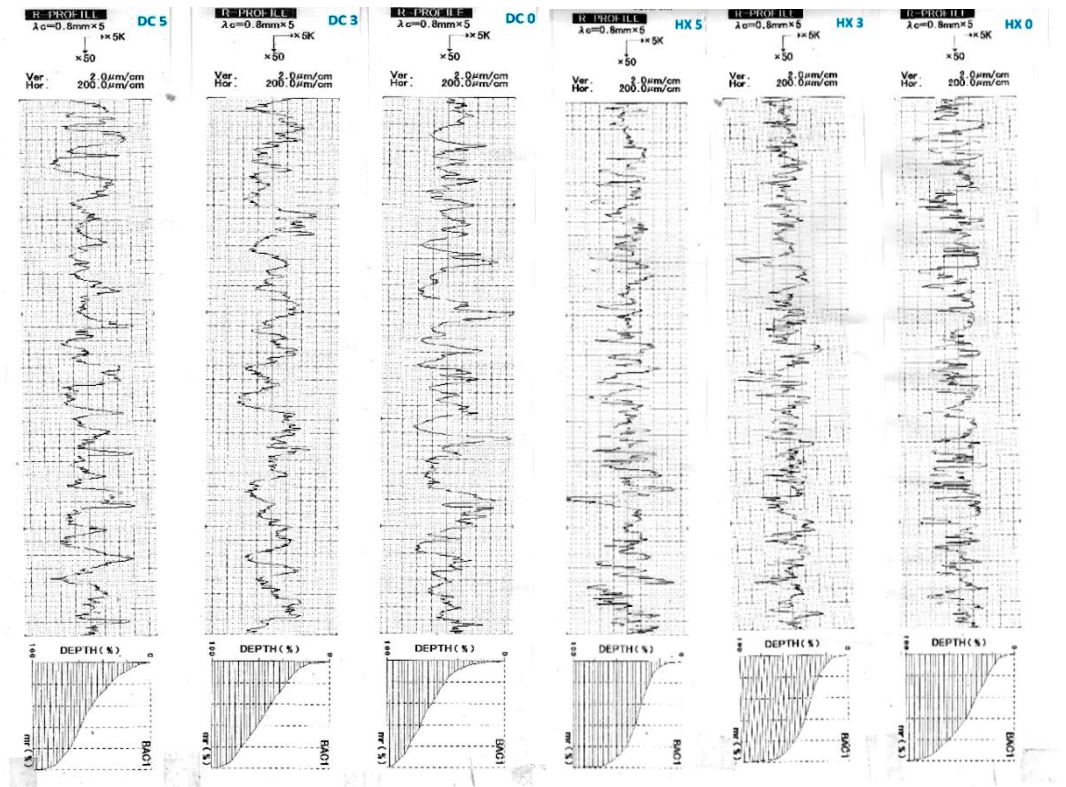
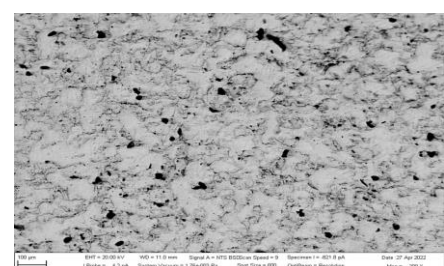
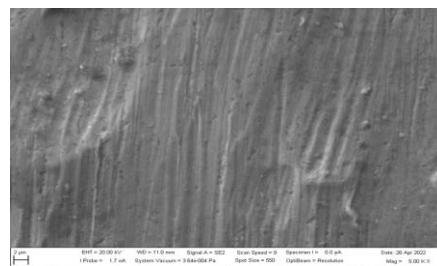
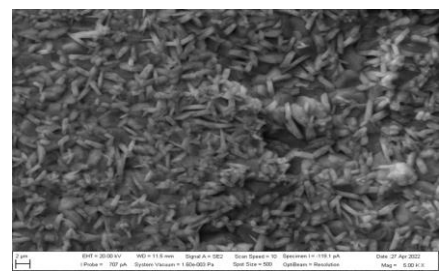
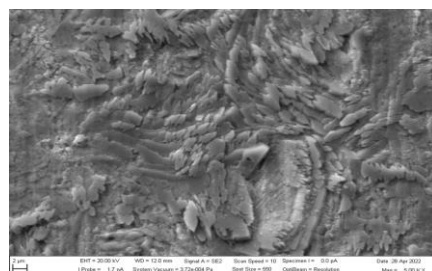


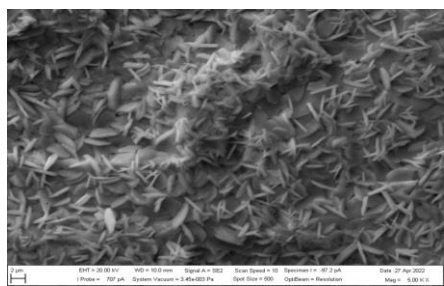
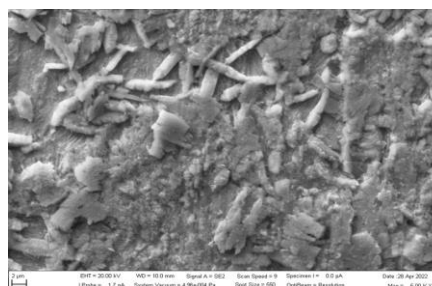
Figure 1. Profilograms of measured DC samples and HX samples



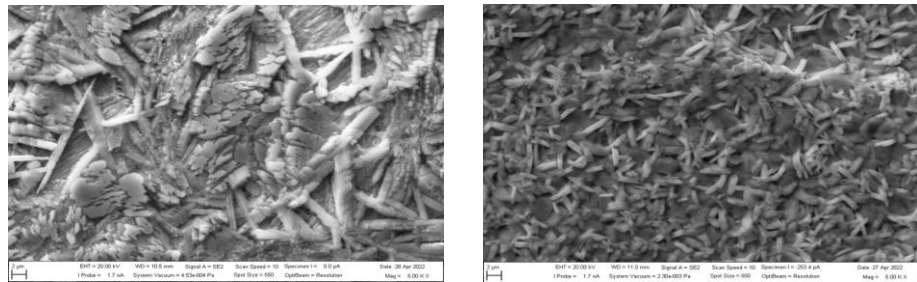
a) The surface of the DC 0 sample and HX 0 sample



b) The surface of the DC 3 sample and HX 3 with sample



c) The surface of the DC 5 sample and HX 5 sample



d) The surface of the DC 10 sample and HX 10 sample

**Figure 2.** SEM appearance of the base material and pretreatment samples

#### 4. Conclusions

Based on the experimental measurements, the following conclusions can be made:

- when measuring the roughness, the value of the parameters Ra and Rz for individual materials does not change significantly after surface treatment by phosphating, the differences were manifested in the parameters RSm and RPc. The RPc parameter of the DC material after phosphating increased compared to the original surface. The surfaces of HX material modified by phosphating copy the original surface, the density of protrusions has not changed significantly. However, the number of protrusions in the HX material was already double that of the DC material in its original state, and after surface treatment with phosphating, the number of protrusions of the HX material is also higher than that of the DC material with the same treatments. For this reason, when using surfaces for adhesive bonding, the HX material and its modified variants are more likely to create a joint with a high load capacity compared to the DC material.

The process of phosphating due to the resulting roughness and fragmentation of the surfaces as well as due to the achievement of lower production costs can be implemented in 5 minutes. Experiments with zinc phosphating confirmed the suitability of the given technology in connection with the further formation of adhesive joints. After phosphating, a favorable surface texture is created in terms of surface fragmentation with the assumption of good anchoring of the adhesive.

**Funding:** The contribution was developed with the support of the VEGA project 1/0154/19.

#### References

1. Guzanová, A.; Draganovská D.; et al. Application of organosilanes in the preparation of metal surfaces for adhesive bonding. *J. Adhes. Sci. Technol.* **2022**, *36*, 1153-1175.
2. Draganovská D.; Ižaríková, G.; Moro, R. Trends in the diagnosis of metal surfaces micro-geometry. *Mach., Technol., Mater.* **2021**, *15*, 146-149.
3. Jane Jiang, X.; Whitehouse, D. J. Technological shifts in surface metrology. *CIRP Annals - Manufacturing Technology* **2012**, *61*, 815-836.
4. Durakbasa, M.N.; Osanna, P.H.; Demircioglu, P. The factors affecting surface roughness measurements of the machined flat – The geometry and the precision of the surface. *Measurement* **2011**, *44*, 1986-1999.
5. Zhang S. L.; Chen, H. H.; Zhang, X. L.; Zhang, M. M. The growth of zinc phosphate coatings on 6061-Al alloy. *Surf. Coat. Technol.* **2008**, *9*, 1674-1680.
6. ISO 4287: Geom. Product Specifications, 1997.
7. Narayanan, T.S.N. Surface pretreatment by phosphate conversion coatings, *Adv. Mater. Sci.* **2005**, *9*, 130-177.

# Analysis of the influence of the porosity of recycled rubber crumb on its acoustic properties

Alžbeta Nováková<sup>1\*</sup>, Kristián Pástor<sup>2</sup> and Miroslav Badida<sup>3</sup>,

<sup>1</sup> alzbeta.novakova@tuke.sk

<sup>2</sup> kristian.pastor@tuke.sk

<sup>3</sup> miroslav.badida@tuke.sk

\* Correspondence: alzbeta.novakova@tuke.sk; Tel.: 055 602 2685

**Abstract:** The paper analyzes the acoustic properties of crumb rubber, which comes from the recycling of old tires from end-of-life vehicles. It is a granular material that can be used as a substitute for traditional materials used in soundproofing applications. The Attenuation index and Sound absorption coefficient were determined for rubber crumbs in three forms – in compact form, loose form and loose form pressed under pressure. The paper presents the research method and the results of the measurement achieved using the Kundt tube.

**Keywords:** rubber granulate; recycling; Kundt tube

## 1. Introduction

In the automotive or construction industry, requirements for the regulation of unwanted noise from the environment are starting to be taken into account more and more, which is also related to the development of materials with better acoustic properties [1,2]. Recycled materials such as rubber, glass, textiles McGinnes C. et al. (2005) described as advantageous for use in building constructions due to their environmental friendliness and easy availability [3].

The paper presents and compares the results of measurements of recycled rubber crumb in three forms. Since the production of compact materials is more expensive in terms of time and materials, and the price of chemical binders is also relatively high, the use of recycled bulk material from end-of-life cars could reduce these disadvantages and contribute to the improvement of the environment.

## 2. Materials and Methods

To determine the Coefficient of sound absorption ( $\alpha$ ) and the Attenuation Index (R), one of the most used methods is the measurement on an impedance tube. It is based on the measurement of the transfer function between two or by four signals from microphones located inside the tube. In accordance with the measuring chain, a loudspeaker is placed at the end of the tube [4]. In Fig. 1 shows the equipment used to measure the Sound Absorption Coefficient ( $\alpha$ ) and the Attenuation Index R. The system includes a tube with an internal diameter of 60 mm (SW060-L) and a test sample holder with an internal diameter of 60 mm (SW060-S).

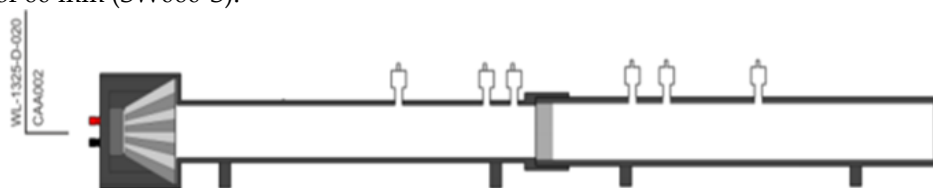
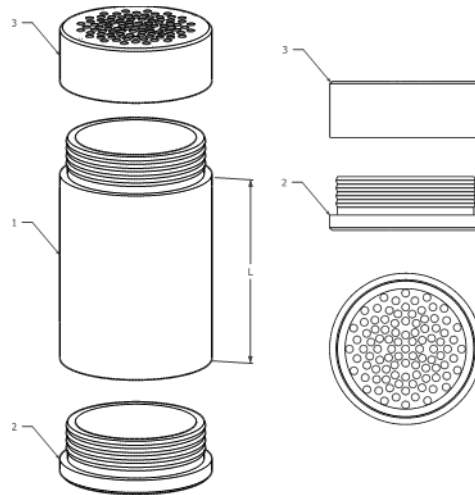


Figure 1. Measurement system of the Attenuation Index (R)

In order to measure the acoustic properties of bulk materials, test cassettes were designed, since these materials cannot be placed directly in the impedance tube (Fig. 2). At the same time, this cartridge made it possible to test the material under pressure in the filling device, which achieved different porosity of the material.

The measurement was performed in a capsule with a length of 50 mm. The body of the capsule is made of aluminum with surface treatment using CNC machining equipment. The test cassette is closed with a perforated sieve, which prevents the tested material from spilling out [5].



Legend: 1 – cartridge case, 2 – lower perforated bottom, 3 – upper perforated lid, L – adjustable length.

**Figure 2.** Test cartridge design

As part of the research, a device was developed for filling test cassettes with loose and compact material. This device is used for compaction, or pressing the material inside the cassette (Fig. 3). The loose material is poured into the cartridge and with the help of a linear piston the loose material is compacted inside. The pressure value in kilograms is displayed on the display of the control element [6].



**Figure 3.** A real view of the developed device for filling test cartridges

The choice of materials was conditioned by the possibilities and laboratory equipment of the workplace, as well as its use in practice as an insulating and noise-absorbing material. On the basis of material, physical and mechanical properties, tires and rubber from cars and recycled rubber granulate from them were selected and used for the purposes of the experiments (Fig. 4). The rubber material was chosen for research purposes

also because this material has good acoustic parameters and is already used in the production of compact acoustic panels.



**Figure 4.** Tested samples of recycled granulate

Measurements were made for one size fraction of rubber granulate 2-3 mm in three forms. The first was a compact panel, which was made using an epoxy-based adhesive and then compacted and pressed. The second sample was loosely poured into the test cassette and the third sample was made by compacting the loose fraction in the test cassette using a device for filling these cassettes under a pressure of 100 kg. The compact recycled rubber had a weight of 88,8 g. The loose recycled rubber had a weight of 43,3 g and the compacted loose rubber had a weight of 52 g.

### 3. Results

A series of measurements of the acoustic properties of the examined samples were carried out, which were then compared, and based on the measurements and subsequent analysis, the suitability of these materials for soundproofing applications was assessed.

Bulk material will always be used in acoustic applications in combination with an outer layer, because by its nature, bulk material cannot be used without an outer cover. When measuring acoustic properties, the test cassette represents the form of the outer casing.

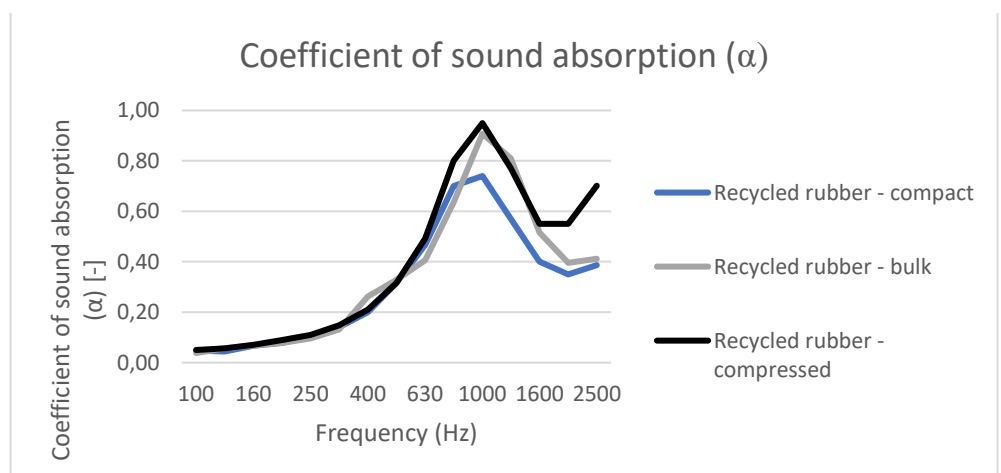


**Figure 5.** Coefficient of sound absorption ( $\alpha$ ) of recycled rubber crumb

Based on the measurements carried out, the compact recycled rubber has the lowest sound absorption, as expected, due to low porosity, since in bulk materials, sound absorption occurs not only by the material itself, but also by the contribution of air gaps between individual rubber particles (Fig. 5). Comparable results were achieved by bulk and compressed rubber. Compressed rubber performed better at high frequencies. The choice of fraction will take into account what use the given material is to have and at what frequencies it will be used.

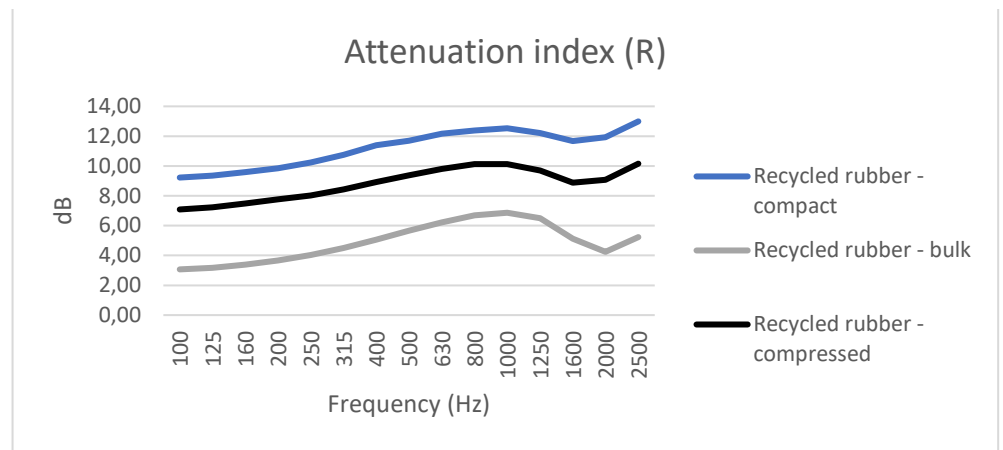


Figure 6. Attenuation index (R) of recycled crumb rubber

When measuring the attenuation index, the compact rubber sample achieves the best values. (Fig. 6) Loose rubber crumb reached lower attenuation index values compared to compressed loose rubber crumb, as the compressed rubber crumb is more compact and therefore transmits less sound. Based on the results, compressed recycled rubber is in the middle between compact and bulk rubber crumb because it is compressed and therefore less porous than loose rubber. On the other hand, it is not as compact as a rubber crumb combined with an epoxy base.

#### 4. Conclusions

The experiment was aimed at determining the sound absorption and attenuation index of recycled rubber crumb from vehicles after the service life. Three types of samples were tested, namely compact, loose and compressed fraction. The results show that both the compressed and the loose sample achieved better sound absorption than the compact sample at higher frequencies, which gives them a good prerequisite for the realization of anti-noise steins or other sound-insulating products. Compared to commercial materials, they are lighter, have a lower price and higher physical and chemical stability.

**Acknowledgments:** The paper was developed within the framework of the grant project of the Ministry of Education of the Slovak Republic KEGA 013TUKE-4/2022 Implementation of the results of scientific and research activities into the processing of a modern university textbook "Psychoacoustics - sound quality and acoustic design of products" and the VEGA project No. 1/0485/22 Development methods of increasing the acoustic quality of the sound of products by visualization and psychoacoustic methods.

#### References

1. Niresh, J.; Neelakrishnan, S.; Subharani, S.; Kannaiyan, T.; Prabhakaran, R. Review of acoustic characteristics of materials using impedance tube. *ARPN J. Eng. Appl. Sci.* 2015, 10.
2. Badida, M.; Lumnitzer, E.; Bartko, L.: Options for reducing traffic noise. ELFA, s.r.o., Košice, 2011, 274 p., ISBN 978-80-8086-181-0.
3. McGinnes, C.; Kleiner, M.; Xiang, N. An environmental and economical solution to sound absorption using straw. *J. Acoust. Soc. Am.* 2005, 118, 1869, doi:10.1121/1.4779138.
4. STN EN ISO 10534-2 (730537) Acoustics - Determination of sound absorption coefficient and impedance in impedances tubes - Part 2: Transfer-function method (ISO 10534-2:1998); 2002.
5. Cassette for expanding the possibilities of measuring bulk materials in an impedance tube Application for utility model 4. 50024-2022/ Miroslav Badida ... [et al.] - Banská Bystrica: ÚPV SR - 2022. - 9 p. Method of access: <https://wbr.indprop.gov.sk/WebRegistre/UzitivkovyVzor/Detail/50024-2022>.
6. Device for metered filling of test cassettes with loose materials Utility model application no. 50031-2022/ Miroslav Badida ... [et al.] - Banská Bystrica: ÚPV SR - 2022. - 7 p. Method of access: <https://bit.ly/3D4V0EG>.



# Antimicrobial photocatalytic devices

Jan Kral, Dominik Novotny

1 Technical university of Kosice, Faculty of Mechanical Engineering, Department of Manufacturing Technologies and Robotics, Slovakia

\* Correspondence: dominik.novotny@tuke.sk

**Abstract:** Photocatalysis represents a unique class of chemical transformations. It uses the energy supplied by light and controls reactions that are difficult, sometimes even impossible, to carry out in the dark. When applied to thermodynamically increasing reactions such as photosynthesis, photocatalysis promises a sustainable solution for large-scale solar energy storage. A large number of photo-catalytic materials have been studied for efficient light absorption, charge separation and charge transfer. The aim of this article is to summarize the basics of photocatalysis and the very functioning of this process through the devices themselves, which use this chemical process with the help of special materials.

**Keywords:** Photocatalysis, photocatalyst, reaction, devices, process

## Introduction

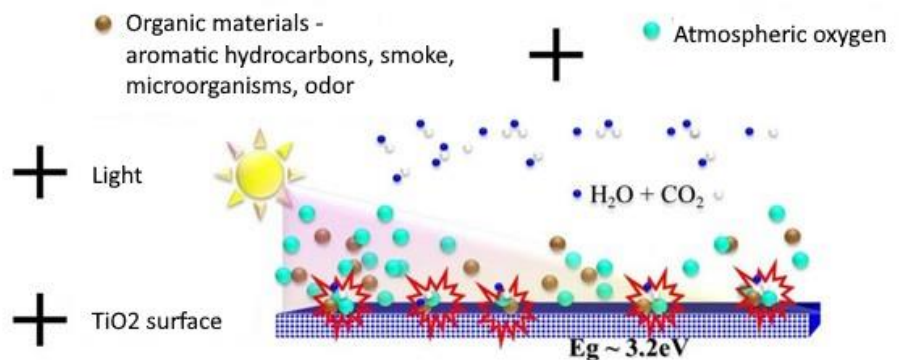
We are currently following the great development of science and research and the use of new technologies in all branches of industry. The 21st century is also marked by the coronavirus pandemic, which significantly affected the functioning of society as such. Deterioration of the health status of the population, significant mortality due to the virulence and variable mutations of the Covid-19 virus and the way it spreads were the reason for the creation of devices that use photocatalysis to eliminate and eliminate pathogens by means of air filtration, which in itself creates a safe environment for operation population in closed spaces.

This article deals with the description of the photocatalysis process and the devices in which this chemical process takes place and offers its use in practice. The use of photocatalysis is also part of my dissertation, because I am designing and developing a device that directly uses this process to eliminate pathogens in the air in a closed space.

## Photocatalysis

Photocatalysis is the process of chemical decomposition of substances in the presence of a photocatalyst and light radiation. In principle, it is based on photolysis, the natural decomposition of some substances by the action of light, accelerated by the presence of a photocatalyst. [1]

If a material with photocatalytic properties is exposed to light radiation of a suitable wavelength, its surface is activated and a characteristic reaction is triggered. The free electron-hole pair created primarily, and the hydroxyl radicals created secondarily by the contact of the excited molecule of the photocatalyst and water vapor decompose the present organic and inorganic substances. [2]



Principle of photocatalysis. [3]

Substances that can be decomposed by photocatalysis include e.g. nitrogen oxides (NO<sub>x</sub>), sulfur oxides (SO<sub>x</sub>), carbon monoxide (CO), ozone (O<sub>3</sub>), ammonia (NH<sub>3</sub>), hydrogen sulfide (H<sub>2</sub>S), chlorinated hydrocarbons, dioxins, chlorobenzene, chlorophenol, simple hydrocarbons, aromatic hydrocarbons and also bacteria, viruses, fungi or micro dust particles.

The final product then tends to be common and stable compounds. Concrete industrial applications of the principle of photocatalysis can differ primarily with the type of catalyst. Nanocrystalline titanium dioxide TiO<sub>2</sub> is most often used, which is activated by UV-A radiation. [2,3]

#### Types of photocatalysis:

- Homogeneous photocatalysis,
- Heterogeneous photocatalysis.

#### Homogeneous photocatalysis

It involves the existence of reactants and photocatalysts in the same phase. One of the very commonly used homogeneous photocatalysts is ozone and photo-Fenton systems. The reactive species here should be the hydroxyl radical, which is used for various purposes. The productivity and efficiency of Fenton-type processes is influenced by various operating parameters, such as hydrogen peroxide concentration, pH, and UV light intensity. [4]

The main advantage of this process is the ability to use sunlight with a sensitivity of up to 450 nm wavelength, so this process is highly economical in terms of operating costs.

#### Heterogeneous photocatalysis

Heterogeneous photocatalysis involves catalysts and reactants in different phases. Heterogeneous photocatalysis includes a large number of reactions, but they are not limited to moderate or complete oxidation reactions such as dehydrogenation process, hydrogen transfer reaction, metal deposition, water detoxification, gaseous pollutant removal process. [3,4]

Commonly used heterogeneous photocatalysts include transition metal oxides and semiconductors, which have unique properties. [5]

#### Factors affecting photocatalysis

- substrate concentration,
- amount of photocatalyst,
- amount of PH solution,
- temperature of the reaction medium,

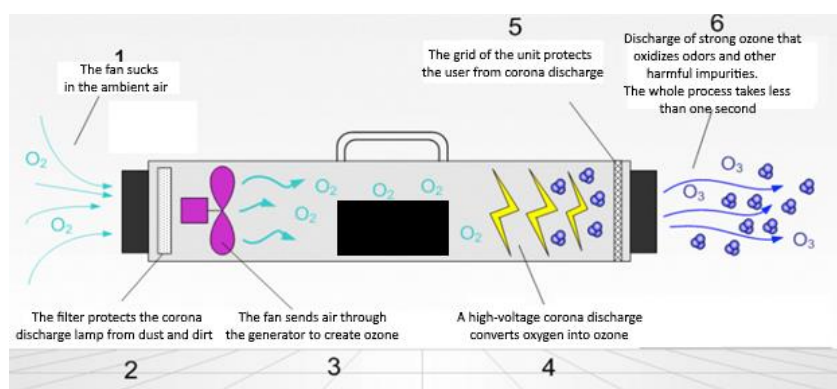
- light irradiation time,
- light intensity,
- surface area of the photocatalyst,
- dissolving oxygen in the reaction medium,
- the nature of the photocatalyst,
- the nature of the substrate,
- doping of metal and non-metal ions,
- structure of photocatalyst and substrate.

### Mechanism of photocatalysis

- Doping - The application of doping is known as the addition of impurities to a pure substance. Doping is divided into two sub-categories, which are: cationic doping and anionic doping. Cation doping involves doping cations into semiconductors such as metals. Anionic doping, on the other hand, involves the use of anions such as nonmetals. [6]
- Composites/couplings - Another technique to make visible light photocatalysts more efficient for various applications is to combine semiconductors or composites so that semiconductors with a large band gap and semiconductors with a small band gap are connected to each other so that they have a more negative conductance level. [6]
- Metallization - Various noble metals are used to improve the photocatalytic activity of the semiconductor. The probability of electron-hole recombination is reduced by this process, leading to efficient charge separation as well as higher photocatalytic reaction rates. Due to these properties of noble metals, electron transfer can be promoted, leading to higher photocatalytic activity. [6,7]
- Dye sensitization - is a favorable technique for surface development and modification of photocatalysts to utilize visible light for energy conversion. The dyes have redox properties as well as sensitivity to visible light, which may be useful for solar cells and in photocatalytic systems. [7]

### Types of photocatalytic devices

**Ozone generators** generate or produce ozone from oxygen, which destroys all organisms. These devices are suitable for disinfecting large spaces. With ozone, you can reliably destroy up to 99.9% of bacteria and viruses from the air and from surfaces, allergens and unpleasant odors. The ozone generator can only be used in closed spaces without the presence of people, animals and plants.

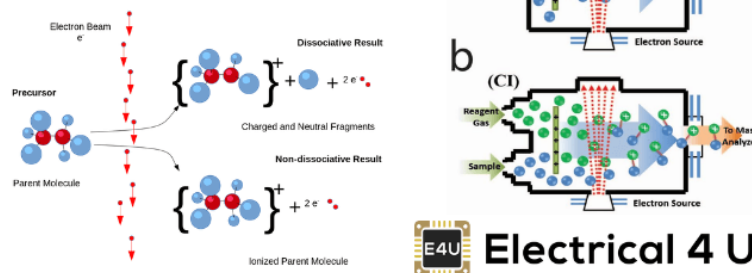


Operation of the ozone generator [8]

### Ionizer and the process of operation

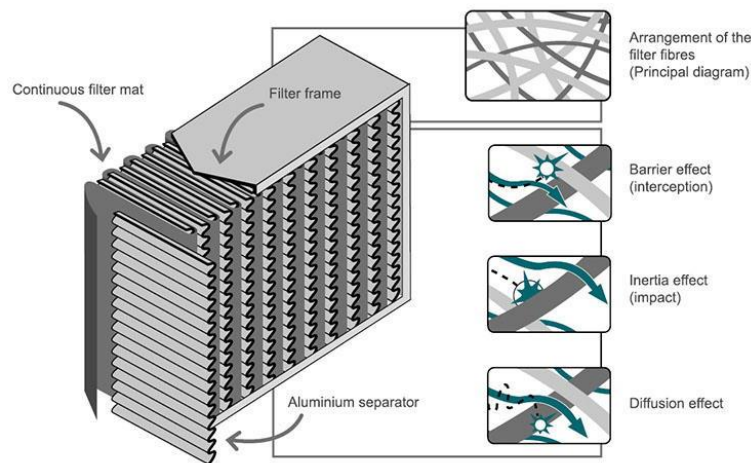
Ionizers help restore the natural balance of positive and negative ions in the interior, i.e. devices that can create ions. They purify the air, effectively neutralize bacteria and viruses, dust particles, absorb odors, aerosols and other volatile organic substances. Air ionizers have a positive effect on immunity, improve blood circulation and are also a great help for allergy sufferers.

### What is the Ionization Process?



Ionization process [9]

**Devices using HEPA filters** is an abbreviation for "High Efficiency Particulate Air filter", which means a highly effective filter of air particles. It was developed by NASA to protect astronauts from dangerous particles. The principle of operation is simple, a large flat filter made of glass microfiber is folded many times and folded into an accordion so that only clean air without any particles passes through it. In one layer, the filter is permeable, and its excellent filtering properties are achieved by consistent layering.



HEPA filter function [10]

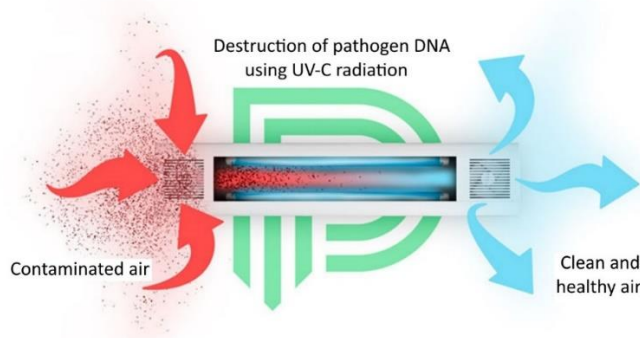
### Devices using UV-c radiation

One of the ultraviolet rays and is commonly used not only in air purifiers but also as a separate disinfectant. It effectively eliminates bacteria, molds and viruses that spread not only through the air, but also on surfaces. UV-C light, like radio waves or X-rays, is an invisible form of electromagnetic radiation. UV light is a type of radiation that cannot be seen with the naked eye because it is part of the invisible part that makes up the electromagnetic spectrum.

According to the method of use, we distinguish between direct and indirect radiation. Direct radiation works based on an open radiator. Disinfection using an open radiator takes place without the presence of people, animals and plants. Direct radiation does not

have a negative effect on the human body. The intensity of UV-C light decreases significantly with distance, the further you are from the light source, the less exposed you are to danger.

Direct contact with the light can cause inflammation of the conjunctiva or, in the worst case, seriously damage the eyesight.



The principle of operation of the ozone generator [11]

On the other hand, air purifiers with a closed emitter are safe and disinfection can take place in the presence of people. This type of air purification takes place in germicidal radiators.

### Conclusions

The aim of this article was to create a research about photocatalysis, its functioning and the processes that take place in the given process and about the devices in which this process takes place and about the possibilities of its use. The two most important conditions are an effective photocatalyst and the use of a suitable range of radiation wavelengths. Each photocatalyst must have the most suitable conditions to achieve the highest possible efficiency. Conditions may vary with each reaction. It is necessary to experimentally determine the correct application of photocatalysts according to the purpose for which we want to use them. No - sometimes it can be a thin layer, other times as an admixture in the material.

This chemical process will continue to expand in various applications for improving the home environment, work space or environment. The use of photocatalysis is also part of my dissertation, in which I focus on the development of an experimental antimicrobial device.

### Acknowledgment

The article was created with the support of the project: ITMS2014+ 313011AVF5 Center for the development of textile intelligence and anti-microbial technologies.

### References

- [1] A. Yousef, N.A.M. Barakat, K.A. Khalil, A.R. Unnithan, G. Panthi, B. Pant, H.Y. Kim, Photocatalytic release of hydrogen from ammonia borane-complex using Ni(0)-doped TiO<sub>2</sub>/C electrospun nanofibers, *Colloids Surf. A: Physicochem. Eng. Aspects* 410 (2012) 59–65, doi:<http://dx.doi.org/10.1016/j.colsurfa.2012.06.017>.
- [2] Zhixin Chen, Jingjing Xu, Zhuyun Ren, Yunhui He, Guangcan Xiao, High efficient photocatalytic selective oxidation of benzylalcohol to benzaldehyde by solvothermal-synthesized ZnIn<sub>2</sub>S<sub>4</sub> microspheres under visible light irradiation, *J. Solid State Chem.* 205 (2013) 134–141, doi:<http://dx.doi.org/10.1016/j.jssc.2013.07.015>.
- [3] V. Kuzhalosai, B. Subash, M. Shanthi, A novel sunshine active cerium loaded zinc oxide photocatalyst for the effective degradation of AR 27 dye, *Mater. Sci.Semicond. Proc.* 27 (2014) 924–933, doi:<http://dx.doi.org/10.1016/j.mssp.2014.08.046>.

- [4] A. Rajan, H.K. Yadav, V. Gupta, M. Tomar, Fast response ultra-violet photodetectors based on sol-gel derived Ga-doped ZnO, *Procedia Eng.* 94(2014) 44–51, doi:<http://dx.doi.org/10.1016/j.proeng.2013.11.046>.
- [5] A. Senthilraja, B. Subash, P. Dhatshanamurthi, M. Swaminathan, M. Shanthi, Photocatalytic detoxification of Acid Red 18 by modified ZnO catalyst under sunlight irradiation, *Spectrochim. Acta Part A: Mol. Biomol. Spectrosc.* 138(2015) 31–37, doi:<http://dx.doi.org/10.1016/j.saa.2014.11.006>.
- [6] H.S.M. Tabaei, M. Kazemeini, M. Fattahi, Preparation and characterization of visible light sensitive nano titanium dioxide photocatalyst, *Sci. Iranica* 19 (2012) 1626–1631, doi:<http://dx.doi.org/10.1016/j.scient.2012.07.005>
- [7] N.M. Mahmoodi, M. Arami, J. Zhang, Preparation and photocatalytic activity of immobilized composite photocatalyst (titania nanoparticle/activated carbon), *J. Alloys Compd.* 509 (2011) 4754–4764, doi:<http://dx.doi.org/10.1016/j.jallcom.2011.01.146>.
- [8] I.A.P. Martínez, V.R. González, S.W. Lee, S. Obregón, Facile synthesis of InVO<sub>4</sub>/TiO<sub>2</sub> heterojunction photocatalysts with enhanced photocatalytic properties under UV-vis irradiation, *J. Photochem. Photobiol. A: Chem.* 299 (2015) 152–158, doi:<http://dx.doi.org/10.1016/j.jphotochem.2014.11.021>.
- [9] Tom Keijer, Tessel Bouwens, Joeri Hessels, Joost N. H. Reek, Supramolecular strategies in artificial photosynthesis, *Chemical Science*, 10.1039/D0SC03715J, 12, 1, (50-70), (2021).
- [10] Jayachandran Jayakumar, Ho-Hsiu Chou, Recent Advances in Visible-Light-Driven Hydrogen Evolution from Water using Polymer Photocatalysts, *ChemCatChem*, 10.1002/cctc.201901725, 12, 3, (689-704), (2020).
- [11] Eric M. Lopato, Stefan Bernhard, Exploring Multidimensional Chemical Spaces: Instrumentation and Chemical Systems for the Parallelization of Hydrogen Evolving Photocatalytic Reactions, *Energy & Fuels*, 10.1021/acs.energyfuels.1c02168, 35, 23, (18957-18981), (2021).



# Use of Matlab - Simulink for calculating the kinematic variables of the mechanism

Ing. Štefan Ondočko\*, prof. Ing. Jozef Svetlík PhD, Ing. Tomáš Stejskal PhD, Ing. Michal Šašala

Technická univerzita v Košiciach, Strojnícka fakulta, Katedra výrobnéj techniky a Robotiky (KVTaR)  
[tomas.stejskal@tuke.sk](mailto:tomas.stejskal@tuke.sk), [jozef.svetlik@tuke.sk](mailto:jozef.svetlik@tuke.sk), [lukas.hrivniak@tuke.sk](mailto:lukas.hrivniak@tuke.sk), [michal.sasala@tuke.sk](mailto:michal.sasala@tuke.sk)

\* [stefan.ondocko@tuke.sk](mailto:stefan.ondocko@tuke.sk); Tel.: +421 55 602 3238 (Letná 9, 042 00 Košice)

**Abstract:** The paper describes the manner of calculating kinematic values on the mechanism. This is done by using homogenous transformations to determine the function of position, velocity, acceleration dependent on a partial turn and shift of the local coordinate systems of the given mechanism's parts with respect to the basic reference cartesian system in a manner which utilizes modern simulation environment, where the probability of calculation error is more a result of bad design or, eventually, swapping the variables, rather than a mistake in the equation.

**Keywords:** Kinematics; Matlab; Simulink; Multibody

## 1. Introduction

Simulink has been developed by "The MathWorks" [1, 2]. It is a commercial tool for modeling, simulation and analysis of dynamic systems. Its primary interface is a graphic tool for creating block diagrams. It contains a set of block libraries. It is closely linked to the rest of the MATLAB environment and may control it or be scripted therefrom. Simulink is widely used in the theory of steering and digital signal processing for simulation and development. It contains many supporting tool packages, designed more specifically to a particular physical and technical area, which makes the work more pleasant and Matlab multifunctional. The paper describes an example of checking analytical calculation of kinematic values in Simulink on the given mechanical model published several times [3, 4, 5] also within the Modular architecture of production technology structural elements APVV-18-0413. This approach is applicable to other types of mechanisms, too.

## 2. Mathematic description

To analytically calculate the kinematic values [6 - 10] such as the trajectory or, alternatively, the position, velocity and acceleration, we must know the geometry and location of the given mechanism's joints. With the help of mathematical operations, we look for a functional dependence between motion of the examined mechanism part and the so-called reference system. In more complicated mechanisms, the risk of an error in calculation is relatively high. That is why it is an advantage to have another option of checking.

The task is to establish the position, velocity, acceleration, eventually other values on the mechanism as needed, see Figure 1. Partial turn in the individual  $i^{\text{th}}$  transformational links is described by the angle variable  $\varphi_i$ , or by the  $\vartheta_i$  for the curvature. In the joints, coordinate systems are defined, the position and orientation of which is indisputably given by  $\varphi_i$ . The structure's size is quantified by position vectors  $p_i(\varphi_i, \vartheta_i)$ , on individual segments -  $r_i$  in the so-called open kinematic chain. It is assumed that the modules, the joints are immaterial and perfectly rigid bodies.

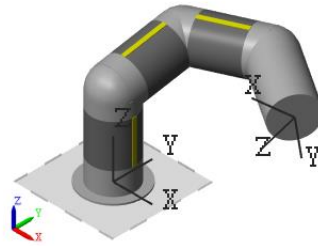


Figure 1. Model

The paper [5] gives a detailed description of the mechanism’s position kinematics, from which only the necessary equations will be mentioned. For the sake of an overview, we will limit ourselves to only a couple of modules from the given chain. In fact, there are six of them in the real model.

2.1. For position

For  $\mathbf{p}_1$

$$\mathbf{p}_1 = \mathbf{R}_{z1}(\varphi_1) \cdot \mathbf{r}_1 \tag{1}$$

For  $\mathbf{p}_2$

$$\mathbf{p}_2 = \mathbf{p}_1 + \mathbf{R}_{z1}(\varphi_1) \cdot \mathbf{R}_{y2}(\vartheta_2) \cdot \mathbf{R}_{z2}(\varphi_2) \cdot \mathbf{r}_2 \tag{2}$$

For  $\mathbf{p}_3$

$$\mathbf{p}_3 = \mathbf{p}_2 + \mathbf{R}_{z1}(\varphi_1) \cdot \mathbf{R}_{y2}(\vartheta_2) \cdot \mathbf{R}_{z2}(\varphi_2) \cdot \mathbf{R}_{y3}(\vartheta_3) \cdot \mathbf{R}_{z3}(\varphi_3) \cdot \mathbf{r}_3 \tag{3}$$

For  $\mathbf{p}_4$

$$\mathbf{p}_4 = \mathbf{p}_3 + \mathbf{R}_{z1}(\varphi_1) \cdot \mathbf{R}_{y2}(\vartheta_2) \cdot \mathbf{R}_{z2}(\varphi_2) \cdot \mathbf{R}_{y3}(\vartheta_3) \cdot \mathbf{R}_{z3}(\varphi_3) \cdot \mathbf{R}_{y4}(\vartheta_4) \cdot \mathbf{r}_4 \tag{4}$$

Thus, we can write the following for  $\mathbf{R}_{zi}(\varphi_i)$

$$\mathbf{R}_{zi}(\varphi_i) = \begin{bmatrix} \cos(\varphi_i) & -\sin(\varphi_i) & 0 \\ \sin(\varphi_i) & \cos(\varphi_i) & 0 \\ 0 & 0 & 1 \end{bmatrix} \tag{5}$$

And the following for  $\mathbf{R}_{yi}(\vartheta_i)$

$$\mathbf{R}_{yi}(\vartheta_i) = \begin{bmatrix} \cos(\vartheta_i) & 0 & \sin(\vartheta_i) \\ 0 & 1 & 0 \\ -\sin(\vartheta_i) & 0 & \cos(\vartheta_i) \end{bmatrix} \tag{6}$$

And the following for  $\mathbf{r}_i$  in centerline

$$\mathbf{r}_i = \begin{bmatrix} 0 \\ 0 \\ L_i \end{bmatrix} \tag{7}$$

Resulting relations describing the individual effector position vector components  $\mathbf{p}_i = [p_{xi}, p_{yi}, p_{zi}]^T$  may be obtained by multiplication of the matrices in (1), (2), (3), (4). They take up too much space to be included here.

2.2. For velocity

We obtain the individual velocities by derivation of the position vectors  $\mathbf{p}_i$  according to time

$$\mathbf{v}_i = \dot{\mathbf{p}}_i = \dot{\mathbf{R}}_{zi}(\varphi_i) \cdot \mathbf{r}_i \tag{8}$$

It may be derived that the following is true

$$\dot{\mathbf{R}}_{zi}(\varphi_i) = \mathbf{R}_{zi} \cdot \boldsymbol{\Omega}_{zi} \tag{9}$$

Where the segment's angular velocity in the space around the  $z_i$  axis is defined by the antisymmetric  $\boldsymbol{\Omega}_{zi}(\omega_i)$  matrix [6, 7, 8, 10]. Thus, for  $\boldsymbol{\Omega}_{zi}(\omega_i)$ , the following may be written

$$\boldsymbol{\Omega}_{zi} = \begin{bmatrix} 0 & -\omega_i & 0 \\ \omega_i & 0 & 0 \\ 0 & 0 & 0 \end{bmatrix} \tag{10}$$

For the  $v_i$  vector of velocities in space and in the individual assemblies coordinate systems,  $\mathbf{v}_i = [v_{xi}, v_{yi}, v_{zi}]^T$ . Then based on (8), (9), we can write the following for  $\mathbf{v}_1$

$$\mathbf{v}_1 = \mathbf{R}_{z1} \cdot \boldsymbol{\Omega}_{z1} \cdot \mathbf{r}_1 \tag{11}$$

For  $\mathbf{v}_2$

$$\mathbf{v}_2 = \mathbf{v}_1 + (\mathbf{R}_{z1} \cdot \mathbf{R}_{y2} \cdot \mathbf{R}_{z2} \cdot \boldsymbol{\Omega}_{z2} + \mathbf{R}_{z1} \cdot \boldsymbol{\Omega}_{z1} \cdot \mathbf{R}_{y2} \cdot \mathbf{R}_{z2}) \cdot \mathbf{r}_2 \tag{12}$$

For  $\mathbf{v}_3$

$$\mathbf{v}_3 = \mathbf{v}_2 + (\mathbf{R}_{z1} \cdot \mathbf{R}_{y2} \cdot \mathbf{R}_{z2} \cdot \mathbf{R}_{y3} \cdot \mathbf{R}_{z3} \cdot \boldsymbol{\Omega}_{z3} + \mathbf{R}_{z1} \cdot \mathbf{R}_{y2} \cdot \mathbf{R}_{z2} \cdot \boldsymbol{\Omega}_{z2} \cdot \mathbf{R}_{y3} \cdot \mathbf{R}_{z3} + \mathbf{R}_{z1} \cdot \boldsymbol{\Omega}_{z1} \cdot \mathbf{R}_{y2} \cdot \mathbf{R}_{z2} \cdot \mathbf{R}_{y3} \cdot \mathbf{R}_{z3}) \cdot \mathbf{r}_3 \tag{13}$$

For  $\mathbf{v}_4$

$$\mathbf{v}_4 = \mathbf{v}_3 + (\mathbf{R}_{z1} \cdot \mathbf{R}_{y2} \cdot \mathbf{R}_{z2} \cdot \mathbf{R}_{y3} \cdot \mathbf{R}_{z3} \cdot \boldsymbol{\Omega}_{z3} \cdot \mathbf{R}_{y4} + \mathbf{R}_{z1} \cdot \mathbf{R}_{y2} \cdot \mathbf{R}_{z2} \cdot \boldsymbol{\Omega}_{z2} \cdot \mathbf{R}_{y3} \cdot \mathbf{R}_{z3} \cdot \mathbf{R}_{y4} + \mathbf{R}_{z1} \cdot \boldsymbol{\Omega}_{z1} \cdot \mathbf{R}_{y2} \cdot \mathbf{R}_{z2} \cdot \mathbf{R}_{y3} \cdot \mathbf{R}_{z3} \cdot \mathbf{R}_{y4}) \cdot \mathbf{r}_4 \tag{14}$$

Resulting relations describing the individual effector velocity vector components  $\mathbf{v}_i = [v_{xi}, v_{yi}, v_{zi}]^T$  may be obtained by multiplication of the matrices in (11), (12), (13), (14). They take up too much space to be included here.

### 2.3. For acceleration

Individual accelerations are obtained from derivation of the position vectors of the velocity  $\mathbf{v}_i$  according to time. Thus, for the  $\mathbf{a}_i$  acceleration, the following is true

$$\mathbf{a}_i = \dot{\mathbf{v}}_i = \ddot{\mathbf{R}}_{zi}(\varphi_i) \cdot \mathbf{r}_i \tag{15}$$

It may be derived that the following is true

$$\ddot{\mathbf{R}}_{zi}(\varphi_i) = \mathbf{R}_{zi} \cdot (\boldsymbol{\Omega}_{zi}^2 + \mathbf{E}_{zi}) \tag{16}$$

Where the segment's angular acceleration in the space around the  $z_i$  axis is defined by the antisymmetric matrix  $\mathbf{E}_{zi}(\varepsilon_i)$  [6, 7, 8, 10]. Thus, the following can be written for  $\mathbf{E}_{zi}(\varepsilon_i)$

$$\mathbf{E}_{zi} = \begin{bmatrix} 0 & -\varepsilon_i & 0 \\ \varepsilon_i & 0 & 0 \\ 0 & 0 & 0 \end{bmatrix} \tag{17}$$

For the acceleration vector  $\mathbf{a}_i$  in space and in the individual coordinate systems:  $\mathbf{a}_i = [a_{xi}, a_{yi}, a_{zi}]^T$ . Then based on (15), (16), we can write the following for  $\mathbf{a}_1$

$$\mathbf{a}_1 = \mathbf{R}_{z1} \cdot (\boldsymbol{\Omega}_{z1}^2 + \mathbf{E}_{z1}) \cdot \mathbf{r}_1 \tag{18}$$

For  $\mathbf{a}_2$

$$\mathbf{a}_2 = \mathbf{a}_1 + (\mathbf{R}_{z1} \cdot \mathbf{R}_{y2} \cdot \mathbf{R}_{z2} \cdot (\Omega_{z2}^2 + \mathbf{E}_{z2}) + \mathbf{R}_{z1} \cdot (\Omega_{z1}^2 + \mathbf{E}_{z1}) \cdot \mathbf{R}_{y2} \cdot \mathbf{R}_{z2} + 2 \cdot \mathbf{R}_{z1} \cdot \Omega_{z1} \cdot \mathbf{R}_{y2} \cdot \mathbf{R}_{z2} \cdot \Omega_{z2}) \cdot \mathbf{r}_2 \quad (19)$$

For  $\mathbf{a}_3$

$$\begin{aligned} \mathbf{a}_3 = \mathbf{a}_2 + & (2 \cdot \mathbf{R}_{z1} \cdot \mathbf{R}_{y2} \cdot \mathbf{R}_{z2} \cdot \Omega_{z2} \cdot \mathbf{R}_{y3} \cdot \mathbf{R}_{z3} \cdot \Omega_{z3} + 2 \cdot \mathbf{R}_{z1} \cdot \Omega_{z1} \cdot \mathbf{R}_{y2} \cdot \mathbf{R}_{z2} \cdot \mathbf{R}_{y3} \cdot \mathbf{R}_{z3} \cdot \Omega_{z3} \\ & + 2 \cdot \mathbf{R}_{z1} \cdot \Omega_{z1} \cdot \mathbf{R}_{y2} \cdot \mathbf{R}_{z2} \cdot \Omega_{z2} \cdot \mathbf{R}_{y3} \cdot \mathbf{R}_{z3} + \mathbf{R}_{z1} \cdot \mathbf{R}_{y2} \cdot \mathbf{R}_{z2} \cdot \mathbf{R}_{y3} \cdot \mathbf{R}_{z3} \cdot (\Omega_{z3}^2 + \mathbf{E}_{z3}) \\ & + \mathbf{R}_{z1} \cdot \mathbf{R}_{y2} \cdot \mathbf{R}_{z2} \cdot (\Omega_{z2}^2 + \mathbf{E}_{z2}) \cdot \mathbf{R}_{y3} \cdot \mathbf{R}_{z3} + \mathbf{R}_{z1} \cdot (\Omega_{z1}^2 + \mathbf{E}_{z1}) \cdot \mathbf{R}_{y2} \cdot \mathbf{R}_{z2} \cdot \mathbf{R}_{y3} \cdot \mathbf{R}_{z3}) \cdot \mathbf{r}_3 \end{aligned} \quad (20)$$

For  $\mathbf{a}_4$

$$\begin{aligned} \mathbf{a}_4 = \mathbf{a}_3 + & (2 \cdot \mathbf{R}_{z1} \cdot \mathbf{R}_{y2} \cdot \mathbf{R}_{z2} \cdot \Omega_{z2} \cdot \mathbf{R}_{y3} \cdot \mathbf{R}_{z3} \cdot \Omega_{z3} \cdot \mathbf{R}_{y4} + 2 \cdot \mathbf{R}_{z1} \cdot \Omega_{z1} \cdot \mathbf{R}_{y2} \cdot \mathbf{R}_{z2} \cdot \mathbf{R}_{y3} \cdot \mathbf{R}_{z3} \cdot \Omega_{z3} \cdot \mathbf{R}_{y4} \\ & + 2 \cdot \mathbf{R}_{z1} \cdot \Omega_{z1} \cdot \mathbf{R}_{y2} \cdot \mathbf{R}_{z2} \cdot \Omega_{z2} \cdot \mathbf{R}_{y3} \cdot \mathbf{R}_{z3} \cdot \mathbf{R}_{y4} + \mathbf{R}_{z1} \cdot \mathbf{R}_{y2} \cdot \mathbf{R}_{z2} \cdot \mathbf{R}_{y3} \cdot \mathbf{R}_{z3} \cdot (\Omega_{z3}^2 + \mathbf{E}_{z3}) \cdot \mathbf{R}_{y4} \\ & + \mathbf{R}_{z1} \cdot \mathbf{R}_{y2} \cdot \mathbf{R}_{z2} \cdot (\Omega_{z2}^2 + \mathbf{E}_{z2}) \cdot \mathbf{R}_{y3} \cdot \mathbf{R}_{z3} \cdot \mathbf{R}_{y4} + \mathbf{R}_{z1} \cdot (\Omega_{z1}^2 + \mathbf{E}_{z1}) \cdot \mathbf{R}_{y2} \cdot \mathbf{R}_{z2} \cdot \mathbf{R}_{y3} \cdot \mathbf{R}_{z3} \cdot \mathbf{R}_{y4}) \cdot \mathbf{r}_4 \end{aligned} \quad (21)$$

Final relations between the individual effector acceleration vector components  $\mathbf{a}_i = [a_{xi}, a_{yi}, a_{zi}]^T$  can be obtained from multiplication of the matrices in (18), (19), (20), (21). They are too extensive to be included here.

### 3. Experimental solution using a model of the mechanism

Calculated kinematic values were checked in the Matlab Simulink toolbox Multibody. First, we correctly assemble the given model. Figure 2. shows blocks – the parts linked together in  $i^{\text{th}}$  coordinate systems of  $S_i\{O_i, x_i, y_i, z_i\}$ . The  $S_1\{O_1, x_1, y_1, z_1\}$  coordinate system makes up a so-called base (the reference cartesian system). Each of the parts, i.e., Part1, Part2, Part3, is able to rotate around its own axis  $z_i$ . The Part1, Part2, Part3 are actuated by the respective angular acceleration  $\epsilon_i$ . The last of the parts, Part4, does not rotate around its own axis. Kinematic vectors ( $\mathbf{p}_i, \mathbf{v}_i, \mathbf{a}_i$ ) are obtained easily from the transformation sensors – Sensor1, Sensor2, Sensor3. Individual blocks can be grouped together and they can be assigned a picture expressing their function. Thus, the resulting model does not have to appear complicated.

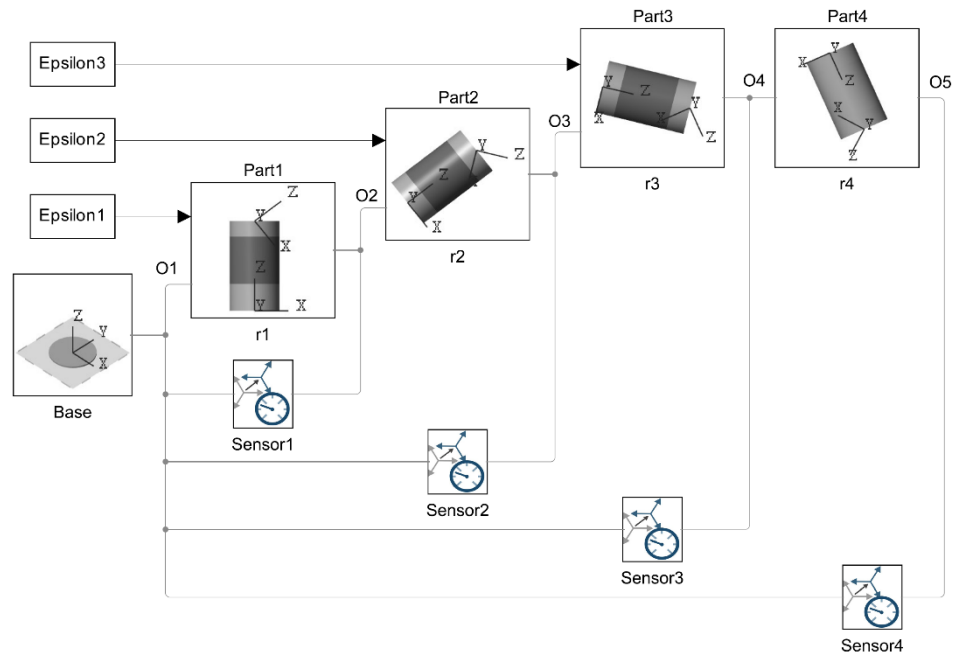


Figure 2. Blocks scheme in the Matlab Simulink Multibody toolbox

The signal used in actuating the individual joints of the mechanism, i.e., Part1 to Part3, must be adjusted following well-known physical equations and rules in Multibody. In our case (around the  $z_i$  axis) the following holds for the angular acceleration  $\epsilon_i$ :

$$\varepsilon_i = \frac{d\omega_i}{dt} \tag{22}$$

Since the angular acceleration  $\varepsilon_i$  will be known, we need to obtain the angular velocity  $\omega_i$ . We are solving a differential equation with the initial condition of  $\omega_i(t=0)=0$ :

$$\int_0^{\omega_i} d\omega_i = \varepsilon_i \int_0^t dt \tag{23}$$

Angular velocity is:

$$\omega_i = \varepsilon_i t \tag{24}$$

For partial turning  $\varphi_i$ , the following is derived by analogy:

$$\omega_i = \frac{d\varphi_i}{dt} \tag{25}$$

From (24) and (25), we get:

$$\int_0^{\varphi_i} d\varphi_i = \varepsilon_i \int_0^t t dt \tag{26}$$

Partial turn with the initial condition of  $\varphi_i(t=0)=0$  will be as follows:

$$\varphi_i = \varepsilon_i \frac{t^2}{2} \tag{27}$$

In this way, we obtained all the values necessary to control the joint (Revolute Joint) see Figure 3. Actuation of the joint is then set to automatically computed torque and motion is provided by input.

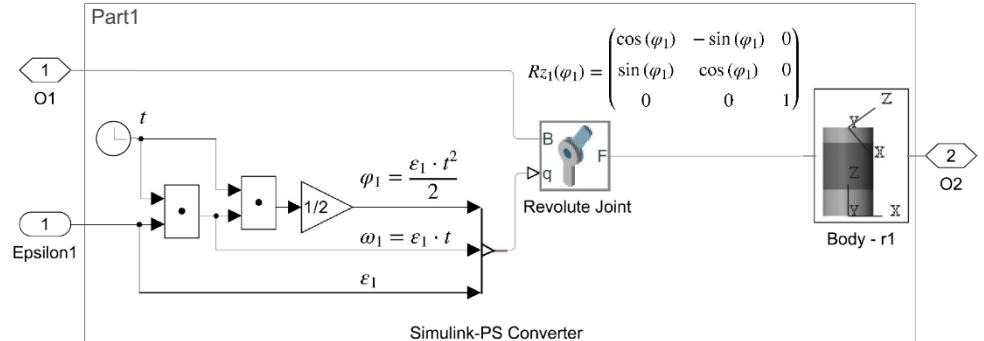


Figure 3. Detail of the Part1

Also important is to correctly set the converter (Simulink - Physical Signal Converter) for the input value itself and for its first, second derivative. Kinematic time-dependent values are exported from individual sensors, see Figure 4.

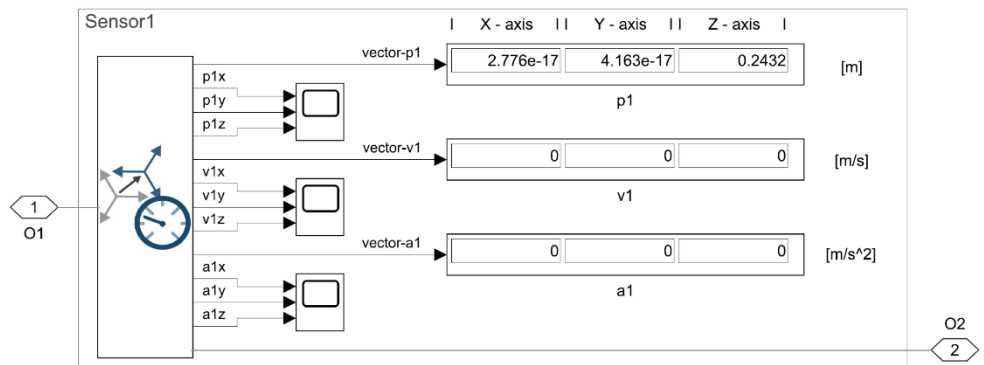


Figure 4. Detail of the Sensor1

#### 4. Results

We compute the results of differential kinematic equations for the given moment in time  $t$  from the equations (1) to (27). Individual parts' lengths are  $L_1=0.2432$  m,  $L_2=0.2124$  m,  $L_3=0.2124$  m,  $L_4=0.2124$  m. For the moment in time  $t=1$  s,  $\varepsilon_1=0.3$  rad.s<sup>-2</sup>,  $\varepsilon_2=0.9$  rad.s<sup>-2</sup>,  $\varepsilon_3=1.8$  rad.s<sup>-2</sup>,  $\varphi_1(t=0)=0$ ,  $\varphi_2(t=0)=0$ ,  $\varphi_3(t=0)=0$ ,  $\vartheta_2=80^\circ$ ,  $\vartheta_3=70^\circ$ ,  $\vartheta_4=52^\circ$ ;

##### 4.1. For position

According to equation (27) the following holds for instantaneous  $\varphi_1$

$$\varphi_1 = 0.3 \frac{1^2}{2} = 0.15 \text{ [rad]} \quad (28)$$

According to equation (1) the following holds for  $\mathbf{p}_1$

$$\mathbf{p}_1 = \begin{bmatrix} \cos(0.15) & -\sin(0.15) & 0 \\ \sin(0.15) & \cos(0.15) & 0 \\ 0 & 0 & 1 \end{bmatrix} \cdot \begin{bmatrix} 0 \\ 0 \\ 0.2432 \end{bmatrix} = \begin{bmatrix} 0 \\ 0 \\ 0.2432 \end{bmatrix} \text{ [m]} \quad (29)$$

Due to extensiveness of some equations, we only present results computed and inserted into the equations below. According to equation (2), the following holds for  $\mathbf{p}_2$

$$\mathbf{p}_2 = \begin{bmatrix} 0.2068 \\ 0.0313 \\ 0.2801 \end{bmatrix} \text{ [m]} \quad (30)$$

According to equation (3), the following holds for  $\mathbf{p}_3$

$$\mathbf{p}_3 = \begin{bmatrix} 0.2955 \\ 0.1325 \\ 0.1157 \end{bmatrix} \text{ [m]} \quad (31)$$

According to equation (4), the following holds for  $\mathbf{p}_4$

$$\mathbf{p}_4 = \begin{bmatrix} 0.2306 \\ 0.3118 \\ -0.0221 \end{bmatrix} \text{ [m]} \quad (32)$$

##### 4.2. For velocity

According to equation (24), the following holds for instantaneous  $\omega_1$

$$\omega_1 = 0,3 \cdot 1 \text{ [rad.s}^{-1}\text{]} \quad (33)$$

According to equation (10), the following holds

$$\mathbf{\Omega}_{z1} = \begin{bmatrix} 0 & -0.3 & 0 \\ 0.3 & 0 & 0 \\ 0 & 0 & 0 \end{bmatrix} \text{ [rad.s}^{-1}\text{]} \quad (34)$$

According to equation (11), the following holds for  $\mathbf{v}_1$

$$\mathbf{v}_1 = \begin{bmatrix} 0.9888 & -0.1494 & 0 \\ 0.1494 & 0.9888 & 0 \\ 0 & 0 & 1 \end{bmatrix} \cdot \begin{bmatrix} 0 & -0,3 & 0 \\ 0.3 & 0 & 0 \\ 0 & 0 & 0 \end{bmatrix} \cdot \begin{bmatrix} 0 \\ 0 \\ 0.2432 \end{bmatrix} = \begin{bmatrix} 0 \\ 0 \\ 0 \end{bmatrix} \text{ [m.s}^{-1}\text{]} \quad (35)$$

Due to extensiveness of equations, we only present results computed and inserted into the equations below. According to equation (12), the following holds for  $\mathbf{v}_2$

$$\mathbf{v}_2 = \begin{bmatrix} -0.0094 \\ 0.0621 \\ 0 \end{bmatrix} \text{ [m.s}^{-1}\text{]} \quad (36)$$

According to equation (13), the following holds for  $\mathbf{v}_3$

$$\mathbf{v}_3 = \begin{bmatrix} -0.0773 \\ 0.2466 \\ 0.0770 \end{bmatrix} \text{ [m.s}^{-1}\text{]} \quad (37)$$

According to equation (14), the following holds for  $\mathbf{v}_4$

$$\mathbf{v}_4 = \begin{bmatrix} -0.0020 \\ 0.4596 \\ 0.4330 \end{bmatrix} \text{ [m.s}^{-1}\text{]} \quad (38)$$

4.3. For acceleration

According to equation (17), the following holds

$$\mathbf{E}_{z1} = \begin{bmatrix} 0 & -0.3 & 0 \\ 0.3 & 0 & 0 \\ 0 & 0 & 0 \end{bmatrix} \text{ [rad.s}^{-2}\text{]} \quad (39)$$

According to equation (18), the following holds for  $\mathbf{a}_1$

$$\mathbf{a}_1 = \begin{bmatrix} 0.9888 & -0.1494 & 0 \\ 0.1494 & 0.9888 & 0 \\ 0 & 0 & 1 \end{bmatrix} \cdot \left( \begin{bmatrix} 0 & -0.3 & 0 \\ 0.3 & 0 & 0 \\ 0 & 0 & 0 \end{bmatrix}^2 + \begin{bmatrix} 0 & -0.3 & 0 \\ 0.3 & 0 & 0 \\ 0 & 0 & 0 \end{bmatrix} \right) \cdot \begin{bmatrix} 0 \\ 0 \\ 0.2432 \end{bmatrix} = \begin{bmatrix} 0 \\ 0 \\ 0 \end{bmatrix} \text{ [m.s}^{-2}\text{]} \quad (40)$$

Due to extensiveness of equations, we only present results computed and inserted into the equations below. According to equation (19), the following holds for  $\mathbf{a}_2$

$$\mathbf{a}_2 = \begin{bmatrix} -0.0280 \\ 0.0592 \\ 0 \end{bmatrix} \text{ [m.s}^{-2}\text{]} \quad (41)$$

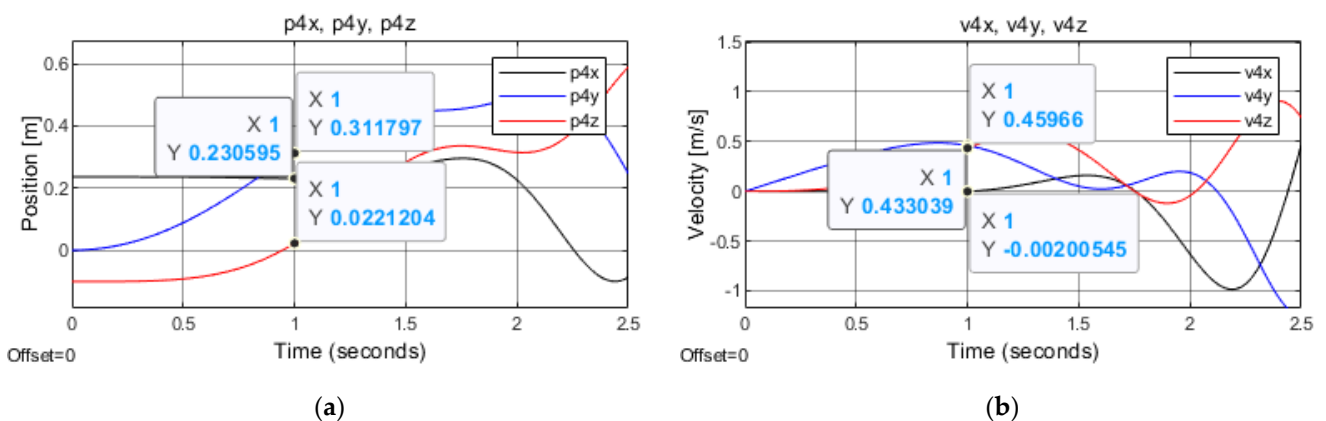
According to equation (20) the following holds for  $\mathbf{a}_3$

$$\mathbf{a}_3 = \begin{bmatrix} -0.2132 \\ 0.1388 \\ 0.2203 \end{bmatrix} \text{ [m.s}^{-2}\text{]} \quad (42)$$

According to equation (21), the following holds for  $\mathbf{a}_4$

$$\mathbf{a}_4 = \begin{bmatrix} 0.1264 \\ -0.3981 \\ 0.8567 \end{bmatrix} \text{ [m.s}^{-2}\text{]} \quad (43)$$

Figure 5 shows the results from Sensor4 (values from the last part of the kinematic chain), for the moment in time  $t=1s$ .



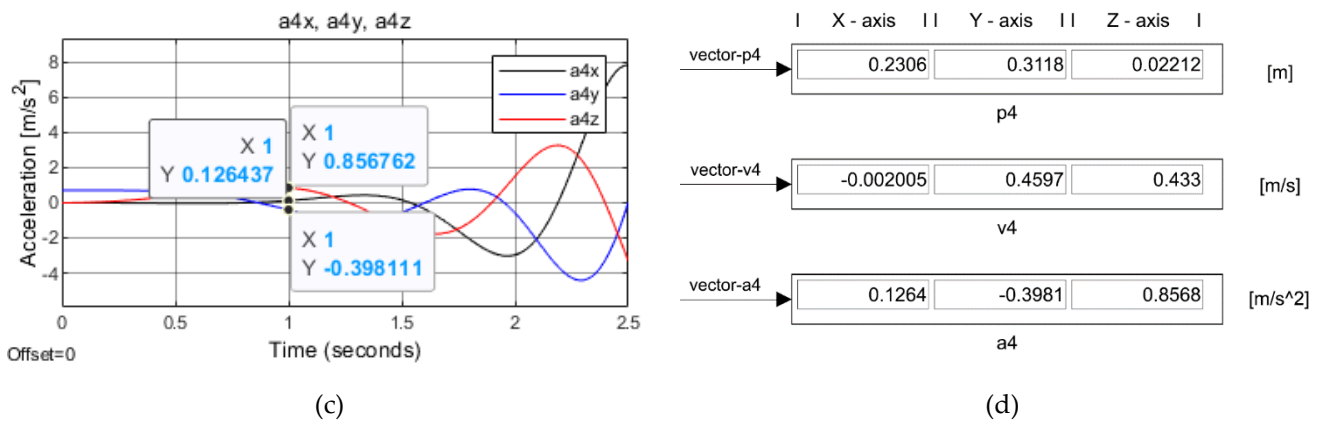


**Figure 5.** Results from Sensor4 (values from the last part of the kinematic chain), for the moment in time  $t=1s$ : (a) Central axis position Part4; (b) Central axis velocity Part4; (c) Central axis acceleration Part4; (d) Kinematic vectors output from Sensor4.

#### 4. Discussion and Conclusions

The results above, see Figure 5, point to the following. Individual kinematic values, i.e., in our case the Part4 position, velocity and the central axis acceleration, are identical (at least to three decimal places) with the values calculated through equations (28) to (43). Other values, such as the angular velocity or the angular partial turn of any mechanism part, can be obtained in this manner, too. The same applies to determining orientation of any mechanism part. As mentioned in the beginning, individual parts of the chain in simulation were modeled as immaterial and perfectly rigid. In the simulation environment, some changes are only a few clicks away, without complicated compilation of equations. However, in some cases, if our requirement is functional dependence of some values, it is good to have both approaches under control.

**Acknowledgement:** This work has been supported by the Research and Development Promotion Agency under the Contract no. APVV-18-0413 Modular architecture of production technology structural elements.

**Conflict of interests:** The authors rule out any conflict of interest. In designing the study, no role was played by any investors and the same holds true for the collection, analyses and interpretation of data, drafting the manuscript or decision making process on publishing the results.

#### References

- MATLAB - MathWorks - MATLAB & Simulink, MATLAB Documentation, <https://ch.mathworks.com/help/matlab/ref/help.html>, 2022.
- Hroncová, D., Huňady, R., Miková, L., Sivák, P., *Simulácia v programe matlab/simulink*. SjF, TU v Košiciach, 2019
- Svetlík, J.; Štofa, M.; Pituk, M. Prototype development of a unique serial kinematic structure of modular configuration. *MM Science Journal*, 2016, 994-998.
- Štofa, M. Experimentálny vývoj rotačných modulov pre stavbu sériových kinematických štruktúr vo výrobnjej technike. Ph.D. Tézý, Technická univerzita Košice, Slovensko, 30 Január 2020.
- Ondočko, Š.; Svetlík, J.; Šašala, M.; Bobovský, Z.; Stejskal, T.; Dobranský, J.; Demeč, P.; Hrivniak, L. *Inverse Kinematics Data Adaptation to Non-Standard Modular Robotiac Arm Consisting of Unique Rotational Modules*. Applied Sciences, 2021, volume 11, issue 3, 0-15.
- BRÁT, Vladimír. *Maticové metody v analýze a syntéze priestorových väzaných mechanických systémů*. Academia, 1981.
- Murray, R. M.; Li, Z.; Sastry, S. S. *A mathematical introduction to robotic manipulation*. CRC press, 2017.
- Grepl, R. *Kinematika a dynamika mechatronických systémů*. Akademické nakladatelství CERM, 2007.
- Smutný V., *Robotika, České vysoké učení technické v Praze, Praha 2019*
- Siciliano, B.; Khatib, O. *Springer handbook of robotics* (2nd Edition). Springer, 2016.



# 3D PRINTED CUSTOMIZED CAST FOR A CHILD WITH UPPER EXTREMITY FRACTURES: A CASE STUDY

Bibiána Ondrejová <sup>1\*</sup>, Branko Štefanovič <sup>1</sup>, Monika Michalíková <sup>1</sup>, Lucia Bednarčíková <sup>1</sup> and Jozef Živčák <sup>1</sup>

<sup>1</sup> Technical University of Košice, Faculty of Mechanical Engineering, Department of Biomedical Engineering and Measurement, Letná 9, 042 00 Košice

\* Correspondence: bibiana.ondrejova@tuke.sk

**Abstract:** In recent years, 3D technologies have become part of medicine thanks to the possibility of personalizing medical devices. This advantage has found its application mainly in prosthetics and orthotics. The work deals with the design and production of a personalized forearm orthosis made of PA12 (polyamide) material using MJF (Multi Jet Fusion) additive technology. The orthosis was designed for an eleven-year-old child with a dislocated elbow, a fracture of the epicondyle of the radius and humerus.

**Keywords:** additive manufacturing, orthosis, MJF technology

## 1. Introduction

Successful treatment of fractures requires immobilization of the damaged site. Traditional methods of immobilization in orthopedics include plastering, which has certain disadvantages, such as the opacity of the molded splint, which prevents control of the condition of soft tissues, postoperative wounds and swelling. Dermatological complications can also occur due to the impermeability of the material. The disadvantages of conventional production also include the weight and volume of the resulting splint. These splints are cheap, strong, easy to apply and ensure stability and limitation of joint mobility. However, this effect can be achieved with orthoses made of polymer materials, which are commonly used in additive manufacturing and, thanks to the diverse possibility of modifying the design, are able to eliminate the disadvantages in traditional manufacturing. [1-3]

This case study presents a practical methodology for manufacturing a 3D printed elbow and wrist immobilization orthosis to overcome the disadvantages of conventional manufacturing in a pediatric setting. It includes the methodology of non-contact acquisition of measurement data, which were used for the subsequent design of a personalized aid, considering limited mobility. At the same time, it describes the procedure for modeling an orthotic device with the required subject design, subsequent production and post-processing.

## 2. Materials and Methods

An eleven-year-old girl fell from her bicycle onto her dominant right upper limb. Immediate swelling and pain were noted around the elbow. During the palpation examination, there was tenderness and swelling of the elbow joint. After performing an X-ray examination, a fracture of the lateral epicondyle of the humerus, the epicondyle of the spindle bone and a dislocated elbow were found. The subject underwent surgery (Fig. 1) and prescribed treatment, which included temporary immobilization through an orthotic device.

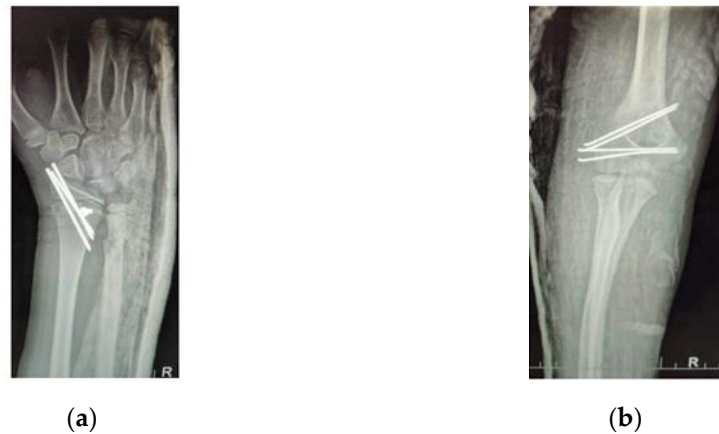


**Figure 2.** Postoperative radiograph of the right hand in neutral position: (a) wrist joint; (b) elbow joint

Before the actual design of the individual prosthesis, it is necessary to obtain anthropometric and morphological measurements of the hand, which will be used for the CAD design of the personalized aid. The method of obtaining measurements was using a 3D handheld Artec Eva scanner (Artec 3D, Luxemburg, Luxembourg), with a scanning frequency of 8 frames per second. The scanning was performed considering the sensitivity and limited mobility of the damaged limb. It was necessary to consider the possibilities of positioning the limb to obtain the highest possible morphological shape of the forearm with the wrist and elbow joint and at the same time. Due to pain, scanning was performed with the elbow joint flexed ( $90^\circ$ ) and with external rotation in the subject's shoulder joint. This position was secured with the assistance of a second person by holding the hand in a hook grip, which ensured sufficient space for moving the handheld scanner around the subject. This process was repeated 2 times due to subject movement during scanning. The resulting model was exported in STL (Standard Tessellation Language) format as a basis for modeling the aid. The resulting STL model had to be modified, as the movement during scanning caused deformations of the 3D model around the arm, the proximal and lateral sides of which were slightly displaced relative to each other (Fig. 2).

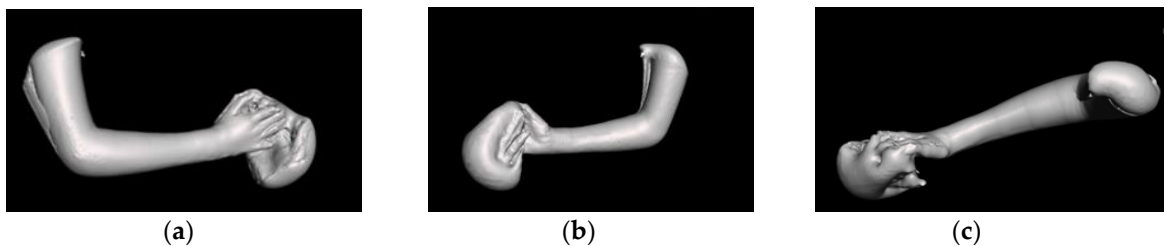


**Figure 2.** Scan of the upper extremity; (a) dorsal, (b) palmar, (c) radial view

After creating a digital positive, its subsequent adjustments were performed in the freely downloadable CAD software Autodesk Meshmixer (Autodesk, Inc., San Rafael, CA, USA), which contains functions for editing 3D models necessary for the creation of orthotic-prosthetic aids.

The surface of the distal part of the shoulder, forearm, and proximal part of the wrist from the obtained 3D model of the pathological hand was used to create the orthosis. This area had to be separated and extruded, to obtain a 3D shape of the orthosis, which copied the anatomical surface of the palmar and dorsal side of the deformed hand, leaving space for fitting the orthosis along the entire arm and forearm. To ensure sufficient strength of the orthosis, a thickness of 3 mm was chosen. The design of the device was supplemented

with a pattern of holes on the entire surface, which will ensure weight reduction and maximize the breathability of the prosthetic device. The attachment to the upper limb was ensured by modeled attachments in the SolidWorks program (Dassault Systemes, Waltham, USA), which are used to put on the Velcro straps. [4]



**Figure 3.** Final 3D model of the personalized orthosis.

A 3D printer type MJF (Multi Jet Fusion) HP Jet Fusion 5200 3D printer (Hewlett Packard, California, USA) was used to produce the orthosis. The MJF printing process consists of applying a layer of powder to the top of the assembly using a roller. The thickness of each layer is approximately 80 microns. Subsequently, fixing, and detailing agents are applied, and the entire layer is exposed to infrared light. The fixing agent determines which places in the layer are connected, and the detailing agent ensures sharp and smooth edges by limiting the adhesion of the powder near the print surface. 214.53 cm<sup>3</sup> of bio-compatible material PA12 (Polyamide) was used to produce the device (Tab. 1).

**Table 1.** Parameters of the model with a price MJF printed orthosis.

Model Dimensions	29.75 x 23.49 x 14.72 cm
Material Volume	214.53 cm <sup>3</sup>
Price <sup>1</sup>	115,79 €

<sup>1</sup> According to [www.hp3dprint.eu](http://www.hp3dprint.eu)

### 3. Results

The final orthosis was sufficiently tight, functional, and comfortable. It corresponded to the morphological shape of the upper limb and sufficiently immobilized the upper limb in a flexed position.



**Figure 2.** Final orthosis manufactured by MJF technology; (a) before postprocessing, (b) after postprocessing on the subject's arm.

#### 4. Discussion

The process of designing and manufacturing the orthosis using innovative additive technology begins with scanning the patient in the desired position. In this case, the scan took about 10 minutes precisely because of the movement of the subject. The editing of the exported STL file together with the CAD modeling of the orthosis took approximately 60 minutes. However, the duration of scanning and modeling is closely related to the skills of the orthopedic technician and the patient's condition, but programmable modeling tools have been developed that reduce the amount of manual CAD operations required, simplify the modeling process for clinicians, and alleviate the need for complex operations or extensive training. The manufactured orthosis can be fixed or removed as needed, which is an advantage mainly from a hygienic and rehabilitation point of view. The application of the orthosis should be after the maximum swelling, which usually occurs three to five days after the injury, which gives room for the manufacture of the orthosis with additive technology. [5-6]

#### 5. Conclusions

Over the past decade, 3D printed orthotics have made significant advances due to their light weight, relatively low cost, rapid production, and ease of customization. Currently, there are still few publications on the treatment of upper limb fractures in children using 3D printed orthoses. Guida et al. developed a protocol to produce custom-made, 3D printed orthoses in a hospital setting [7-8]. According to the study, eighteen children were successfully treated with a 3D printed orthosis with high patient satisfaction. [9-10]

The aim of the work was to design and manufacture a personalized forearm orthosis for a subject with multiple fractures using progressive methods. When scanning the subject, it was necessary to consider the soreness of the upper limb during mobility, which was limited to a minimum through the assistance of a second person. It was also necessary, from a time point of view, to take care of the fastest possible procedure of designing and manufacturing the orthosis due to the need for an aid after surgery.

With the technologies used, the entire process from obtaining anthropometric data to testing the orthosis took 3 days. After printing, color was applied to the orthosis according to the wishes of the pediatric subject, which also contributed to a psychologically better tolerance of the necessity of wearing the orthosis. The purpose of further research is to compare upper limb orthoses made by different types of additive technology and at the same time price comparison. It would also be possible to create an accurate design of the methodology to produce functional low-cost 3D printed orthoses.

**Acknowledgments:** This article was developed with the support of the project KEGA 023TUKE-4/2020 "Increasing the synergy of teaching methods of biophysics using laboratory equipment and diagnostic instruments aimed at measuring physical and technical quantities", KEGA 044TUKE-4/2022 "Implementation of progressive technologies in prosthetics and orthotics education and support integration with practice" and Slovak Research and Development Agency under the contract No. APVV-19-0290.

**Conflicts of Interest:** The authors declare no conflict of interest.

#### References

1. Md, Hasibuzzaman & Abdul Wahab, Asnida & Gan, Hong & Ramlee, Muhammad Hanif. (2021). Three-dimensional printed orthosis in biomedical application: A short review. *Journal of Physics: Conference Series*. 2071. 012025. 10.1088/1742-6596/2071/1/012025.
2. Oud, Tanja & Lazzari, E. & Gijssbers, Harm & Gobbo, Massimiliano & Nollet, Frans & Brehm, Merel-Anne. (2021). Effectiveness of 3D-printed orthoses for traumatic and chronic hand conditions: A scoping review. *PLOS ONE*. 16. e0260271. 10.1371/journal.pone.0260271

3. Waldburger, Leonie & Schaller, Romain & Furthmüller, Christina & Schaefer, Dirk & Kaempfen, Alexandre. (2021). 3D-Printed Hand Splints versus Thermoplastic Splints: A Randomized Controlled Pilot Feasibility Trial. *International Journal of Bioprinting*. 8. 474. 10.18063/ijb.v8i1.474
4. Surucu, Serkan & Aydın, Mahmud & Batmaz, Guray & Karasahin, Deniz & Mahirogullari, Mahir. (2022). Evaluation of the patient satisfaction of using a 3D printed medical casting in fracture treatment. *Joint Diseases and Related Surgery*. 3. 180-186. 10.52312/jdrs.2022.372.
5. Buonamici, Francesco & Furferi, Rocco & Governi, Lapo & Lazzeri, Simone & McGreevy, Kathleen & Servi, Michaela & Talanti, Emiliano & Uccheddu, Francesca & Volpe, Yary. (2020). A practical methodology for computer-aided design of custom 3D printable casts for wrist fractures. *The Visual Computer*. 36. 10.1007/s00371-018-01624-z.
6. Chen, Yanjun & Lin, Hui & Yu, Qinqin & Zhang, Xiaodong & Wang, Defeng & Shi, Lin & Wenhua, Huang & Zhong, Shizhen. (2020). Application of 3D-Printed Orthopedic Cast for the Treatment of Forearm Fractures: Finite Element Analysis and Comparative Clinical Assessment. *BioMed Research International*. 2020. 1-12. 10.1155/2020/9569530.
7. Katt, Brian & Imbergamo, Casey & Seigerman, Daniel & Rivlin, Michael & Beredjiklian, Pedro. (2021). The Use of 3D Printed Customized Casts in Children with Upper Extremity Fractures: A Report of Two Cases. *The archives of bone and joint surgery*. 9. 126-130. 10.22038/abjs.2020.47722.2342.
8. Guida P, Casaburi A, Busiello T, Lamberti D, Sorrentino A, Iuppariello L, et al. An alternative to plaster casttreatment in a pediatric trauma center using the CAD/CAM technology to manufacture customized three-dimensional-printed orthoses in a totally hospitalcontext: a feasibility study. *Journal of PediatricOrthopaedics B*. 2019; 28(3):248-55.
9. Schwartz, Deborah & Schofield, Katherine. (2021). Utilization of 3D printed or-thoses for musculoskeletal conditions of the upper extremity: A systematic review. *Journal of Hand Therapy*. 10.1016/j.jht.2021.10.005.
10. Choo, Yoo & Boudier-Revéret, Mathieu & Chang, Min. (2020). 3D printing technology applied to orthosis manufacturing: Narrative review. *Annals of Palliative Medicine*. 10.21037/apm-20-1185.

# Homogenization of composite material reinforced with discontinuous fibers

Peter Palička<sup>1,\*</sup>, Róbert Huňady<sup>1</sup> and Sára Janigová<sup>1</sup>

<sup>1</sup> Department of Applied Mechanics and Mechanical Engineering, Faculty of Mechanical Engineering, Technical University of Košice, Letná 9/B, 042 00 Košice, Slovakia; peter.palicka@tuke.sk; robert.hunady@tuke.sk; sara.janigova@tuke.sk;

\* Correspondence: peter.palicka@tuke.sk;

**Abstract:** Composite materials are increasingly being applied in the industry in many technical fields. They are mainly used when it is necessary to reduce the price and weight of the final product while maintaining its original mechanical properties. In numerical analysis, the building of composite FEM model is significantly difficult. If it is not necessary to investigate the deformation of the individual fibers and layers of the composite, homogenization is a suitable tool for describing the composite from a macroscopic point of view. In this work a composite with epoxy matrix reinforced with discontinuous short glass fibers is homogenized using representative volume element and Mori-Tanaka method. The cube-shaped RVE and the same cube-shaped model with a defined homogenized material model with proposed material properties by Mori-Tanaka method is subjected to the tensile loading. The aim of this work is to validate and correlate the simulation results for these composite homogenized by two different homogenization methods.

**Keywords:** Composite; FEM; Representative volume element (RVE); Mean-field homogenization Mori-Tanaka method.

## 1. Introduction

A composite is a heterogeneous material that is made up of at least two or more materials [1]. A composite consists of a matrix and a reinforcement. In the matrix of the composite, the reinforcements may be layered on top of each other at different angles. The composite may be reinforced with small particles, discontinuous fibers or continuous fibers. Thus composites can be classified into discontinuously reinforced or continuously reinforced (see Figure 1).

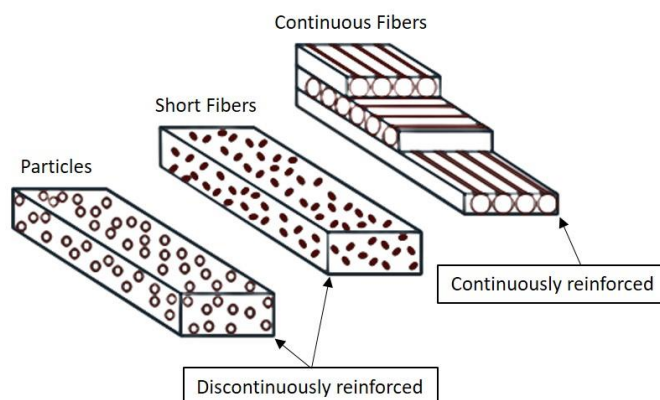
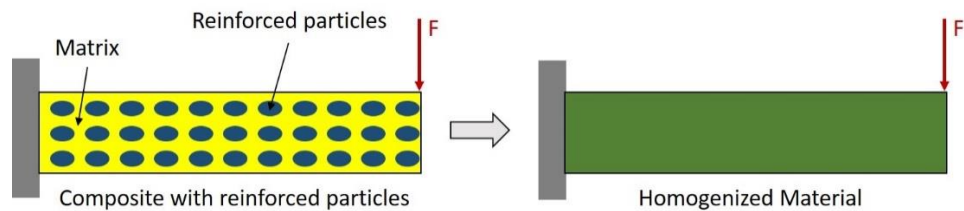


Figure 1. Composite material.

Both the matrix and the individual layers of the composite have different material properties. The aim of homogenization is to determine such material properties that describe the relationship between microstructure and the macroscopic response of a composite material. In other words, homogenization allows to create from a heterogeneous composite material an "equivalent" homogeneous material to solve global and macroscopic problems. The disadvantage of homogenization is the loss of local stress fields in the layers of the composite, where plastic deformation and failure of layer integrity can occur. The above-mentioned characteristic of homogenization is illustrated in Figure 2, where it can be seen that the homogenization of the composite results in a material model that describes the global deformation with sufficient accuracy. The results of strain and displacement would be approximately the same for both models.



**Figure 2.** Homogenization of composite.

There are many homogenization methods but among the most used and implemented by researchers around the world is the so-called mean-field homogenization and multi-scale homogenization which is based on the approaches of the finite element method. Mean-field homogenization is an effective tool for describing and predicting the behaviour of heterogeneous material. This method was established for the description of a linear elastic region but over time new techniques have been developed that allow to describe also the elasto-plastic region even the visco-plastic region. The range of mean-field homogenization extends from the simplest stress-strain hypotheses, where no analytical solution is required on the associated boundary-value problem (Voigt and Reuss estimates), to more complex geometric models based on the solution of a boundary value problem (self-consistent schemes). The concept of a representative volume element is related to the concept of microhomogeneity, i.e. homogeneous properties of a heterogeneous material at the microscopic level. However, the microstructure of a heterogeneous composite is in many cases very complex and random. Therefore, a necessary condition for defining a representative volume element is that this element is created from a statistically representative region from the composite material. This means that the RVE must contain as many heterogeneities as possible from the given composite [2,3].

The homogenization of composite materials is being studied by researchers around the world, resulting in papers comparing different homogenization techniques and methods for investigating composites in both the elastic and plastic regions [4,5].

The prediction of the stress-strain response in a composite material from a macroscopic point of view is closely related to the description of its complex microstructural behaviour [6,7]. Riecky et al. [8] in their work dealt with micromechanical modelling of composites. The goal was to determine the elastic properties of the homogenized material. The composite consisted of an epoxy matrix reinforced with carbon, glass and kevlar fibers. A three-dimensional representative volume element (RVE) of the polymer matrix was modelled using the finite element method (FEM). MATLAB and ANSYS software were used to homogenize the composite plate. The direct homogenization method was used. This method is based on the volumetric average of the stresses in the RVE. As a result of their study, the elastic properties of the homogenized composite were calculated.

RVE homogenization and mean-field homogenization using the Mori-Tanaka method in elasto-plastic deformation are being investigated by scientists all over the world and it is still a very actual and interesting field of research [9-14].

## 2. Homogenization and simulation of composite material

A cube-shaped model with a 1 mm long edge i.e. with volume of 1 mm<sup>3</sup> was result of RVE homogenization method. This model consisted of pure epoxy resin and randomly generated discontinuous short glass fibers in the x-axis direction with volume fraction ( $V_f$ ) of 0.166 (see Figure 3a). The RVE model consisted of 238 985 solid tetra elements and two material cards, one for inclusions and one for matrix. The homogenized material model (see Figure 3b) created by mean-field homogenization with the efficient material properties proposed by the Mori-Tanaka method is applied to the same size cube-shaped model. It is consisted of 230 521 solid tetra elements.

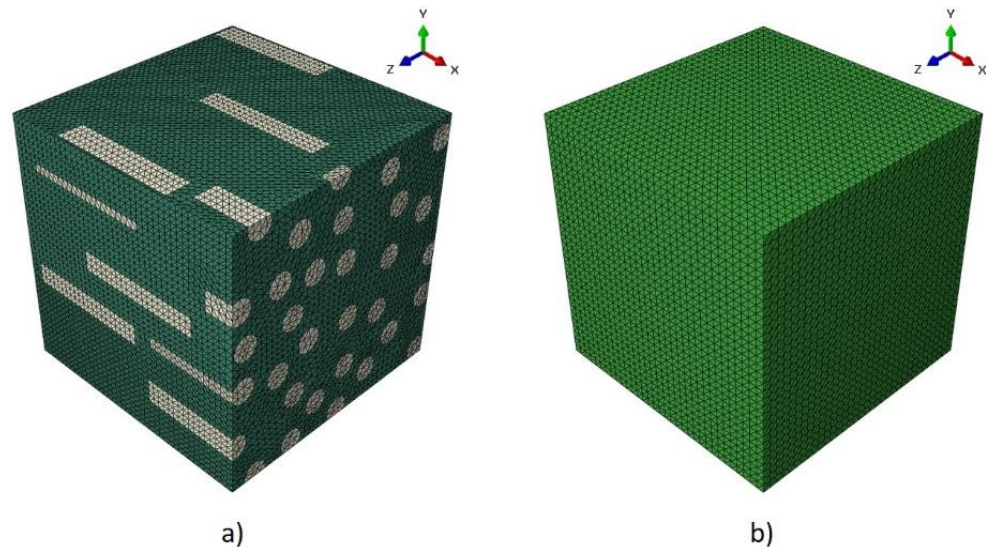


Figure 3. a) RVE model; b) Model with homogenized material.

The material properties of the transversely isotropic RVE are shown in Table 1.

Table 1. The material properties of the components of transversely isotropic material.

Material properties	$E$ [MPa]	$\nu$ [-]	$\rho$ [kg.m <sup>3</sup> ]	$G$ [MPa]
Epoxy resin	3400	0.3	1100	-
Glass fibers	85 000	0.22	2460	30 974.6

The material properties of homogenized composite determined by Mori-Tanaka method are shown in Table 2.

Table 2. Efficient material properties of homogenized material proposed by Mori-Tanaka method.

Material properties	$\rho$ [kg.m <sup>3</sup> ]	$E_1$ [MPa]	$E_2, E_3$ [MPa]	$\nu_{12}, \nu_{13}$ [-]	$\nu_{23}$ [-]	$G_{12}, G_{13}$ [MPa]	$G_{23}$ [MPa]
Homogenized material	1461.4	10605.95	4608.43	0.29	0.36	1794.47	1689.27

The boundary conditions (see Figure 4) were identical for both models. A kinematic coupling was used, which tied all nodes on the cube surface to a reference point at which a displacement of 0.01 mm was defined. The kinematic coupling reinforces the entire surface of the cube so that there is no torsion or bending on the surface. In other words all points tied by the kinematic coupling are displaced in the same way as the reference point.

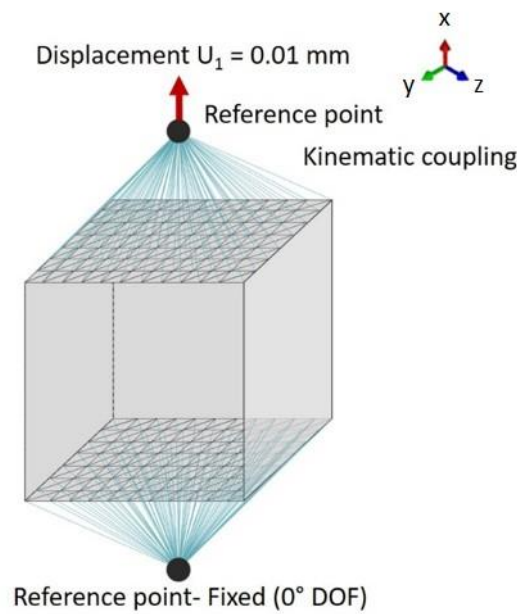


Figure 4. Boundary conditions for simulations.

### 3. Results and discussion

At the defined displacement the reaction force was measured. This force was necessary to be included in the relation to calculate the Young's modulus of elasticity. Figure 5 shows the displacement field in the x-axis direction and it is possible to see similarly distributed displacement field for both models. The maximum displacement is 0.01 mm as was set in simulation. The reaction force that was caused by this displacement had a value of 91.79 N for the RVE and 108.2 N for the Mori-Tanaka model.

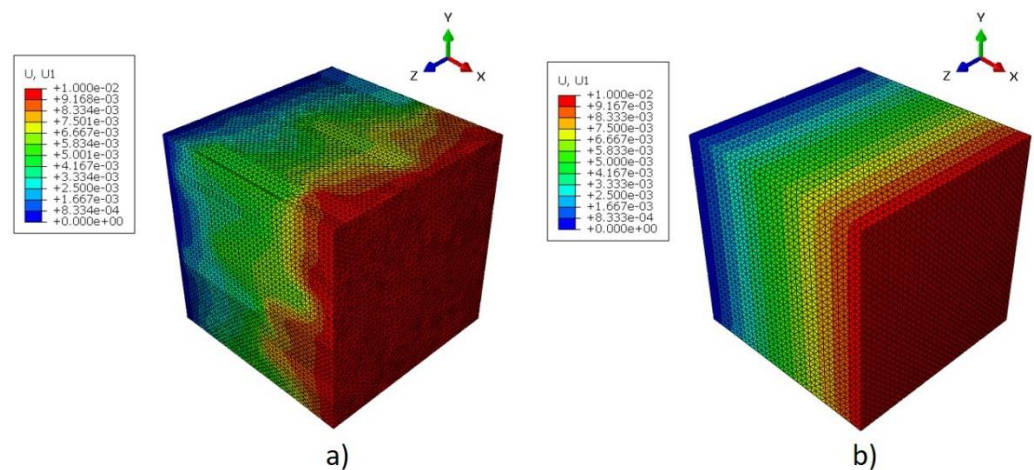


Figure 5. Displacement field of: a) RVE model; b) Mori\_Tanaka model.

Young's modulus of RVE is 9179 MPa and 10 820 MPa of Mori-Tanaka model. The Young's modulus results are slightly different. It is difficult to specify what caused this difference in results. One possibility is that the composite was reinforced with randomly generated discontinuous fibers, which caused a significant complication in homogenizing the material. It is reasonable to think that if the composite had been reinforced with regularly aligned continuous fibers the results of both homogenizations would have been much more accurate and thus the difference between the results would have been either very small or none.

#### 4. Conclusion

The goal of this paper was to homogenize the composite material by two different homogenization methods and to compare the results of Young's modulus. The obtained results shows that both homogenization methods were able to homogenize the composite approximately equally. However, it cannot be stated whether this composite is homogenized correctly, as this study was purely numerical and no real samples of the composite material were observed experimentally. This means that the results from the numerical analysis are not experimentally verified and so their correctness cannot be unequivocally confirmed. Homogenization is based on an approximate estimation of material properties and should be compared with experimental results.

**Acknowledgments:** This research was funded by Scientific Grant Agency of the Ministry of Education and Science of the Slovak Republic and the Slovak Academy of Sciences, grant number VEGA 1/0500/20 "Investigation of mechanical properties of materials with complex internal structure by numerical and experimental methods of mechanics" and KEGA 018TUKE-4/2020 "Increasing of professional and language knowledge and abilities of students by teaching of subjects of technical mechanics in English".

**Conflicts of Interest:** The authors declare no conflict of interest.

#### References

1. Barbero EJ. *Introduction to composite materials design*, 3rd ed.; Taylor & Francis: Boca Raton, Florida, 2017; pp. 1-5.
2. Ortolano J.M.; Hernández J.A.; Oliver J. *A Comparative Study on Homogenization Strategies for Multi-Scale Analysis of Materials*, 1<sup>st</sup> ed.; International Center for Numerical Methods in Engineering: Barcelona, Spain, 2013, pp. 9-87
3. Latypov M.I.; Toth L.S.; Kalidindi S.R. Materials knowledge system for nonlinear composites. *Computer Methods in Applied Mechanics and Engineering* **2019**, Volume 346, pp. 180-196.
4. Otero F.; Oller S.; Martínez X.; Salomón O. Numerical homogenization for composite materials analysis. Comparison with other micro mechanical formulations. *Composite Structures* **2015**, Volume 122, pp. 405-416.
5. Chatzigeorgiou G. Study of multilayered composites through periodic homogenization and Mori–Tanaka methods. *Mechanics of Materials* **2022**, Volume 164, pp. 104 - 110.
6. Caporale A.; Luciano R.; Sacco E. Micromechanical Analysis of Interfacial Debonding in Unidirectional Fiberreinforced Composites. *Computers and Structures* **2006**, Volume 84, pp. 2200-2211.
7. Dekys V.; Kopas P.; Sapieta M.; Stevka O. A Detection of Deformation Mechanisms using Infrared Thermography and Acoustic Emission. *Applied Mechanics and Materials* **2014**, Volume 474, pp. 315-320.
8. Riecky D.; Zmindak M.; Pelagic Z. Numerical Finite Element Method Homogenization of Composite Materials Reinforced With Fibers. *Communications - Scientific letters of the University of Zilina*, 16(3A), 2014, pp. 142-147.
9. Harper L.T.; Qian C.; Turner T.A.; Li S.; Warrior N.A. Representative volume elements for discontinuous carbon fibre composites – Part 1: Boundary conditions. *Composites Science and Technology* **2012**, Volume 72, pp. 225-234.
10. Tian W.; Qi L.; Zhou J.; Liang J.; Ma Y. Representative volume element for composites reinforced by spatially randomly distributed discontinuous fibers and its applications. *Composite Structures* **2015**, Volume 131, pp. 366-373.
11. González C.; Segurado J.; LLorca J. Numerical simulation of elasto-plastic deformation of composites: evolution of stress microfields and implications for homogenization models. *Journal of the Mechanics and Physics of Solids* **2004**, Volume 52, pp. 1573-1593.
12. Pierard O.; González C.; Segurado J.; LLorca J.; Doghri I. Micromechanics of elasto-plastic materials reinforced with ellipsoidal inclusions. *International Journal of Solids and Structures* **2007**, Volume 44, pp. 6945-6962.
13. Tian W.; Qi L.; Su C.; Liang J.; Zhou J. Numerical evaluation on mechanical properties of short-fiber-reinforced metal matrix composites: Two-step mean-field homogenization procedure. *Composite Structures* **2016**, Volume 139, pp. 96-103.
14. Song Z.; Peng X.; Tang S.; Fu T. A homogenization scheme for elastoplastic composites using concept of Mori-Tanaka method and average deformation power rate density. *International Journal of Plasticity* **2020**, Volume 128, 102652.



# Analysis of the sound of selected automobile powertrains using psychoacoustic methods

Kristián Pástor <sup>1\*</sup>, Miroslav Badida <sup>2</sup>, Alžbeta Nováková <sup>3</sup> and Anna Badidová <sup>4</sup>,

<sup>1</sup> Technical University of Košice, Faculty of Mechanical Engineering, Department of Environmental Engineering; [kristian.pastor@tuke.sk](mailto:kristian.pastor@tuke.sk)

<sup>2</sup> Technical University of Košice, Faculty of Mechanical Engineering, Department of Environmental Engineering; [miroslav.badida@tuke.sk](mailto:miroslav.badida@tuke.sk)

<sup>3</sup> Technical University of Košice, Faculty of Mechanical Engineering, Department of Environmental Engineering; [alzbeta.novakova@tuke.sk](mailto:alzbeta.novakova@tuke.sk)

<sup>4</sup> Technical University of Košice, Faculty of Mechanical Engineering, Department of Environmental Engineering; [anna.badidova@tuke.sk](mailto:anna.badidova@tuke.sk)

\* Correspondence: [kristian.pastor@tuke.sk](mailto:kristian.pastor@tuke.sk); Tel.: 055 602 2721

**Abstract:** The article is focused on the assessment of psychoacoustic parameters in the interior of selected types of vehicles. Measurements were made on vehicles with gasoline, diesel and electric engines. Five psychoacoustic parameters were measured and a psychoacoustic head was used for the measurement. The measurements were carried out at different speeds and the measured values were processed and evaluated. The measurements showed the effect of motorization and car speed on selected psychoacoustic parameters. They also showed that the electric car achieved the lowest values of the evaluated parameters in most cases.

**Keywords:** Sound; noise; psychoacoustics; car; powertrain;

## 1. Introduction

Different types of vehicle powertrains have different effects on the environment. In addition to the positive aspects of transport, one can also observe the negative impact of the development of motoring, mainly in connection with the production of more emissions and the generation of sound, or noise, which significantly negatively affects the environment, the health of the car crew, but also the health of the population in general.

## 2. Psychoacoustics as a tool for creating acoustic design of cars

Psychoacoustics, as a relatively new field of acoustics, deals with the subjective perception of sound, its effect on a person and the analysis of its possible effects. A significant area of psychoacoustics is the so-called experimental psychoacoustics, in which the subjective reaction of a person to the investigated sound is evaluated.

One of the practical applications of psychoacoustics is the evaluation of sound quality. Driving comfort in cars is currently becoming an important demand of customers [1][2].

Marketing studies have shown that customers pay close attention to sound quality not only in situations where sound is the primary object of interest, but also when sound is only a side effect of the product's operation [3].

Sound quality assessment is carried out in two ways, which can be classified into two categories:

- subjective psychoacoustic assessment methods,
- objective psychoacoustic assessment methods.

### Subjective psychoacoustic methods

There are several ways to implement the sound quality evaluation process, from formal evaluation to informal listening of the recording (listening, respectively listening).[1][4][5]

Psychoacoustic methods can include:

- classic psychoacoustic methods,
- scaling psychoacoustic methods,
- adaptive psychoacoustic methods.

### Objective psychoacoustic methods

In recent times, for the purposes of psychoacoustic measurements, technical means have also been increasingly promoted. They are highly sophisticated systems, developed to measure selected psychoacoustic parameters with highly specialized software support.

Perceiving sound through two ears is called binaural hearing. It is the ability to hear sounds from the left ear and the right ear in parallel and the ability to locate the direction of the incoming sound. This type of hearing strongly depends on the geometric parameters of the human body (ears, head and trunk). Important and highly effective technical means for measuring psychoacoustic parameters include the so-called "artificial head" (or psychoacoustic head) (Fig. 1). It is an identical form with a human head. The psychoacoustic head has two microphones that are installed in the ears. It is characterized by the same acoustic and auditory properties as the human head. The goal is to achieve a state so that the evaluator of the quality of the sound event, who listens to the sound recordings obtained from the psychoacoustic headset, has the impression that he is part of the space of the acoustic event [1][6][7][8].



Figure 1 Examples of making psychoacoustic heads

### 3. Measurement of selected psychoacoustic parameters in the car interior

The aim of the measurements performed using a binaural measuring device, the so-called of the psychoacoustic head was to determine the values of selected psychoacoustic parameters under the conditions of different car speeds when using gasoline, diesel and electric car drives. For the needs of the research, the psychoacoustic parameters loudness (N), sharpness (S), roughness (R), tonality (T) and strength of fluctuation were selected, which were measured and subsequently evaluated using sound signals. For the purposes of the psychoacoustic experiment, sound signals obtained at speeds of 50 km/h, 90 km/h, 110 km/h and 130 km/h were used.

The subject of the research were three passenger cars of the same brand, same model, but with different engines (gasoline, diesel, electric). Specifically, it is the Volkswagen Golf Edition Highline 1.5 TSI ACT 6G – 110 kW/150 hp, the Volkswagen Golf 2.0 TDI – 100 kW/150 hp and the Volkswagen eGolf – 100 kW/136 hp.

For the purpose of measuring selected psychoacoustic parameters, a binaural measuring apparatus (psychoacoustic head) with a recording unit, a two-channel binaural

equalizer BEQ II and a laptop with the appropriate software equipment ArtemiS (Advanced Research Technology for Measurement and Investigation of Sound and Vibration) was used.

As part of the psychoacoustic experiment, measurements of selected psychoacoustic parameters were carried out on VW Golf diesel, VW Golf petrol and VW eGolf electric vehicles. The psychoacoustic head was placed in the interior of the vehicle in the position of the passenger on the front seat. The location of the psychoacoustic head in the tested vehicles is shown in Fig. 2.



**Figure 2** Placement of the psychoacoustic head in the vehicle

Measurements of selected psychoacoustic parameters (sharpness, harshness, tonality, loudness and power of oscillation) were carried out at steady speeds (50 km/h, 90 km/h, 110 km/h and 130 km/h) on the R4 expressway Košice - Milhošť. The audio recordings obtained were processed, unwanted and random ambient sounds (e.g. passing nearby cars, etc.) were removed. Monitored psychoacoustic parameters were determined using the evaluation software ArtemiS.

#### 4. Results of measurements

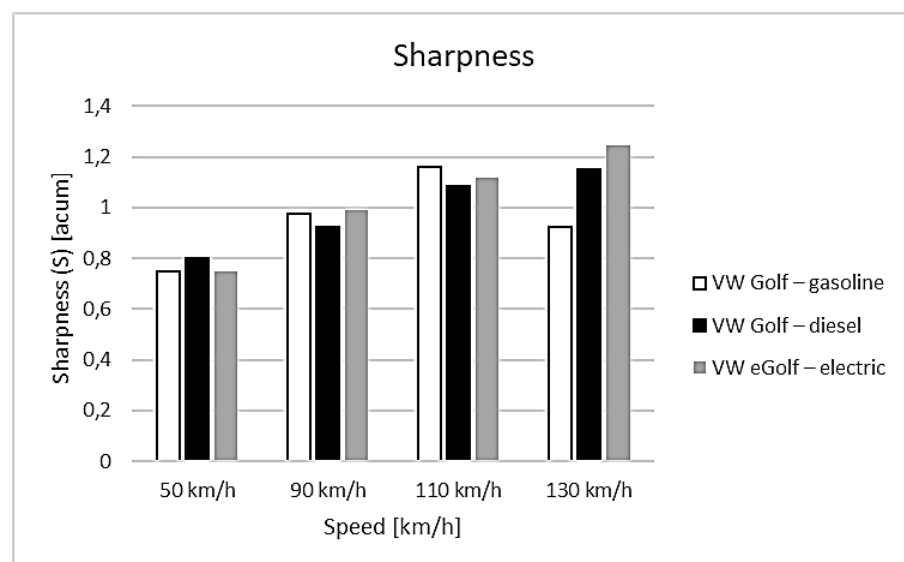


**Figure 3** Dependence of sharpness on vehicle speed

Based on the results obtained from the performed sound measurements, it can be concluded that the psychoacoustic parameter "sharpness" with increasing speed tends to grow almost linearly for all types of motorization. A certain anomaly is that the sharpness

parameter at a speed of 130 km/h. has a decreasing tendency. When using a gasoline engine, the graph shows that the sharpness value is mostly higher for all speeds with a gasoline engine up to a speed of 130 km/h, when the highest sharpness value was measured with an electric motor. The sharpness values of the diesel engine constantly move between the sharpness values for gasoline and electric motors (Fig. 3).

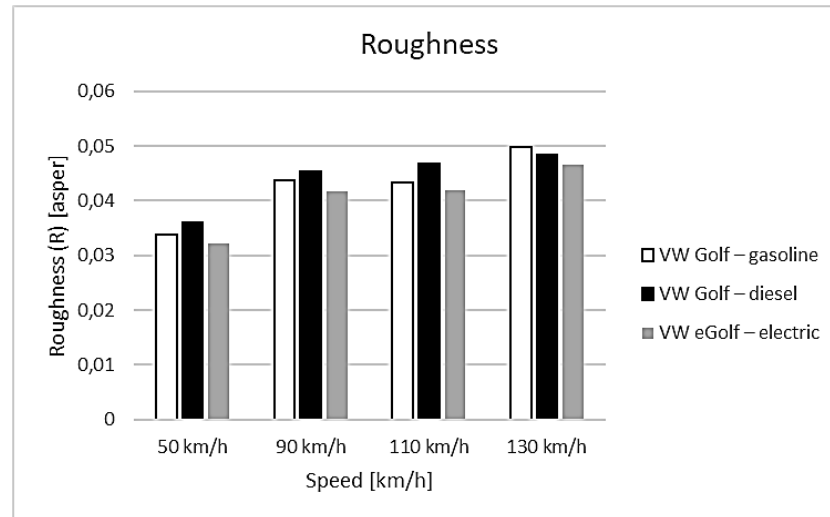


Figure 4 Dependence of roughness on vehicle speed

Based on the obtained results from the measurement of the psychoacoustic parameter "roughness", it can be concluded that this parameter has a growing tendency for all types of motorization with increasing speed. This fact applies up to a speed of 110 km/h. The highest roughness value can be observed for the diesel engine, lower for the gasoline engine. And the lowest for an electric motor. At a speed of 130 km/h. however, the order changes and the gasoline engine shows the smallest sharpness value, the diesel engine the lowest, and the electric engine the lowest (Fig. 4).

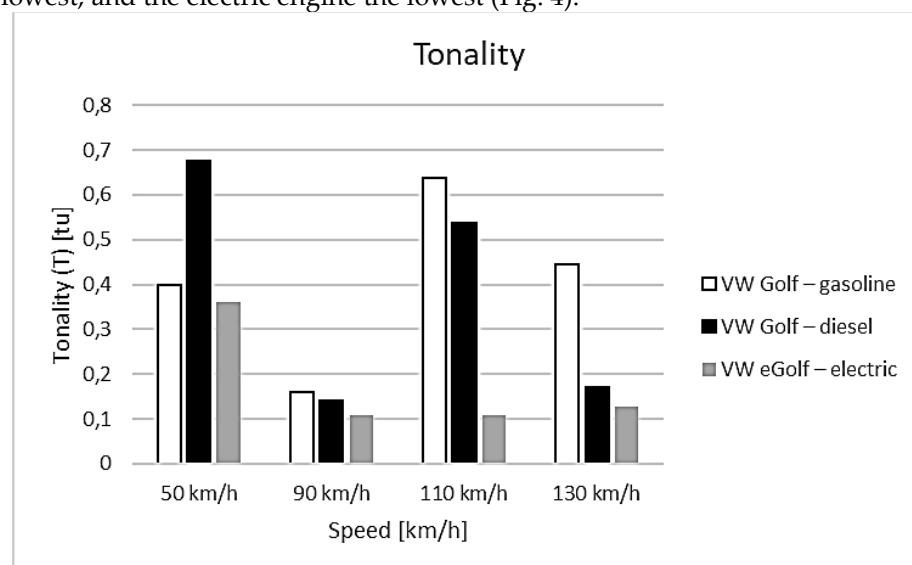


Figure 5 Dependence of tonality on vehicle speed

Measurements of the psychoacoustic parameter "tonality" have shown that the tonality of a car with a diesel engine reaches the highest values at lower speeds. Subsequently, it tends to gradually decrease at higher speeds from 130 km/h. rise again. In the case of the gasoline engine, the lowest tonality value was found at a speed of 90 km/h. The highest value of the monitored parameter was found at a speed of 110 km/h. with increasing

speed, the tonality tended to decrease. In a car with an electric drive, the psychoacoustic parameter tonality increases at lower speeds, decreases with increasing speed, and is almost constant at higher speeds (Fig. 5).

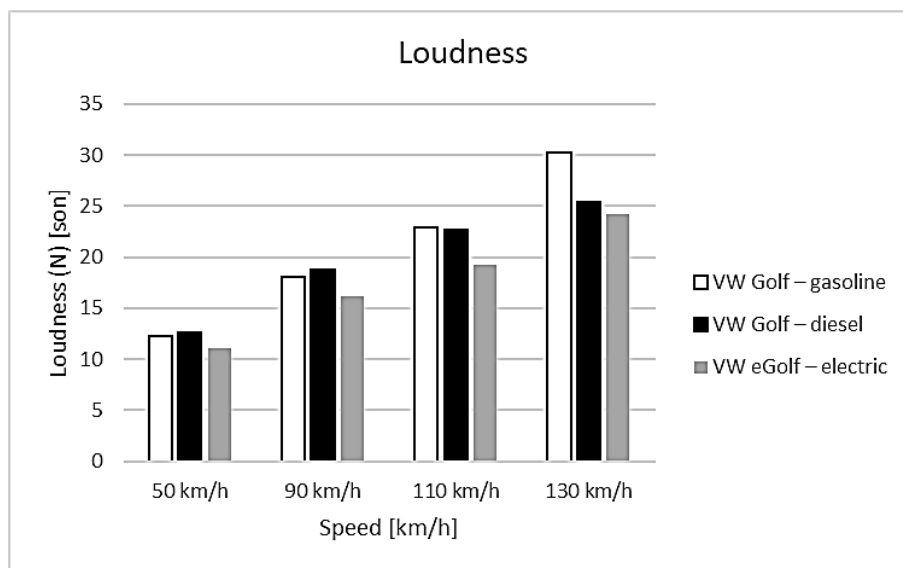


Figure 6 Dependence of loudness on vehicle speed

Based on the sound measurements of cars with different engines, it can be concluded that the psychoacoustic parameter "volume" increases linearly with increasing speed in the case of all three drives. At lower speeds, the highest values are achieved by the diesel engine, lower values by the gasoline engine and the lowest by the electric engine. At higher speeds, the psychoacoustic parameter volume is almost the same for diesel and gasoline engines. With electric motorization, the volume value is lower. At speeds from 130 km/h. the volume rises in the case of petrol engine (it is the highest). Lower values are achieved by the diesel motorization and the lowest values by the electric motorization (Fig. 6).

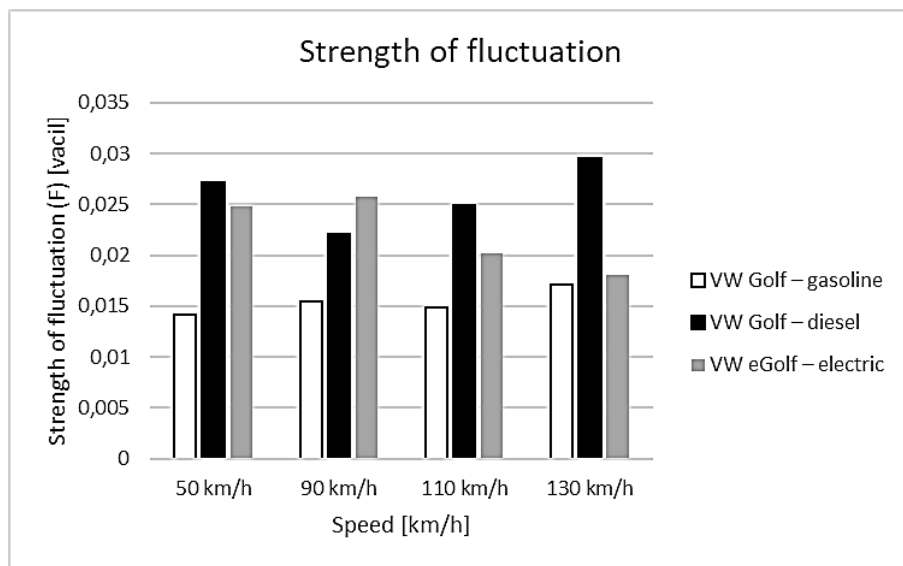


Figure 7 Dependence of strength of fluctuation on vehicle speed

The results of measurements of the psychoacoustic parameter " strength of fluctuation " proved that the observed parameter in the case of gasoline engines is stable and

almost constant. In the case of a diesel engine, the parameter at a speed of 90 km/h. decreases and subsequently increases linearly with increasing speed. In the case of electric motorization, the monitored parameter rises again with increasing speed. After reaching a speed of approximately 90 km/h. the monitored parameter has a linear decreasing tendency (Fig. 7).

### Conclusion

On the basis of the presented results, it can be concluded that the values of the psychoacoustic parameters are influenced by the speed of the vehicle as well as the motorization of the vehicle. For most parameters, the values of psychoacoustic parameters increase with increasing speed. However, from the motorization point of view, it affects individual parameters differently and at different speeds. From the point of view of motorization, a direct proportionality between motorization and the values of psychoacoustic parameters is not visible.

### Acknowledgment

The contribution was developed within the framework of the grant project of the Ministry of Education of the Slovak Republic KEGA 013TUKE-4/2022 Implementation of the results of scientific and research activities into the processing of a modern university textbook "Psychoacoustics - sound quality and acoustic design of products" and the VEGA project No. 1/0485/22 Development methods of increasing the acoustic quality of the sound of products by visualization and psychoacoustic methods.

### References

1. Badidová, A; Moravec, M.; Badida, M; Sobotová, L.: Research of sound quality in interior of automobile by psychoacoustics evaluation methods. In.: Proceedings ICEEE, 2017, Óbuda University, Budapest, Hungary, 158 – 162 p.
2. Badidová, A.; Moravec, M.; Sobotová, L.; Analysis of Various Sound Sources Inside and Outside the Vehicle, 2019. In: Scientific Letters of Academic Society of Michal Baludansky. - Košice (Slovensko): Akademická spoločnosť Michala Baludanského Vol. 7, No. 6 (2019), p. 17-24 [print]. - ISSN 1338-9432
3. Badidová, A.; Sobotová, L.; Badida, M.; Psychoakustika v technickej diagnostike, 2020. In: Strojárstvo/Strojnírenství = Engineering Magazine. - Žilina (Slovensko) : Media/ST Vol. 24, No. 10 (2020), pp. 60-61 [print]. - ISSN 1335-2938
4. Rychtáriková, M.: Psychoakustické testy v stavebnej akustike. Monee, IL, USA, 2020, ISBN 978-80-971993-6-4
5. Zwicker, E.: Psychoakustik. Springer Verlag, Berlin, Heidelberg, 2009, 198 p.
6. Andrew, Ch.; Randolph, C.: Initial investigation into the psychoacoustic properties of small unmanned aerial system noise, 2015, 21 p.
7. Fastl, M.; Zwicker, E.: Psycho-Acoustics. Facts and Models. Springer, 2007, 462 p. ISBN 0720-678
8. Lentz, J., J.: Psychoacoustics. Perception of Normal and Impaired Hearing with Audiology Applications. Plural Publishing, Inc., 2020, 227 - 236 p., ISBN 159-7-56989-5
9. Badidová, A. 2011. Návrh metodiky posudzovania kvality zvuku v interiéri automobilu psychoakustickými metódami [Doctoral dissertation]. Košice: technická univerzita v Košiciach [s. n.], 2020. 187 p.



# Ergonomic Assessment of Physical Load in the Mechanical Engineering Industry

Denisa Porubčanová<sup>1\*</sup>, Kristína Lengyelová<sup>2</sup>, Miroslav Čička<sup>3</sup>, Ferdinand Kóča<sup>4</sup> and Michaela Balážiková<sup>5</sup>

<sup>1</sup> Technical University of Košice, Faculty of Mechanical Engineering, Department of Safety and Quality; denisa.porubcanova@tuke.sk

<sup>2</sup> Technical University of Košice, Faculty of Mechanical Engineering, Department of Safety and Quality; [kristina.lengyelova@tuke.sk](mailto:kristina.lengyelova@tuke.sk)

<sup>3</sup> Technical University of Košice, Faculty of Mechanical Engineering, Department of Safety and Quality; miroslav.cicka@tuke.sk

<sup>4</sup> Technical University of Košice, Faculty of Mechanical Engineering, Department of Safety and Quality; ferdinand.koca@tuke.sk

<sup>5</sup> Technical University of Košice, Faculty of Mechanical Engineering, Department of Safety and Quality; michaela.balazikova@tuke.sk

\* Correspondence: [denisa.porubcanova@tuke.sk](mailto:denisa.porubcanova@tuke.sk)

**Abstract:** The paper is devoted to ergonomic assessment of physical load during the work and is based on the current issue of frequent occurrence of injuries of the support and movement system due to inappropriate movements and positions at work, which has a consequent impact on the employee and also on the society as a whole. Many methods are currently used to measure and evaluate workload, which must take into account the specific type of work to be evaluated. An example of a suitable system for addressing the possibility of workload assessment is the CAPTIV system. However, when trying to set the right thresholds to meet our standards, we found that Decree 542/2007 Coll. and STN EN 1005-4+A1, which are applicable in our territory, do not correspond in the area of workload assessment with regard to risk positions.

**Keywords:** ergonomics, workload, standard

## 1. Introduction

The increasing pace of work and the ever-increasing demands on workers are leading to higher rates of accidents and sick leave due to disproportionate body strain. Musculoskeletal disorders (MSDs) have become a phenomenon in this area in recent years. A significant contributing factor is that workers are often placed in positions requiring monotonous, unilateral movements, cyclical loading of the same body segments, or work in unnatural or loading positions. However, as technologies and techniques develop and advance, the possibilities for measuring and evaluating workload are also improving, which should lead to improved safety and the development of appropriate protective work equipment to help reduce the effects of workload on the human body and health, as well as to assist in planning the correct workplace layout or training of workers.

## 2. Current Status of the Issue

The latest surveys and statistics on occupational diseases in the territory of Slovakia for the year 2021 show an upward trend in the incidence of occupational diseases. Compared to 2020, an increase in the number of occupational diseases by 169 cases was recorded. The total number of detected cases for 2021 is 423. The most frequently occurring type of disease was just a disease of the support and musculoskeletal system, which was recorded in 175 patients, representing more than 41.3%. This is followed by infectious diseases, vibration sickness and hearing disorders [1].

Occupational diseases were most common in health care workers, specifically in 163 cases, which is a significant proportion compared to other industries. The other unspecified manufacturing industry ranked second with 38, followed by manufacture of fabricated metal structures except machinery and equipment and manufacture of motor vehicles, trailers and semi-trailers, with an identical number of 37 workers with an occupational disease. According to the NCZI, occupational diseases in 2021 occurred mostly in the 50-59 age group [1].

These statistics prove that the increase in the incidence of work-related injuries to the musculoskeletal system is a hot topic that not only impacts the health of employees, but ultimately affects the economy, operations and productivity of the plant itself, as well as impacting the overall economy of the state. Therefore, we consider it important to ensure that suitable working conditions are provided, with the correct assessment of the workload and working positions being necessary.

## 3. Workload Measurement and Assessment

Various tools, systems, scales and standards are currently used for ergonomic workload assessment. Most rating scales and standards are based on long-term research that establishes appropriate working body positions. However, these are not the only aspects influencing the development of MSDs.

MSDs usually arise as a result of the interaction of multiple factors over time. The influencing factors can be divided into physical, biomechanical and also organisational, psychosocial. The first group includes the aforementioned uncomfortable, incorrect positions, repetitive movements at work, handling of loads, the influence of vibrations, light and environmental temperature. The category of organisational and psychosocial risk factors is made up of high work demands, high work pace, long shifts and lack of breaks, discrimination and poor workplace relations, as well as low job satisfaction. All of these factors work together with the employee's medical and physical history, physical endurance and lifestyle to create a risk of developing a musculoskeletal disorder [2].

For the measurement and ergonomic assessment of workload, various types of equipment, systems and rating scales are used in practice, which allow the determination of correct, conditionally acceptable and unacceptable positions, or by means of software processing, it is also possible to determine the percentage of time spent in the given positions, thus obtaining a graphical evaluation of the measurement. The methods used for MSDs assessment can be divided into 3 groups, namely direct, semi-direct and indirect. Direct methods are those that use different types of sensors for measurement. Semi-direct methods use

assessment by computer programs, but based on video recordings and photographs. Indirect methods refer to various forms of questionnaires [3].

A typical indirect method is the Nordic Questionnaire, which is based on the worker's subjective answers regarding his/her work and problems with individual body segments. This is a frequently used method. Semi-direct methods can be e.g. RULA, REBA, OWAS, etc., which are based on standardized scales and require video or photographs for evaluation [4]. An example of a direct method is the CAPTIV system, which allows the application of sensors directly on the body of the observed subject and allows the subsequent processing of the measured data into graphical form. The development of new systems is moving towards the use of wireless sensing systems, interfaced with appropriate software for processing and evaluation of the measurements. In addition to TEA CAPTIV, companies such as Xsens, VelocityEHS Industrial Ergonomics or EWI works, which has even developed a system that enables the assessment of movement and posture remotely, offer ergonomic systems for the assessment of movement. It is sufficient to take a video and then send it to the software, which evaluates the movements according to set standards [5-7].

#### **4. CAPTIV**

The CAPTIV system is a multisensory system that allows the measurement of various parameters necessary for ergonomic workload assessment. For the purpose of measurement in our department we have chosen to measure movements and postures at work, we will also work with EMG sensors and also with ECG sensors. TEA CAPTIV T-SENS MOTION sensors were used for the measurements that have been performed so far in the department. The course of the measurements and the results were published in paper [8].

These sensors belong to the group of M-IMU sensors. It is an inertial measurement unit which is extended by a magnetometer. Using these devices we can estimate both translational and rotational motions. Conventional IMUs contain a gyroscope and an accelerometer for measuring angular velocity and acceleration. However, it is typical for gyroscopes to drift, which causes measurement errors. The combination with a magnetometer is used precisely for the purpose of compensating for drift and thus for refining the measurement results. However, for M-IMU sensors, careful control of the surrounding environment is necessary to ensure that no ferromagnetic materials are present near the measurement site that cause signal interference. Fusion algorithms are used for accurate estimation of the position and motion of the body in space [9].

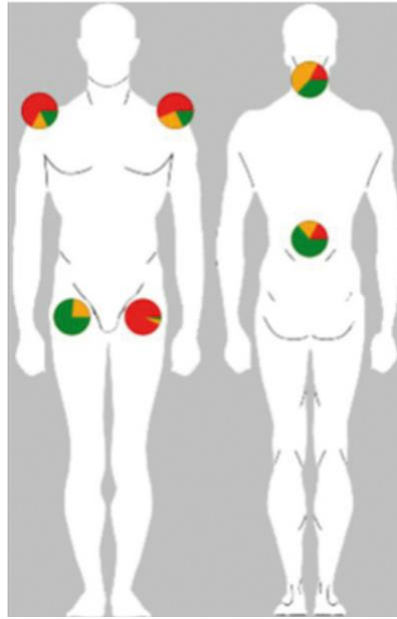


Figure 1: Graphical evaluation of the percentage of working positions using the CAPTIV system. Green indicates a correct position, yellow a conditionally acceptable position and red an unacceptable position that is directly associated with the risk of MSDs and therefore correction of this position is required [10]

### 5. Assessment of Parameters Obtained Using the CAPTIV System and Differences in Applicable Standards

The CAPTIV software itself is used to evaluate the parameters obtained by the TEA CAPTIV T-SENS MOTION sensors, which have pre-built threshold values for conditionally acceptable and unacceptable positions at work. As the values are pre-set to be subject to the standards in force in the territory of France - AFNOR and INRIS - the software allows the limit values to be changed to be subject to the standards and legislation in force in the specific country where the measurements are carried out and evaluated. However, we have encountered an obstacle in this area of work in the form of disagreements on standards. The European standard STN EN 1005-4+A1 and the decree 542/2007 Coll. are valid in Slovakia. Both of these standards set the limit values of positions at work, but they differ in many parameters and also in the starting positions, from which the subsequent determination of the ranges of movements is based. Thus, the question arises as to which standard should be followed when evaluating workload measurements so that these evaluations are correct and therefore publishable and usable for practical application [11,12]. We also compared these standards with the CAPTIV system preset values. These also differ in most parameters.

A significant difference occurs in the assessment of head and neck forward bending, where Decree 542/2007 sets 25° as the limiting angle, STN EN 1005-4+A1 sets the limit at 40°, while CAPTIV considers 30° as the limit. Similarly, differences in the range of 5-10° arise in the assessment of side bend. Interestingly, STN EN 1005-4+A1, unlike the decree, does not mention the concept of backward bend [11,12].

Agreement arises in the assessment of unacceptable positions for static work in the trunk area, where both standards refer to a 60° angle as the limiting angle of forward bend. When determining conditionally acceptable positions, the standards agree in several parameters; CAPTIV has deviations in most positions [11,12].

Regarding the assessment of upper and lower limb positions, it can be deduced that the standards do not agree in the style of assessment; for the lower limb area even STN EN 1005-4+A1 does not provide a specific assessment. In this respect, the CPATIV is a more reliable assessment tool as it can determine inappropriate positions for these segments as well, even with much more consideration of the biomechanics of the limbs and also the presence and work of the individual joints [11,12].

Therefore, we consider it necessary to address the issue of ergonomic assessment of workload not only in practical terms, i.e. by measuring and specifying appropriate measures to minimize risks, but also in legislative terms, so that these measurements and measures are also covered by uniform legislation, which is based on the conducted long-term research and at the same time takes into account the needs of the worker and the biomechanics of the human body.

### Discussion

Workload assessment is nowadays a very important aspect for the protection of worker's health and also for the support of the company's economy. For a proper assessment, a suitably selected tool or system and the determination of risk thresholds are necessary, forming the basis for the subsequent implementation of protective measures. These values should comply with the standards in force in the country concerned. Decree 542/2007 Coll. applies in the territory of the Slovak Republic, and at the same time the standard STN EN 1005-4+A1, which delimit the hazardous working positions, but the data in these standards are not identical. We therefore consider it necessary to review the legislation in force, in accordance with the proven facts, and also taking into account human biomechanics, so as to ensure the protection of workers' health and also to minimise workplace risks which, especially with prolonged exposure, lead to damage to the body and the development of occupational diseases.

**Acknowledgments:** The paper was prepared within the framework of the grant project of the Ministry of Education APVV-19-0367 Framework Integrated Process Safety Management Approach for Smart Enterprise.

### References

1. National Health Information Centre (NCZI). (18 May 2022). NCZI - Occupational diseases or risk of occupational disease. Available on the Internet: [www.nczisk.sk](http://www.nczisk.sk): [https://www.nczisk.sk/statisticke\\_vystupy/tematicke\\_statisticke\\_vystupy/choroby\\_povolania\\_alebo\\_ohrozenia\\_chorobou\\_povolania/Pages/default.aspx](https://www.nczisk.sk/statisticke_vystupy/tematicke_statisticke_vystupy/choroby_povolania_alebo_ohrozenia_chorobou_povolania/Pages/default.aspx)
2. European Agency for Safety and Health at Work. (2021). OSHA Europa - Musculoskeletal disorders. Available on the Internet: [www.osha.europa.eu](http://www.osha.europa.eu): <https://osha.europa.eu/en/themes/musculoskeletal-disorders>

3. Gómez-Galán, M.; Pérez-Alonso, J.; Callejón-Ferre, Á.J.; López-Martínez, J. (8 August 2017). Musculoskeletal disorders: OWAS review. Available on the Internet: PubMed: <https://doi.org/10.2486/indhealth.2016-0191>
4. Nguyen, J.K.; Le, D.K. (2017). Working analysis and design using ergonomics methods and simulation software in brick production process at Truong Viet Company. *Environmental Technology and Innovations* (p. 263-267). London: Taylor&Francis Group.
5. Xsens Company. (13. 11 2022). Xsens - Wearables. Available on the Internet: [www.xsens.com](http://www.xsens.com): <https://www.xsens.com/wearables>
6. Velocity EHS. (15. 11.2022). Velocity EHS - The Benefits of Sensorless Motion Capture for Ergonomics Assessments. Available on the Internet [www.ehs.com](http://www.ehs.com): <https://www.ehs.com/2021/06/the-benefits-of-sensorless-motion-capture-for-ergonomics-assessments/>
7. Golabchi, A. (8 11. 2022). EWIworks-Vision-Based Motion Capture Technology: A New Era for Ergonomics. Available on the Internet: [www.ewiworks.com](http://www.ewiworks.com): <https://www.ewiworks.com/blog/vision-based-motion-capture-technology-ergonomics/>
8. Onofrejová, D.; Balážiková, M.; Glatz, J.; Kotianová, Z.; Vaškovičová, K. (2022). Ergonomic Assessment of Physical Load in Slovak Industry Using Wearable Technologies. *Applied Sciences* [online]. 12 (7), 3607; <https://doi.org/10.3390/app12073607>
9. Carnevale, A. et al. (15.11.2019). Wearable systems for shoulder kinematics assessment: a systematic review. *BMC Musculoskeletal Disorders*. 20 (546), p.2-24; doi:<https://doi.org/10.1186/s12891-019-2930-4>
10. Balážiková, M.; Onofrejová, D.;Tomašková, M.; Vaškovičová, K. (22 April 2022). Meranie fyzickej záťaže ako súčasť prevencie pri práci so strojovými zariadeniami. *ATP journal*. Available on the Internet [https://www.atpjournalsk.com/rubriky/prehľadove-clanky/meranie-fyzickej-zataze-ako-sucast-prevencie-pri-praci-so-strojovymi-zariadeniami.html?page\\_id=34678](https://www.atpjournalsk.com/rubriky/prehľadove-clanky/meranie-fyzickej-zataze-ako-sucast-prevencie-pri-praci-so-strojovymi-zariadeniami.html?page_id=34678)
11. Standard STN EN 1005-4+A1
12. Decree of the Slovak Republic No. 542/2007 Coll.



# THE QUALITY EVALUATION OF THE CUTTING SURFACE BY MICROSCOPIC ANALYSIS

Vladimír Rohal<sup>1</sup>, Emil Spišák<sup>2</sup>

<sup>1</sup> Department of Technology, Materials and Computer Supported Production, Faculty of Mechanical Engineering, Technical University of Košice, Mäsiarska 74, 040 01 Košice, Slovakia; vladimir.rohal@tuke.sk (V.R.); emil.spisak@tuke.sk (E.S.)

\* Correspondence: vladimir.rohal@tuke.sk; Tel.: +421556023519

**Abstract:** In this article the influence of the cutting gap on the quality of the cutting surface is described. In the first part, the individual parameters of electrical steel sheets given by the manufacturers themselves are presented. The second part of the paper is devoted to the experimental verification of the influence of the cutting gap on the quality of the cutting surface. The experimental results show that the cutting gap has a major influence on the formation of the cutting surface and its shape. It also influences the actual hardening of the material during cutting and the distribution of the individual zones on the cutting surface. In the experimental part of this work, the results of the shear zone size, which is one of the main parameters for evaluating the quality of the cutting surface, are recorded. It is characterized as the ratio of the shear zone height to the fracture zone height. Cutting materials in a tool with a cutting gap of 3% of the material thickness results in a reduction in the size of the shear zone, especially for materials with higher ductility values. When cutting sheet in a tool with a cutting gap of 5 and 7 % of the material thickness, the shear zones were reduced for all materials examined.

**Keywords:** cutting gap, cutting surface, shear zone, fracture zone, electrical steel

## 1. Introduction

Today, the emphasis is on efficiency and optimization in all directions, whether it is the cost of individual production operations or the optimization of individual aspects of production and technological processes, which ultimately determine the competitiveness of products in the market.

At present, steels with higher strength properties are coming to the market and used in the industry, so it is necessary to thoroughly investigate their behavior and use suitable tool steels for their processing, machining. Since cutting is one of the most frequently used surfaces forming operations, it is necessary to know its principles, regularities, and correct setting of conditions during the cutting process.

Silicon steels are the essence of electrical appliances, and they provide the best combination for electricity distribution and transmission. Desired properties of these steels are low magnetic losses, high permeability, and induction and low magnetostriction. Low magnetic losses reduce heat generation and power consumption, a high permeability and induction result in reduced size and mass of the parts, and low magnetostriction decreases the noise (manifested as buzzing) in transformers and large capacity machines. [1]

The silicon content increases the electrical resistance, reduces the electrical losses caused by eddy currents and magnetic hysteresis. Alloys of iron and silicon, characterized as magnetic hard, are used for transformer sheets, while for dynamo sheets, materials characterized as magnetic soft are used. These are characterized by a simple change in the direction of magnetization and low energy losses associated with remagnetization.

Recently, sheet metal has been extensively used in various industries such as electronics, automotive, aerospace, etc. Most commonly, shearing is used as the primary process to reduce the rolled sheet to a shape as close as possible to the desired product shape. Other manufacturing processes must be used to achieve the final shape of the product. In most cases, the most accurate dimensions and the shortest product manufacturing process are required, which has a favorable impact on the production costs and the usability of the product. During the shearing process, unwanted burr formation occurs on the shearing surfaces. The aim of every manufacturer is to produce semi-finished products with as few burrs as possible. [2]

Nowadays, the industry places various demands on components created by shearing. One of them is the requirement of a burr-free cutting edge, which allows better processing of components with a more economical result in the work process and their safer handling. Efforts are therefore being made to reduce burr formation to avoid subsequent deburring. Currently, this process is carried out in a further component processing step such as mechanical deburring [3], belt grinding [4], sliding surface grinding [5], or burr pressing [6]. Material removal during the shearing process results in lower dimensional accuracy [7]. All these additional technical processes are labor, time and cost intensive.

The shear cutting process is one of the most economical separation processes since it combines high production rates with low costs. The quality of the shear cut edge depends on the material properties, material thickness, die clearance, cutting edge radius, tool wear and shear cutting strategy. [8]

In general, the shearing surface of the materials that have undergone shear deformation due to the compressive stress of punch and die are composed of 4 parts: rollover, burnish zone, fracture zone and burr. An ideal shearing surface is created by 100% of the burnish zone, and without rollover, fracture zone or burr. At the beginning of the shearing process, elastic and plastic deformations usually occur, which subsequently produce rollover and burr. Burr after shearing process is the plastic deformity, which remains on the surface and lowers the products quality by influencing roughness and accuracy. In addition, burrs on the surface of inside or outside cut-outs can affect negatively to the cost efficiency of products and the safety of the workers. [9]

## 2. Materials and Methods

For the needs of experimental verification of cutting conditions of electrical sheets, 3 types of electrical steels from different manufacturers were used. The individual sheet metal parameters are recorded in the Table 1.

Table 1. Sheet metal parameters

Samples	Embraco designation	Dimension [mm]	Sheet thickness [mm]	Presence of coating Y/N
A	T.K. 037 M660-50K S5H Tökölt	1070x1050	0,50	Y
B	V.A. 036 S1S-IS450- 50K HE	1380x1050	0,50	Y
C	A.M. 036 S1S M450-50K	1130x1150	0,50	Y
D	034 USS S3S-M350-50A	880x1060	0,50	N
E	T.K 033 S1S-M450- 50PP	1050x1110	0,50	N

Electrical sheets were characterized (table 2) by a thickness of 0.5 mm, hardness at the level of 60 to 90 HRB, density at 7.65 to 7.85 g / cm<sup>3</sup>, tensile strength 380 to 620 N / mm<sup>2</sup> and an elongation of 10 to 25%.

Table 2. Characteristics of materials

Material designation	Sheet thickness [mm]	Hardness HBR	Density [g/cm <sup>3</sup> ]	Rolling direction characteristics	
				Tensile strength [N/mm <sup>2</sup> ]	Elongation [%]
S1S	0,50	65-85	7,75	380-550	10-20
S3S	0,50	75-90	7,65	520-620	10-20
S5H	0,50	60-80	7,85	380-490	10-25

The largest producers of electrical steel in Europe are ThyssenKrupp Bochum, Arcelor Mittal Luxemburg, VoestAlpine Austria, Wälzholz Hagen. As for the Asian producers operating on the European market, they are BaoSteel, WuGan and TaiYuan.

The reason for the chemical analysis (tab.3 - 7) was to make sure that the delivered semi-finished products had the same chemical composition as the one declared by the manufacturer for the semi-finished products

Table 3. Chemical composition of M660-50K steel in %

C	Mn	Si	P	S	Al	Cu	Ni	Cr	As	Ti	V
0.0042	0.339	0.171	0.088	0.0014	0.145	0.014	0.025	0.042	<0.001	0.005	<0.001
Nb	Mo	Co	Sn	Sb	W	B	Ca	Zr	N <sub>2</sub>	O <sub>2</sub>	Als
<0.002	0.003	<0.002	<0.002	<0.002	<0.003	<0.0002	0.001	<0.001	0.0027	0.0036	0.144

Table 4. Chemical composition of M450-50K HE steel in %

C	Mn	Si	P	S	Al	Cu	Ni	Cr	As	Ti	V
0.0059	0.506	0,574	0.03	0.0036	0.418	0.01	0.01	0.019	<0.01	0.001	<0.001
Nb	Mo	Co	Sn	Sb	W	B	Ca	Zr	N <sub>2</sub>	O <sub>2</sub>	Als
<0.02	<0.02	<0.02	0.02	<0.002	<0.03	<0.002	<0.002	<0.001	0.002	0.004	0.416

Table 5. Chemical composition of M450-50K steel in %

C	Mn	Si	P	S	Al	Cu	Ni	Cr	As	Ti	V
0.0026	0.609	0.148	0.089	0.0074	0.117	0.017	0.021	0.028	<0.001	0.001	0.001
Nb	Mo	Co	Sn	Sb	W	B	Ca	Zr	N <sub>2</sub>	O <sub>2</sub>	Als
<0.002	<0.002	<0.002	<0.002	<0.002	<0.003	0.0002	<0.0002	<0.001	0.0024	0.0021	0.115

Table 6. Chemical composition of M350-50A steel in %

C	Mn	Si	P	S	Al	Cu	Ni	Cr	As	Ti	V
0.0023	0.268	2.419	0.014	0.0054	0.388	0.014	0.006	0.022	<0.001	<0.001	<0.001
Nb	Mo	Co	Sn	Sb	W	B	Ca	Zr	N <sub>2</sub>	O <sub>2</sub>	Als
<0.002	<0.002	<0.002	<0.02	0.056	<0.003	<0.002	<0.002	<0.01	0.002	0.002	0.387

Table 7. Chemical composition of M450-50PP steel in %

C	Mn	Si	P	S	Al	Cu	Ni	Cr	As	Ti	V
0.003	0.209	1.630	0.046	0.001	0.138	0.013	0.018	0.030	<0.001	0.002	<0.001
Nb	Mo	Co	Sn	Sb	W	B	Ca	Zr	N <sub>2</sub>	O <sub>2</sub>	Als
<0.002	<0.002	<0.002	<0.002	<0.002	<0.003	0.0002	0.0002	<0.001	0.0056	0.006	0.136

### 3. Cutting tool and cutting process

Rotating electrical machines are characterized by the variability of the magnetic induction flux. For this reason, the sheets used for their production must be isotropic. The material of stator and rotor made from electrical sheets should have an isotropic structure after final processing. However, the plastic deformation accompanying the cutting process worsens the magnetic properties of the finished electrical sheet products. The production of rotors by cutting electrical sheets is therefore always accompanied by the occurrence of an area with other magnetic properties.

A burr is formed (figure 1), the formation of which cannot be prevented during the cutting of electrical sheets, therefore the plates for the rotors and stators are sometimes subjected to an additional deburring operation. The influence of burr on the blades of rotors and stators, on the output characteristics of the electric motor is unfavorable.

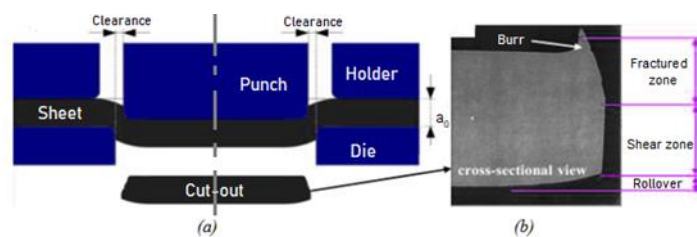


Figure 1: Schematic of the cutting process and different zones of the cutting edge

During winding of the coil and during electric motor operation, the insulation may be broken, the winding may be short-circuited, and the rotor of the electric motor may burn out. Then, it is necessary to cut these sheets with the smallest possible burrs, of course, while maintaining the conditions of economy of production. At the same time, the requirements for electric motors stipulate that the size of the burr of the cut sheets, for stators and rotors, in small and medium-sized electric motors, should not exceed 10% of the nominal thickness of the sheet used. [12]

The table 8 shows the real values of punch diameters (figure 2) at 1,3,5 and 7% cutting gap. The correctness of the punches dimensions was tested using a digital micrometer and a Zeiss industrial coordinate measuring device.

Table 8. Parameters of the cutting gap and punches

Cutting gap thickness to sheet thickness [%]	Diameter $\phi$ of larger punch [mm]	Diameter $\phi$ of smaller punch [mm]
1	25,003	15,039
3	24,983	15,019
5	24,963	14,989
7	24,943	14,979

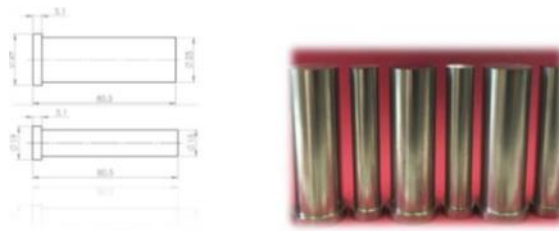


Figure 2. Punches

For the purpose of experimental verification of shearing conditions, a shearing tool was developed (figure 3). The designed shearing tool is constructed as a progressive tool. The tool cuts in three steps. In the first step, the side lateral punch cuts and centers the strip of sheet metal. In the second step, a small diameter hole of 15 mm is cut. The holes cut out in the first step are used in the second step for the viewfinders which centre the strip of sheet metal. The centering of the strip of sheet metal serves to create a cut-out with a precise and coaxial dimension. In the third and final step, the outer diameter of 25 mm is cut out to form the final cut-out.



Figure 3. Experimental cutting tool

All components of the shearing tool (Fig. 3) except shear bars  $\phi$  15 and  $\phi$  25 mm, springs, guide bushings and fasteners were made from Meusburger Georg GmbH tool steel of designation 1.1730, DIN C 45 U, AFNOR XC 48, AISI 1045. This steel type belongs to the non-alloyed tool steels with good machinability, it is suitable for hardening and annealing, with a hardness of 58 HRC.

Steel 1.1730 contains 0.45% C, 0.30% Si, 0.70% Mn, strength reaches at 640 N/mm<sup>2</sup>. It is a non-alloyed flame hardened steel. This type of steel can be used in in the manufacture of tools and jigs such as base plates, posts and moulds.

#### 4. Results

Experimental verification of the shear area by microscopic analysis was performed on a Keyence VHX-5000 (Figure 4).



Figure 4. Digital microscope Keyence VHX-5000

Table 6 and Figures 5, 6 show the microscopic analysis of samples A1-A7. As was mentioned above, the designation A is for sample from sheet M660-50K. The samples show the quality of the cutting surface as a function of the cutting gap (clearance). Cutting gaps for the purposes of for the experiment were chosen at 1,3,5,7 % of the thickness of the sheet.

Table 6. Results of the microscopic analysis of sample A

Samples	Thickness [mm]	Shear zone [mm]	Fracture zone [mm]	Shear zone [%]	Fracture zone [%]
A1	0,500	0,4756	0,0244	95,12	4,88
A3	0,500	0,4572	0,0428	91,44	8,56
A5	0,500	0,2836	0,2164	56,72	43,28
A7	0,500	0,3326	0,1674	66,52	33,48

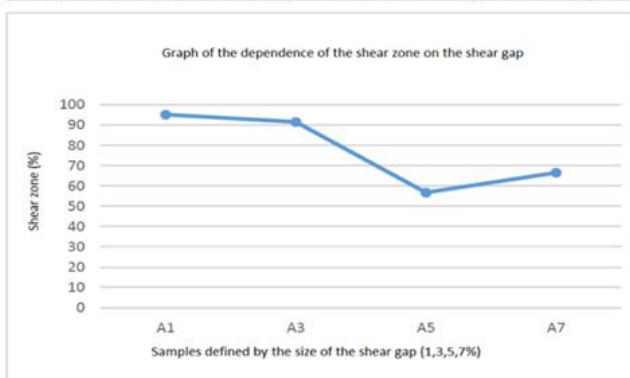


Figure 5. Graph of the dependence of the shear zone on the cutting gap of sample A

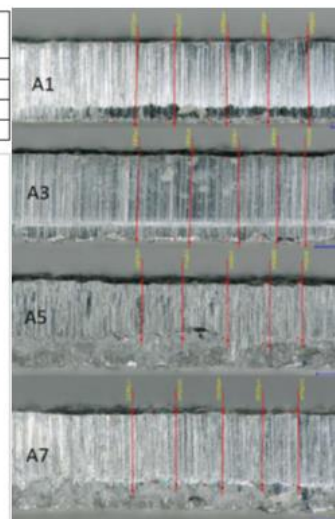


Figure 6. Microscopic analysis of sample A

The optimal cutting gap for cutting samples from M660-50K material is at the level of 1%. This fact also shows that the 1% gap is optimal for cutting these electrical sheets, as its content structure has the largest share of the shear zone, which in practice eliminates short circuits and undesirable processes in the proper operation of electric motors.

Table 7 and Figures 7, 8 show the microscopic analysis of samples B1-B7. As was mentioned above, the designation B is for sample from sheet M450-50K HE. The samples show the quality of the cutting surface as a function of the cutting gap (clearance). Cutting

gaps for the purposes of for the experiment were chosen at 1,3,5,7 % of the thickness of the sheet.

Table 7. Results of the microscopic analysis of sample B

Samples	Thickness [mm]	Shear zone [mm]	Fracture zone [mm]	Shear zone [%]	Fracture zone [%]
B1	0,500	0,4788	0,0212	95,76	4,24
B3	0,500	0,4644	0,0356	92,88	7,12
B5	0,500	0,2496	0,2504	49,92	50,08
B7	0,500	0,305	0,195	61	39

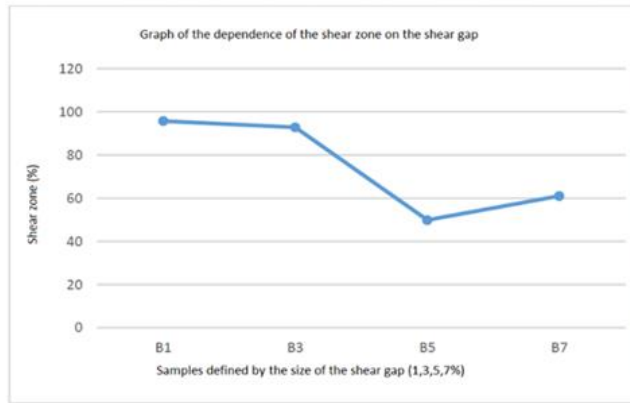


Figure 7. Graph of the dependence of the shear zone on the cutting gap of sample B

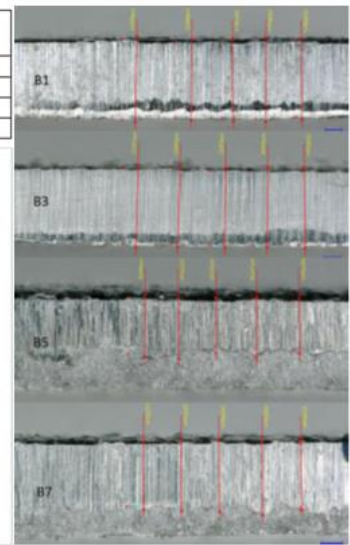


Figure 8. Microscopic analysis of sample B

The ISOVAC M450-50K HE samples with a 1% shear gap showed the best parameters for the quality of the cutting surface based on the measurement of the microscopic analysis. The shear zone had a thickness of 0.4788 mm and a fracture zone of 0.0212 mm, i.e., 95.76% and 4.24%, respectively.

Table 8 and Figures 9, 10 show the microscopic analysis of samples C1-C7. As was mentioned above, the designation C is for sample from sheet M450-50K. The samples show the quality of the cutting surface as a function of the cutting gap (clearance). Cutting gaps for the purposes of for the experiment were chosen at 1,3,5,7 % of the thickness of the sheet.

Table 8. Results of the microscopic analysis of sample C

Samples	Thickness [mm]	Shear zone [mm]	Fracture zone [mm]	Shear zone [%]	Fracture zone [%]
C1	0,500	0,4446	0,0554	88,92	11,08
C3	0,500	0,3036	0,1964	60,72	39,28
C5	0,500	0,2994	0,2006	59,88	40,12
C7	0,500	0,2574	0,2426	51,48	48,52

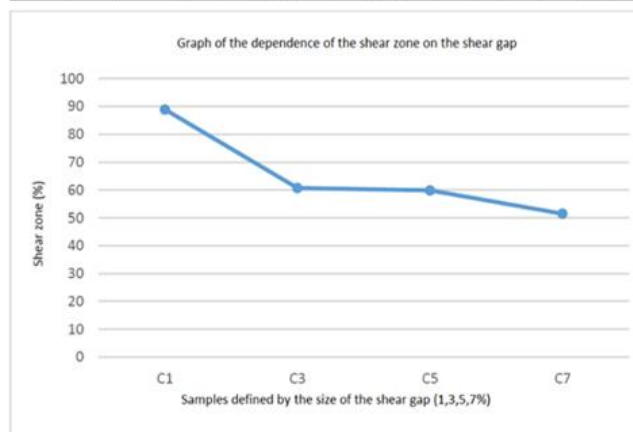


Figure 9. Graph of the dependence of the shear zone on the cutting gap of sample C

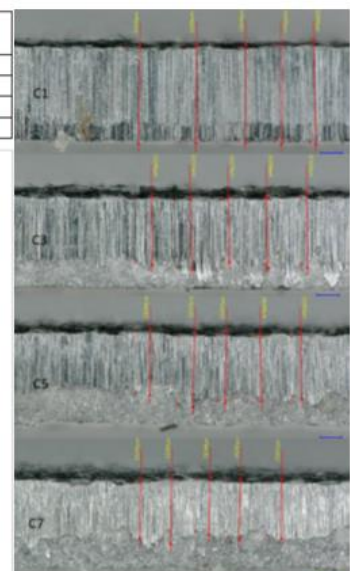


Figure 10. Microscopic analysis of sample C

As with all other observed samples, in the case of sample C-M450-50K, the 1% shear gap showed the best parameters of the plastic shear zone and the fracture zone in the ratio 0.4446mm: 0.0554mm, 88.92%: 11.08%.

Table 9 and Figures 11, 12 show the microscopic analysis of samples D1-D7. As was mentioned above, the designation D is for sample from sheet M350-50A. The samples

show the quality of the cutting surface as a function of the cutting gap (clearance). Cutting gaps for the purposes of for the experiment were chosen at 1,3,5,7 % of the thickness of the sheet.

Table 9. Results of the microscopic analysis of sample D

Samples	Thickness [mm]	Shear zone, average value [mm]	Fracture zone, average value [mm]	Shear zone [%]	Fracture zone [%]
D1	0,500	0,4342	0,0658	86,84	13,16
D3	0,500	0,3640	0,1360	72,80	27,20
D5	0,500	0,2732	0,2268	54,64	45,36
D7	0,500	0,2046	0,2954	40,92	59,08

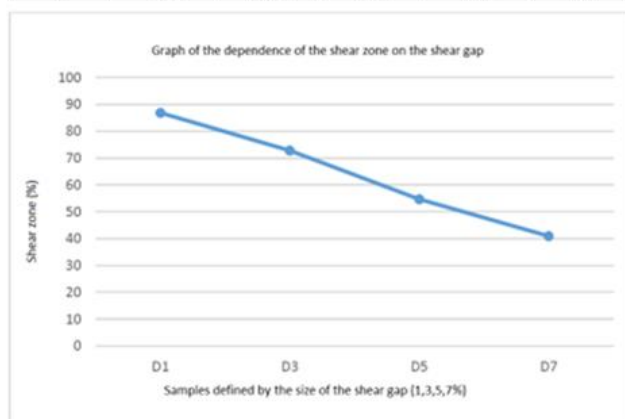


Figure 11. Graph of the dependence of the shear zone on the cutting gap of sample D

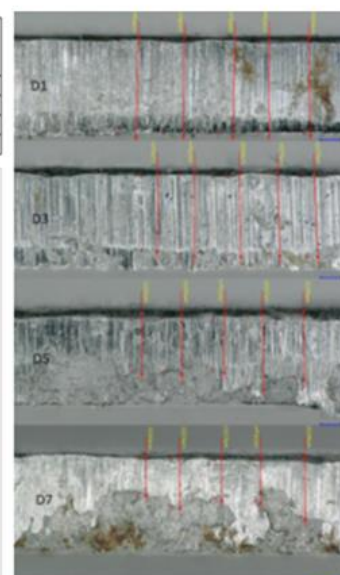


Figure 12. Microscopic analysis of sample D

Table 10 and Figures 13, 14 show the microscopic analysis of samples E1-E7. As was mentioned above, the designation E is for sample from sheet M450-50PP. The samples show the quality of the cutting surface as a function of the cutting gap (clearance). Cutting gaps for the purposes of for the experiment were chosen at 1,3,5,7 % of the thickness of the sheet.

Table 10. Results of the microscopic analysis of sample E

Samples	Thickness [mm]	Shear zone, average value [mm]	Fracture zone, average value [mm]	Shear zone [%]	Fracture zone [%]
E1	0,500	0,4526	0,0474	90,52	9,48
E3	0,500	0,2382	0,2618	47,64	52,36
E5	0,500	0,3086	0,1914	61,72	38,28
E7	0,500	0,2814	0,2186	56,28	43,72

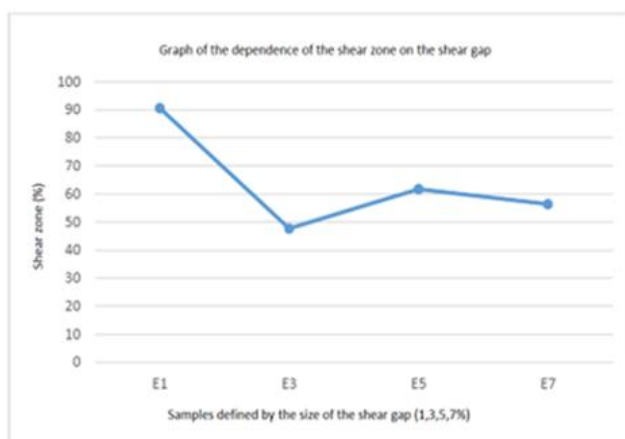


Figure 13. Graph of the dependence of the shear zone on the cutting gap of sample E

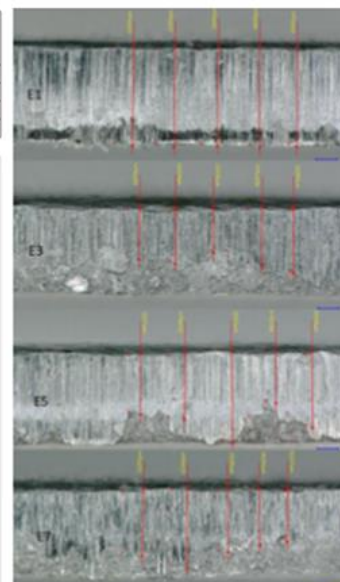


Figure 14. Microscopic analysis of sample E

The 1% shear gap exhibited standard optimal conditions for the shear surface quality of the M450-50PP sample, where the ratio of shear zone to fracture zone was 90.52%:9.48%, 0.4526 mm:0.0474 mm.

The quality of the shear area is defined by its "smoothness". This non-technical term is the ratio of the thickness of the shear zone to the fracture zone. The larger the shear zone, the higher the quality of the shear surface. In terms of the characteristics and behavior of electric motors, we assume that the larger the shear zone, the higher the elimination of undesirable phenomena such as short circuits, losses, and electric motor failures.

## 5. Conclusions

Based on the experimental results of the influence of the cutting gap on the quality of the cutting surface, the following conclusions can be established:

- 1) when cutting electrical steel sheets in a tool with a cutting gap of 1% of the material thickness neither the chemical composition nor the mechanical properties have any influence on the quality of the cutting surface, which is characterized by the size of the shear zone,
- 2) cutting materials in a tool with a cutting gap of 3% of the material thickness results in a reduction in the size of the shear zone, especially for materials with higher ductility values,
- 3) when cutting sheet in a tool with a cutting gap of 5 and 7 % of the material thickness, the shear zones were reduced for all materials examined. The largest inhomogeneity of the shear zone was measured for the sheets with the highest ductility. In these sheets, the in-homogeneity is mainly due to the tearing off large grains of material during cutting.

Based on the experiments carried out, it is recommended to use cutting tools with the cutting gaps in the range of 1-2 % of the material thickness for smooth cutting of circular cutouts from electrical steel sheets (rotors and stators of electric rotating machines).

**Acknowledgments:** This paper was written with the financial support of the granting agency VEGA within the project solution VEGA 1/0384/20 and KEGA 036TUKE-4/2021.

## References

1. P. Rodriguez-Calvillo, Structure Development during Hot Rolling, Proceedings of 3rd International Conference on Magnetism and Metallurgy, Ghent University, Ghent-Zwijnaarde, 2008.
2. Jyotiranjana Barik, Vijayalaxmi Sonkamble and K Narasimhan. Burr formation and shear strain field evolution studies during sheet metal blanking. IOP Conference Series Materials Science and Engineering. Vol. 418, no. 1 (2018), 012068.
3. Thilow A. Entgrattechnik Entwicklungsstand und Problemlösung. 4. Auflage; Ehningen bei Böblingen: Expert Verlag; 2012
4. Osterrath H. Bandschleifen. Entwicklung und Anwendung in der Industrie - Chronologie eines Zerspanungsverfahrens. Ehningen bei Böblingen: Expert Verlag; 1993.
5. Prüller H. Praxiswissen Gleitschleifen, Leitfaden für die Produktionsplanung und Prozessoptimierung. Wiesbaden: Vieweg+Teubner Verlag; 2012.
6. Klocke F, König W. Fertigungsverfahren Umformen. 5. Auflage; Berlin: Springer Verlag; 2006.
7. Bartz W E, Hintz H E. Gleitschlifftechnik. Ehningen bei Böblingen: Expert Verlag; 1989.
8. Spišák, E., Majerníková, J., Kaščák, L., Šlota, J. (2015). Influence of cutting on the properties of clippings from electrical sheets. Acta Metallurgica Slovaca, Vol. 21, No. 4, pp. 302-310.
9. Vladimír Rohaľ, Emil Spišák. Evaluation of influence of cutting gap on the quality of the cutting surface when cutting of electrical steel. (2021). The international Journal of Engineering and Science. Vol. 10, No. 2, pp. 49-55.



# Development and testing of collaborative workplace with 2D camera system

Jaroslav Romancík, Marek Vagaš

<sup>1</sup> Technical University of Kosice, Faculty of Mechanical Engineering, Department of Industrial Automation and Mechatronics; jaroslav.romancik@tuke.sk

<sup>2</sup> Technical University of Kosice, Faculty of Mechanical Engineering, Department of Industrial Automation and Mechatronics; marek.vagas@tuke.sk

**Abstract:** This article presents a method of Ethernet communication between control PLC and collaborative mechatronic system based on the secure protocol CC-Link IE Field Basic. The proposed method is then tested on the example of an experimental workplace with 2D visual camera system to test the principles of recognition, processing, and aggregation of collected image data on the application example of an automated workplace of the "Pick & Place" type. Implemented experimental results demonstrate the robustness and performance of the process, a high degree of reliability, and low hardware requirements.

**Keywords:** camera system, Pick & Place, Ethernet, Mitsubishi, protocol CC-Link IE Field Basic, communication

## 1. Introduction

The arrival of collaborative robotics naturally also brought a new nature of requirements placed on communication methods to cooperate with the selected mechatronic system. Nowadays, however, many companies (especially SMEs) are unwilling to invest in a complete reconstruction of their automated workplace, which includes the often laborious and expensive replacement of many peripherals. They think the automated workplace's innovation or reconstruction ends with the collaborative robot deployment. The reason is mainly high-quality monitoring, diagnostics, and ensuring trouble-free automated operation. Subsequently, problems often arise in communication because outdated communication interfaces do not allow connection between robots, machines, or other devices. Simple and application-friendly automated operations, like Pick & Place applications usually use only one robotic system one PLC, if the application requires it a visual camera system [1].

## 2. Materials and Methods

This chapter briefly describes the process that affects the proposed and tested unified (and partially universal) communication solution, focusing on only one specific type, Ethernet. Explaining all the way and possibilities would be very lengthy. In principle, we can view the proposed communication process from two points (from the side of the robotic system and the side of the PLC component) [2]. Methods of robotic system control with the participation of an industrial PLC currently allow the implementation of complex calculation sequences that we can directly integrate into the control of the robotic system. At the same time, it is possible to choose control either through the robot's control system or by using a PLC [3], [4]. The hardware connection of the individual components is an essential prerequisite for the next steps, *Fig. 1*.

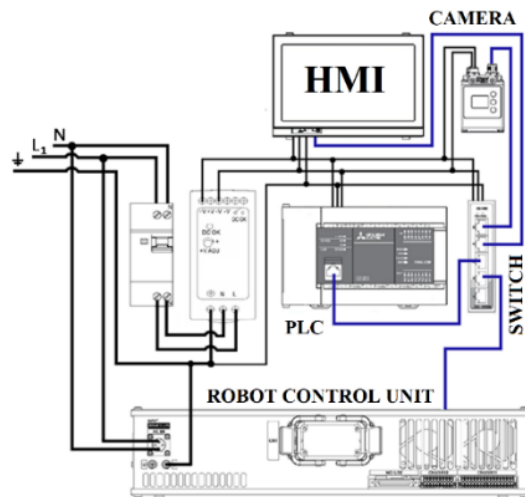


Fig. 1. Components connection

To correctly set up the communication between the FX5U PLC system and the Melfa Assista robot when using the CC-Link IE Field Basic communication protocol, it is necessary to first enable this type of communication on the robot side. Subsequently, on the PLC side, we will set the range of received and sent data types in bit and word format. In the application we created, we attach a 2D camera sensor to the robot's effector, Fig. 2.



Fig. 2. Attaching 2D camera sensor to the robot Melfa Assista

When considering an object in 2D, we get the horizontal ( $x$ ) and vertical ( $y$ ) coordinates. Also, the linear rotation around its centre axis ( $R_z$ ) is available [5]. It changes the object's angle (called 'roll'). But there's no tilt. The part remains flat, Fig. 3.

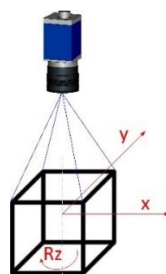


Fig. 3. 2D vision principle

*Dimensional Accuracy Check* allows image processing to determine whether geometric quantities (distance, diameter, or angle) comply with the specified tolerances [6]. In addition, it can be used for monochrome and color types of the obtained image. *Object Counting* function declares the number of the detected objects. We can recognize the values as surface area, circumference, compactness, or other [7]. *Pixel Counting* is a function that adds up a reference object's pixels (pixels). *Tracking* means tracing an object's regions (region, ROI: region of interest). Then, various evaluations are conducted within these regions [8].

### 3. Results

This case study aims to verify the parameterization of a 2D visual camera system in cooperation with a collaborative robot (from MITSUBISHI) and a superior system based on a PLC automaton (FX5U, also from MITSUBISHI). Following the above, we will experimentally test the "Pick & Place" application, Fig. 4.



Fig. 4. The layout of the experimental collaborative workplace

The algorithm uses the position of the PLC device FX5U in the Master role, while the collaborative robot and other peripheral devices (2D camera system, etc.) act in the Slave position. We can understand PLC as an automated workplace's connecting or connecting communication node, Fig. 5. Creating a functional communication link between the 2D visual camera system and the Mitsubishi FX5U PLC is a fundamental prerequisite for reliable communication.

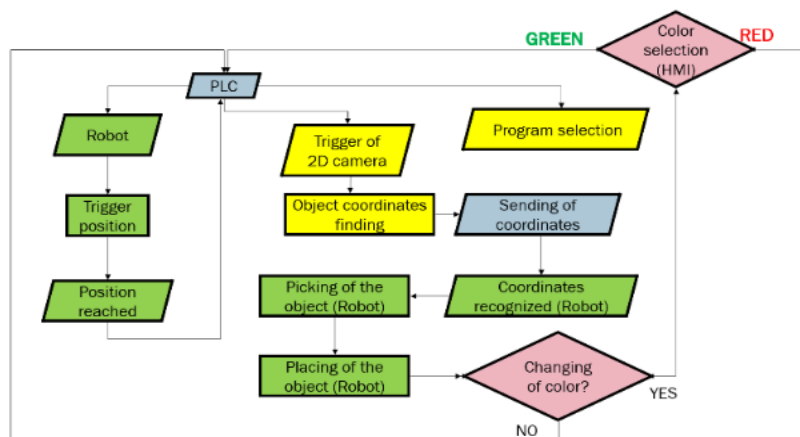


Fig. 5. Algorithm for the collaborative process

In essence, with the CC-Link IE Field basic communication protocol, we ensure the connection between the PLC and external devices via Ethernet parameters (IP address, port number), on which the PLC should expect incoming information from the camera system. Since both PLC and robot are from MITSUBISHI, establishing communication between these devices is very easy. Here, we can observe the advantages of applications built on one platform. The only condition is that the devices are on the same subnet. We realize the recognition, processing, and aggregation of the collected image data by selecting and combining the built-in functional modules of the 2D visual camera system. The sequence of image creation and the use of available functionalities (regarding the final goal, which is to obtain the coordination coordinates of the scanned object) assumes implementation in the form of the following steps:

- We are starting the "trigger" function based on the instructions in the "Device Camera" module to obtain image data from the captured scene of the camera system, Fig. 6.

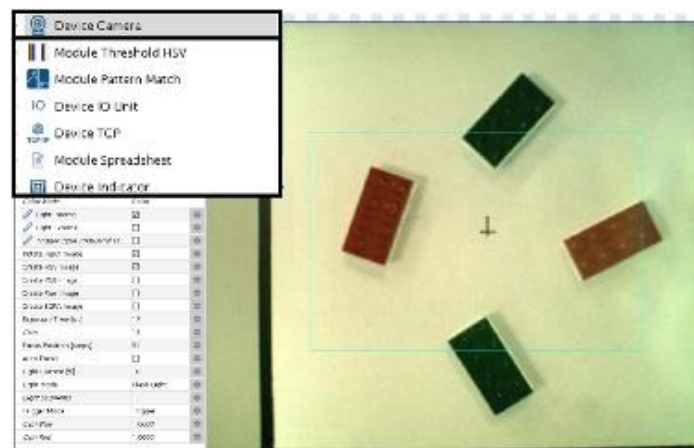


Fig. 6. Picture obtaining (triggering) from the camera sensor scene (area)

- Pixel selection according to the specified parameters based on the instructions in the "Threshold HSV" module. This step aims to sort and display the appropriate

pixels in white. Pixels that do not match the set parameters are shown as black. In this way, we achieve the display of objects on the captured scene, Fig. 7.

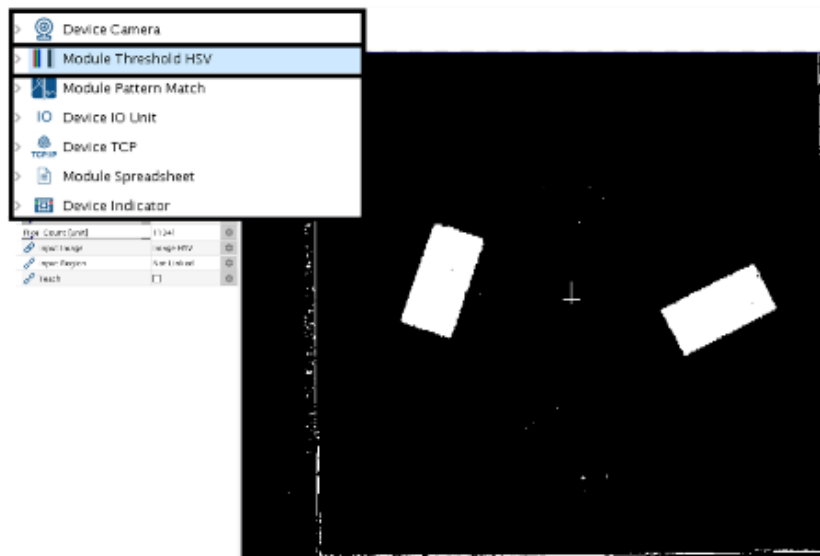


Fig. 7. Selection of suitable pixels from the 2D visual camera system

- The following (logical) step for obtaining the object's coordinates is to find the coordinates of the center of gravity of the scanned object. Fig. 8.

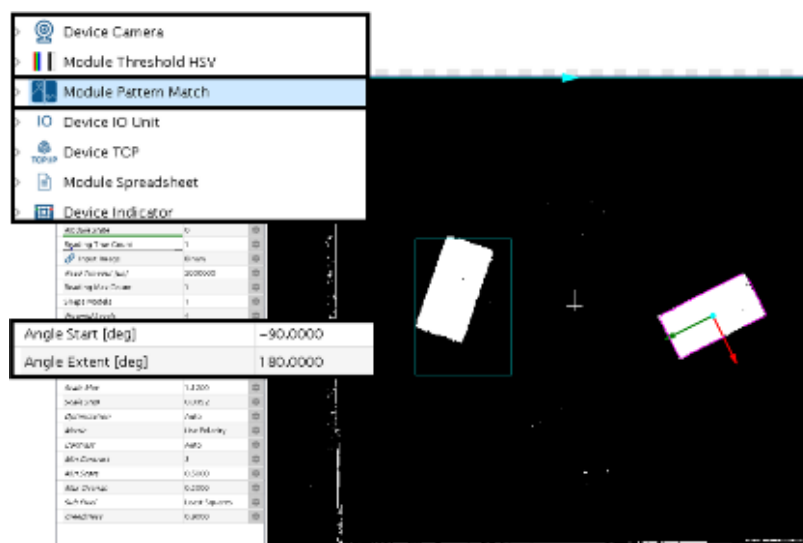


Fig. 8. Data determination from obtained picture

- The coordination coordinates processed this way are sent (in the form of output) directly to the PLC using the "Device TCP" module.

The openness of the communication and sending the coordinates to the data register in the PLC. The data is transmitted in the form of a 16-character "String" type. This format is split into variables for each coordinate and transformed into the "Integer" data type. The robotic system then writes them into variables ( $mX1$ ,  $mY1$ ,  $mC1$ ). After this conversion, the "Pick & Place" application considers the distinguished color, Fig. 9.

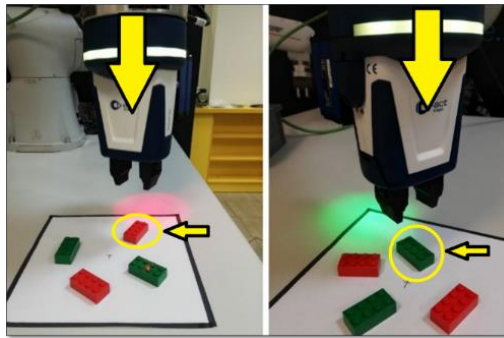


Fig. 9. Pick & place the application

## 5. Conclusions

The article aims to present the Ethernet method of communication between the control PLC and the collaborative mechatronic system in the application example of sorting and storing selected (different-colored) objects using a 2D camera system. The benefit of the article is the description and use of the CC-Link IE Field Basic communication protocol to create a seamless and efficient connection between peripheral devices of various manufacturers, e.g., MITSUBISHI, WENGLOR, and others. Furthermore, the presented case study verifies the proposed approach in the example of an experimental collaborative workplace. Finally, it offers a procedural scenario in the form of an algorithm for the solution of similarly focused automated workplaces with the participation of a robotic system.

**Acknowledgments:** This work was supported by the Slovak Research and Development Agency under Contract no 1/0169/22 New methodics approaches to data from automated and robotized workplaces.

## References

1. R. Holubek, M. Vagas, "Center of gravity coordinates estimation based on an overall brightness average determined from the 3d vision system". In: *Applied sciences. Basel: Multidisciplinary Digital Publishing Institute*, Switzerland (2022). ISSN: 2076-3417
2. R. Drath, et al. "Vendor-Independent modeling and exchange of Fieldbus Topologies with AutomationML." In: 5th AutomationML User Conference, (2018), pp. 956-963, DOI: 10.1109/ETFA.2018.8502630.
3. M. Vagas et al., "Wireless data acquisition from automated workplaces based on RFID technology," In *16th IFAC conference on programmable devices and embedded systems*, (2019), IFAC, pp. 299-304. ISSN 2405-8963
4. M. Vagas, et al., "The view to the current state of robotics," In *International Proceedings of Computer Science and Information Technology, 6th IEEE/IACSIT International Conference on Optimization of the Robots and Manipulators*, 2011. Sinaia, Romania, Vol. 8, pp. 205-209. ISSN 2010-460X
5. A. Senior, et al., "Appearance models for occlusion handling." In: *Image and Vision Computing*. 2006, pp. 1233-1243. Volume 24, Issue 11, ISSN 0262-8856
6. T. Lojka, M. Bundzel and I. Zolotova. "Detection of unexpected data changes in a monitored system," In *IEEE 13th International Symposium on Applied Machine Intelligence and Informatics (SAMI)*. 2015. pp. 93-96. DOI: 10.1109/SAMI.2015.7061853.
7. S. Szénási. "Analysis of historical road accident data supporting autonomous vehicle control strategies," In *PeerJ Computer Science* 7. 2015. DOI: 10.7717/peerj-cs.399
8. E. Lindbeck, J. Conenna and N. Rahnavard,. "A Low-Cost and Portable Single-Pixel Camera," In *55th Asilomar Conference on Signals, Systems, and Computers*. 2021. pp. 1704-1709. DOI: 10.1109/IEEECONF53345.2021.9723132.



# Detection of nickel and chromium release in the oral cavity in patients with metal-ceramic dental prostheses

Svetlana Rusnáková<sup>1</sup>, Jozef Živčák<sup>2</sup>

<sup>1</sup> svetlana.rusnakova@gmail.com

<sup>2</sup> Technical university of Košice, Letná 1/9, 04200, Košice, Slovakia, jozef.zivcak@tuke.sk

\* Correspondence: svetlana.rusnakova@gmail.com

**Abstract:** In past, metal materials occupied an important place in dentistry. The reason was the favourable mechanical properties, which made them unrivalled on the market at the time. After the application of modern materials in practice, the negative properties of metal materials began to be pointed out more and more. These properties include poor aesthetics, electrical and thermal conductivity, patient allergies and negative impact on the environment. Other significant disadvantages include electrogalvanism and metal corrosion. The article will show the data measured from swabs of the oral cavity in patients with fixed metal-ceramic restorations.

**Keywords:** metal, chrome, nickel, fixed metal-ceramic prostheses, corrosion

## 1. Introduction

Metals and its alloys are among the oldest materials used in dentistry. In addition to positive properties, this group of materials also has a number of negative properties, which include electrogalvanism and corrosion. The oral cavity is a complex chemical environment. Saliva, but also the acids that are created during food processing, together create an electrolyte into which, if we apply a metal - electrode, electrochemical corrosion occurs. The cause of electrochemical corrosion is a galvanic current that arises when two or more metals with different electrical potentials are immersed in the electrolyte. Released oxides formed during metal corrosion in contact with saliva and periodontal tissues begin to release metal ions, which can have a toxic effect either locally or spread throughout the body. Metal ions are the cause of bleeding gums, ulcers on the oral mucosa, stomatitis, redness of the tongue, distortion of taste sensations, hyperplasia of the gums in combination with chronic periodontitis and excessive plaque formation. As for the general consequences of metal corrosion, they can manifest themselves in the form of allergies, eczema, vision disorders, neurological disorders, gastrointestinal pathologies, rhinitis, pharyngitis and tinnitus. In any case, it must be remembered that there are no inert materials that do not corrode in the oral cavity, since any metal in contact with another in a moist environment will cause an oxidation reaction. As a result of corrosion, a metal product can lose a number of useful technical properties. Corrosion reduces the strength and plasticity of the metal, damages the surface of the metal and worsens its electrical and other properties. Dental materials should have increased resistance to oral fluid and the environment that is present in the oral cavity during food intake. Corrosion is promoted by temperature conditions and alternating loads to which metal dental structures are exposed. [1] [2] [3] [4] [5]

## 2. Problem description

The research was aimed at detecting the release of nickel and chromium in case of patients with metal-ceramic dentures. The main data on the effect of metal alloys on the

body, their corrosion properties and the rate of absorption of nanoparticles were obtained based on the results from patients who underwent a procedure called joint arthroplasty. General data on the toxicity, toxicokinetics and toxicodynamics of metals are not sufficient to understand the full impact of the contact effect of metals and their alloys on the mucosa. Although the biological effects of metal nanoparticles have been widely studied in plants, microorganisms and experimental animals, their toxicological characterization for humans is far from complete, and therefore any new studies of this area are undoubtedly relevant.

Nickel and chromium have dermatological, toxicological and possibly mutagenic effects. It is estimated that 4.5 to 28.5% of the population has nickel hypersensitivity, with a higher prevalence in women. Chromium allergy is estimated at 10% in men and 3% in women. Symptoms of nickel hypersensitivity include the presence of vesicles, allergies, lung disorders, ear infections, and tinnitus. Nickel is the most common cause of allergic contact dermatitis caused by the metal. In second place is chrome. In addition to the allergic effect, nickel and, to a lesser extent, chromium are also carcinogenic, mutagenic and cytotoxic.

Alloys of nickel and chromium, which are used in metal-ceramic constructions, are considered a cheap alternative to noble alloys. In the case of a sufficiently high concentration of chromium (more than 20%), they are chemically stable and thus resistant to corrosion in the oral cavity. Therefore, only nickel-chromium alloys with a chromium content higher than 20% should be used in prosthetics. In the case of a known allergy to one or more components of the alloy, their use is not recommended. This recommendation applies to all other alloys. [6] [7] [8] [9] [10] [11] [12]

Figure 1. and Figure 2. below shows photos of metal-ceramic prostheses of 2 out of 30 patients that were subjected to my research.



**Figure 1.** Patient – woman, 45 years, 10-year metal-ceramic bridges. Metallic staining of the gingiva in the DN 11, 12 area.

Subj.- The patient experiences a peculiar taste in the mouth, irritability, gum pain developed over time.



**Figure 2.** Patient - woman, 69 years, 38-year-old metal crown DN 11. Metallic discoloration of the gingiva in the area of the crown.

Subj.- The patient is satisfied, but feels a metallic taste in the mouth and observes discoloration of the gums.

### 3. Preparation of the experiment methodology

For the most reliable result of the experiment, the methodology was applied to a sample of 30 patients. 2 samples were taken from the oral cavity of each of them and were marked with the letters A and B. Sample A indicated a swab from the area of immediate contact of the metal-ceramic prosthetic work with the gingiva. Sample B represented a swab from an area (surface of intact teeth and gingiva, palate) where no metal-ceramic work or other metal filling is present. The samples were examined for the presence of chromium and nickel. The sample was taken using a wooden cotton swab, which was packed in Lukasterik bags, and then sent to the laboratory for analytical expertise. After the expert examination, the amount of chromium and nickel in the oral cavity was determined. Subsequently, the results were compared between both categories of patients. Table 1 below describes ICP-MS and measurement conditions of the examination.

**Table 1.** ICP-MS and measurement conditions

Spectrometer	Sciex Elan 5000 (Perkin-Elmer, Norwalk, CT) Perkin Elmer Model Optima 3100 XL
Nebuliser	Transverse flow type, with Rytan condensation chamber
Interface	Pt-Rh alloy sample and skimmer cones
Output	1000 kW
Argon flow (l/min)	Plasma gas, 16; auxiliary gas, 0,5; aerosol gas, 1,0
Scanning conditions	residence time, 100 ms; sweeps for reading, 10; values per replicate, 5; number of replicates, 3; points over the top, 3; normal resolution, 0.8
Analytical determination	Cr, Ni
Reference weight	103Rh

Samples from patients were first sterilized by heat inactivation for 24 hours, 95°C. Next, the samples were incubated in concentrated nitric acid in a Teflon container using multi-cycle microwave heating. Heating was performed in a microwave system (Ultrawave system, Milestone, Italy). A typical procedure included the following steps: 4 mL of 69–70% HNO<sub>3</sub> (Sigma-Aldrich, Darmstadt, Germany) was added to 4 mL of each sample. The acid was added in small portions due to the highly exothermic nature of the reaction. In the next step, the aforementioned microwave mineralization was used. After the

mineralization process, the contents of the test tubes were quantitatively transferred into flasks with a volume of 25 ml. A standard with a certified concentration (Merck, Germany) was used as an internal standard for monitoring signal stability. To measure the indicated elements, it was necessary to prepare calibration curves based on a standard solution (Multi-element ICP standard, Merck, Germany). Preparation of standards was carried out by the subsequent dilution method. Blank samples were prepared in the same way as the studied samples. ICP-MS was performed on a Perkin-Elmer Sciex Elan 5000 and Model Optima 3100 XL. The excerpt from the results is showed in Table 2. The orange columns contain the measured results from examination, For the most precise results, the green columns contain the measured results of examination minus the average value of nickel / chromium values found on the spatula used in the examination (the exact values of the spatula are included in Table 3). The last two columns of the Table 2 contain the age of the examined metal-ceramic prostheses and the number of metal-ceramic crowns.

**Table 2.** Results of individual measurements (an excerpt from the full table)

Sample	Sample no.	Sample type	Measured value		The result value (after subtracting the values from the spatula)		No. of years of wearing the prosthesis	No. of crowns
			Cr ng/r	Ni ng/r	Cr ng/ml (	Ni ng/ml (		
20227g1	1a	a	10,2	23,2	2,6	16,6	10	2
20227g2	1b	b	12,3	26,5	4,7	19,9	10	2
20227g3	2a	a	81,4	34,4	73,8	27,8	10	2
20227g4	2b	b	16,2	38,8	8,6	32,2	10	2
20227g5	3a	a	89,7	20,8	82,1	14,2	21	3
20227g6	3b	b	26,2	29,5	18,6	22,9	21	3
20227g7	4a	a	143,1	40,7	135,5	34,1	30	8
20227g8	4b	b	20,5	46,4	12,9	39,8	30	8
20227g9	5a	a	17,2	35,8	9,6	29,2	7	2
20227g10	5b	b	11,2	44,7	3,6	38,1	7	2
20227g11	6a	a	90,8	39,1	83,2	32,5	16	24
20227g12	6b	b	10,8	47,9	3,2	41,3	16	24
20227g13	7a	a	56,2	21,2	48,6	14,6	50	9
20227g14	7b	b	19,3	23,5	11,7	16,9	50	9
20227g15	8a	a	27,4	43,7	19,8	37,1	7	20
20227g16	8b	b	14,2	50,5	6,6	43,9	7	20
20227g17	9a	a	68,5	33,6	60,9	27,0	11	11
20227g18	9b	b	13,3	41,3	5,7	34,7	11	11
20227g19	10a	a	157,4	38,6	149,8	32,0	5	19
20227g20	10b	b	28,1	43,2	20,5	36,6	5	19
20227g21	11a	a	44,5	46,5	36,9	39,9	20	16
20227g22	11b	b	16,8	50,1	9,2	43,5	20	16
20227g23	12a	a	198,7	47,4	191,1	40,8	8	16

**Table 3.** Measured results of the spatula

	Cr ng/ml	Ni ng/ml
	8,1	7,3
	7,2	6,5
	7,8	6,8
	7,1	6,2
	7,9	6,3
<b>AVG:</b>	<b>7,6</b>	<b>6,6</b>

#### 4. Output / Comparison

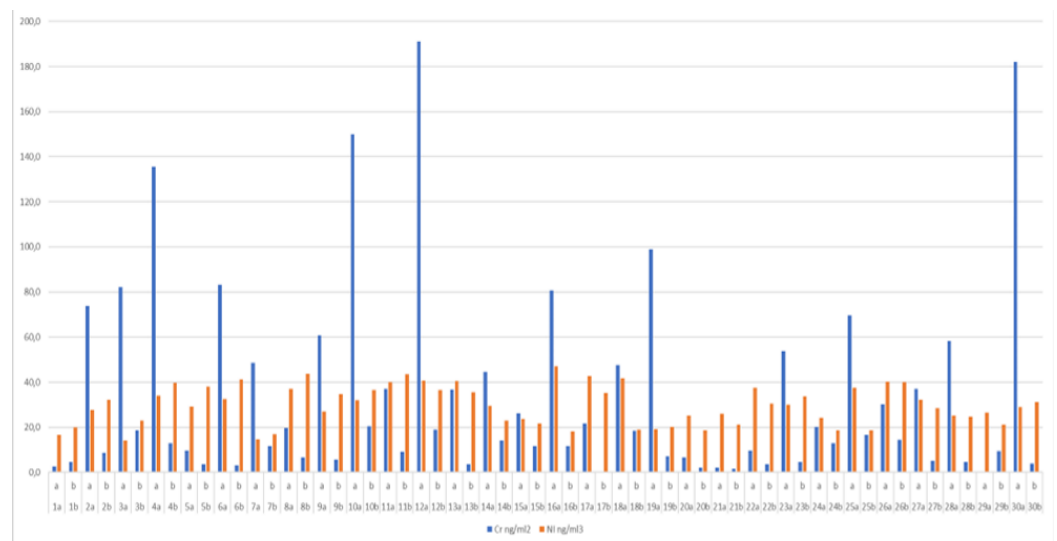
The analysis of the measurements confirms that the release of Cr and Ni into the oral cavity environment really occurs, as the values of metal particles were measured both in the immediate proximity of metal-ceramic works and in remote areas of the oral cavity where the prosthetic work is not located. This fact is described in Chart 1.

Chart 2 shows the measured values of Cr and Ni based on a smear of the gingiva in the immediate proximity of the metal-ceramic work. It can be observed on the chart that Cr is released in a much larger amount than Ni in most cases.

On the other hand, Chart 3 points to the fact that in the more distant parts of the oral cavity from the metal-ceramic restoration, on the contrary, there is a more significant release of Ni compared to Cr.

From the comparison of the results contained in Charts 2 and 3, it is possible to deduce the different extent of spread of the observed metals in the oral cavity. Although Cr occurs in the immediate proximity of the metal-ceramic restoration in very high quantities, its occurrence is essentially negligible in the rest of the oral cavity. On the other hand, based on the measurements, Ni occurs relatively evenly in the oral cavity space, regardless of the location of the metal-ceramic restoration.

**Chart 1.** Results of measured Cr and Ni values



**Chart 2.** The results of the measured values of Cr and Ni - the area of immediate proximity to the metal-ceramic restoration

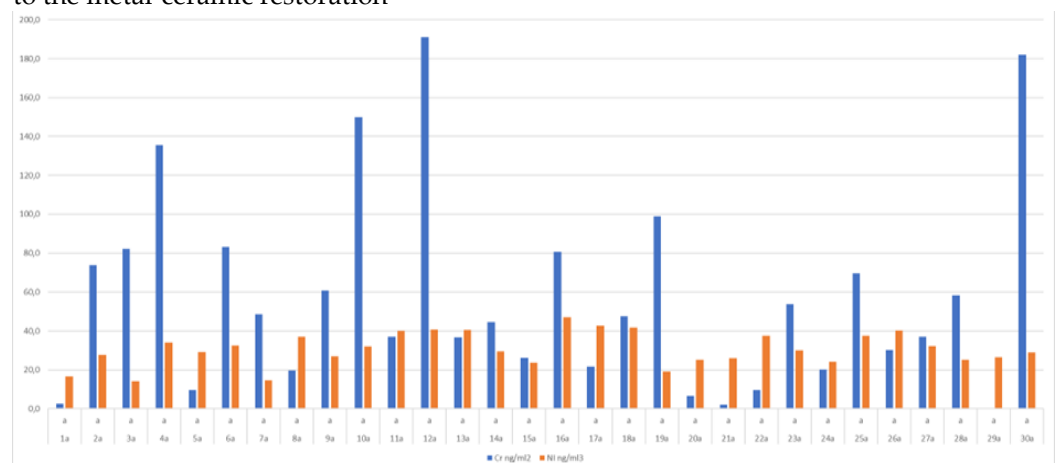
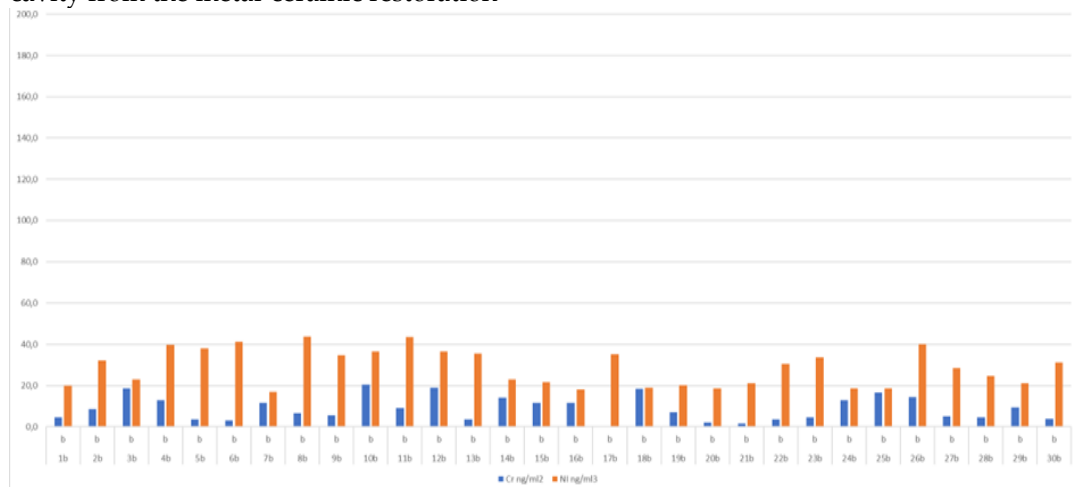


**Chart 3.** The results of the measured values of Cr and Ni – the furthest area of the oral cavity from the metal-ceramic restoration



## 5. Conclusion

The main goal of the research was the analytical expertise of swabs taken from soft tissues and proving that despite the fact that suppliers of dental metal alloys try to refine the composition and ratio of individual components in a given alloy to have the most biocompatible properties and claim that currently there are metals on the market that are not subject to corrosion, the release of metals into the oral cavity continues to occur. It was also found that the release of metals does not occur only in the case of structures older than 15 years, but also in structures that are much younger (less than 5 years). Even the fact that the structure was completely covered with ceramics did not stop the release of metal. The most significant finding of this work can be attributed to the fact that the extent and uniformity of the spread of metals in the oral cavity varies significantly depending on the metal as such.

## References

- ZICHA, A. Stomatologie. Vybrané kapitoly pro zubní techniky. 1. vyd. Praha: UK, 1998.
- CRAIG, RG. Ceramic-metal systems. In Craig, RG., et al., Restorative dental materials. St. Louis: Mosby, 2002, p.575-592.
- BITTNER, J. Protetická technológia. Brno: IDVZP, 1989, 145 p.
- BITTNER, J., J. SEDLÁČEK. Technológia pre zubných laborantov. Martin: Osveta, 1981, p. 157-190.
- KOMRSKA, J. Materiály pro protetickou stomatologii. Brno: IDVZP, 1991, 120 p.
- РЕВА, И. В. – КИМ, А. Р. – БОЧАРОВ, В. С. – ТОЛМАЧЁВ, В. Е. – РЕВА, Г. В. РЕАКЦИЯ СЛИЗИСТОЙ ОБОЛОЧКИ ПОЛОСТИ РТА НА ОРТОПЕДИЧЕСКИЕ КОНСТРУКЦИИ ИЗ СПЛАВОВ, СОДЕРЖАЩИХ НИКЕЛЬ, Современные проблемы науки и образования, 2016, DOI: 10.17513/spno.24556. Dostupné na: <https://science-education.ru/ru/article/view?id=24556>
- CAESAR, HH. Stomatologická protetika pre zubných technikov II. Martin: Osveta, 2004, p. 311-422, 451-498, 578-598.
- WAGNER, R., S. HELMLINGM. AGC-Galvanotechnic- ein Verfahren mit Zukunft. Quintessenz Za-hntechnik, 1998, 24 (5), p. 499-507.
- WAGNER, R. AGC – Galvanotechnik – ein Verfahren mit Zukunft. Quintessenz Zahntechnik, 1998, 25 (5), p. 499-507.
- HOUBALKOVĀ, H., J.KRŇOLOVĀ. Materiály a technologie v protetickém zubním lékařství, Praha: Galen, vydanie č.1, 2009, 301 p (267), ISBN 978-80-7262-581-9.
- TVRDOŇ, M. at all. Protetická stomatológia. Bratislava: Science, 2001. WEBER, T. Memorix zubního lékařství. Překlad 2. vyd. Praha: Grada Publishing, 2006. 430 p. ISBN 802471017x.

12. ŠEDÝ, J. a kol. Komentium stomatologie, Vydavatelstvo TRITON, 2012, 1196 p. ISBN: 9788073875435.



# Evaluation of the quality of renovation layers in tribological conditions

Henrich Sailer<sup>1,\*</sup>, Janette Brezinova<sup>2</sup>

<sup>1</sup> henrich.sailer@tuke.sk

<sup>2</sup> janette.brezinova@tuke.sk

\* Technical university of Kosice, Faculty of mechanical engineering, Letna 9 Kosice 04001, Slovakia

**Abstract:** Presented article is focused on the analysis of the quality of two types of welds intended for the renovation of molds during high-pressure aluminum casting. Two different cladding processes were used for the production of samples, disk laser technology and TOPTIG cladding. In all samples, Uddeholm Dievar 1.2344 wire was used as an additional material, because this material is used in the restoration and renovation of functional parts of molds for aluminum pressure die-casting. The quality of the clads was evaluated on the basis of the heat-affected zone, which was determined from the course of the graphs during the hardness measurement. The tribological parameters of the clads were investigated using the Pin-on-disc test. Based on the experimental work carried out, these cladding technologies can be recommended in practice for the renovation of molds. Better results were achieved with the TOPTIG clad sample.

**Keywords:** Die casting, damage surface, casting dies, molten Aluminium, cladding, high temperature corrosion, Laser, TOPTIG

## 1. Introduction

High Pressure Die Casting (HDPC) is a technological process widely used for casting complex aluminum castings, mainly associated with the automotive industry. In this process, molten metal with a temperature of 670-710 °C is forced into the cavities of the molds at filling speeds of 30-100m/s, under pressures ranging from 40-80MPa [1]. This-loading, in combination with the corrosive properties of liquid aluminum, leads to aluminization or oxidation of them old surface, which results in thermal fatigue of the surfaces followed by cracking, soldering and erosive wear. The service life of die matrices-made of steel alloys is approximately 100,000 cycles and can be increased either by heat-treatment, thin coating or cladding [2-4]. At present, the issue of surface treatment of various materials is becoming more and more important. It offers savings in strategic materials and at the same time enables the production of components with specific surface and volume properties. Because resources are limited by conventional technologies, it is becoming increasingly difficult to meet more advanced customer needs [5-6]. There are many methods for substrate treatment, but coatings developed, for example, by electrostatic, chemical, physical deposition techniques, have lower bond strengths or very low reproducibility than surfacing. Refurbishing worn parts of machines is a very efficient and environmentally friendly form of their maintenance. This option can reduce the environmental impact over the whole lifecycle of the component by up to 63.8% [7].

### Laser cladding:

Laser cladding is a technology used to create coating layers with improved properties, or to recovered effects in worn parts of the surface and base layers of components. Due to the high energy density and relatively small heat affected area, this method is suitable for-processing a wide range of materials. It is mainly used in the automotive, aerospace, medical, nuclear and oil industries. In the aerospace industry, the cladding of

layers to aluminum alloys has an increasing potential to improve their surface properties [8-10]. This technology uses highly concentrated waves of light, concentrated at a certain point. In the area affected by the laser beam, atomic bonds disintegrate, causing it to heat up. The three most common types of lasers used in laser cladding equipment are gas, semiconductor and fiber. The laser beam is guided into the cladding device by one or more optical fibers concentrated at one point. With each fiber added, the intensity of the laser beam also increases [11-14]. Before the laser beam leaves the cladding device, a combination of collimator and focusing lenses is often used to direct this radiation to a very small area. An important part of the laser cladding equipment is also the nozzle supplying the protective atmosphere gas, most often CO<sub>2</sub>. Vacuum cladding is possible but difficult to use, due to the high demands on the construction of the cladding equipment [13].

### TIG (Tungsten Inert Gas):

Non-melting tungsten electrode (TIG) cladding technology, otherwise known as Gas Tungsten Arc Cladding (GTAW), is a cladding method in which the gas protecting the cladding bath and the non-melting electrode is usually argon fed to a cladding nozzle at the end. The additional material is fed to the cladding bath in the form of a wire [15].

The TIG method also enables cladding without additional material. Its main advantage is the cladding of thin materials from 0.3 to 5 mm. The main disadvantage of this technology is low productivity, which limits it to smaller-scale work. The cladding torches used in the TIG method are divided into two types. The first type is an air-cooled burner used for smaller operations, loaded with a current of up to 200A. At a high current density of up to about 400A, burners are used which are cooled mainly by water [16-18].

The non-melting cladding electrode material must have a high melting point, good electrical, thermal conductivity and low electrical resistance. Tungsten with a melting point of 3370°C meets these requirements. Pure tungsten electrodes are used in predominantly alternating current cladding of light metals, but more often, electrodes with an admixture of thorium oxide, cerium or zirconium are used, which improves the stability of the electric arc and improves its ignition. Another parameter of the cladding electrode is its shape. When cladding with direct current, its tip is sharpened at an angle of 45°, but when alternating current they are not ground, instead they melt slightly with increasing current until they are rounded [19-20].

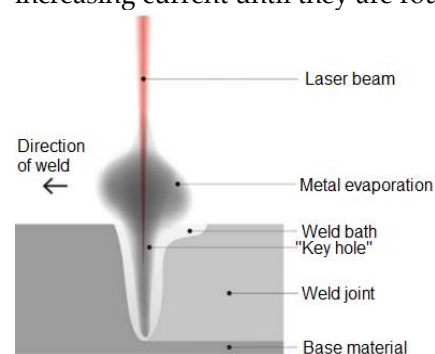


**Figure. 1** Schematic representation of laser beam cladding [13]

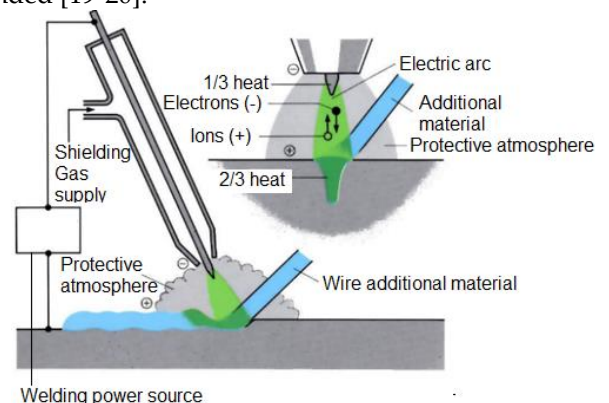


**Figure. 2** Schematic representation of the TIG method [18]

## 2. Materials and Methods

Two different technologies were used for the production of the samples below, while the aim of the work was to determine the impact of individual technologies not

only the quality but also the chemical composition of the clads and the minimization of the heat-affected area. Each of the technologies listed below has a different heat input, which is reflected not only in the quality of the clad but also in the degree of mixing of the base material with the clad metal.

Two disk laser clad samples (sample 01), TOPTIG (sample 02), were applied to the additive material. Sample clads marked 01, 02 were applied on a substrate of nickel - chromium - molybdenum - vanadium steel 1.2714, DIN - 56NiCrMoV7. Uddeholm Deivar 1.2344, DIN - X40CrMoV51 1.2 mm diameter cladding wire was used as an additional material. Pin on disk tests and hardness curves were performed on the samples.

The clads were applied to samples of two base materials. On base material made of nickel - chrome - molybdenum vanadium steel 1.2714, DIN - 56NiCrMoV7, with hardness 44 HRC Tab. 1.

**Table 1.** Chemical composition of the base material

Element	C	Mn	Si	P	S	Cr	Fe	Ni	Mo	V	W
Wt. [%]	0.397	0.72	0.238	0.004	0.002	0.969	95.76	1.253	0.438	0.089	0.12

**Table 2.** Chemical composition of the additive material [8]

Element	C	Cr	Si	Mo	Mn	V
Wt. [%]	0.35	5.0	0.2	2.3	0.5	0.6

Uddeholm Deivar 1.2344 cladding wire, DIN-X40CrMoV51 with a diameter of 1.2 mm and a hardness of 51 HRC was used as an additional material for the formation of cladding layers [8].

**Table 3.** Parameters of cladding

Cladding technology	Disc laser cladding	Cladding technology	TOPTIG cladding:
Cladding equipment	The TruDisk 4002 solid-state disk laser with BEO D70 focusing	Cladding equipment	Fronius TPS600i cladding power source
Focal length	200 mm	Cladding current	196 A
Laser power	1.8 kW	Cladding voltage	23.8 V
Optical fiber diameter	400 $\mu\text{m}$	Wirefeed speed	6.5 m. min <sup>-1</sup>
Cladding speed	10 mm. s <sup>-1</sup>	Cladding speed	8 mm. s <sup>-1</sup>
Focusing	+/- 6 mm	Arc length correction	3
Wire feed speed	70 cm. min <sup>-1</sup>	Pulse/dynamics correction	0.0
Shielding gas flow rate	Ar 30 l. min <sup>-1</sup>	Shielding gas flow rate	Ar 30 l. min <sup>-1</sup>
		Pre heating of base material	preheated to 300 ° C before welding
		Distance burner sheet metal surface	19 mm

### 3. Results

For structural analysis of the clads, Tescan Vega-3 scanning electron microscope (SEM) images were selected, capturing the interface of the base material and the clads as well as the heat affected area. The chemical analysis of the individual clads was evaluated for each sample from the base material area, the mixing zone and the Clad metal pool.

Clad 01 (disk laser)

Clad 02 (TOPTIG)

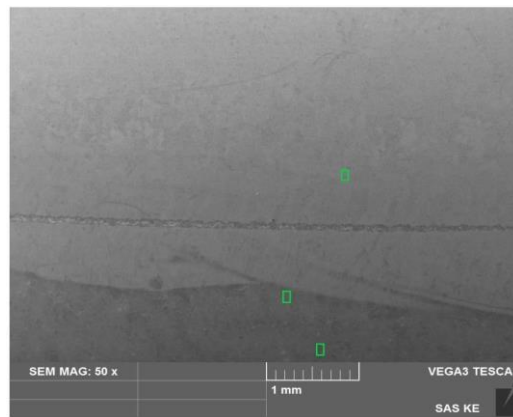


**Figure. 3** Clad 01. Electron microscope image, capturing the interface of a) cladded metal, b) heat affected area, c) base material

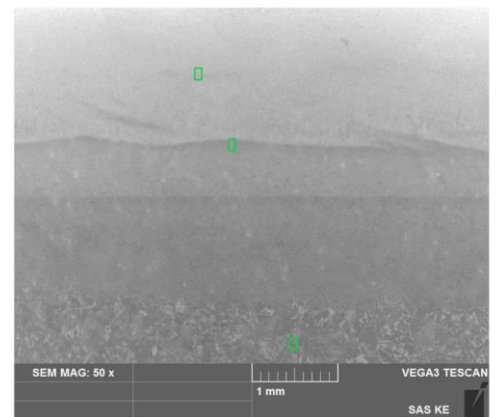


**Figure. 4** Clad 02. Electron microscope image, capturing the interface of a) cladded metal, b) heat affected area, c) base material

Based on the chemical analysis of the clad metal 01 formed by the disk laser, it is possible to evaluate that due to the mixing of the base material and the cladded metal, the original value of chromium in the upper cladded metal layer was not reached. Another element for which a visible increase can be observed is vanadium.

During the chemical analysis of the clad marked 02 made by the TOPTIG technology, the smallest decrease of the elements, especially chromium in the cladded metal, is visible, in comparison with the elements contained in the additional material.

Chemical analyzes have shown that in the heat-affected area, individual materials are mixed, ie. base and additional material in the cladded metal. The value of chromium in the cladded metal is crucial, which in no case reached the limit of 5.00%, soaked in the additive material. The decrease of this element can be attributed mainly to the thermal influence of the material in the process of cladding. The value of mixing the base material and the cladded metal is minimal, which is confirmed by the fact that the hardness of all clads evaluated in the previous analysis was around 500 HV0.5.

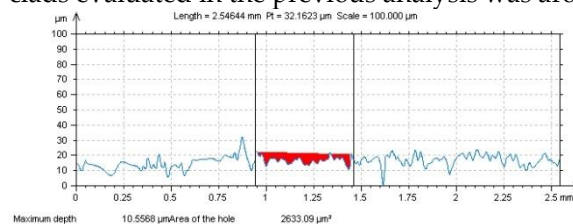


**Figure. 5** Scheme of the tribo wear track on sample 01 produced by the Pin-on-Disc test

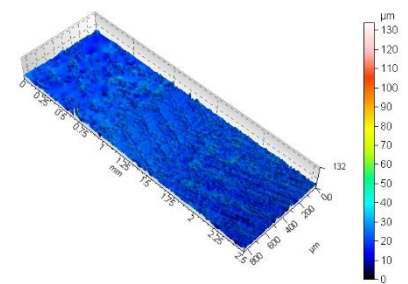


**Figure. 6** 3D picture of the tribo wear track on sample 01 produced by the Pin-on-Disc test

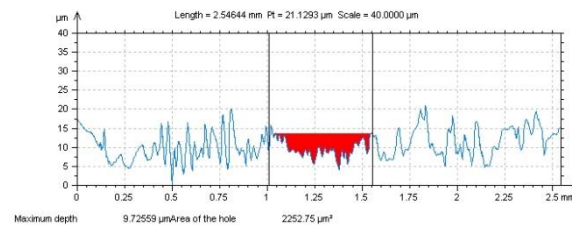


**Figure. 7** Scheme of the tribo wear track on sample 02 produced by the Pin-on-Disc test

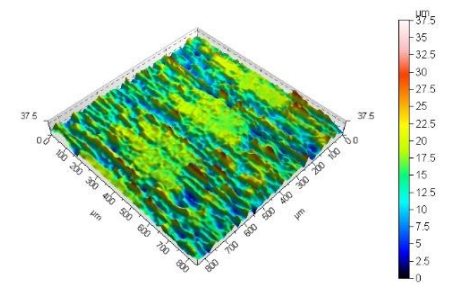


**Figure. 8** 3D picture of the tribo wear track on sample 02 produced by the Pin-on-Disc test

## 5. Conclusions

The presented article is focused on the analysis of the quality of two types of clads intended for the renovation of molds in high-pressure aluminum casting. Two different claddings, disk laser cladding technologies and TOPTIG cladding were used to produce the test specimens. Uddeholm Dievar 1.2344 cladding wire was used as an additional material in all samples due to the fact that this material is used in the renewal and renovation of functional parts of molds, for die-casting of aluminum. In the theoretical part, the problems and mechanisms of wear of die matrices for high-pressure aluminum casting are characterized, together with an overview of cladding technologies used in the formation of cladding layers in various industries. The experimental part was focused on determining the quality of the above clads. The quality of the clads was assessed on the basis of the heat-affected zone, which was determined from the course of the graphs, when measuring the hardness. Tribological parameters of the clads were investigated using the Pin-on-disc test. From the measurement of the hardness of individual samples, it is possible to deduce that the narrowest heat-affected area had a clad marked 02, created by the TOPTIG method. The widest heat affected area was recorded on a sample labeled 01, created by a disk laser. Based on the Pin-on-disc test, it is possible to use that sample 02 is much smoother and the shift of the coating material from the center to the wear sides was less pronounced. Based on the implemented experimental work, it is possible to recommend these technologies in practice in order to renovate the molds. Better results were obtained with a sample of clad marked 02 TOPTIG.

**Acknowledgments:** This contribution is the result of the project implementation: “Innovative approaches to the restoration of functional surfaces by laser cladding overlaying” (APVV-20-0303), supported by the Slovak Research and Development Agency and supported by the Ministry of Education of Slovakia Foundation under grant projects VEGA No. 1/0597/23 “Application of progressive technologies in restoration of functional surfaces of products” and KEGA 036TUKE-4/2021 “Distance form of education in the field of engineering technologies using modern IT tools for foreign students”. This support is highly appreciated by the authors. Conflicts of Interest: The authors declare no conflict of interest.

## References

1. Changrong Chen et al.: Energy based approach to thermal fatigue life of tool steels for die casting dies. In: International Journal of Fatigue Volume 92, Part 1, November 2016, Pages 166-178.
2. J. Lin et al.: Design methodology for optimized die coatings: The case for aluminum pressure die-casting In: Surface and Coatings Technology 201 (2006) pp. 2930–2941.
3. K. Domkin, J.H. Hattel, J. Thorborg, Modeling of high temperature- and diffusion-controlled die soldering in aluminum high pressure die casting, J. Mater. Process. Technol. 209 (8) (2009) 4051–4061.
4. Sundqvist M., Hogmark S.: Effects of liquid aluminium on hot-work tool steel Tribol. Int. 26 (1993) in International Journal of

Fatigue p. 129.

5. H. Zhu, J. Guo, J. Jia, Experimental study and theoretical analysis on die soldering in aluminum die casting, *J. Mater. Process. Technol.* 123 (2) (2002) 229–235.
6. Z.W. Chen, M.Z. Jahedi, Die erosion and its effect on soldering formation in high pressure die casting of aluminium alloys, *Mater. Des.* 20 (6) (1999) 303–309.
7. K. Venkatesan, R. Shivpuri, Experimental and numerical investigation of the effect of process parameters on the erosive wear of die casting dies, *J. Mater. Eng. Perform.* 4 (2) (1995) 166–174. R. Markežič et al. *Engineering Failure Analysis* 95 (2019) 171–180179.
8. A Mohammed, M.B. Marshall, R. Lewis, Development of a method for assessing erosive wear damage on dies used in aluminium casting, *Wear* 332–333 (2015)1215–1224.
9. LF. Hou, Y.H. Wei, Y.G. Li, B.S. Liu, H.Y. Du, C.L. Guo, Erosion process analysis of die-casting inserts for magnesium alloy components, *Eng. Fail. Anal.* 33 (2013)457–564.
10. D.W.C. Baker, K.H. Jolliffe, D. Pearson, The resistance of materials to impact erosion damage, *Philos. Trans. R. Soc. A Math. Phys. Eng. Sci.* 260 (1110) (1966) 193–203.
11. Persson, S. Hogmark, J. Bergström, Temperature profiles and conditions for thermal fatigue cracking in brass die casting dies, *J. Mater. Process. Technol.* 152(2) (2004) 228–236.
12. C. Rosbrook, Analysis of Thermal Fatigue and Heat Checking in Die-Casting Dies: A Finite Element Approach, PhD thesis Ohio State University, 1992.
13. F. Medjedoub, G. Dour, S. Le Roux, P. Lamesle, M. Salem, P. Hairry, F. Rézaï-Aria, Experimental conditions and environment effects on thermal fatigue damageaccumulation and life of die-casting steel X38CrMoV5 (AISI H11), *Int. J. Microstruct. Mater. Propert.* 3 (2–3) (2008).
14. P. Hansson, “Modern prehardened tool steels in die-casting applications,” *Materials and Manufacturing Processes*, vol. 24, no. 7-8, pp. 824–827, 2009.
15. Uddeholm, “Dievar,” 2014, (18.10.2021) internet: <http://www.uddeholm.com>
16. D. Klobčar, J. Tušek, B. Taljat, Thermal fatigue of materials for die-casting tooling, *Mater. Sci. Eng. A* 472 (1) (2008) 198–207.
17. D. Schwam, J. F. Wallace, and S. Birceanu, “Die Materials for Critical Applications and Increased Production Rates,” Case Western Reserve University, 2002.
18. Methodical measurement and evaluation of adhesive cohesive behavior of thin film-substrate systems,2005, (19.10.2021)internet: <https://www.opi.zcu.cz/adheze.html>
19. Z. Yuan, C. Wang, F. Li, Y. Hu, Y. Guo, Q. Chen, Y. Wang, M. Guo Investigation on Behavior of Elastoplastic Deformation for Ti-48Al-2Cr-2Nb Alloy by Micro-indentation and FEM-reverse Algorithm[J] *Advanced Engineering Materials*, 19 (8) (2017), Article 1700097
20. D. Klobčar, et al.: Thermo fatigue cracking of die casting dies. In: *Engineering Failure Analysis* Volume 20, March 2012, pp. 43-53.



# Continuum robot control based on reinforcement learning

Peter Ján Sinčák <sup>1\*</sup>, Ivan Virgala <sup>1</sup> and Martin Varga <sup>1</sup>

<sup>1\*</sup> Department of Industrial Automation and Mechatronics, Faculty of Mechanical Engineering, Technical University of Košice, 04200 Košice, Slovakia; peter.jan.sincak@tuke.sk (P.J.S.); ivan.virgala@tuke.sk (I.V.); martin.varga2@tuke.sk (M.V.)

\*Correspondence: peter.jan.sincak@tuke.sk

**Abstract:** One of the disadvantages of the conventional robotic manipulators is their hard body, that is not compliant and unable to adapt to the sensitive and complicated environment. This disadvantage is compensated in the continuum robots. Their structure allows them to be compliant and dexterous in various sensitive and complicated environments. The modeling of these robots can be divided in two main groups. Where one is using classical analytical methods and other is using modern learning-based techniques to learn the kinematics and dynamic models of the robot. This work is describing the use of reinforcement learning method called deep Q learning to learn the control of a tendon driven robot in order to position itself to the desired position. The algorithm is trained on a constant curvature approximation model of the robot. The achieved results show that the agent was able to learn to get towards the goal, however the accuracy needs to be improved. Further work will focus on implementation of multiple agents to study how the distribution of the task will improve the accuracy and training time.

**Keywords:** robotics, control algorithm, mathematical modeling, simulation

## 1. Introduction

Conventional robotic manipulators can be defined by various criteria like numbers of joints, types of joints connecting the links of the robot, etc. By kinematic structure, the robotic manipulators are classified as serial, parallel, and hybrid manipulators. One of the important properties of robotic manipulators are the number of their joints that correspond to their degrees of freedom. When it comes to the continuum robots, most of them have a high or virtually infinite number of degrees of freedom. Therefore, continuum robots can be classified as redundant or hyper-redundant robots. The continuum robots are essentially biologically inspired robots whose capabilities were inspired by snakes, elephant trunks, and all kinds of tentacles. The mechanical configuration of continuum robots allows them to move in various complicated environments as well as adapt to the obstacles and barriers. These properties are the main advantage of the continuum robots that are allowing them to be used for various complex tasks, where complex environments can cause problems to conventional rigid robots. There are many different applications of continuum robots, where their properties can be fully utilized.

This paper is focusing on the use of reinforcement learning for the control of tendon driven continuum robots. The structure of the paper is as follows: 1. Introduction, 2. Mathematical modeling of continuum robots, 3. Reinforcement learning based control algorithm, 4. Conclusion.

## 2. Mathematical modeling of continuum robots

One of the key components of the robot is the controller that dictates to the robot how to activate its actuators to achieve the desired position or coordinates in the coordinate system. The controller is acting in the actuator space, therefore, mapping between multiple coordinate systems is required.

There are multiple approaches of mapping between the coordinate systems and describing the kinematics of the continuum robots. These approaches can be categorized into two main groups, where one uses classical analytical methods to develop and describe the relationship between multiple coordinate systems and the other group uses modern learning-based approaches to learn these relationships either directly from the robot or its model.

### *2.2. Model-based modeling*

Model based approaches focus on analytical methods. The most common approach here is constant curvature approximation (CC). This approach assumes that the configuration space of a continuum robot is parameterized by three variables that represent the curve that is formed along the center line of the robot [1]. This approach reduces and ignores large amount of the robot's dynamics and trades it with the computation speed and simplicity of the model. The limitations of this approach are in its use, in cases, when the robot's actuation is symmetric and its shape uniform. This means that the tendons that are controlling the robot must be evenly distributed around the center line of the robot, so that the actuation can be symmetrical. Another approach similar to the CC approximation is the piecewise constant-curvature approximation (PCC) [2], [3]. In this case, the backbone is parameterized as a series of interconnected tangent sections, where each section is approximated as an arc with constant curvature [4]. The backbone is described by two parameters  $\kappa$ ,  $\Phi$ . In this description,  $\kappa$  is the curvature of the arc that represents the backbone of the robot,  $\Phi$  is the angle of rotation of the plane in which the robot is bending. The X, Y, Z coordinates of task space can be obtained from these two parameters by use of D-H parameters, Frenet-Serret frames, and other approaches that are described in detail and compared in [3].

The model-based methods are the most studied and researched methods right now. These methods rely mostly on the constant curvature approximation, due to its fast computation and easy implementation. All the mentioned models have its advantages and disadvantages based on various factors like external loading, mechanical design, number of sub-segments etc. In comparison, the accuracy does not change significantly between the models, however the computation time does [4]. This factor, therefore, plays the biggest role when choosing the right mathematical model of the continuum robot.

### *2.3. Model-free modeling*

Unlike model-based approaches of modelling, the model free approaches are newer and less explored. These approaches are based on the data that are gathered and generated by either mathematical model or real robot. Based on these data, various techniques are used to learn forward or inverse kinematics and actuate the robot with highest possible precision and speed. In [5], the author proposed to use neural networks to learn directly the inverse kinematics of a three-tendon driven robot. This approach showed good results, however drawbacks of this approach is its application to different continuum robots or even extending the segment on the original one, therefore this method is very specific to the robot designed in this paper. One of the proposed methods for solving the control task of a continuum robot can be seen in [6]. In this paper, the authors proposed a reinforcement learning approach to learn the control strategy for a pneumatically actuated soft robot. The movement of the robot is restricted to 2D space. The authors opted, for using Q-Learning, which guides the robot in any given state by choosing the appropriate action, based on the learnt policy. It is trained to move towards the randomly selected target and the iteration ends when the robot reaches the target with acceptable accuracy. The state space is discretized so that there are finite numbers of states that can occur, and the action space is limited to four actions that are enough to achieve every point in the 2D space. The application of reinforcement learning was also used in [7] to learn the closed-loop dynamic control of the soft robot. The authors have used recurrent neural networks to learn the forward dynamic model. In combination with trajectory optimization algo-

rithm and learnt forward model control policies are sampled on real robot, which is generating new trajectories. These are used in supervised learning to train the closed-loop predictive controller based on multilayer perceptron. In addition to classical Q-Learning, the use of Deep-Q Learning was introduced in [8]. The soft pneumatically controlled robot achieves its position, with combination of the unidirectional bending and bidirectional torsional deformation. The control policy is learnt on simulation of the robot by using the Deep-Q Learning with the experience replay. The use of reinforcement learning was also mentioned in [9]. In this paper, the authors proposed using the Deep-Q Learning approach on a tendon driven continuum robot. The robot was controlled by 4 motors so that the movement in the x-y coordinate system would be handled by 2 agents. Each agent was trained to move in one direction of the coordinate system in order to achieve the desired target. So called shielding scheme was also introduced. The shielding is adapting the actions of the agents to the actual Euclidean distance of the actual position and the target position. The variable actions allow for quicker achievement of the target point.

The use of model-free methods in the field of continuum robotics is relatively new and less explored than model-based methods. These methods are data dependent, and the learning uses the data to learn the proper kinematics. The main advantage of these methods is in the cases when the mathematical model is too complicated or just not available. Even though, the learning can take considerable amount of time, the subsequent deployment is fast, and the control is often very precise.

### 3. Reinforcement learning based control algorithm

The main objective of this research is to develop a control algorithm for positioning a continuum robot in 3D space. The robot platform can be seen in the following figure 1b.

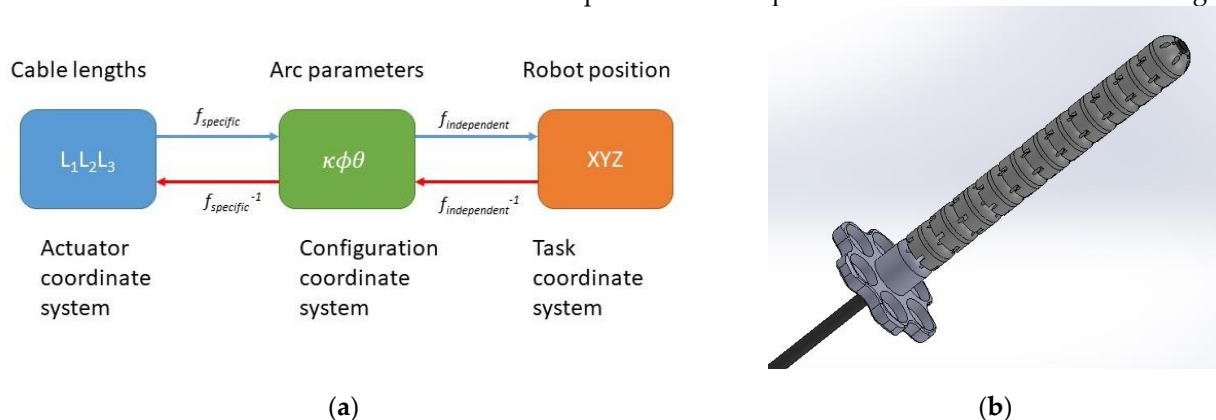
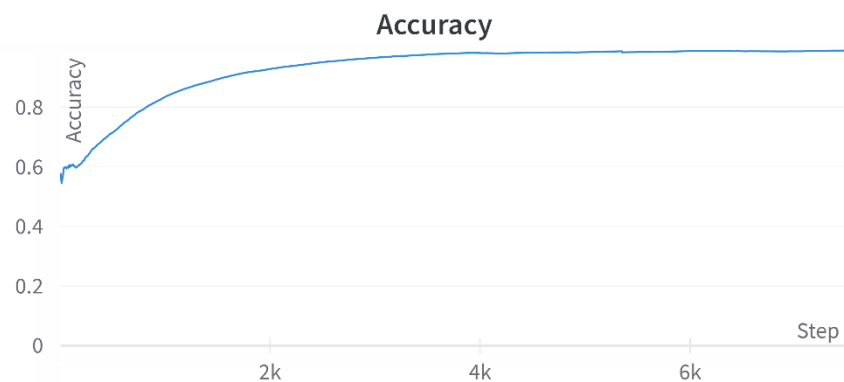


**Figure 1.** The modeled system: (a) The mapping between the multiple coordinate systems of the tendon driven continuum robot; (b) Hardware design of controlled and modelled continuum robot driven by tendons.

It consists of 11 sub-segments that are forming 1 large segment of the continuum robot. The robot is controlled by 3 tendons that are either shortened or extended in order to position the robot into the desired position. Since, the reinforcement learning based algorithms are based the interaction between the agent, which is an entity that is learning a policy, and the environment that represents the robot, either real or simulated, for the purpose of learning the policy a model of the proposed robot was created. The scheme of the model can be seen in the figure 1a. It is a constant curvature approximation model, where robot is approximated as a constant curve. The mapping is then done from cable lengths to the arc parameters all the way to the Cartesian coordinates of the end point of the robot. This model is then used as part of the environment to train the agent.

The proposed algorithm is based on so called Deep Q Learning. It consists of one DQN agent that is interacting with the environment. The agent is sending the appropriate actions to the environment, based this the environment gets into the state and sends reward signal to the agent depending on the chosen action. The agent contains 2 networks, where the main network is being trained and its weights are used to update the weights of the target network depending on the update interval. The main network is used to approximate the action-value  $Q(s, a, \theta)$ . The output of the target network  $Q^*(s_{j+1}, a_{j+1}, \theta^-)$  is to calculate the loss function that is being minimized during the training. The policy used for training is called  $\epsilon$ -greedy policy. The  $\epsilon$  parameter is used to determine how often does the agent take an exploratory action. The higher the parameter, the more likely is the agent to take a random action to explore the space. The action space is consisting of twelve possible action combinations that the agent can take to control all three tendons of the robot.

**Figure 2.** Training accuracy



The algorithm was training for 1500 episodes and each episode was set to have maximum 400 steps, depending on the termination condition. After each episode the robot was reset to initial position and start again. The algorithm was using an off-policy training and the robot's task was to achieve a desired point that was set at the beginning of the training. In figure 2 and figure 3 the graphs from the training can be seen.

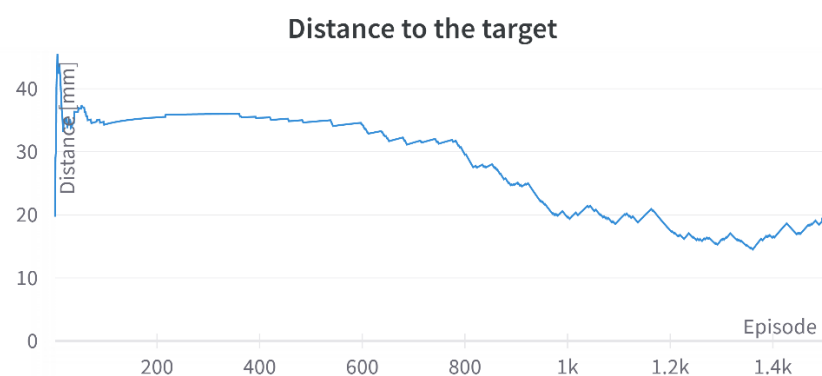


**Figure 3.** Distance to the target measured during the training

In figure 2, the training accuracy graph can be seen. The accuracy during training is slowly increasing as the agent learns the appropriate actions, and eventually the accuracy is converging. The objective of the training is to maximize the accuracy and minimize the loss function. In the figure 3, the error or distance of the robot's tip to the target point can be seen. As the training is progressing the error is slowly decreasing. The total training time of the algorithm was about 17-hours. During this time, the agent was learning the policy for action selection given the state. The initial position of the robot was 36.1 mm

away from the target point. The achieved Euclidean distance after the training was 19.3 mm.

#### 4. Conclusions

The objective of this paper was to present reinforcement learning based control algorithm for the position control of a continuum robot driven by tendons. To train the algorithm a mathematical model, based on constant curvature approximation, of continuum robot driven by tendons was implemented in the training algorithm. The training of the algorithm was done in batches so that 100 samples were randomly selected from the buffer, to train the neural network. The neural network had 3 input neurons representing the Euclidean distance from the actual position to the target point. As a result, one of the 12 possible actins was selected and used. After the 17-hour of training the achieved accuracy of the robot was about 19 mm. These results could be influenced by the number of factors. One of the factors is the number of actions that the agent could take. The limited action space can, therefore, limit the performance of the agent. Another limiting factor can be the number of the agents that are used to control the robot. In the current state a single agent must handle for all the tendons by itself, by introducing more agents the task can be distributed which would potentially simplify the task for each agent and which could also result in faster training times. The future work will consist of implementation of multiple agents to lighten the workload for each agent and achieve better accuracy and training times.

**Acknowledgments:** The authors would like to thank to the Slovak Grant Agency VEGA 1/0201/21, VEGA 1/0436/22 and KEGA 030TUKÉ-4/2020.

**Conflicts of Interest:** The authors declare no conflict of interest. The funders had no role in the design of the study; in the collection, analyses, or interpretation of data; in the writing of the manuscript; or in the decision to publish the results.

#### References

- [1] M. W. Hannan and I. D. Walker, "Kinematics and the Implementation of an Elephant's Trunk Manipulator and Other Continuum Style Robots," *Journal of Robotic Systems*, vol. 20, pp. 45-63, February 2003.
- [2] B. A. Jones and I. D. Walker, "Kinematics for multisection continuum robots," *IEEE Transactions on Robotics*, vol. 22, p. 43-55, February 2006.
- [3] R. J. WebsterIII and B. A. Jones, "Design and Kinematic Modeling of Constant Curvature Continuum Robots: A Review," *I. J. Robotic Res.*, vol. 29, p. 1661-1683, November 2010.
- [4] P. Rao, Q. Peyron, S. Lilge and J. Burgner-Kahrs, "How to Model Tendon-Driven Continuum Robots and Benchmark Modelling Performance," *Frontiers in Robotics and AI*, vol. 7, p. 223, 2021.
- [5] M. Giorelli, F. Renda, G. Ferri and C. Laschi, "A feed-forward neural network learning the inverse kinetics of a soft cable-driven manipulator moving in three-dimensional space," in *2013 IEEE/RSJ International Conference on Intelligent Robots and Systems*, 2013.
- [6] X. You, Y. Zhang, X. Chen, X. Liu, Z. Wang, H. Jiang and X. Chen, "Model-free control for soft manipulators based on reinforcement learning," in *2017 IEEE/RSJ International Conference on Intelligent Robots and Systems (IROS)*, 2017.

- [7] T. George Thuruthel, E. Falotico, F. Renda and C. Laschi, "Model-Based Reinforcement Learning for Closed-Loop Dynamic Control of Soft Robotic Manipulators," *IEEE Transactions on Robotics*, vol. PP, p. 1–11, November 2018.
- [8] S. Satheeshbabu, N. K. Uppalapati, G. Chowdhary and G. Krishnan, "Open Loop Position Control of Soft Continuum Arm Using Deep Reinforcement Learning," in *2019 International Conference on Robotics and Automation (ICRA)*, 2019.
- [9] G. Ji, J. Yan, J. Du, W. Yan, J. Chen, Y. Lu, J. Rojas and S. S. Cheng, "Towards Safe Control of Continuum Manipulator Using Shielded Multiagent Reinforcement Learning," *arXiv:2106.07892 [cs]*, June 2021.



# Introduction of Generative Design for Spur Gear Wheel Bodies

Samuel Sivák<sup>1, \*</sup>, Silvia Maláková<sup>1</sup>, Matúš Virostko<sup>1</sup>

<sup>1</sup> Faculty of Mechanical Engineering, Technical University of Košice, Letná 9, 042 00 Košice, Slovakia; saumel.sivak@tuke.sk, [silvia.malakova@tuke.sk](mailto:silvia.malakova@tuke.sk), matus.virostko@tuke.sk

\* Correspondence: samuel.sivak@tuke.sk

**Abstract:** A paper was written about recent developments in design engineering. These techniques included generative design and topological optimization. Following chapters described the process of topology optimization. Each step is divided into subsection, where it is described, alongside the image demonstration. Topology optimization is described step by step in a SolidWorks software. Advantages and disadvantages of this process in this software are summarized in the last section, where the next approach and other options are laid out.

**Keywords:** generative design; topology; spur gear body; SolidWorks

## 1. Introduction

During the conceptual design stage of the product development process, engineers and designers develop and assess numerous design choices in search of the best solutions. The procedures selected and choices made during this phase have a significant impact on all later stages of product development, including areas like manufacturing, production, quality, expense, and others [1]. Up to 80% of a product's cost can reportedly be identified by the end of the design phase, according to Anderson [2]. Multiple criteria must therefore be taken into account during the design stage in order to prevent unnecessary expenses later in the development process.

Technology developments, particularly in processing power, machine learning, and related algorithms, have contributed to the creation of intelligent design automation systems. Thanks to the high-performance computing capacity offered by the cloud, complex optimization computations and iterations that were before impossible to complete are now viable. This enables designers to quickly perform intricate simulations to test various product configurations under a variety of circumstances, providing important information for selecting the optimal design options. On the other hand, the rapid advancement of additive manufacturing technology is leading to significant changes in component production and design. They make it possible to produce complex geometries that are otherwise impossible to make using conventional production techniques [3].

The usage of CAD systems is being incorporated into the design process more and more often, and this incorporation is being supported by the expanding range and capabilities of the systems [4]. Engineers started creating CAD-based topology optimization (TO) software that can provide the best designs for certain structures. However, this has been mostly acknowledged by designers and engineers, rather than the more general area of product design [5]. Such programs may change current designs, include explicit features into the design, and build whole new designs. This issue has recently been resolved by the inclusion of generative design (GD) algorithms in CAD software. These programs' primary objective is to foster designers' creativity by producing a wide range of design solutions. The aim of this article is to lay the foundation for the research based on GD, which will be compared to commonly used methods for optimization as well as the use of TO.

## 2. Materials and Methods

The conventional design process starts with the process of developing functional specifications over the user needs, which are included in the following modelling phase. These are transformed into geometric shapes using CAD systems. CAD systems are mainly used to create a detailed 3D model of the final element and to produce accurate engineering drawings. The three-dimensional models are then verified by simulation programs, i.e. CAE (Computer Aided Engineering) and CAM (Computer Aided Manufacturing) programs, using analytical and testing functions, before they are sent to production machines, such as machining centers, lathes or milling machines, to produce the final product. The use of CAx (Computer Aided Technologies) systems [6] is used to support and simplify design on the one hand, while on the other hand such systems can limit the creativity of designers [7]. This is mainly because current CAD systems allow designers to create 3D models according to parametric feature-based modelling, which was introduced in the late 1980s. The main advantage of this technique was its ability to produce flexible designs defined by design variables and parametric character. In the following years, CAD systems were enriched with additional modelling and specific functions and were also integrated with CAE and CAM modules, allowing users to work in a single virtual environment. In particular, the CAE modules enable finite element analysis (FEM/FEA), in which structural studies are solved by defining geo-metrics, boundary conditions and initial conditions [8], while CAM is used to assess the manufacturing geometry created in the CAD environment. Once the program and path are selected, code can be created and used in the CNC machine to create the product. However, the modelling approach has remained essentially unchanged and thus does not support designers in building complex geometry models [9].

Unlike the traditional design process, in which CAD systems are used to generate precise geometry that follows user specifications, the introduction of TO and GD allows designers to focus primarily on the function of the designed product instead of the form, using optimization programs to generate design alternatives. In fact, as shown in Figure 1, the first stage is common to both methods, where the CAD system has to be used, but only for the definition of the functional surfaces. Moreover, the last stage is common to both methods and consists of the use of CAM systems to ensure precise manufacturing. In contrast to the CAM systems mentioned above, these systems, specific to AM, are designed to enhance the printing capabilities, optimizing the orientation of the part, the number and type of supports and, only recently, to predict the deformation of the part due to the high stress gradient created during printing [10].

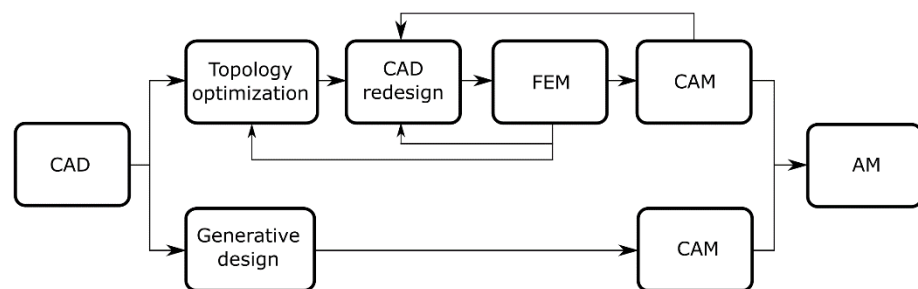


**Figure 1.** Scheme of optimization using TO and GD.

### 2.1. Generative design

Research on generative design started in the 1980s, but much of it published at the time, was completely theoretical and lacked any real-world applications. The field of architecture first attracted interest [11], but soon after, academics started considering opportunities and applications in other domains that may profit from the convergence of computer and evolutionary theory parallels. In the field of design, Vajna et al. [12] developed

the autogenetic design theory by examining the similarities between the design process as it relates to product creation and the natural process of evolution (Figure 2).

According to evolutionary theory, the product development process may be described as the continual improvement of a fundamental solution under the influence of beginning conditions, boundary conditions, and constraints. These factors influence the development of design and open up new spaces for it. Given the variety of uses, generative design currently lacks a widely accepted concept. In accordance with Shea et al. [11], "Generative design systems are targeted at producing novel design processes that provide spatially inventive, yet efficient and buildable designs by employing current computational and manufacturing capabilities". According to Krish [13], "generative design" is a design-driven, parametrically constrained exploratory technique that utilizes parametric-based CAD tools intended to support design as an emerging process. However, there are presently design applications that go beyond the usage of standard CAD tools and are not constrained by parametric models [14, 15].

Using a process known as generative design, which includes some automation and autonomy in the process, several designs are created. The design process mimics nature's evolutionary process by starting with one or more different designs and changing them through time into ones that are more suited to the demands of particular contexts. Design criteria that are not met or circumstances that are not met are discarded, and the search (evolution) process moves in new directions.

The term "generative design" is frequently used to refer to computationally aided design, despite the fact that it can only be performed with a pen and paper and a set of rules. The created results can be in a variety of formats, including images, models, sounds, and animations. Generative design is typically thought of as using algorithms as a foundation for the production of designs.



**Figure 2.** Progress of generative design [16]

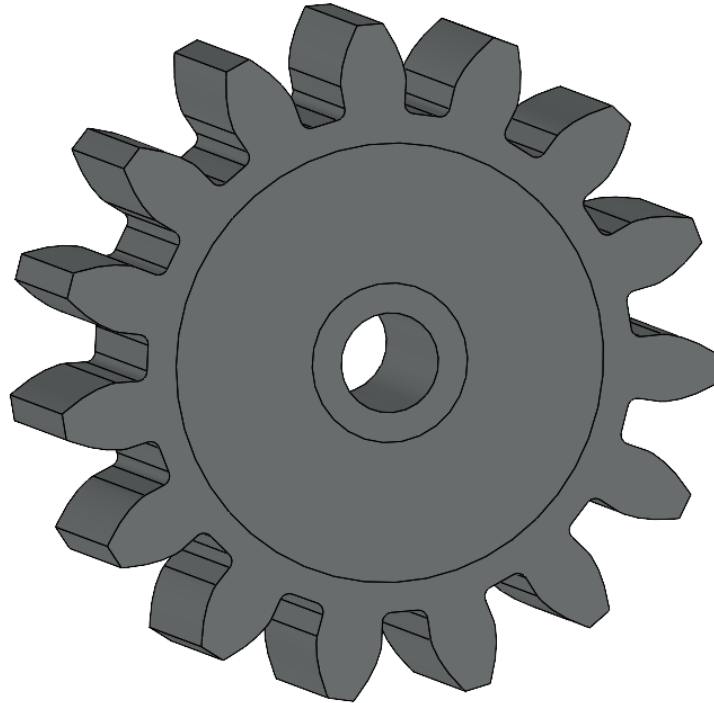
### 3. Practical demonstration of the problem solution in SolidWorks

This chapter is aimed at definition of conditions needed for topology optimization of a part, mainly the gear wheel body. Next steps are described step by step of what they mean and how to use them.

#### 3.1. Digitization of the Model

The 3D modeling capabilities and effective design automation tools built into SolidWorks were utilized to digitize the model. Although, in reality the designer needs to take into account that the optimized model cannot have more bodies than one and needs to be unified. This is a crucial requirement because the SolidWorks topology optimization mod-

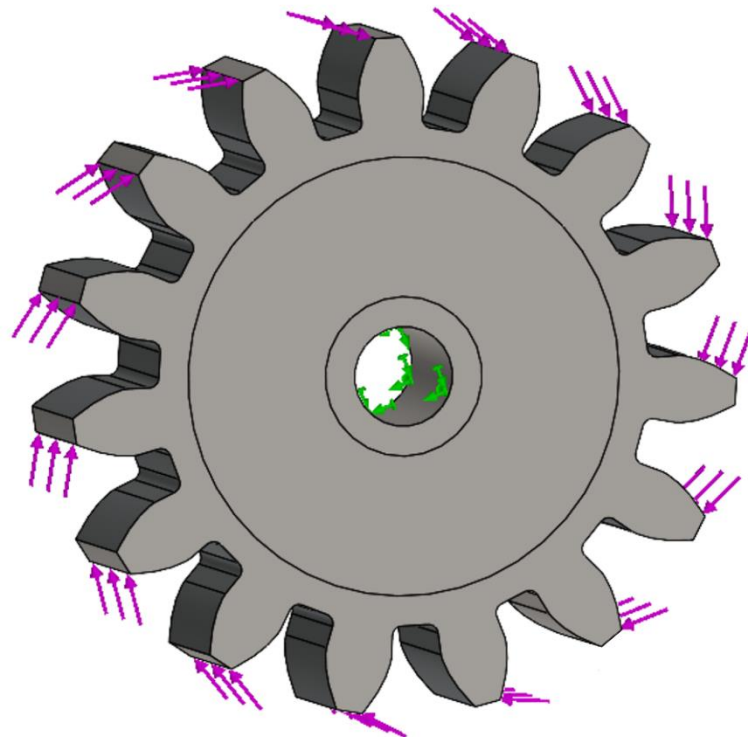
ule does not support the simultaneous optimization of many parts or assemblies. Although it needs to be taken into account that some areas need to be unchanged from geometry point of view (holes, functional profiles...). In that case the model needs to have boundaries limiting the area (Figure 3).



**Figure 3.** Digitalized model with boundary curves

### 3.2. *Defining the External Loads and Fixtures*

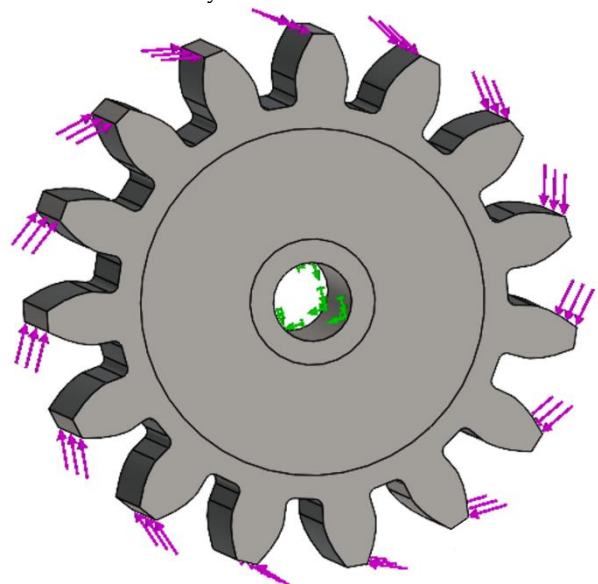
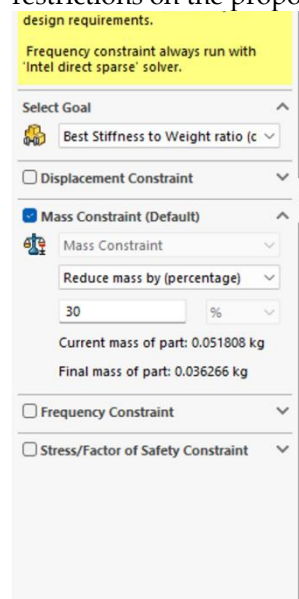
External loads and fixtures are defined in the same way as for FEM simulation. Only difference is that the force load is place upon every tooth of the gearing to ensure the “pattern” shape of the optimized gear wheel, which means that there will not be sections with less or no support without pattern (Figure 4).



**Figure 4.** Boundary and load characteristics for gear wheel

### 3.3. Defining Goals and Constraints of the Model

The topology optimization study's optimization objectives and constraints must be determined in this part. Given a particular amount of material reduction, the topology analysis will try to determine the stiffest structure achievable. The aim and limitations definition will affect the material removal. The geometry of the 3D model's most stiff components is determined by the amount of mass that is eliminated from the initial maximum design space by the optimization process. When "Best Stiffness to Weight ratio" is chosen, the algorithm will attempt to reduce the 3D model's global compliance, which is an indicator of the model's overall flexibility (contrary to stiffness) (Figure 5). Compliance is defined by the sum of strain energies of all elements. Constraints define upper and lower limitations for the largest displacement that can be shown in the 3D model, or they impose restrictions on the proportion of the mass that may be removed.

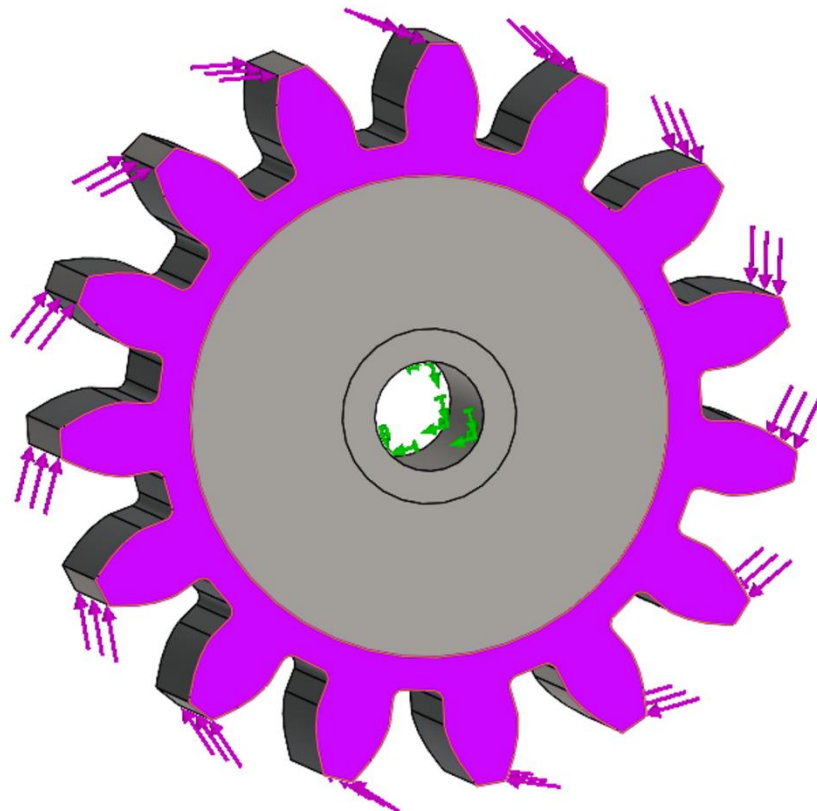


**Figure 5.** Goals and constraints for gear wheel

### 3.4. Defining the Manufacturing Controls

The material is laid out in a way by the topology optimization process that adheres to the optimization objective under the given geometric constraints. However, utilizing conventional manufacturing techniques like casting or forging may make it difficult to produce the 3D model. The application of appropriate production controls in the optimization model can prevent the creation of undercuts and hollow pieces. Manufacturing boundaries guarantee that the optimized 3D model can be correctly stamped or removed from a mold, for example. Four different manufacturing control types are available in SolidWorks simulation. They are listed below:

- Thickness Control. limits the topology optimization of the model to avoid producing regions with difficult-to-manufacture walls that are too thin or regions that are too thick.
- Preserved Region(s). This characteristic adds conserved region(s) to the 3D model that won't be altered during topology optimization, maintaining the geometry of those surfaces that are crucial to the model's functionality (Figure 6).
- Symmetry Control. The optimized 3D model is made symmetric to one or more pre-determined planes using symmetry control. Depending on the design layout, a planar symmetry can be adopted that is either half, quarter, or one-eighth.
- De-mold Control. This feature brings the extraction of the optimum 3D model from a mold.

**Figure 6.** Preserved regions defined in manufacturing controls

#### 4. Conclusions

The 3D model that has been optimized can be exported as a surface body, solid body, or graphic body. When the model will be created on a 3D printer without additional design modification, the alternatives "Surface body" and "Solid body" are appropriate. When "Graphic body" is selected, an optimal design is exported in a boundary geometry representation format, which is better suited for alterations and additional editing. In the first 3D model, SolidWorks enables the insertion of an exported graphic body. After superimposing two 3D models, the initial step is to determine their differences. The simplest approach to achieve this is to make the optimized model opaque and adjust the initial model's transparency to semitransparent.

The program SolidWorks reported an errors with regions to preserve which needs to be addressed. Preserved regions for topology optimization are the hub which is mounted on shaft and gearing with some rim thickness under it to ensure the gearing stiffness. Other disadvantage of this work is that the rim thickness was chosen but not optimized. These points will be added and solved in future works.

Future works will be performed not only in SolidWorks software but also in other ones such as NX or Fusion 360. This will be done to ensure and choose in needed of the best software to optimize the gear wheel body. One of the missing features of SolidWorks software is also a lack of generative design options. This will be addressed in future works alongside the comparisons of software capabilities and optimized shapes.

**Acknowledgments:** This paper was written in the framework of Grant Project VEGA: „1/0528/20 and KEGA 029TUKE-4/2021.

**Conflicts of Interest:** The authors declare no conflict of interest.

#### References

1. Wang, L., Shen, W., Xie, H., Neelamkavil, J. and Pardasani, A. Collaborative conceptual design—state of the art and future trends. *Computer-Aided Design* 2002, 34(13), pp.981-996.
2. Anderson, D. *Design for Manufacturability*, CRC Press, 2014.
3. Bici, M., Broggiato, G. and Campana, F. Topological Optimization in Concept Design: starting approach and a validation case study. *Lecture Notes in Mechanical Engineering* 2016, pp.289-299.
4. Horváth, I. On some Crucial Issues of Computer Support of Conceptual Design. *Product Engineering* 2004, pp.123-142.
5. Querin, O. *Topology design methods for structural optimization*. 2017. London, United Kingdom: Academic Press.
6. Werner Dankwort, C., Weidlich, R., Guenther, B. and Blaurock, J. Engineers' CAx education—it's not only CAD. *Computer-Aided Design* 2004, 36(14), pp.1439-1450.
7. Barbieri, L., Calzone, F. And Muzzupappa, M. Form and Function: Functional Optimization and Additive Manufacturing. *Springer: Cham, Switzerland* 2019, pp. 649–658
8. Bathe, K. *Finite element procedures in engineering analysis*. Englewood Cliffs 1982, N.J.: Prentice-Hall.
9. Tang, Y. And Zhao, Y. A survey of the design methods for additive manufacturing to improve functional performance. *Rapid Prototyping Journal* 2016, 22(3), pp.569-590.
10. Pagac, M., Hajnys, J., Halama, R., Aldabash, T., Mesicek, J., Jancar, L. and Jansa, J. Prediction of Model Distortion by FEM in 3D Printing via the Selective Laser Melting of Stainless Steel AISI 316L. *Applied Sciences* 2021, 11(4), p.1656
11. Vajna, S. et al. The Autogenetic Design Theory: An evolutionary view of the design process. *Journal of Engineering Design* 2005, 16(4), pp. 423-440.
12. Krish, S. A practical generative design method. *Computer-Aided Design* 2011, 43(1), pp. 88-100.
13. Chen, X. et al. Forte: User-Driven Generative Design. *Proceedings of the 2018 CHI Conference on Human Factors in Computing Systems* 2018, ACM Press, New York, New York, USA, pp. 1-12.
14. Kazi, R.H. et al. DreamSketch: Early Stage 3D Design Explorations with Sketching and Generative Design. *Proceedings of the 30th Annual ACM Symposium on User Interface Software and Technology - UIST '17* 2017, ACM Press, New York, New York, USA, pp. 401-414.
15. Tyflopoulos, E. et al. State of the art of generative design and topology optimization and potential research needs. 2018.
16. Add it. Available online: <https://www.add-it.tech/en/services/design/generative-design> (5.11.2022).



# Digitization and virtual reality in industrial enterprises

Dominika Sukopová \*, Jaroslava Kádárová and Juraj Kováč

Department of Industrial and Digital Engineering, Institute of Industrial Engineering, Management and Environmental Engineering, Technical University of Košice, Park Komenského 9, 040 01 Košice, Slovakia; dominika.sukopova@tuke.sk; jaroslava.kadarova@tuke.sk; juraj.kovac@tuke.sk

\* Correspondence: dominika.sukopova@tuke.sk; Tel.: + 421 55 602 2724

**Abstract:** The constant evolution of technology has a profound impact on people, their skills, knowledge and desire to own or use these new technologies. The same is true for entrepreneurs, for whom technology can greatly help to improve their skills, enhance their market position and undermine their competitors. One possibility is to embrace digitization. Creating a digital model that saves time and financial costs. The use of virtual reality will give the user a more realistic view of the enterprise space. These conveniences have also helped in various areas of business during the COVID-19 pandemic by enabling online interviews for workers or instant site visits.

**Keywords:** digitization, production hall, SketchUp, Twinmotion, virtual reality

## 1. Introduction

If businesses want to remain competitive, they need to be responsive to innovation and the changes that innovation brings to the world. Technology is increasingly encroaching on business processes. Virtual reality is currently under development, but is expected to be widely used in the market in the future. Which means the opportunity to bring a competitive advantage. However, the importance lies in responding to innovation in its early stages [1]. It is necessary to think about the possibilities of using virtual reality because they can bring added value not only to customers but also to the enterprise.

## 2. Digitization and visualization of the production hall model

The first part of the work consisted of creating a model of the production hall. For an illustrative example, a model of the production hall PK12a was made, which is part of the Technical University in Košice referred to as the prototype and innovation center of the Faculty of Mechanical Engineering.

The software products SketchUp and Twinmotion were chosen for making the model. The SketchUp software made it easy to create the basic space of the production hall, to design the individual machines and equipment. Some of them were inserted into the environment from the respective library. The Twinmotion program allowed important changes of materials and colors, addition of the surrounding environment, of course addition of other objects as well as addition of workers, machine and equipment operators.

The following figures show the model created in the aforementioned programs [2].



**Figure 1** Created model of the hall in SketchUp

Figure 1 shows the formation of the basic space of the production hall, complete with machinery and equipment. In the figure it is also possible to see the tools used by the program.



**Figure 2** Created model of the hall in Twinmotion

The changes made to the production hall environment and the addition of production machine and equipment operators are shown in Figure 2.

### **3. Virtual reality**

The use of virtual reality enriches all of the entrepreneur's options mentioned in the introduction. Its use has been high even in the case of pandemic period. It has enabled various meetings or visits to distant places [3].

#### *3.1. The importance of virtual reality*

The improvement and advancement of technology can also be seen in the wide range of applications of virtual reality [4]. It has become an essential part of industry, healthcare, sport or architecture.

##### **3.1.1. Virtual reality and employee training**

More and more companies are procuring virtual reality assets every day. It allows them to train or train their staff in one place, easily and at a savings time [4].



**Figure 3** worker training

Figure 3 shows the training of an employee using virtual reality tools.

### 3.1.2. Virtual reality and communication

The influx of the COVID-19 pandemic has also severely disrupted and limited communication between companies around the world.

Suspension of flights, banning movement between countries was addressed using virtual reality tools that allowed users to communicate in the same room. In this way communication allows viewing videos, images, PDF files in individual rooms [4].



**Figure 4** communication using virtual reality

### 3.1.3. Virtual reality and automotive production

Virtual reality also has its place in the automotive industry. A team of engineers can use it to design a new car model, saving money and time [5].



**Figure 5** Creating a car design through virtual reality

The use of virtual reality is also used in other areas mentioned above. In each of them, its use has a different meaning, a different goal, and in each of them, different means of virtual reality are used.

### 3.2. Virtual reality resources

In some cases, interaction is provided by basic computer equipment such as a mouse or keyboard, on the other hand, the current era brings some additional means of virtual reality.

#### 3.2.1. Head-up display

This means of virtual reality can be considered the simplest. The head-mounted display is a display device with a varied shape [6]. We include here display goggles or helmets.



**Figure 6** Headset of virtual reality

This virtual reality tool is increasingly being sold alongside game controllers, displayed in Figure 6.

#### 3.2.2. Data gloves

This means allows the user to move, rotate components, fold objects in the virtual world [7].



**Figure 7** Data gloves

#### 3.2.3. Leap Motion Controller

Leap Motion Controller maps hand movement in real time, enabling natural integration with digital content [8].



Figure 8 Using the Leap Motion controller

The following virtual reality tools were used for the created model of the production hall:

- Head-up display
- gaming controllers



Figure 9 Use of virtual reality tools

#### 4. Price appreciation

The aim of the article was to introduce digitization, its conveniences and the switching of digitized model into virtual reality.

Use of the software products was available free of charge with student registration, but for businesses these programs would require a fee. The same initial investment is required for the virtual reality resources used.

A table was created to give an idea and approximation of the investment.

Table 1 Display of expenditure

Product	Price
SketchUp	328, 80 €
Twinmotion	473, 83 €
virtual reality resources used (headset)	490 €
Computer for VR	1 248 €
training programs	175 €
Total	2 715, 63 €

The price evaluation includes the average prices of the virtual reality assets used as well as the individual programs. The price depends on the level of the program. However, higher editions of the programs are suitable for more demanding users, for example in the medical or architectural fields. In the same way, in the industry, the entrepreneur

could reduce his expenditure by the value of the training, as the level of use of SketchUp and Twinmotion is not high.

## 5. Conclusions

This paper has highlighted the increasing use of digitization and virtual reality in business. The article included the creation of a manufacturing floor space and its transformation into a program that allows the model to be linked to virtual reality. Its inventiveness lay in the possibility of viewing the created space and doing so instantly. The article also included several other benefits of using virtual reality, in different areas of business. The price evaluation highlights the initial financial costs that a business needs to incur if it is interested in this way of increasing the efficiency of the business.

**Acknowledgments:** This article was created with the support of projects: KEGA 009TUKE-4/2020 "Transfer of Digitization into Education in the Study Program Business Management and Economics", VEGA 1/0340/21 "The impact of a pandemic and the subsequent economic crisis on the development of digitization of enterprises and society in Slovakia", VEGA 1/0438/20 "Interaction of digital technologies to support software and hardware communication of the advanced production system platform" and KEGA 001TUKE-4/2020 "Modernizing Industrial Engineering education to Develop Existing Training Program Skills in a Specialized Laboratory."

**Conflicts of Interest:** The authors declare no conflict of interest.

## References

1. Garcia-Ortega, B., Lopez-Navarro, MA, Galan-Cubillo, J. Top Management Support in the Implementation of Industry 4.0 and Business Digitization: The Case of Companies in the Main European Stock Indices. **2021**. Available online: <https://www.webof-science.com/wos/woscc/full-record/WOS:000709063900001>
2. Askin, R. G., Tandrige, Ch.: Modeling and Analysis of Manufacturing Systems. John Wiley & Sons, **1993**, ISBN: 978-0-471-51418-3
3. Mižikova, A. What is virtual reality? Definition. **2018**. Available online: <https://blogit.sk/co-je-virtualna-realita/>
4. Šubák, M. What you can do in virtual reality. **2019**. Available online: <https://virtualnarealita.eu/vseobecne-virtualna-realita/co-sa-da-robit-vo-vr/>
5. López, J. El diseño de los CUPRA: así se ha conferido al Formentor, el último concept car de la marca Española. **2019**. Available online : <https://www.highmotor.com/cupra-formentor-diseno-creacion.html>
6. Přecechtěl P. VR - Virtual Reality: from the first steps to the present. **2019**. Available online: <https://www.alza.sk/vr-virtualna-realita>
7. Kováč J., Rudy V., Malega P., Connecting robotic systems with the Cyber Glove II data glove. **2021**. In: PRŮMYSLOVÉ INŽENÝRSTVÍ 2021 : Mezinárodní studentská vědecká konference : Sborník příspěvků. - Plzeň (Česko). s. 102-109. ISBN 978-80-261-0792-7. Available online: [https://dspace5.zcu.cz/bitstream/11025/46405/2/PI2021%20-%20sbornik\\_komplet-106-113.pdf](https://dspace5.zcu.cz/bitstream/11025/46405/2/PI2021%20-%20sbornik_komplet-106-113.pdf)
8. Carter T. and the collective. Leap Motion Controller. **2020**. Available online: <https://www.ultraleap.com/product/leap-motion-controller/>

# Analysis of available torque on the output shaft for Universal Rotary Module prototype

Michal Sasala <sup>1,\*</sup>, Jozef Svetlik <sup>1</sup>, Tomas Stejskal<sup>1</sup> and Stefan Ondocko<sup>1</sup>

<sup>1</sup> Department of Production Technique and Robotics, Faculty of Mechanical Engineering, Technical University of Kosice, Slovakia, michal.sasala@tuke.sk

**Abstract:** This article deals with analysis of available torque on prototype device with unlimited degree of rotation. This device is developed at Technical University of Kosice. Current generation is able to rotate on their own, however the capability of current generation is still unknown. This is holding back the future development, as we do not know, what current generation is capable of. Therefore, in this article we are going to test highest available torque on one of the modules to evaluate, if current design of mechanics is good for future development. To achieve this task, we build custom setup and we are going to compare real measurements with theoretical values.

**Keywords:** modular system, URM, torque

## 1. Introduction

URM is short term for Universal Rotary Module. This device is developed at Technical University of Kosice. It is based on modular architecture, and it is important for modular robotic arm. The main advantage is ability to rotate continually without need to rotate back. Communication between modules is wireless. The power delivery to each module is done from previous module trough contact pins and coils for wireless power transfer. Other advantage is building a kinematic chain with degrees of freedom depending on required application. For that, we are connecting active parts of the module with passive interconnections called Bend. These bends can be manufactured with any angle, but for now we are working with angle  $52^\circ$ . However different angles can be manufactured based on specific task and requirements. Same size modules are identical, therefore there can be change in kinematic chain with each other in case of failure. [1,2]

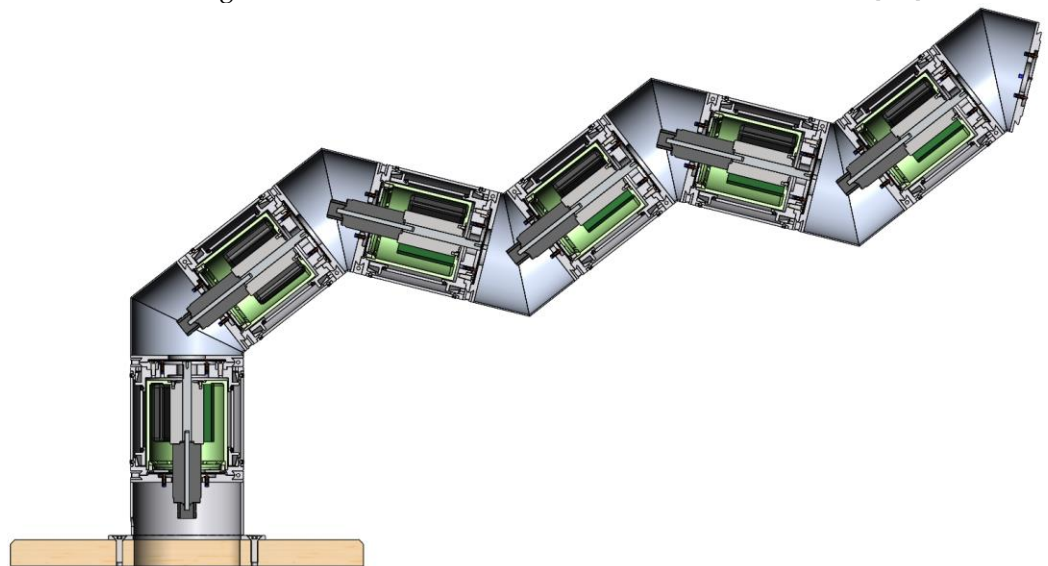


Figure 1. Kinematic chain from URM modules in section view

The second generation of these modules was manufactured in 2019 [3]. This generation consists of 3 different sizes named as Large, Medium and Small. All modules have height identical with outside diameter. Large is 128 mm, Medium 108 mm and Small is 88 mm. For mechanical connection they are requiring passive parts. This part does not have any mechanical parts, batteries or logic. It only connects two active modules together. However it is necessary to have this part, as the servo with gearbox is longer than the shell of the URM.

## 2. URM SPECIFICATION

### 3.1. Original Design

All modules of URM have their own logical circuit, their own power management, batteries, servo and power transfer features. The main difference is size of each module and servos used in each size. The general comparison of servo is in the table below. These values are also considered to be the base for our future measurements. All sections are manufactured primarily from aluminium alloys.

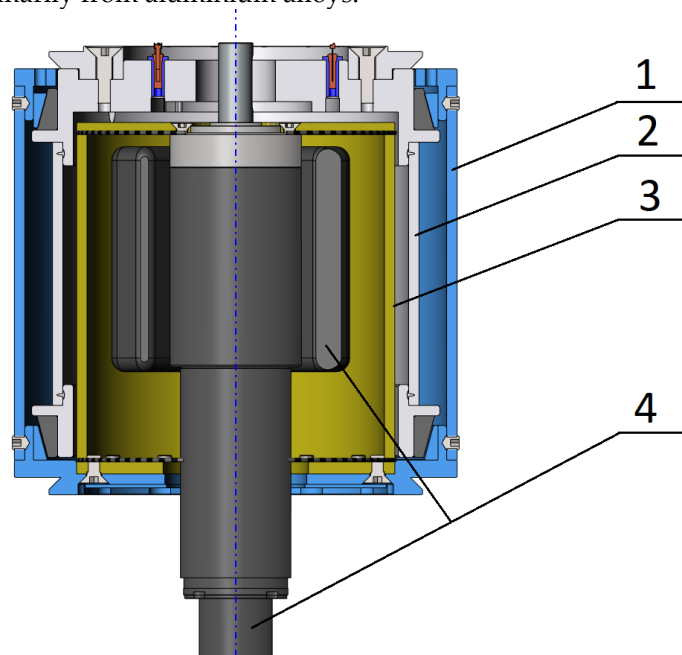


**Figure 2.** Description of section in URM. 1.) outside shell, 2.) rotating section 3.) core holder, 4.) servo, batteries, control unit.

The other modules are sized down version of the largest module. Therefore, we are focusing on improving this variant first, before we are implementing changes in the other variants. With smaller sizes, we are also using smaller servos. All servos can use up to 24 Volts. This allows us to use same control board for all sizes. The smaller servos have also lower torque and different gearbox. Selected values for each size are in the table below. These are only theoretical values, however the manufacturer can often guarantee performance close to these values. [4]

**Table 1.** This is a table. Tables should be placed in the main text near to the first time they are cited.

Sizes of URM	Small	Medium	Large
Outside diameter	88 mm	108 mm	128 mm
Gearbox	1:159	1:159	1:116
Model of servo	1741U024CXR	2642W024CR	3272G024CR
Max Torque	1.1 Nm	4.5 Nm	32.0 Nm
Continuous torque	0.8 Nm	3.5 Nm	13.2 Nm

Current generation was already improved by optimizing the core holder. This moved the prototype into working state, because till this point, modules were unable to move on their own. One of the main parameters in designing these modules was torque requirement. This is important, because each part of the robotic arm needs to be able to move in the most difficult position. Therefore, we need to know, how much performance is lost due to friction, resistance etc. This will also affect the battery life, lifespan of the bearings, and also the overall performance of the module.

The bearings are custom made taper plain bearings manufactured by Igus from material Iglidur G. [5]

For bearing arrangements we had two main options, called Face-To-Face arrangement or Back-To-Back arrangement. These arrangements are also referred to as X and O arrangement respectively.

Advantage of O configuration is higher rigidity and stability of assembly. It is also better for preloading the bearings. This arrangement can take very well both, axial and radial loads. X arrangement is better for tolerating misalignments. [6] The example of bearing alignment is shown below.

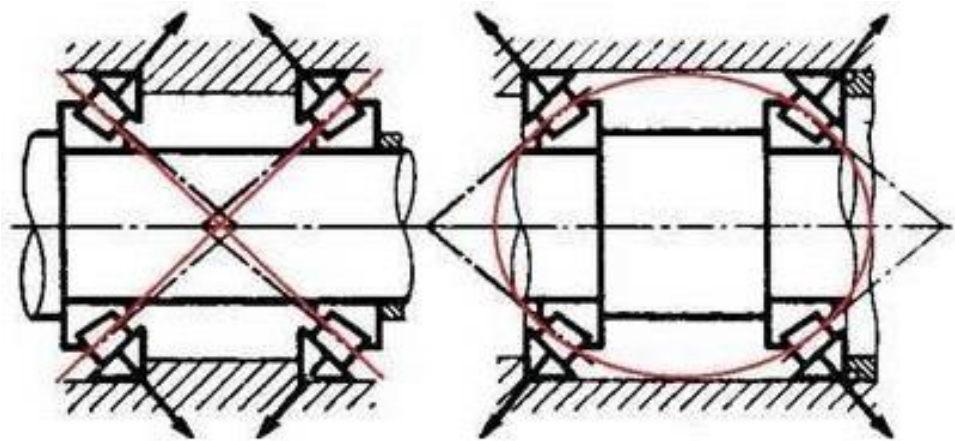


**Figure 3.** Face-To-Face and Back-To-Back configuration [7]

With experience from our first prototype generation, we used Back-To-Back configuration in current generation.

### 3.1. Changes in prototype

Original concept had manufacturing defects, that was fixed by manufacturing spare parts. The original design of the core holder was welded together from four individual parts. That introduce large deviation in concentricity between output shaft from gearbox and rotary section of URM. The radial forces on the gearbox were so large, it was unable to move on its own. Therefore, we manufactured spare part from PLA on 3d printer. These segments are interchangeable. [8]

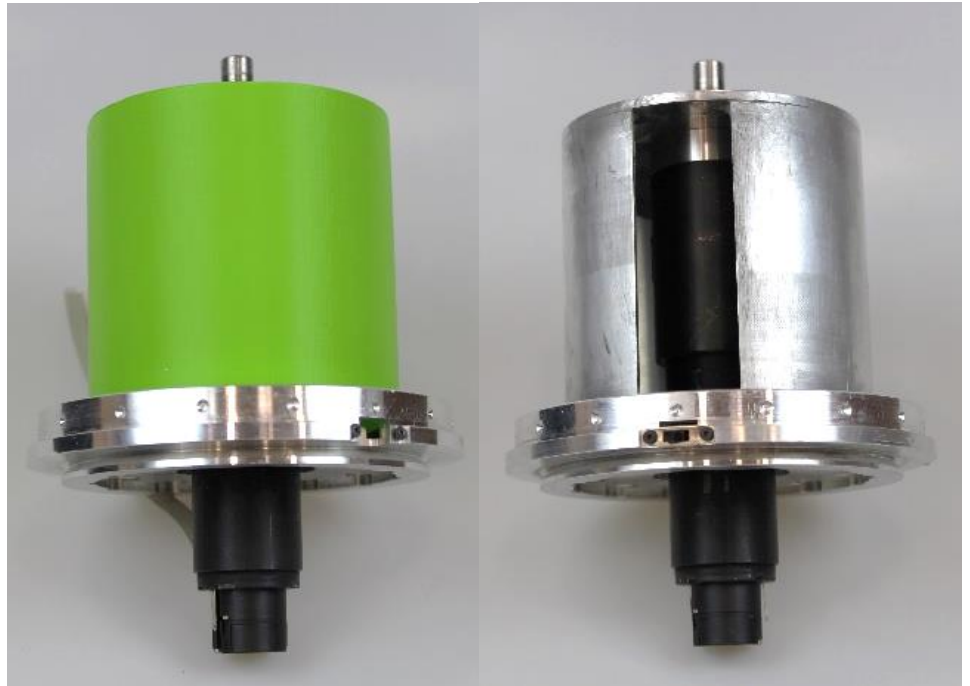


**Figure 4.** New core holder from PLA and old core holder from aluminium

### 3. Testing setup

For purpose of this article, we are testing only larger module, as it is only size that can be fixed in the testing setup and it is only module, that is currently working. We secured the module in the fixture and created tower, where we can fix lever for our torque meter. Then we proceeded to take measurements every 60 degrees in both directions. The Clockwise direction is defined as the top fixture is trying to rotate clockwise. The Counterclockwise direction is done analogically. We also reset the torque meter after few measurements to ensure proper calibration of the device. For moving the servo we used power supply with current and voltage control. The power supply has limit up to 30 V and 5 A of current. Our servo is however limited to 24 V and 3.5 A.

During the testing, we needed around 20 degrees in both directions, before torque meter started showing values. This was because the backlash in the system and also the meter is only showing value, if the torque exceeds 6 Nm. However, we do not believe this will significantly affect the results.

In testing we set voltage for maximum, that is 30 V and limited the current to 0 A. Then, we connected positive and negative cable and slowly increase the limit for current, till the all backlash was gone. Once we were sure, that all backlash was eliminated, we increased current limit to maximum, and read out the torque on the torque meter. While the power supply can provide 30V 5A, maximum values reached 24 V and around 4 A. This means, the limits were set by the servo electronic, and servo always used maximum available power. For changing directions, we manually changed the cables and repeated the measurement in other direction.



**Figure 5** Testing setup

The torque meter has operating range from 6 Nm up to 30 Nm with resolution 0.1 Nm. The torque meter was connected to the Trantorque M shaft/hub connection on the one end, and on the second end was connected to the lever. This lever was not fixed, however its movement was limited by two small towers. During the testing, we did not observe any slips, strokes or jerks, that could invalidate the results.

#### 4. RESULTS

We took multiple measurements in both directions. After few cycles, we noticed that the values were repeating itself. Table below shows the highest measured value for each segment of rotation.

**Table 2.** This is a table. Tables should be placed in the main text near to the first time they are cited.

Rotation	Clockwise	Counterclockwise
0°	9.5 Nm	21.6 Nm
60°	9.5 Nm	21.2 Nm
120°	9.8 Nm	20.2 Nm
180°	9.9 Nm	20.2 Nm
240°	9.0 Nm	19.1 Nm
300°	9.0 Nm	21.0 Nm

We were able to reach up to 62.5 % of maximum possible torque for the counterclockwise direction and 75 % of continuous maximum torque for clockwise direction. That indicates very high internal friction, or big manufacturing imperfection.

One of the ways for decreasing the friction is to use different material for bearing with lower friction coefficient. This will however mean changing the entire inner parts, and

also redesign the tensioning mechanism, as well as entire rotating section. These changes are too radical for implementing in this prototype. Therefore, we are going to design new improved version as new generation. This will also allow us to change bearings configuration from Back-To-Back to Front-To-Front, which should further improve efficiency of the servo.

## 5. Conclusions

In this article we measured the available torque in multiple positions for Universal Rotary Module. These tests were important to evaluate, how friction and manufacturing imperfections are impacting the performance of our prototype. We discovered, that the device has only 75% of maximum possible torque. Based on that we can assume, we need to further improve bearings by changing the material with lower friction coefficient and also change alignment of these bearings, as these losses can negatively impact performance. For future prototype we would like to achieve at least 95% efficiency. All these changes are going to be implemented in future generation of URM. Old generation is going to be used for different tests.

**Acknowledgments:** This work was supported by the Slovak Research and Development Agency under the Contract no. APVV-18-0413.

## References

1. Svetlák, J.; Demeč, P.; Semjon, J. Rotational Kinetic Module with Unlimited Angle of Rotation. In Proceedings of the Applied Mechanics and Materials; Trans Tech Publ, 2013; Vol. 282, pp. 175–181.
2. Svetlák, J. *Modulárna Architektúra Výrobnej Techniky*; Edícia vedeckej a odbornej literatúry – Strojnícka fakulta Technickej Univerzity v Košiciach; I.; Košice; ISBN 978-80-553-1928-5.
3. Štofa, M. Experimentálny Vývoj Rotačných Modulov Pre Stavbu Sériových Kinematických Štruktúr vo Výrobnej Technike. *Dizertačná práca, Košice: TU 2019*.
4. FAULHABER BXT 4221 ... BXT R Available online: <https://www.faulhaber.com/en/products/series/4221bxtr/> (accessed on 25 February 2022).
5. Iglidur® G, Sleeve Bearing with Flange, Mm Available online: <https://www.igus.eu/product/64?artNr=GFM-03040-15> (accessed on 10 October 2022).
6. Understanding Back-to-Back & Face-to-Face Bearing Arrangements Available online: <https://www.pumpsandsystems.com/understanding-back-back-face-face-bearing-arrangements> (accessed on 10 October 2022).
7. Orlov, P.; Troitsky, A. *Fundamentals of Machine Design*; vol 4.; Mir Publishers: Moscow, 1977;
8. Šašala, M.; Hrivniak, L.; Ondočko, Š.; Svetlák, J. Topologická Optimalizácia Konštrukcie Rotačného Modulu s Použitím Metód Aditívnej Výroby. *Novus Scientia 2021*.



# Individual arm and forearm orthosis CAD design

Branko Štefanovič<sup>1,\*</sup>, Lucia Bednarčíková<sup>1</sup>, Richard Staško<sup>1</sup> and Jozef Živčák<sup>1</sup>

<sup>1</sup> Technical university of Košice, Letná 1/9, 04200, Košice, Slovakia; [branko.stefanovic@tuke.sk](mailto:branko.stefanovic@tuke.sk), [lucia.bednarcikova@tuke.sk](mailto:lucia.bednarcikova@tuke.sk), [jozef.zivcak@tuke.sk](mailto:jozef.zivcak@tuke.sk)

\* Correspondence: [branko.stefanovic@tuke.sk](mailto:branko.stefanovic@tuke.sk)

**Abstract:** The aim of this article is to propose a methodology for individual arm and forearm orthosis design using innovative methods such as 3D scanning, CAD modeling and additive manufacturing. The orthosis was designed in a CAD software and the development process was based on a subject's 3D scan of the upper limb. A specific pattern has been applied on the orthosis and the manufacturing simulation has been performed.

**Keywords:** upper limb orthosis, body 3D scanning, orthotic device design, CAD modeling, additive manufacturing

## 1. Introduction

An orthosis, or orthotic device, is a device applied to the body that replaces lost musculoskeletal function or helps to restore lost or damaged function, stabilize, or immobilize a body part, correct position, prevent deformation, protect against injury, or assist in movement. [1,2]

The innovation of the technological process of orthosis production with the use of modern technologies may consist in the phase of collection of measurement data and subsequent conventional production or in the modernization of the whole process of taking measurements, orthotic device design and its production. The innovation of the technological process of data collection consists in the use of 3D scanners and computer processing of scanned data into a 3D model, which replaces manual sampling and acquisition of gypsum positive and use of subtractive or additive method of positive production. The innovation of the orthosis production process also consists in the digital CAD (Computer Aided Design) modeling of an individual orthosis in a suitable software, which is produced using additive technologies. [3-11]

The aim of this article is to propose a methodology for individual arm and forearm orthosis design using innovative methods and technologies.

## 2. Materials and Methods

### 2.1. Individual orthosis design

Autodesk Meshmixer software (Autodesk, Inc., San Rafael, CA, USA) was used to create the digital orthosis model. It is a freely available modeling software in which it is possible to create and edit 3D objects and contains functions suitable for the design of prosthetic and orthotic devices. The individual hand and forearm orthosis design consists of three parts:

1. Sketch of the contact surface of the orthosis,
2. Creation of the orthosis shell,
3. Dividing the orthosis into 2 halves.

In the first step, it is necessary to sketch the contact area of the orthosis with its boundaries on the 3D positive (Figure 1a). At the distal end, the orthosis should encircle the thumb with the area of its MCP (metacarpophalangeal) joint and the MCP finger joints

at the proximal side, and at the proximal end of the orthosis, it should encircle the forearm, distal to the elbow bone. Its boundaries are drawn transversely across the forearm at the proximal end and transversely across the MCP areas of the hand joints, omitting the area between the thumb and forefinger.

After creating a sketch of the contact surface of the orthosis, it is necessary to create a gap/offset (1 mm) between the orthosis and the positive. With this setting, an orthosis shell is created at a constant distance from the surface of the 3D positive.

After the shell creation and separation from the 3D positive model, it must be divided into 2 halves (Figure 1b). The division of the device model is necessary to be able to apply the device to the given area of interest. The division is made by cross-sections along the orthosis model on the radial and ulnar side of the forearm and at the point between the thumb and forefinger.

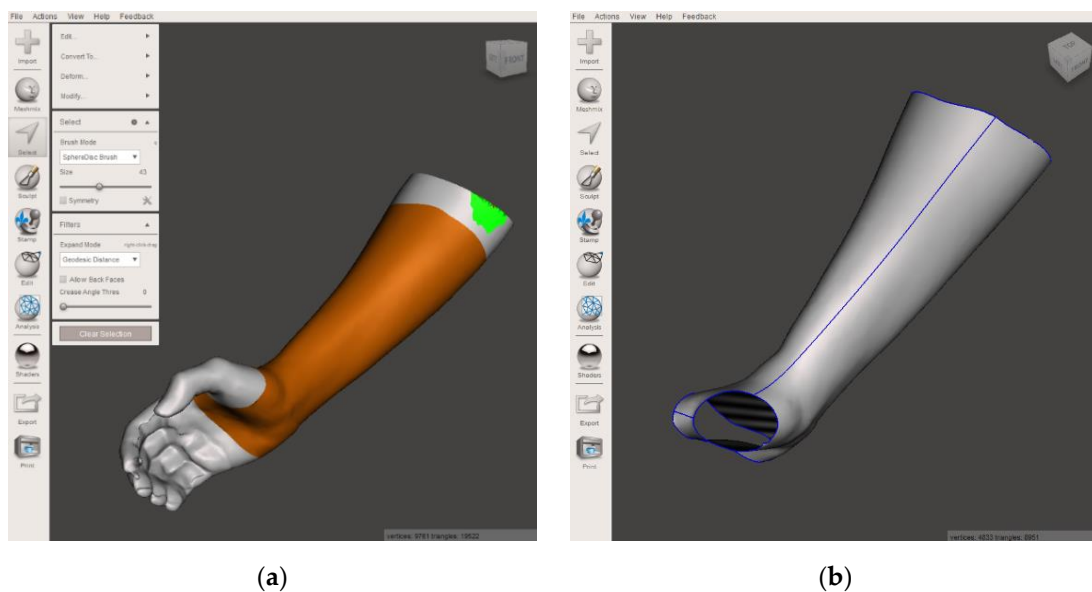
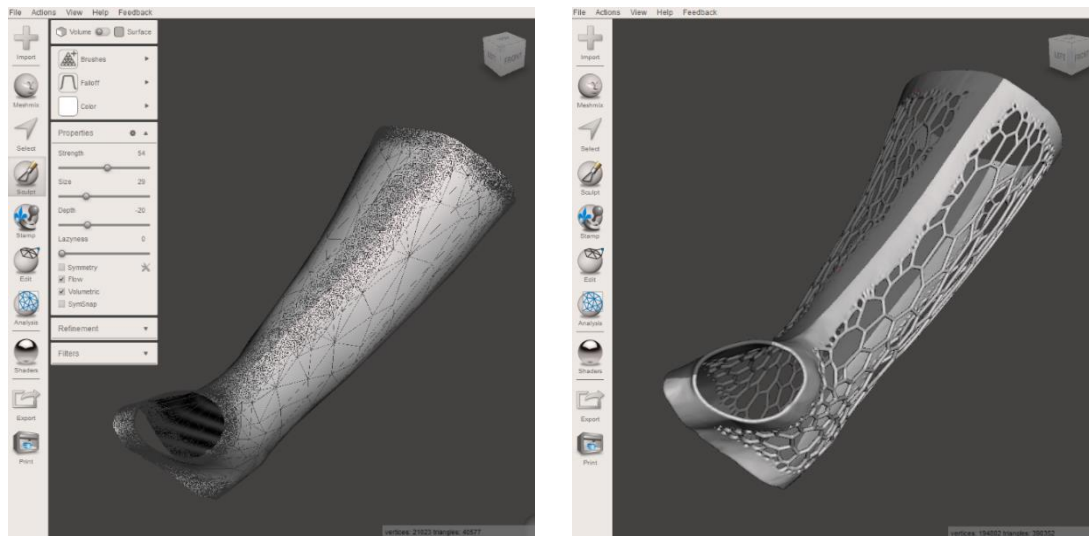


**Figure 1.** (a) Sketch of the contact surface; (b) Two halves of the orthosis shell.

## 2.2. Applying patterns in individual orthosis design

Before applying a pattern to a device, it is important to evaluate the number of triangles on the device model. The pattern function works with this triangle grid and the final design depends on the layout and size of the triangles. The thinner the network, the greater the space between the individual elements and vice versa. As the design depends on the size, number, and arrangement of the triangles, it is necessary to increase the density at the edges of the models to maintain the boundaries of the device after the application of the pattern (Figure 2a). After activating the function, it is necessary to set the parameters as required. In this case the pattern element dimension is 2 mm, and the spacing of the pattern element is 0,2 mm (Figure 2b).



(a)

(b)

**Figure 2.** (a) Increasing of the density of triangles at the edges of the models; (b) Orthosis with applied patter.

At this stage, it is necessary to design the components that will serve to connect the two halves of the orthotic device. These handles are designed in SOLIDWORKS software (Dassault Systems, Waltham, USA), as Meshmixer is not suited for parametric model design. These parts must be positioned where the dividing line of the orthosis halves is created. It is advisable to place 3 handles on the radial side, 3 on the ulnar side and 1 on the area between the thumb and finger (Figure 3).

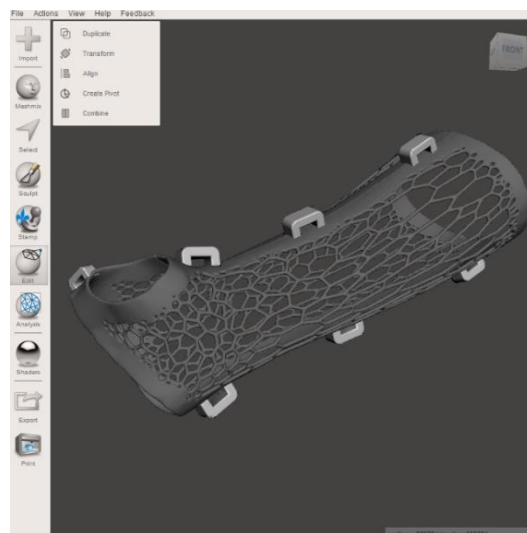


**Figure 3.** Orthosis with applied handles.

After the final inspection of the 3D orthosis model and evaluating that the model is suitable for production, it is necessary to export the model to STL format so it can be imported into the 3D printer software (Figure 4).

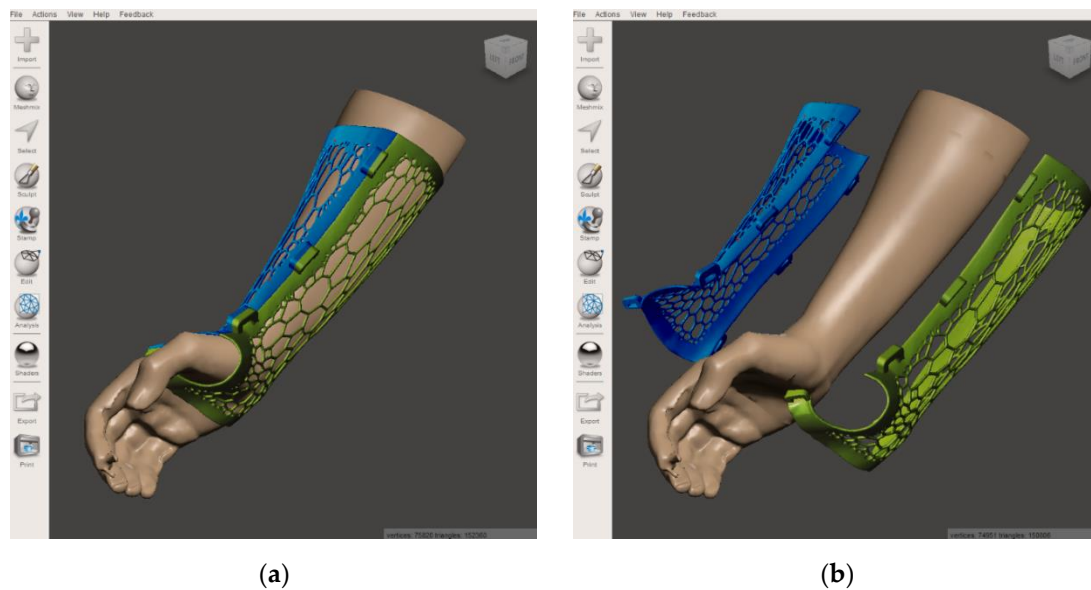


Figure 4. (a) Final orthosis model assembly; (b) Final orthosis model assembly divided into 2 halves.

### 3. Results

Preparation of CAD models for additive production consist in uploading the model to software designed to set individual parameters of the 3D printing process. The choice of software depends on the additive production technology used. Since prosthetic and orthotic devices are designed for production using FFF (Fused Filament Fabrication) technology, a suitable software for setting printing parameters is, for example, the freely downloadable PrusaSlicer (Prusa Research, Prague, Czech Republic).

In the case of the hand and forearm orthosis with an individual design, positioning to the ideal position is more complicated, due to the number of perforations on the surface of the device. In this case, it is necessary to focus mainly on the fact that no support structures are generated on the contact surface, that the layering orientation is in the transverse plane and that it is a large model to have enough support structure on the model to prevent deformation. For these reasons, it is necessary to position the model so that the dorsal surface of the orthosis is positioned towards the working platform and the angle that the model arch towards the platform is large enough to meet the layering orientation and the amount of support material conditions (Figure 5).

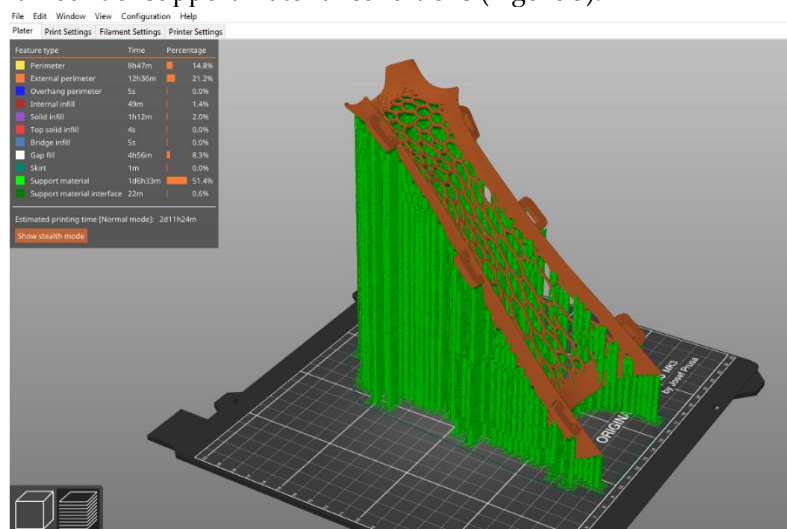


Figure 5. Production simulation of 1 half of the orthosis.

After setting important production parameters and thorough positioning of the model on the virtual platform, it is necessary to export this arrangement to a G-code file, which is a file that is supported by desktop 3D printers of the FFF type. The code is loaded into the printer's memory and the production is manually activated.

#### 4. Discussion

The modern approach to creating orthotic devices begins with the digitization of the human body and its parts to obtain input data from the patient's body for the needs of modeling the orthotic device in CAD software, and subsequent additive manufacturing. This innovative method in the hands of experts replaces unpleasant and time-consuming plastering. Thanks to this technological process, it is possible to achieve higher accuracy, speed of production of the device, a new level of comfort for the patient and functionality in the field of orthotics and prosthetics. The 3D scanning technique is used for data collection. The obtained data are processed by a computer software that creates a three-dimensional image of the model, where the CPO (Certified Prosthetist Orthotist) can make corrections to create the final positive model. Software tools allow the professional to use a wide range of adjustment tools, including rotation, rotation, scaling, levelling, and adding pressure or relief points.

Digitization brings better control over the creation of orthotic devices and at the same time respects the "know-how" of the traditional method of production and the creativity of the CPO.

The creation of digital models also brings other possibilities, such as the analysis of possible problems that may arise because of the design, material selection and errors in connection with the production process. The virtual model of the orthotic device in the appropriate format includes not only the device model itself, but also the parameters of the production process and the choice of material.

#### 5. Conclusions

The methodology of design and preparation of an individual arm and forearm orthosis using CAD technology was presented. The procedures given in the methodology can also be used in the production process of other prosthetic and orthotic aids and devices, in the design of new, low-cost prostheses and orthoses, and for educational purposes in the field of prosthetics and orthotics.

**Acknowledgments:** This article was developed with support Slovak Research and Development Agency under the contract No. APVV-19-0290, project KEGA 044TUKE-4/2022 Implementation of progressive technologies in prosthetics and orthotics education and support integration with practice, project KEGA 023TUKE-4/2020 Increasing the synergy of methods of teaching biophysics using laboratory equipment and diagnostic devices aimed at measuring physical and is the result of the project implementation CEMBAM - Center for Medical Bioadditive Research and Production, ITMS2014+: 313011V358 supported by the Operational Programme Integrated Infrastructure funded by the European Regional Development Fund.

**Conflicts of Interest:** The authors declare no conflict of interest.

#### References

- [1] Živčák, J. et al.: *Individuálna ortotika horných končatín* - 1. ed. Košice. 2016. p. 179 s. ISBN 978-80-553-3110-2.
- [2] Bowers DM, Chui KK. Neurological and Neuromuscular Disease Implications for Orthotic Use. In: *Orthotics and Prosthetics in Rehabilitation*. 4th ed. 2020. p. 259-293. DOI: 10.1016/B978-0-323-60913-5.00010-6.
- [3] Lunsford TR, Contoyannis B. Materials Science. In: *Atlas of Orthoses and Assistive Devices*. 5th ed. Philadelphia. 2019. p. 7-41, DOI: 10.1016/B978-0-323-48323-0.00002-0.

- [4] Supan TJ. Principles of Fabrication. In: Atlas of Orthoses and Assistive Devices. 5th ed. Philadelphia. 2019. p. 42-48. DOI: 10.1016/B978-0-323-48323-0.00003-2.
- [5] Jorge M. Orthotics and Prosthetics in Rehabilitation: Multidisciplinary Approach. In: Orthotics and Prosthetics in Rehabilitation. 4th ed. 2020. p. 2-13. DOI: 10.1016/B978-0-323-60913-5.00001-5
- [6] Palousek D. et al. Pilot study of the wrist orthosis design process. Rapid Prototyping Journal, 2014, 20.1: 27-32.
- [7] Zuniga J. et al. Cyborg beast: a low-cost 3d-printed prosthetic hand for children with upper-limb differences. BMC research notes, 2015, 8.1: 10.
- [8] Zuniga J. M., et al. An open-source 3D-printed transitional hand prosthesis for children. JPO: Journal of Prosthetics and Orthotics, 2016, 28.3: 103-108.
- [9] Buonamici F. et al. A Practical Methodology for Computer-Aided Design of Custom 3D Printable Casts for Wrist Fractures. The Visual Computer, 36:375-390. DOI: <https://doi.org/10.1007/S00371-018-01624-Z>.
- [10] Hale L., Linley E., Kalaskar, D.M. A Digital Workflow for Design and Fabrication of Bespoke Orthoses Using 3d Scanning And 3D Printing, A Patient-Based Case Study. Scientific Reports, 2020, 10:7028. DOI: 10.1038/S41598-020-63937-1.
- [11] Štefanovič B. et al. Arm and Forearm Scanning Methodology for The Development of An Orthotic Device for Tetraplegic Patients. In: Proceedings Of 3dbody.Tech 2020 - 11th International Conference and Expo On 3D Body Scanning and Processing Technologies. 17-18 November 2020. Online/Virtual.



# Design and setup of a robotic workstation for additive manufacturing

Pavol Štefčák <sup>1\*</sup>, Ivan Gajdoš <sup>2\*</sup>, Ján Slota <sup>3\*</sup>

<sup>1</sup> pavol.stefcak@tuke.sk

<sup>2</sup> ivan.gajdos@tuke.sk

<sup>3</sup> jan.slota@tuke.sk

\* Slovakia, Technical University of Košice, Department of Technology, Materials and Computer Supported production, Mäsiarska 74,040 01 Košice

Additive manufacturing based on thermoplastic polymers has expanded into several areas of production in recent years due to its increasingly affordable cost. One of the biggest limitations of conventional polymer 3D printers is the size of the build space they offer, their printing speed and the cost of the filament needed for printing. The current solution to these limitations is the continued development of ever larger AM devices. Current trends include the development of large gantry printers and the development of Robotic 3D Printers which are a cheaper alternative while still being able to offer superior print volume and performance. The content of the study discusses the current status and trends in the field of Large format additive manufacturing (LFAM), the technology of fused granular fabrication (FGF) and the functional design of a robotic workstation for large-scale additive manufacturing and its set up. Several CAx technologies were used in the implementation of the work. CAD software Solidworks, CAM software RoboDK and Slicer Ultimaker Cura. The first print samples were subsequently produced using these tools.

**Keywords:** Robotic additive manufacturing; Large format additive manufacturing; Fused Granular Fabrication; CAx;

## 1. Introduction

LFAM is slowly coming to the fore as a cost-effective and flexible solution for the production of large parts and components in specific areas of industry. It has the potential to solve many of the challenges that manufacturers face in producing larger parts, but given that most of the currently available 3D printers have been developed for smaller parts, components of greater size and weight, such as aircraft wings, various ship parts, moulds or turbines require larger printing areas and tooling to produce. This ultimately translates into higher production costs and longer lead times. This is where 3D printing technologies that can produce large parts faster and cheaper come into play [1]. One of the current challenges is not only to meet the demand for the production of large-scale components where conventional 3D printers are reaching their limits in terms of print space and flexibility, but also to identify new areas of application. The ability to print components with a volume of several cubic meters and to print on curved surfaces thanks to the flexible motion of the robot are processes that are difficult to implement using conventional printing methods while maintaining the process speed and build quality expected from conventional 3D printing. The current state of development is impressive, high-temperature components as well as heat treatment capabilities of plastics should enable the use of high-performance plastics in the near future [2].

Currently, several types of additive technologies are used for the needs of LFAM by gantry and robotic workplaces, with the help of which is possible to produce three-dimensional products for example by:

- Polymer extrusion
- Concrete and ceramics extrusion
- Extrusion of continuous carbon filament with thermoplastics
- Coating and other methods [3].

Due to the mentioned advantages and the need of implementation of this technology, relatively low cost large-scale additive manufacturing workplace was Designed and operationalized, using-FANUC M-20iB/25 industrial robot [4], which was complemented by the end part of the MDPH2 extrusion head from Massive Dimension with FGF technology that allows printing of commonly available thermoplastic materials in the form of granulates [5]. Material extrusion with FGF technology in general allows material flow rates 200 times higher than conventional FFF technology [6], Thanks to the printing material used in the form of granules, which are extruded directly onto the substrate after melting, additive manufacturing eliminates the heating cycle required for filament production. The result is an increase in the mechanical properties of the printed product, a reduction in the cost of the input material for its production (Table 1) and reduction in the delivery time to the end customer [7]. The input material in pellet form, together with new ways of generating layers, enables new applications of high performance plastics while maintaining the speed of the process and the required quality of the product [8].

*Table 1.* Comparison of prices of filament and granules [9].

Type	Filament price [€/Kg]	Price of granulate [€/kg]
PLA	30,52	8,39
PLA+ CF	61,04	7,66
PETG	30,52	4,5
ABS	30,52	8,39
ABS+CF	45,78	27,66
HIPS	30,52	8,4
PEEK	567,48	16,03
PEI	209,82	26,72

In context of design and set up of large scale robotics additive workstation several CAx technologies have been used such as:

- Solidworks CAD software with XTract3D reverse engineering plugin
- CAM software RoboDK for the purpose of offline simulation of toolpath motion and conversion of NC code into code for industrial robots
- Cura, a freely available slicing software from Ultimaker for nozzle path motion generation

The design of the workstation involved the use of reverse engineering to create a CAD model of the printhead which was only available in STL format. The CAD model of the printhead was then used to model an adapter to connect the printhead to the FANUC robotic arm and the RoboDK CAM software to simulate the movement of the printhead and avoid collision with the robotic arm.

The CAD model of the print head will find its use in future workstation improvements and new additive manufacturing methods using 6 degrees of freedom, gradient

printing and non-planar printing. The CAD model of the FANUC robot can be accessed in the RoboDK CAM software as part of the robot library.

The design of the new robot frame ensured the required stiffness of the arm and its easy handling using available scrap material of faculty. The design of the building platform with the print pad allows the full potential of the robotic arm's reach to be exploited, with an emphasis on maximising the size of the print volume (Figure 1).

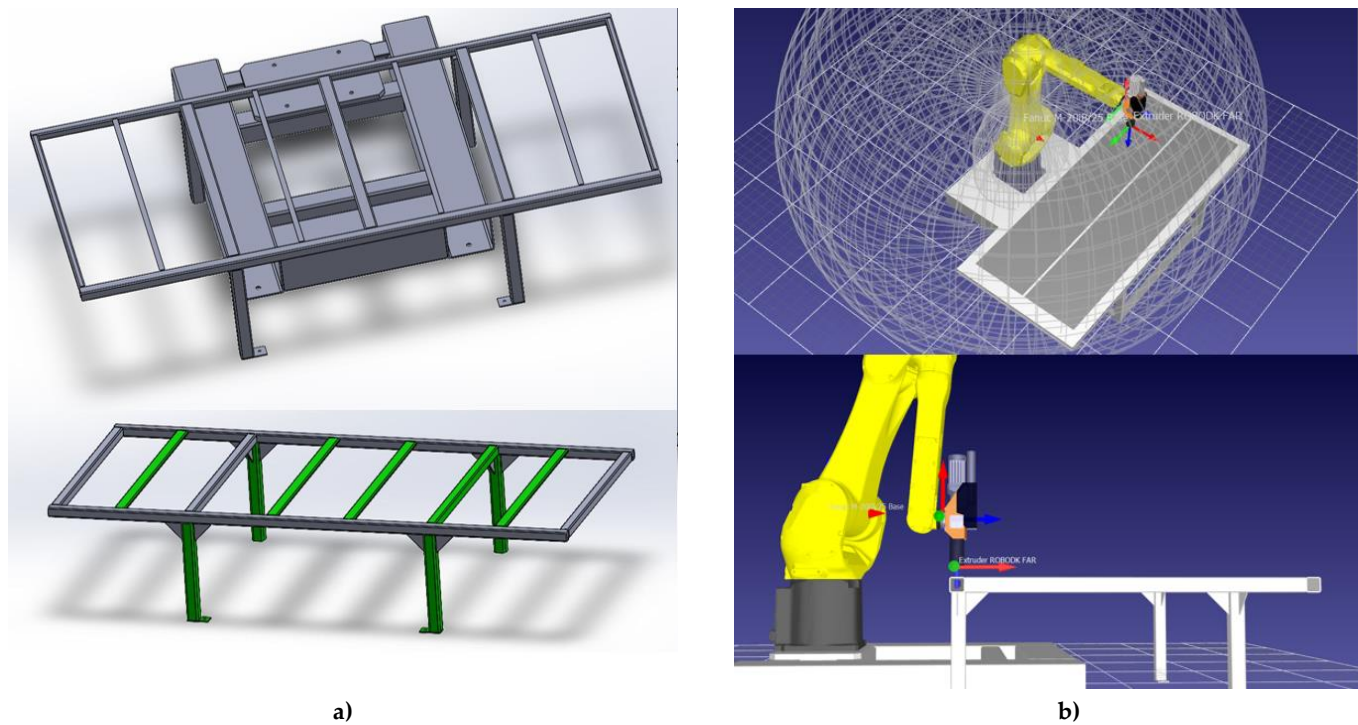


**Figure 1.** Model of robotics additive manufacturing workstation in a) Solidwork CAD software and b) RoboDK CAM software [10].

MDPH2 Massive Dimension extrusion head allows extrusion of commonly available thermoplastic materials with a melting temperature of up to 450°C and a throughput of up to 1kg/h. This extrusion head can be fitted with a nozzle diameter of 1.5mm, 3mm or nozzles with a slightly smaller or larger diameter can be used as required [5]. After the electrical connection and subsequent recovery of the robotic workstation followed the printing of the first test samples and optimization of production parameters such as the speed of movement of the print head, granulate melting temperature, material extrusion speed and adjustment of input data related to the setting of G-code generation in Slicer Ultimaker Cura and CAM program RoboDK. PETG pellets were used to print the samples.

In the preprocessing process, we varied the size of the print nozzle diameter in Slicer and changed the distance of the zero point from the print nozzle in the CAM program RoboDK in order to achieve a satisfactory printing result of the first layer.

The best first layer printing results were with a nozzle diameter of 1.55mm. In order to maximize the speed of the robotic arm, we tried to find the maximum possible printing speed. At a speed of 100 mm/s, we re-calibrated the material extrusion speed by increasing the time interval of sending pulses to the extrusion motor via the Modbus Poll program. The best results were obtained at 210°C and with a pulse every 2600 [ms] (Figure 2).

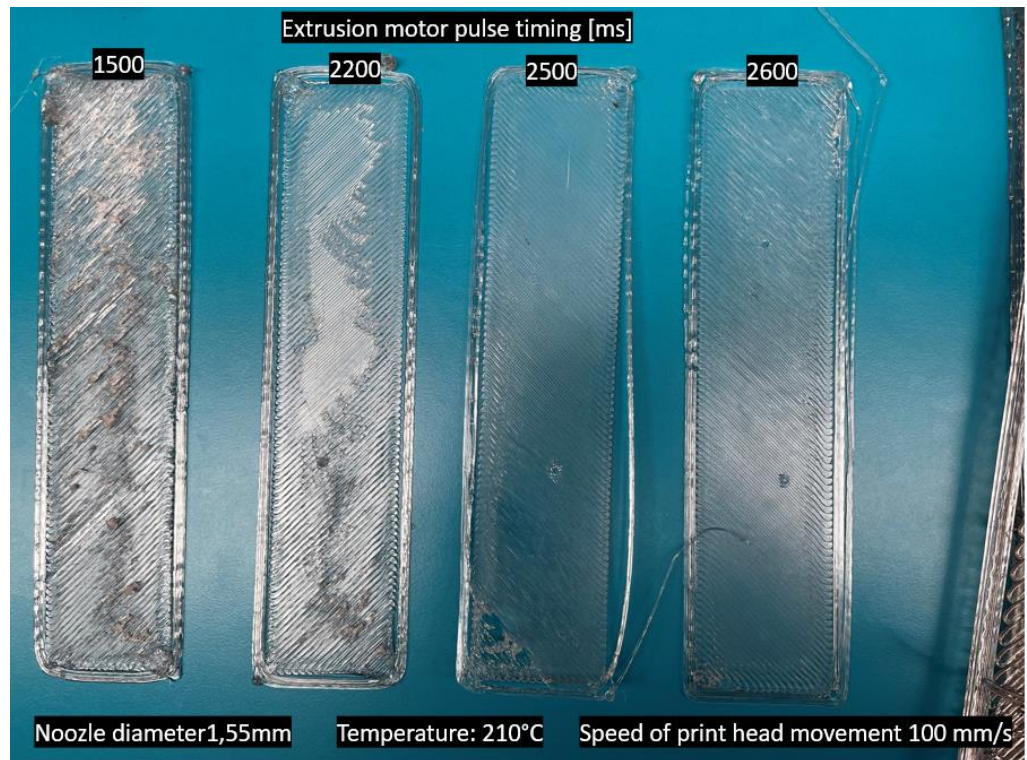


**Figure 2.** Samples at a print speed of 100 mm/s with increasing pulse interval to the extruder motor [10].

After successfully managing the printing of the first layer, we moved on to multi-layer printing where we found out right after the first sample that the speed of 100 mm/s was too high and the material was not able to cool down fast enough to keep the desired shape. It was therefore necessary to reduce the printing speed to 50 mm/s to increase the pulse transmission interval or to use additional cooling (Fig. 5).

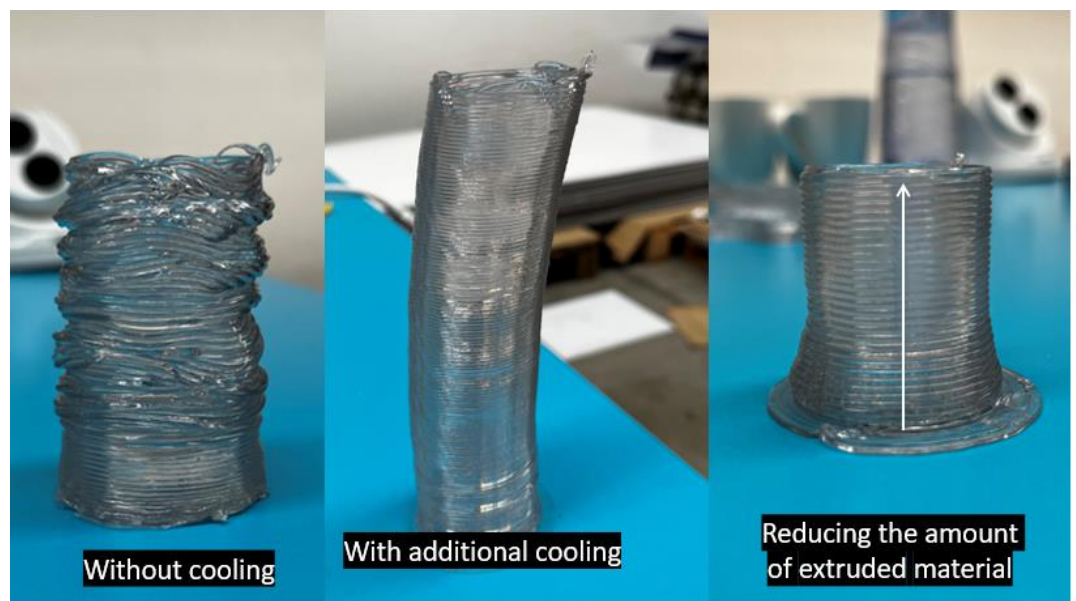


**Figure 3.** First three dimensional samples printed on robotics additive manufacturing workstation [10].

To verify the printing of overhangs, we designed a custom sample to verify the maximum overhang angle that can be printed in this configuration, given the parameters and material used, how it can handle the printing of internal and external curves, and how the surface will look at obtuse and acute angles (Figure 4).

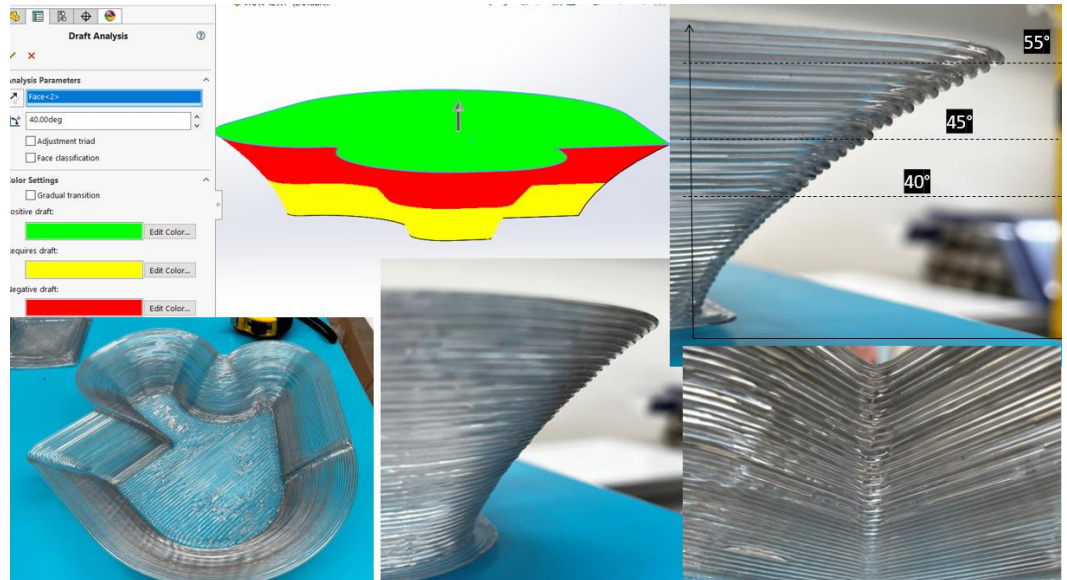


Figure 4. Print results of designed sample [10].

### 3. Results

The printing results (Figure 4) of the test sample showed that the robotic workstation has successfully passed the implementation phase and has the ability to print overhangs up to  $40^\circ$  inclination while maintaining a constant product shape. The design quality of overhangs larger than  $40^\circ$  decreases with increasing inclination, but under certain conditions, for example, when the product allowance is set correctly for subsequent machining by milling or grinding, they can be considered an acceptable compromise of design and resulting print quality.

Since we were able to print multiple samples and other three-dimensional objects with the current process parameter settings, we will need to use a nozzle with a larger diameter when printing large objects in order to achieve acceptable production times and re-adjust the process parameters individually.

### 4. Discussion

We have created a robotic workstation providing a printing volume of  $2.5 \text{ m}^3$ . By optimizing production parameters such as the speed of the print head movement, granulate melting temperature, material extrusion speed and by adjusting the input data related to G-code generation settings in Slicer Ultimaker Cura and CAM program RoboDK, the workplace is able to print objects in three degrees of freedom up to a height of 1m with 40% overhangs of acceptable quality.

Further research will focus on the area of non-planar 3D printing with full use of the robot's 6 degrees of freedom, algorithmic layer generation for large-scale additive manufacturing, and a deeper exploration of the possibilities of hybrid robot manufacturing using a milling spindle to create dimensionally accurate products.

## References

1. Paolini, A., Kollmannsberger, S., Rank, E.: Additive manufacturing in construction: a review on processes, applications, and digital planning methods. *Addit. Manuf.* 30, 100894 (2019) . [ONLINE].[cit. 2022.12.04] dostupné na internete: <https://reader.elsevier.com/reader/sd/pii/S2214860419309029?token=E19C33EF8C4051DE952DFEB1DA399915C05AB518701799E643D47366F8810CA6710FC683D4CE70D8B5AC671B3D3E24E2&originRegion=eu-west-1&originCreation=20220505192933>
2. Reich, M.J., Woern, A.L., Tanikella, N.G., Pearce, J.M.: Mechanical properties and applications of recycled polycarbonate particle material extrusion-based additive manufacturing. *Materials* 12(10), 1642 (2019) [ONLINE].[cit. 2022.12.04] dostupné na internete: <https://www.mdpi.com/1996-1944/12/10/1642/htm>
3. Largescale additive manufacturing. [ONLINE].[cit. 2022.12.04] dostupné na internete: <https://ewi.org/capabilities/additive-manufacturing/large-scale-additive-manufacturing/>
4. Fanuc M-20iB/2: datasheet [ONLINE].[cit. 2022.28.04] dostupné na internete: <https://www.fanuc.eu/~media/files/pdf/products/robots/robots-datasheets-en/m20ib/datasheet%20m-20ib-25-en.pdf?la=en>
5. MDPH2 - PELLET HEAD EXTRUDER [ONLINE].[cit. 2022.28.04] dostupné na internete: <https://massivedimension.com/collections/extruders/products/mdphe-v1-pellet-headextruder-system>
6. Stefan Otto Felber, Mohamed Aburaia, Wilfried Wöber, and Maximilian Lackner: Parameter Optimization for the 3D Print of Thermo-Plastic Pellets with an Industrial Robot. Wien:UAS Technikum Wien. ISBN 978-3-030-62784-3. page 253.
7. Greg Costantino, Covestro Additive Manufacturing, and Zac DiVencenzo, Juggernaut: 3D Printing with Fused Filament Fabrication and Fused Granulate Fabrication (Pellet Printing) [ONLINE].[cit. 2022.05.05] available on the internet: [https://am.covestro.com/en\\_US/insights/blog/3d-printing-with-fused-filamentfabrication-and-fused-granulate-fabrication.html](https://am.covestro.com/en_US/insights/blog/3d-printing-with-fused-filamentfabrication-and-fused-granulate-fabrication.html)
8. Next generation of 3D printing- robot guided additive manufacturing. [ONLINE].[cit.2022.12.04] available on the internet: <https://zal.aero/en/news/next-generation-3dprinting-robot-guided-additive-manufacturing/?cookie-statechange=1648994679559>
9. 3DXTECH: products. [ONLINE].[cit. 2022.28.04] available on the internet: <https://www.3dxtech.com/products/>
10. Own photos



# Advanced exhaust system for vehicles' emission footprint reduction

Pavol Tarbajovský <sup>1\*</sup>, Michal Puškár <sup>2</sup>, Matúš Lavčák <sup>3</sup>

<sup>1</sup> Faculty of Mechanical Engineering, TU Košice, Letná 9, 040 01 Košice, Slovak Republic; pavol.tarbajovsky@tuke.sk

<sup>2</sup> Faculty of Mechanical Engineering, TU Košice, Letná 9, 040 01 Košice, Slovak Republic; michal.puskar@tuke.sk

<sup>3</sup> Faculty of Mechanical Engineering, TU Košice, Letná 9, 040 01 Košice, Slovak Republic; matus.lavcak@tuke.sk

\* Correspondence: e-mail@e-mail.com: pavol.tarbajovsky@tuke.sk; Tel.: +421 55 602 2355

**Abstract:** Automobile emission standards are becoming increasingly strict, resulting in the creation of new technologies to reduce toxic matters which are present in exhaust gases while reaching maximum possible performance of the vehicle' combustion engine. One of the possible solution is cylinder deactivation technology. Under suitable conditions, this technology turns off combustion on the required cylinders, thereby reducing the emissions produced by the engine during combustion process. A catalytic converter is another emission reducing technology used in automotive industry. The catalytic converter belongs to the most important part of the exhaust system, due to the removal of toxic matter from exhaust gases and which ensures meeting emissions standards. Possibility to maintain maximum engine performance and minimum emission values for reaching emission standards can be achieved by combining these two technologies. The article' main goal is construction idea of exhaust system which utilizes cylinder deactivation and catalytic convertor technology.

**Keywords:** exhaust, emissions, exhaust valve, cylinder deactivation

## 1. Introduction

One of the ways manufacturers reduce fuel consumption is by reducing the sizes of the engines they build and offer in production cars. However, the volume of the cylinder can only be reduced to a certain extent in order to maintain the thermodynamically ideal volume capacity of 400 to 500 cm<sup>3</sup> per cylinder. In practice, therefore, downsizing often leads to a reduction in the number of cylinders.

"Temporary downsizing" in the form of cylinder deactivation offers an attractive compromise as it allows the engine to shift its operating mode to achieve specific consumption values for which it is designed, especially at low loads and operating speeds. At the same time, the user still has sufficient engine power available, which ensures the same level of driving dynamics and comfort with respect to acoustics and vibration characteristics.

Cylinder deactivation technology can be integrated into already existing engine concepts, allowing for a reduction in research and development costs.

The catalyst as a part of the exhaust system is an indispensable part in today's cars, thanks to which the emissions produced by the internal combustion taking place in the internal combustion engine are reduced.

The 3D design of the exhaust system, specially designed for the cylinder deactivation technology, which utilizes a valve system to bypass the primary catalyst after the engine has warmed up to operating temperature is one of the possible solutions that can be used

in modern cars. The exhaust construction design was the main goal of the article for further analysis and tests to optimize the design of the exhaust system. The proposal is detailed in the text of the article [1-8].

## 2. Cylinder Deactivation Technology

The most consistent form of cylinder deactivation is not only the interruption of injection and ignition for the respective cylinders, but also the stopping of all moving parts (including pistons). This in turn uses the entire available thermodynamic potential and significantly reduces the friction that arises inside the engine. It goes without saying that there are trade-offs to be made when it comes to firing order and dynamic balance. But far more important is the cost required to separate the engine into an area that continues to run while the other area is activated and deactivated as needed. Even the connecting mechanisms on the crankshaft and camshaft cannot be justified by cost-benefit analysis, and therefore the implementation of the system is currently not easy. Almost all cylinder deactivation systems in use today interrupt the injection and ignition as well as valve actuation sequences for the cylinders to be deactivated. Today's applications range from 4 to 12 cylinder engines. However, the analyzes carried out show that temporarily deactivating one of the cylinders in a three-cylinder engine can also reduce consumption. To ensure that the engine continues to run smoothly enough, only certain cylinders are deactivated according to the firing order.

If there is a specific performance requirement, cylinders that are still in operation after cylinder deactivation must produce a higher mean pressure. This displacement of the load point leads to a reduction in engine losses and ultimately helps to save fuel. Valve deactivation also reduces friction losses in the cylinder head, which further minimizes consumption.

The potential for reduced consumption when the engine is operated on two cylinders instead of four can be graphically displayed in Figure 1. The red line shows the mean pressures at which an engine operating in two-cylinder mode can reach its optimal combustion point (crankshaft position  $8^\circ$  after TDC.).

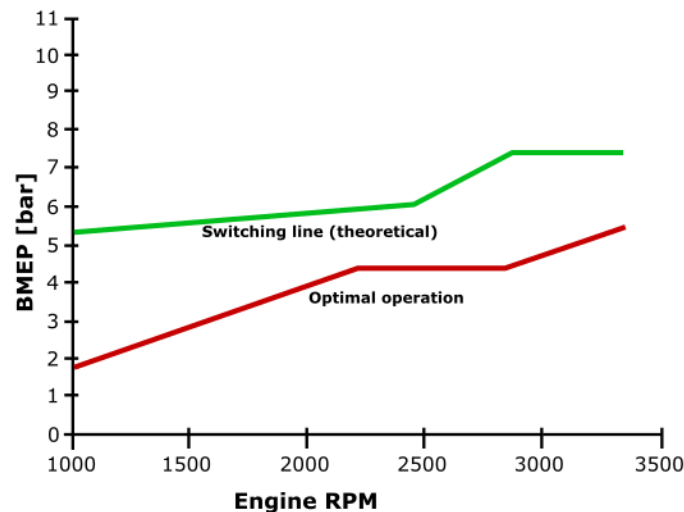


Figure 1 Four-cylinder and two-cylinder mode comparison

When higher intermediate pressures are introduced in two-cylinder mode, the ignition sequence must be slowed to prevent knocking. As a result, combustion no longer reaches its peak efficiency and more fuel is consumed. Opening the throttle prevents this even more and has a positive effect on consumption in cylinders with higher mean pressure. The green line represents the theoretical switching or transition line, as operating the engine above these values in twin-cylinder mode results in additional fuel consumption [1-4].

### 3. Catalytic Converter

In the casing of this exhaust part, there is a chamber called a catalyst, which serves to change harmful compounds from engine emissions into safe gases, such as steam. The function is that it breaks down the dangerous molecules in the gases produced by the combustion engine before they enter the air.

The catalytic converter (Figure 2) is located on the underside of the vehicle. Two pipes come out of it. The converter uses these two pipes and the catalyst during the process of ensuring the discharge of gases.

Gases are supplied from an inlet pipe connected to the vehicle's engine. These are blown through a catalytic converter, which causes a chemical reaction that breaks down pollutants. Less harmful gases pass through a second pipe or outlet that is connected to the car's exhaust.

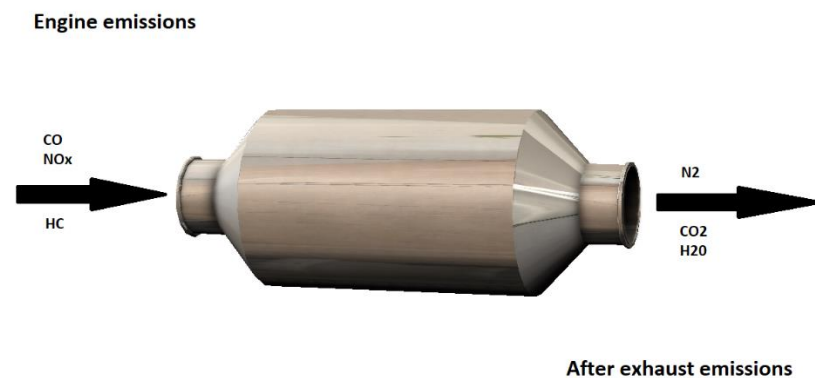


Figure 2 Catalytic Converter

There is also an oxygen sensor near the catalytic converter that informs the electronic control unit about how much oxygen is in the exhaust gases. This helps create a more efficient air/fuel ratio, allowing the engine to supply enough oxygen to the catalytic converter to complete the oxidation process [1-4].

### 4. Structural design of the cylinder deactivation exhaust system and catalyst

The design of the exhaust system specially adapted for this specific use is based on systems that can be found in cars already in production. The goal of the exhaust system is to increase engine performance while maintaining the required emission standards.

The overall design is based on the operation of the engine with cylinder deactivation, with cylinders 1 and 3 operating continuously after the engine start with the possibility of supercharging the engine (passage of exhaust gases through the turbocharger) and cylinders 2 and 4 operating as needed higher performance (constant passage of exhaust gases through the turbocharger) such as when overtaking or driving uphill.

The designed exhaust system consists of several elements. The exhaust manifold that connects the cylinders with opposite work cycles was designed first, otherwise, the operation of the engine would be impossible or significantly more difficult.

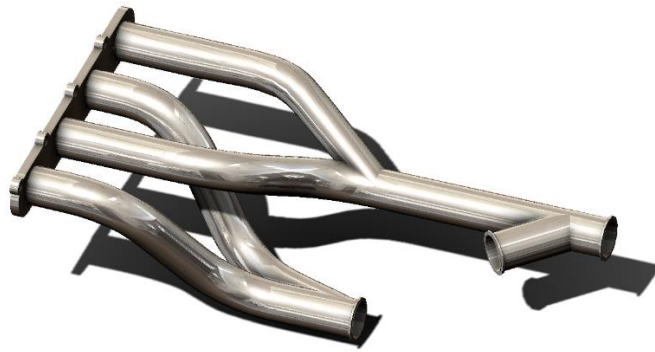


**Figure 3 Exhaust manifold design**

Figure 3 shows the designed exhaust pipes for an engine whose 1 and 3 cylinders operate in opposite combustion cycles as well as cylinders 2 and 4.

The design includes a valve system, the function of which is to divert exhaust gases from the pipe leading to the turbocharger during the time until the engine reaches operating temperature together with the secondary catalyst.



**Figure 4 Exhaust valve**

The exhaust valve, which serves to direct the exhaust gases, is shown in Figure 4. This flap is used to split the exhaust gases between the two pipes of the exhaust system, with one pipe leading the exhaust gases through the turbocharger to the secondary catalytic converter and the other bypassing it and leading through the primary catalytic converter to the secondary catalytic converter.

The exhaust pipes together with the exhaust valve are shown in Figure 5.



**Figure 5 Exhaust manifold with exhaust valve**

The exhaust pipes of cylinders 1 and 3 can lead the exhaust gases through the open valve to the turbocharger or, with the valve closed, through the primary catalyst as mentioned earlier in the article. At an engine temperature other than the operating one, the exhaust valve is closed due to higher emissions produced by the engine during its operations, and for that reason, the gases flow through the primary catalyst, where they partially get rid of toxic substances. The primary catalyst is shown together with the pipeline in Figure 6.



**Figure 6 Exhaust system with primary catalytic converter**

The exhaust gases, partially freed of toxic substances, flow into the main catalyst, which they heat up, thereby increasing its efficiency, and subsequently, freed of toxic substances, they proceed to the remaining parts of the exhaust system. The function of the gases to heat the main catalyst is very important, since when the remaining cylinders are activated, the toxic gases flow directly through the turbocharger, without getting rid of unwanted substances, which must be removed due to emission standards. The main catalyst, heated to operating temperature, subsequently rids the exhaust gases of toxic substances flowing from the turbocharger, but also from the primary catalyst.

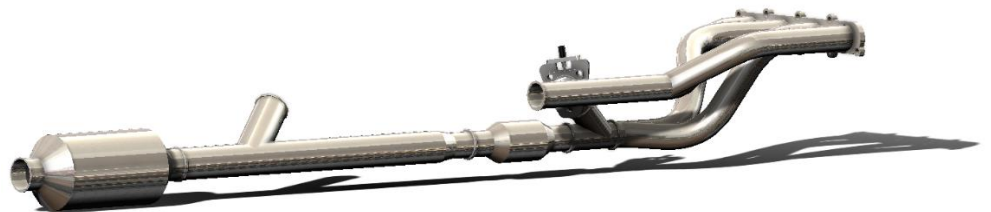


**Figure 7 Exhaust system with primary and main catalytic converter**

Cylinders 2 and 4 connect to a second manifold that directs the flow of exhaust gases to a turbocharger that increases engine power by compressing the intake air. The exhaust pipes of cylinders 2 and 4 are shown in Figure 8.



**Figure 8 Exhaust system with turbocharger**

Exhaust gases from the turbocharger are combined with gases from the primary catalyst and subsequently flow into the main catalyst, where they get rid of toxic substances.

Figures 9 show the overall design of a valve exhaust system for an internal combustion engine with cylinder deactivation.

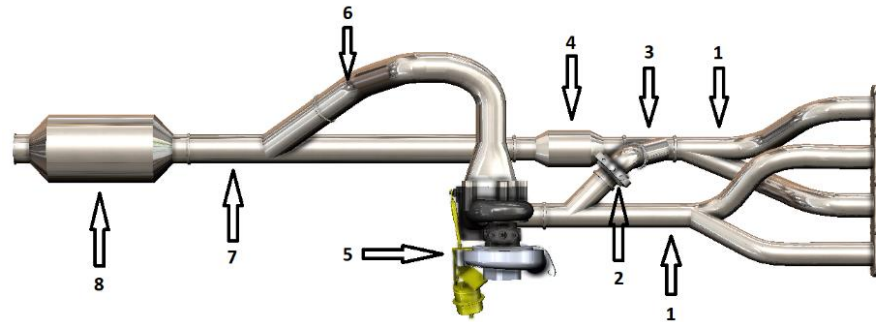


**Figure 9 Overall design of the exhaust system with description: 1. Exhaust manifold, 2. Exhaust valve with exhaust pipes, 3. Exhaust coupling, 4. Primary catalytic converter, 5. Turbocharger, 6. Turbocharger downpipe, 7. Exhaust pipe with exhaust coupling Main catalyst, 8 Main catalytic converter**

## 5. Conclusions

The aim of this article was the design of an exhaust system for application in an engine with a cylinder deactivation system. The technical solution was based on information and knowledge from real cars available on the car market.

The proposal consisted of the creation of important components of the exhaust system, which are essential for the proper removal of exhaust gases and the removal of toxic substances of these gases.

The created exhaust system was designed to optimize vehicle performance in conditions where maximum engine power is required and in conditions when minimum power is sufficient, with an emphasis on maintaining the emission standards required by individual states.

With further research and simulations in 3D simulation programs, it is possible to optimize the shape and eliminate the errors that may be present in this design.

**Acknowledgments:** This work was supported by the Slovak Research and Development Agency under the Contract no. APVV-19-0328. The article was written in the framework of Grant Projects: VEGA 1/0318/21 "Research and development of innovations for more efficient utilization of renewable energy sources and for reduction of the carbon footprint of vehicles" and KEGA 007TUKE-4/2023 "Transfer of innovations and advanced technologies, determined for more ecological and more efficient vehicle drive systems, into the educational process."

**Conflicts of Interest:** The authors declare no conflict of interest.

## References

1. Dons, Evi et al. Concern over health effects of air pollution is associated to NO<sub>2</sub> in seven European cities. In *Air Quality, Atmosphere & Health*. 2018, vol. 11, no. 5, s. 591–599.
2. Han, Lijian et al. Global population exposed to fine particulate pollution by population increase and pollution expansion. In *Air Quality, Atmosphere & Health*. 2017, vol. 10, no. 10, s. 1221–1226.
3. Li, Yaopeng et al. Evaluation of the necessity of exhaust gas recirculation employment for a methanol/diesel reactivity controlled compression ignition engine operated at medium loads. In *Energy Conversion and Management*. 2015, vol. 101, s. 40–51.

4. Puškár, Michal et al. Environmental study focused on the suitability of vehicle certifications using the new European driving cycle (NEDC) with regard to the affair "Dieselgate" and the risks of nox emissions in urban destinations. In *Air Quality, Atmosphere & Health*. 2018, vol. 12, no. 2, s. 251–257.
5. Fridrichová, K. et al. Overview of the potential and limitations of cylinder deactivation. In *Renewable and Sustainable Energy Reviews*. 2021, vol. 146, s. 111196.
6. Vinodh, B. Technology for Cylinder deactivation. In *SAE Technical Paper Series*. 2005
7. Mahadeven, Ganesan, Sendilvelan, Subramanian. Temperature analysis of dynamic catalytic convertor system with pre-catalyst in a multi cylinder spark ignition engine to reduce light-off time. In *International Journal of Heat and Technology*. 2017, vol. 35, no. 1, s. 97–102.
8. Balaji, G et al. Experimental analysis of exhaust emissions using catalytic converter. In *IOP Conference Series: Materials Science and Engineering*. 2018, vol. 402, s. 012200.



# New trends in industrial robot research and application: redundant robots

Martin VARGA<sup>1</sup>, Ivan VIRGALA<sup>2</sup> and Michal KELEMEN<sup>3</sup>

<sup>1</sup> Technical university of Košice, Faculty of Mechanical Engineering, Department of Mechatronics, Slovakia; martin.varga.2@tuke.sk

<sup>2</sup> Technical university of Košice, Faculty of Mechanical Engineering, Department of Mechatronics, Slovakia; ivan.virgala@tuke.sk

<sup>3</sup> Technical university of Košice, Faculty of Mechanical Engineering, Department of Mechatronics, Slovakia  
michal.kelemen@tuke.sk

**Abstract:** Industrial robots are an essential part of manufacturing. Redundant robots are a subclass of robot with unique characteristics like compliance and high dexterity ideal for applications in agriculture, medicine, or collaborative tasks in general. In this paper an overview of research articles dealing with the design and control of redundant robots was presented and an analysis containing the publishing dates was carried out. The interest in research on the topic of redundant robots is accelerating. The robots in question were mostly different from standard industrial robots not only by a greater number of degrees of freedom but also by their morphology. The probable reasons are also discussed.

**Keywords:** industrial robot, redundant, trends

## 1. Introduction

Industrial robots are a critical part of manufacturing industry like car manufacturing, integrated circuit manufacturing and many others. In these traditional fields of industrial robot use the task, workspace and boundary conditions are well defined. The research and development of these robots has been done for many decades and they are well understood. These robots are usually driven by electrical or hydraulic actuators. In recent years there is a push to apply industrial robots and robots similar to them in applications that have a variable time dependent task, workspace and boundary conditions. Examples of such applications are produce picking, selective weeding, applications in agriculture in general and applications in medicine like minimally invasive surgery. Robots that can fulfill these tasks need to have properties that standard robots lack, mainly compliance and high obstacle avoidance capability. Both requirements can be facilitated by redundancy. The basic definition of redundancy is given by [1] and it says that a redundant robot is every robot that has more degrees of freedom than is necessary for completing a certain task. Redundancy is task dependent. Nevertheless, in a loose sense for a general-purpose robot and for general tasks that need to be performed in 3d space several degrees of freedom greater than six are considered to be redundant. In this article new designs of robots will be discussed, their applications and the overall interest for these robots in research will be presented.

## 2. New types of redundant robots

Redundant robots can have a vastly different morphology and be driven by more exotic types of actuators compared to classic 6R serial industrial robots. According to [2] and [3] redundant robots can be categorized according to their morphology in to the following categories and shown in **Figure 1**:

- **Discrete robots-** redundant robots most resembling basic industrial robots, but with more joints/links
- **Cascade robots-** In general these robots consist of in serial connected parallel platforms
- **Continuum robots-** they have infinite or queasy infinite underactuated degrees of freedom. They can be further subdivided into three categories:
  - **Soft continuum robots-** have infinite degrees of freedom in all parts of the robot
  - **Hard continuum robots-** has infinite degrees of freedom but they are situated along a central spine
  - **Discrete continuum robots-** have similar macroscopic behavior than hard continuum robots but do not have infinite degrees of freedom

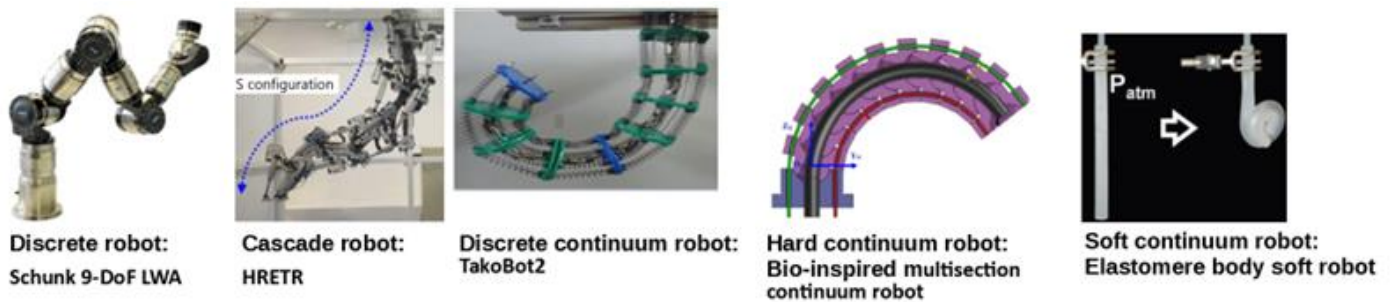


Figure 1 Redundant robot types

#### 4. Current fields of research in redundant robots

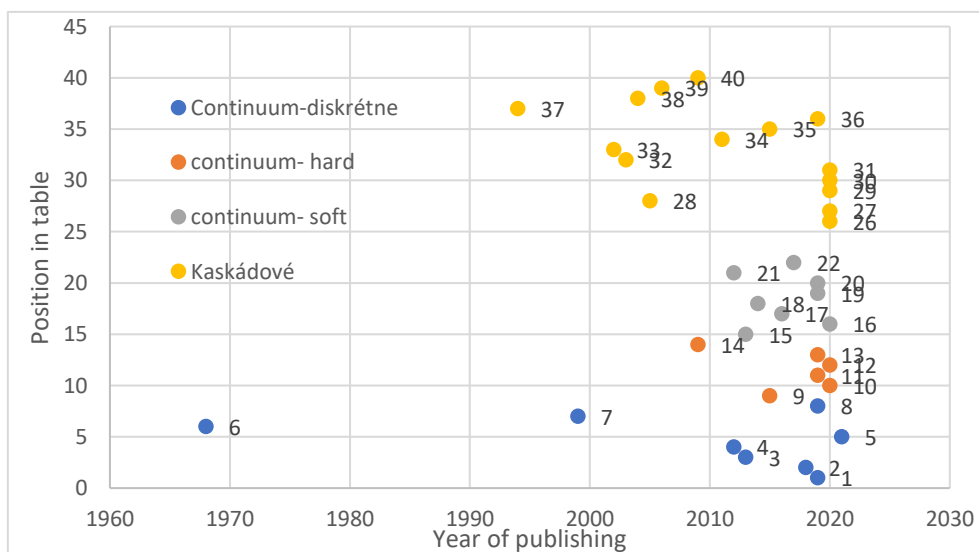
In the **Table 1** it can see the types and some of the design properties of redundant robots used both in research and in the industry. The overview was done for articles published up to year 2021

**Table 1** Overview of articles involving redundant robots

n.o	Arti- cle	Type	Subtype	Total dof	Actuator	Year	Use	n.o	Arti- cle	Type	Subtype	Total dof	Actuator	Year	Use
1	[4]	continuum	discrete	16	el. mot.	2019	research	21	[24]	continuum	soft	n	bellows	2019	research
2	[5]	continuum	discrete	20	el. mot.	2018	research	22	[25]	continuum	soft	n	bellows	2012	research
3	[6]	continuum	discrete	30	el. mot.	2013	research	23	[26]	continuum	soft	n	bellows	2017	research
4	[7]	continuum	discrete	30	el. mot.	2012	research	24	[27]	discrete		9	el. mot.		industrial
5	[8]	continuum	discrete	97	el. mot.	2021	inšpekcia	25	[28]	discrete		7	el. mot.		industrial
6	[9]	continuum	discrete	20	el. mot.	1968	research; un- derwater	26	[29]	cascade		3	bellows	2020	research
7	[10]	continuum	discrete	32	el. mot.	1999	research	27	[30]	cascade		18	el. mot.	2020	research

8	[11]	continuum	discrete	7+ (19)	bellows + pneu rotation mot	2019	colaborative	28	[31]	cascade		3	el. mot.	2005	research
9	[12]	continuum	hard	n	el. mot.	2015	research	29	[32]	cascade		15	el. mot./ nylon muscles	2020	research
10	[13]	continuum	hard	n	el. mot.	2020	research	30	[33]	cascade	snake	14	el. mot.	2020	research; inspection
11	[14]	continuum	hard	n	bellows	2019	research	31	[34]	cascade	snake	20	el. mot.	2020	research
12	[15]	continuum	hard	n	el. mot.	2020	research	32	[35]	cascade	snake	15	el. mot.	2003	inspection
13	[16]	continuum	hard	n	bellows	2019	research; podmorský zber	33	[36]	cascade		3	el act. polymér	2002	research
14	[17]	continuum	hard	n	bellows	2009	loboratórne, inšpekčné	34	[37]	cascade	snake	7	el. mot.	2011	surgical
15	[18]	continuum	soft	n	hybrid- el. mot./ bellows	2015	research	35	[38]	cascade	snake	9	el. mot.	2015	surgical
16	[19]	continuum	soft	n	bellows	2013	research	36	[39]	cascade	snake	32	el. mot.	2019	research, surgical
17	[20]	continuum	soft	n	bellows	2020	research	37	[40]	cascade	snake	30	el. mot.	1994	research
18	[21]	continuum	soft	n	hybrid- el. mot./ bellows	2016	research	38	[41]	cascade		7	el. mot.	2004	research
19	[22]	continuum	soft	n	bellows	2014	research, surgical	39	[42]	cascade	snake	-	el. mot.	2006	research, surgical
20	[23]	continuum	soft	n	bellows	2019	research	40	[43]	cascade	snake	105	el. mot.	2009	research, surgical

The above table is summarized in Figure 2, where the x axis is the year of publishing of an article describing a redundant robot and the y axis is the number of the article in the table.



#### 4. Discussion

As can be seen from the above overview, the interest in research and development in the field of redundant robots has increased dramatically in the past twenty years. New and exotic designs emerge mainly as research platforms. The reasons for this trend are multiple. The first is the need to automate processes that had traditionally been performed by human laborers like the already mentioned produce picking, in other words, processes with not fully defined parameters. The second mayor factor is the decreasing cost of rapid prototyping technologies and increased availability of cheap powerful electronic hardware and the advent of new materials allowing for quick and cheap development of prototypes. The last factor is the fact that all new research regarding classic industrial robot design and control because of the extend of previous research usually yields only incremental results whereas research in the design and control of redundant robots gives ample opportunity for significant contributions. It is safe to assume that thanks to these factors, the field of redundant robotics will continue to rapidly evolve and the application of redundant industrial robots in agriculture and medicine will follow in the next years.

#### 5. Conclusions

This article discusses new trends in industrial robot research which mainly focus on development of redundant robots of nonstandard morphology. An overview of the research on this topic has been performed and summarized both in a graph and table form. An appreciable increase in the amount of research papers on the topic of redundant robots can be seen starting from year 2000. Possible reasons for this development were discussed and three were identified as simple and cheap prototype manufacturing, emergence of new fields of application and non-exhausted field of research. It can be expected that the trend of high interest in the field of redundant robot research and development will continue in the future.

**Acknowledgments:** The authors would like to thank Slovak grant agency- project VEGA 1/0436/22.

**Conflicts of Interest:** The authors declare no conflict of interest.

#### References

1. Chiaverini, S., Oriolo, G., and Walker, I., "Kinematically Redundant Manipulators", In *Springer Handbook of Robotics*, Springer, Berlin, Heidelberg, pp. 245–268 (January 1, 2008).
2. V. C. ANDERSON et A and R. C. Horn, "SENSOR ARM MANIPULATOR", United States Patent Office patent US3497083A (1968).
3. Robinson, G. and Davies, J. B. C., "Continuum robots - a state of the art", *Proceedings 1999 IEEE International Conference on Robotics and Automation (Cat. No.99CH36288C)*, pp. 2849–2854 vol.4 (1999).
4. Yeshmukhametov, A., Koganezawa, K., and Yamamoto, Y., "Designing of Novel Wire-Driven Continuum Robot Arm with Passive Sliding Disc Mechanism: Forward and Inverse Kinematics", *2019 19th International Conference on Control, Automation and Systems (ICCAS)*, pp. 218–223 (2019).
5. Stevanović, I., Rodić, A., Jovanović, M., and Tomić, M., "Building of Hyper-redundant Under-Actuated Soft Robotic Arm with 20 DOF", *Advances in Service and Industrial Robotics*, C. Ferraresi and G. Quaglia, Eds., Mechanisms and Machine Science, Springer International Publishing, Cham, pp. 681–688 (2018).
6. Li, Z. and Du, R., "Design and Analysis of a Bio-Inspired Wire-Driven Multi-Section Flexible Robot", *International Journal of Advanced Robotic Systems*, **10**(4), p. 209 (2013).
7. Jagadeesan, P., Sivaprakasham, S., Kumar, D., and Madhu, M., "A 'Multilink Spatial Hyper Redundant' Manipulator", *Advances in Reconfigurable Mechanisms and Robots I*, J. S. Dai, M. Zoppi, and X. Kong, Eds., Springer, London, pp. 869–875 (2012).
8. Wang, M., Dong, X., Ba, W., Mohammad, A., Axinte, D., and Norton, A., "Design, modelling and validation of a novel extra slender continuum robot for in-situ inspection and repair in aeroengine", *Robotics and Computer-Integrated Manufacturing*, **67**, p. 102054 (2021).
9. V. C. ANDERSON et A and R. C. Horn, "SENSOR ARM ANIPULATOR" (1968).

10. Walker, I. D. and Hannan, M. W., "A novel 'elephant's trunk' robot", *1999 IEEE/ASME International Conference on Advanced Intelligent Mechatronics (Cat. No.99TH8399)*, pp. 410–415 (1999).
11. "BionicSoftArm | Festo Corporate", <https://www.festo.com/group/en/cms/13527.htm>.
12. Yang, Y. and Zhang, W., "ET Arm: Highly Compliant Elephant-Trunk Continuum Manipulator", *Intelligent Robotics and Applications*, X. Zhang, H. Liu, Z. Chen, and N. Wang, Eds., Lecture Notes in Computer Science, Springer International Publishing, Cham, pp. 288–299 (2014).
13. Zhiguang Xing, Pengyuan Wang, and Jianwen Zhao, "A novel design of a contractible, tubular continuum manipulator" (2020).
14. Bao, G., Chen, L., Zhang, Y., Cai, S., Xu, F., Yang, Q., and Zhang, L., "Trunk-like Soft Actuator: Design, Modeling, and Experiments", *Robotica*, **38**, pp. 1–15 (2019).
15. Yang, C., Geng, S., Walker, I., Branson, D., Liu, J., Dai, J., and Kang, R., "Geometric constraint-based modeling and analysis of a novel continuum robot with Shape Memory Alloy initiated variable stiffness", *The International Journal of Robotics Research*, **39**, p. 027836492091392 (2020).
16. Gong, Z., Chen, B., Liu, J., Fang, X., Liu, Z., Wang, T., and Wen, L., "An Opposite-Bending-and-Extension Soft Robotic Manipulator for Delicate Grasping in Shallow Water", *Frontiers in Robotics and AI*, **6** (2019).
17. Walker, I. D. and Green, K. E., "Continuum Robots", In *Encyclopedia of Complexity and Systems Science*, R. A. Meyers, Ed., Springer, New York, NY, pp. 1475–1485 (2009).
18. Wurdemann, H., Stilli, A., and Althoefer, K., *An Antagonistic Actuation Technique for Simultaneous Stiffness and Position Control* (2015).
19. Martinez, R. V., Branch, J. L., Fish, C. R., Jin, L., Shepherd, R. F., Nunes, R. M. D., Suo, Z., and Whitesides, G. M., "Robotic Tentacles with Three-Dimensional Mobility Based on Flexible Elastomers", *Advanced Materials*, **25**(2), pp. 205–212 (2013).
20. Zolfagharian, A., Mahmud, M., Gharaie, S., Bodaghi, M., Kouzani, A., and Kaynak, A., "3D/4D-printed bending-type soft pneumatic actuators: fabrication, modelling, and control", *Virtual and Physical Prototyping*, **15**, pp. 1–30 (2020).
21. Shiva, A., Stilli, A., Noh, Y., Faragasso, A., Falco, I. D., Gerboni, G., Cianchetti, M., Menciassi, A., Althoefer, K., and Wurdemann, H. A., "Tendon-Based Stiffening for a Pneumatically Actuated Soft Manipulator", *IEEE Robotics and Automation Letters*, **1**(2), pp. 632–637 (2016).
22. Fraś, J., Czarnowski, J., Maciaś, M., and Głowka, J., "Static Modeling of Multisection Soft Continuum Manipulator for Stiff-Flop Project", *Recent Advances in Automation, Robotics and Measuring Techniques*, R. Szewczyk, C. Zieliński, and M. Kaliczyńska, Eds., Advances in Intelligent Systems and Computing, Springer International Publishing, Cham, pp. 365–375 (2014).
23. Drotman, D., Ishida, M., Jadhav, S., and Tolley, M. T., "Application-Driven Design of Soft, 3-D Printed, Pneumatic Actuators With Bellows", *IEEE/ASME Transactions on Mechatronics*, **24**(1), pp. 78–87 (2019).
24. Ren, T., Li, Y., Xu, M., Li, Y., Xiong, C., and Chen, Y., "A Novel Tendon-Driven Soft Actuator with Self-Pumping Property", *Soft Robotics*, **7**(2), pp. 130–139 (2019).
25. Jiang, A., Xynogalas, G., Dasgupta, P., Althoefer, K., and Nanayakkara, T., "Design of a variable stiffness flexible manipulator with composite granular jamming and membrane coupling", *2012 IEEE/RSJ International Conference on Intelligent Robots and Systems*, pp. 2922–2927 (2012).
26. Anver, H. M. C. M., Mutlu, R., and Alici, G., "3D printing of a thin-wall soft and monolithic gripper using fused filament fabrication", *2017 IEEE International Conference on Advanced Intelligent Mechatronics (AIM)*, pp. 442–447 (2017).
27. Lehmann, J., "Jens Lehmann stands for precise gripping, and concentrated safe holding. As a brand ambassador of the SCHUNK team, the No. 1 goalkeeper represents our global competence leadership for clamping technology and gripping systems. The top performance of SCHUNK and Jens Lehmann are characterized by dynamics, precision, and reliability.", p. 32 (n.d.).
28. "LBR iiwa", <https://www.kuka.com/sk-sk/produkty-a-sluzby/robotické-systémy/industrial-robots/lbr-iiwa>.

29. Zhang, J., Wei, H., Shan, Y., Li, P., Zhao, Y., Qi, L., and Yu, H., "Modeling and Experimental Study of a Novel Multi-DOF Parallel Soft Robot", *IEEE Access*, **8**, pp. 62932–62942 (2020).
30. Zhao, Y., Song, X., Zhang, X., and Lu, X., "A Hyper-redundant Elephant's Trunk Robot with an Open Structure: Design, Kinematics, Control and Prototype", *Chin. J. Mech. Eng.*, **33**(1), p. 96 (2020).
31. Koganezawa, K., "Hyper redundant manipulator using compound three-bar linkages", *J Mech Sci Technol*, **19**(1), pp. 320–327 (2005).
32. Jiang, Z., Huang, H., Huang, H., and Li, B., "A Truss-type Deployable Manipulator Actuated by Parallel Twisted and Coiled Nylon Fiber Actuator\*", *2020 IEEE International Conference on Real-Time Computing and Robotics (RCAR)*, pp. 105–110 (2020).
33. Martín-Barrio, A., Roldán Gómez, J., Rodríguez, I., Cerro, J., and Barrientos, A., "Design of a Hyper-Redundant Robot and Teleoperation Using Mixed Reality for Inspection Tasks", *Sensors*, **20**, p. 2181 (2020).
34. Xu, D., Li, E., Liang, Z., and Gao, Z., "Design and Tension Modeling of a Novel Cable-Driven Rigid Snake-Like Manipulator", *J Intell Robot Syst*, **99**(2), pp. 211–228 (2020).
35. Wolf, A., Brown, H. B., Casciola, R., Costa, A., Schwerin, M., Shamas, E., and Choset, H., "A Mobile Hyper Redundant Mechanism for Search and Rescue Tasks", pp. 2889–2895 (2003).
36. Wingert, A., Lichter, M., Dubowsky, S., and Hafez, M., "Hyper-redundant robot manipulators actuated by optimized binary-dielectric polymers", *Proceedings of SPIE - The International Society for Optical Engineering*, **4695**, pp. 415–423 (2002).
37. Shang, J., Noonan, D. P., Payne, C., Clark, J., Sodergren, M. H., Darzi, A., and Yang, G.-, "An articulated universal joint based flexible access robot for minimally invasive surgery", *2011 IEEE International Conference on Robotics and Automation*, pp. 1147–1152 (2011).
38. Clark, J., Noonan, D. P., Vitiello, V., Sodergren, M. H., Shang, J., Payne, C. J., Cundy, T. P., Yang, G.-Z., and Darzi, A., "A novel flexible hyper-redundant surgical robot: prototype evaluation using a single incision flexible access pelvic application as a clinical exemplar", *Surg Endosc*, **29**(3), pp. 658–667 (2015).
39. Liu, T., Mu, Z., Xu, W., Yang, T., You, K., Fu, H., and Li, Y., *Improved Mechanical Design and Simplified Motion Planning of Hybrid Active and Passive Cable-Driven Segmented Manipulator with Coupled Motion* (2019).
40. Chirikjian, G. S. and Burdick, J. W., "A hyper-redundant manipulator", *IEEE Robotics Automation Magazine*, **1**(4), pp. 22–29 (1994).
41. Suthakorn, J. and Chirikjian, G., *Design and Implementation of a New Discretely-Actuated Manipulator* (2000).
42. Degani, A., Choset, H., Wolf, A., and Zenati, M., *Highly Articulated Robotic Probe for Minimally Invasive Surgery* (2006).
43. Ota, T., Degani, A., Schwartzman, D., Zubiate, B., McGarvey, J., Choset, H., and Zenati, M. A., "A Highly Articulated Robotic Surgical System for Minimally Invasive Surgery", *The Annals of Thoracic Surgery*, **87**(4), pp. 1253–1256 (2009).



# Evaluation of accuracy and porosity of FDM 3D printed PEEK implants

Patrik Varga<sup>1\*</sup>, Radovan Hudák<sup>2</sup>, Teodor Tóth<sup>3</sup>, Marek Schnitzer<sup>4</sup>

1 Technical University of Kosice, Faculty of Mechanical Engineering, Department of Biomedical Engineering and measurement, Slovakia; [patrik.varga@tuke.sk](mailto:patrik.varga@tuke.sk)

2 Technical University of Kosice, Faculty of Mechanical Engineering, Department of Biomedical Engineering and measurement, Slovakia; [radovan.hudak@tuke.sk](mailto:radovan.hudak@tuke.sk)

3 Technical University of Kosice, Faculty of Mechanical Engineering, Department of Biomedical Engineering and measurement, Slovakia; [teodor.toth@tuke.sk](mailto:teodor.toth@tuke.sk)

4 Technical University of Kosice, Faculty of Mechanical Engineering, Department of Biomedical Engineering and measurement, Slovakia; [marek.schnitzer@tuke.sk](mailto:marek.schnitzer@tuke.sk)

\* Correspondence: [patrik.varga@tuke.sk](mailto:patrik.varga@tuke.sk); Tel.: 055 602 2378

**Abstract:** Despite the rapid progress of several additive technologies, there is a critical barrier to the processability of high-performance materials. Polyether-ether-ketone (PEEK) is known for its mechanical properties, biological and chemical stability and biocompatibility suitable for biomedical applications. The main challenges of using PEEK material in additive FDM technology are the high melting temperature of 340°C and viscosity. The paper deals with the evaluation of printed implant deviations, wall thickness and porosity of the implant in VGStudio MAX software. The results show that 90% of the implant surface has a deviation of less than or equal to 0.66 mm. The analysis shows that the total pore volume of the manufactured implant is 464 mm<sup>3</sup> pores, which represents 0.77% of the implant volume, and also the average thickness of the implant is 4.84 mm with a standard deviation of 1.4 mm.

**Keywords:** additive manufacturing 1; PEEK 2; patient specific implant 3; FDM 4

## 1. Introduction

Brain-sparing cranioplasty is most often performed after a previous craniectomy for traumatic brain injury, stroke, intracranial tumour surgery, and intracranial infections. Like any procedure, cranioplasty also carries risks, including infection, postoperative edema, and other complications [1]. The construction of cranial implants must include two factors: the suitability of the contour of the cranial implant defect for each patient and the biocompatibility of the material [2]. Over time, the production techniques and the materials used have evolved. The first reports described the use of metals (gold, silver) for the replacement of intervertebral discs, and then progress was made to bone grafts and eventually to polymer (PEEK) implants [3–5]. One of the most important factors that surgeons must consider is the nature of the material used [6]. Implants were made by FDM 3D printer Apium M220 (Germany) which has been developed for use in the field of healthcare. PEEK implants have several advantages: they are chemically inert, maintain structural integrity at temperatures above 300°C, and can be sterilized using gamma radiation with steam [12]. Due to the availability of computer-aided design (CAD) surgical planning, PEEK implants can be easily manufactured using 3D printing to meet the individual requirements of each patient [7–9]. The elasticity and energy-absorbing properties of the PEEK material are closer to the bone than the mechanical properties of titanium. In general, custom-made implants are constructed using patient CT imaging data and are required to exhibit long-term stability, good osseointegration, and high geometric accuracy after insertion. The

main challenges of using PEEK material in additive FFF technology are the high melting temperature of 340 °C and viscosity [10]. This melting temperature brings high demands on processing equipment and later prevents the melting of the melt and further affects the strength of the 3D models. This is because the melting point drops rapidly after 3D printing [11]. Regarding FDM equipment, one of the most important issues is the design of the nozzle, which determines the heat transfer, melt flow and melt condition. Regarding dimensional accuracy, there are many parameters such as 3D printing growth angle, layer thickness, nozzle temperature, etc., which can significantly affect the quality of 3D models [11-12]. The aim of this study is to evaluate the accuracy of 3D printing, which is affected by the setting of the input printing parameters. These settings also affect the connection of individual layers and the porosity of the implant. For a comprehensive assessment of the shape, an analysis of the thickness of the implant wall and a nominal-actual analysis was performed, where the nominal object is the STL model used for production and the actual object is a scan obtained by computer tomography.

## 2. Methodology

This study describes data processing to evaluate the CAD model of the printed implant, and to evaluate the porosity and wall thickness of the implant. VGStudio MAX software (Volume Graphics, Germany) was used for data processing.

### 2.1 Comparison of the printed implant with the CAD model

For comparison, the Nominal-Actual Comparison module was used, in which the reconstructed implant model was aligned to the CAD model using the Best Fit function. Figure 1 shows the distribution of deviations with respect to the CAD model.

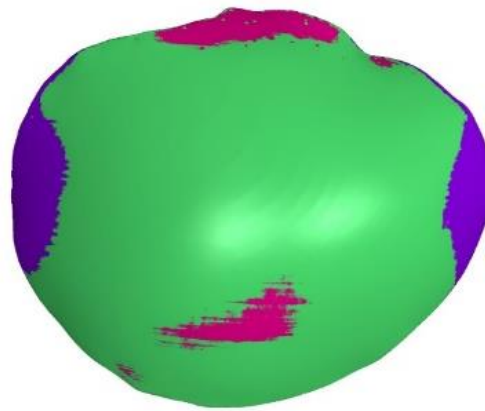


**Figure 1.** Distribution of deviations on 3D implant models

The results show that 90% of the implant surface has a deviation less than or equal to 0.66 mm.

### 2.2 The thickness of the implant wall

The thickness of the wall of the proposed implant is based on the thickness of the bone wall in the healthy part of the skull and is therefore not the same. To perform data analysis, when determining the surface, the possibility of removing internal defects of the material was chosen, so that the wall thickness would not be divided into 2 or more parts during the detection of the pore. Figure 2 shows the wall thickness distribution on the manufactured implant. The analysis shows that the average thickness of the implant is 4.84 mm with a standard deviation of 1.4 mm.

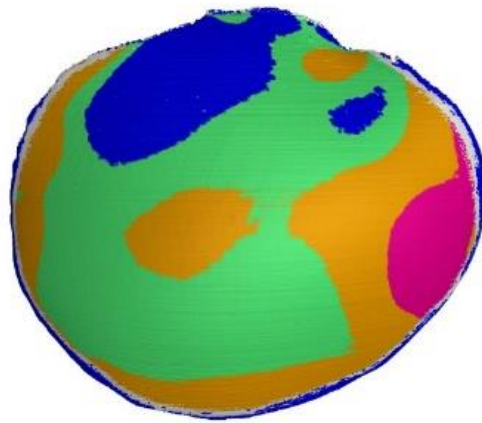


**Figure 2.** The distribution of the thickness of the implant walls shown on the 3D models of the implant

### 2.3 Porosity

The porosity of the manufactured implant was evaluated as part of the study. The pore search was set to a minimum volume of 0.03 mm<sup>3</sup> (8 voxels) and a maximum diameter of 2 mm. In the monitored volume, 464 mm<sup>3</sup> of pores were identified, which represents 0.77% of the implant volume. Figure 3 shows the distribution of pores in the 3D volume.

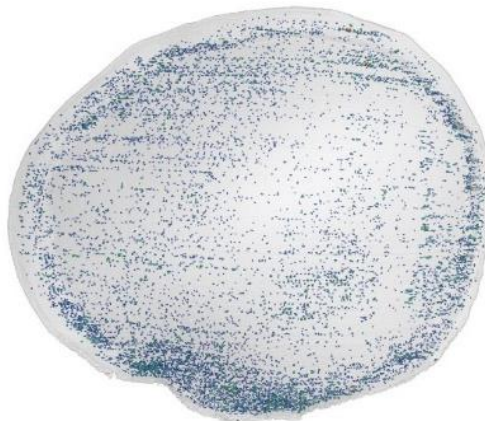


**Figure 3.** Layout The layout of the pores in the 3D volume

It is clearly visible in the picture that the pores are distributed over the printing layers. This porosity of the product can be influenced by changing the input production parameters.

### 3. Conclusions

It can be seen from the output that the biggest deviations of the printed implant from the CAD model occurred in the outer parts of the model or in the part of the implant touching the supporting structures and the heated plate affected by the heat flow. From the evaluation of the pores of the implant, it is clearly visible that the pores are distributed over the printing layers. For the correct placement and attachment of the implant to the bone, it is necessary to ensure that the shape of the implant is inverse to the shape of the bearing surface on the skull. The manufactured implant must copy the thickness of the bones of the healthy part of the skull. Thus, the implant must not touch soft tissues. The analysis of bone thickness shows that the maximum thickness reaches 8.67 mm.

**Acknowledgment:** This article was developed on the basis of support obtained from the projects: ITMS2014+: 313011V358, 01/2020 - 06/2023; VEGA 1/0599/22; KEGA 021TUKE-4/2022; CEMBAM

**Conflicts of Interest:** The authors declare no conflict of interest.

## References

- SCHOEKLER, Bernadette a Martin TRUMMER. Prediction parameters of bone flap resorption following cranioplasty with autologous bone. *Clinical Neurology and Neurosurgery*. 2014, 120, 64-67. ISSN 03038467. doi:10.1016/j.clineuro.2014.02.014.
- PIITULAINEN, Jaakko M., Tommi KAUKO, Kalle M.J. AITASALO, Ville VUORINEN, Pekka K. VALLITTU a Jussi P. POSTI. Outcomes of Cranioplasty with Synthetic Materials and Autologous Bone Grafts. *World Neurosurgery*. 2015, 83(5), 708-714. ISSN 18788750. doi:10.1016/j.wneu.2015.01.014
- STULA, Dragoslav. The problem of the "sinking skin-flap syndrome" in cranioplasty. *Journal of Maxillofacial Surgery*. 1982, 10, 142-145. ISSN 03010503. doi:10.1016/S0301-0503(82)80030-1.
- KUO, Jinn-Rung, Che-Chuan WANG, Chung-Ching CHIO a Tain-Junn CHENG. Neurological improvement after cranioplasty – analysis by transcranial doppler ultrasonography. *Journal of Clinical Neuroscience*. 2004, 11(5), 486-489. ISSN 09675868. doi:10.1016/j.jocn.2003.06.005.
- ZANATY, Mario, Nohra CHALOUHI, Robert M. STARKE, et al. Complications following cranioplasty: incidence and predictors in 348 cases. *Journal of Neurosurgery*. 2015, 123(1), 182-188. ISSN 0022-3085. doi:10.3171/2014.9.JNS14405.
- EL HALABI, F., J.F. RODRIGUEZ, L. REBOLLEDO, E. HURTÓS a M. DOBLARÉ. Mechanical characterization and numerical simulation of polyether-ether-ketone (PEEK) cranial implants. *Journal of the Mechanical Behavior of Biomedical Materials*. 2011, 4(8), 1819-1832. ISSN 17516161. doi:10.1016/j.jmbbm.2011.05.039
- FEROZE, Abdullah H., Graham G. WALMSLEY, Omar CHOUDHRI, H. Peter LORENZ, Gerald A. GRANT a Michael S. B. EDWARDS. Evolution of cranioplasty techniques in neurosurgery: historical review, pediatric considerations, and current trends. *Journal of Neurosurgery*. 2015, 123(4), 1098-1107. ISSN 0022-3085. doi:10.3171/2014.11.JNS14622
- SHAH, Aatman M., Henry JUNG a Stephen SKIRBOLL. Materials used in cranioplasty: a history and analysis. *Neurosurgical Focus*. 2014, 36(4). ISSN 1092-0684. doi:10.3171/2014.2.FOCUS13561.
- NORTHAM, Weston, Avinash CHANDRAN, Crystal ADAMS, Nikki E. BARCZAK-SCARBORO a Carolyn QUINSEY. Cranioplasty length of stay: Relationship with indication, surgical decision-making factors, and sex. *Trauma*. 2020, 22(4), 256-264. ISSN 1460-4086. doi:10.1177/1460408619892141.
- LIU, Liming, Shou-Tao LU, Ai-Hua LIU, et al. Comparison of complications in cranioplasty with various materials: a systematic review and meta-analysis. *British Journal of Neurosurgery*. 2020, 34(4), 388-396. ISSN 0268-8697. doi:10.1080/02688697.2020.1742291.
- MATSUNO, A., H. TANAKA, H. IWAMURO, S. TAKANASHI, S. MIYAWAKI, M. NAKASHIMA, H. NAKAGUCHI a T. NAGASHIMA. Analyses of the factors influencing bone graft infection after delayed cranioplasty. *Acta Neurochirurgica*. 2006, 148(5), 535-540. ISSN 0001-6268. doi:10.1007/s00701-006-0740-6.
- ZHAO, Yachen, Kai ZHAO, Yuchan LI a Fei CHEN. Mechanical characterization of biocompatible PEEK by FDM. *Journal of Manufacturing Processes*. 2020, 56, 28-42. ISSN 15266125. doi:10.1016/j.jmapro.2020.04.063.
- TSENG, Jian-Wei, Chao-Yuan LIU, Yi-Kuang YEN, Johannes BELKNER, Tobias BREMICKER, Bernard Haochih LIU, Ta-Ju SUN a An-Bang WANG. Screw extrusion-based additive manufacturing of PEEK. *Materials & Design*. 2018, 140, 209-221. ISSN 02641275. doi:10.1016/j.matdes.2017.11.032.



# Influence of selected process parameters on joint formation by thermal drilling technology

Nikita Veligotskyi \*, Erik Janoško <sup>1</sup> and Anna Guzanová <sup>2,\*</sup>

<sup>1</sup> Technical University of Košice, Faculty of Mechanical Engineering, Department of Technologies, Materials and Computer Aided Production, Slovakia; [erik.janosko@tuke.sk](mailto:erik.janosko@tuke.sk); [anna.guzanova@tuke.sk](mailto:anna.guzanova@tuke.sk)

\* Correspondence: [nikita.veligotskyi@tuke.sk](mailto:nikita.veligotskyi@tuke.sk)

**Abstract:** The paper is aimed at verifying the influence of the change in feed rate on the shape and dimensions of the bushing formed when joining two overlapped thin-walled materials by thermal drilling technology. Pairs of materials - dissimilar steels and steel with aluminium alloy - were joined. Three strategies for changing the feed rate during the tool cycle were tested. The shape and dimensions of the formed bushings – form fit joints were studied on metallographic sections. For joining steels with aluminium alloys, a strategy involving start the working feed at the value of 250 mm.min<sup>-1</sup> and gradually increase it to the value of 700 mm.min<sup>-1</sup> can be recommended for the tested materials and a tool diameter of 5.3 mm.

**Keywords:** joining; dissimilar materials; flowdrill; rotational speed; tool feed; metallography

## 1. Introduction

Joining dissimilar materials is currently a highly topical. In order to save material resources and make utilization of the material characteristics of structural materials more effective, conventional steels are gradually being replaced by non-conventional high-strength steels, as well as other materials with good specific strength, such as aluminum, magnesium alloys or even composite materials [1-2]. The main problem that needs to be solved is the joining of these dissimilar materials. They differ from each other in their nature, internal arrangement of individual elements (e.g. metals versus plastics), or microstructure, mechanical, physical properties, as well as the nature of the response of these materials to different types of load [3-8]. The problem arises especially when joining steels with aluminium, which differ in melting temperature, very low mutual solubility of the constituents (Fe-Al) and the formation of brittle intermetallic compounds at the interface of the joined materials. There are different ways how to solve these problems, such as the use of interlayers when welding dissimilar materials, or modifying technologies to decrease heat input - CMT welding, welding with high-energy beams - laser, electron beam, etc. Technologies using the principles of mechanical joining, such as clinching, riveting and their numerous modifications, or combinations with adhesive bonding or resistance welding, appear to be very promising. Their disadvantage is that in many cases they require two-sided access to the parts to be joined, and problems can also be caused by the different formability of dissimilar materials, which is essential for form fit joints formation [9-10].

One of the possibilities of joining dissimilar materials could be the thermal drilling technology, which was founded in 1923 by Jan Claude de Valliere. He tried to create a tool that would be able to make a hole in thin-walled steel sheets without cutting, only using frictional heat. The result of his efforts is friction-forming technology, known as Flowdrill [11]. Flowdrill technology is mainly used for joining thin-walled materials.

It is the joining by the action of a relatively high axial force and friction induced by the tool (forming drill) on the workpiece. In the process, the material is rapidly heated and

becomes soft, allowing the tool to penetrate the entire cross-section of the workpiece and form a bushing on the bottom of the workpiece corresponding to the size of the tool used. Sufficient threads can be then placed in the bushing to allow mechanical connection to other material by means of a screw.

The paper deals with the verification of the possibility of using flowdrill technology to connect a pair of thin overlapped sheets without thread and screw, just by creating two coaxial embedded bushings with form contact. Various process parameters were tested during the formation of joints. Their effect was manifested in the shape and dimensions of the resulting bushing, which was verified by observation of metallographic sections [12].

## 2. Materials and Methods

The following materials were used for the joints formation:

- Cold rolled uncoated deep drawing steel DC04 (hereinafter referred to as DC). The thickness of the material is 0.8 mm.
- Hot-dip zinc coated fine-grained HSLA steel TL 1550-220+Z with increased cold formability (hereinafter referred to as TL). The thickness of the material is 0.8 mm.
- Precipitation hardened aluminum alloy EN AW-6082 T6 (AlSi1MgMn, hereinafter referred to as Al). The thickness of the material is 1,0 mm.

The chemical composition of steels is shown in Table 1, the chemical composition of the aluminum alloy is shown in Table 2.

**Table 1.** Chemical composition of steels, wt. %.

DC									
C	Mn		P	S					Fe
0.04	0.25		0.009	0.008					bal.
TL									
C	Mn	Si	P	S	Al	Nb	Ti	Cu	Fe
0.10	1.00	0.50	0.08	0.03	0.015	0.10	0.15	0.20	bal.

**Table 2.** Chemical composition of aluminum alloy, wt. %.

Al								
Si	Fe	Cu	Mn	Mg	Cr	Zn	Ti	Al
1.00	0.40	0.06	0.44	0.70	0.02	0.08	0.03	bal.

Mechanical properties, surface conditions and/or thermal treatment of the materials used are listed in Table 3.

**Table 3.** Mechanical properties, surface conditions and/or thermal treatment of the materials.

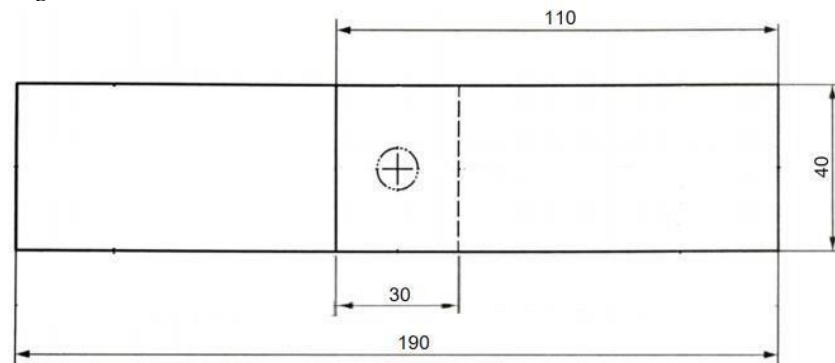
Materials	YS [MPa]	UTS [MPa]	Elongation [%]	Thickness [mm]	Condition
DC	197	327	39	0.8	electrostatically oiled
TL	292	373	34	0.8	Zn coated 100 g.m <sup>-2</sup>
Al	290	340	14	1.0	Solution treated, artificially aged

Table 4 shows selected physical properties of the tested materials.

**Table 4.** Physical properties of materials.

Materials	Density [kg.m <sup>-3</sup> ]	Melting point [°C]	Thermal conduc- tivity [W/m·K]	Coefficient of ther- mal expansion [10 <sup>-6</sup> /K]	Modulus of elasticity [GPa]
DC, TL	7860	~1500	45	10.8-12.5	~210
Al	2700	555	180	24	~70

The shape and dimensions of the test specimens were designed according to EN ISO 12996 depending on the thickness of the materials to be joined and the diameter of the tool used, Fig. 1.



**Figure 1.** Shape and dimensions of joint assembly.

To create connections was elected the thermal drilling tool Flowdrill Long  $\varnothing$  5.3 mm, Fig. 2.



**Figure 2.** Tool Flowdrill Long  $\varnothing$  5.3 mm.

In thermal drilling, in order to achieve the maximum tool life, it is necessary to choose rotational speed at the lowest possible limit. The choice of rotational speed primarily depends on the drilled material and its thickness. Thicker anti-corrosion and high-carbon steels require lower speeds, which usually result in lower tool life. In general, non-ferrous metal alloys require higher speeds, the higher the softer material we are drilling. When joining steel and aluminum alloy, we are therefore forced to make a compromise when choosing rotational speed - and thus we chose a higher speed than required by steel and lower than required by aluminum alloy. Rotational speed was constant during the formation of the joints. By changing rotational speed in the work cycle, we would needlessly extend the drilling time at the expense of the efficiency of the process. It is much more efficient to use a variable feed in the drilling process. By changing it, we can influence the shape and dimensions of the resulting bushing.

The feed is determined by the pressure - the resistance of the material against the penetration of the tool. The initial pressure is quite high to generate frictional heat. As the material softens, it allows the drill bit to advance into the material, the rate of advancement increasing with temperature and progress in penetrating the material.

The required feed motion can be achieved manually or by means of pneumatic systems. If a CNC machining center is used to produce the holes, the above procedure can be simulated by creating a program with a slow initial feed rate that gradually increases to the level of the selected maximum feed value. The feed and its change will also depend on the dimensions of the tool, the tool speed and the type and thickness of the material. The appropriate feed can be determined relatively easily by experiment and observation.

The correct feed is selected when a constant dark red coloring of the material during drilling is achieved (applies to steels).

When joining dissimilar steels and steels with aluminum alloy, the following three different strategies – feed courses - were chosen, Fig. 3.

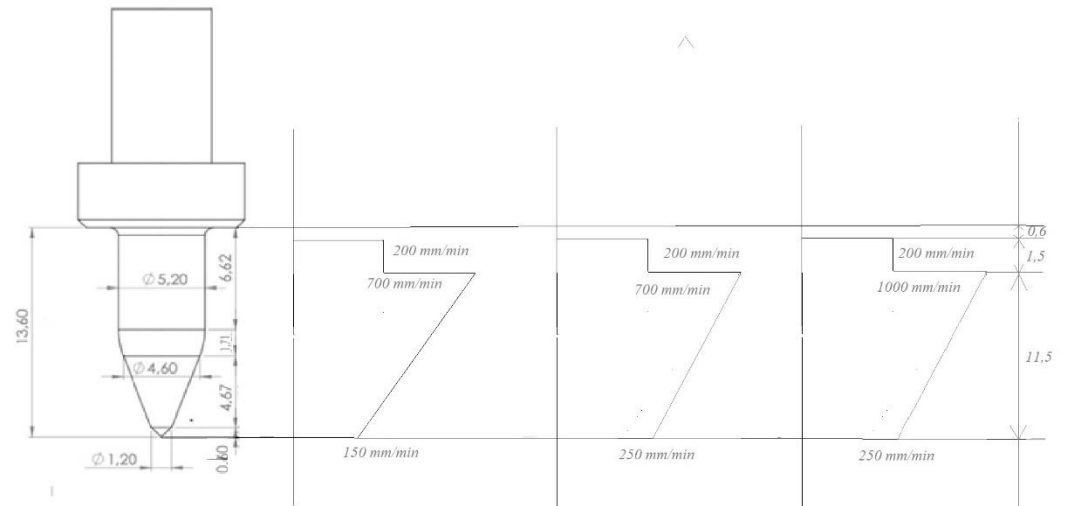


**Figure 3.** Representation of the tool feed change in the work cycle.

**Strategy 1:** when the tip of the tool get in contact with the material, the initial feed is  $150 \text{ mm}\cdot\text{min}^{-1}$ , on a tool path of  $11.5 \text{ mm}$  it continuously increased to a value of  $700 \text{ mm}\cdot\text{min}^{-1}$ , then on a path of  $1.5 \text{ mm}$  the feed was reduced to a value of  $200 \text{ mm}\cdot\text{min}^{-1}$ . Finally, the tool stopped  $0.6 \text{ mm}$  below the tool collar to avoid deformation of the resulting rim. The revolutions were constant:  $3800 \text{ min}^{-1}$ . Abbreviated designation: 3800, 150-700, 200

**Strategy 2:** 3800, 250-700, 200

**Strategy 3:** 3800, 250-1000, 200

For setting and clamping the materials to be joined and for joints making, a fixture was designed, manufactured and used, shown in Fig.4.

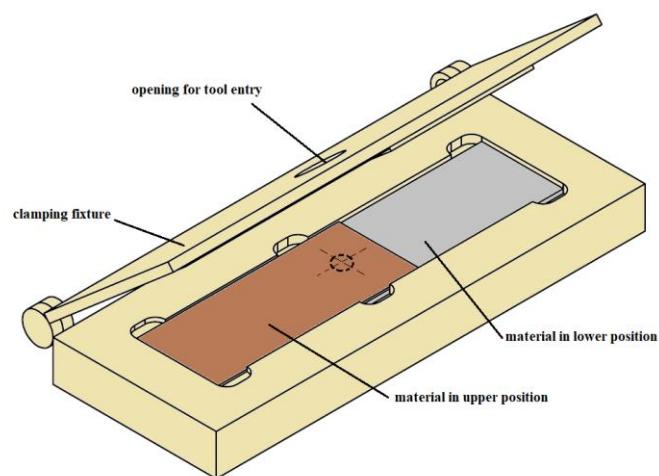


**Figure 4.** Fixture for clamping materials and leading the tool during joining.

The joints were created on a 5-axis CNC milling machine DMG MORI DMU 60 eVO, Fig. 6, using the indicated production strategies.



**Figure 5.** 5-axis CNC milling machine DMG MORI DMU 60 eVO.

A simulation of the process was carried out before the process of creating joints. Figure 7 shows the tool in the bottom reversal point in the simulation software Simufact forming [13]. It is clear from the simulation that in the process of creating the hole, the materials are pushed away from each other to a certain extent, which will be a possible obstacle for the creation of joints.

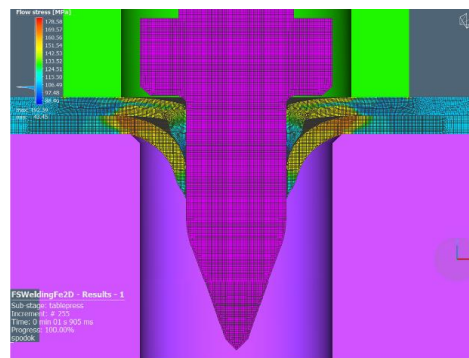


**Figure 6.** Simulation tool in the bottom reversal point.

Thermal drilling technology has been tested on various combinations of materials. It is necessary to realize that when joining dissimilar materials, the position of the material in the joint matters, as dissimilar materials differ both in mechanical properties, in formability, and in thermal conductivity, which are properties that significantly affect the flow of the material during joining and the shape and dimensions of the created bushings. Through previous research, it was found that when joining the mentioned steels and Al, it is necessary to put steel in the upper position and Al in the lower position. The opposite arrangement does not lead to the desired results. The tested material combinations are listed in Tab. 5.

**Table 5.** Matrix of created joints.

Materials in upper position	Materials in lower position
DC	DC; TL; Al
TL	TL; DC; Al
Al	Al

The created joints were subjected to metallographic analysis. Metallographic cuts were made from them through the axis of the hole, then they were mounted in resin, ground and polished using a classic metallographic procedure. The created sections were observed using an optical microscope,

and then the lengths and thicknesses of the created bushings of the individual materials in the joint were measured on the images.

### 3. Results

The appearance of some created joints is shown in Tab. 6.

**Table 6.** Appearance of created joints.

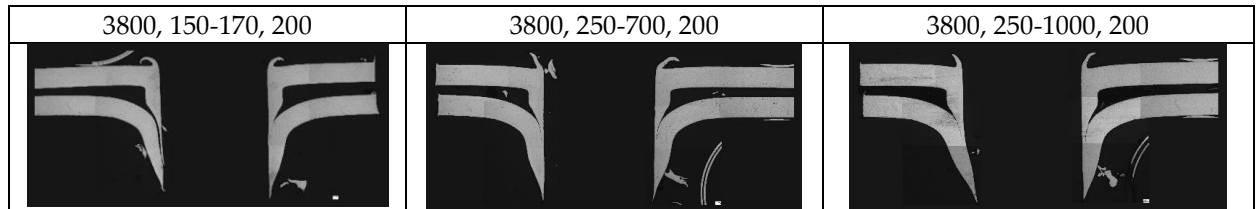
Materials	Top view	Bottom view
DC-DC		
TL-TL		
DC-TL		
TL-DC		
DC-Al		
TL-Al		
Al-Al		

As shown in Table 6, a continuous rim can be seen on some joints (DC-DC, TL-TL, DC-TL, TL-Al), on some it is fragmented (TL-DC) or separated from the material (Al-Al). When looking at the joint bushing, there are visible continuous, intact bushings (DC-DC, TL-DC, Al-Al), some show circumferential cracks (TL-TL, DC-TL) and some even show petals (DC-Al and TL-Al). From the point of view of the design of the joint, it is desirable

that the bushing is continuous, without cracks. A cracked bushing up to the formation of petals can lead to the opening of the joint and loss of cohesion of the materials already during manual handling, even if the bushings were well shaped, embedded coaxially.

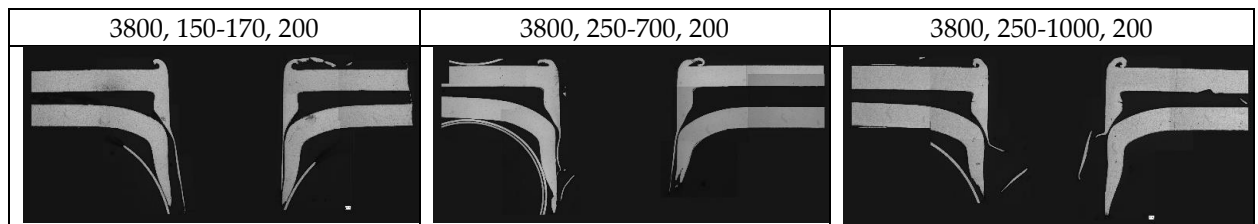
Tables 7-13 show resulting metallographic sections of all formed joints. The sections are presented in full, showing both sides of hole, so that all the details of the joint are clear.

**Table 7.** Metallographic sections of the DC-DC connection.



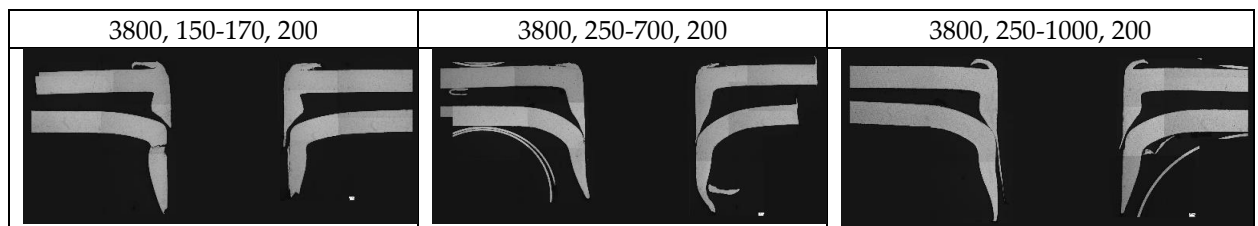
When joining a pair of sheets of uncoated low-carbon steel DC-DC, although concentric embedded bushings were formed, however, due to the springback effect and greater distance between the sheets, we assume that the joint will undergo shear stress at the point of its smallest thickness, and that already at low load. The influence of the used drilling strategy on the shape of the resulting joint is not apparent. The resulting bushings are almost identical in terms of length and thickness. Their shape and mutual position are not suitable for creating a functional connection capable of carrying loads.

**Table 8.** Metallographic sections of the TL-TL connection.



The situation is similar with the material pair TL-TL, concentric bushings have been created, but their shape is not suitable for creating a functional joint. On the lower material, a bushing with a suitable thickness and length was created, but the bushing made from the upper material has a suitable thickness in the place that does not touch the bottom plate. Vice versa, in the place where both bushings touch each other, the thickness of the inner bushing, which finally fails under shear stress, and is responsible for the bearing capacity of the joint, is only of a few micrometers. The influence of the change in the process parameters did not significantly affect the quality of the formed joint.

**Table 9.** Metallographic sections of the DC-TL connection.



At the DC-TL joints on the left, you can see a significantly shortened inner bushing, significant spring back effect, deformation (bending) of the bottom plate and the formation of a gap between the materials. Using strategy 2 (picture in the middle), both bushings are of suitable length and thickness, but they are independent, not embedded in each other, which means an open, broken joint.

**Table 10.** Metallographic sections of the TL-DC connection.



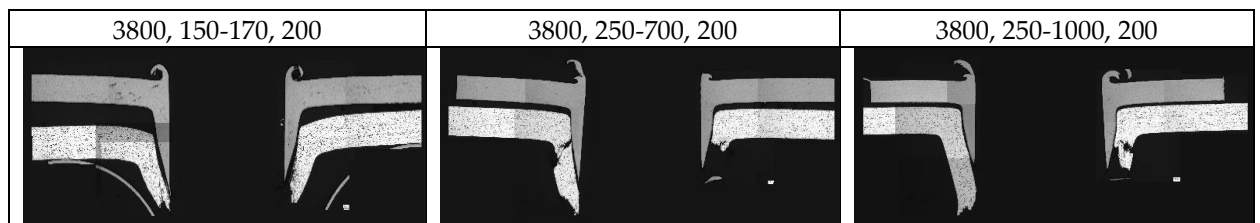
For TL-DC connections and strategy 1 (left), the situation is the same as for a DC-TL connection made with the same strategy. A significant improvement in joint formation was brought by strategy 2 (in the middle) and 3 (right), when the embedding of the sleeves is evident from the metallographic section, while the inner bushing has a greater thickness and can therefore ensure a higher bearing capacity of the joint than the joint of the same material pair joined in the reverse order (DC-TL) created by the same strategy.

**Table 11.** Metallographic sections of the DC-AI connection.



For DC-AI joints, strategies 2 and 3 led to satisfactory results, when joints with concentric embedded bushings were created. The inner bushing shows considerable thickness at the point of future failure and sufficient length, both bushings are in close contact, copy the shape, which will contribute to the load-bearing capacity of the joint. This means that a higher feed at the beginning of drilling is positive, while increasing the feed at the end of the tool's working movement to 1000 mm.min<sup>-1</sup> (strategy 3, right) is not desirable, because both bushings are tightly fitting, but the inner bushing has a slightly less thickness compared to strategy 2 (in the middle).

**Table 12.** Metallographic sections of the TL-AI connection.



The TL-AI joint shows the same behavior as the DC-AI joint when the process parameters are changed. Strategy 2 or 3 can be recommended for this material pair.

**Table 13.** Metallographic sections of the AI-AI connection.

3800, 150-170, 200		3800, 250-700, 200		3800, 250-1000, 200	



In the material pair Al-Al, no joint was formed. Although a bushing was formed on the lower plate, the material of the upper plate was concentrated in the gap between the plates, there was no formation of two embedded coaxial bushings. Al-Al material pair is not suitable for making joints.

#### 4. Conclusions

The following recommendations result from the metallographic analysis of the joints made of dissimilar materials:

- Flowdrill technology can be used to make mechanical joints with form contact
- To ensure the correct function of the joint - load transfer - it is necessary that the joint consists of two concentric embedded bushings
- Flowdrill technology is suitable for joining materials with significantly different mechanical properties, e.g. steel – aluminum alloy
- When joining steels and aluminum alloys, it is advisable to place the steel in the upper position
- The load bearing capacity of the joint depends mainly on the thickness of the inner bushing, as well as on the length of contact between the bushings
- When joining steels with aluminum alloy in the lower position, it is possible to recommend strategy 2: start the working feed at the value of 250 mm.min<sup>-1</sup> and gradually increase it to the value of 700 mm.min<sup>-1</sup>. The strategy can be recommended is for the listed materials and a tool diameter of 5.3 mm.

**Acknowledgments:** This research was funded by the Scientific Grant Agency of the Ministry of Education, Science, Research and Sports of the Slovak Republic under project VEGA 1/0154/19: Research of the combined technologies of joining dissimilar materials for automotive industry.

#### References

1. K. Mori, N. Bay, L. Frantini, F. Micari, A.E. Tekkaya, *CIRP Annals – Manuf. Technol.* 2013, 62, 673-694.
2. K. Martinsen, S.J. Hu, B.E. Carlson, *CIRP Annals – Manuf. Technol.* 2015, 64, 679-699.
3. F. Aslan, L. Langlois, T. Balan, *Int. J. Adv. Manuf. Technol.* 2019, 104, 2377 – 2388.
4. P. Krasauskas, *Mechanika (Kaunas)* 2011, 17, 681-686..
5. C. Özek, Z. Demir, *TEM-Journal* 2013, 2, 93 – 101.
6. R. Kumar, N.R.J. Hynes, *Int. J. Light. Mat. Manuf.* 2019, 2, 193 – 205.
7. R. Kumar, N.R.J. Hynes, C.I. Pruncu, J.A.J. Sujana, *J. Clean. Prod.* 2019, 236, 117711.
8. P. Shalamov, M. Pivtsaeva, A. Chvanova, Shamgunov, A., *Mater. Today* 2021, 38, 1931-1935.
9. Innovative Manufacturing Research Centre, Faculty of Mechanical and Electrical Engineering, Kunming University of Science and Technology, Clinching for sheet materials. *Science Technology of Advanced Materials*, 2017, pp. 381–405.
10. Ebnesajjad, S.; Landrock H. Arthur.; *Adhesives Technology*, 3rd ed.; Elsevier, United States, 2014; pp. 3-4
11. Flowdrill. User Guide. Copyright, 2003. Available online: [https://www.ipro.si/upload/articles\\_files/articles\\_file1503317485.pdf](https://www.ipro.si/upload/articles_files/articles_file1503317485.pdf) (17.11.2022)
12. Heiler R. Flow drilling technology and thread forming - an economical and secure connection in hollow sections and thin-walled components. *Web of Conferences* 97, 2019, 8.
13. Simufact Forming. Available online: <https://www.simufact.com/simufactforming-forming-simulation.html> (20.11.2022)



# Assessment of the effect of blank holding pressure on the formability of DC04 sheet metal using Simufact software

Samuel Vilkovský<sup>1,\*</sup>, Janka Majerníková<sup>2</sup>

<sup>1</sup> Technical University of Košice, Department of Technology, Materials and Computer Aided Production

\* email: Samuel.vilkovsky@tuke.sk

**Abstract:** This paper deals with the numerical simulation of deep drawing using Simufact software. DC04 metal sheet was used with a thickness of 0.7 mm. The simulation of the manufacturing process is an integral part of engineering production. Deep drawing is a complex process affected by several factors, including the blank holding pressure.

In this paper, the blank holding pressure will be evaluated by the earing formation on the cylindrical cup with different hardening models.

**Keywords:** Deep drawing, DC04, anisotropy, earing, Simufact, blank holding pressure

## 1. Introduction

Deep drawing is a widely used sheet metal forming process. Automotive parts, arms industry products, aerospace parts, medication and perfume tubes, pots, pans, and kitchen appliances such as pots and pans are examples of the different applications of this process [1,2,3].

Deep drawing is based on production parts with simple or complex shapes through large plastic deformation [1,4]. During the deep drawing process, several defects can occur such as surface scratches, wall and flange wrinkling tearing, or earing [5].

The process of deep drawing is highly sensitive to material properties, geometrical and technological parameters. Elasticity, plasticity, and anisotropy are crucial material parameters. Punch velocity, blank holding pressure, and lubrication have been as much influence as the radius of punch and die, blank thickness, or clearance between punch and die. If some of these parameters are not defined properly several defects can occur such as surface scratches, wall, and flange wrinkling, tearing, or earing [7,8].

One of the most common defects that occur in the deep drawing process is earing, defined as the formation of a wavy edge at the open end of the cup. Many studies dealing with earing defects have been published in recent years [8,9].

The blank holding force is a crucial parameter and has a significant influence on the process of deep drawing [10]. Recently, some research papers have been published to study the influence of friction conditions and blank holding pressure on the deep-drawing process.

The effect of blank shape on earing was studied by Nagda et al. [12]. The anisotropy effect on earing defects was published by Yoon et al. [13]. Tran et al. [14] studied the influence of earing reduction in the deep drawing process of an aluminum alloy sheet based on the method of varying blank holding pressure with the segmental blank holder.

In the conventional deep drawing, a uniform blank holding pressure is used, which keeps constant throughout the process. It is generally used for shallow parts with relatively simple shapes [10].

With the development of computer-aided engineering, numerical simulation has become widely used in the metal forming process [11]. The paper aims to study the effect of blank holding pressures on the formability of DC04 material with a thickness of 0.7 mm through FEM simulation using Simufact forming software.

## 2. Materials and Methods

In this experimental research Simufact forming software was used to simulate effect of the blank holding pressure on the earing of material DC04 with the diameter of 55 mm and thickness of 0.7 mm. Mechanical, anisotropy properties and chemical composition are shown in Tab. 1-3.

Tab. 1 Mechanical properties of DC04

Material	Density [kg/m <sup>3</sup> ]	Young's modulus [MPa]	Yield strength [MPa]	Ultimate tensile strength [MPa]	Ultimate strain [%]	Strain hardening exponent [-]
DC04	7851	210000	231	350	38	0.18

Tab. 2 Anisotropy values of DC04

Material	r <sub>0°</sub>	r <sub>45°</sub>	r <sub>90°</sub>	r <sub>m</sub>
DC04	1.6	1.4	2.0	1.6

Tab. 3 Chemical composition of DC04

	C <sub>max</sub>	P <sub>max</sub>	S <sub>max</sub>	Mn <sub>max</sub>	Si <sub>max</sub>	Al <sub>min</sub>	Ti <sub>max</sub>
Weight %	0.08	0.030	0.030	0.40	-	-	-

Dimensions of the tool are shown in Tab. 4.

Tab. 4 Dimensions of deep drawing tool

Parameters	Length [mm]
Die diameter - d <sub>d</sub>	35
Punch diameter - d <sub>p</sub>	36.6
Clearance between punch and die - c <sub>pd</sub>	0.8
Punch radius - r <sub>p</sub>	5.5
Die radius - r <sub>d</sub>	5.5

Numerical simulation was performed with a coefficient of friction of 0.2 using Coulomb friction law. Parameters of the deep drawing process are shown in Tab.5.

Tab. 5 Deep drawing process parameters

Parameter	Value
Punch velocity	20 mm/s
Blank holding pressure 1	1.8 MPa
Blank holding pressure 2	2.4 MPa
Blank holding pressure 3	9.2 MPa
Friction coefficient	0.2

The mesh was created with hexahedral elements with a size of 0.07 mm. According to Hu et al. [15] three layers of elements have been used through the thickness. Kura et al. [16] used five elements per thickness. More elements will bring more accurate results at the expense of computational time. In our research, ten elements per sheet thickness were used (Figure 1). The software automatically remeshed the metal sheet if the accumulated strain of any element reached the value of 0.2.

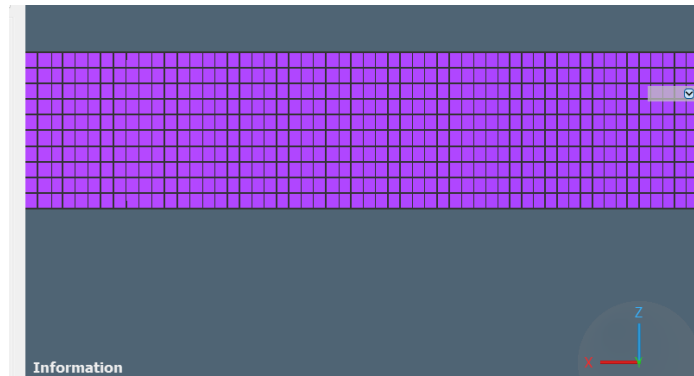


Figure 1 Mesh of the metal sheet

To save computational time two symmetry planes were used (Figure 2). Only 90° of the metal sheet was considered in the simulation.

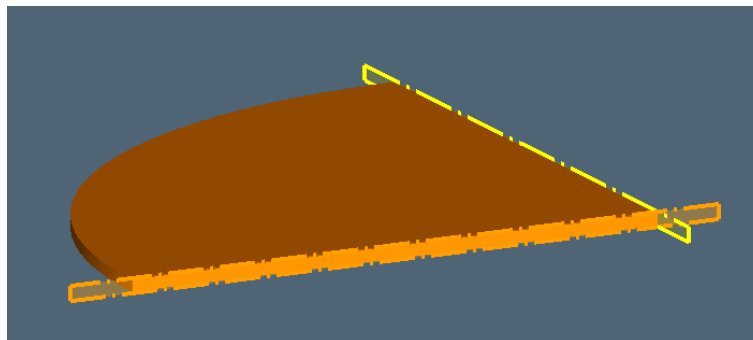


Figure 2 Symmetry planes

For the simulation, Barlat yield criteria with the combination of hardening model Holomon and Simufact CFM plasticity model were used. The heights of cups in directions 0°, 45°, 90° were evaluated.

### 3. Results

Based on the parameters mentioned above, six independent (Figure 3-4) simulations with different hardening models were performed with the blank holding pressure of 1.8, 2.4, and 3.0 MPa.

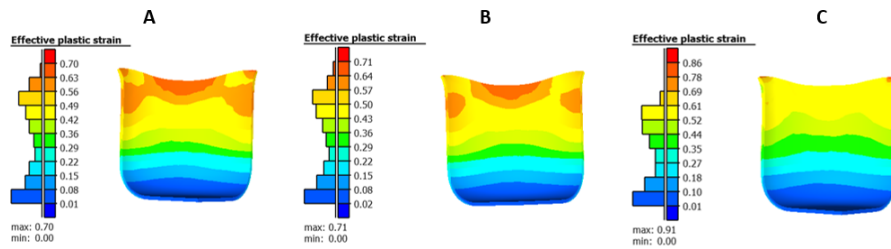


Figure 3 Deep drawing using Barlat-Holomon models A) Blank holding pressure = 1.8 MPa, B) Blank holding pressure = 2.4 MPa, C) Blank holding pressure = 3.0 MPa

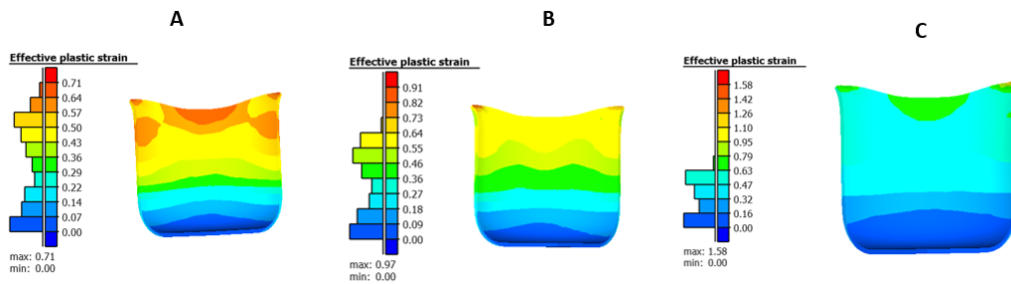


Figure 4 Deep drawing using Barlat-CFM models A) Blank holding pressure = 1.8 MPa, B) Blank holding pressure = 2.4 MPa, C) Blank holding pressure = 3.0 MPa

A comparison of cup heights with the use of different hardening models is shown in Figure 5-7.

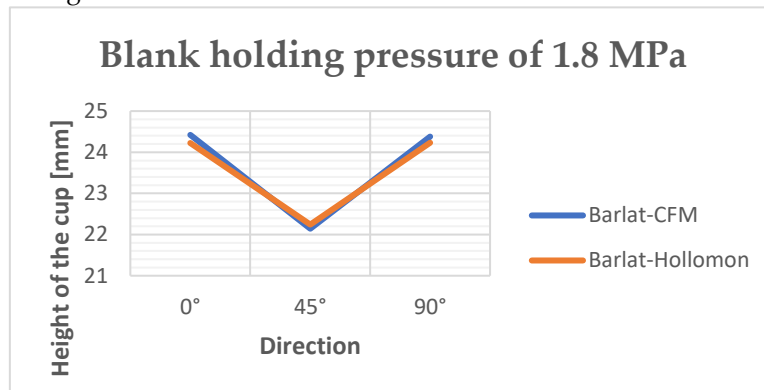


Figure 5 Cup heights with the blank holding pressure of 1.8 MPa

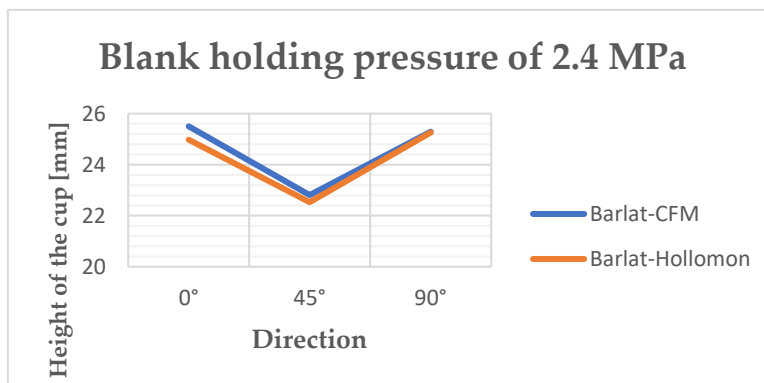


Figure 6 Cup heights with the blank holding pressure of 2.4 MPa

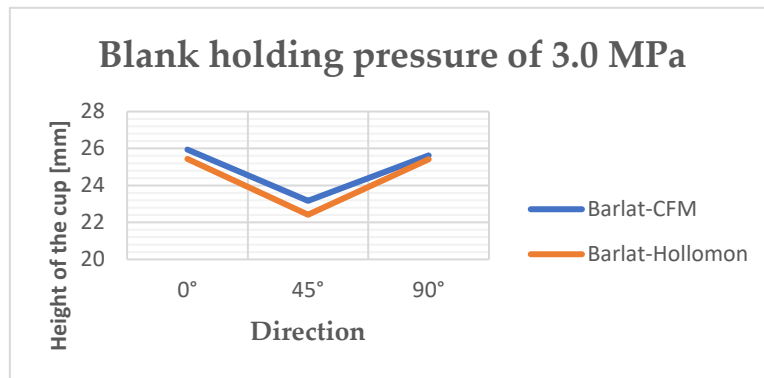


Figure 7 Cup heights with the blank holding pressure of 3.0 MPa

A comparison of the cup heights using the same models with different blank holding pressure is shown in Figures 8-9.

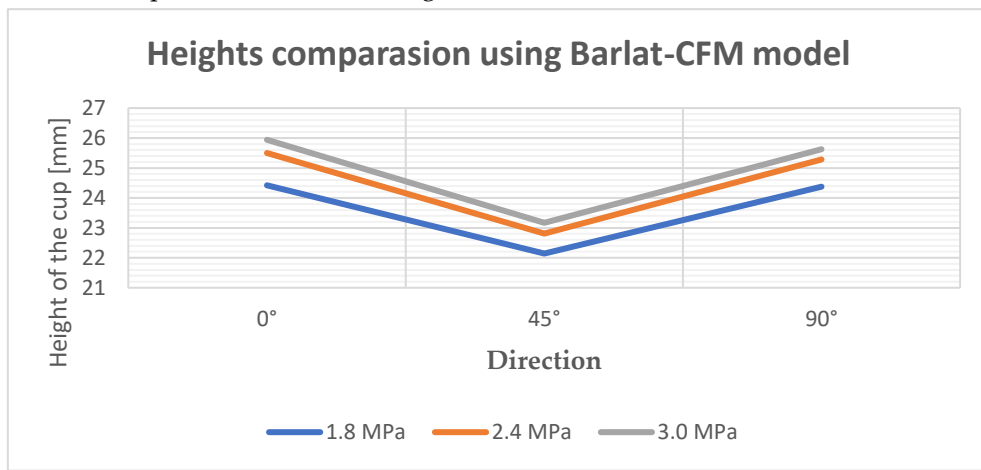


Figure 8 Cup heights using different blank holding pressure

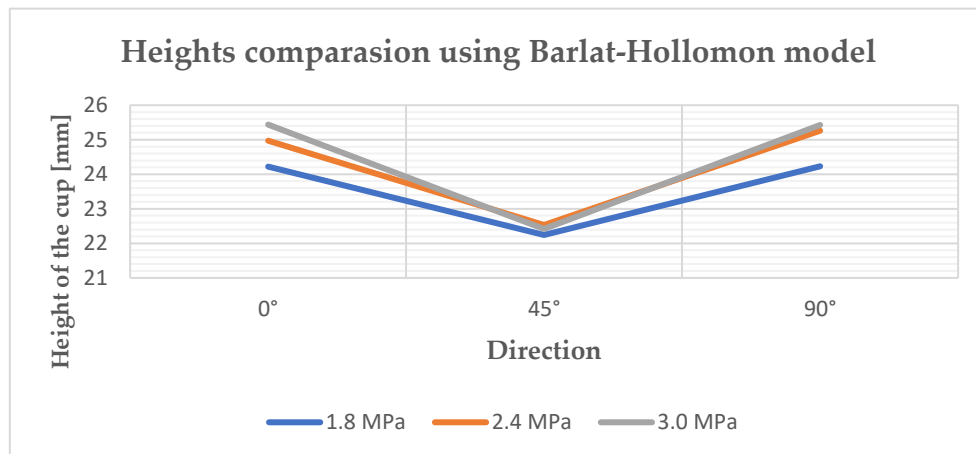


Figure 9 Cup heights using different Blank holding pressure

### 5. Conclusions

In conclusion, FEM simulations of deep drawing were conducted using blank holding pressures of 1.8, 2.4, and 3.0 MPa. It was noticed that earing occurred in the direction 0° and 90°. As the planar anisotropy was positive the formation of earing occurred at 0° and 90° directions, which correlated with the theoretical knowledge.

The results showed (Figure 8-9) that the height of ears increased with the increase of blank holding pressure. A significant increase in earing height was observed at 0° and 90° and 270° with the larger pressure for both hardening models.

Moreover, comparing the various blank holding pressures of deep drawing illustrated that the equivalent plastic strain in the case of blank holding pressure using 3.0 MPa was more critical than that of using the uniform blank holding pressures of 1.8 MPa and 2.4 MPa. This high level of plastic strain can cause defects in deep drawing when a larger blank holding pressure is introduced.

Comparing the hardening models, there is no significant deviation.

**Acknowledgments:** The authors are grateful to VEGA 1/0384/20 and KEGA 036TUKE-4/2021.

## References

1. SPIŠÁK, E., et al. Strojárske technológie. Košice: Strojnícka fakulta TU v Košiciach, 2011. Edícia vedeckej a odbornej literatúry. Strojnícka fakulta TU v Košiciach. ISBN 978-80-553-0820-3. RONG, Yi et.al.: Structural topology optimization with an adaptive design domain. In: Computer Methods in Applied Mechanics and Engineering. Vol.389, (2022), ISSN: 0045-7825
2. Özdilli, Ö., Erdin, E.: Comparison of Common Deep Drawing Steel Sheets in terms of Blank Holder Force and Friction Conditions. In: International journal of automotive science and technology. Vol. 2, Issue: 4 (2018). e-ISSN: 2587-0963
3. Gürün, G., Karaağaç, I.: The Experimental Investigation of Effects of Multiple Parameters on the Formability of the DC01 Sheet Metal. In: Strojníški vestnik - Journal of Mechanical Engineering. Vol. 61, Issue: 11, p. 651-662. ISSN 2536-3948 (online).
4. Dwivedi, R., Agnihotri, G.: Study of Deep Drawing Process Parameters. In: Materials Today: Proceedings. Vol. 4, Issue 2. (2017), p. 820-826, ISSN: 2214-7853
5. Semiatin, S.L.: Introduction to Sheet-Forming Processes. In: Metalworking: Sheet Forming 9<sup>th</sup> edition, Vol.14 B. Ohio: ASM International, 2006 pp 319-33. ISBN electronic: 978-1-62708-186-3
6. Bouchaâla, K. et al.: Prediction of Earing in Cylindrical Deep Drawing of Aluminum Alloys Using Finite Element Analysis. In: International Journal of Mechanical and Production Engineering, Vol 6, Issue 10. (2018). ISSN(e): 2321-2071
7. Joshi, A.R. et al.: Effects Of Different Parameters On Deep Drawing Process: Review. In: International Journal of Engineering Research & Technolog. Vol. 2, Issue: 3. (2013). ISSN: 2278-0181
8. Benke, M.; Schweitzer, B.; Hlavacs, A.; Mertinger, V. Prediction of Earing of Cross-Rolled Al Sheets from {h00} Pole Figures. Metals **2020**, 10, 192. DOI: <https://doi.org/10.3390/met10020192>
9. Hlavacs, A.; Szucs, M.; Mertinger, V.; Benke, M. Prediction of Earing of Hot-Rolled Al Sheets from Pole Figures. Metals **2021**, 11, 99. DOI: <https://doi.org/10.3390/met11010099>
10. Feng, Y. et al.: Optimization of variable blank holder force in deep drawing based on support vector regression model and trust region. In: The International Journal of Advanced Manufacturing Technology. (2019). Vol. 105, ISSN: 4265-4278. DOI: <https://doi.org/10.1007/s00170-019-04477-5>
11. Weiping, D. et al.: Stress analysis of cylindrical parts during deep drawing based on Dynaform. 2018 IOP Conf. Ser.: MaterSci. Eng. 423 012166
12. Nagda P.S. et al.: Finite element simulation of deep drawing process to minimize earing. In: World Acad Sci Eng Technol Int J Mech Mechatron Eng (2017) 11(2), p. 413-416
13. Yoon J. W. et al.: A new analytical theory for earing generated from anisotropic plasticity. In: International Journal of Plasticity 27(8), (2011), p. 1165-1184. ISSN: ISSN: 0749-6419. DOI: 10.1016/j.ijplas.2011.01.002
14. Tran, T.M. et al.: Earing Reduction by Varying Blank Holding Force in Deep Drawing with Deep Neural Network. In: Metals Metals 2021, 11(3), p. 395; ISSN: 2075-4701. DOI: <https://doi.org/10.3390/met11030395>
15. Hu, J.G. et al.: Finite element analysis of damage evolution and the prediction of the limiting draw ratio in textured aluminum sheets. In: Journal of Materials Processing Technology, 103 (2000), p. 374-382. ISSN: ISSN: 1873-4774 DOI:
16. Kurra, S. et al: Experimental and numerical studies on formability of extra-deep drawing steel in incremental sheet metal forming. In: Journal of Materials Research and Technology (2014). 3 (2), p. 158-171. ISSN: ISSN: 2214-0697

# Introduction to Generative Design

Matúš Virostko <sup>1\*</sup>, Martin Mantič <sup>2</sup> and Samuel Sivák <sup>3</sup>

<sup>1</sup> Faculty of Mechanical Engineering, Technical university of Košice, Slovakia; matus.virostko@tuke.sk

<sup>2</sup> Faculty of Mechanical Engineering, Technical university of Košice, Slovakia; martin.mantic@tuke.sk

<sup>3</sup> Faculty of Mechanical Engineering, Technical university of Košice, Slovakia; samuel.sivak@tuke.sk

\* Correspondence: matus.virostko@tuke.sk; Tel.: +421 55 602 2354

**Abstract:** The thesis covers the basic knowledge of generative design, comparing the nature of software operation in comparison to the process of topological optimization. Following that, programs that support generative design using this technology are discussed in detail. Finally, the benefits and drawbacks of the mentioned technology.

**Keywords:** generative design; optimalization; topology optimalization

## 1. Introduction

Product design is a difficult discipline to master today. The more technologies and manufacturing methods are integrated into products, the greater the complexity. Timelines are getting shorter in the race to get to market as soon as possible. Engineers, who are burdened with a variety of tasks, are thus looking for the best possible solution for a feasible design [1]

Generative design offers a new solution for them. It is a new technology that uses algorithms such as topology optimization and natural algorithms to automatically generate many designs. It occurs when in a context where an engineer defines certain constraints that the technology must meet. Generative design allows software to present its capabilities to engineers. This allows engineers to consider many more options than usual thanks to autonomous software. It has many applications in both conceptual and practical design. [1]

CAD software is currently at the beginning of integrating topological optimization functions in the context of generative design, where parametric modeling is linked to direct modeling. This is a critical process, and they must collaborate closely. [1]



Figure 1. In-practice application of generative design [10]

In a typical design, several types of product visualization are mostly created, then a few alternatives are evaluated through optimizations based on the goals set by the engineer. In generative design, the engineer first defines the input conditions with constraints, after which the software uses algorithms to generate a series of designs based on these parameters. Once the generation is complete, the software then offers a subsequent selection of the most optimal alternative, which the engineer can further examine in detail. This significantly shortens the design phase without requiring the engineer to become fully immersed in the process. [2][3]

Consider the following scenario: a designer wishes to design the construction of a mechanism. Instead of going through the design and then experimenting with a few shapes, he can provide the mechanical properties, material, loads, and so on to the software. [4]

## 2. Differences between Generative Design and Topological Optimization

Generative Design and Topological Optimization have become a trend in the fields of design and design in CAD environments, but it is important to note that the two spheres are not even synonymous as some people mistakenly think. [5]

Topological optimization is a mathematical method, accessible that has been available in some CAD tools for quite some time and it is not that new. At the very beginning, a model has to be created, then input conditions and parameters are defined. As a result, the software generates an optimal shape for the model, which the engineer then examines. In short, Topological Optimization requires a basic model from the start in order to function, thereby defining the process's boundaries. Although in part, topological optimization is the basis for generative design. [5]

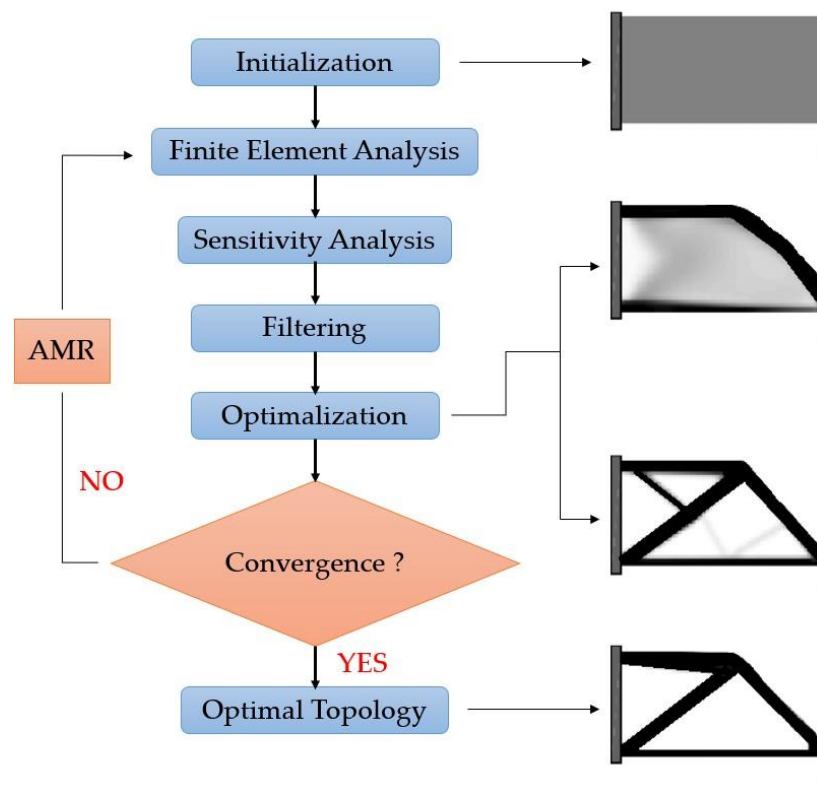
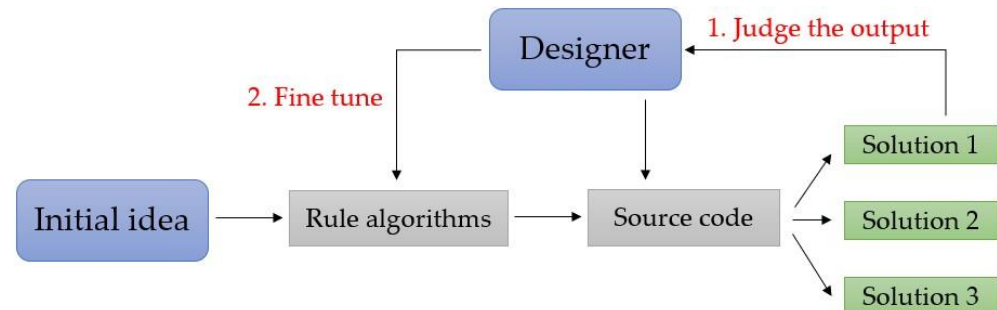


Figure 2. Topology Optimization Process Scheme. [11]

Generative Design takes this process to a higher level by eliminating the need for the engineer to create a model from the start, instead taking over this task based on the constraints provided by the engineer. However, still the essential gro in the design is done

by a human where he must know and be able to specify in detail the input constraints and constraints based on which the software generates the final visualizations. As a result, for the time being, the engineer will be required to continue developing and improving the algorithms for Generative Design as well as the specifics it requires. [11]



**Figure 3.** Generative Design Process Scheme. [5]

Will artificial intelligence eventually replace humans in the generation process?

When that Generative Design has been used for some time now, but has not yet had such widespread use in various industries as this time. So replacing the work of engineers with artificial intelligence is unlikely at the moment. There are no pre-set algorithms in Generative Design for creating different object design options autonomously. The engineer must create that process based on knowledge, which is a difficult task. Artificial intelligence cannot automatically evaluate pluses and minuses but performs them given the input design goals. [6]

### 3. Software for Generative Design

Generative Design is used in many industries such as automotive, aerospace or architecture. When designing in different areas, Generative Design mainly focuses on weight loss, performance improvement or cost reduction. Engineers with CAD experience, have the ability to easily convert to Generative Design. This software provides more options than the usual CAD software functions, such as inputting information about materials, forces, mechanical properties, and so on. [5]

This is a short list when compared to the software's requirements. The following section introduces software programs for working with generative lay-up: [5]

- Fusion 360 (Autodesk)
- Creo generative Design (PTC)
- nTop (nTopology)
- NX (Siemens)

The choice of software is up to each user individually, but there are a few key questions for choosing the optimal software: [7]

- In which part of the process can generative design be applied ?
- What range of parameters can be defined in the software ?
- What manufacturing options will be available after the application of GD ?
- Will the generated designs be usable later for other evaluation methods ?

**3.1 Fusion 360** – an Autodesk program that is interested in generative design. It includes a wide range of modeling tools for direct and parametric modeling, design exploration, surface creation, and rendering. The generative design extension mainly uses machine learning and artificial intelligence to autonomously generate specific solutions with respect to specified constraints, defining parameters for each type of manufacturing process. [8][5][7]

The Fusion 360 Generative Design extension lets you compare and select manufacturing methods for a given model, as well as see the sequence of constraints placed on the processes for the designed model. 3D products using additive technology can clearly have properties that cannot be achieved with traditional manufacturing methods. The add-in also includes a cost comparison tool for identifying part designs that would be expensive to produce. [8][5][7]

**3.2 Creo generative design** – PTC program with cloud-based main support and CAD, PLM, and simulation integrated into this platform. This allows for the creation of optimised designs and, in parallel, the testing and solving of different iterations of the generated models. These connections are taken care of by two software interfaces, the cloud-based Generative Design Extension (GDX) and the Generative Topology Optimization (GTO) extensions. The aforementioned extensions automatically point out the best design variants, which it can also divide according to the desired manufacturing method. The software in the Creo working environment strives to generate high-quality, affordable, and manufacturable designs in the shortest amount of time. [8][7]

**3.3 nTop** – nTopology's program offers engineers complete control over design optimization. With which it can create specific procedures for generating and using combinations of user knowledge, simulation and database data for the most optimal design variants. [7]

According to this company, generative design has three key characteristics: [7]

- Creation of geometry
- Model optimization with constraints
- Design loops that are automated

nTopology is supported by an implicit generative module. 3D geometry is conceived of as a mathematical function in implicit nav-design, allowing users to quickly create specific structures. Finally, one of the nTop software's capabilities is the ability to re-create previously used processes, which are saved and imported when the input conditions change. [7]

**3.4 NX** – Siemens program with the novelty of this software, in addition to generative design. Specifically, it is a digital twin technology that offers flexibility and performance with solutions for streamlining designs. The inclusion of design, simulation and manufacturing in one package is also an added value. The software can integrate topology optimization via simulation into a generative design environment powered by convergent modeling. [7] [5]

When an engineer specifies a set of constraints, the technology self-generates a number of alternative designs. In a single environment, you can modify scanned data or topology optimization results alongside the standard CAD model using NX. There is no interleaving or switching between programs.

Siemens NX helps design engineers by providing a set of tools to efficiently implement generative engineering. [7]

#### **4. Advantages and disadvantages of generative design**

A significant positive of generative design is the linking of several areas into a common whole. When software allows the engineer to visualize and compare generated designs in order to find the most optimal designs for the needs in a given area in the shortest amount of time. [5]

The use of artificial intelligence in generative design allows for a significant reduction of time in the development and actual generation of new designs, leading to a competitive capability in bringing products to market quickly. [5]

The limitations of generative design are primarily due to the requirement to master machine learning, i.e. artificial intelligence, when it is necessary to insert various new algorithms or input conditions for the subsequent generation of designs. Not all engineers are equally skilled in this area, which creates obstacles. As a result, continuous learning is required throughout the process. [8]

The current costs associated with generative design are quite high for ordinary users. Free versions are also available, however, where custom algorithms for generation need to be entered. However, because of cloud computing, generative design is now much more affordable for every user. [8]

## 5. Conclusions

Generative Design is currently transforming the way engineers approach engineering design. AI's added value allows for a more efficient and automated path in generating different design variations that push the boundaries and bring a much wider range of possibilities to the work. It is not a traditional topology optimization, but rather connects multiple optimization components to determine the topology in relation to defined constraints and requirements. This technology was created not to replace the human component in the process, but to change the perspective in design engineering, allowing for greater detail and efficiency. One of the benefits of generative design is the ability to create designs for additive manufacturing. [9] [8]

## Acknowledgment

The contribution was created within the framework of the solution of the projects VEGA 1/0528/20 and KEGA 029TUKE-4/2021.

## References

1. Chad Jackson. (2017) Empowering engineers with generative design and facet modeling. Available online: [https://static.sw.cdn.siemens.com/siemens-disw-assets/public/2dhrNXsZVjzFCb94OnAO9D/en-US/eBook--Empowering-Engineers-with-Generative-Design-and-Facet-Modeling\\_tcm27-12349.pdf](https://static.sw.cdn.siemens.com/siemens-disw-assets/public/2dhrNXsZVjzFCb94OnAO9D/en-US/eBook--Empowering-Engineers-with-Generative-Design-and-Facet-Modeling_tcm27-12349.pdf) (accessed on 20.11.2022)
2. Siemens e-book. (2017) Generative design. Available online: [www.plm.automation.siemens.com/media/global/en/Siemens-PLM-Generative-Design-ebook-mi-63757\\_tcm27-31974.pdf](http://www.plm.automation.siemens.com/media/global/en/Siemens-PLM-Generative-Design-ebook-mi-63757_tcm27-31974.pdf) (accessed on 22.11.2022)
3. Siemens. (2017) Generative design. Available online: [www.plm.automation.siemens.com/global/en/our-story/glossary/generative-design/27063](http://www.plm.automation.siemens.com/global/en/our-story/glossary/generative-design/27063) (accessed on 22.11.2022)
4. Trautmann Laura. Product customization and generative design (2021), Vol. 11 No. 4, pp. 87-95 <https://doi.org/10.35925/j.multi.2021.4.10>
5. Formlabs, Generative Design 101, Available online: [formlabs.com/eu/blog/generative-design](https://formlabs.com/eu/blog/generative-design) (accessed on 22.11.2022)
6. Vectornator, What Is Generative Design ? A Full Guide. Available online: [www.vectornator.io/blog/generative-design/](http://www.vectornator.io/blog/generative-design/) (accessed on 24.11.2022)
7. All3dp, The Best Generative Design Software of 2022. Available online: [all3dp.com/1/the-best-generative-design-software-of-2022/](https://all3dp.com/1/the-best-generative-design-software-of-2022/) (accessed on 24.11.2022)
8. Bigrep, A Short introduction To Generative Design. Available online: [bigrep.com/posts/generative-design/](https://bigrep.com/posts/generative-design/) (accessed on 24.11.2022)
9. S. Bagassi, F. Lucchi, F. De Crescenzo, F. Persiani. Generative Design: Advanced Design Optimization Processes For Aeronautical Applications (2016), Vol. 7
10. Dassault systems. (2022) Generative Design Engineering. Available online: [events.3ds.com/generative-design-engineering](https://events.3ds.com/generative-design-engineering) (accessed on 26.11.2022)
11. ResearchGate. Scheme of topology optimization. Available online: [www.researchgate.net/figure/General-scheme-of-topology-optimization-using-SIMP-14-courtesy-of-Shun-Wang\\_fig4\\_289325331](https://www.researchgate.net/figure/General-scheme-of-topology-optimization-using-SIMP-14-courtesy-of-Shun-Wang_fig4_289325331) (accessed on 26.11.2022)



# Assessment of the acoustic performance of different categories of drones

Ing. Anna Yehorova<sup>1\*</sup> prof. Ing. Ervin Lumnitzer, PhD.<sup>1</sup> and Ing. Elena Jurgovská<sup>1</sup>.

<sup>1</sup> Technical University of Košice, Faculty of Mechanical Engineering, Department of Environmental Engineering

\* Correspondence: anna.yehorova@tuke.sk

**Abstract:** The number of drone applications on a global scale has been steadily increasing lately and will continue to increase in the future. A serious aspect of the drone using is the noise produced by the flight. Thus it causes disturbance and harassment of the population and accelerates the effects on people. The intention of the authors is to create a methodology for assessing the impact of drones on the population, since such a methodology does not currently exist. The presented paper is intended to assess the appropriateness and completeness of acoustic performance measurement according to current legislation.

**Keywords:** drones, categories of drones, noise, impact on residents, measurement surface, acoustic performance, measurements

## 1. Introduction

There are many devices, appliances, devices or machines that emit noise into the environment in which we live. In some cases, the noise levels we are exposed to are assessed as harmful to hearing and/or disruptive to comfort and daily life. Drone noise is quite new and has until now been an exploratory noise source characterized by a specific noise spectral composition and an often subjectively perceived high degree of intrusiveness. Therefore, it is necessary to carry out extensive research and assess the increasing noise burden of the population and the suitability of the existing requirements of directives and standards.

Currently, the number of applications for small unmanned aerial vehicles (UAVs) is growing rapidly. While initially used and developed mainly for military purposes, they are becoming increasingly important in civilian applications as well. In particular, the use of drones has increased during the COVID epidemic, when humanity has been forced to use largely contactless methods of communication and transportation. Relatively new consumer markets for drones include forestry, agriculture and road management, energy and communications, oil and gas production and transportation, safety and environmental protection, etc. Several drones have become available to ordinary users, and their equipment is quite complex and includes photo and video cameras, an autopilot system and navigation systems that make controlling such aircraft relatively easy.

Several authors dealt with the issue in question. N. Kloet in the publication "Drone on: a preliminary investigation of the acoustic impact of unmanned aircraft systems (UAS)" deal with the problem of the use of a quadcopter and acoustic nuisance for the public [1]. They also propose a way to reduce the acoustic impact, by using propellers with lower noise. The use of drones in security areas was also discussed by L. Shi in the article "Hidden Markov Model based Drone Sound Recognition using MFCC Technique in Practical Noisy Environments" [2]. Experiments were conducted by the authors in order to recognize the sound of drones in a noisy environment. S. Perron in the article "Review of the effect of aircraft noise on sleep disturbance in adults" [3] deals with the effects

of noise from aircraft traffic on the sleep of residents. It has been found that there is a causal link between exposure to drone noise and sleep disturbances, specifically awakenings, reduced sleep time, or the use of sleep medications.

For the needs of the publication, 3 drones from different categories, but from the same manufacturer, were selected. It is DJI mini 2 (C0), DJI Mavic 3 (C1) and DJI Phantom 4 Pro (C2).

## 2. Measurement of acoustic performance

There are different methods of measuring acoustic power with different levels of accuracy in different acoustic fields. The generally preferred method is to measure the sound pressure level over a hypothetical surface of size  $S$  surrounding the source and then calculate the sound power level using the average sound pressure level and the measured surface area. The standard prescribes one of two shapes of measuring surfaces: a rectangular parallelepiped distant from the reference parallelepiped by a measuring distance  $d$  and a hemispherical surface or a part of a hemispherical surface with radius  $r$ . For our needs, it was more appropriate to choose a measurement on a hemispherical surface. This measurement method is standardized in STN EN ISO 3744 2010 [4] for free field. In fig. 1 shows a hemispherical measuring surface with the measurement points marked.

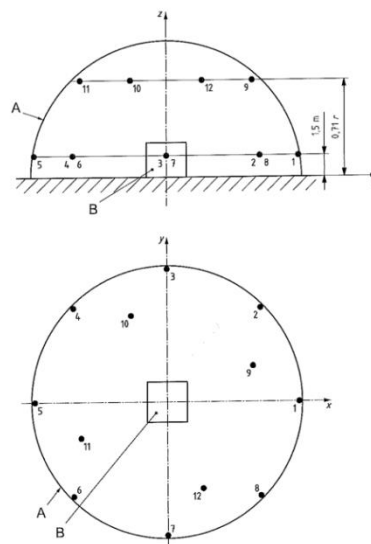


**Figure 1.** Positions of microphones on the hemispherical measuring surface.

For stationary noise sources emitting broadband sound and tested near a single reflecting plane, the microphone must be placed in the 12 positions listed in the annex to ISO 3744. For moving noise sources in motion near a single reflecting surface, the microphones must be placed in six positions numbered 2, 4, 6, 8, 10 and 12.

During the experiment, two types of measurements were performed:

- stationary flight – hovering the drone at a height of 0.5 m above ground level, in accordance with the wording of the delegated regulation [6],
- overflights – at a height of 0.5 m above ground level, at two different speeds.

During stationary flights, 5 series of measurements were performed, for the purpose of statistical evaluation of the data. Figure 2 shows a view of the measurement during stationary drone flights.

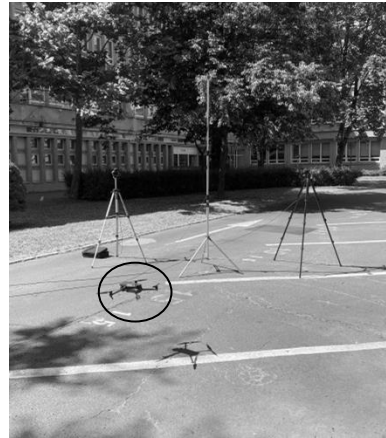


**Figure 2.** View at the measurement point during the drone's stationary flight – hovering.

When measuring the acoustic performance of flights, 5 repeated flights were performed at a slow ( $5 \text{ kmh}^{-1}$ ) and a higher ( $8 \text{ km}^{-1}$ ) speed. The measurement was performed on a reflective surface - asphalt carpet, smooth. A view of the measurement location is shown in Figure 3. The measurement time was chosen so that the influence of background noise on the measurement results was zero.



**Figure 3.** View at the measuring point during the flyovers.

### 3. Measurement results

The following figures show time records from three different measurement locations (M1, M2 and M9) for drones from all three considered categories.

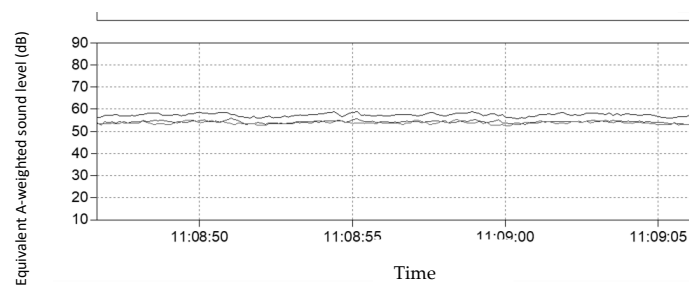


**Figure 4.** Time recording from measurement locations M1, M2 and M9 for the DJI mini 2 drone.

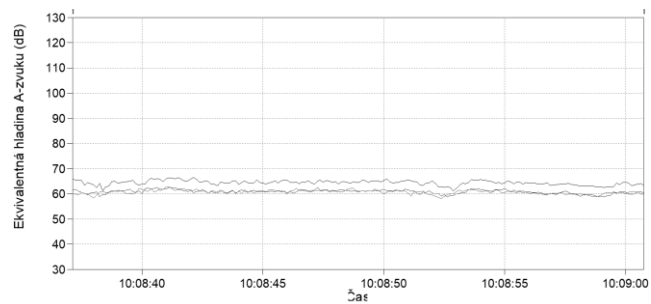


**Figure 5.** Time recording from measurement locations M1, M2 and M9 for the DJI Mavic 3 drone.

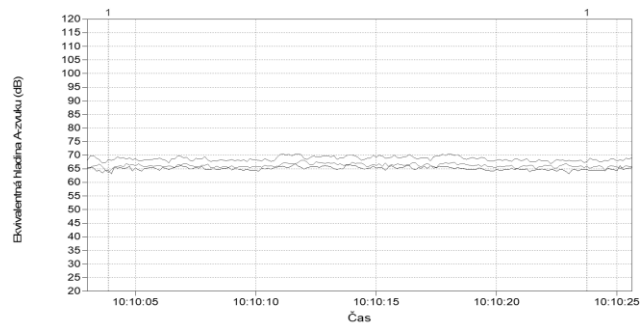


**Figure 6.** Time recording from measurement locations M1, M2 and M9 for the DJI Phantom 4 Pro drone.

Subsequently, calculations were made of the acoustic power level for all three investigated drones. Table 1 shows the calculated result values of the acoustic power level from five series of measurements.

**Table 1.** Comparison of acoustic power level values for all drones while hovering.

	DJI mini 2	DJI Mavic 3	DJI Phantom Pro 4
$L_{WA}$ [dB]	76,6	84,7	90,7

From the above results, we can conclude that the acoustic power values are significantly different for the individual categories of drones. While the drone from the CO category reached an acoustic power of almost 79 dB, which also indicates its use for leisure activities. The drone from category C1 achieved acoustic power values 8 dB higher and the drone from category C2 even 14 dB higher. Please note, however, that these are values achieved when the drone is hovering, which is required by legislation.

Subsequently, we performed measurements of the acoustic performance of flights at two speeds. The acoustic performance of a moving object is calculated from the emission values obtained from the moment of entry into the hemispherical measuring surface until the moment of leaving the measuring surface. The following images show sample flights at speeds of 5 and 8 kmh<sup>-1</sup> for the DJI mini 2 drone. The apparent shift of the time course curves is caused by the position of the individual measurement points on the measurement surface.

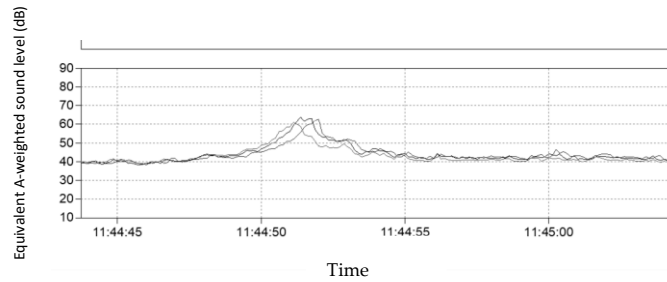


**Figure 7.** Time record from measurement points M6, M8 and M12 during flight at a speed of 5 kmh<sup>-1</sup> for the DJI mini 2 drone

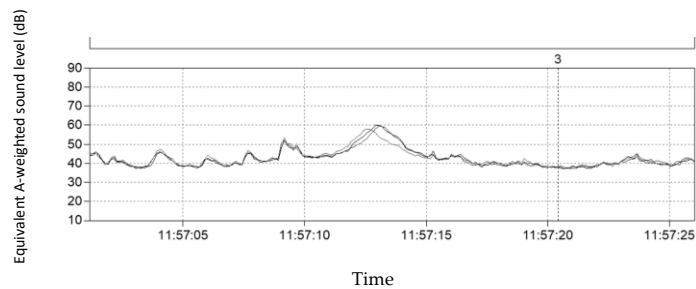


**Figure 8.** Time record from measurement points M6, M8 and M12 during flight at a speed of 8 kmh<sup>-1</sup> for the DJI mini 2 drone

As in the case of stationary measurements, calculations of the acoustic power level were made for all three investigated drones. Table 2 shows the resulting sound power level values.

**Table 2.** Comparison of acoustic power level values for all drones during overflights.

L <sub>WA</sub>	DJI mini 2	DJI Mavic 3	DJI Phantom Pro 4
Speed 5 kmh <sup>-1</sup> [dB]	79,2	81,0	85,3
Speed 8 kmh <sup>-1</sup> [dB]	80,2	82,0	89,0

From the measured and calculated values, we found seemingly illogical results. For drones from category C0, the acoustic power increased by 2-3 db, for drones from category C1 or C2, the acoustic power decreased by 3-5 dB. This reduction was also subjectively observed. We assume that it is caused by the proximity of the reflection surface and strong air swirl during static measurement. Adherence to the flight path can also be problematic, which is especially problematic for larger drones (category C1 and C2) and higher speeds, and largely depends on the experience and skills of the drone operator.

The graphs below show the frequency spectrum of emitted sound in fractional-octave bands for individual drones under consideration and all types of measurements – hovering, flying at a speed of 5 kmh<sup>-1</sup> and flying at a speed of 8 kmh<sup>-1</sup>.

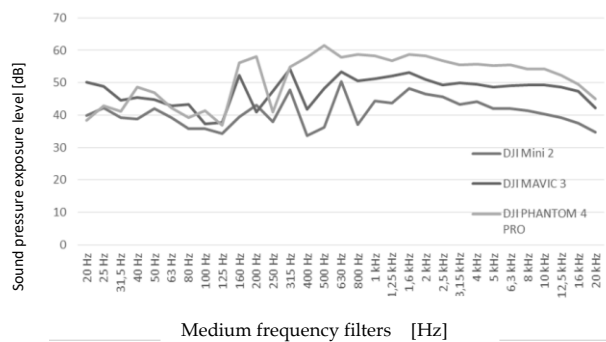


Figure 9. Frequency spectrum of emitted sound during hovering for all drones

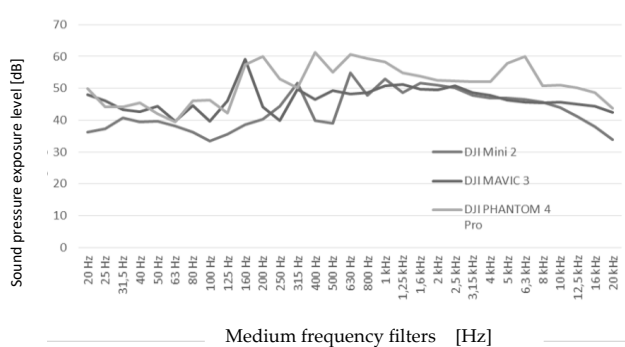


Figure 10. Frequency spectrum of emitted sound during flight at a speed of 5 kmh<sup>-1</sup> for all drones

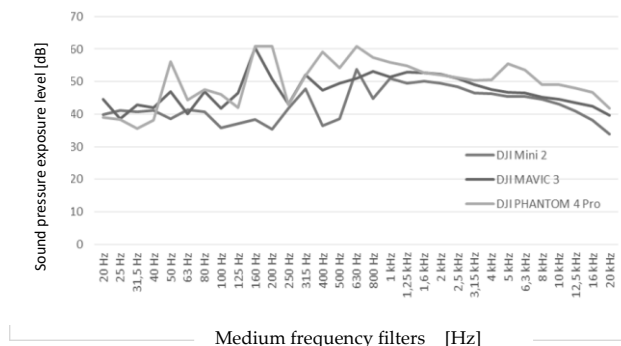


Figure 11. Frequency spectrum of emitted sound during flight at a speed of 8 kmh<sup>-1</sup> for all drones

### 5. Conclusions

The presented contribution deals with the issue of a more detailed analysis of noise sources. It specifies the analyzed source of noise - the drone - in more detail. This noise source was chosen because of its significantly increasing application areas. The number of drones, whether for amateur or professional use, is growing significantly and will continue to grow in the near future. And that is why we are trying to create a complete methodology, suitable for assessing all types of drones. In the current stage, we focused on comparing the acoustic performance of drones with the aim of assessing the suitability of this methodology. We found that such kind of measurements can be included in the newly conceived methodology.

**Acknowledgments:** This paper was created within the project KEGA 011TUKE-4/2021.

**Conflicts of Interest:** The authors declare no conflict of interest.

## References

1. Kloet, N. Drone on: a preliminary investigation of the acoustic impact of unmanned aircraft systems (UAS). 24th International congress of sound and vibration, 2017.
2. Shi, L. Hidden Markov Model based Drone Sound Recognition using MFCC Technique in Practical Noisy Environments. Journal of communications and networks, vol. 20, no. 5, oct. 2018.
3. Perron, S. Review of the effect of aircraft noise on sleep disturbance in adults. Noise and Health, 2012.
4. STN EN ISO 3744 2010. Akustika. Určovanie hladín akustického výkonu a hladín akustickej energie pomocou akustického tlaku. Technické metódy merania pre prevažujúce voľné zvukové pole nad rovinou odrážajúcou zvuk.
5. Nariadenie Európskeho parlamentu a rady (es) č. 216/2008 z 20. februára 2008 o spoločných pravidlách v oblasti civilného letectva a o zriadení Európskej agentúry pre bezpečnosť letectva, ktorým sa zrušuje smernica Rady 91/670/EHS, nariadenie (ES) č. 1592/2002 a smernica 2004/36/ES.
6. Delegované nariadenie komisie (EÚ) 2019/945 z 12. marca 2019 o bezpilotných leteckých systémoch a o prevádzkovateľoch bezpilotných leteckých systémov z tretích krajín.
7. Lumnitzer, E. et al. Hodnotenie vplyvov fyzikálnych faktorov na zdravie človeka. Objektivizácia a hodnotenie faktorov prostredia - 1. vyd - Košice : TU - 2014. - 159 s.. - ISBN 978-80-553-1632-1.



# Verification of the causal dependence of noise and vibration on a mechanical drive with a piston compressor.

Lucia Žulová<sup>1\*</sup>, Robert Grega<sup>2</sup>, Marián Siman<sup>3</sup>

<sup>1</sup> Faculty of Mechanical Engineering, Technical University of Košice, Slovakia; [lucia.zulova@tuke.sk](mailto:lucia.zulova@tuke.sk)

<sup>2</sup> Faculty of Mechanical Engineering, Technical University of Košice, Slovakia; [robert.grega@tuke.sk](mailto:robert.grega@tuke.sk)

<sup>3</sup> Faculty of Mechanical Engineering, Technical University of Košice, Slovakia; [marian.siman@tuke.sk](mailto:marian.siman@tuke.sk)

\* Correspondence: [lucia.zulova@tuke.sk](mailto:lucia.zulova@tuke.sk); Tel.: +421 55 602 2354

**Abstract:** One of the accompanying phenomena of the operation of any machine is a mechanical oscillation. From the point of view of operation and maintenance of machines, the basic methods are aimed at monitoring and analyzing this mechanical oscillation. Mechanical oscillation, technically known as vibration, manifests itself in the environment as a noise. Noise and vibration are very close quantities, the dependence of which can be observed both by sensory perception and by monitoring their emitted values. They formed the basis for the research in this article, the aim of which is to verify the causal dependence of noise and vibration in mechanical drives. An experimental mechanical drive with a compressor was assembled to demonstrate the dependence. In order to obtain results for different parameter variations, a pneumatic flexible coupling was applied to this mechanical drive for continuously tuning of its dynamic properties. The article deals with finding out the possibility of using the course of one physical quantity to identify the course of another physical quantity with the aim of controlling noise and vibrations in machines.

**Keywords:** noise, vibration, mechanical drive

## 1. Introduction

An essential part of increasing the machines operability is a monitoring of their technical properties through the measurement and analysis of mechanical oscillations. The latest knowledge in that field of assessment consists in the mutual correlation of data obtained from technical diagnostics [1]. The main purpose of this diagnostics is primarily the safety of the machine and its parts, and subsequently to increase its operability, for example lifetime, failure-free operation, reliability, etc. Diagnostics of vibration and noise of the machine can be one of the parameters ensuring the continuous operation of the machine [5,6].

Controlling of vibrations and the resulting noise is a complex process that requires both theoretical knowledge and practical experience. The concept of vibration and noise control in machines can be understood as a way of their elimination, but also as a possibility of their control and diagnostics [1], [5,6]. The term "elimination" means reducing them to a level that does not negatively affect humans or workers and environment. These topics are discussed among many experts who deal with the appropriate tuning of mechanical drives in these machines [2-4], [7,8].

The field of mechanical oscillation tuning is covered by our department, which has a torsional oscillation laboratory. The centers of interest are pneumatic tuners of torsional vibrations, specifically pneumatic flexible couplings, which can continuously change the dynamic properties of the entire mechanical drive [2-4], [10-11]. Just such a pneumatic

flexible coupling was a part of the investigated mechanical drive, on which vibration and noise values were recorded. These values were obtained for the purpose of diagnosing the mechanical drive in terms of determining the dependence of these two quantities. Vibrations occur as mechanical oscillations of particles in the construction, whose waves into the surrounding environment are perceived as sound [5,6]. From the point of view of its intensity, in practice it is perceived as a noise [7-9].

The latest concept in the field of assessing the technical condition of machines consists in monitoring and obtaining their parameters, such as vibration and noise values, which can be compared with each other. The aim of this article is to verify the causal dependence of noise and vibration in mechanical drives. Noise and vibration monitoring was carried out in laboratory conditions with a mechanical drive with a compressor.

## 2. Materials and Methods

### 2.1 Designed mechanical drive

In order to obtain measurement results, we assembled a mechanical drive with a piston compressor (Fig.1) in our torsional vibration laboratory. The examined mechanical drive consists of a tree-cylinder compressor (4), which is driven via pneumatic flexible coupling (3) by a three-phase asynchronous electric motor (1) which drives a two-speed gearbox (2). Individual positions of parts of the mechanical drive correspond to the indications in Fig. 1.

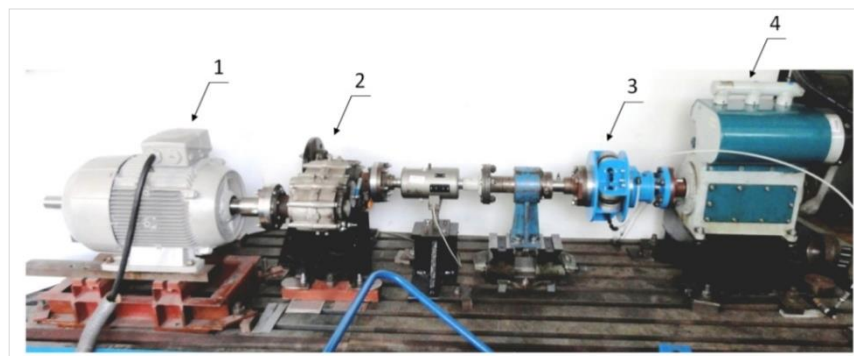


Figure 1. Mechanical drive used during measurements.

### 2.2 Measuring apparatus

The following devices were used to measure a noise:

- handheld sound level meter analyzer Brüel&Kjær Type 2250,
- Microphone Type 4189, nominal sensitivity 50 mV/Pa,
- Tripod carrying sound level meter.

After consideration, as a measuring quantity was chosen A-weighted equivalent sound pressure level  $L_{Aeq}$  in dB, that values were obtained from sound-level meter during the measurements. During measurement, a sound-level meter was placed at a height of 1.5 m from the floor on a tripod. Distance of sound-level meter from the mechanical drive was 1 m.

As a measuring device for vibrations was used:

- ADASH 4100, which allows the connection of different types of measuring sensors,
- speed sensor Wilcoxon Research (model 784A).

For such measuring apparatus a time record and the basic vibration parameters were measured. Hereby, it was also defined following unit of measurement - speed ( $\text{mm}\cdot\text{s}^{-1}$ ) and the measurement range from  $10 \div 1000$  Hz.

### 2.3 Methods of measurement

Measurement of noise and vibration requires a consistent preparation. As mentioned in the introduction, by using a pneumatic flexible coupling in a mechanical drive, we can affect the dynamic properties of the entire drive, which has a direct effect on the magnitude of vibrations and consequently the noise intensity of this drive [2, 4]. As a method of influencing these dynamic properties, we chose a pressure change of the gas medium in chambers of pneumatic flexible coupling from 200 to 700 kPa, and subsequently the noise and vibration values were recorded. At the same time, the speed of the electric motor was continuously changed in the range of 500 to 700 rpm.

### 3. Results and Discussion

Considering creation of vibration is usually associated with creation of noise, and the physics of vibration and noise are similar, our verification of their causal dependence will be based on created graphs (Figure 2 and 3) of obtained measurement values. During the running of the mechanical drive with variable operating speeds of the electric motor, individual noise and vibration values were recorded, which are shown in the following graphs in Fig. 2 and 3.

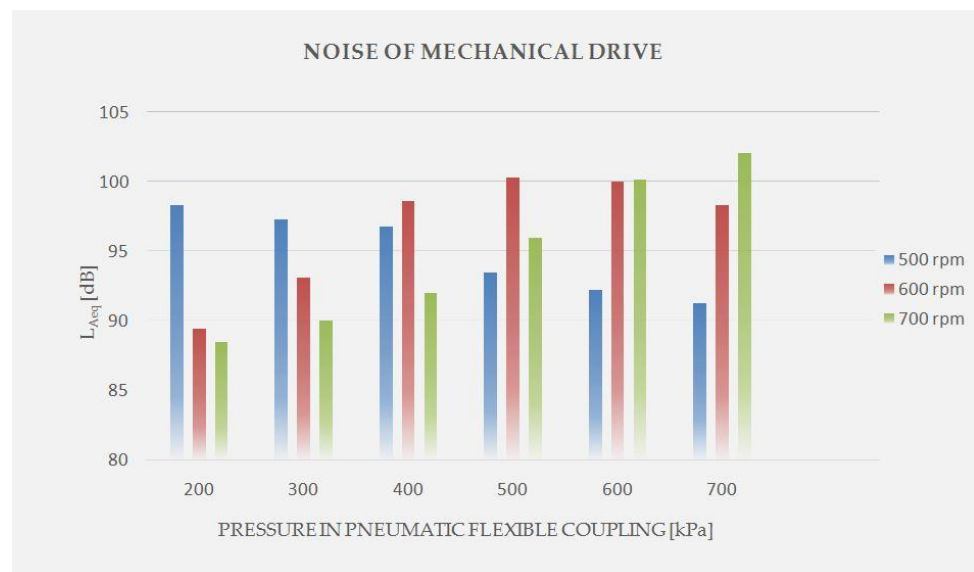


**Figure 2.** Measured values of noise of mechanical drive.

As can be seen from figure 2, the noise values during the measurements reach level of 88 to 102 dB. These values belong to the noise of the electric motor at 700 rpm (labeled as green column). Noise values at operating speed 600 rpm are in the range of 89-100 dB (labeled as red column). During the operation of the mechanical drive with a speed of 500 rpm, it reached the smallest noise interval of only 7 db (labeled as blue column). Furthermore, from the graphs, it is possible to observe the interesting changes in the increase or decrease of noise values with increasing pressure in the pneumatic flexible coupling. If the performance of the mechanical drive was required at the level of 500 rpm, then the pneumatic flexible coupling is suitable as a tuner for such a drive.

Examining the fact that noise and vibration are closely connected with each other, it is also proven in Fig.3. The tendency of the increase and decrease of vibration values with

the speed of the electric motor and the increase of pressure in the pneumatic flexible coupling have almost identical courses.

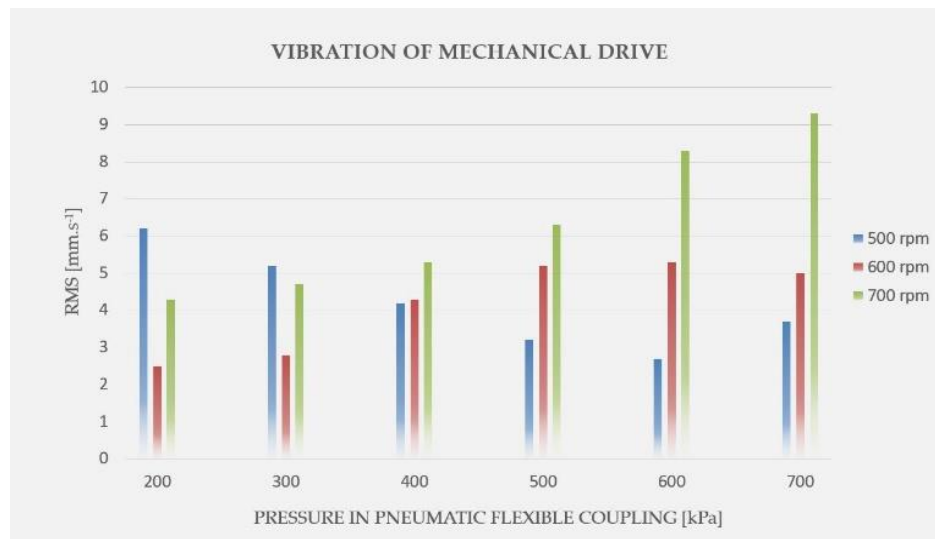


Figure 3. Measured values of vibration of mechanical drive.

Both observed quantities and their measured values are shown together in Figure 4. A line graph was used for the clarity of their courses. As it can be seen, the causal dependence of these two quantities is demonstrable. Due to the different measurement units, it is possible to neglect their numerical values, but on the other hand, it is possible to compare their courses. The most similar, almost the same course has values at 700 rpm (green course). This fact can be considered as a confirmation of the experimental aim, namely the verification of the causal dependence of noise and vibrations in the mechanical drive. This conclusion proves the extended possibilities of using the quantity of noise as an accompanying phenomenon of vibrations, and vice

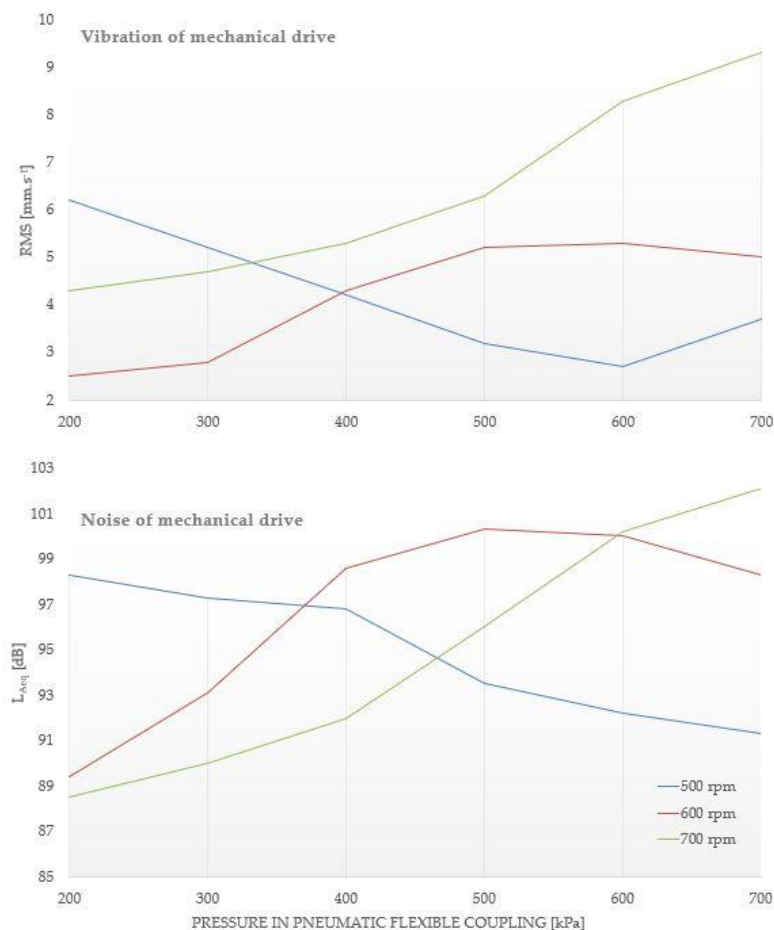


Figure 4. Courses of noise and vibration measured values

versa. On the other hand, when diagnosing mechanical drives, i.e. the machine or its components, it is possible to consider the value of one quantity (e.g. noise) as reliable for the needs of vibration diagnostics during rapid diagnostics. The proof is the course of the measured values of the quantities in our experimental measurement. These findings can be a assumption for our future research on this causal dependence on a wider scale, that is, measuring the noise and vibration of machines directly in the factory.

## 5. Conclusions

Firstly, from the measured values and analysis during the observation of the occurrence of vibrations accompanied by noise, the aim of the article can be confirmed, namely the verification of the causal dependence of noise and vibrations in a mechanical drive. This aim is proven on the displayed graphs, on which you can observe not only the actual values of the quantities, but also the graphs of the individual parameters of the mechanical drive. Secondly, it should be taken into account that these measurements are demonstrated only in laboratory conditions, and therefore we have to consider their inaccuracies and deviations from the conditions outside the laboratory. However, this does not refute the article that noise and vibrations can be considered as an extremely close physical quantities. In a certain approximation, the rule applies that where there is vibration there is also noise, and of course vice versa.

**Acknowledgments:** This paper was written in the framework of Grant Project **VEGA**: „1/0528/20 and **KEGA** 029TUKE-4/2021.

**Conflicts of Interest:** The authors declare no conflict of interest.

## References

1. Peter Tirinda: Trendy v oblasti ochrany, monitorovania a technickej diagnostiky strojov., Strojárstvo/Strojírrenství . 12.2021-01.2022, s.66-68, ISSN:1335-2938, Available online: <https://www.engineering.sk/clanky2/udrzba/23903-trendy-v-oblasti-ochrany-monitorovania-a-technickej-diagnostiky-strojov>.
2. Grega R., Homišin J., et. al.: The chances for reduction of vibrations in mechanical system with low-emission ships combustion engines. International Journal of Maritime Engineering: Transactions of The Royal Institution of Naval Architects. Vol. 157 (2015).
3. J. Homišin [et al.]: Removal of systematic failure of belt conveyor drive by reducing vibrations, In: Engineering Failure Analysis. č. 99 (2019), s. 192-202, ISSN 1350-6307.
4. Grega R., [et al.]: Failure analysis of driveshaft of truck body caused by vibrations. In: Engineering Failure Analysis. Vol. 79. (2017) ISSN 1350-6307.
5. HaSPA (Health and Safety Professionals Alliance): The Core Body of Knowledge for Generalist OHS Professionals. Tullamarine, VIC. Safety Institute of Australia, 2012, ISBN 978-0-9808743-1-0.
6. Konrad Wegener, Friedrich Bleicher, Uwe Heisel, Hans-Werner Hoffmeister, Hans-Christian Möhring, Noise and vibrations in machine tools, CIRP Annals, Volume 70, Issue 2, 2021, ISSN 0007-8506.
7. S. J. Idehara, F. L. Flach, D. Lemes, Modeling of nonlinear torsional vibration of the automotive powertrain, Journal of Vibration and Control, (2018), Vol. 24(9) 1774–1786, DOI:10.1177/1077546316668687.
8. Grega R, [et al.]: Failure analysis of driveshaft of truck body caused by vibrations. In: Engineering Failure Analysis. Vol. 79. (2017) ISSN 1350-6307.
9. Homišin J: Characteristics of pneumatic tuners of torsional oscillation as a result of patent activity, ACTA MECHANICA ET AUTOMATICA Volume: 10 Issue: 4 (2016).
10. Grega R, Homišin J, et. al.: The chances for reduction of vibrations in mechanical system with low-emission ships combustion engines. International Journal of Maritime Engineering: Transactions of The Royal Institution of Naval Architects. Vol. 157 (2015).
11. Krajňak J, Grega R: Analysis of external temperature in flexible element at various speed levels. Projektowanie, badania i eksploatacja Tom 1. - Bielsko-Biała: Akademia Techniczno-Humanistyczna w Bielsku-Białej (2018) 191-198 ISBN 978-83-65182-93-7.



# 3D bioprinting using stem cells in regenerative medicine

Jana Demeterová <sup>1\*</sup>, Marianna Trebuňová <sup>1</sup>, Darina Bačenková <sup>1</sup> and Jozef Živčák <sup>1</sup>

<sup>1</sup> Department of Biomedical Engineering and Measurement, Faculty of Mechanical Engineering, Technical University of Košice, Letná 9, 042 00 Košice, Slovakia; marianna.trebunova@tuke.sk (M.T.), darina.bacenkova@tuke.sk (D.B.) jozef.zivcak@tuke.sk (J.Ž.)

\* Correspondence: jana.demeterova@tuke.sk

**Abstract:** 3D bioprinting is an innovative technology that supports the production of biomimetic, multicellular tissues in a highly complex microenvironment. The great potential of three-dimensional bioprinting using stem cells lies in a great source of cell cultures and tissues for drug testing, academic research, and last but not least, for tissue and potentially whole organ transplantation. It is essential for these cells to get as close as possible to their natural environment for optimal and healthy growth. However, when cultured in 2D space, cells lose their natural properties, such as morphology, basic structure, polarity, gene expression and especially tissue specificity. 3D bioprinting of living cells into functional tissue could be the solution. By granting the spatial structure, the cells are presented with nature-like environment, where they differentiate and proliferate as they are programmed to by nature. This paper reviews current possibilities of bioprinting of tissues with use of stem cells, various hydrogel bioinks, differences between printing techniques and unique properties of stem cells with all their advantages and setbacks, as this field carries a great potential in regenerative medicine.

**Keywords:** bioprinting; stem cells; bioink; hydrogel

## 1. Introduction

The success of any medical device is influenced by the initial physical interaction between the cells and the surface of the implant. Almost 1.2 million patients use cardiovascular, dental, orthopedic, and other types of implanted devices, as well as external devices in contact with the skin or blood [1].

The ability of stem cells to make identical copies of themselves and differentiate into various types of cells makes them perfect candidates for prosperous tissue engineering. However, the expansion of these cells is not equivalent *in vivo* and *in vitro*. Outside the body, cells can form nourishing and viable tissue only if placed in a suitable *in vitro* environment where preferably appropriate spatial arrangement is preserved, along with growth factors and signals from the environment necessary for healthy development. Without these essential factors, cell development can be chaotic and imprecise - leading to unwanted differentiation or even a cell death [2]. 3D bioprinting is a technology that could solve this difficulty, as it brings biomimetic complex microenvironment for the cells to differentiate and proliferate. Due to the huge demand for organ transplants, along with limited donors, bioprinting is a potential technology that could unravel this issue of organ shortage. The precise control over the deposition of bioink into complex structures was shown to be possible by many researcher groups. The fabrication of complex structures such as designed scaffolds for tissue engineering with controlled porosity, permeability and mechanical properties could be future of tissue engineering and regenerative medicine [3].

## 2. Stem cells

The most unique biological property of MSCs is their capacity for mesenchymal differentiation. This means that they can develop into osteoblasts, adipocytes, and chondroblasts under standard *in vitro* tissue culture differentiation conditions. MSCs have the ability to express and secrete cytokines and growth factors, even in hypoxic conditions thus they stimulate the migration of endothelial cells, the formation of vascular tubular structures and stabilize the newly formed vascular structures with the help of pericytes [4].

## 3. Methods of 3D bioprinting

3D bioprinting is a large subset of 3D printing itself, which is mainly used in tissue engineering for biomimetic production of tissues. Additive manufacturing brings broad flexibility and reproducibility in mechanical production stable, biocompatible tissue, and organ structures [5]. The requirements for the production of biological tissues by 3D bioprinting have been summarized by various researchers' groups. However, there is disagreement regarding the solution and organization of the required criteria for the microscopic level. Researchers believe that biological tissues should be cultured with the highest possible resolution to be able to mimic the functions and behavior of cells in an *in vitro* 3D environment. At the same time, great emphasis is placed on being able to accurately control and edit the emerging 3D construct. However, other researchers, on the contrary, believe that already the printing alone of cell aggregates allows cells to organize themselves, to form tissues, given that cells have genetically encoded organizational abilities. For example, endothelial cells naturally form tubular structures under optimal environmental conditions [3].

### 3.1. Inkjet bioprinting

Inkjet bioprinting is a promising biological approach to printing. It is a non-contact technique that creates layer by layer by depositing drops of ink on top of each other. The printing process consists of two phases. The first phase represents the application of drops of bioink on specific substrate sites. The second phase involves the interaction between the droplets and the substrate - cross-linking and gelation. All the processes need to be precisely controlled because we are working with living cells, so the conditions must be set up accordingly. That is the main difference compared to basic 3D printing [6].

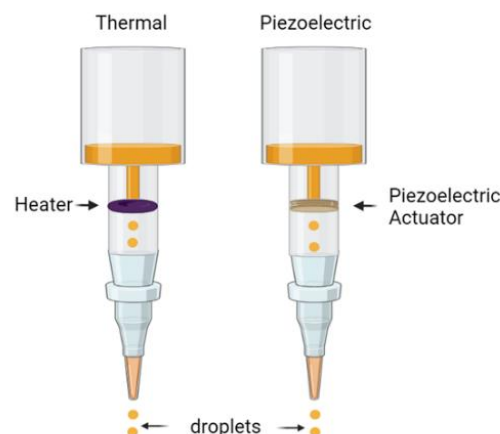


Figure 1. Schematic of a thermal and piezoelectric inkjet printing, where droplets are generated by the heat and then ejected or droplets are made with piezoelectric actuator by its vibration.

### 3.2. Extrusion bioprinting

An extrusion bioprinter consists of two or more printing heads (Fig. 2,) extruding bioink consisting of cells, growth factors, and biomaterials by applying pressure, providing the dispersion of bioink filaments through a small or micro-sized nozzle. The cartridge is set on a print arm moving in a z-y direction. The collector is moving in the x-axis [4]. Extrusion bioprinting has been used to create 3D tissues and organ constructs such as kidney, liver, adipose tissues, tracheal grafts, vascularized soft tissue, skin grafts, neural tissues, cartilage tissue, renal tissue, bone tissue, and other engineered structures [7].

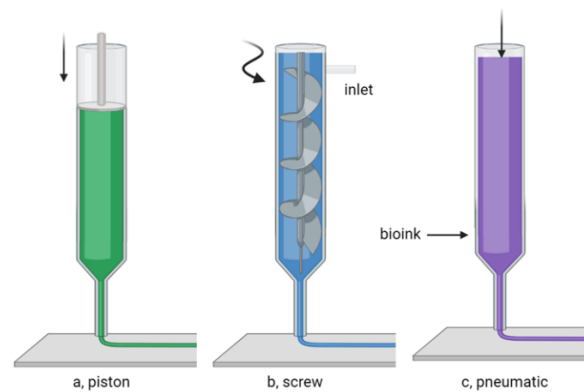
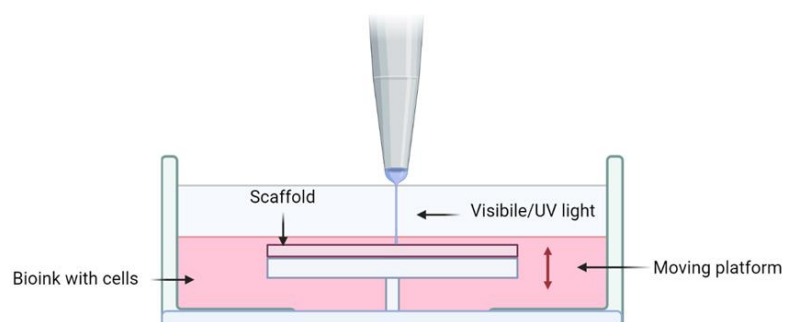


Figure 2. A scheme that shows various types of extrudations. (a) Shows pneumatic extrusion with compressed gas. (b) Extrusion using a mechanical force in form of a piston. (c) Extrusion using a mechanical force in form of a screw.

### 3.3. Stereolithography bioprinting

The principle of SLA printing is a laser light applied to a photosensitive liquid material in a point-by-point manner creating a solidified layer (Figure 3.). After the solidification of the first layer, the platform rises by an exactly defined height and the second layer is photo-crosslinked. Bioink used in SLA bioprinting is photocrosslinkable so the solution is cross-linked by light illumination during the printing process. Bioink consists of cells and a photosensitive prepolymer solution. The use of non-toxic crosslinking is necessary to prevent cell damage. Some natural polymers, such as chitosan, have a great advantage in their self-gelation property, therefore there is no need for often harming chemicals [8].



**Figure 3.** Stereolithography. An advantage of SLA is that it does not require extrusion through a nozzle, and is faster, and more accurate with higher resolution ( $< 100\mu\text{m}$ ) than extrusion-based printing.

#### 4. Hydrogel bioinks

Hydrogels are highly hydrated polymeric materials containing more than 90% water. They are biomaterials of natural origin, such as collagen, gelatin, alginate, fibrin, hyaluronic acid, silk proteins, chitosan, or decellularized ECM (dECM). Natural resources are advantageous biomaterials due to their biocompatibility, controlled degradation, and similarity with native ECM [9]. However, common disadvantages are weak mechanical strength and inconsistency of the composition and properties between production batches. Due to this reason, natural hydrogels are often combined to create ideal properties prior to and after printing. Decellularized ECM as a bioink provides unique three-dimensional distribution of structural and functional components, and diversity is what distinguishes it from other biomaterials [10].

#### 5. Discussion

Recent developments in tissue engineering may hold great promise for the development of new 3D tissue models for pre-clinical drug testing, toxicology studies, or although far-reaching but desirable whole 3D printed whole organ transplant. Table 1. shows examples of what is possible to create by bioprinting using stem cells to this date [11].

**Table 1.** Disadvantages of current 2D tissue models with counterpart solution by 3D printed models. Each method has its benefits and difficulties, however, 2D platforms produced a lot of scientific discoveries and data, therefore without them, the process of bioprinting would not be possible.

Current 2D models: Problem	3D printed models: Solution	Ref.
Multi-stage production methods	Automated and reproducible production of tissue models	[11],[5]
Absence of a specific extracellular matrix environment	Creation of a cell-specific microenvironment	[3], [11]
Absence of structural hierarchy	Generation of tissue of specific architecture	[5], [12]
Low efficiency perfusion	Integration of microfluidics with 3D structure	[4],[5]
Difficult to obtain a vascularization	Production of vascularized tissue <sup>1</sup>	[13]
Unpredictable false-positive or false-negative results from testing for animal models	Sidestepping tightening controls on the use of animals for scientific purposes and experiments	[2],[10], [14]

<sup>1</sup>Still in development. Certain research results of 3D bioprinting were applied into developing of vascular tissue however 3D printed vascular scaffolds are still limited in mechanical strength, biodegradation, and printability restricted to simple linear vascularization.

In the last decade, the use of *in vitro* 3D models has increased significantly due to the developments new supporting technologies (Table 2.) and the tightening of the use of animal models for scientific purposes and experimentation [12].

**Table 2.** A summarization of bioprinting technique, frequently used materials for bioinks and examples of products that can be created by bioprinting to this date

Technique	Bioink materials	Products
Extrusion Inkjet Stereolithography Cryoprinting LIFT <sup>3</sup>	Collagen Gelatin Alginate Hyaluronic acid Silk fibroin Hydroxyapatite Chitosan Nanocellulose Methylcellulose Composites of bioinks	Skin tissue Neural tissue Cartilage tissue Cardiac tissue Liver tissue Adipose tissue Renal tissue Cell laden products iPSCs <sup>1</sup> encapsulated in hydrogel Vascularization <sup>2</sup>
[13], [4]	[5], [11], [4]	[11], [15], [6], [16], [17]

<sup>1</sup> Induced pluripotent stem cells; <sup>2</sup> Certain research results of 3D bioprinting were applied into developing of vascular tissue however 3D printed vascular scaffolds are still limited in mechanical strength, biodegradation, and printability restricted to simple linear vascularization; <sup>3</sup> Laser-induced forward transfer

Our plan in the future is to study and possibly design a bioink based on decellularized extracellular matrix (dECM), which brings a native environment for cells to develop. The use of dECM could bring great opportunities when in use, due to its composition, as it already contains the much-needed potential for the spatial organization and grow factors with other various biomolecules, that cells are used to in their natural differentiation when *in vivo*. The extracellular matrix naturally “knows” what cells need to thrive and differentiate into various cell types, so we see great promise in its future use in regenerative medicine.

**Funding:** 021TUKE-4/2022, 044TUKE-4/2022

**Conflicts of Interest:** The authors declare no conflict of interest.

## References

1. Jain, P.; Kathuria, H.; Dubey, N. Advances in 3D Bioprinting of Tissues/Organs for Regenerative Medicine and in-Vitro Models. *Biomaterials* **2022**, *287*, 121639. <https://doi.org/10.1016/j.biomaterials.2022.121639>.
2. Dominici, M.; Le Blanc, K.; Mueller, I.; Slaper-Cortenbach, I.; Marini, F.; Krause, D.; Deans, R.; Keating, A.; Prockop, D.; Horwitz, E. Minimal Criteria for Defining Multipotent Mesenchymal Stromal Cells. The International Society for Cellular Therapy Position Statement. *Cytotherapy* **2006**, *8* (4), 315–317. <https://doi.org/10.1080/14653240600855905>.
3. Tan, C. T.; Liang, K.; Ngo, Z. H.; Dube, C. T.; Lim, C. Y. Application of 3D Bioprinting Technologies to the Management and Treatment of Diabetic Foot Ulcers. *Biomedicines* **2020**, *8* (10). <https://doi.org/10.3390/biomedicines8100441>.
4. Messaoudi, O.; Henrionnet, C.; Bourge, K.; Loeuille, D.; Gillet, P.; Pinzano, A. Stem Cells and Extrusion 3D Printing for Hyaline Cartilage Engineering. *Cells* **2021**, *10* (1). <https://doi.org/10.3390/cells10010002>.
5. Chia, H. N.; Wu, B. M. Recent Advances in 3D Printing of Biomaterials. *J. Biol. Eng.* **2015**, *9* (1), 4. <https://doi.org/10.1186/s13036-015-0001-4>.
6. Murphy, S. V.; Atala, A. 3D Bioprinting of Tissues and Organs. *Nat. Biotechnol.* **2014**, *32* (8), 773–785. <https://doi.org/10.1038/nbt.2958>.
7. Zhang, Y. S.; Haghighashtiani, G.; Hübscher, T.; Kelly, D. J.; Lee, J. M.; Lutolf, M.; McAlpine, M. C.; Yeong, W. Y.; Zenobi-Wong, M.; Malda, J. 3D Extrusion Bioprinting. *Nat. Rev. Methods Primer* **2021**, *1* (1), 75. <https://doi.org/10.1038/s43586-021-00073-8>.
8. Kumar, H.; Kim, K. Stereolithography 3D Bioprinting. In *3D Bioprinting: Principles and Protocols*; Crook, J. M., Ed.; Springer US: New York, NY, 2020; pp 93–108. [https://doi.org/10.1007/978-1-0716-0520-2\\_6](https://doi.org/10.1007/978-1-0716-0520-2_6).
9. Kim, Y. S.; Majid, M.; Melchiorri, A. J.; Mikos, A. G. Applications of Decellularized Extracellular Matrix in Bone and Cartilage Tissue Engineering. *Bioeng. Transl. Med.* **2019**, *4* (1), 83–95. <https://doi.org/10.1002/btm2.10110>.
10. Unagolla, J. M.; Jayasuriya, A. C. Hydrogel-Based 3D Bioprinting: A Comprehensive Review on Cell-Laden Hydrogels, Bioink Formulations, and Future Perspectives. *Appl. Mater. Today* **2020**, *18*, 100479. <https://doi.org/10.1016/j.apmt.2019.100479>.
11. Zhang, Y. S.; Yue, K.; Aleman, J.; Mollazadeh-Moghaddam, K.; Bakht, S. M.; Yang, J.; Jia, W.; Dell'Erba, V.; Assawes, P.; Shin, S. R.; Dokmeci, M. R.; Oklu, R.; Khademhosseini, A. 3D Bioprinting for Tissue and Organ Fabrication. *Ann. Biomed. Eng.* **2017**, *45* (1), 148–163. <https://doi.org/10.1007/s10439-016-1612-8>.
12. Gao, Q.; Kim, B.-S.; Gao, G. Advanced Strategies for 3D Bioprinting of Tissue and Organ Analogs Using Alginate Hydrogel Bioinks. *Mar. Drugs* **2021**, *19* (12). <https://doi.org/10.3390/md19120708>.
13. Semba, J. A.; Mieloch, A. A.; Rybka, J. D. Introduction to the State-of-the-Art 3D Bioprinting Methods, Design, and Applications in Orthopedics. *Bioprinting* **2020**, *18*, e00070. <https://doi.org/10.1016/j.bprint.2019.e00070>.
14. Germain, N.; Dhayer, M.; Dekioui, S.; Marchetti, P. Current Advances in 3D Bioprinting for Cancer Modeling and Personalized Medicine. *Int. J. Mol. Sci.* **2022**, *23* (7). <https://doi.org/10.3390/ijms23073432>.
15. Ouyang, L.; Yao, R.; Zhao, Y.; Sun, W. Effect of Bioink Properties on Printability and Cell Viability for 3D Bioplotting of Embryonic Stem Cells. *Biofabrication* **2016**, *8* (3), 035020. <https://doi.org/10.1088/1758-5090/8/3/035020>.
16. Piola, B.; Sabbatini, M.; Gino, S.; Invernizzi, M.; Renò, F. 3D Bioprinting of Gelatin–Xanthan Gum Composite Hydrogels for Growth of Human Skin Cells. *Int. J. Mol. Sci.* **2022**, *23* (1). <https://doi.org/10.3390/ijms23010539>.
17. Ma, L.; Wu, Y.; Li, Y.; Aazmi, A.; Zhou, H.; Zhang, B.; Yang, H. Current Advances on 3D-Bioprinted Liver Tissue Models. *Adv. Healthc. Mater.* **2020**, *9* (24), 2001517. <https://doi.org/10.1002/adhm.202001517>.



# Proposal of a methodology for evaluating the placement of dental implants using dental surgical guides

Luboš Chromý <sup>1\*</sup>, Viktória Rajtúková <sup>1</sup> Radovan Hudák <sup>1</sup>

<sup>1</sup> Technical University of Košice, Faculty of Mechanical Engineering, Department of Biomedical Engineering and Measurement, Letná 1/9, Košice, 04200; lubos.chromy@tuke.sk, viktorija.rajtukova@tuke.sk, radovan.hudak@tuke.sk

\* Correspondence: lubos.chromy@tuke.sk; Tel.: +421556022651

**Abstract:** This study deals with the evaluation of the dental implant placement using surgical guidance systems. The purpose of this study is to examine various evaluation methods in order to compare the accuracy between virtually planned and clinically achieved implant positions. The paper describes comparative methods using preoperative and postoperative computed tomography (CT) data and digital stamp for the definitive prosthesis. The method of measuring displacement and stress for quantification of errors is also examined. The difference between the planned and actual position of the implant placement in a controlled implant operation is expressed as a deviation. Assessing the accuracy of controlled surgical implantation can play an important role in avoiding errors. All evaluation methods have their necessary errors and require careful interpretation during evaluation. The result of the work is a proposal for a methodology for evaluating the placement of dental implants.

**Keywords:** dental implant placement; placement evaluation; surgical guide systems.

## 1. Introduction

The successful introduction of a dental implant depends not only on proper osseointegration, but also on the proper function and aesthetics of the final dental prosthesis [1,2,3]. Conventional implant placement is a workflow that was used before the development of digital technology. The workflow includes making impressions and diagnostic waxing on a plaster model. However, implant placement that considers the correct angle and position in relation to the adjacent tooth and bone is gradually coming to the fore. It is a controlled implantation operation enabling precise, safe and predictable placement of the implant. The most prominent in guided implantation are the deviations between the planned and positional placement of the implant, which can include several factors, for example, problems with spatial resolution in CT, combining imaging techniques and scanned data, errors in the manufacture of surgical guides, insufficient stability of surgical guides, drilling errors such as the clearance between the socket and the drill, the thickness of the soft tissues, the movements of the patient as well as the type of software used. An evaluation of the accuracy is therefore necessary if the clinical control of guided surgery is not convincing. [4,5,6]

## 2. Materials and Methods

The current position of the implant is determined in two basic ways. The first is the use of postoperative CBCT images of the implant after implantation; the second method is indirect estimation of the position from plaster models or scanned abutment on which the respective implants are attached (Fig. 1). [7]

Another method of assessing implant placement is to quantify the degree of displacement by assessing the tension applied when attaching a specially designed suprastructure to an analog model made of acrylic resin [8,9,10,11]

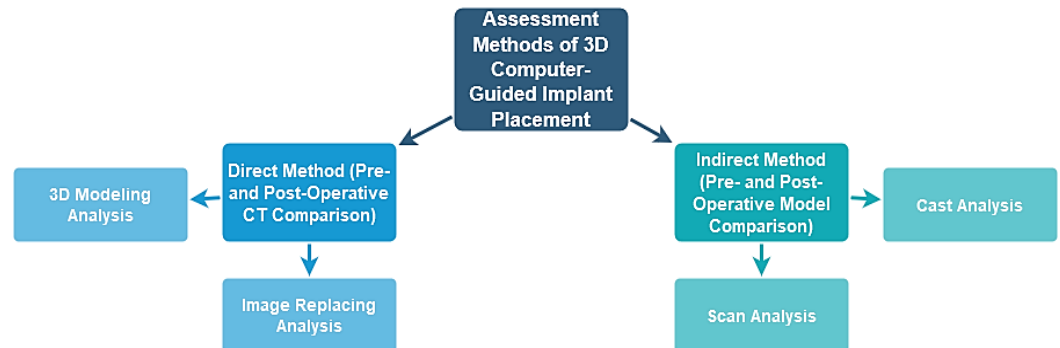


**Figure 1.** Evaluation methods for 3D computer-guided implant placement.

*2.1. Superimposition of planned and actual implant placement*

The planned and actual position of the implant is analyzed to evaluate deviations. Two pieces of 3D information must be superimposed into 1 identical plane. Overlapping two planes requires 3 or more different reference points that are not in a straight line. In partial edentulousness, the 2 data may be overlaid with reference points such as three distinct teeth. However, in completely edentulous patients, special reference points are needed for superposition [12].

In fig. 2 it is possible to see the information about the planned position of the implant extracted from the CT images, where the current position of the implant was confirmed by the analysis by replacing the CT images. Reference point and background data for comparison are all in CT. Therefore, the accuracy of the superposition is determined by the resolution of the CT, which consists of a DICOM file [14]

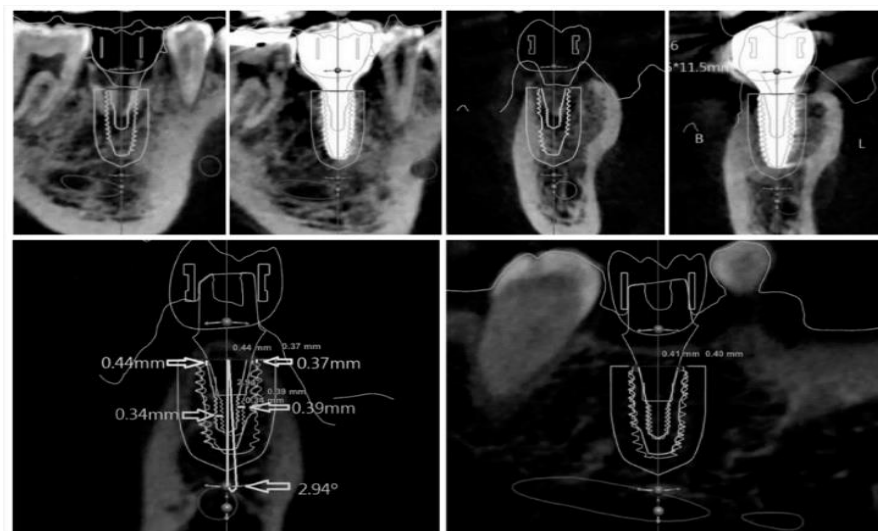


**Figure 2.** Displacement measurement by the direct method - overlapping of the planned and actual position. [12]

## 2.2. Quantification of errors

The magnitude of the error of the planned and actual position superimposed by the direct or indirect method can be analyzed by measuring the displacement. To specify the displacement, it is necessary to determine a standard parameter to quantify the position of the implant. To measure displacement (Fig. 3), parameters such as linear deviations of the implant, angular deviation and vertical deviation in height or depth. All these parameters can be recorded as distance or as two separate vectors (with horizontal and vertical distance) [13]

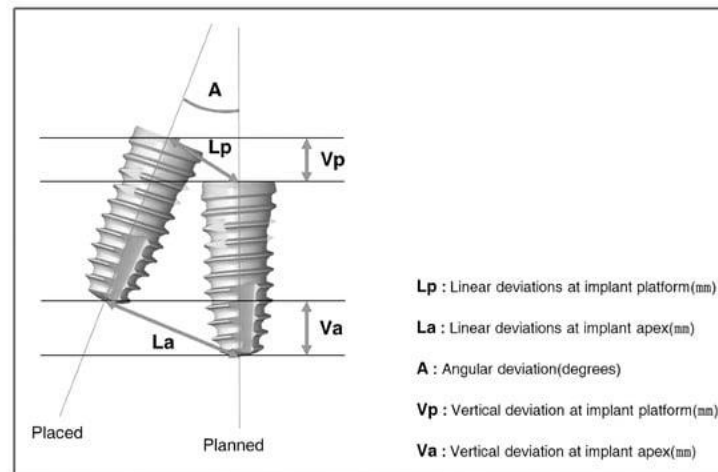


**Figure 3.** The parameters used to measure displacement,  $L_p$  and  $L_a$ , can be determined using distance or 2 individual vectors (with horizontal and vertical distance). [12]

## 2.3. Voltage measurement

To successfully evaluate the deviation, Tahmaseb et al. [11] determined a method to quantify the strain (force) on each implant using strain gauge measurements. In this research, 6 implants were placed in the mouth using surgical guides fixed with anchor pins. After the final impression of the implants, a milled titanium structure was produced. Four strain gauges were attached along the long axis of each superstructure cylinder at an angle of  $90^\circ$  to each other. Each frame was measured by the three-dimensional method of tension measurement using strain gauges. They found that this method has the advantage of being able to numerically express the indistinguishable error. Although there are limitations to strain gauges such as location, number and area of application, their role should not be overlooked. In addition, this method is not possible with a digital-type virtual model, so it is necessary to create an analog dental plaster model [12][16].

## 3. Results

In his study, Jacques Vermeulen investigated the difference in accuracy between implant placement without the use of a guide and guided implant placement by experienced surgeons. 10 experienced clinicians placed a total of 80 implants using both approaches in the anterior part of the SIMPLANT Guide maxillary models and placed them in the mouth of the head model. For all 80 implants, the average vertical, lateral and angular deviations between the virtually planned and achieved implant positions based on CBCT scans were measured. The angular deviation of the entire sample was  $7.63^\circ$  for the unguided method and  $2.19^\circ$  for the guided procedure. The mean difference in angular deviation differed significantly between groups and was more than three times greater for the non-guidance

method. The lateral deviation at the coronal level of the implants was 0.42 mm for the guided method and 1.27 mm for the non-guided method, and at the apical level it was 0.52 mm for the guided method and 1.28 mm for the non-guided method; deviation at the coronal and apical levels was significantly less with the guided procedure than with the non-guided method ( $P = 0.001$ ). The differences in depth deviation at the apical and coronal levels were smaller (guided vs. non-guided surgery at the coronal level: 0.54 vs 0.78 mm; apical level: 0.54 vs 0.73 mm), but also statistically significant ( $P = 0.05$ ). Differences in angular, global and lateral deviations were also significantly smaller with the guided procedure, while deviations in depth revealed no statistically significant difference between the methods. [17][18]

Kivovics et al. were the first in their in vitro study to compare the accuracy of implant placement in model operations implemented by implementing 3 different methods. The study was conducted on 3D printed models randomly assigned to 3 studied groups. In the 1st group, the model operation was performed through dynamic navigation. In the 2nd group, the implants were placed using a method without guidance, and in the 3rd group, static computer-assisted implant surgery (CAIS-Computer Assisted Implant Surgery) was used. A total of 48 dental implants were placed. Angular, coronal and apical global deviations were primarily monitored (Fig. 4). These were calculated for all implants based on preoperative registration of the operative plan and postoperative CBCT reconstruction. The postoperative CBCT scan was performed using the same scanning conditions as the preoperative CBCT scan.

The accuracy of implant placement using dynamic navigation showed no significant difference compared to static CAIS (angular deviation:  $4.09 \pm 2.79^\circ$  and  $3.21 \pm 1.52^\circ$ ; coronal deviation:  $1.27 \pm 0.40$  mm and  $1.31 \pm 0.42$  mm; and apical global deviation:  $1.34 \pm 0.41$  mm and  $1.38 \pm 0.41$  mm). Global deviation results were significantly lower using dynamic navigation than with the unguided method (coronal and apical global deviation, respectively:  $1.93 \pm 0.79$  mm and  $2.28 \pm 0.74$  mm). According to the results of this preclinical study, the accuracy of implant placement by dynamic navigation was comparable to that of the static CAIS method and better than that obtained by the manual method without guidance [15][19].

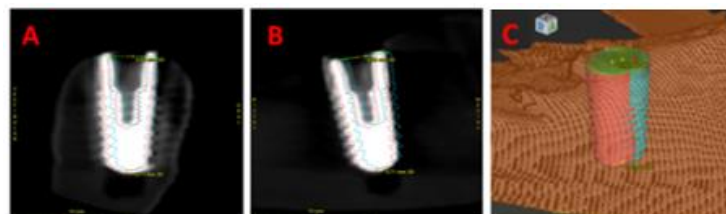


**Figure 4.** Measurement of angular, coronal, and apical global deviation of planned (blue) and achieved (red) implant placements in coDiagnostiX software (Dental Wings, Montreal, CA, USA): A) orthoradial, B) tangential cross-sections, and C) three-dimensional visualization. [19]

#### 4. Discussion

In guided surgery, it is appropriate to use direct and indirect methods to determine the location of implants within the current technical limits. The development of an optimization algorithm capable of automatically recognizing and accurately extracting implant boundaries from CT images is expected soon, using artificial intelligence. Artificial intelligence will be able to extract the edges of implants and also overlay pre- and post-operative data. The result of the development of the process of extraction and superposition with the help of artificial intelligence will be a significant elimination of the process of

creating dental impressions. This will enable the automation of the denture manufacturing process and facilitate the work of dental technicians. In the future, it is possible to expect the development of technology using information about the current position of the implant in real time. This means that the guided implantation surgery will be replaced by the navigated implantation surgery. This will lead to controlled implantation with the help of a robot, which will reduce the efforts of the dentist. [12].

## 5. Conclusions

The aim of this study was to compare the methodologies for evaluating the placement of dental implants and to propose the most suitable ones for the most accurate placement.

It was pointed out the benefit of using static surgical guidance systems or dynamic guidance systems compared to the usual conventional methods of evaluating the location with the free hand, i.e. without the use of any guides during the implantation procedure. During controlled surgery, within the current technical limits, it is appropriate to use direct and indirect methods to determine the location of the implants. Soon, the development of an optimization algorithm that will be able to automatically recognize and accurately extract implant boundaries from CT images is expected. However, this algorithm will require the help of artificial intelligence. Artificial intelligence can not only extract the edges of implants, but also overlay preoperative and postoperative data.

In the future, the development of technology using information about the position of the implant in real time is expected. This means that guided implantation surgery will be replaced by navigated implantation surgery. Guided implantation surgery will lead to robotic surgical implantation and the dentist's effort will be reduced [12].

**Acknowledgments:** This research was supported by project KEGA 050TUKE-4/2022 “Additive manufacturing in medicine - creation of multimedia material and tools to support teaching in biomedical engineering”.

**Conflicts of Interest:** The authors declare no conflict of interest.

## References

1. Motta, M.; Monsano, R.; Velloso, G.R.; de Oliveira Silva, J.C.; Luvizuto, E.R.; Margonar, R.; Queiroz, T.P. Guided Surgery in Esthetic Region. *J. Craniofac. Surg.* 2016, 27, e262-5.
2. Margonar, R.; Queiroz, T.P.; Luvizuto, E.R.; Betoni-Júnior, W.; Zocal, E.A. Mandibular re-habilitation using immediate implant loading after computer-guided surgery. *J. Craniofac. Surg.* 2012, 23, e129-32.
3. Vercruyssen, M., W. Coucke, I. Naert, R. Jacobs, W. Teughels a M. Quirynen. Depth and lateral deviations in guided implant surgery: an RCT comparing guided surgery with mental navigation or the use of a pilot-drill template. *Clinical Oral Implants Research* [online]. 2015, 26(11), 1315-1320 [cit. 2022-05-10]. ISSN 09057161.: Available from doi:10.1111/clr.12460
4. Jung, R.E.; Schneider, D.; Ganeles, J.; Wismeijer, D.; Zwahlen, M.; Hämmerle, C.H.; Tah-maseb, A. Computer technology applications in surgical implant dentistry: A systematic review. *Int. J. Oral Maxillofac. Implants* 2009, 24, 92–109.
5. Vercruyssen, M.; Fortin, T.; Widmann, G.; Jacobs, R.; Quirynen, M. Different techniques of static/dynamic guided implant surgery: Modalities and indications. *Periodontology* 2014, 66, 214–227.
6. Behneke, A.; Burwinkel, M.; Behneke, N. Factors influencing transfer accuracy of cone beam CT-derived template-based implant placement. *Clin. Oral Implants Res.* 2012, 23, 416–423.
7. Tahmaseb, A.; Wismeijer D.; Coucke W.; Derksen W. Computer Technology Applications in Surgical Implant Dentistry: A Systematic Review. *The International Journal of Oral & Maxillofacial Implants* [online]. 2014, 29(Supplement), 25-42 [cit. 2022-05-08]. ISSN 08822786. Available from: doi:10.11607/jomi.2014suppl.g1.2
8. Platzer, S.; Bertha, G.; Heschl, A.; Wegscheider, W.A.; Lorenzoni, M. Three-dimensional accuracy of guided implant placement: Indirect assessment of clinical outcomes. *Clin. Implant Dent. Relat. Res.* 2013, 15, 724–734.
9. Cristache, C.M.; Gurbanescu, S. Accuracy Evaluation of a Stereolithographic Surgical Template for Dental Implant Insertion Using 3D Superimposition Protocol. *Int. J. Dent.* 2017, 2017, 4292081.

10. Sun, Y.; Luebbbers, H.T.; Agbaje, J.O.; Schepers, S.; Politis, C.; Van Slycke, S.; Vrielinck, L. Accuracy of Dental Implant Placement Using CBCT-Derived Mucosa-Supported Stereo-lithographic Template. *Clin. Implant Dent. Relat. Res.* 2015, 17, 862–870.
11. Tahmaseb, A.; van de Weijden, J.J.; Mercelis, P.; De Clerck, R.; Wismeijer, D. Parameters of passive fit using a new technique to mill implant-supported superstructures: An in vitro study of a novel three-dimensional force measurement-misfit method. *Int. J. Oral Maxillo-fac. Implants* 2010, 25, 247–257.
12. Pyo, S.-W.; Lim, Y.-J.; Koo, K.-T.; Lee, J. Methods Used to Assess the 3D Accuracy of Dental Implant Positions in Computer-Guided Implant Placement: A Review. *J. Clin. Med.* 2019, 8, 54.
13. Marzieh Alikhasi, Hakime Siadat, Alireza Nasirpour, Mahya Hasanzade, "Three-Dimensional Accuracy of Digital Impression versus Conventional Method: Effect of Implant Angulation and Connection Type", *International Journal of Dentistry*, vol. 2018, Article ID 3761750, 9 pages, 2018. <https://doi.org/10.1155/2018/3761750>
14. Park, J.H. Accuracy of Implant Placement with a Stereolithographic Surgical Template on Mandibular Molar Sites Measured by Two Methods; Pre- and Postoperative CT Method and Postoperative Digital Impression Method. Ph.D. Thesis, Seoul National University, Seoul, Korea, 2018.
15. Maes, F., A. Collignon, D. Vandermeulen, G. Marchal a P. Suetens. Multi-modality image registration by maximization of mutual information. *IEEE Transactions on Medical Imaging* [online]. 16(2), 187-198 [cit. 2022-05-09]. ISSN 02780062. Available from: doi:10.1109/42.563664
16. Emery, Robert W, Scott A Merritt, Kathryn Lank a Jason D Gibbs. Accuracy of Dynamic Navigation for Dental Implant Placement–Model-Based Evaluation. *Journal of Oral Implantology* [online]. 2016, 42(5), 399-405 [cit. 2022-05-07]. ISSN 0160-6972. Available from: doi:10.1563/aaid-joi-D-16-00025
17. Kang, Sang-Hoon, Jae-Won Lee, Se-Ho Lim, Yeon-Ho Kim a Moon-Key Kim. Verification of the usability of a navigation method in dental implant surgery: In vitro comparison with the stereolithographic surgical guide template method. *Journal of Cra-nio-Maxillofacial Surgery* [online]. 2014, 42(7), 1530-1535 [cit. 2022-05-07]. ISSN 10105182. Available from: doi:10.1016/j.jcms.2014.04.025
18. Wu, Dong, Lin Zhou, Jin Yang, Bao Zhang, Yanjun Lin, Jiang Chen, Wenxiu Huang a Yonghui Chen. Accuracy of dynamic navigation compared to static surgical guide for dental implant placement. *International Journal of Implant Dentistry* [online]. 2020, 6(1) [cit. 2022-05-07]. ISSN 2198-4034. Available from: doi:10.1186/s40729-020-00272-0
19. Son, KeunBaDa, Mei-Yang Huang a Kyu-Bok Lee. A method to evaluate the accuracy of dental implant placement without postoperative radiography after computer-guided implant surgery: A dental technique. *The Journal of Prosthetic Dentistry* [online]. 2020, 123(5), 661-666 [cit. 2022-05-07]. ISSN 00223913. Available from: doi:10.1016/j.prosdent.2019.04.015

## Novus Scientia 2023

Zborník príspevkov z XX. Medzinárodnej vedeckej konferencie doktorandov  
strojnícych fakúlt technických univerzít a vysokých škôl

<b>Názov:</b>	Novus Scientia 2023
<b>Editor:</b>	© prof. Ing. Ján Slotá, PhD. © Ing. Matúš Matiscsák © Ing. Ján Kopec © Ing. Laura Lachvajderová © Ing. Dominika Sukopová © Ing. Marek Mizerák
<b>Vydavateľ:</b>	Technická univerzita v Košiciach, Strojnícka fakulta, Letná 1/9, 042 00 Košice-Sever
<b>Rok:</b>	2023
<b>Náklad:</b>	70 výtlačkov
<b>Rozsah:</b>	337 strán
<b>Miesto konania:</b>	Strojnícka fakulta, Technická univerzita v Košiciach
<b>Dátum konania:</b>	26.01.2023
<b>ISBN</b>	<b>978-80-553-4369-3</b>